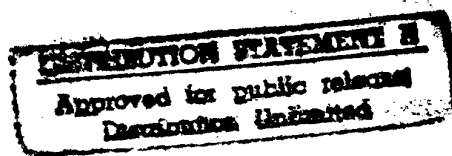
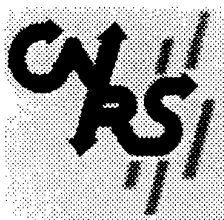


ARO 35545-1-6S-CF



Seventh International Symposium on Long Range Sound Propagation

24-26 JULY 1996

19970321 025

DTIC QUALITY INSPECTED 2

ECOLE CENTRALE DE LYON

Laboratoire de Mécanique des Fluides et d'Acoustique

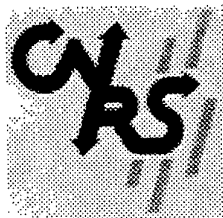
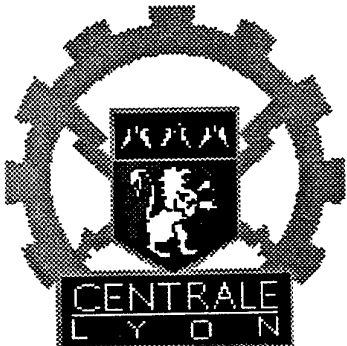
ECULLY, FRANCE

REPORT DOCUMENTATION PAGE

*Form Approved
OMB NO. 0704-0188*

Public reporting burden for this collection of information is estimated to average 1 hour per response, including the time for reviewing instructions, searching existing data sources, gathering and maintaining the data needed, and completing and reviewing the collection of information. Send comment regarding this burden estimates or any other aspect of this collection of information, including suggestions for reducing this burden, to Washington Headquarters Services, Directorate for Information Operations and Reports, 1215 Jefferson Davis Highway, Suite 1204, Arlington, VA 22202-4302, and to the Office of Management and Budget, Paperwork Reduction Project (0704-0188), Washington, DC 20503.

1. AGENCY USE ONLY (Leave blank)			2. REPORT DATE 1996	3. REPORT TYPE AND DATES COVERED Final
4. TITLE AND SUBTITLE Seventh International Symposium on Long Range Sound Propagation			5. FUNDING NUMBERS DAAH04-96-1-0090	
6. AUTHOR(S) Henry E. Bass (principal investigator)				
7. PERFORMING ORGANIZATION NAMES(S) AND ADDRESS(ES) University of Mississippi University, MS 38677			8. PERFORMING ORGANIZATION REPORT NUMBER	
9. SPONSORING / MONITORING AGENCY NAME(S) AND ADDRESS(ES) U.S. Army Research Office P.O. Box 12211 Research Triangle Park., NC 27709-2211			10. SPONSORING / MONITORING AGENCY REPORT NUMBER ARO 35545.1-GS-CF	
11. SUPPLEMENTARY NOTES The views, opinions and/or findings contained in this report are those of the author(s) and should not be construed as an official Department of the Army position, policy or decision, unless so designated by other documentation.				
12a. DISTRIBUTION / AVAILABILITY STATEMENT Approved for public release; distribution unlimited.			12 b. DISTRIBUTION CODE	
13. ABSTRACT (Maximum 200 words) As with previous symposia, the purpose of the meeting was to exchange information on current research, identify areas needing additional work, and coordinate activities as much as possible. Attendees at the meeting included representatives from most groups with active research programs in the area of atmospheric sound propagation. The meeting was divided into seven short sessions : sound propagation in the atmosphere, diffraction and ground effects, meteorology, non linear propagation, computational models, ground effects, turbulence and scattering. The symposium ended with an open discussion and plans for a future meeting in 1998. The Seventh Symposium confirmed current interest in the effects of atmospheric turbulence. The final lively discussion clearly showed that strong interactions between acousticians and specialists of fluid dynamics are needed to make significant progress in this area.				
14. SUBJECT TERMS			15. NUMBER OF PAGES	
			16. PRICE CODE	
17. SECURITY CLASSIFICATION OR REPORT UNCLASSIFIED	18. SECURITY CLASSIFICATION OF THIS PAGE UNCLASSIFIED	19. SECURITY CLASSIFICATION OF ABSTRACT UNCLASSIFIED	20. LIMITATION OF ABSTRACT UL	



Seventh International Symposium on Long Range Sound Propagation

24-26 JULY 1996

ECOLE CENTRALE DE LYON

Laboratoire de Mécanique des Fluides et d'Acoustique
36 Avenue Guy de Collongue-BP 163
69131 Ecully Cedex - France

*Fax 04 72 18 91 43 - Tél. 04 72 18 60 09
e-mail : acous@ec-lyon.fr*

Supported by

L'Ecole Centrale de Lyon
La Société Française d'Acoustique
La Délégation Générale de l'Armement
The University of Mississippi
The US Army Research Office
The European Research Office of the US Army

"The views, opinions, and/or findings contained in these proceedings are those of the authors and should not be construed as an official Department of the Army position, policy, or decision, unless so designated by other documentation"

PREFACE

Every two years since the first meeting in 1981, the University of Mississippi and the Open University have cooperated with a third institution in organizing a symposium on Long Range Sound Propagation. The Seventh International Symposium was held 24-26 July 1996 in the Ecole Centrale de Lyon, France.

As with previous symposia, the purpose of the meeting was to exchange information on current research, identify areas needing additional work, and coordinate activities as much as possible. Attendees at the meeting included representatives from most groups with active research programs in the area of atmospheric sound propagation. The meeting was divided into seven short sessions: sound propagation in the atmosphere, diffraction and ground effects, meteorology, non linear propagation, computational models, ground effects, turbulence and scattering. The symposium ended with an open discussion and plans for a future meeting in 1998. The Seventh Symposium confirmed current interest in the effects of atmospheric turbulence. The final lively discussion clearly showed that strong interactions between acousticians and specialists of fluid dynamics are needed to make significant progress in this area.

The hosts would like to express their appreciation to the participants for attending and for sharing their knowledge and expertise and to Evelyne Roche for invaluable assistance with organisation of the meeting and preparation of the proceedings.

Daniel Juvé

Ecole Centrale de Lyon
BP 163, 69131 Ecully Cedex
France

Henry E. Bass

National Center for Physical Acoustics
University of Mississippi
University, MS 38677
USA

Keith Attenborough

Faculty of Technology
The Open University
Milton Keynes MK7 6A
England

Seventh International Symposium on Long Range Sound Propagation

Session I : Sound propagation in the atmosphere (chair: Henry E. Bass)

Atmospheric absorption in the atmosphere at high altitudes.....	1-15
L.C. Sutherland, H.E. Bass	
Seasonal and diurnal variations of atmospheric absorption for horizontal sound propagation.....	17-26
C. Larsson	
Infrasonic signals from an accidental chemical explosion.....	27-34
J.P. Mutschlechner, R.W. Whitaker	
Some results of sound propagation experiments.....	35-48
P. Naz, G. Parmentier	

Session II : Diffraction and Ground effects (chair : Louis C. Sutherland)

Ground effect for a-weighted noise in the presence of turbulence and refraction ...	49-62
K. Attenborough, K.M. Li	
New analytical expressions for predicting diffraction and ground effects.....	63-77
J. Defrance, Y. Gabillet	
On the analogy between sound propagation over a rough surface and sound propagation over a smooth surface with modified surface impedance.....	79-93
Y.H. Berthelot, J.P. Chambers	
The prediction of sound field above a curved surface.....	95-109
Q. Wang, K.M. Li	

Session III : Meteorology (chair : Yannick Gabillet)

A brief tutorial on atmospheric boundary-layer turbulence for acousticians.....	111-121
D.K. Wilson	
Estimating long-term microclimatic conditions for long-range sound propagation studies.....	123-136
Y. Brunet, J.P. Lagourde, V. Zouboff	
Meteorological measurements for use in sound propagation calculations.....	137-147
M.R. Stinson, G.A. Daigle	
Temporal coherence of a soundfield in the turbulent atmosphere near the ground	149-159
M. Galindo, D.I. Havelock	

Comparison of coherent summation to incoherent summation of acoustic signals scattered from turbulence.....	161-173
H.J. Auvermann	

Session IV : Non Linear Propagation (chair : Yves H. Berthelot)

Sonic Boom research at Applied Research Laboratories.....	175
D.T. Blackstock	
Influence of molecular relaxation on the rise time of sonic booms.....	177-191
F. Coulouvrat, T. Auger	
Sonic boom scattering from anisotropic turbules.....	193-207
M. Kelly, R. Raspet, H.E. Bass	
Description of acoustical channels : linear and non linear approximate methods	209-221
R. Burvingt	

Session V : Computational models (chair : Kenneth E. Gilbert)

Towards a multiazimuth field prediction algorithm based on a new fast PE which includes turbulence.....	223-234
M. West	
Approximations in the PE method. Phase and level errors in a downward refracting atmosphere.....	235-255
M. Galindo	
Atmospheric sound propagation using the wide-angle parabolic equation.....	257-269
P. Malbequi	
Computational model for propagation of bullet noise.....	271-278
N.A. Kinneging, F.H.A. van den Berg	

Session VI : Ground effects (chair : Volker Mellert)

An efficient algorithm for predicting sound propagation at long range in the presence of wind and temperature gradients.....	279-289
K.M. Li, S. Taherzadeh, K. Attenborough	
Models and measurements of sound propagation from a point source over mixed impedance ground.....	291-305
P. Boulanger, T. Waters-Fuller, K. Attenborough, K .M. Li	
Computer cost of a 3D numerical model for noise barrier insertion loss.....	307-321
A. Tekatlian, E. Premat	
Lamb waves from airborne explosion sources : viscous effects and comparisons to ducted acoustic arrivals.....	323-337
D.O. ReVelle, R.W. Whitaker	

Session VII : Turbulence and scattering (chair : David I. Havelock)

Line-of-sight propagation in the turbulent atmosphere with Gaussian correlation functions of temperature and wind velocity fluctuations.....	339-348
V.E. Ostashev, G. Goedecke, F. Gerdes, R. Wandelt, J. Noble	
Coherence functions of plane and spherical sound waves in the turbulent atmosphere with von Karman spectra of temperature and wind velocity fluctuations.....	349-357
V.E. Ostashev, G. Goedecke, B. Brähler, V. Mellert, H. Auvermann	
Propagation of acoustic pulses in a turbulent refractive atmosphere.....	359-372
Ph. Blanc-Benon, D. Juvé	
Distorted-wave Born approximation analysis of sound levels in a refractive shadow zone.....	373-389
K.E. Gilbert, X. Di, R.R. Korte	
Correlation and coherence measurements of a spherical wave travelling in the atmospheric boundary layer.....	391-405
V. Mellert, B. Schwarz-Roehr	

LIST OF ATTENDEES

ATTENBOROUGH Keith

The Open University
Faculty of Technology

Milton Keynes MK7 6AA
United Kingdom

BLANC-BENON Philippe

Ecole Centrale de Lyon
Départ. Acoustique UMR CNRS 5509
36 Avenue Guy de Collongue
69131 Ecully Cedex
France

BACH Walter D., Jr

U.S. Army Research Office
Atmospheric Sciences Branch
P.O. Box 12211
Research Triangle Park, NC 27709-2211
USA

BOBIN Léo

Institut Franco-Allemand
de Recherche de Saint-Louis
5 rue du Général Cassagnou BP 34
68301 SAINT LOUIS Cedex
France

BAILLY Christophe

Ecole Centrale de Lyon
Départ. Acoustique LMFA URA CNRS 5509
36 Avenue Guy de Collongue
69131 ECULLY Cedex
France

BOULANGER Patrice

The Open University
Engineering Mechanics
Walton Hall
MK7 6AA
United Kingdom

BASS Henry E.

University of Mississippi
National Center for Physical Acoustics

University MS 38677
USA

BRASSEUR J.G.

Pennsylvania State University
Department Mechanical Engineering
205 Rever Building
University Park PA 16802-1413
USA

BERENGIER Michel

Laboratoire Central des Ponts & Chaussées
Centre de Nantes
BP 19
44340 BOUGUENAIS
France

BRUNEAU Michel

Université du Maine
Laboratoire d'Acoustique
BP 535
72017 LE MANS Cedex
France

BERTHELOT Yves

Georgia Institute of Technology
Mechanical Engineering

Atlanta GA 30332-0405
USA

BRUNET Y.

INRIA
Bioclimatologie
B.P. 81
33883 Villenave d'Ornon Cedex
France

BLACKSTOCK David T.

University of Texas at Austin
Applied Research Laboratories
PO BOX 8029
AUSTIN TX 78713-8029
USA

BURVINGT Raymond

THOMSON-CSF
Applications Radar
6 rue Nieuport - BP 86
78143 Velizy Villacoubray Cx
France

COMATI Jerry C.
U.S. Army Research
Environmental Sciences Branch
223 Old Marylebone Road
London NW1 5TH
United Kingdom

COMTE-BELLOT Geneviève
Ecole Centrale de Lyon
Départ. Acoustique UMR CNRS 5509
36 Avenue de Collongue
69131 Ecully Cedex
France

COLOUVRAT François
Université Pierre & Marie Curie URA 229
Laboratoire de Modélisation en Mécanique
Case 162, 4 Place Jussieu
75252 PARIS Cedex 05
France

DAIGLE Gilles
National Research Council
Institute for Microstructural Sciences

Ottawa Canada K1A 0R6
Canada

DEFRANCE Jérôme
Centre Scientifique et Technique du Bâtiment

24 rue Joseph Fourier
38400 Saint Martin d'Hères
France

FAURE Thierry
Ecole Centrale de Lyon
Départ. Acoustique UMR CNRS 5509
36 Avenue de Collongue
69131 Ecully Cedex
France

FIORINA David
CEA - Centre d'Etudes de Cadarache
DER/SSAE - Bât. 238

13106 St Paul lez Durance Cedex
France

GABILLET Yannick
Centre Scientifique et Technique du Bâtiment

24 rue Joseph Fourier
38400 Saint Martin d'Hères
France

GALINDO Marta
Institut for Akustisk Teknologi
Danmarks Tekniske Universitet
Bygning 353
2800 Lyngby
Danmark

GILBERT Kenneth E.
Pennsylvania State University
Applied Research Laboratory
Post Office Box 30
State College PA 16804
USA

HAVELOCK David I.
National Research Council
Institut for Microstructural Sciences

Ottawa Canada K1A 0R6
Canada

JUVE Daniel
Ecole Centrale de Lyon
Départ. Acoustique UMR CNRS 5509
36 Avenue Guy de Collongue
69131 Ecully Cedex
France

KINNEGING Niels
Institute of Applied Physics
TNO
P.O. Box 155
2600 AD Delft
The Netherlands

LARSSON Conny
Uppsala University
Department of Meteorology
Box 516
S-751 20 Uppsala
Sweden

LI Kai Ming
The Open University
Engineering Mechanics
Walton Hall
MK7 6AA
United Kingdom

REMY Hugues
AEROSPATIALE Toulouse
Service Acoustique
316 route de Bourgogne
31000 TOULOUSE
France

MALBEQUI Patrice
ONERA
29 Avenue de la Division Leclerc
92322 CHATILLON Cedex
France

REVELLE Douglas O.
Los Alamos National Lab.
Los Alamos
New Mexico 87545
USA

MELLERT V.
Universitat Oldenburg
Fachbereich Physik-Arbeitsgruppe Akustik
Oldenburg D-26111
Germany

SMART Eugène
HQ AFTAC/TTR
1030 5.HWY.A1A
PAFB, FL 32925
USA

NAZ Pierre
Institut FrancAllemand
de Recherche de Saint Louis
5 rue du Général Cassagnou BP 34
68301 SAINT LOUIS Cedex
France

SUNYACH Michel
Ecole Centrale de Lyon
Départ. Acoustique UMR CNRS 5509
36 Avenue Guy de Collongue
69131 Ecully Cedex
France

OSTASHEV Vladimir
New Mexico State University
Department of Physics
Box 30001/Dept. 3D
Las Cruces, New Mexico 88003-0001
USA

SUTHERLAND Louis C.
Rancho Palos Verdes
27803 Longhill Dr.
CA 90275-3908
USA

PINTON Jean-François
Ecole Normale Supérieure de Lyon
Laboratoire de Physique
46 allée d'Italie
69364 LYON Cedex 07
France

TEKATLIAN Annick
Ecole National des Travaux Publics
de l'Etat
2 rue Maurice Audin
69518 Vaulx en Velin Cedex
France

PREMAT Eric
Ecole Nationale des Travaux Publics
de l'Etat
2 rue Maurice Audin
69518 Vaulx en Velin Cedex
France

TROCCAZ Philippe
DGA-DRET
SDCT
4 rue de la Porte d'Issy
PARIS
00460 ARMEES

VOISIN Philippe
Institut Franco-Allemand
de Recherche de Saint-Louis
5 rue du Général Cassagnou BP 34
68301 SAINT LOUIS Cedex
France

WANG Qiang
The Open University
Engineering Mechanics Department
Walton Hall
Milton Keynes MK7 6 AA
United Kingdom

WEST Martin
University of Salford
Dept. of Applied Acoustics

Salford M5 4 WT
United Kingdom

Sound propagation in the atmosphere

ATMOSPHERIC ABSORPTION IN THE ATMOSPHERE AT HIGH ALTITUDES

LOUIS C. SUTHERLAND, 27803 Longhill Dr., Rancho Palos Verdes,
CA 90275-3908

and

HENRY E. BASS, National Center for Physical Acoustics,
University of Mississippi, University, MS 38677.

FAX (1st Author, +1-310-541-7795, 2nd Author, +1-601-232-5045)

1.0 INTRODUCTION

A long range sound propagation topic which frequently receives attention is the evaluation of blast waves propagating through the atmosphere at high altitudes.¹ Altitudes of concern can include the thermosphere up to about 160 km where blast overpressure pulses can propagate initially upward before being refracted down to the ground. Thus, propagation of such high altitude blast waves requires consideration of atmospheric absorption under conditions very different from those normally encountered near or on the ground. These conditions are not covered by current ISO or ANSI standards² on atmospheric absorption of sound.

New algorithms, not previously available, are developed for predicting atmospheric absorption of sound at high altitudes up to the thermosphere (up to about 160 km). At such high altitudes, classical and rotational relaxation absorption are dominant, as opposed to absorption by molecular vibrational relaxation that is normally considered the primary atmospheric absorption loss mechanism for sound propagation at audio frequencies near the ground. The former varies inversely with atmospheric pressure thus increasing in magnitude at high altitudes. For the latter, the relaxation frequencies vary directly with atmospheric pressure and depend on moisture content in the atmosphere. The resulting molecular relaxation losses decrease rapidly at high altitudes. However, classical and rotational losses also relax at the high values of frequency/pressure reached at high altitudes and thus, for audio and infrasonic frequencies, begin to decrease at altitudes in the vicinity of 90 km.

Modifications, some of them major, are defined for the existing algorithms in the ISO/ANSI standards for atmospheric absorption at high altitudes. Classical and rotational loss including a minor correction for diffusion loss are treated in Section 2 and molecular vibration relaxation loss in Section 3. Section 4 defines mean atmospheric conditions, including typical humidity content, up to and above 90 km. Also included are algorithms for viscosity and specific heat ratio as a function of temperature since these parameters are involved in defining atmospheric absorption for the temperatures encountered at high altitudes.

The paper includes consideration of the added effects of molecular relaxation loss by carbon dioxide and ozone and an accurate assessment of temperature effects³ on the molecular vibration relaxation frequencies for each of the four primary gases in the atmosphere, O₂, N₂, CO₂, and O₃. The first two appear in both molecular and atomic form at high altitudes. The paper shows that molecular relaxation by carbon dioxide, not covered by the current ANSI or ISO standards, is the dominant source of molecular

relaxation at altitudes above 60 km at a frequency of 1 Hz and above about 10 km at a frequency of 10 kHz. However, at such high altitudes, classical plus rotational losses predominate reaching maximum values at about 80-160 km, depending on frequency.

The variation in mole fractions of the atmospheric constituents is assumed to have only a second order effect on viscosity and specific heat ratio. The complex methods available to take such effects into account⁴ were not considered for this paper.

2.0 CLASSICAL and ROTATIONAL LOSS

Sound propagating through the atmosphere is subject to two forms of energy loss:⁵ classical and relaxation losses. The former is associated with energy transfer from the organized kinetic energy of molecules due to passage of a sound wave to equivalent heat energy or random kinetic energy of translation of the molecules. The relaxation form of energy loss is associated with redistribution of translational or internal energy of the molecules. Relaxation losses break down into rotational and vibrational relaxation losses - the former generally being more significant at high values of frequency/pressure.

A rigorous presentation of the theoretical background involved in these processes is given in Ref. 5. However, the revised expressions developed in this paper for the classical and rotational relaxation losses are based primarily on theoretical^{6,7} and experimental⁷ work by Greenspan.

The total attenuation coefficient, α_t in Np/m due to atmospheric absorption can be defined in a general form by the summation:⁵

$$\alpha_t = \alpha_{cr} + \alpha_{diff} + \sum_i [A_{max,i}/c] [(2f^2/f_{vib,i})/(1+(f/f_{vib,i})^2)] \quad (1)$$

where α_{cr} is the combined attenuation coefficient for classical plus rotational relaxation losses,

α_{diff} is the attenuation coefficient for diffusion loss and

$A_{max,i}$ is the maximum loss per wavelength for the i th molecular vibration relaxation component with a relaxation frequency $f_{vib,i}$, f is the frequency and c is the speed of sound.

From Greenspan^{6,7}, the normalized complex propagation constant, k_{cr} for the combined classical (translational) and rotational losses is:

$$k_{cr} = -i k_1 \cdot k_2 \quad (2)$$

where k_1 and k_2 are the normalized complex propagation constants for the classical and rotational losses, respectively, each having the general form:

$$k_j = \alpha_j / \beta_0 + i \beta_j / \beta_0 \quad (3)$$

where β_0 is the phase constant ($= 2\pi f/c_0$) associated with the low frequency speed of sound, c_0 .

Inserting Eq. (3) into (2), it can be shown that the real part of k_{cr} , which is the attenuation coefficient, α_{cr} , is given by:

$$\alpha_{cr} = \alpha_1 \cdot \beta_2 / \beta_0 + \alpha_2 \cdot \beta_1 / \beta_0 \quad (4)$$

At low frequencies, the ratios β_1 / β_0 and $\beta_2 / \beta_0 = 1.0$ so that Eq. (4) reduces to the usual summation, $\alpha_{cr} \approx \alpha_1 + \alpha_2$.

From Greenspan's earlier paper⁶, simplified versions of the real and imaginary parts of k_1 [i.e. $i = 1$ in Eq. (3)] are given by:

$$\alpha_1 / \beta_0 = \{ \frac{1}{2} [(1+v^2)^{1/2} - 1] / (1+v^2) \}^{1/2} \quad (5a)$$

$$\text{and } \beta_1 / \beta_0 = \{ \frac{1}{2} [(1+v^2)^{1/2} + 1] / (1+v^2) \}^{1/2} \quad (5b)$$

where $v = 8\pi f \mu / 3P$, a non-dimensional frequency. (This more useful variable is employed here in place of Greenspan's r ($= (4/3)/v$). For this variable, f is the frequency, in Hz, μ is the viscosity in $\text{Kg} \cdot \text{m}^{-1} \cdot \text{s}^{-1}$ and P is the atmospheric pressure in Pascals.

For low frequencies, ($v \ll 1$), with Eq. (5a) and (5b), k_1 reduces to:

$$k_1 = [2\pi^2 f^2 \mu / cP] \cdot [4/3] + i \cdot 1 = [2\pi^2 f^2 \mu / k cP] \cdot [4k/3] + i \cdot 1 \quad (6)$$

where k = the specific heat ratio, c_p / c_v .

and c_0 = the ambient speed of sound = $[k R_0 T / M]$, m/s (Note that c_0 is this ambient sound speed without dispersion.)

R_0 = the Universal Gas Constant = 8,314.48 J/kmole K

M = Molecular weight $\approx 28.964 \text{ Kg/Kmole}$ for altitudes below 90 km.

The unity imaginary term in Eq. (6) shows, as required, that there is no dispersion at low frequencies. For $k = 7/5$ for air, the value of the second bracketed term in the real part is 1.867, just 0.5% below the value of 1.876 in Eq. (18) in Bass, et al⁵ for the low frequency attenuation coefficient for classical losses. In fact, employing a close approximation to the Eucken relationship between viscosity, μ and the ratio of thermal conductivity, K to the specific heat for constant pressure, c_p [i.e. $\mu / (K/c_p) = 14/19 = 0.737 \approx 3/4$], the real part of this equation can be expressed in exactly the same form as in Eq. (11) of Ref. 5.

It should be noted that the theoretical expression employed here for k_1 is a simplified version⁶ and is not the more exact but complex 6th order polynomial Greenspan used later.⁷

Greenspan⁷ shows that the normalized real and imaginary parts of the propagation constant, k_2 for rotational loss can be expressed as:

$$\alpha_2 / \beta_0 = (\sigma/2 - 1/2\sigma)(x) / [(1+x^2) \cdot (1+(\sigma x)^2)]^{1/2} \quad (7a)$$

$$\text{and } \beta_2 / \beta_0 = [(1+x^2) / (1+(\sigma x)^2)]^{1/2} \quad (7b)$$

where $x = 3nv/4$ is a modified non-dimensional frequency,

$$n = 4/5[(C_p^\infty \cdot C_v^\infty) / (C_p^0 \cdot C_v^0)]^{1/2} \cdot Z_{\text{rot}}$$

$$\sigma = c_\infty / c_0 = [k_\infty / k_0]^{1/2} = [(C_p^\infty / C_v^\infty) / (C_p^0 / C_v^0)]^{1/2}$$

and Z_{rot} is the rotational collision number for air.⁸

The superscripts ∞ and 0 applied to the specific heats at constant pressure, C_p and constant volume, C_v denote conditions, respectively, at frequencies well above and below the rotational relaxation frequency (i.e. $v \gg 1$ or $\ll 1$).

We can write $C_p \equiv C_v + R$, and, for diatomic molecules, $C_v^\infty \equiv 3R/2$, so $C_p^\infty \equiv 5R/2$. At low frequencies, well below the rotational relaxation peak and for moderate temperatures (< 400 K), $C_v^0 = 5R/2 + \Sigma C' v_i \approx 5R/2$ where $C' v_i$ are the vibrational relaxation specific heats and their sum is much less than $5R/2$. Thus $C_p^0 \approx 7R/2$ and it is readily found that, to a close approximation:

$$n = (4/5) \cdot (3/7)^{1/2} \cdot Z_{\text{rot}} \quad \text{and} \quad \sigma \approx 5/(21)^{1/2} \quad (8a)$$

To allow for changes in the mixture ratio of oxygen and nitrogen in air at altitudes above the stratosphere, Z_{rot} is given in a more general form by⁸:

$$Z_{\text{rot}} = 1/[(X_{N2}/Z_{\text{rot},N2}) + (X_{O2}/Z_{\text{rot},O2})] \quad (8b)$$

where $Z_{\text{rot},N2} = 63.3 \exp[-16.7(T^{-1/3})]$, the collision number for N₂,

$Z_{\text{rot},O2} = 54.1 \exp[-17.3(T^{-1/3})]$, the collision number for O₂,

and X_{N2} and X_{O2} are the mole fractions of N₂ and O₂.

For low frequencies, ($v \ll 1$), Eq. (7) reduces to:

$$(\alpha_2/B_0) + i(\beta_2/B_0) \approx [2\pi^2 f^2 \mu / k c P] \cdot [16k/175] \cdot Z_{\text{rot}} + i \cdot 1 \quad (9)$$

For $k \approx 7/5$ for air, the second bracketed term is 0.128, exactly the same is in Eq. (29) of Ref. 5.

From Eq. (4), (5a) and (7a), the attenuation coefficient α_{cr} for classical plus rotational loss at a frequency, f , in Nepers/m can be represented in a more familiar form as the sum of the attenuation coefficients for the classical, α_{cl} and rotational, α_{rot} losses respectively. However, both of these terms exhibit a relaxation-type behavior at values of f/P^* of the order of 200 to 1,000 MHz/atm where P^* is the pressure in atmospheres. Associated with this relaxation behavior, an empirical adjustment, explained later, is included for the value of the parameter x in both the numerator and denominator of the phase term, B_2/B_0 of Eq. (7b). Then, using $B_0 = 2\pi f/c_0$, the classical loss attenuation coefficient, α_{cl} , can be expressed as:

$$\alpha_{\text{cl}} = \alpha_1 \cdot B_2/B_0 = (2\pi f/c_0) \left[\frac{\frac{1}{2}[(1+v^2)^{1/2}-1]}{[1+v^2]} \cdot \frac{[1+(x')^2]}{[1+(\sigma x')^2]} \right]^{1/2} \quad (10)$$

where $v =$ the same nondimensional frequency $= 8\pi f \mu / 3P$ and the only new variable is $x' = 2.36 \cdot x$ where 2.36 is the empirical adjustment factor.

The classical attenuation coefficient, α_{cl} , exhibits a relaxation-type behavior with a maximum value for the α_1 term at $v_{max} = 8\pi f_{max}\mu/3P = \sqrt{3}$ or $f_{max}/(P/P_0) = 3\sqrt{3} \cdot P_0/(8\pi\mu) \approx 1 \cdot 10^9$ Hz/atm. At an altitude of 140 km, P/P_0 is of the order of 10^{-8} and, neglecting temperature effects, the "relaxation" peak frequency, f_{max} occurs at about 10 Hz! This expression for α_{cl} reduces to the usual form showing a dependency with f^2 at low frequencies well below the rotational relaxation frequency.

The viscosity, μ , included in the dimensionless frequency, v , is given by the following modified version of the well-known Sutherland equation.⁷ This is shown later to provide a very good fit to published viscosity data.

$$\mu/\mu_0 = (T/T_0)^{1/2} [1 + S/T_0] / [1 + S/T] \quad (11)$$

where μ_0 = the reference viscosity at $T_0 = 18.192 \cdot 10^{-6}$ kg·m⁻¹·s⁻¹
 $T_0 = 293.15$ K (20 °C) and $S = 117$ K.

In the expression for the attenuation coefficient, α_{rot} for rotational loss (i.e., $\alpha_{rot} = \alpha_2 \cdot \beta_1 / \beta_0$), one basic change and one empirical adjustment are required for this paper where the value of frequency/pressure can exceed 1,000 MHz/atm. The change is that α_{rot} must be multiplied by the sum of the mole fractions for molecular oxygen and nitrogen, ($X_{O2} + X_{N2}$), normalized by its sea level value of 0.9903. The quantity, α_{rot} defines the rotational loss for the diatomic molecules, O₂ and N₂ and does not apply for atomic oxygen and nitrogen which do not exhibit rotational relaxation. Although the correction is essentially unity at altitudes below about 85 km, this normalized mole fraction sum falls to a value of about 0.75 at an altitude of 125 km.

The adjustment is the same empirical adjustment to the parameter, x , (i.e. - using $x' = 2.36 \cdot x$) but only for the x terms in the denominator of Eq. (7b). With these two changes, the attenuation coefficient, α_{rot} for the rotational vibration loss, is given in Nepers/m by:

$$\alpha_{rot} = (2\pi f/c_0) \cdot X_{ON} \left[\frac{(\sigma^2 - 1)x}{2\sigma} \right] \cdot \left[\frac{\frac{1}{2}[(1 + v^2)^{1/2} + 1]}{[1 + v^2] \cdot [1 + (x')^2] \cdot [1 + (\sigma x')^2]} \right]^{1/2} \quad (12)$$

where $X_{ON} = (X_{O2} + X_{N2}) / (X_{O2,0} + X_{N2,0})$ ($X_{O2} + X_{N2}$) = the sum of the mole fractions at any altitude,
 $(X_{O2,0} + X_{N2,0})$ = the sea level value, 0.9903 (for dry air),
and the remaining parameters, v , x , x' and σ are the same as for Eq. (7) and (10).

Fig 1. compares the predicted values for α_{cr} computed using Eq. (10) and (12), with Greenspan's data for air.⁷ The data and theory are plotted as non-dimensional values of α_{cr}/β_0 versus the non-dimensional frequency $v = 8\pi f\mu/3P$ where $\beta_0 = (2\pi f/c_0)$ is the phase constant at the reference temperature, T_0 .

The uppermost line in Fig. 1 is the theoretical result computed with Eq. (10) and (12) but without any empirical adjustment - i.e with $x' = x$. The line closest to the data is the theory with the empirical adjustment using $x' = 2.36 \cdot x$ as explained above. This adjustment reduces the effect of the rotational relaxation peak and adjusts the "theory" line to provide better agreement with Greenspan's measured data. This purely empirical adjustment is considered a reasonable artifice for this paper to allow use of practical computational algorithms for α_{rot} .

Moreover, this empirical modification does not change the low frequency value of α_{rot} since the denominator $\rightarrow 1$ for x or $x' \ll 1$. The theoretical and empirically-adjusted values for α_{rot} predicted by Eq. (12), without and with the empirical adjustment, (i.e. - with $x' = 1.0$ or 2.36 times x), are shown by the lower 2 lines in Fig. 1.

In summary, Eq. (10) and (12) are the basic expressions employed in this paper to compute classical and rotational loss in the atmosphere. Eq. (11) is employed to compute viscosity as a function of temperature. The ambient speed of sound, c_0 , in the absence of dispersion, is a basic temperature-dependent parameter required in Eq. (10) and (12). The computation of c_0 as a function of altitude is considered in Section 4.0 which also defines the default values for atmospheric pressure and temperature.

2.1 DIFFUSION LOSS A small addition to classical plus rotational relaxation loss, too small to be readily apparent in measured data, is provided by a mass and thermal diffusion loss signified by α_{diff} . A brief evaluation of this term indicates that it is reasonable to assume that the attenuation coefficient, α_{diff} for this diffusion loss is approximately equal to its low frequency value, 0.3% of the classical loss, α_{cl} as defined by Eq. (10). This assumption provides the correct low frequency value but also accounts for an expected relaxation behavior at high values of f/P for the diffusion loss, a behavior not indicated by current theoretical models^{3,9}.

After adding this minor diffusion loss to the total classical plus rotational relaxation loss, the predicted value for $\alpha_{\text{cr}} + \alpha_{\text{diff}}$ is $1.84 \cdot 10^{-11} \cdot f^2 \text{ Np/m}$ at the reference temperature and pressure, T_0 and P_0 . This agrees within 0.5% (well within experimental error) with the average from an extensive evaluation of experimental data¹⁰ obtained in air under conditions and for frequencies where the only significant losses are classical, rotational and diffusion losses.

3.0 VIBRATIONAL RELAXATION LOSS

This section defines the algorithms for the maximum loss per wavelength at the relaxation peak frequencies for each of the four primary gas components in air, O_2 , N_2 , CO_2 and O_3 . This is followed by estimates of the relaxation frequencies for each of these primary components.

3.1 Maximum Loss per Wavelength The maximum loss per wavelength, $A_{\text{max},i}$ from vibrational relaxation for the i^{th} gas component is defined by:⁵

$$A_{\text{max},i} = X_i \cdot (\pi/2) \cdot (C'_i/R) / [(C_p^{\text{av}}/R)(C_v^{\text{av}}/R + C'_i/R)] \quad (13)$$

where X_i = the mole fraction of the i^{th} gas constituent

C'_i/R = the relaxing specific heat for this gas normalized by the universal gas constant, R, is given in terms of its characteristic temperature, Θ_i and the atmospheric temperature, T by the following Planck-Einstein equation as:

$$C'_i/R = (\Theta_i/T)^2 \exp(-\Theta_i/T)/[1 - \exp(-\Theta_i/T)]^2 \quad (14)$$

The parameters C_v^{∞}/R and C_p^{∞}/R , similar but not identical to those defined for Eq. (7), are summarized below for the four components considered along values for Θ_i and sea level values for the mole fractions, X_i .

Table 1. Parameters used to define the maximum absorption loss per wavelength for the four major constituents of air.

MOLECULE	C_v^{∞}/R a)	C_p^{∞}/R a)	Θ_i , K	X_i
Diatomeric, O ₂	5/2	7/2	2239.1	0.20948
, N ₂ ,	5/2	7/2	3352	0.78084
Triatomic, CO ₂ b)	3	4	915	2 x 0.000314 c)
, O ₃ d)	3	4	1037	0->7·10 ⁻⁸ e)

a) For frequencies below the rotational relaxation frequency.

b) Known to be a linear molecule.

c) For CO₂, X_{CO_2} , is multiplied by 2 to account for the double degeneracy of its two orthogonal vibration modes.

d) O₃ may not be a linear molecule in which case, C_v^{∞}/R would be = 7/2 and C_p^{∞}/R would be 9/2. (This would introduce a negligible change in the total atmospheric loss.)

e) X_{O_3} reaches a maximum at an altitude of about 26 km

Although a simpler form of Eq. (13) is normally employed⁵ since it is usually assumed that $(C'_i/R) \ll 1$, the general form of Eq. (13) is retained for this paper to insure accuracy for the higher temperature range found at high altitudes where (C'_i/R) can approach 0.3 (i.e. not $\ll 1$).

One aspect of the final results conveniently mentioned here is to point out how the temperature-dependent relaxation strength, C_i/R varies with temperature for the four gases identified in Table 1. Applying Eq. (14), the value of C_i/R , relative to its value at the sea level temperature, T_0 , increases substantially but the increase for nitrogen is especially marked. Nitrogen shows an increase by a factor of 500 in its molecular vibration relaxation strength at a temperature of 1,000 K over the sea level value. Such a temperature is reached at the upper altitude of 160 km considered in this paper. This behavior, caused by its higher characteristic temperature, Θ_i , will be apparent later when examining the variation in the molecular relaxation loss for each of the four gases.

3.2 Vibrational Relaxation Frequencies. Based on the current ANSI/ISO Standards², on other published data,³ and on estimates by the second author of this paper where data were not available, the following expressions have been developed to estimate the molecular vibration relaxation frequencies under the unusual atmospheric composition and temperature conditions at high altitudes.

3.2.1 OXYGEN In a variation on the ANSI/ISO standards, the molecular vibration relaxation frequency for oxygen, f_{vib,O_2} , in Hz, is estimated to be given by^{2,3}:

$$f_{vib,O_2} = (P/P_o)(\mu_o/\mu)[A_1 + A_2 + B h'(C + h')/(D + h')] \quad (15)$$

where $A_1 = (X_{O_2} + X_{N_2}) \cdot 24 \exp(-9.16 T_r)$, Hz

$$A_2 = (X_0 + X_N) \cdot 2400, \text{ Hz}; \quad B = 40,400 \exp(+10.0 T_r), \text{ Hz}/\%$$

$$C = 0.02 \exp(-11.2 T_r), \text{ \%}; \quad D = 0.391 \exp(+8.41 T_r), \text{ \%}$$

$$T_r = [(T/T_o)^{-1/3} - 1] \text{ K}; \quad T_o = 293.15 \text{ K} \text{ and}$$

$h' = 100[(X_{H_2O}) + X_{O_3}]$, the mole concentration, in %, of water vapor plus ozone (Note the distinction between the mole concentration, h , in percent for water vapor and the corresponding mole fraction, X_{H_2O} .)

The various mole fractions, X_i , where i corresponds to O_2 , N_2 , O_3 , O , N , and H_2O , are their fractional parts, by volume, in the mixture of moist air. The A_2 term in the above expression is an estimated correction for the presence of atomic oxygen and nitrogen. (The mole fraction of the former exceeds that for O_2 at altitudes above about 95 km.) The term, $(P/P_o)(\mu_o/\mu)$ accounts for the inherent effect of the pressure- and viscosity-dependent molecular collision frequency, $f_{col} = 1.25P/\mu$, on all vibrational relaxation frequencies.⁵ The ratio (μ_o/μ) is obtained by inverting Eq. (11) given earlier.

The temperature correction factors in Eq. (15) are defined in terms of the relative temperature variable, T_r , which is zero at the reference temperature, T_o , so the temperature correction factor is unity at T_o . For each component, the exponents are based on the experimental data reviewed in Ref. 3.

3.2.2 NITROGEN The relaxation frequency for nitrogen is also modified from the ANSI/ISO standards² to account for the atypical conditions at high altitudes. The resulting new expression is:

$$f_{vib,N_2} = (P/P_o)(\mu_o/\mu)[E + F \cdot X_{O_3} + G \cdot X_{H_2O}] \quad (16)$$

where $E = 9 \cdot \exp(-19.9 T_r)$. This includes a temperature correction³ for the low humidity term believed to represent relaxation of N_2 by CO_2 .

$F = 60,000 \text{ Hz}$, an estimate for relaxation of N_2 by ozone.

$G = 28,000 \cdot \exp(-4.17 T_r)$. This is the same term as in the ANSI/ISO Standards to account for relaxation of N_2 by water vapor.

3.2.3 CARBON DIOXIDE For carbon dioxide, based on experimentally-based relaxation rates specified in Ref. 3 for CO_2 , O_2 , N_2 , H_2O and on rough estimates for O , N and O_3 , the relaxation frequency, f_{vib,CO_2} is given by the following approximation.

$$f_{vib,CO_2} = (P/P_0)(\mu_0/\mu) \cdot [H \cdot X_{CO_2} + I \cdot (X_{O_2} + 0.5 \cdot X_O) + J \cdot (X_{N_2} + 0.5 \cdot X_N) + K \cdot (X_{H_2O} + X_{O_3})] \quad (17)$$

where $H = 22,000 \exp(-7.68 T_r)$, Hz; $I = 15,100 \exp(-10.4 T_r)$, Hz
 $J = 11,500 \exp(-9.17 T_r)$, Hz and $K = 8.48 \cdot 10^8 \exp(+9.17 T_r)$, Hz.

While data are available³ to support the temperature correction factors in the above expression for the molecular species (i.e. - O₂ and N₂), adding 50 % of the mole fraction of atomic oxygen and nitrogen to the mole fraction for their respective molecular forms is only an estimate, not supported by data, to approximate the relaxation rates for the atomic species.

3.2.4 OZONE The relaxation frequency, f_{vib,O_3} for ozone, based on limited data,³ is estimated to be:

$$f_{vib,O_3} = (P/P_0)(\mu_0/\mu) \cdot (1.2 \cdot 10^5) \cdot \exp(-7.72 \cdot T_r) \quad (18)$$

The relaxation time, τ_v corresponding to this estimate is $\tau_v = 1/(2\pi \cdot 1.2 \cdot 10^5) = 1.3 \cdot 10^{-6}$ sec.

For Eq. (16-18), T_r is the same as defined for Eq. (15).

The preceding expressions can now be used to compute atmospheric absorption as a function of altitude given a model, or models, for the atmospheric pressure, temperature and composition of the atmosphere.

4.0 ATMOSPHERIC CONDITIONS

Mean annual values for atmospheric pressure and temperature up to 160 km were defined primarily by a NASA model for Cape Kennedy weather.¹¹ Below 50 km, this model predicted temperatures slightly higher than given by the U.S. or ICAO Standard Atmosphere^{12,13}. Therefore, the U.S Standard Atmosphere (1962) profile was employed below 50 km. Above 50 km, the NASA model was used after incorporating a small offset adjustment to provide a smooth transition to the U.S. Standard Atmosphere.

The vertical profile of water vapor was based on the data in Ref. 14 which extended to 100 km. However, it was readily extrapolated to 160 km since: 1) a log-linear decrease in mole fraction of H₂O vs altitude was clearly indicated by the data in Ref. 14 for altitudes from 50 to 100 km and 2) water vapor plays little or no role in atmospheric absorption above about 80 km and then only for very low frequencies.

The mole fractions of the constituent gases (i.e. - N₂, O₂, N, O, CO₂, O₃ and H₂O) are also based on the data in Ref. 14. The later defined the mole fractions for these constituent gases, except CO₂, to an altitude of 240 km. For CO₂, available information^{14,15} indicated a constant mole ratio equal to 375 PPM at all altitudes is a reasonable projection for CO₂ in the atmosphere for the year 2000.

4.1 Reference values for atmospheric pressure and temperature.

Atmospheric pressure and temperature are defined by the following two polynomial equations (up to 5th order) with geometric altitude, Y, in km, as

the independent variable. Each equation utilizes different sets of polynomial coefficients to cover seven altitude ranges or legs. These coefficients and the equations to which they apply are specified in Table 2.

The atmospheric pressure, P in Pascals, and absolute temperature, T in kelvin, for Y = 0 to 160 km, are given by:

$$P = 10^5 \cdot \exp(A_0 + A_1 \cdot Y + A_2 \cdot Y^2 + A_3 \cdot Y^3 + A_4 \cdot Y^4 + A_5 \cdot Y^5) \quad (19)$$

$$T = A_0 + A_1 \cdot Y + A_2 \cdot Y^2 + A_3 \cdot Y^3 + A_4 \cdot Y^4 + A_5 \cdot Y^5 \quad (20)$$

The above equations and Table 2 are used to define the profiles for mean atmospheric pressure and temperature shown in Figure 2 and 3 respectively. Temperature profiles, for any one time period, show considerably more variation than the pressure profiles - they vary widely with time of day and location - a detail not reflected in the models considered for this paper.

Table 2. Coefficients for Polynomial Expressions for Atmospheric Pressure and Temperature vs Altitude.

PRESSURE

Altitude		Use		Coefficients						
Range, km		with								
Lower	Upper	Leg	Eqn.	No.	Ao	A1	A2	A3	A4	A5
0	11	I	19	1.68716E-02	-1.14252E-01	-1.36123E-03	7.36241E-05	-1.08003E-05	3.30464E-07	
11	18	II	19	-7.99108E-02	-8.10464E-02	-5.55224E-03	3.11170E-04	-1.66878E-05	3.83200E-07	
18	28	III	19	9.84143E-01	-2.69769E-01	8.52275E-03	-3.96203E-04	1.01465E-05	-1.02643E-07	
28	50	IV	19	2.18198E+00	-4.11497E-01	1.33665E-02	-3.59519E-04	5.10097E-06	-2.89056E-08	
50	83	V	19	7.63380E+00	-2.58298E-01	3.76139E-03	-4.20887E-05	1.60200E-07	-1.92509E-10	
83	90	VI	19	-1.12790E+01	3.19820E-01	-5.80930E-03	2.23310E-05	0	0	
90	160	VII	19	-1.09914E+02	4.71430E+00	-8.21230E-02	6.62200E-04	-2.55930E-06	3.84825e-09	

TEMPERATURE

Altitude		Use		Coefficients						
Range, km		with								
Lower	Upper	Leg	Eqn.	No.	Ao	A1	A2	A3	A4	A5
0	11	I	20	2.85000E+02	-5.07619E+00	1.97780E-01	-5.61320E-02	1.46360E-03	1.42000E-04	
11	18	II	20	1.25350E+03	-3.28270E+02	4.18980E+01	-2.67240E+00	8.44850E-02	-1.05260E-03	
18	28	III	20	2.12120E+03	-4.19180E+02	3.64740E+01	-1.57300E+00	3.36670E-02	-2.85790E-04	
28	50	IV	20	-9.01040E+02	1.58750E+02	-8.92550E+00	2.46170E-01	-3.28070E-03	1.68830E-05	
50	83	V	20	-5.03980E+02	3.92140E+01	-4.95180E-01	-3.26220E-03	9.66650E-05	-4.78800E-07	
83	90	VI	20	1.75740E+02	0	0	0	0	0	
90	160	VII	20	-6.84520E+04	2.82794E+03	-4.57421E+01	3.62065E-01	-1.39987E-03	2.12100E-06	

4.2 Reference values for Composition of the Atmosphere

Reference 14 contained a plot of density of molecules or atoms of the atmospheric constituents as a function of altitude. Careful reconstruction of this plot provided the data for Fig. 4. Although the model provides

reasonable approximations of these average values for this paper, some constituents, such as water vapor and ozone, have significant variations with location and time - a detail not considered in this paper.

For the humidity profile, regression equations were developed from the data in Ref. 14. to define the mole fraction of water vapor, X_{H2O} in 3 legs: from 0 to 30, 30 to 100 km and, by extrapolation, from 100 to 160 km. The results are compared in Fig. 5 to other humidity profile data^{2,11}.

Thus, for the i^{th} component, the mole fraction, X_i vs altitude is given by the following generic expression.

$$X_i = 10^{-5} [A_0 + A_1 \cdot Y + A_2 \cdot Y^2 + A_3 \cdot Y^3 + A_4 \cdot Y^4 + A_5 \cdot Y^5] \quad (21)$$

The coefficients, defined by Table 3, cover the entire altitude range from 0 to 240 km. The total mole fraction over all constituents considered, except water vapor, was very nearly equal to the theoretical value of about 0.99 at any altitude. Argon and other trace constituents make up the remaining 1%. Thus, to provide the correct mole fractions for moist air, argon was added to dry air as 1.2 % of the mole fraction of nitrogen; the mole ratio for H_2O , derived from Fig. 4 was then added and the new total for moist air normalized to unity.

Table 3. Coefficients for Polynomial Expressions for Atmospheric Composition

COMPONENT >	O2	N2	CO2	O3	O	N	H2O
ALT.,km >	0-90	0-76	0-240	0-80	0-95	0-240	0-30
A0	-0.67887	-0.10744	-3.3979	-1.9027E+01	-1.1195E+01	-5.3746E+01	-1.7491E+00
A1				1.3093E+00	1.5408E-01	1.5439E+00	4.4986E-02
A2				-4.6496E-02	-1.4348E-03	-1.8824E-02	-6.8549E-02
A3				7.8543E-04	1.0166E-05	1.1587E-04	5.4639E-03
A4				-6.5169E-06		-3.5399E-07	-1.5539E-04
A5				2.1343E-08		4.2609E-10	1.5063E-06
ALT.,km >	90-240	76-240		80-240	95-240		30-100
A0	4.9296E+01	1.3972E-01		-4.2340E+00	-3.2456E+00		-4.2563E+00
A1	-1.5524E+00	-5.6269E-03		-3.0975E-02	4.6642E-02		7.6245E-02
A2	1.8714E-02	3.9407E-05			-2.6894E-04		-2.1824E-03
A3	-1.1069E-04	-1.0737E-07			5.2640E-07		-2.3010E-06
A4	3.1990E-07						2.4265E-07
A5	-3.6211E-10						-1.2500E-09
ALT.,km >							100-240
A0							-6.2534E-01
A1							-8.3665E-02

4.3 Temperature-dependent Parameters Three basic temperature-dependent parameters are needed for evaluation of atmospheric absorption of sound at high altitudes: 1) the ambient speed of sound, c_0 , 2) the specific heat ratio, k to define c_0 and 3) viscosity, μ , for computing the classical

plus rotational relaxation losses.

For an ideal gas⁵, in the absence of dispersion, the ambient speed of sound in air, c_0 , in m/s, is given by:

$$c_0 = [kR_0T/M]^{1/2} \quad (22)$$

where k = the ratio of specific heats, C_p/C_v .

R_0 = the Universal Gas Constant, 8314.48 J/Kmole·K

T = Absolute temperature, K

M = Molecular weight, kg/Kmole, a weighted value computed from the mole fractions and well-known molecular weights of each component.¹³

For the specific heat ratio, k , ignoring any second-order variation due to changes in atmosphere composition above the stratosphere, the following empirical expression defines the variation in k with temperature, T (K).

$$k = A_0 + A_1 \cdot T + A_2 \cdot T^2 + A_3 \cdot T^3 + A_4 \cdot T^4 + A_5 \cdot T^5 \quad (23)$$

where $A_0 = 1.371E+00$, $A_1 = 2.460E-04$, $A_2 = -6.436E-07$,
 $A_3 = 5.200E-10$, $A_4 = -1.796E-13$ and $A_5 = 2.182E-17$

This expression evolved from a regression fit to what are considered the most credible data¹⁶⁻¹⁹ for k shown in Fig. 6. For viscosity, the slightly modified Sutherland equation⁷, given earlier by Eq. (11), was used for μ vs temperature. The model and data^{12,16,18} for μ are compared in Fig. 7.

5.0 ATMOSPHERIC ABSORPTION TO 160 km and SUMMARY

Applying the preceding sections, the absorption coefficients are converted from Nepers/m to decibels/km by multiplying by 8685.9. Typical results are shown in Fig. 8 and 9 by the attenuation coefficient in dB/km for altitudes from 0 to 160 km and for frequencies of 1 and 1,000 Hz respectively. The top of each figure shows the classical loss and added 0.3% diffusion loss, the rotational relaxation loss, the total molecular relaxation losses and the resultant total attenuation coefficient. The bottom shows each molecular relaxation component and the total attenuation coefficient.

Summarizing the results: a) classical plus rotational losses predominate over molecular relaxation losses from 60 km at 1 Hz to 10 km at 10,000 Hz, b) the former will be most important for propagation of high altitude blast waves, c) molecular relaxation by CO₂ dominates these relaxation losses at altitudes above where classical plus rotational relaxation begin to control. The algorithms provide estimates of atmospheric absorption at altitudes well beyond the range of applicability of the existing ANSI and ISO Standards. They are based on well-founded, but simplified, theoretical models for classical plus rotational relaxation losses and a combination of theory, experimental data and estimates for molecular vibration relaxation losses. Unlike a previous study of atmospheric absorption at high altitudes²⁰, it is also shown that classical and rotational losses undergo relaxation at the very high values of frequency/pressure encountered at high altitudes and thus begin to decrease at very high altitudes.

REFERENCES

1. Besset, C. and Blanc, E., J. Acoust. Soc. Am. 95, 1830-1839, (1994).
2. American National Standard, ANSI S1-26-1995 (ASA 113-1995), July, 1995.
(See also, International Organization for Standards, ISO 9613-1, 1993.)
3. Bass, Henry E., J. Acoust. Soc. Am. 69, 124-138, (1981).
4. Hirschfelder, J.O, Curtiss, C.F. and Bird, R.B., "Molecular Theory of Gases and Liquids", Wiley Book Co., New York, (1954).
5. Bass, H. E., Sutherland, L.C., Piercy, J. and Evans, L., "Absorption of Sound by the Atmosphere", Chap 3, Physical Acoustics, Vol. XVII, Academic Press, Inc., N.Y. (1984)
6. Greenspan, Martin, J.Acoust. Soc. Am. 26, 70-73, (1954).
7. Greenspan, Martin, J.Acoust. Soc. Am. 31, 155-160, (1959).
8. Bass, H.E. & Sutherland, L.C., J.Acoust. Soc. Am., 59, 1317-1318, (1976).
9. Roberts, R.C. Chap. 2s, Amer. Inst. of Physics Handbook, D. E. Gray (ed), McGraw-Hill Book Co., N.Y. (1972).
10. Sutherland, L.C., U.S. Dept. of Trans. Report No. TST-75-87, (1975).
11. Smith, O.E. & Weidner, D. K, "A Reference atmosphere for Patrick AFB, Florida, Annual (1963 Revision), NASA TM X-53139, Sept.((1964)
12. Valley, S.L. (ed), "Handbook of Geophysics and Space Environments", McGraw-Hill Book Co., (1965).
13. International Civil Aviation Organization, "Manual of the ICAO Standard Atmosphere", Second Edition, Doc. 7488/2, (1964)
14. Air Force Geophysics Directorate, "Handbook of Geophysics", The Macmillan Co., (1960).
15. Keeling, Charles, Director, CO₂ Research Group, Institute of Oceanography, La Jolla, CA., Personal Communication, Aug. (1996)
16. Keenan, J.H. and Kaye, J. "Gas Tables, Thermodynamic Properties of Air", John Wiley & Sons, N.Y, (1945).
17. Hilsenrath, J., et al., "Tables of Thermal Properties of Gases", National Bureau of Standards Circular 564, Nov. (1955).
18. Chemical Rubber Co., Handbook of Chemistry and Physics, 67th Edition, Cleveland, OH, (1986).
19. Cramer, O., J. Acoust. Soc. Am., 93, 2510-2516, (1993).
20. Rind, D., , J. Atmosph. and Terrestrial Physics, 39, 445-456, (1977)

FIG. 1. CLASSICAL & ROTATIONAL LOSS PER WAVELENGTH

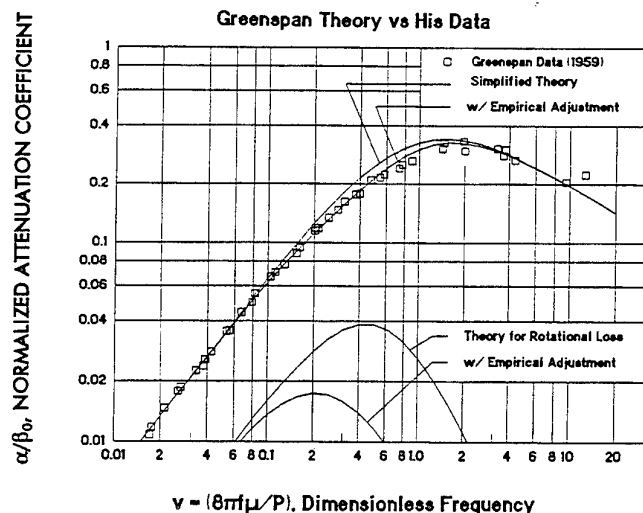


FIG. 2 ATMOSPHERIC PRESSURE MODELS

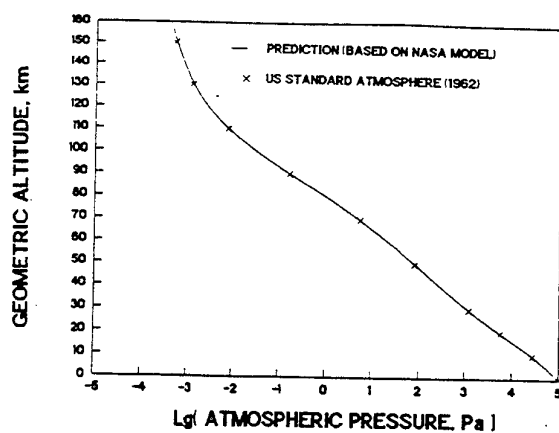


FIG. 3 ATMOSPHERIC TEMPERATURE MODELS

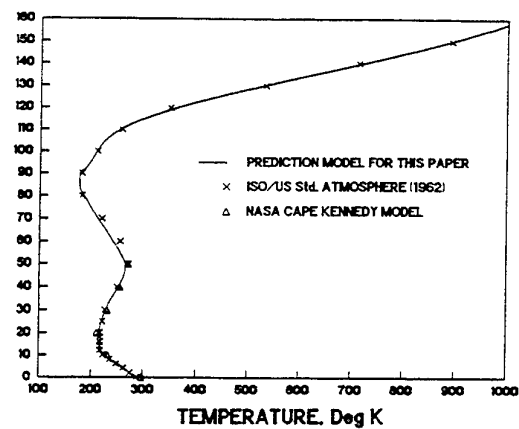
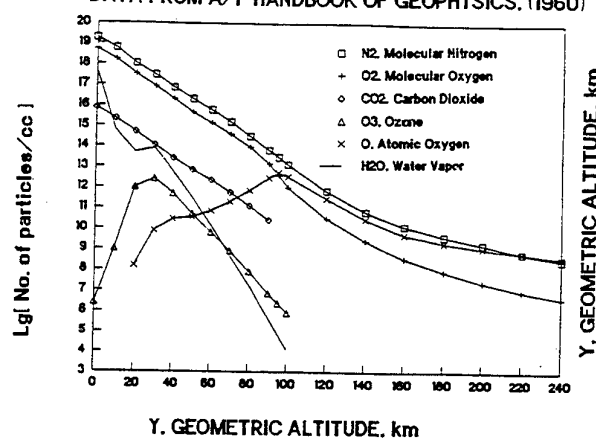
FIG. 4 DENSITY OF ATMOSPHERIC COMPONENTS
DATA FROM A/F HANDBOOK OF GEOPHYSICS, (1960)

FIG. 5 HUMIDITY PROFILE VS ALTITUDE

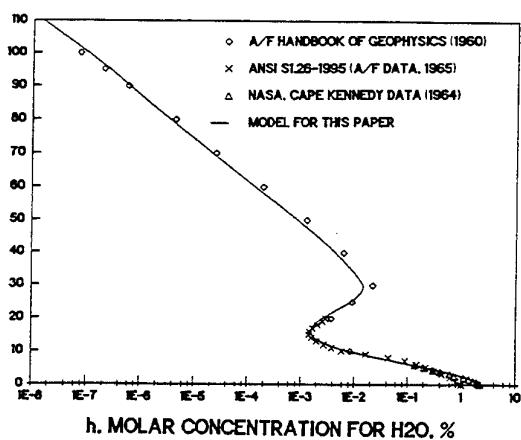


FIG. 6 k. RATIO OF SPECIFIC HEATS FOR AIR

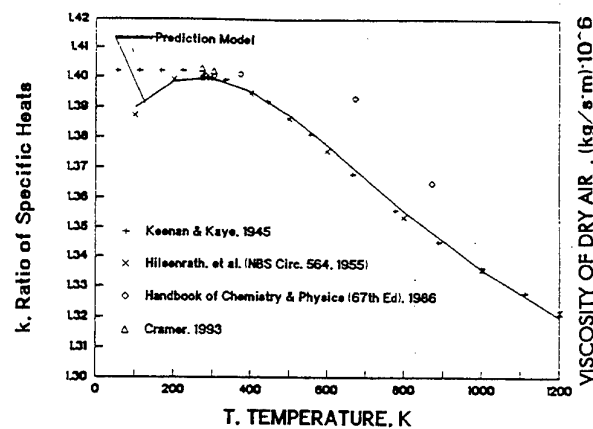


FIG. 7 VISCOSITY OF DRY AIR

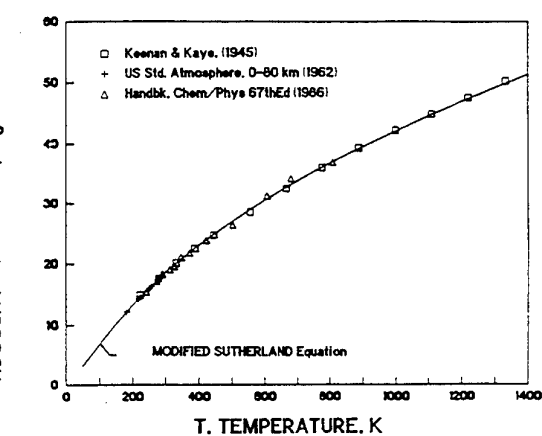


FIG. 8 COMPONENTS OF ATMOSPHERIC ABSORPTION, FREQUENCY = 1 Hz

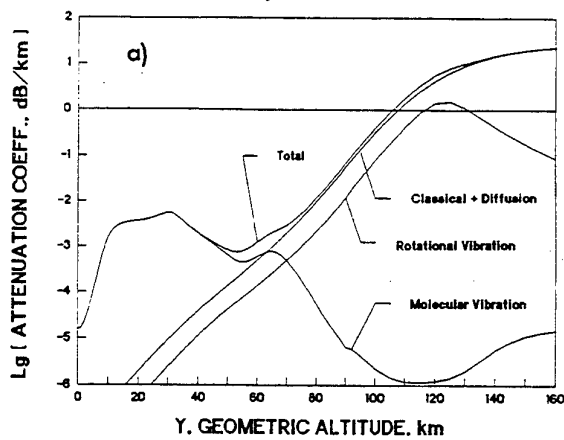
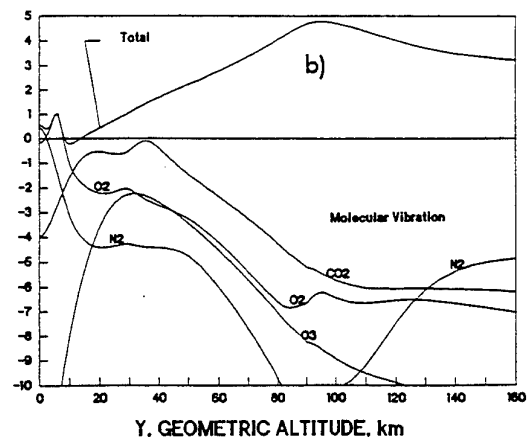
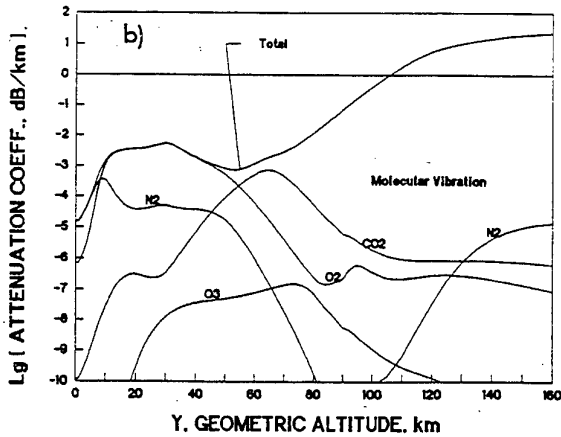
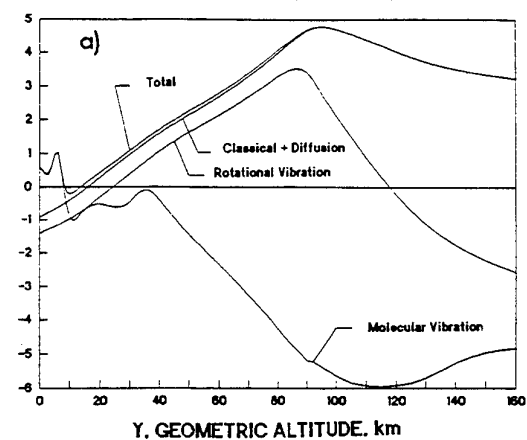


FIG. 9 COMPONENTS OF ATMOSPHERIC ABSORPTION FREQUENCY = 1,000 Hz



Seasonal and Diurnal Variations of Atmospheric Absorption for Horizontal Sound Propagation

Conny Larsson

Department of Meteorology
Uppsala University
Box 516
S-751 20 Uppsala, Sweden
Conny.Larsson@met.uu.se

ABSTRACT

Atmospheric absorption is important for outdoor sound propagation. Weather changes over the day and the year and this alters the atmospheric absorption. Thirty years of meteorological measurements from three stations in Sweden were used to determine the conditions for atmospheric absorption. The size of the monthly and daily variances was frequency-dependent. The most accurate information about atmospheric absorption climate is achieved if hourly values over thirty years are used. An increase in the accuracy of calculations of outdoor sound levels can be made by taking the local climate into consideration.

INTRODUCTION

Our understanding of sound propagation outdoors has increased considerably over the past few decades. However, meteorological conditions are seldom used as input to the different prediction models. Mean values for the conditions are sometimes used in the predictions, but two radically different condition distributions can have the same mean, thus including considerable errors. Use of more complete distributions gives more information and it has been found necessary to use continuous measurements of different meteorological variables over a longer period in order to get good models. Reviews of meteorological effects on sound propagation have been published.¹⁻³

These distributions can be obtained by expensive, long-term sound level measurements. This weather and climate information can be included in theoretical calculations.

The climate for an area or place is given by the mean value of fluctuating meteorological variables. However, the values of these variables are not constant over time. It is also necessary to know how large these fluctuations are. Calculated mean values naturally become more certain the longer the period over which they are calculated. On the other hand, climatic change can be masked if the period chosen is too long. Periods of thirty years are therefore used as climatological standards, sometimes called "normals".⁴ This "normal" climate is defined to assume comparability between data collected at various stations. The latest global standard normal period is 1961-1990.

This paper deals with such normals for three stations in Sweden. Hourly meteorological values for the years 1961-1990 have been used. The data have been provided by the Swedish Meteorological and Hydrological Institute. From this data, sound atmospheric absorption and

monthly and daily variations have been calculated.

METEOROLOGICAL EFFECTS ON SOUND PROPAGATION

Since 1976, investigations concerning meteorological effects on sound propagation have been carried out at the Department of Meteorology at Uppsala University. Many experimental and theoretical studies⁵⁻¹³ have been performed. Meteorological effects were noticeable even at a distance of twenty-five metres from the source and increased with decreasing receiver height.

The three most significant meteorological effects on sound propagation are: *refraction*, *scattering by turbulence* and *atmospheric absorption*. This paper will focus on the last effect. The other effects will only be discussed briefly.

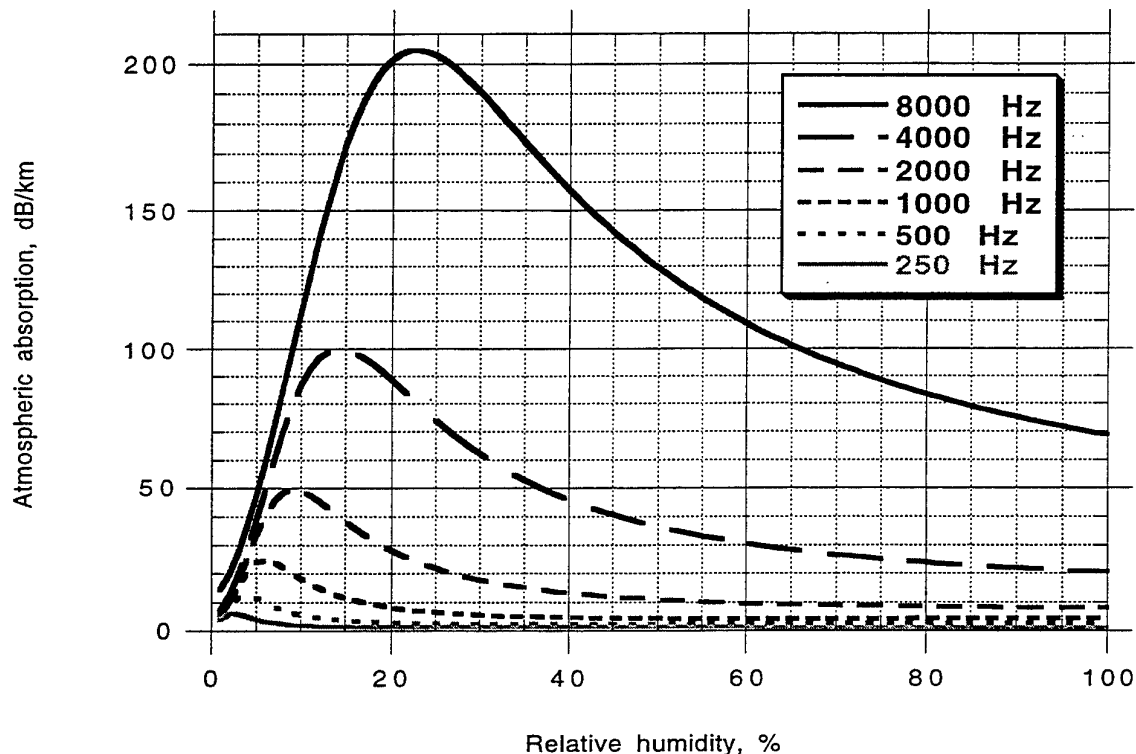


Fig. 1. Atmospheric absorption¹⁴(dB/km) for different sound frequencies (250-8000 Hz) under various conditions of relative humidity (%) at 15° C and normal air pressure (101.325 kPa).

Refraction

Refraction of sound rays occurs if the sound velocity and/or wind speed changes along the ray path, i.e., there are gradients of wind and temperature^{9,10}. The refraction influences the sound level. The angle of sound incidence at the ground changes, which results in varying ground attenuation. In downwind conditions and/or temperature inversion, the sound rays are bent downwards, and in upwind conditions and/or lapse, they are bent upwards. Upwind

conditions and/or lapse create areas, known as sound shadow zones, where no direct sound ray can reach. The refractive effects of temperature gradients and wind component gradients in the direction of propagation are additive. As the refractive conditions change, the path lengths of the various waves intersecting at the receiver change. Thus, depending on the phase relationships between these waves, some frequencies will be amplified and others muted.

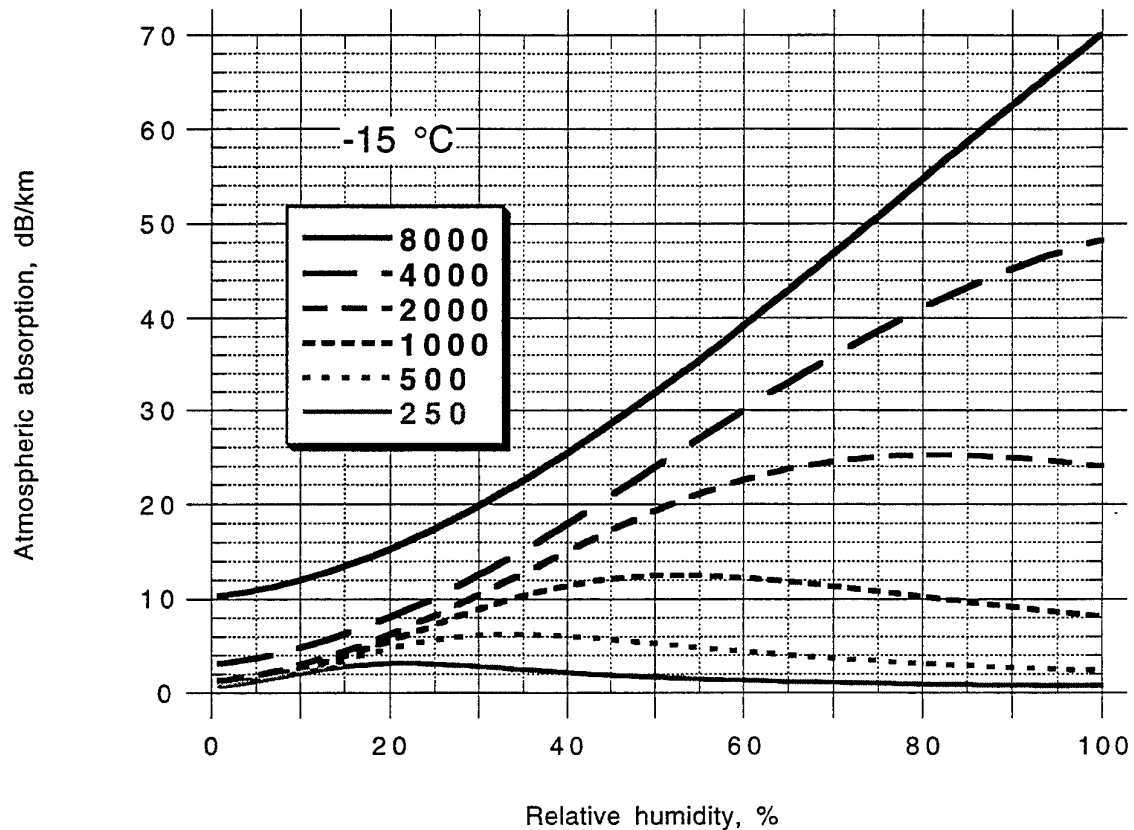


Fig. 2. Atmospheric absorption 14 (dB/km) for different sound frequencies (250-8000 Hz) under various conditions of relative humidity (%) at -15°C and normal air pressure (101.325 kPa).

Turbulence

Turbulence has a twofold effect on sound propagation. First, temperature fluctuations lead to fluctuations in the velocity of sound. Secondly, turbulence velocity fluctuations produce additional random distortions of the sound wave front. Turbulence scatters sound into sound shadow zones and causes fluctuations of the phase and the amplitude of the sound waves, thus destroying the interference between different rays reaching the receiver. This gives higher sound levels than expected for frequencies where the ground effect has its maximum. The effect of turbulence can be disregarded for low frequencies and distances up to a few hundred metres. When making measurements, integration over many turbulence cycles reduces the effect of turbulence on the sound level. Mean values over 5-10 minutes give more reproducible results than just an instantaneous measurement.

Atmospheric absorption

Atmospheric absorption depends on frequency, relative humidity, temperature and atmospheric pressure. A small part of a sound wave is lost to the air or other media through various physical processes. One important process is the direct conduction of the vibration into the medium as heat caused by the conversion of the coherent molecular motion of the sound wave into incoherent molecular motion in the air or other absorptive material. The viscosity of the medium also affects sound transmission. These two physical causes combine to produce the classical attenuation of a sound wave. Sound attenuation due to absorption can be calculated.¹⁴ Atmospheric absorption increases linearly with distance and becomes more important the longer sound propagation is under study. Figures 1 and 2 shows the atmospheric absorption for different frequencies and relative humidity at 15° C and for -15° C, respectively

Very little attenuation is found for low values of relative humidity or temperature. Monthly and diurnal variations in relative humidity and temperature introduce large variations in atmospheric absorption. Usually, relative humidity reaches its maximum soon after sunrise and its minimum in the afternoon when temperature is highest. The diurnal variations are greatest during the summer.

RESULTS

The ISO standard 9613 specifies methods of calculating the attenuation of sound propagation outdoors. Part 1¹⁴ is a detailed treatment restricted to attenuation by atmospheric absorption. Part 2¹⁵ is a more approximate and empirical treatment of attenuation by all physical mechanisms. This part states about atmospheric absorption "For calculation of environmental noise levels, an average atmospheric attenuation coefficient should be used based on the values determined by the range of ambient weather which is relevant to the locality." The discussion below shows the need for using the local climate and not just the average values. Differences in the results depending on how accurately the climate is described are also shown.

A computer program was written to calculate the atmospheric absorption based on the methods in ref. 14. Further developments of atmospheric absorption have been added.^{16,17} Hourly values of temperature and relative humidity at a height of 1.5 m above the ground and at atmospheric pressure were used to compute the atmospheric absorption. Long-term measurements of temperature and humidity close to the ground at three stations in Sweden were used as raw data to calculate the distribution for horizontal sound propagation.

Calculations based on complete distributions

Table 1 shows the location of the stations and Tables 2-3 gives some statistics for the calculated atmospheric absorption for Luleå and Ljungbyhed.

Table 1

The various stations used.

Name	Latitude, ° N	Longitude, ° E	Altitude above sea level, m
Luleå	65° 33'	22° 08'	10
Uppsala	59° 53'	17° 36'	18
Ljungbyhed	56° 05'	13° 14'	43

Table 2

Calculated atmospheric absorption in dB/km for Luleå based on hourly values of temperature, relative humidity and atmospheric pressure over thirty years (1961 to 1990).

Frequency, Hz	Mean	Maximum	Minimum
63	0.12	1.09	0.05
125	0.37	2.57	0.22
250	0.91	5.94	0.60
500	2.05	10.61	1.25
1000	4.96	15.96	1.38
2000	13.77	48.87	1.82
4000	40.15	108.32	3.54
8000	111.47	220.64	10.34

Table 3

Calculated atmospheric absorption in dB/km for Ljungbyhed based on hourly values of temperature, relative humidity and atmospheric pressure over thirty years (1961 to 1990).

Frequency, Hz	Mean	Maximum	Minimum
63	0.11	0.57	0.06
125	0.35	1.70	0.23
250	0.92	5.15	0.60
500	1.92	11.85	1.35
1000	4.01	17.89	3.12
2000	10.76	50.42	7.61
4000	34.66	102.55	11.11
8000	111.38	232.24	18.20

The cumulative distributions for the three stations are given in Figs. 3-5. These distributions give valuable information about the amount of atmospheric absorption and how often it occurs. From an environmental point of view, it is of special interest to know what the smallest absorption can be. The highest sound levels would occur during such a situation. Instead of looking at the smallest value during the thirty year normal, the 95% percentile can be used. That is the absorption value that is exceeded 95% of the time. For only 5% or 18 days and 6 hours during a year the atmospheric absorptions are lower. The data from this most northerly station varies over a wider range than from the other stations.

The three stations: Luleå, Uppsala and Ljungbyhed are located from north to south in Sweden. From Figs. 3-5, we can see that atmospheric absorptions increase the further south we go for 500 Hz and higher frequencies. For lower frequencies we see the opposite trend.

Large differences were found between the three locations. Comparison with a standard for atmospheric absorption from aircraft¹⁸, (Table 4 and Figs. 3-5) showed an overestimation of the absorption values between 7 and 70% of the time for these sites. Overestimation increased at higher frequency.

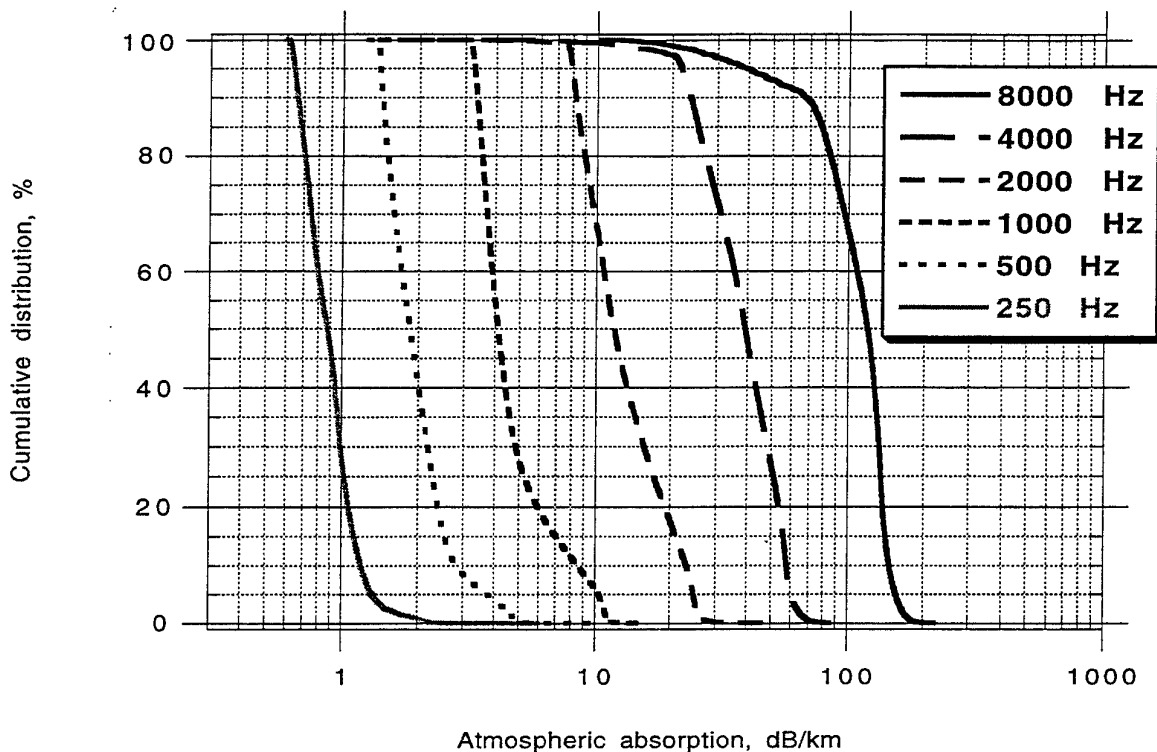


Fig. 3. Cumulative distributions for atmospheric absorption in dB/km at Luleå , Sweden.

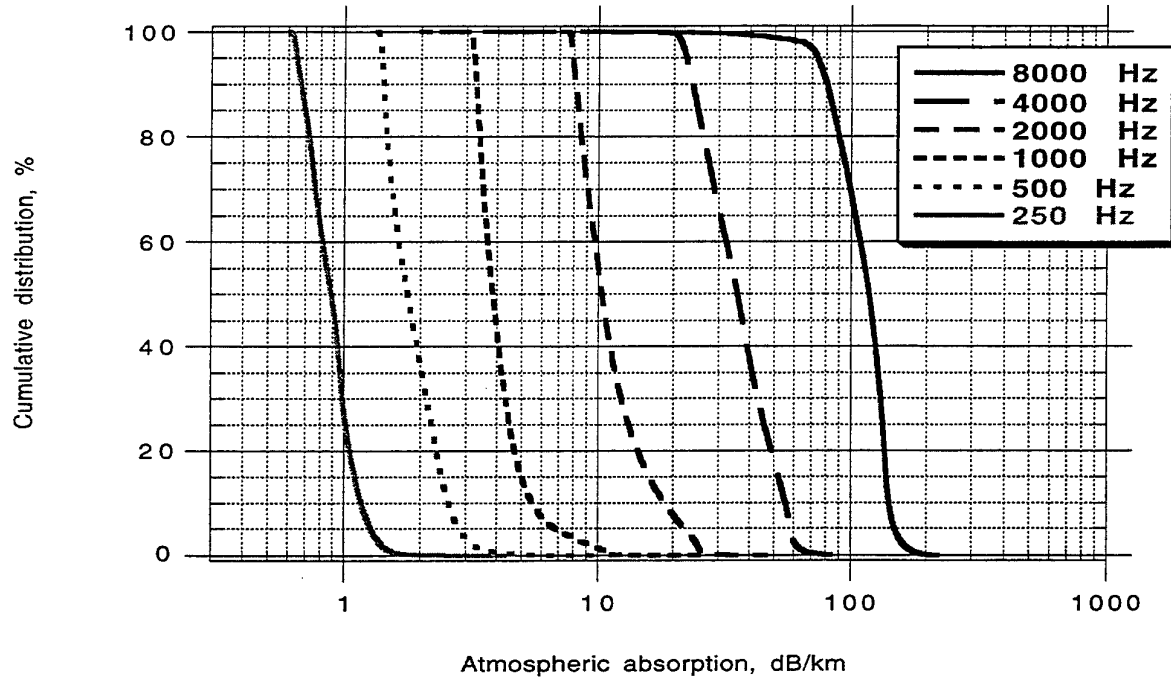


Fig. 4. Cumulative distributions for atmospheric absorption in dB/km at Uppsala, Sweden.

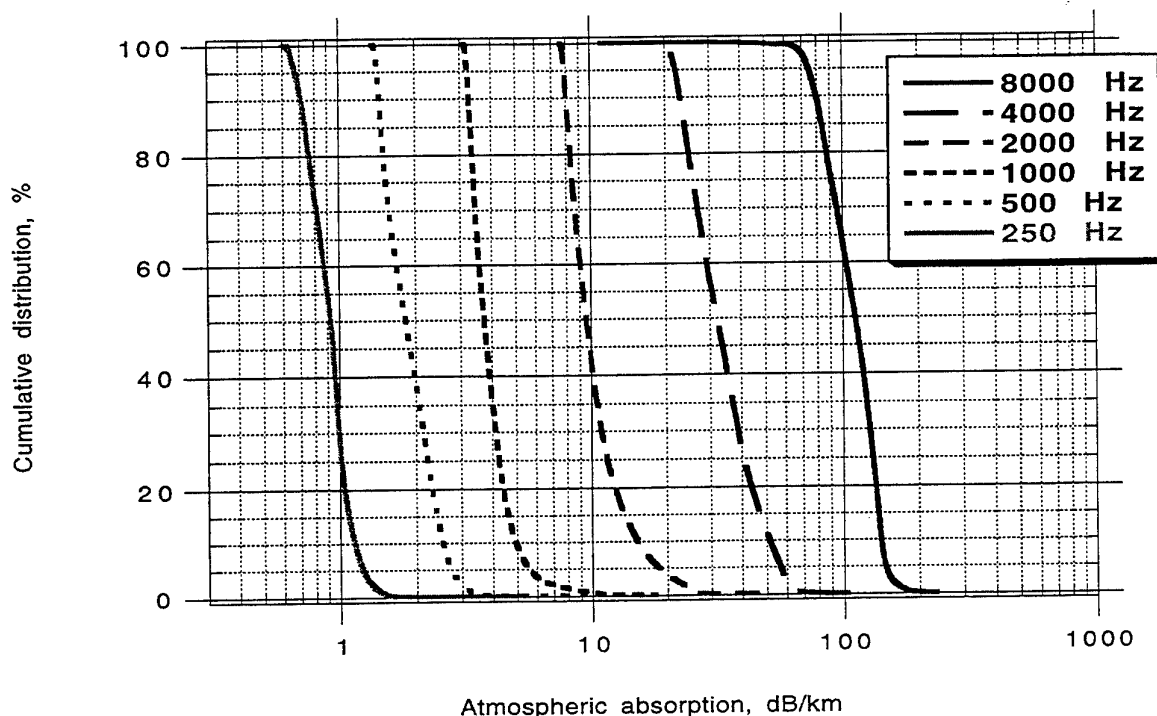


Fig. 5. Cumulative distributions for atmospheric absorption in dB/km at Ljungbyhed, Sweden.

Table 4.

Atmospheric absorption in dB/km according to ISO standard 3891¹⁸

125 Hz	250 Hz	500 Hz	1 kHz	2 kHz	4 kHz	8 kHz
0.381	1.13	2.36	4.08	8.75	26.4	93.7

Annual and diurnal variations

Let us now study the variations over the normal year and the normal day. The mean values for every hour and month for Uppsala are presented in Figs. 6-8. The frequencies 250, 1000 and 4000 Hz are given. Atmospheric absorption for the high frequencies changes at different times of the year. The absorption for low frequencies varies both over the day and the year. The size of the monthly and diurnal variance is frequency-dependent.

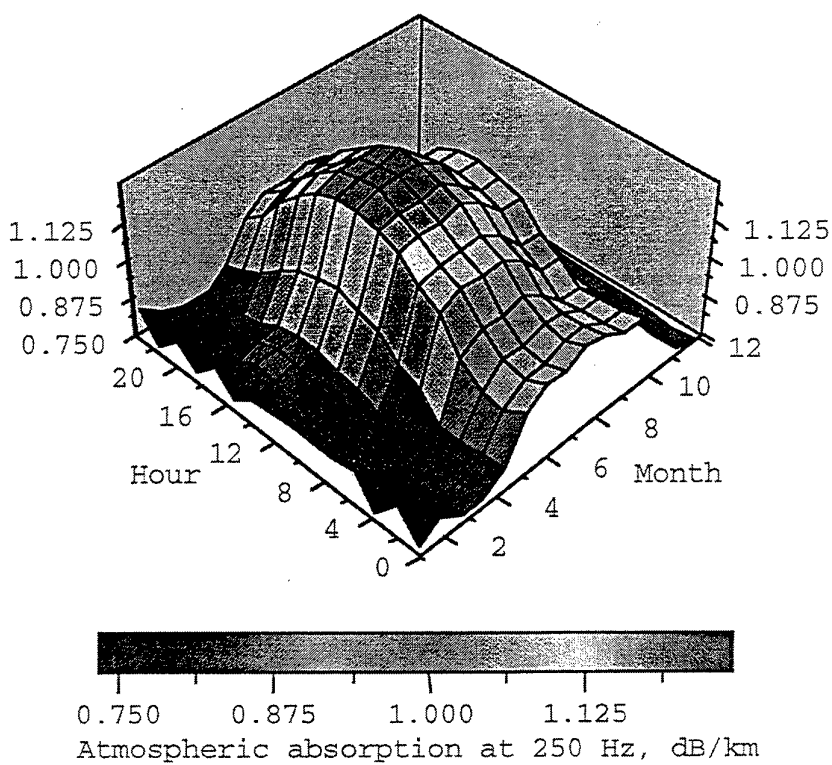


Fig. 6. Mean atmospheric absorptions in dB/km at 250 Hz for different times of day over the course of a year for Uppsala 1961-1990.

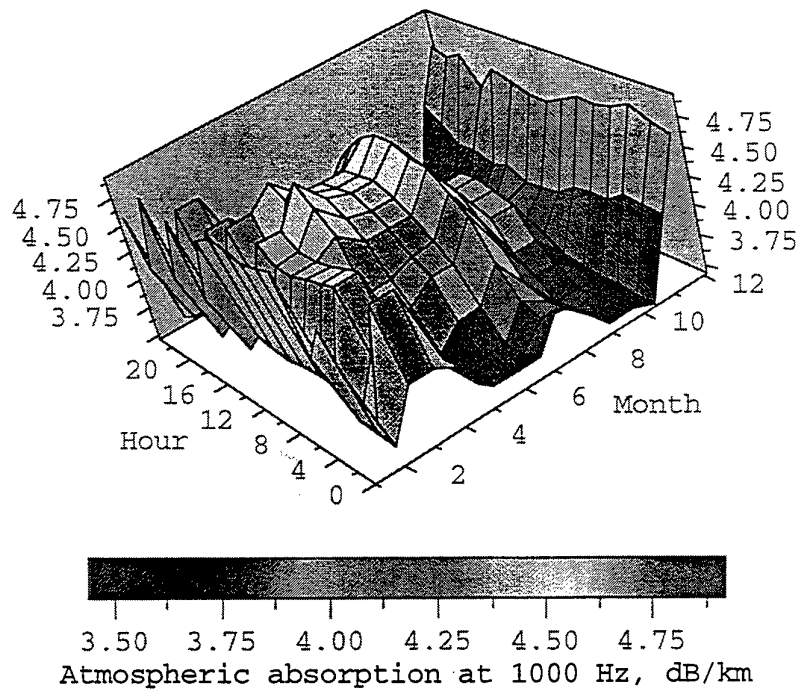


Fig. 7. Mean atmospheric absorptions in dB/km at 1000 Hz for different times of day over the course of a year for Uppsala 1961-1990.

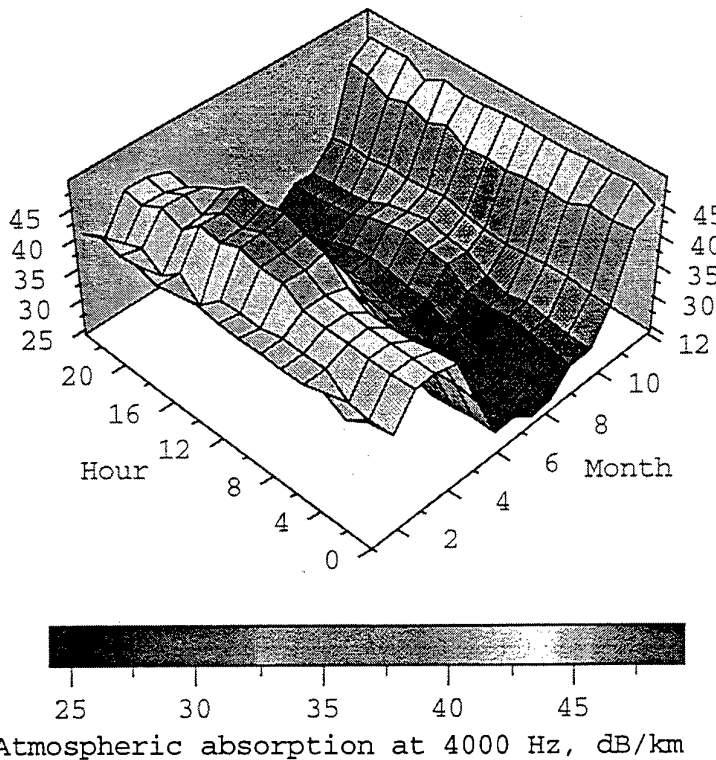


Fig. 8. Mean atmospheric absorptions in dB/km at 4000 Hz for different times of day over the course of a year for Uppsala 1961-1990.

CONCLUSIONS

Atmospheric absorption is important for long range sound propagation. Correct estimates of long range sound propagation need correct information for temperature and humidity.

Data-sets from local weather stations should be used. The accuracy of a predicted sound level is increased by using local data if thirty years of hourly measurements are used. The values of atmospheric absorption need to be calculated for the local climate instead of using some global mean value. The time has come to use data from local meteorological stations.

ACKNOWLEDGEMENTS

This study was supported by the Swedish Environmental Protection Agency.

REFERENCES

- 1 Delany, M. E., Sound propagation in the atmosphere: A historical review. *Acustica*, **38** (1977), pp. 201-23.
- 2 Piercy, J. E., Embleton, T. F. W. & Sutherland, L. C., Review of noise propagation in the atmosphere. *J. Acoust. Soc. Am.*, **61**(6) (1977), pp. 1403-18.
- 3 Larsson, C.: Meteorological effects on sound propagation. Current topics in acoustical research. Council of Scientific Information, India (1994).
- 4 Guttman, N.B.: Statistical descriptors of climate. *Bulletin of the American Meteorological Society*, **70**(6), (1989), pp. 602-607.

- 5 Larsson, C. and Israelsson, S.: The influence of the meteorological parameters on the sound propagation from a traffic road. Inter-Noise 79, Warszawa, Poland (1979), pp. 513-516.
- 6 Larsson, C. and Israelsson, S.: The effects of meteorological parameters on sound propagation from a point source. Report No. 67, Dept. of Meteorology, Uppsala (1982).
- 7 Hallberg, B., Larsson, C. and Israelsson, S.: Measurements of meteorological effects on long-range sound propagation using m-sequence correlation. J. Acoust. Soc. Am. **78**(3) (1985), pp. 1038-1044.
- 8 Larsson, C., Hallberg, B. and Israelsson, S.: Long-term audible noise and radio noise performance from an operating 400-kV transmission line. IEEE. Transactions on Power Delivery, 3(4) (1988), pp. 1842-1846.
- 9 Larsson, C. and Israelsson, S.: Effects of meteorological conditions and source height on sound propagation near the ground. Applied Acoustics **33** (1991), pp 109-121.
- 10 Larsson, C., Hallberg, B. and Israelsson, S.: A method to estimate meteorological effects on sound propagation near the ground. Applied Acoustics **25** (1988), pp. 17-31.
- 11 Larsson, C: Weather effects on sound propagation near the ground. Second International Congress on recent developments in air & structure-borne sound and vibration, Auburn, Alabama, U.S.A. (1992).
- 12 Hallberg, B., Larsson, C. and Israelsson, S.: A numerical ray tracing model for sound propagation. Department of Meteorology, Uppsala (1988) (in Swedish).
- 13 Hallberg, B., Larsson, C. and Israelsson, S.: Numerical ray tracing in the atmospheric surface layer. J. Acoust. Soc. Am. **83**(6) (1988), pp. 2059-2068.
- 14 International Standard Organization 9613 (1993): Attenuation of sound during propagation outdoors. Part 1: Calculation of the absorption of sound by the atmosphere.
- 15 Draft International Standard 9613-2.2 (1994): Attenuation of sound during propagation outdoors. Part 2: General method of calculation.
- 16 Bass, H.E., Sutherland, L.C., Zuckerwar, A.J., Blackstock, D.T. and Hester, D.M. (1995).: Atmospheric absorption of sound: Further developments. Journal of the acoustical Society of American, Vol **97**(1) January 1995. pp. 680-683.
- 17 Bass, H.E., Sutherland, L.C., Zuckerwar, A.J., Blackstock, D.T. and Hester, D.M. (1996).: Erratum: Atmospheric absorption of sound: Further developments. Journal of the acoustical Society of American, Vol **99**(2) January 1996. p. 1259.
- 18 International Standard Organization 3891: (1978): Acoustics - Procedure for describing aircraft noise heard on the ground.

Infrasonic Signals from an Accidental Chemical Explosion

J. P. MUTSCHLECNER and R. W. WHITAKER

*Los Alamos National Laboratory
Los Alamos, New Mexico, U.S.A.
Fax (505) 665-3687*

BACKGROUND

A series of large accidental explosions occurred at a chemical plant in Henderson, Nevada on May 4, 1988. The explosions were produced by the ignition of stores of ammonium perchlorate produced for solid rocket fuel at the Pacific Engineering and Production Co. This material, prior to the incident, had been believed to be non explosive. The blasts destroyed the plant and caused one death. There was a series of explosions over a period of time with two major explosions which we will identify as A at 18:53:34 (all times herein will be given in C.U.T.) and B at 18:57:35. J. W. Reed (1992) provides further details of the explosions in his report on near-field blast damage. Signals from events A and B as well as smaller events were detected by the infrasound arrays operated by the Los Alamos National Laboratory at St. George, Utah (distance 159 km) and at Los Alamos, N.M. (distance 774 km).

EQUIPMENT

The two infrasonic arrays are operated in a continuous mode and thus were able to monitor these explosions. Both arrays utilize 100C microphones produced by the Chapparal Physics Co. There were five microphones at St. George and four at Los Alamos. The microphones are connected to noise reducers consisting of a series of porous hoses radiating from the microphones. The overall size of the arrays is about 200 m. In typical operation the sampling rates are 20 samples per second and the frequency band analyzed is 0.5 to 3 Hz. A standard beam-forming procedure is employed in the analysis.

THE DETECTIONS

Figure 1 shows a portion of the analysis output for St. George. Each dot represents the results for a 20 second window of the azimuth; the trace velocity, and the average correlation coefficient between the sensor pairs; the multiple signals are obvious in the change in character from the random pattern of the dots to lines. Events A and B both produced two signal at each array due to differing propagation paths.

Table I provides the details of the signals and shows, in order, the signal name, the peak arrival time T, peak-to-peak amplitude A, peak frequency F, the trace velocity V_t, the azimuth Θ, and the average propagation velocity V. The azimuths show reasonable accord with

the expected great-circle azimuths of 230.5° for St. George and 274.0° for Los Alamos. The differences are close to our usual variance of about 3° .

INTERPRETATION

The occurrence of double signals for each event at both arrays indicates that two propagation channels were present for signal transmission to each site. However the differing velocities between the two sites strongly suggests that the physical mechanisms were different for the two arrays.

The St. George site is located only about 0.6 of a typical ozonospheric bounce distance from the source and so the signals there are unlikely to be ozonospheric returns according to our present understanding. Other possible mechanisms for the high velocity St. George signals are tropospheric returns or Lamb wave propagation. From the trace velocities we deduce an inclination angle to the surface of the arriving rays of about 9° . This, in turn, implies a maximum propagation height of about 12 km. A preliminary examination of the atmospheric profiles up to about 10 km in the source area does not appear to support the notion of tropospheric propagation. In Figure 2 we show a portion of the signal B1. The abrupt onset of the signal is suggestive of a Lamb wave. The signal A1 shows a very similar character. On the other hand, there is some question of the ability of Lamb waves to be effective at such short ranges. ReVelle and Whitaker (1996) provide further discussion of Lamb wave characteristics. The secondary signals at St. George with $V = 0.275$ km/s appear to have V too low for normal ionospheric returns. At the same time the trace velocities are too low for normal ozonospheric returns and, again, ionospheric or ozonospheric returns normally would not be expected at this short range from the source. Consequently at present we cannot explain the nature of A2 and B2. The peak frequencies show reasonable consistency between A1 and B1 and again between A2 and B2.

At Los Alamos the principal signals from A and B have $V = 0.297$ km/s which is normal for ozonospheric propagation. Los Alamos is about 3.1 ozonospheric bounces from the source. The trace velocities give an inclination angle of about 17° which suggests a maximum propagation height of about 36 km. This is low but plausible for ozonospheric propagation. The smaller signals with $V = 0.280$ km/s are also probably ozonospheric since their trace velocities support this. It should be noted that in our experience there are frequently two or more signals near the ozonospheric return velocity from large sources. The peak frequencies are considerably larger than those at St. George except for B2.

It is clear that a full interpretation of the signals at St. George will require further analysis including possible modeling efforts using available wind data.

SIGNAL CONGRUENCE

One of the interesting features of the signals at St. George is the close congruence of some of the signals over a period of time. Figure 3 gives a comparison of the signals A2 and B2 for a period of over one minute near their peaks. There is a striking agreement of the two signals for features of about 2 second period and longer with some agreement even for shorter periods. These two signal regions are separated by four minutes. Presumably this gives an indication of atmospheric constancy for infrasound propagation over this interval of time and at this distance; an interpretation might be possible in terms of atmospheric turbulent element "lifetime". The fact that A and B are distinctly different sources in terms of configuration, size and perhaps detonation characteristics and yet produce such signal similarity is an indication that at a range as small as that to St. George the local source character is effectively reduced to a "point source" for propagation purposes.

EXPLOSION YIELDS

We attempt to make an estimate of the explosive yield for sources A and B using the relation

$$A^* = 4.69 \times 10^4 \times (R/W^{1/2})^{-1.35} \quad (1)$$

where A^* is an amplitude in microbars corrected for the effects of stratospheric winds as previously described by Mutschlechner and Whitaker (1990), R is the range in kilometers, and W is the explosive yield expressed in kilotons of nuclear free air burst. The expression 1 is an improved version, using two additional events, of that given by Whitaker et al (1990) derived empirically from the observation of experimental chemical high explosive sources. Since this relation was derived for ozonospheric signals, we employ the signals A1 and B1 at Los Alamos. Available stratospheric observations of the zonal and meridional components of the winds were used to estimate the correction from A to A^* but these corrections are quite small since May 4 is close to the transition time of the stratospheric zonal winds. We obtain for sources A and B respectively 1.4 and 3.7 kilotons nuclear equivalent free air burst yields or about 0.7 and 1.8 kilotons of surface burst. Reed (1992) has estimated the explosive size by his analysis method which employs close-in blast damage reports, in this case from Henderson and Las Vegas, Nevada. He finds a source size of 227 Mg of HE on the surface which is approximately equivalent to a 1 kiloton nuclear air burst. Thus our estimate is larger than Reed's by nearly a factor of four. At the present time the cause of this disagreement is not understood although it may be related to the fact that the blast damage is probably caused by low elevation propagation whereas the ozonospheric signals are produced by the launch of much higher elevation rays.

CONCLUSIONS

The Henderson explosions present an interesting and challenging set of infrasound observations. The case may be unique in providing two very large sources separated in time by only four minutes. To fully understand the propagation details will require further analysis and probably a modeling effort. The understanding of the St. George signals in the context of Lamb waves would be valuable for a better understanding of this mode of propagation.

The improved understanding of long range infrasonic propagation is now especially important in the context of the Comprehensive Test Ban Treaty (CTBT). A portion of the plan for CTBT monitoring includes a global distribution of sixty infrasound arrays to provide for the monitoring of signals in as uniform a way as possible. It is expected that under this global network many signals and interpretation questions of the type described here will be encountered. Investigations of propagation over the ranges of hundreds to thousands of kilometers will be highly desired.

ACKNOWLEDGMENTS

We are grateful to Douglas ReVelle for discussion of the work, to Jack Reed for providing details of his analysis, and to Masha Davidson for assistance with the data analysis. The work was supported by the Department of Energy, Office of Nonproliferation and International Security, DOE HQ, NN-20.

REFERENCES

- Mutschlechner, J. P. and R. W. Whitaker, Correction of Infrasonic Signals for Upper Atmospheric Winds, Fourth International Symposium on Long-Range Sound Propagation, NASA Conference Publication 3101, 143, 1990.
- Reed, J. W., Analysis of the Accidental Explosion at PEPCON, Henderson, Nevada, on May 4, 1988, Propellants, Explosives, Pyrotechnics, 17, 88-95, 1992.

ReVelle, D. O. and R. W. Whitaker, Lamb Waves from Airborne Explosion Sources: Viscous Effects and Comparison to Ducted Acoustic Arrivals, Seventh Long Range Sound Propagation Symposium, 1996.

Whitaker, R. W., J. P. Mutschlechner, M. B. Davidson, and S. D. Noel, Infrasonic Observations of Large-Scale HE Events, Fourth International Symposium on Long-Range Sound Propagation, NASA Conference Publication 3101, 133, 1990.

TABLE I: SIGNALS FROM THE HENDERSON EXPLOSIONSt. George, Utah

Sig ID	T	A	F	V _t	Θ	V
A1	01:33	92	0.643	347	236	332
A2	03:13	43	0.536	347	236	275
B1	05:33	108	0.621	347	236	333
B2	07:14	72	0.566	347	236	275

Los Alamos, New Mexico

Sig ID	T	A	F	V _t	Θ	V
A1	36:58	6.8	0.820	354	278	297
A2	39:40	4.7	0.810	354	278	280
B1	40:57	12.9	0.830	354	278	297
B2	43.34	3.0	0.689	354	278	280

Column Notes

T = minutes : seconds after 19 hours C.U.T.

A = p-p amplitude in μ bar

F = peak frequency in Hz

 V_t = trace velocity in m/s Θ = azimuth in degrees from N through E

V = average signal velocity in m/s

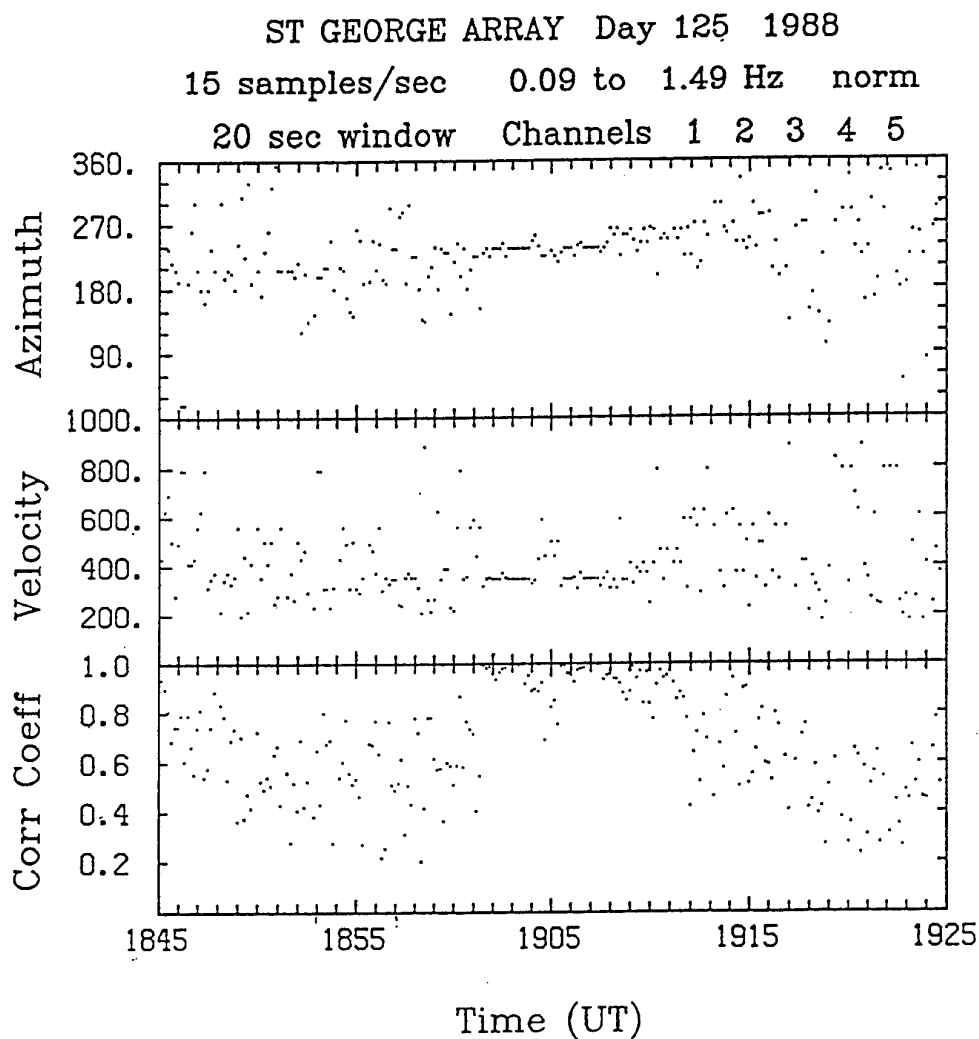


FIGURE 1. Survey plot showing the analysis of St. George data for the Henderson event. The panels from top to bottom show the azimuth from the array in degrees, the trace velocity in meters / second, and the average correlation coefficient.

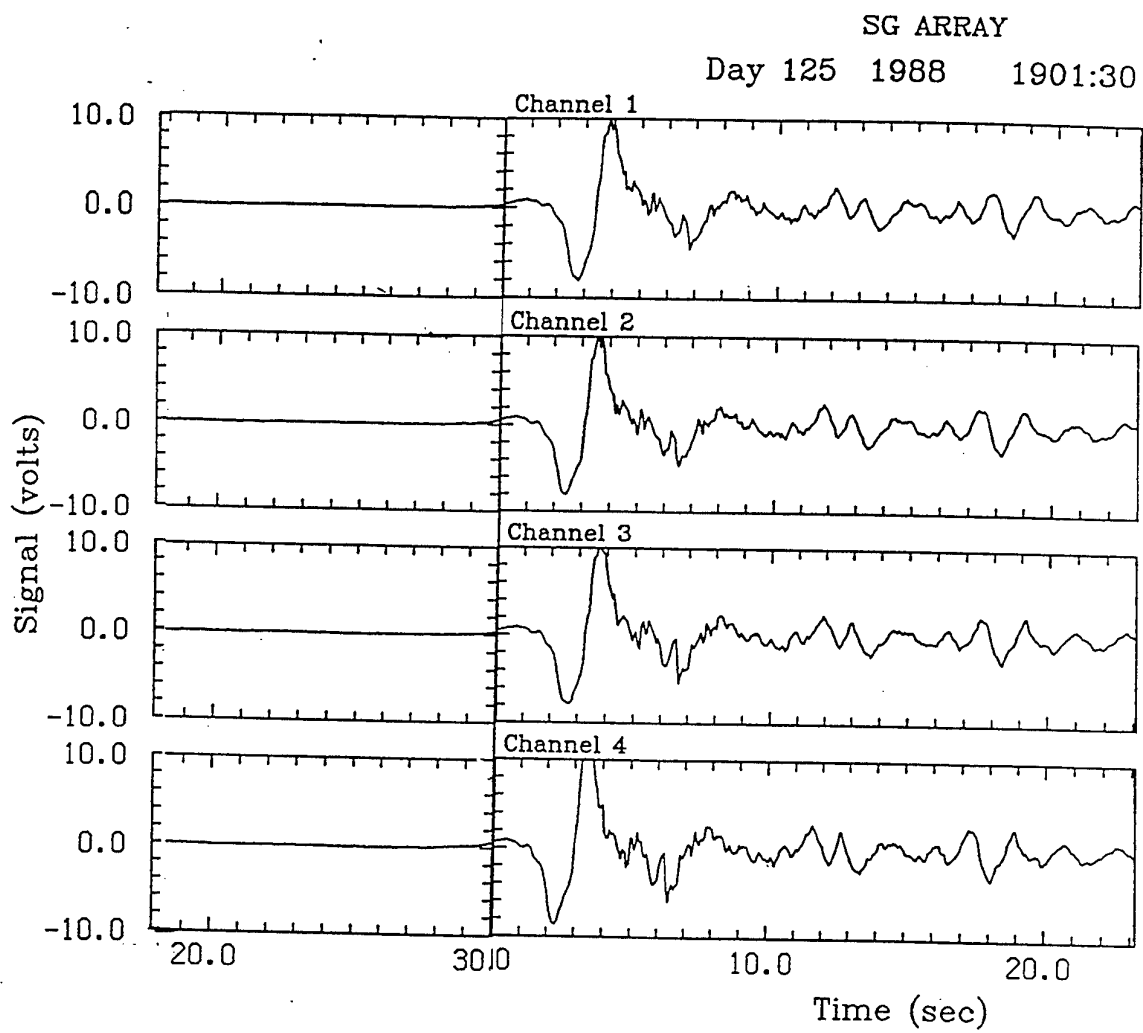


FIGURE 2. A portion of the signal B1 seen at St George showing the abrupt onset of the signal. Signal level is given in microphone volts (about 0.2 volts / μ bar).

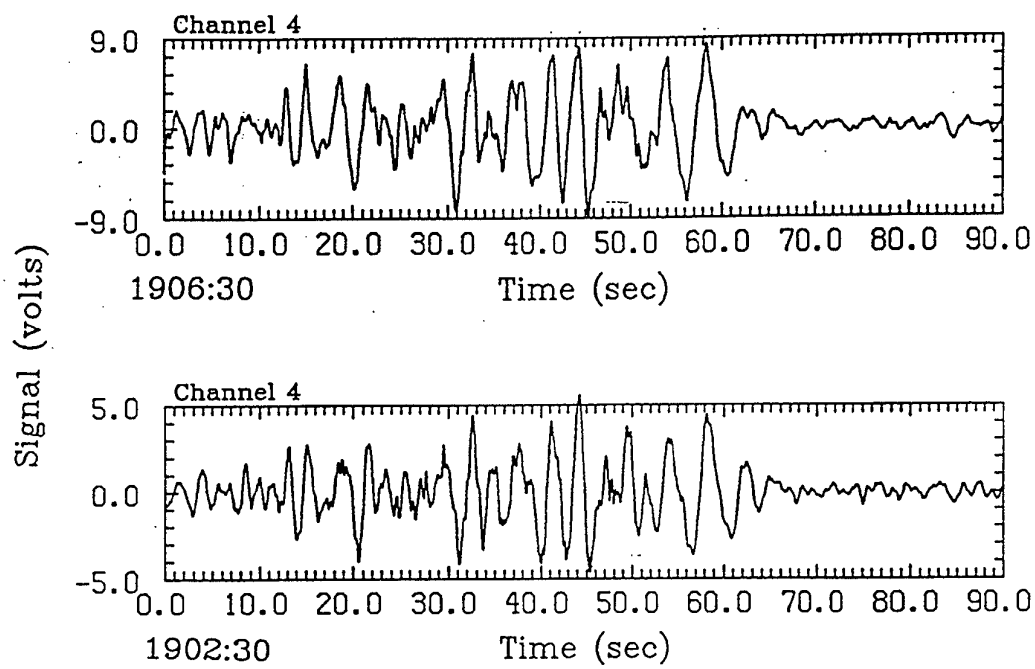


FIGURE 3. A comparison of a portion of the signals B2 (top) and A2 (bottom) at St. George showing the close similarity of the signals.

Some Results of Sound Propagation Experiments

P. Naz, G. Parmentier

*French-German Research Institute of Saint-Louis (ISL)
PO Box 34, 68301 SAINT LOUIS Cedex (France)*

Abstract

In the last years, several experiments have been carried out to study the acoustic noise propagation in the low atmosphere. The NATO experiments (JAPE-91, AMI-2, etc.) have been carried out in cooperation between several laboratories. The acoustic data collected have been merged and the influence of some physical parameters is noticeable:

- influence of the frequency of sound,
- influence of the height of the source,
- influence of the direction of propagation, related to the meteorological conditions.

In most cases, when the environmental conditions are well known, it is found that the FFP algorithm or the ray tracing model give a relatively good prediction. The predictions given by these numerical models have been compared to the experimental data obtained during the field trials. The necessity to have meteorological profiles, carefully measured or predicted by a numerical model is noted.

1 - Introduction

Long-range sound propagation through the lower layer of the atmosphere has been studied intensively during the past decade, due to environmental consideration (traffic noise, airport noise, etc.) and to military applications (helicopter detection, etc.). For these two kinds of applications, it is necessary to know the sound at its source as well as the changes brought about by the propagation through the atmosphere and signal reception. Acoustic signals are influenced by the medium of propagation, the nature of the ground, the terrain features and vegetation. In the context of defense applications, and in order to support the development of the theoretical part of these subjects, international experiments have been carried out to study experimentally some of these phenomena and to collect data for the validation of numerical models. The field trials in which ISL has been involved and which will be referred to in this paper, have been organized by the NATO P III, Research Study Group 11 (Experiment AMI-2 and JAPE [1]). These experiments involving specialists in different branches of physics have permitted to do acoustic measurements in parallel to the characterization of the environmental conditions (meteorology, site characteristics, etc.). With the same goal, benchmark cases for outdoor propagation models [2] have been proposed by members of the RSG 11.

In France, under the coordination of the DGA/DRET, work has been done by ONERA, CSTB and ISL on the numerical simulations of the acoustic propagation phenomena. The research carried out in coordination between these laboratories has allowed the evaluation of different numerical methods and the comparison of the predictions with the experimental results.

2 - Experiment AMI-2 (*Acoustic Measurement Initiative*)

The AMI-2 experiment carried out as part of an international cooperative effort has shown the effects of meteorological conditions on the range of hearing of helicopter noise. In addition to its operational interest, the use of a helicopter as a sound source allows the generation of a high-power, low-frequency noise that is propagated over great distances.

Considering the combined effects of temperature and wind gradients, it has been observed during these tests that the attenuation of sound is more important in the middle of the day than at sunset or sunrise. The wind causes a convection of the acoustic waves, as the temperature gradient deviates its trajectories. So shadow zones, as well as focalization zones may be observed. In intermediate meteorological conditions, the sound becomes more noticeably attenuated against the wind, and is reinforced in the opposite direction.

From an operational point of view, it means that the detection range may be modified by the meteorological conditions and may vary with the azimuth of observation.

The plot of the pressure field at ground level (fig. 1) shows an example of the directivity of the acoustic propagation. This characteristic, associated with the intrinsic directivity of the source, has to be taken into account for the exact estimation of the noise level map and for the prediction of the detection distances.

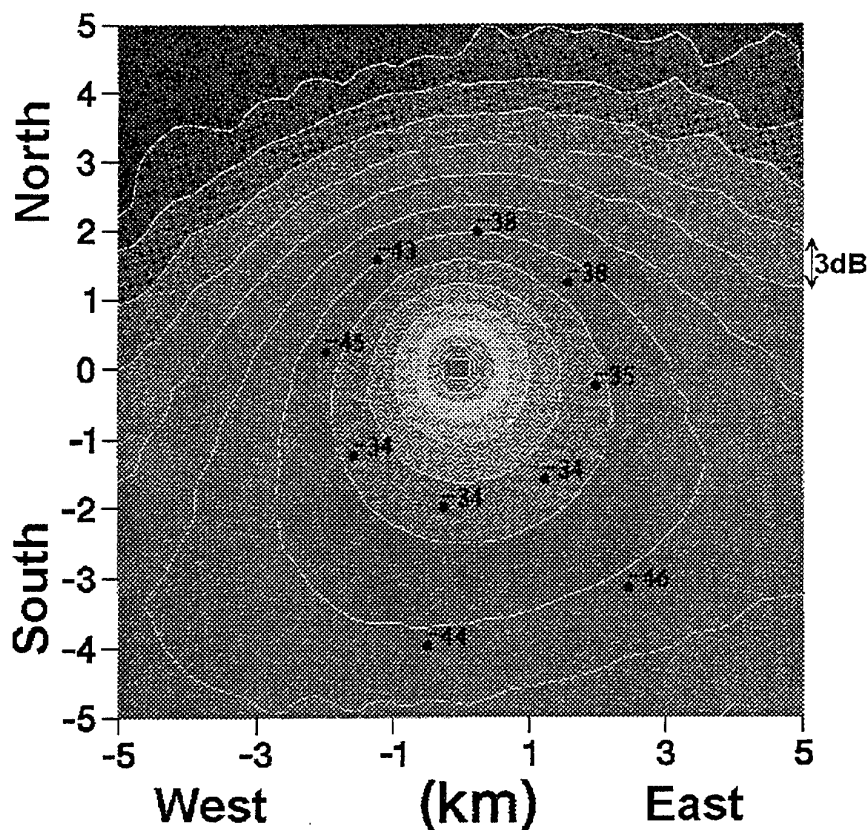


Fig. 1: Pressure field at ground level (computation - experiment comparison)

These factors of influence are complex but quantifiable, and taking them into account by solving the mathematical equations relating to the various physical phenomena (absorption, reflection, refraction) will improve the results of detection and localization algorithms.

The first standard approach is based on ray trace modeling. This method allows the computation of the trajectories of acoustic rays emitted by the source (fig. 2), taking into account their curvatures as a function of the meteorological profiles and of their reflection on the ground ((1) to (3)).

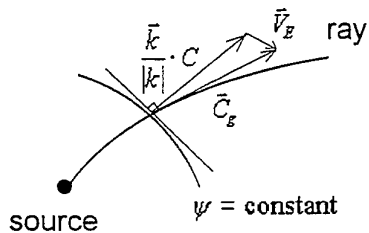


Fig. 2: Acoustic ray

$$\frac{d\vec{r}}{dt} = \vec{C}_g = \vec{V}_E + \frac{\vec{k}}{|k|} \cdot C \quad (1)$$

$$\frac{d\vec{k}}{dt} = -\vec{k} \cdot \vec{g} \nabla \text{ad } C - k_j \cdot \vec{g} \nabla \text{ad } V_{E_j} \quad (2)$$

$$\frac{d\psi}{dt} = 0 \quad (3)$$

with:
 C : sound velocity
 \vec{k} : wave vector
 t : time
 V_E : wind velocity
 ψ : phase

The second approach is based on the classical wave propagation for the acoustic pressure. Assuming that the acoustic pressure can be described by a cylindrical wave, slowly modulated by the distance of propagation, the wave equation can be written in the classical parabolic form (4):

$$\nabla^2 p - \frac{1}{C^2} \cdot \frac{\partial^2 p}{\partial t^2} = -4\pi \cdot \delta(x, y, z), \quad (4)$$

$\nabla^2 p$: Laplacian operator applied to pressure
 x, y, z : Cartesian coordinates
 δ : delta function

This equation can be discretized and solved numerically step by step, a method known as the parabolic approximation. If the Hankel transform is applied to the equation (4), an ordinary differential equation is obtained. The numerical integration of this equation can be processed for each elementary frequency after the introduction of the adequate Green function. A lot of progress has been achieved on FFP and PE (Parabolic Equation) methods during the last years.

The following figures show, for the same meteorological configuration, the results of computations done with the ISL ray tracing model (fig. 3) and with the CERL-FFP method (fig. 4). The computations of the acoustic propagation are done either in the two vertical half-planes corresponding to the measurement axis, or for a number of adjacent angular sectors covering the 360° surrounding the acoustic source. The map of the acoustic level in the horizontal plane corresponding to the microphone height can be reconstructed with these results. This type of graphical plot allows an easy representation of the directivity of the propagation (fig. 1). This characteristic, associated with the directivity of the source, has to be taken into account for a better prediction of the detection distances.

The values of the sound pressure level computed with these two methods (ray tracing and FFP) are very close to one another and also to the experimental values measured during the AMI-2 campaign, at least for propagation ranges in the order of 4 km [3].

Applied at the limit of its theoretical domain of validity, the ray tracing model has allowed to obtain satisfactory results for the low frequencies studied. The introduction of the meteorological profiles and of the ground characteristics in the numerical models has made it possible to improve the predictions as compared with the simple isotropic propagation equation.

The differences observed between the predictions and the experimental values are between 3 and 5 dB (fig. 5). These differences, even small in mean values, may be locally (and temporarily) in the order of 10 dB. During these trials only a few shadow zones were observed; but it is suspected that in these configurations, the differences between the predictions made with the two methods would be more noticeable.

A more detailed analysis of the comparisons between the computations and these experiences [3] shows that the precision of the prediction may be increased if some efforts are made concerning the following points:

- prediction in the shadow zones,
- profiles of the meteorological parameters,
- measurement and modelisation of the fluctuations of the meteorological data.

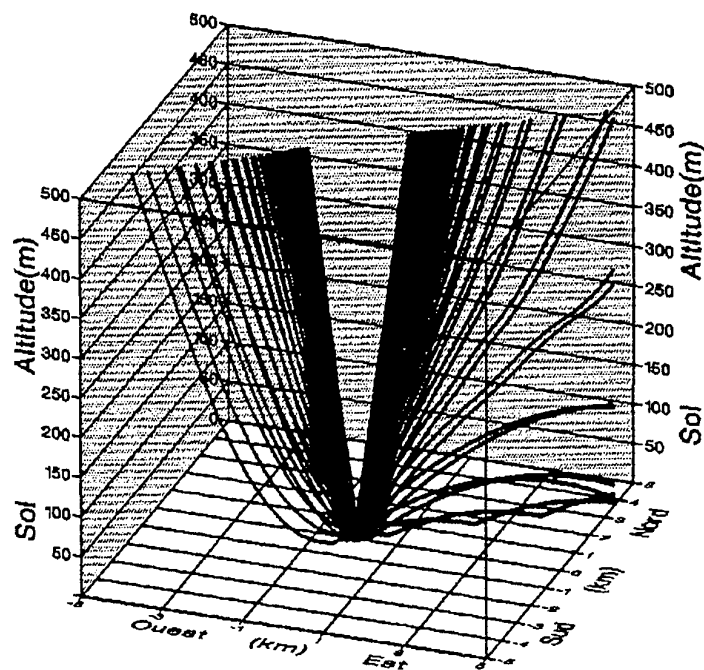


Fig. 3: Ray traces corresponding to the measurement axis

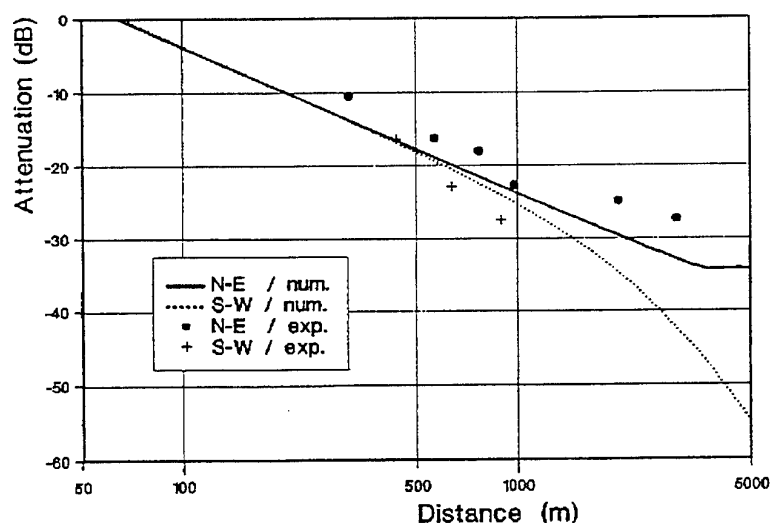


Fig. 4: Comparison of the prediction-experimental values (case corresponding to fig. 3)

distance	$r = 2 \text{ km}$	$r = 4 \text{ km}$
flying height		
$h = 5 \text{ m}$	2.5 ± 2.2	2.5 ± 4
$h = 50 \text{ m}$	2.9 ± 2.5	4.6 ± 3

Fig. 5: Difference between prediction and experimental attenuations
(mean value, standard deviation (dB))

3 - JAPE-91 (*Joint Acoustic Propagation Experiment*)

During field trials such as those described in chapter 2, some of the flight or environmental parameters are neither constant nor easily verifiable. So during the JAPE-91 experiments, also organized with the NATO RSG 11 group, some more academic tests were carried out. The objectives of these tests are to complete the studies of physical phenomena occurring during the propagation of acoustic waves through the atmosphere, accompanied by carefully documented meteorological and terrain conditions. For this purpose, a substantial instrumentation (acoustical, meteorological, etc.) has been brought into operation on the field and by different laboratories (US-ARL, WES, Univ. of Mississippi, MIT, KAE, ISL, etc.). Pure tones and mixed tones have been broadcast successively by four loudspeakers (fig. 6).

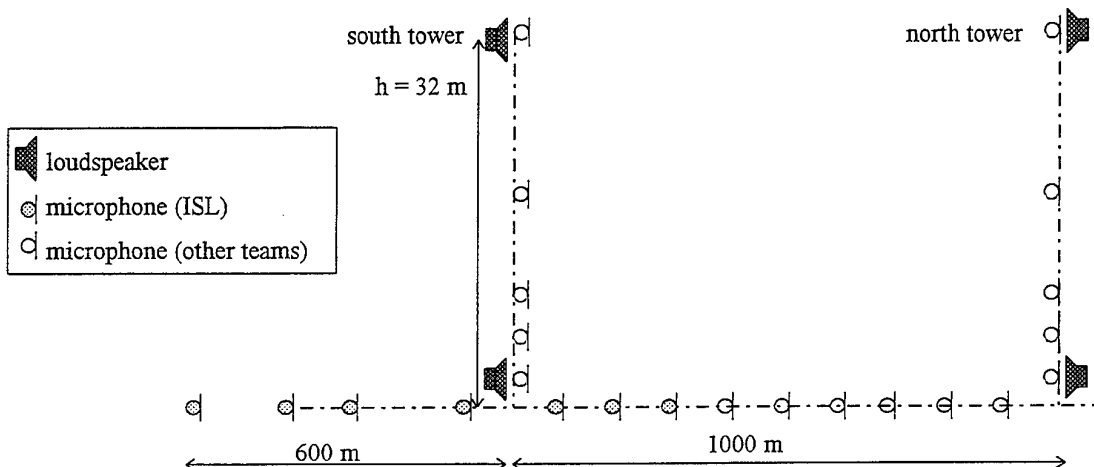


Fig. 6: Geometrical configuration of the measurement set-up

The data measured by some of the laboratories have been merged, allowing to analyse and to quantify the influence of some physical parameters:

- Effect of the wind:

the differences between the two opposite directions show the influence of the shadow zones and the sunny ones (upward and downward refractive conditions). The sunny or shadowy character (acoustically) is much pronounced if the difference, between the two sides, of the sound speed gradient is important. This characteristic is accentuated if the source is close to the ground (fig. 7).

- Influence of the height of the source:

The decrease of the sound level is more important if the source is close to the ground (fig. 8). On these two figures (7, 8), the rays traces corresponding to the experimental conditions have been plotted on the right-hand side of the figure for a quick look at the propagation conditions.

- Influence of the frequency : globally, the classical feature is observed; the low frequencies are less attenuated than the higher ones. Two kinds of tests have been done : for the first one, 3 pure tones have been mixed and broadcast simultaneously. For the second kind of test, a series of pure tones following one another has been broadcast. The homogeneity of the data obtained during the first kind of test has been much greater than

during the second one, illustrating once more the influence of the fluctuation of the meteorological conditions.

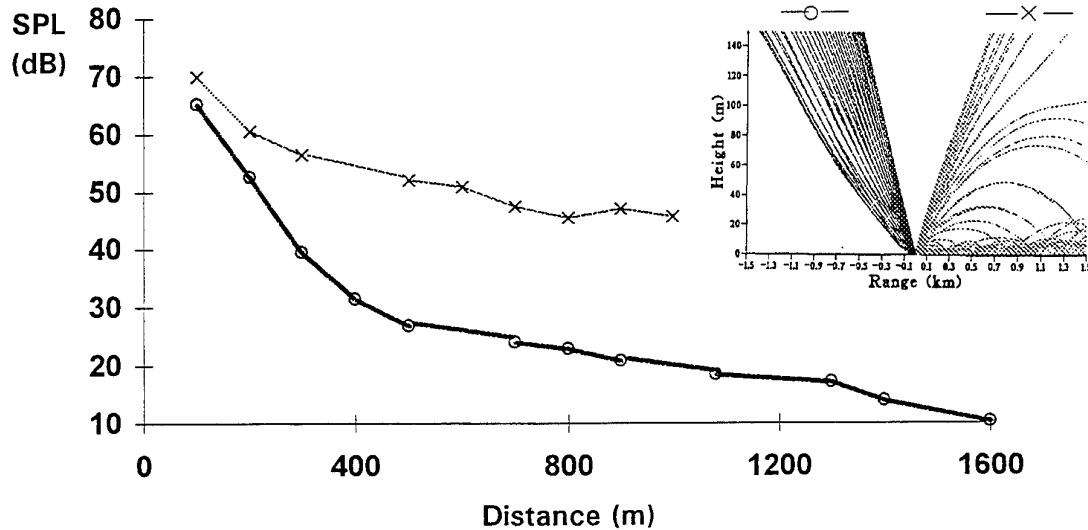


Fig. 7: Influence of the direction of propagation on the acoustic level received ($f = 500$ Hz)

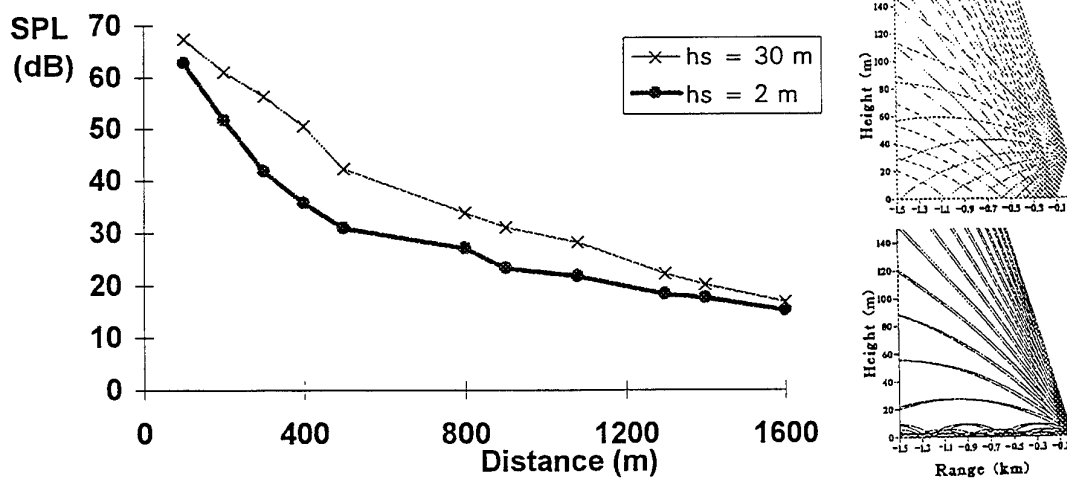


Fig. 8: Influence of the height of the source ($f = 500$ Hz)

During most of the time that these experimental trials lasted, the meteorological situations observed were relatively simple. In these configurations, the effects observed were the increase - to a certain extent - of the acoustic level received under the wind and the creation of a more or less pronounced shadow zone on the opposite side (fig. 9). The acoustical ray traces corresponding to figure 10 illustrate an uncommon propagation situation. An acoustic channel is observed in the layers of the atmosphere between 50 and 200 m over the ground level. This configuration has its origin in the double thermal inversion and is well-known in under-water acoustics, but it has never again been

observed during our tests. In this case, the sound can have a long-range propagation, but it is difficult to predict, with a ray trace model, if the acoustic waves « trapped » in an upper layer of the atmosphere will be deviated down to the ground or not.

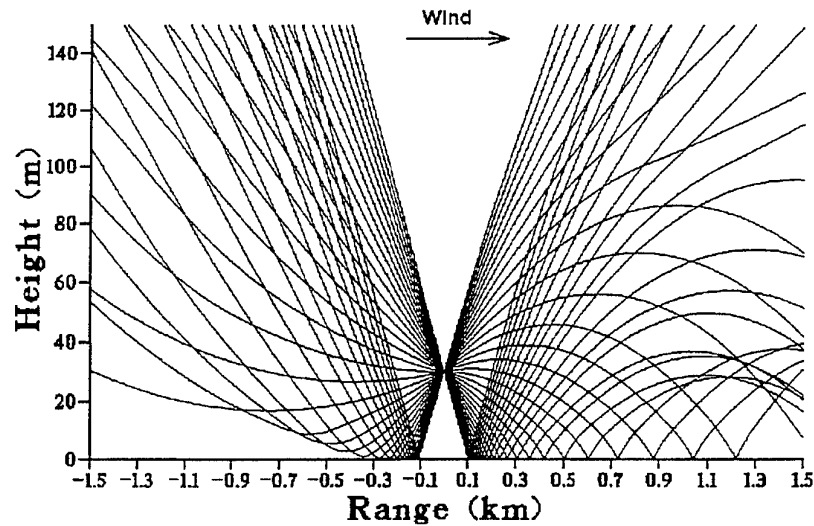


Fig. 9: Ray traces corresponding to typical meteorological conditions

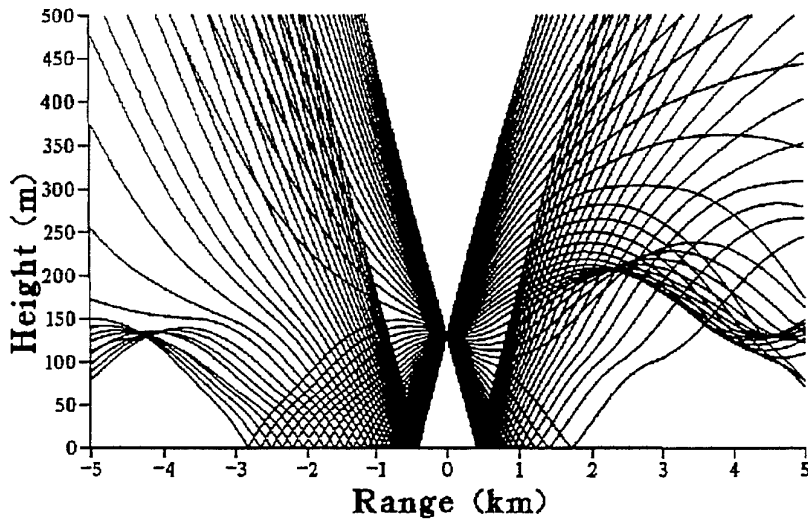


Fig. 10: Ray traces corresponding to an aerial acoustic channel

4 - Prediction of micrometeorological profiles

During those field trials it was observed that, if the meteorological profiles were not updated fast enough, the quality of the prediction was poor. It seems to be necessary to do some meteorological sounding every 10 or 20 minutes and this at different locations

of the field of interest. One can easily understand that it is not simple to obtain these measurements in the field.

With this in view, the possibility of reconstructing the profiles of the atmospheric parameters (wind and temperature) by carrying out only a limited number of measurements is envisaged. In a first stage, the CRPE has studied a method based on the similarity law of Monin-Obukov. This kind of numerical method can be applied with data measured punctually at two different heights by two classical meteorological stations (fig. 11).

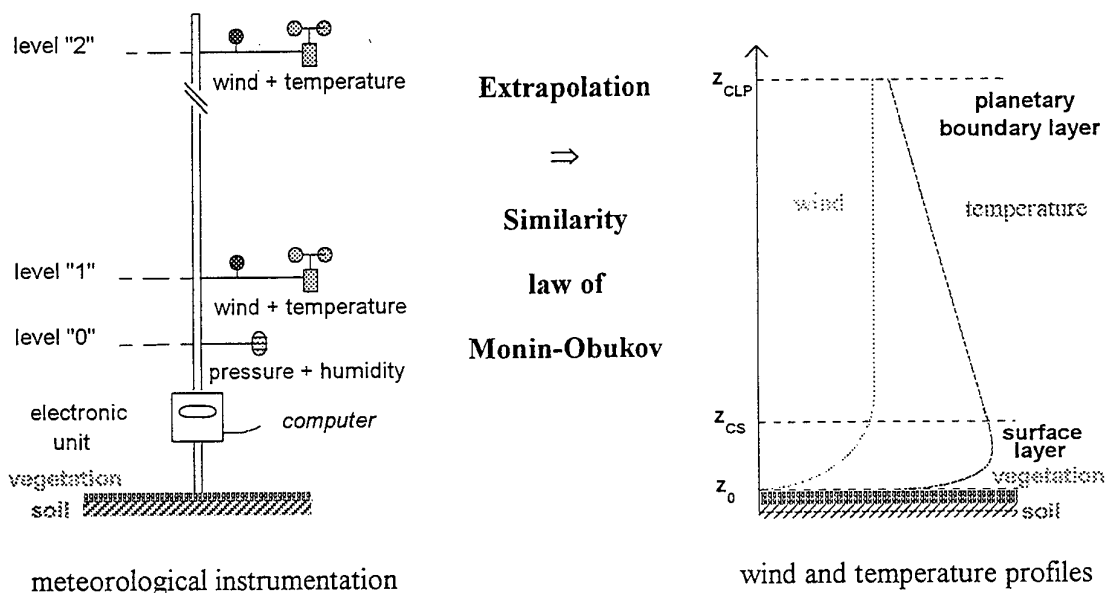


Fig. 11: Prediction of the micrometeorological profiles (*from A. Weill et J.P. Frangi*)

This modelisation allows to predict whether the atmosphere is stable, neutral or unstable. The equations describing the evolution with the height of the wind and temperature (i.e. meteorological profiles) are different, depending on this character (fig. 12).

The method was applied at different periods of the JAPE-91 campaign and the results were compared to the measured profiles provided by US-ARL. These profiles have been obtained by merging data from SODAR and meteorological masts. The comparison is based on measurements carried out at 17 different heights and on 5 test cases. The mean values of the errors are reported in the following table (fig. 13). The precision of the prediction for the temperature and wind profiles is very good when the atmosphere is unstable (but stationary). In unstable conditions, which may occur during the night or at sunrise, the precision is not so good. The direction of the wind, in particular when the wind is not settled, is very variable and the prediction is bad; however, in this specific case, this inaccuracy is of little consequence on the quality of the predictions.

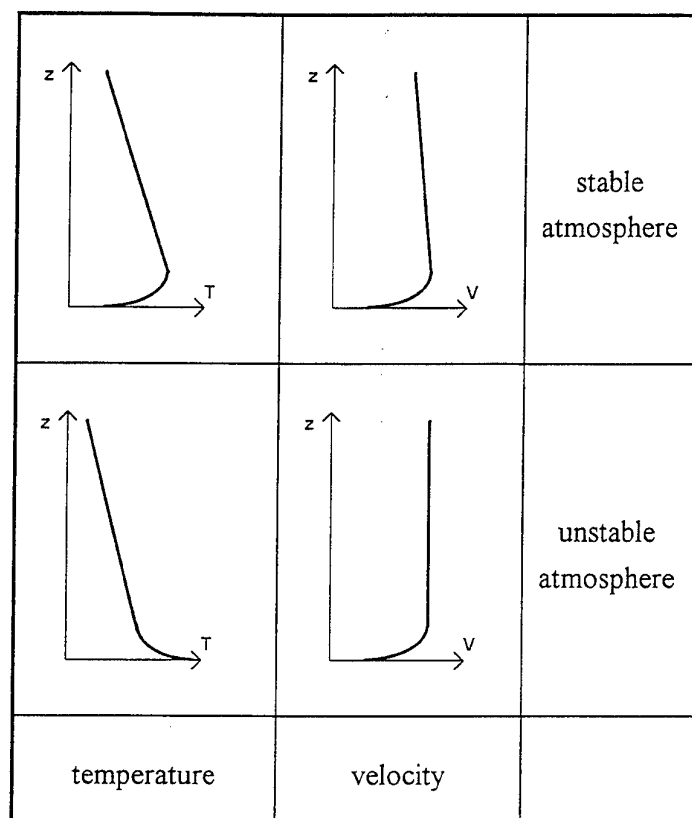


Fig. 12: Shape of the profiles as a function of the meteorological category

Wind velocity (module)	15 %
Wind direction	-
Temperature (°C)	5 %

Fig. 13: Mean value of the prediction errors

For the establishment of this model, it was assumed that the atmosphere was horizontally homogeneous. It means that only vertical interactions are taken into account, and local parameters can be used to solve the problem. The model will be adequate to describe a situation that is well established or slowly evolutive. In an unsteady configuration, as for example the transit of a cold front, it will be necessary to have a real-time measurement of the profile (SODAR, RASS, etc.), or to have a more sophisticated meteorological model. A macrometeorological model predicting the horizontal displacement of the atmosphere, coupled with the previous « local » model for the vertical profiles may be a possible evolution.

The acoustical propagation distances corresponding to our applications are relatively long, so this kind of model can only be considered to be a first approach. The extension of the model to take into account spatial inhomogeneities (hills, forests, lakes, etc.) is also to be elaborated.

5 - Atmospheric turbulence

For the previous calculations, it was assumed that the acoustical waves propagated in a homogeneous atmosphere. However, the latter is always more or less turbulent, and it is a difficult point to estimate. These fluctuations of the medium introduce a modulation of the phase and of the amplitude of the acoustic pressure and they also contribute to decrease the coherence between the signals measured with neighbouring sensors (fig. 14). This possible lack of coherence is of particular consequence for the application of acoustic antennas. The localization of an acoustic source is generally performed by algorithms based on the correlation matrix of the data measured by the different microphones that constitute the antennas. The decrease of the coherence between these signals may have some consequences on the precision of the predicted angle.

The results of the measurements carried out during three consecutive days in Dreux (AMI-2 experiment) show a typical evolution of the intensity of the turbulence, with a maximum for the middle of the day, and a minimum in the night-time (fig. 15).

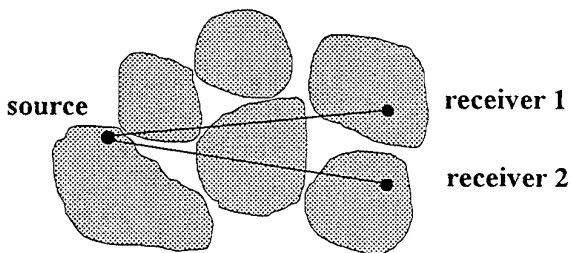


Fig. 14: Schematic view of the turbulent medium

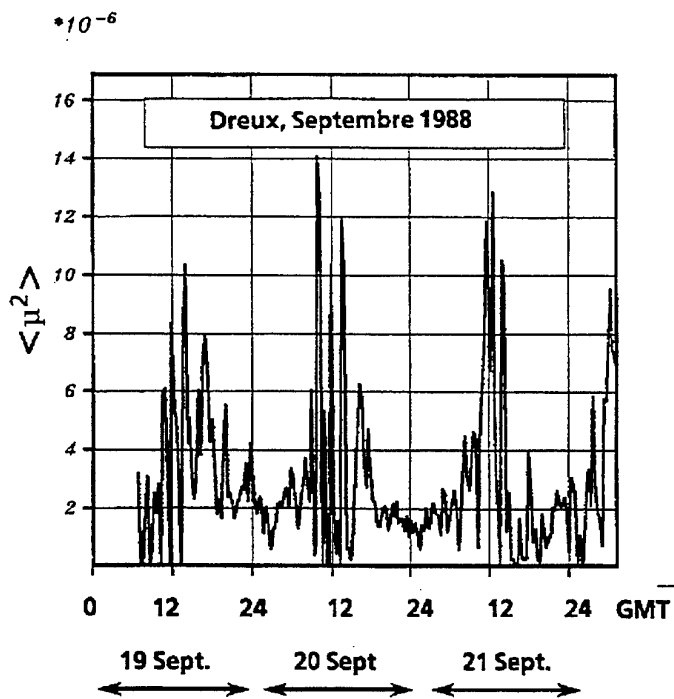


Fig. 15: Evolution of the intensity of the turbulence during 3 consecutive days

This difficulty in taking into account the atmospheric turbulence exists in the experimental approach as well as in the theoretical one. Experimentally, it is necessary to measure the turbulence by taking into account the different scales (from some centimeters to some hundreds of meters) and to describe it in the appropriate statistical manner (distribution of the scale of the whirls, etc.). Then it is necessary to revise the theoretical equations of propagation in order to introduce these statistical aspects; it is not always evident or possible in every method to do this, due to the deterministic aspect of these equations. We have investigated the possibility of describing a random velocity field generated by the terms of discrete Fourier modes. This velocity field is introduced in the ray-tracing equation in a manner similar to that described in [4]. In this case, the trajectories of the rays are less rectilinear than in the case of those drawn with the homogeneous atmosphere (fig. 16 et 17). Corresponding to each of the velocity field realizations, and after the ray tracing calculation, values of sound pressure level on the ground are obtained. Mean values and standard deviations of the pressure values deduced by these calculations provide the confidence interval we can expect for the acoustical prediction. These calculations allow a better representation of the propagation conditions and the first comparisons made show that the experimental data are included in the computed interval [5].

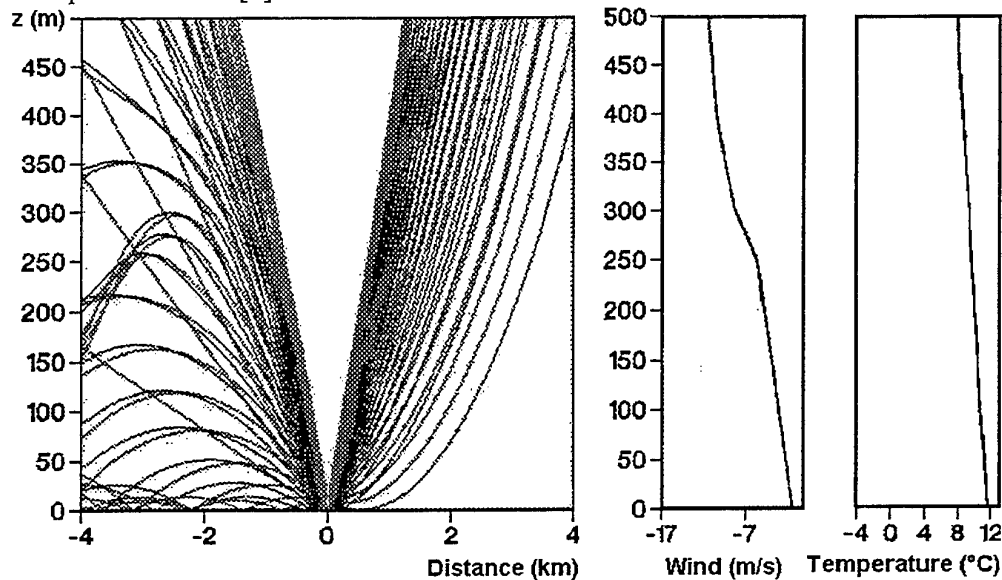


Fig. 16: Acoustic rays - calculation with mean profiles (no turbulence)

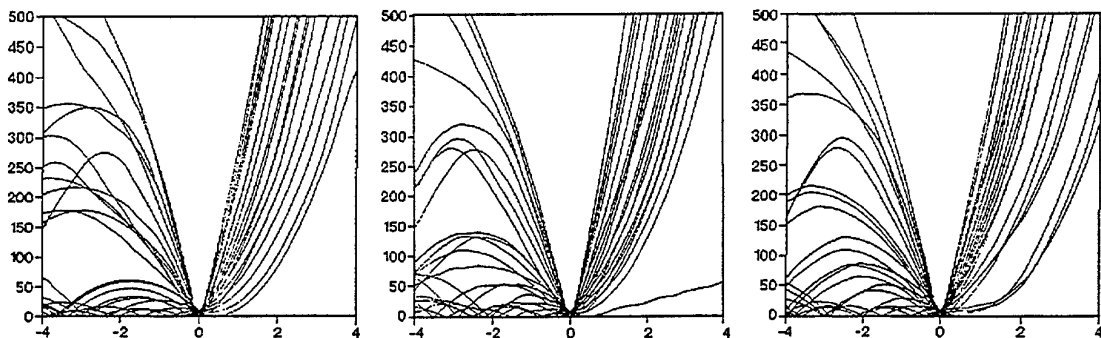


Fig. 17: Acoustic rays (example of 3 plots of turbulent atmosphere)

The response of an acoustic antenna after the propagation of the sound in a turbulent atmosphere is not well-known in aerial acoustics yet [6]. In the future, we consider studying the influence of the turbulence on the coherence of the acoustic wave measured with an antenna designed with 7 microphones (fig. 18).

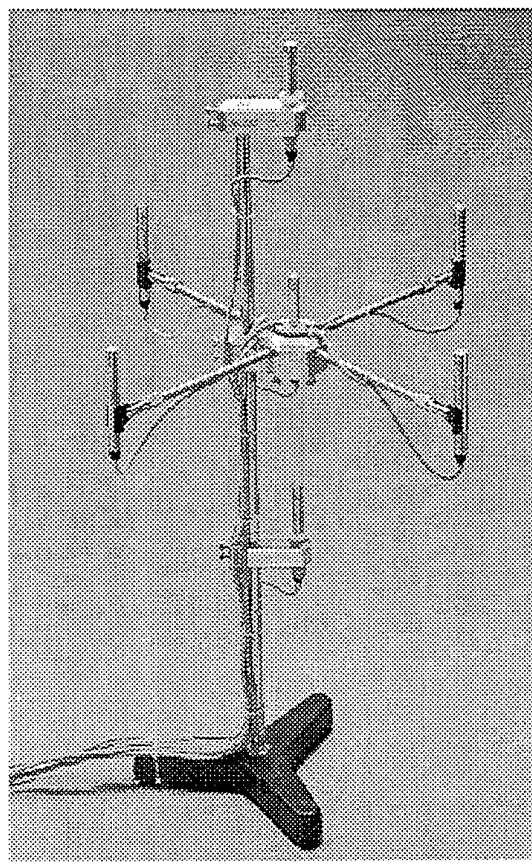


Fig. 18: Acoustic antenna (microphones)

6 - Conclusions

This paper makes a survey of the main experimental results gained during the last years on long-range sound propagation. In particular, the results of the AMI-2 and JAPE-91 experiments have completed our knowledge of acoustical and micrometeorological phenomena specific to the lower part of the atmosphere. In parallel to these experimental measurements, the use of propagation models has shown a mean precision between 3 and 5 dB. Nevertheless, to obtain this precision, it is necessary to characterize carefully the medium of propagation, which is not simple to carry out in the field. Some of the physical phenomena like turbulence are not well-known yet and the studies in this field have to be continued.

References:

- [1] Joint Acoustic Propagation Experiment (JAPE-91) Workshop.
Hampton/VA, USA, April 26-28, 1993
NASA Conference, Publication No. 3231
- [2] K. Attenborough et al.
Benchmark cases for outdoor sound propagation models.
JASA 97 (1), January 1995, pp. 173-191
- [3] P. Naz, F. Riedlinger, E. Burde
Propagation du bruit des hélicoptères dans la basse atmosphère.
Comparaison calcul-expérience AMI-2.
ISL, RT 505/93
- [4] Ph. Blanc Benon, D. Juvé
Simulation numérique de la propagation des ondes acoustiques dans une turbulence bidimensionnelle par une méthode de rayons.
Journal de physique, Suppl. n° 2, Tome 51, pp. 1149-1152, février 1990
- [5] P. Naz, G. Parmentier
Influence des fluctuations des facteurs météorologiques sur la propagation du bruit des hélicoptères dans la basse atmosphère.
ISL, R 112/90
- [6] D. Havelock, M. Stinson, G. Daigle
Beamforming in an Acoustic Shadow.
JAPE-91 Workshop, NASA CP 3231

Diffraction and Ground effects

GROUND EFFECT FOR A-WEIGHTED NOISE IN THE PRESENCE OF TURBULENCE AND REFRACTION

Keith Attenborough and Kai Ming Li

Faculty of Technology
The Open University
Milton Keynes MK7 6AA
England

Abstract

Closed-form approximations, of ground effect for A-weighted noise from a point source near to finite impedance ground, obtained by Li *et al* (J.Acoust. Soc. Am. **88** (2) 1170 - 1172 and Makarewicz [J.Acoust. Soc. Am. **82** 1706 - 1711 (1987) and J.Acoust. Soc. Am. **88** (2) 1172 - 1175], are extended to take account of more general models for ground impedance including revised variable-porosity, thin-layer and rough porous ground where the roughness is small compared with incident wavelengths. The influences of both turbulence and weak atmospheric refraction are included. Approximate relationships between optimum ground effect for A-weighted noise, ground parameters, source spectrum, source and receiver heights are predicted and explored. For low source heights and noise sources with a low frequency A-weighted spectrum, it is possible to indicate ground surface parameters that will give significantly higher excess attenuation than those typical of grass-covered ground. It is predicted that the optimum ground effect parameters are fairly robust to weak refraction effects particularly for low-frequency sources and low source heights.

1 Introduction

Although the phenomenon of ground effect is taken into account in many prediction schemes for sound propagating in open areas near to the ground, there have been few attempts to exploit current knowledge and understanding of the phenomenon for passive noise control. A notable exception is the design and deployment of porous road surfaces which act to reduce road/tire noise both at source and during subsequent propagation¹.

In the absence of meteorological effects, ground effect may be predicted as a function of frequency by means of the classical theory for the propagation of sound from a point source over finite impedance ground together with either measured impedance or an impedance model². Rasmussen³ has derived an empirical approximate formula for ground effect as a function of frequency and has found it to be reliable for short-range propagation.

Most community noise problems require information about the attenuation of A-weighted noise. There are empirical schemes for predicting such attenuation for specific noise sources. However these empirical methods are not well-suited for exploring ground effect optimisation. For example the empirical schemes for predicting attenuation of A-weighted noise assume that all porous ground surfaces may be treated as giving identical excess

attenuation within the accuracy of the scheme. In fact ground surfaces display a wide range of porosities and flow resistivities that vary over nearly three orders of magnitude.

By using exponential functions to represent A-weighting and air absorption and the Delany-Bazley single parameter model of ground impedance⁴, Makaraewicz⁵ derived an approximation for ground effect at relatively long range which could be used to calculate the effective flow resistivity that maximizes ground effect for a given point source-receiver geometry. Li *et al*⁶ pointed out sign errors in this work, used a two-parameter impedance model⁷, and deduced alternative closed-form results for ground effect and optimum parameters. Makarewicz⁸ subsequently extended this model to take account of different source spectra and atmospheric turbulence.

In this paper, we extend this latest work to allow for a more general range of ground impedance and the effects of small scale roughness on the coherent sound field. For a given source-receiver geometry, this enables prediction of ground types that will achieve maximum excess attenuation and estimation of the magnitudes of the optimized excess attenuation. We make use of an approximation for propagation in a linear sound velocity gradient to explore the extent to which the optimised ground effect is affected by atmospheric refraction.

In the next section we review the general basis for the approximations. In the third section we review of various ground impedance models and introduce a new approximation for the effective impedance of rough finite impedance ground. In the fourth section, an approximate method for including weak refraction effects is outlined and justified. Subsequently we derive expressions for excess attenuation and optimum ground parameters and make numerical explorations of their sensitivities to source-receiver geometry and refraction. Finally we offer some conclusions based on these predictions.

2 Integral expressions for A-weighted mean square sound pressure

The basis for this and previous work is the classical analytic approximation, sometimes called the Weyl-van der Pol formula, for the sound field due to a point source above an impedance plane². After further approximation for near-grazing incidence, inclusion of exponential factors to allow for A-weighting, source spectrum, air absorption and turbulence, and integration over frequency (f), an expression for the A-weighted mean square sound pressure may be deduced^{5,8}.

Hence

$$P_A^2 = (\rho_0 c_0 / 4\pi d^2) [P_A + P_{A1} + P_{A2}] \quad (1)$$

where $P_A = \int_0^\infty W_0 P^{(0)} f^m \exp(-\mu_A f - 2\alpha(f)) df , \quad (2a)$

$$P_{A1} = \int_0^\infty W_0 P^{(0)} f^m (Q_1^2 + Q_2^2) \exp(-\mu_A f - 2\alpha(f)) df , \quad (2b)$$

$$P_{A2} = 2 \int_0^\infty W_0 P^{(0)} f^m T \{Q_1 \cos(k_0 \Delta r) + Q_2 \sin(k_0 \Delta r)\} \exp(-\mu_A f - 2\alpha(f)) df \quad (2c)$$

and in equations (2a) - (2c), $W_0 = 1.4676 \times 10^{-6}$; $\mu_A = \delta + \mu$, δ is an A-weighting parameter ($= 6.1413 \times 10^{-4}$), m , μ and $P^{(0)}$ relate to the source power spectrum such that the total A-weighted power of the source is $(P^{(0)} / \mu_A) [\Gamma(m+1) / \mu_A^m] W_0$ W (Γ is the gamma function) and

the A-weighted power spectrum peaks at $f_m = m / \mu_A$ Hz. The air absorption parameter

$\alpha(f) = a_1 f + a_2 f^2$ where a_1 and a_2 are constants with $a_2 \ll a_1$, $T = \exp(-\gamma_f d)$,

$\gamma_f = \epsilon (4\pi^2 / c_0^2) \langle n^2 \rangle L_0 (1 - \rho)$ is a turbulence parameter depending on mean square refractive

index $\langle n^2 \rangle$, the largest turbulence scale (L_0 m) and transverse correlation (ρ), ε is a constant (= 1/2 or 1), Δr m is the path length difference between direct and ground reflected rays, d m is the range and $k_0 \text{ m}^{-1}$ is the wave number for sound in air. In the presence of a linear sound speed profile, and subject to certain constraints, equation (2) remains valid as long as Δr in 2(c) and the angle of specular reflection θ at the ground are calculated for curved ray paths (see section 4).

Q_1 and Q_2 are the real and imaginary parts of the spherical wave reflection coefficient. Assuming that A-weighting reduces any contributions from frequencies less than 250 Hz to insignificance, that $d \geq 10$, that $Z \cos \theta \ll 1$, where $Z = R - iX$, is the normal surface impedance of the ground, θ is the angle of specular reflection, and, using harmonic time-dependence $\exp(i\omega t)$ where $\omega = 2\pi f$, the spherical wave reflection coefficient may be approximated considerably. Hence

$$Q_1 = -1 + 2R \cos \theta - \frac{2c_0}{\pi df} RX - 2(R^2 - X^2) \cos^2 \theta \quad (3a)$$

$$Q_2 \approx -2X \cos \theta + 4RX \cos^2 \theta - \frac{c_0}{\pi df} (R^2 - X^2) \quad (3b)$$

and $Q_1^2 + Q_2^2 \approx 1 - 4R \cos \theta + \frac{4c_0}{\pi df} RX + 8R^2 \cos^2 \theta \quad (3c)$

Note that equations 3a - 3c correct sign errors in the corresponding equations in refs. 5 and 8 and misprints in ref. 6.

It is interesting to observe that when $X > R$, the terms in $(R^2 - X^2)$ serve to increase Q_1 and Q_2 , and hence the integrands in equations (2b) and (2c).

An example simulation of an A-weighted source power spectrum is illustrated in Figure 1. The crosses corresponds to $m = 2.55$, $P^{(0)} = 10^8$ and $\mu_A = 4.03 \times 10^{-3}$, giving a peak sound power level at 633 Hz and the open boxes represent A-weighted octave band power levels deduced from the measured sound level spectrum at 152.4m from a fixed Avon engine at a disused airfield during low wind, low turbulence conditions by correcting for spherical spreading, ground effect, air absorption and turbulence^{9,10}. In principle it should be possible to fit m , $P^{(0)}$ and μ_A , analytically, given f_m , the peak A-weighted sound power level and P_A . However, in this instance the values are the result of trial-and-error best-fitting.

3 Approximate Models for Ground Impedance

Li *et al*⁶ use a model based partly on numerical simulation of the impedance of a porous material with porosity that is exponentially-decreasing with depth⁷. This may be expressed as

$$Z = \frac{1-i}{\sqrt{\pi \eta p_0}} \sqrt{\frac{\sigma_e}{f}} - \frac{ic_0 \alpha_e}{4\pi \eta} \quad (4a),$$

where $\sigma_e = s_p^2 \sigma / \Omega$ and $\alpha_e = n' \alpha / \Omega$; σ , Ω , α , s_p and n' are the flow resistivity and porosity at the surface, the rate of change of porosity, the pore shape and grain shape factors respectively. When its flow resistivity is high, pore shape has relatively little effect on the acoustical properties of a rigid porous medium¹¹. Moreover, to be consistent with the expected low-frequency limit, s_p should be set equal to 0.5 without loss of generality. Recently a more rigorous derivation of the approximate surface impedance of a rigid porous medium in which the porosity decreases exponentially with depth has been given¹³. Hence

$$Z = \frac{1-i}{\sqrt{\pi\rho_0}} \sqrt{\frac{\sigma_e}{f}} - \frac{ic_0\alpha_e}{8\pi\gamma f} \quad (4b),$$

where $\alpha_e = (n' + 2)\alpha/\Omega$. An approximation for the surface impedance of a high flow resistivity porous medium with the porosity *increasing* exponentially with depth is given by (4b) with negative α_e . If α_e is negative then (4b) predicts a resistance that exceeds the reactance at all frequencies.

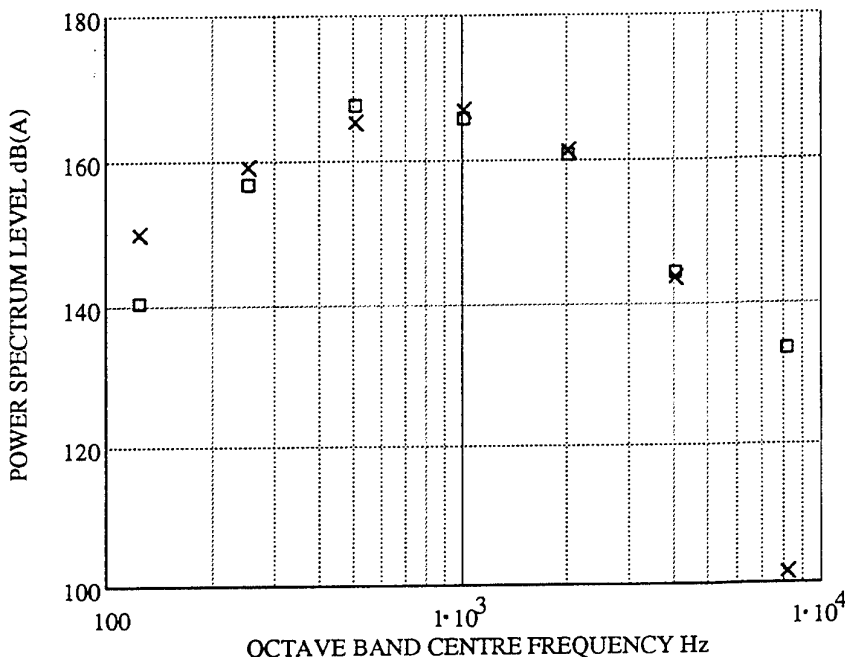


Figure 1 Example simulation of an A-weighted octave band power spectrum (x) compared with that deduced from measurements (□) obtained at 1.2m height with a fixed Rolls Royce Avon jet engine mounted at 2.16m height over grassland. The simulation uses $m = 2.55$, $P^{(0)} = 10^8$ and $\mu_A = 4.03 \times 10^{-3}$.

The surface impedance of a hard-backed thin high-flow-resistivity layer may be approximated by⁷

$$Z = \frac{1-i}{\sqrt{\pi\rho_0}} \sqrt{\frac{\sigma_e}{f}} - \frac{ic_0}{2\pi d_e f} \quad (4c),$$

where $d_e = \Omega d$ and d is the layer thickness.

In general impedances of these types, both of which imply $X > R$ (as long as α_e is positive), may be written

$$Z = a(1-i) \sqrt{\frac{\sigma_e}{f}} - \frac{ib\alpha_e}{f} \quad (4d),$$

where $a = 1/\sqrt{\pi\rho_0\gamma}$ and $b = c_0/8\pi\gamma$. In the latter case, $\alpha_e = 4/d_e$.

The effective normalised surface admittance of a rigid-porous boundary roughened by 3-D or 2-D identical bosses, the heights and spacing of which are small compared with an incident wavelength, may be approximated by¹³

$$\beta_{3D} = \beta_s + i \frac{2\pi f \sigma_v}{c_0} \left(\frac{3s_{3D}}{2v_{3D}} - 1 + \beta_s \frac{c_0}{c_s} \right) \quad (5a),$$

or $\beta_{2D} = \beta_s + i \frac{2\pi f \sigma_v}{c_0} \left(\frac{2s_{2D}}{v_{2D}} - 1 + \beta_s \frac{c_0}{c_s} \right) \quad (5b),$

for 3-D and 2-D bosses respectively, where β_s is the normalised surface impedance of the rigid-porous material surface if it were plane, s and v are shape and close-interaction factors, σ_v is the volume of bosses above the base-plane per unit area of surface, and c_s is the complex speed of sound within the rigid-porous material. For a high flow resistivity semi-infinite rigid-

porous material, $\beta_s \approx \frac{1}{2}(1+i)\sqrt{\frac{\pi\rho_0\gamma}{\sigma_e}}$ and $\frac{2\pi f \beta_s}{c_s} \approx \gamma\Omega$. Hence the rough surface effective

admittance may be approximated by

$$\beta_r = A(1+i)\sqrt{f} + i(C + Df) \quad (5c),$$

where $A = \frac{1}{2}\sqrt{\frac{\pi\rho_0\gamma}{\sigma_e}}$, $C = \sigma_v\gamma\Omega$ and $D = \frac{2\pi\sigma_v}{c_0} \left(\frac{3s_{3D}}{2v_{3D}} - 1 \right)$ or $D = \frac{2\pi\sigma_v}{c_0} \left(\frac{2s_{2D}}{v_{2D}} - 1 \right)$.

With $C \ll A\sqrt{f}$ and $D\sqrt{f} \ll A$, the effective normalised impedance of the rough porous surface is approximated by

$$Z_r \approx \frac{1}{2A\sqrt{f}}(1-i) - \frac{1}{2A^2}(Cf + D) \quad (5d).$$

Figure 2 shows example predictions of equations (5a) and (5d) for the special case of close-packed hemi-spherical bosses of radius r for which

$$C = \pi\gamma\Omega r/6 \text{ and } D = (2\pi r/3c_0) \left[\left(1 - \frac{\pi^2}{16}\right) / \left(1 + \frac{\pi^2}{32}\right) \right].$$

For close-packed identical semi-cylinders of radius r , $D = (\pi r^2/2c_0) \left[1 - \frac{\pi^2}{12} / 1 + \frac{\pi^2}{12} \right]$.

This figure also demonstrates empirically that a valid approximation for the effective impedance of a rough porous surface of high flow resistivity is given by the relatively simple expression

$$Z_r \approx \frac{1}{2A\sqrt{f}}(1+i) - \frac{D}{A^2} \quad (5e).$$

$c_0 D / 2\pi$ may be treated as an effective roughness volume per unit area.

4. Effects of weak refraction

Apart from turbulence, meteorological effects were ignored in Makerewicz^{5,8} derivation of a closed form expression for an A-weighted mean square sound pressure. However, it has been identified¹⁴ that variations in temperature and wind with height cause the speed of sound to vary with height and lead to refraction effects. Without inclusion of refraction the applicability of the model is limited. In the past ten years, there has been considerable progress in the prediction of sound propagation outdoors. Recent developments have been summarized in Ref. 15. In the present context, these numerical methods are not appropriate because the direct and

reflected sound waves are not separated out explicitly as two terms and the evaluation of A-weighted mean square pressure by these numerical methods demands considerable computational resources.

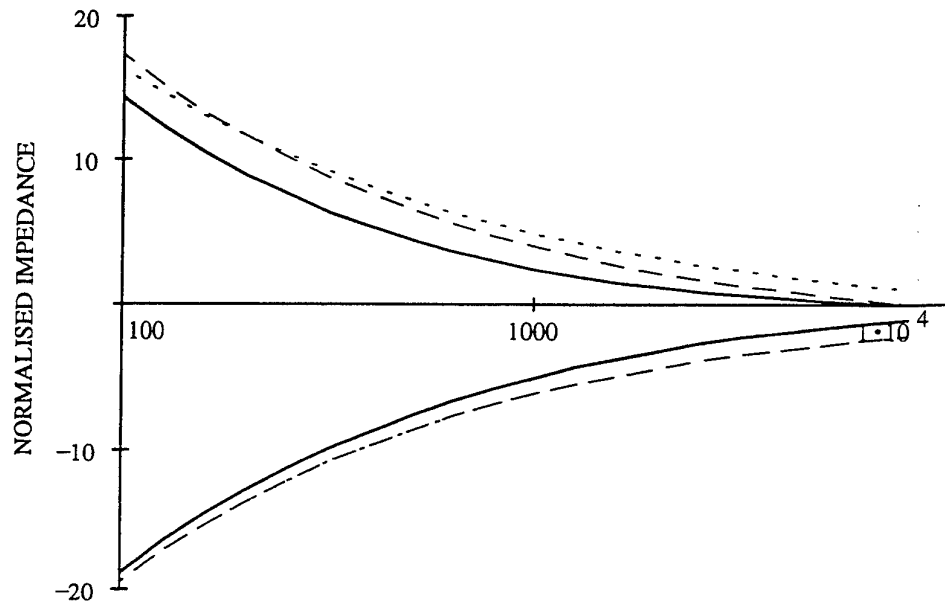


Figure 2 Comparison of predictions of equations (5c) - solid line; (5d) - dotted line; and (5e) - dashed line; for the effective impedance of a rough porous surface with $\sigma_e = 200 \text{ kPa s m}^{-2}$ and close-packed hemispherical bosses of radius 0.01m. Note that (5d) and (5e) give identical predictions for the reactance.

For engineering applications, it is far more convenient to use the ray-trace approach. In the past, the ray-trace approach has been included in a heuristic modification of the Weyl-Van der Pol formula.^{6,16} It has been shown recently that the resulting formulation represents the first term of an asymptotic solution of the full wave equation.^{17,18} In addition, it has been demonstrated numerically that the ray-trace solution agrees reasonably well with other numerical schemes.^{16,19} In the following analysis, we shall use the ray-trace approach in deriving the expression for the A-weighted mean square sound pressure.

It is useful to assume that the atmosphere is vertically stratified and that the effective sound speed gradient can be used to replace wind and temperature gradients.¹⁴ In order to present a tractable analytical solution, the effective sound speed, c is assumed to vary linearly with height,

$$c(z) = c_0(1 + \zeta z) \quad (6)$$

where ζ is the normalised sound velocity gradient and z is the height above ground. There is a distinct advantage for this choice because the use of a linear profile leads to a circular ray path.¹⁴ It is relatively easy to trace the direct and reflected waves. Furthermore, the experimental data obtained by Li *et al*²⁰ agrees tolerably well with the theoretical predictions based a linear sound speed profile.

To simplify our subsequent analysis, the sound field is approximated by

$$P = \{\exp(ik_0\xi_1) + [Q_1 + iQ_2]\exp(ik_0\xi_2)\}/4\pi d \quad (7a)$$

where Q_1 and Q_2 are given by Eqs. (3a) and (3b), respectively. Here, in Eq. (7a), d is the horizontal separation between the source and receiver, ξ_1 and ξ_2 are, respectively, the acoustical path lengths of the direct and reflected waves. The acoustical path lengths can be determined by^{14,16}

$$\xi_1 = \int_{\phi_<}^{\phi_>} \frac{d\phi}{\zeta \sin \phi} = \zeta^{-1} \log_e [\tan(\phi_>/2)/\tan(\phi_</2)] \quad (7b)$$

and

$$\xi_2 = \int_{\theta_<}^{\theta_>} \frac{d\theta}{\zeta \sin \theta} = \zeta^{-1} \log_e [\tan(\theta_>/2) \tan^2(\theta_0/2)/\tan(\theta_</2)] , \quad (7c)$$

where $\phi(z)$ and $\theta(z)$ are the polar angles (measured from the positive z -axis) of the direct and reflected waves. The subscripts $>$ and $<$ denote the corresponding parameters evaluated at $z_>$ and $z_<$, respectively, $z_> \equiv \max(z_s, z_r)$ and $z_< \equiv \min(z_s, z_r)$. We remark that Hidaka *et al*²¹ have used the travel time of the curve ray to characterize the acoustical path length. It is straightforward to show that Eqs. (7b) and (7c) can be reduced to their equations. Additionally, it is possible to show, in the limit of $\zeta \rightarrow 0$ (*i.e.* a homogeneous medium), the acoustical path lengths can be reduced to

$$\xi_1 = \sqrt{(z_> - z_<)^2 + d^2}$$

and

$$\xi_2 = \sqrt{(z_> + z_<)^2 + d^2}$$

which are the corresponding geometrical path lengths of the direct and reflected waves.

To allow for the computation of $\phi(z)$ and $\theta(z)$, we need to find the corresponding polar angles (ϕ_0 and θ_0) at $z = 0$. Formulas for finding ϕ_0 and θ_0 in terms of sound velocity gradient are given elsewhere.^{20,21} Once the polar angles are determined at $z = 0$, $\phi(z)$ and $\theta(z)$ at other heights can be found by using Snell's Law:

$$\sin \vartheta = (1 + \zeta z) \sin \vartheta_0 ,$$

where $\vartheta = \phi$ or θ . Substituting these angles into Eqs. (7b) and (7c) and, in turn, into Eq. (7a), we can calculate the sound field in the presence of a linear sound velocity gradient. In particular, the path length difference, Δr is given by

$$\Delta r = \xi_2 - \xi_1 \quad (7d)$$

If we confine predictions to a horizontal separation of about 1 km and weak refraction so that the receiver is in the illuminated zone, it is reasonable to restrict the ray trace model to a single bounce. L'Esperance *et al*¹⁸ point out, for downward refraction, that the additional rays will cause a discontinuity in the predicted sound level because of the inherent approximation used in the ray-trace model. It is possible to determine the critical range, r_c , where there are two additional rays in the ray-trace solution. It is tedious but straightforward to show that the critical range, for $\zeta > 0$, is given by

$$r_c = \frac{\left\{ \left[\sqrt{(\zeta z_>)^2 + 2\zeta z_>} + \sqrt{(\zeta z_<)^2 + 2\zeta z_<} \right]^{2/3} + \left[\sqrt{(\zeta z_>)^2 + 2\zeta z_>} - \sqrt{(\zeta z_<)^2 + 2\zeta z_<} \right]^{2/3} \right\}^{3/2}}{\zeta} \quad (8a)$$

On the other hand, the ray-trace solution for upward refracting conditions is incorrect when the receiver is located in shadow and penumbra zones. The shadow boundary can be

determined from geometrical considerations. For a given source and receiver heights, the critical range, r'_c is determined as

$$r'_c = \frac{\sqrt{(\zeta' z_s)^2 + 2\zeta' z_s} + \sqrt{\zeta'^2 z_s(2z_s - z_c) + 2\zeta' z_c}}{\zeta'}, \quad (8b)$$

where $\zeta' = \frac{|\zeta|}{1 - |\zeta| z_s}$.

Using Eq. (6) and following the methods detailed in Ref. 5, we can derive the A-weighted mean square sound pressure in the presence of weak effective sound speed gradients. The expression will be given in the next section where all other factors are included in the analysis.

5. Approximations for excess attenuation

Variable porosity or thin layer ground

Substitution of equations (4d) and (3) into (2) leads to integrals of the form

$$G_1(k) = \int_0^\infty x^k e^{-(gx+hx^2)} \cos(lx) dx \text{ and } G_2(k) = \int_0^\infty x^k e^{-(gx+hx^2)} \sin(lx) dx \text{ where}$$

$g = \mu_A + 2a_1 d$, $h = (2a_2 + \gamma_t)d$ and $l = 0$ or $2\pi\Delta r/c_0$. These may be evaluated in closed form by means of products of gamma and parabolic cylinder functions^{5,23}. If d is sufficiently large and a_2 and γ_t are sufficiently small, then $g^2 + l^2 \gg 6h$ and $l/g \ll 1$, so that⁵

$$\text{for } l = 0, \quad G_1(k) \rightarrow C(k) \approx \Gamma(k+1) / (\mu_A + 2a_1 d)^{-(k+1)} \quad (8a),$$

$$\text{for } l \neq 0, \quad G_1(k) \approx C(k) - \frac{1}{2} C(k+1) l^2 - (2a_2 + \gamma_t) d C(k+2) \quad (8b),$$

$$\text{and } G_2(k) \approx C(k+1) l - (2a_2 + \gamma_t) d C(k+3) l \quad (8c).$$

Finally, use of these and further approximations leads to

$$P_A^2 = (P_A / 4\pi d^2) [S(\sigma_e, \alpha_e, g, m, \gamma_t, l, \theta_0, d)] \quad (9a),$$

$$\text{where } S = B_0 d + B_1 l^2 - B_2 l \cos \theta_0 + B_3 \cos^2 \theta_0 + B_4 l \quad (9b),$$

$$B_0 = \frac{2(2a_2 + \gamma_t)}{g^2} \frac{\Gamma(m+3)}{\Gamma(m+1)} \quad (9c),$$

$$B_1 = \frac{1}{g^2} \frac{\Gamma(m+3)}{\Gamma(m+1)} \quad (9d),$$

$$B_2 = 4 \left[\frac{\Gamma(m+\frac{3}{2})}{\Gamma(m+1)} \frac{a\sqrt{\sigma_e}}{\sqrt{g}} + b\alpha_e \right] \quad (9e),$$

$$B_3 = \frac{4g}{\Gamma(m+1)} [2\Gamma(m)a^2\sigma_e + 2\sqrt{g}\Gamma(m-\frac{1}{2})ab\sqrt{\sigma_e}\alpha_e + g\Gamma(m-1)b^2\alpha_e^2] \quad (9f),$$

$$B_4 = \frac{2c_0 g}{\pi d \Gamma(m+1)} [2\Gamma(m-\frac{1}{2})aba\sqrt{\sigma_e g} + g\Gamma(m-1)b^2\alpha_e^2] \quad (9g).$$

The ground parameters that minimize S and hence give maximum excess attenuation, for a given geometry, are given by

$$\sqrt{\sigma_{em}} = \frac{A_2 A_4 - 2A_1 A_3}{A_4^2 - 4A_3 A_5} \quad (10a),$$

and $\alpha_{em} = \frac{A_4 A_4 - 2A_2 A_3}{A_4^2 - 4A_3 A_5}$ (10b),

where $A_1 = \frac{4a}{\sqrt{g}} \frac{\Gamma(m+\frac{3}{2})}{\Gamma(m+1)} l \cos \theta_0$ (10c),

$$A_2 = 4bl \cos \theta_0 \quad (10d),$$

$$A_3 = 8a^2 g \frac{\Gamma(m)}{\Gamma(m+1)} \cos^2 \theta_0 \quad (10e),$$

$$A_4 = 8abg^{\frac{1}{2}} \frac{\Gamma(m-\frac{1}{2})}{\Gamma(m+1)} \left(\cos^2 \theta_0 + \frac{c_0 l}{2\pi d} \right) \quad (10f)$$

and $A_4 = 4b^2 g^2 \frac{\Gamma(m-1)}{\Gamma(m+1)} \left(\cos^2 \theta_0 + \frac{c_0 l}{2\pi d} \right) \quad (10g).$

A similar procedure starting with the approximate rough porous surface impedance given by equation (5e) yields equations (7a) - (7d) together with

$$B_2 = 4 \left[\frac{\Gamma(m+\frac{3}{2})}{\Gamma(m+1)} \frac{a \sqrt{\sigma_e}}{\sqrt{g}} \right] \quad (11a),$$

$$B_3 = 8a^2 \sigma_e \left[g \frac{\Gamma(m)}{\Gamma(m+1)} - 2aD \sqrt{\sigma_e} g \frac{\Gamma(m+\frac{1}{2})}{\Gamma(m+1)} + 2a^2 \sigma_e D^2 \right] \quad (11b),$$

$$B_4 = -8a^3 \sigma_e D \left[a \sigma_e D - \sqrt{\sigma_e} g \frac{\Gamma(m+\frac{1}{2})}{\Gamma(m+1)} \right] \quad (11c).$$

The rough ground parameters that minimise S are given by

$$\sqrt{\sigma_{em}} = A_2 \left/ 2 \left(A_3 + \frac{A_4^2}{4A_5} \right) \right. \quad (12a)$$

and $D_m = \frac{A_4}{2A_5 \sqrt{\sigma_{em}}}$ (12b)

where $A_2 = \frac{4a}{\sqrt{g}} \frac{\Gamma(m+\frac{3}{2})}{\Gamma(m+1)} l \cos \theta_0$ (12c),

$$A_3 = 8a^2 g \frac{\Gamma(m)}{\Gamma(m+1)} \cos^2 \theta_0 \quad (12d),$$

$$A_4 = -16a^3 \sqrt{g} \frac{\Gamma(m+\frac{1}{2})}{\Gamma(m+1)} \left(\cos^2 \theta_0 - \frac{c_0 l}{2\pi d} \right) \quad (12e),$$

and $A_4 = -16a^4 \left(\cos^2 \theta_0 - \frac{c_0 l}{2\pi d} \right)$ (12f).

If the atmosphere is homogeneous, then $l = 4\pi h_r h_s / c_0 d$ and $\cos \theta_0 \approx (h_s + h_r)/d$ and

$$\sqrt{\sigma_{em}} = \frac{2\pi}{ac_0 g^{\frac{3}{2}}} \frac{\Gamma(m+\frac{3}{2})(h_r h_s)(h_r + h_s)}{2\Gamma(m)(h_r + h_s)^2 - (\Gamma(m+\frac{1}{2}))^2 \Gamma(m+1)(h_r^2 + h_s^2)} \quad (12g)$$

and $D_m = \frac{c_0 g^2}{2\pi} \frac{2\Gamma(m)(h_r + h_s)^2 - (\Gamma(m+\frac{1}{2}))^2 \Gamma(m+1)(h_r^2 + h_s^2)}{(2m+1)\Gamma(m+\frac{3}{2})(h_r h_s)(h_r + h_s)}$ (12h).

For completeness, the optimum effective flow resistivity for a semi-infinite smooth rigid-porous high flow resistivity surface, such that $Z = a(1-i)\sqrt{\frac{\sigma_e}{f}}$, under homogeneous atmosphere, is given by

$$\sigma_{em} = \frac{\pi^2}{a^2 c_0^2 g^3} \left(\frac{\Gamma(m + \frac{3}{2})}{\Gamma(m)} \right)^2 \frac{h_r^2 h_s^2}{(h_r + h_s)^2} \quad (12i).$$

Where S is given by equation (9b) together with equations (9c)-(9g), or 9(c) and 9(d), with (11), the excess attenuation may be calculated for optimum or other parameter values from^{3,4}

$$EA = 10 \log(S) \quad (13).$$

6 Numerical examples and Discussion

6.1 Comparison with data: Avon Jet engine source

With $\mu_A = 4.03 \times 10^{-3}$, $P^{(0)} = 10^8$ and $m = 2.55$, the exponentially-modelled A-weighted source spectrum peaks at 633 Hz and simulates Avon jet-engine noise. The A-weighted sound levels predicted by the approximate theory over a variable porosity ground characterised by $\sigma_e = 30$ kPa s m⁻² and $\alpha_e = 16$ m⁻¹, are compared with measurements obtained under zero wind, low turbulence conditions⁹, in Figure 3. Other parameter values used in the predictions are $\langle n^2 \rangle = 10^{-8}$, $L_0 = 1$ m, $\rho = 0$, $\varepsilon = 0.5$, $a_1 = 5 \times 10^{-7}$, $a_2 = 2 \times 10^{-12}$.

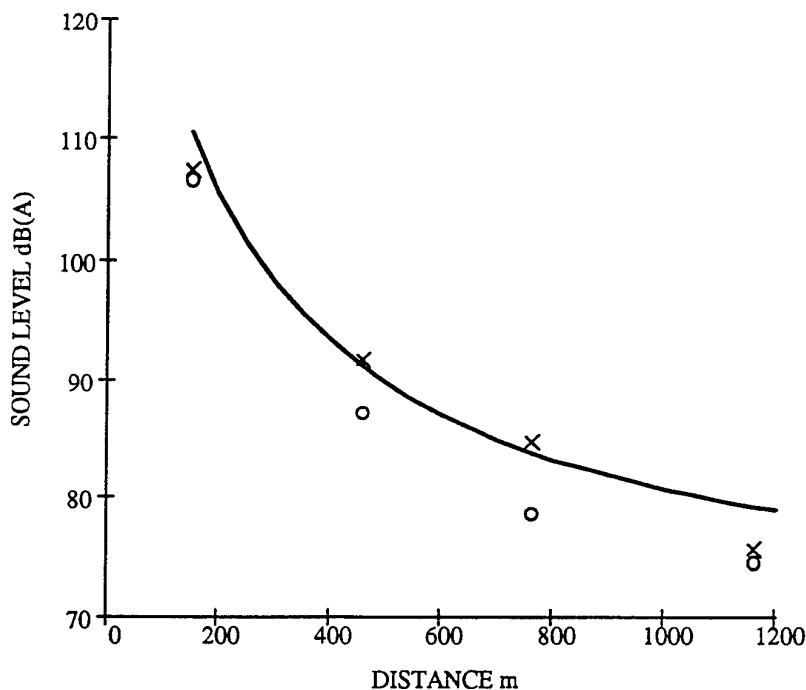


Figure 3 Comparison of predicted and measured sound level as a function of range from a fixed Avon jet engine ($h_s = 2.16$ m, $h_r = 1.2$ m) under zero wind low turbulence conditions. The data correspond to two twenty six second samples.

6.2 Sensitivity to spectrum and source height

Adopting the variable porosity ground model, a range of 500 m, the air absorption, turbulence and spectrum parameter values used for Figures 2 and 3, the optimum parameters are predicted to be $\sigma_{em} = 58.8 \text{ kPa s m}^{-2}$ and $\alpha_{em} = 7.74 \text{ m}^{-1}$. However, for the given A-weighted spectrum and source height, Figure 4 shows that the predicted excess attenuation is rather insensitive to variation in either of the ground parameters below certain values of them (say $\sigma_{em} < 10^3 \text{ kPa s m}^{-2}$ and $\alpha_{em} < 400 \text{ m}^{-1}$). Two decades of variation in flow resistivity or large variations in α_e below these values produce only 1 dB(A) change in predicted excess attenuation. Typical airport grassland^{9,10} with an effective flow resistivity of approximately 30 kPa s m^{-2} and α_e of approximately 15 m^{-1} is predicted to give a ground effect fairly near to the optimum. Such a surface is predicted to give a distinctly greater excess attenuation than acoustically-harder surfaces; specifically the excess attenuation is predicted to be approximately 19 dB(A) different from that predicted for an acoustically-hard surface (+ 3 dB(A)).

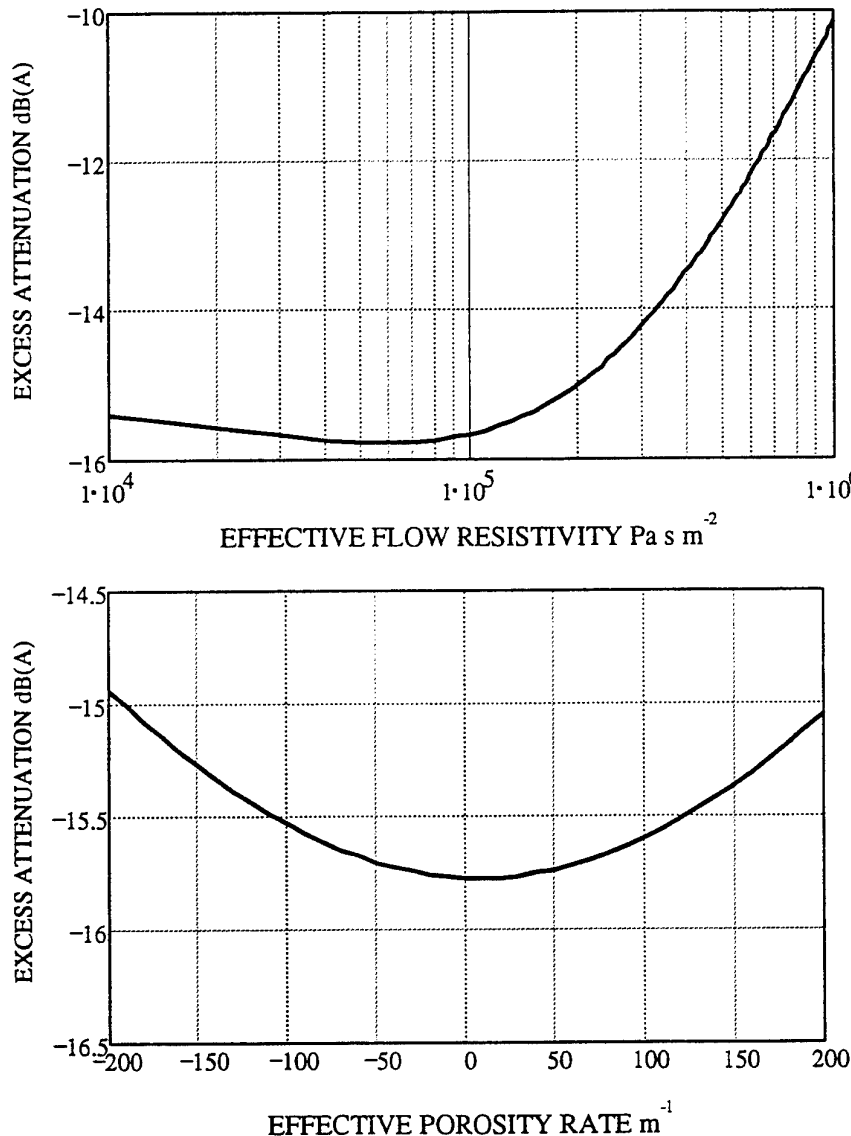


Figure 4 Predicted variation of excess attenuation at 500 m with variable porosity ground parameters for a source at 2.16 m height, receiver at 1.2 m height, an A-weighted spectrum simulated by $m = 2.55$ and $\mu_A = 4.03 \times 10^{-3}$, air absorption given by $a_1 = 5 \times 10^{-7}$, $a_2 = 2 \times 10^{-12}$, turbulence represented by $\langle n^2 \rangle = 10^{-8}$, $L_0 = 1$, $\rho = 0$, and no refraction.

Similar results are predicted, if the approximate rough porous surface impedance model is adopted. For example, the optimum rough ground parameters, for the source-receiver geometry and spectrum used for Figure 4, are predicted to be an effective flow resistivity of 107 kPa s m^{-2} and a roughness volume per unit area of 0.0077 m . This represents soil with roughness equivalent to close-packed hemi-spherical bosses of radius 0.08 m . Figure 5 shows the sensitivity of the predicted optimum excess attenuation to source height and turbulence. Although the optimum ground parameters are predicted to vary with distance from the source, choice of constant parameters within the optimum range is predicted to lead to near optimum excess attenuation.

The most useful optimisations of the excess attenuation of A-weighted noise due to ground effect are predicted to occur for low source heights, low peak frequencies in the A-weighted source spectrum and low turbulence. It should be noted that the predictions for low flow resistivities will be somewhat suspect since high flow resistivity impedance models have been assumed. Considerable increase in predicted excess attenuation over that for typical grassland is predicted to be possible for low source heights if the flow resistivity is low and either the porosity is near constant with depth or the roughness is fairly large. This suggests potential noise reduction from plowing or disking ground since either reduces flow resistivity while increasing roughness.

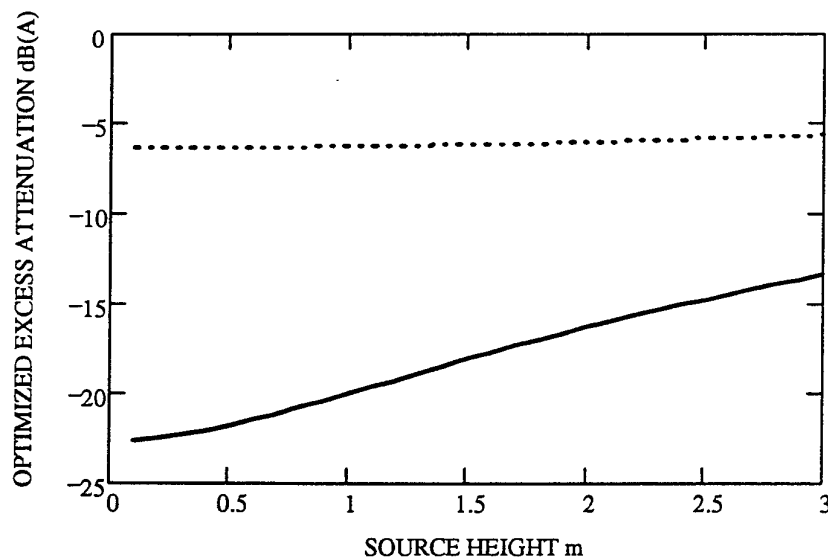


Figure 5 Variation of predicted optimum excess attenuation with source height for variable porosity or thin layer ground with source height: $h_r = 1.2 \text{ m}$, $d = 200$, $m = 2.55$, $\mu_A = 4.03 \times 10^{-3}$, $\beta = 5 \times 10^{-6}$. Dotted and solid lines represent predictions with strong and weak turbulence ($\langle n \rangle = 10^{-6}$ and 10^{-8} respectively).

6.3 Effects of refraction

The predicted optimum ground parameters represent increasingly hard ground under increasing downward refraction conditions and increasingly soft ground under increasing upward refraction conditions. The predicted optimum excess attenuations decrease as downward refraction increases and increase as upward refraction increases. The dependence is relatively slight for the given conditions, so that the predicted optimum ground effect is fairly robust to weak refraction.

7. Concluding remarks

By means of approximations of the classical theory for a point source above an impedance surface and approximate effective impedance models it is possible to derive closed-form relationships between excess attenuation ground effect, parameters relating to the A-weighted source power spectrum and the ground and source and receiver heights. Although the resulting predictions are approximate they suggest practical possibilities for optimising excess attenuation by means of controlling the ground characteristics. The greatest opportunities for such optimisation are predicted for sources with low frequency A-weighted spectral peaks and at ranges of less than 200 m under weak turbulence conditions and require rather acoustically-soft ground. The resulting predictions are fairly robust to weak atmospheric refraction. The optimum attenuations are predicted to be much higher for sources close to the ground. Since it may not be practicable to lower source heights for many noise sources, an alternative strategy is to raise the ground near the area of specular reflection, perhaps through landscaping. This possibility will be the subject of future work.

Acknowledgements

This work was supported in part by BBSRC Research Grant CTE 02649.

References

1. K.Attenborough and C.Howorth, Proc. Int.Tire-Road Noise Conference (Swedish National Board for Technical Development 1990)
2. K.Attenborough Applied Acoustics **25** 289 - 319 (1988)
3. K.B.Rasmussen Applied Acoustics **29** 313 - 324 (1990)
4. Delany and Bazley Applied Acoustics **3** 105-116 1970
5. R.Makarewicz J.Acoust. Soc. Am. **82** 1706 - 1711 (1987)
6. K.M.Li, K.Attenborough and N.W.Heap, J.Acoust.Soc.Am. **88** (2) 1170 - 1172 (1990)
7. K.Attenborough J.Acoust.Soc. Am. **92** 418-427 (1992)
8. R.Makarewicz J.Acoust. Soc. Am. **88** (2) 1172 - 1175 (1990)
9. K.Attenborough, S.Taherzadeh and K.M.Li Proc. INTERNOISE 95 **1** 319-322 (1995)
10. ESDU Data Item No.940355 "The correction of measured noise spectra for the effects of ground reflection" ESDU International plc, London (1994)
11. K.Attenborough, Acta Acustica **1** 213-226 (1993)
12. R.Raspel and J.M.Sabatier J.Acoust.Soc. Am. **99**(1) 147-152 (1996)
- 13.K.Attenborough and S.Taherzadeh, J.Acoust. Soc. Am. **98**(3) 1717-1722 (1995)
14. I. Rudnick, "Propagation of sound in open air", in *Handbook of Noise Control*, edited by C. M. Harris (McGraw Hill, New York, 1957), Chap. 3, pp. 3:1-3:17.

15. K. Attenborough *et al*, J. Acoust. Soc. Am. **97**, 173-191 (1995).
16. A L'Esperance, P.Herzog, G.A.Daigle and J.R.Nicolas, Applied Acoustics **37** 111-139 (1992)
17. K. M. Li, J. Acoust. Soc. Am. **93** 1727-1735 (1993).
18. K. M. Li, J. Acoust. Soc. Am. **99**, 746-754 (1996).
19. R. Raspet, A. L'Esperance and G. A. Daigle, J. Acoust. Soc. Am. **97**, 154-158 (1995).
20. K.M.Li, K.Attenborough and N.W.Heap, J.Sound Vib. **145** 11-128 (1991)
21. T. Hidaka, K. Kageyama and S. Masuda J. Acoust. Soc. Jpn (E) **6**, 117-125 (1985).
22. In Ref. 20 the angles are measured from the horizontal axis whereas, in this paper, the angle is measured from the vertical z-axis.
23. I.Gradshteyn and I.Ryzhik, Tables of Integrals, Series and Products (Academic, New York, 1980) 496, 3.953.1 and 2

New Analytical Expressions for Predicting Diffraction and Ground Effects

J. DEFRENCE and Y. GABILLET

*Centre Scientifique et Technique du Bâtiment
24, rue Joseph Fourier
38400 Saint-Martin-d'Hères, FRANCE
FAX (33) 76 44 20 46*

Abstract

New analytical expressions have been found to evaluate both ground and diffraction effects for traffic noise situations at quite large distances. The ground effect expression is an approximation at grazing angles of the well-known Chien and Soroka formulation. The diffraction expression is based on the properties of the first Fresnel ellipsoid applied to single screen attenuation. Then it is expressed by means of approximations of UTD to more complex impenant barriers such as embankments, wedges and three-sided obstacles. The complete model in an homogeneous atmosphere (called MAPB-H) is obtained by combinig these expressions using a classical geometrical method. In the case of an atmosphere with a constant celerity gradient, the use of corrective length and height terms gives the complete formulation for the MAPB-F (for a positive gradient favourable to propagation) and for the MAPB-D (for a negative gradient unfavourable to propagation). Comparisons with results obtained from BEM and from a Rasmussen-Brekhovskikh numerical method have shown good agreement.

Introduction

This work is undertaken at a time when French regulations for traffic noise are becoming more and more demanding: maximum acceptable sound levels are decreasing. This has brought about the need of sound prediction at long ranges including meteorological effects. Thus, a simple and fast Analytical Method for Noise Prediction (called MAPB in French) has been developed for engineering purpose (meaning *no numerical calculation*) in order to answer this need. The source, considered as spherical and harmonic, is close to an asphalt type surface. Receiver is above a grass type ground and is in the far field of the emission. There may be an obstacle between source and receiver, in the close field of the source. A typical case of interest is shown in Fig.1.

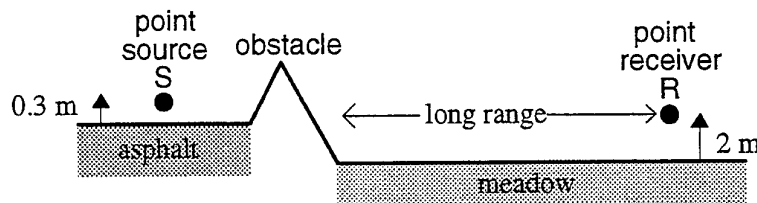


Fig.1. Geometry of a typical case of interest for the MAPB

1. Ground effect expressions

Reference model

The one-parameter Delany and Bazley's model [1] is used to calculate the normalized ground admittance β for a locally reacting surface which is characterized by its flow resistivity σ and an infinite thickness [Fig.2].

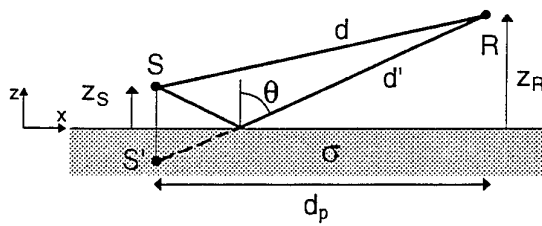


Fig.2. Geometry for the reflexion above an impedance plane

The reference model for the ground effect is the Chien and Soroka's formulation [2] derived from the Weyl-Van der Pol theory. Attenuation Att_{grd} is thus given by [see notations on Fig.2]:

$$Att_{grd} = 20 \log \left| 1 + \Omega \frac{d}{d'} e^{jk(d-d')} \right| \quad (1a)$$

k being the wave number and Ω being the spherical reflexion coefficient such as:

$$\Omega = R_p + (1 - R_p) F(w) \quad (1b)$$

with: $R_p = \frac{\cos \theta - \beta}{\cos \theta + \beta}$,

$$F(w) = 1 + j\sqrt{\pi w} e^{-w^2} erfc(-jw) ,$$

$$erfc(z) = \int_z^\infty e^{-ju^2} du ,$$

$$w = \sqrt{jkd'/2}(\beta + \cos \theta) , \quad \text{where } \sqrt{j} = e^{+j\pi/4} .$$

The calculation of $F(w)$ is carried out with the help of a numerical method [3]. However, this method, giving a reference result, is not appropriate for engineering purpose and thus new formulations of attenuation have been developed.

Short range and reflective ground expression

On the source side, the surface is reflective and distance between source and point of diffraction (at top of the obstacle) is not large. Approximation of attenuation is carried out by means of the following hypotheses:

$$k(d' - d) \approx \frac{2k z_s z_r}{d_p}, \quad |\beta| \ll \cos \theta \ll 1, \quad \Omega \approx R_p.$$

Moreover, for $(f/\sigma) < 40 \text{ Hz/rayls cgs}$, one has $\beta \approx |\beta| e^{-j\pi/4}$.

After some calculations, one gets the simplified MAPB expression of the attenuation Att_{grd}^{refl} for a reflective ground [4]:

$$Att_{grd}^{refl} = 10 \log \left[\left\{ 1 - \delta/d_p - A + \cos(k\delta) \right\}^2 + \left\{ A - \sin(k\delta) \right\}^2 \right] \quad (2)$$

with : $A = (1 - \delta/d_p) \frac{\sqrt{2}|\beta|d_p}{z_s + z_r}$, where : $\delta = \frac{2z_s z_r}{d_p}$

Long range and absorbing ground expression

On the receiver side, the surface is absorbing and distance between point of diffraction and receiver is large. Approximation of attenuation is carried out by means of the following hypotheses:

$$k(d' - d) \approx \frac{2k z_s z_r}{d_p}, \quad \cos \theta \approx \frac{z_s + z_r}{d_p} \ll |\beta|,$$

$$F(w) \approx \frac{j}{kd_p \beta^2}, \quad \beta \approx |\beta| e^{-j\pi/4}.$$

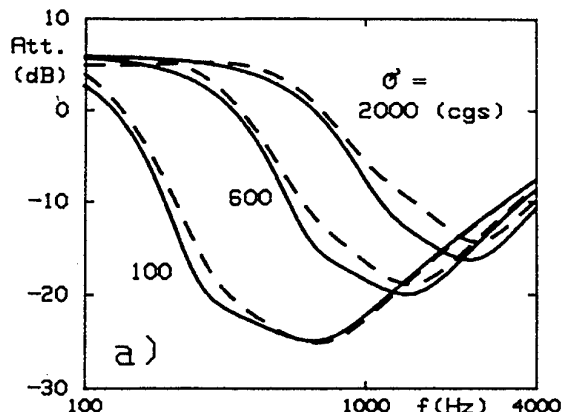
The simplified MAPB expression of the attenuation Att_{grd}^{abs} for an absorbing ground is [4]:

$$Att_{grd}^{abs} = 10 \log \left[\frac{4k^2}{d_p^2} (z_s^2 - \sqrt{2} C z_s + C^2)(z_r^2 - \sqrt{2} C z_r + C^2) \right] \leq 6 \text{ dB} \quad (3)$$

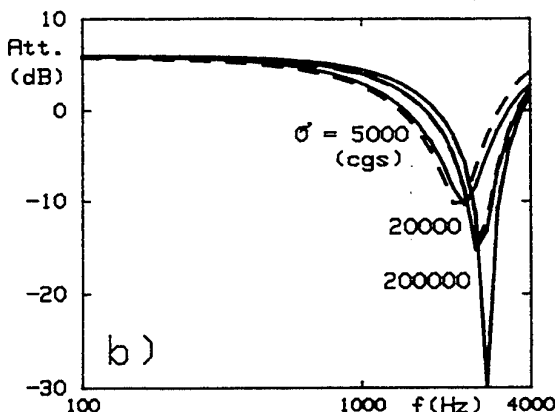
with : $C^2 = \frac{d_p}{k} \cdot \frac{1 + 3We^{-\sqrt{W}}}{1 + W}$, where : $W = kd_p |\beta|^2$.

Validation

Comparisons of Eq.(2) and Eq.(3) with the reference Eq.(1a) for different values of flow resistivity σ show good agreement [Fig.3].



MAPB calculation with Eq.(3)



MAPB calculation with Eq.(2)

Fig.3. Attenuation spectra from: Chien and Soroka ———, MAPB - - -
a) absorbing ground, $z_s=0,3\text{ m}$, $z_R=2\text{ m}$, $d_p=200\text{ m}$, $\sigma=100, 600$ et $2000 \text{ kPa.s.m}^{-2}$
b) reflective ground, $z_s=0,3\text{ m}$, $z_R=2\text{ m}$, $d_p=20\text{ m}$, $\sigma=5000, 20000$ et $200000 \text{ kPa.s.m}^{-2}$

2. Diffraction expressions

Single screen expression

The case of a reflective screen standing between source S and receiver R perpendicularly to the line of sight is considered. Geometry and notations are given in Fig.4.

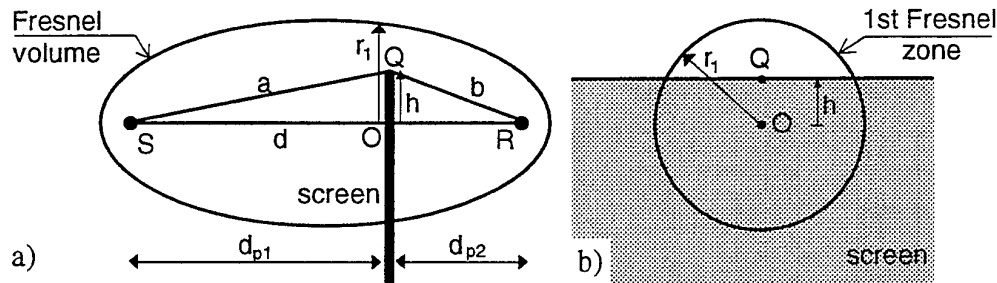


Fig.4. Geometry for the diffraction by a screen
a) view in the vertical plane containing S and R, b) view in the plane of the screen

Here r_1 is the radius of the first Fresnel zone in the plane of the screen [5]. If one introduces the non-dimensional so-called Fresnel number N defined as (λ being the wavelength):

$$N = \text{sign}(h) \frac{a+b-d}{\lambda/2},$$

one may write when $|h| \ll d_{p1}, d_{p2}$:

$$\sqrt[4]{N} \approx \frac{h}{r_1}$$

with: $\sqrt[4]{x} = \text{sign}(x)\sqrt{|x|}$.

Thus, N quantifies the penetration of the screen in the first Fresnel zone. With the use of this variable, the diffraction attenuation Att_{dif} according to Fresnel theory is given, when $d_{p1}, d_{p2} \gg r_1$, by [6]:

$$Att_{dif} = 20 \log \left| \frac{F_f(\sqrt[4]{\pi N})}{\sqrt{\pi}} \right| \quad (4)$$

where $F_f(x) = \int_x^{\infty} e^{j\tau^2} d\tau$ is the complex Fresnel integral.

The MAPB expression Δ_{dif} for the diffraction attenuation by a single screen is an analytical approximation of Eq.(4) and is given by [4,7]:

$\Delta_{dif}(N) = 0$	$N < -0,25$
$\Delta_{dif}(N) = -6 - 12 \sqrt[4]{N}$	$-0,25 \leq N < 0,25$
$\Delta_{dif}(N) = -8 - 8 \sqrt{N}$	$0,25 \leq N < 1$
$\Delta_{dif}(N) = -16 - 10 \log(N)$	$N \geq 1$

Double screen expression

The geometry of the double parallel screen problem is shown in Fig.5.

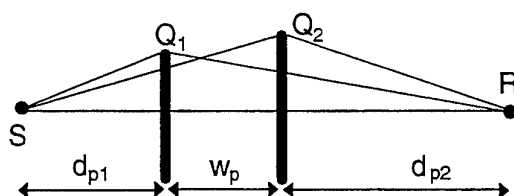


Fig.5. Geometry for the diffraction by a double screen

Here we consider that d_{p1}, w_p, d_{p2} are much bigger than the heights of the screens above the line of sight S-R. Then, if N_1 et N_2 are the Fresnel numbers relative to the paths S-Q₁-R and S-Q₂-R, diffraction attenuation by a double screen according to MAPB is given by [8]:

$$Att_{dif} = \Delta_{dif}(N_1) + \Delta_{dif}(N_2) + 6 + \left[12 - 20 \log \left(\frac{2}{1 - \alpha/\pi} \right) \right] \left(\frac{q}{p} \right)^{2p} \quad (6)$$

where: $\alpha = \operatorname{arctg} \left(\frac{w_p(d_{p1} + w_p + d_{p2})}{d_{p1} + d_{p2}} \right)^{1/2}$ and $p, q = \max, \min(\sqrt{2N_1}; \sqrt{2N_2})$.

Wedge expression

The geometry of the wedge problem is shown in Fig.6.

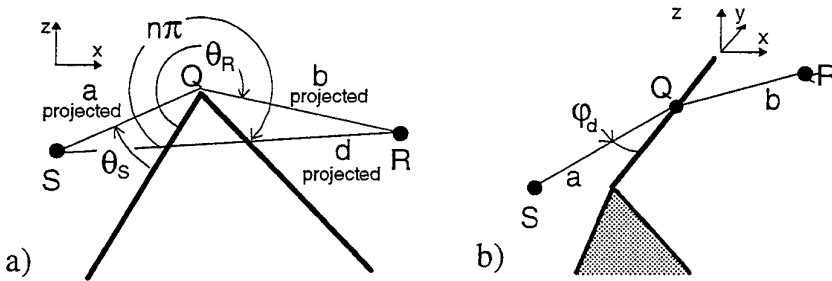


Fig.6. Geometry for the diffraction by a wedge
a) section view , b) perspective view

The reference model for calculating the attenuation is the UTD (Uniform Theory of Diffraction) [9]. Assuming that $\varphi_d \approx \pi/2$ and that, for $\pi \leq \alpha_i \leq (2n-1)\pi$ with $1 < n \leq 2$ [4]:

$$\frac{1}{n} \cot g \left(\frac{\pi - \alpha_i}{2n} \right) \approx \frac{1}{2} \cot g \left(\frac{\pi - \alpha_i}{4} \right),$$

one gets the MAPB expression for the diffraction by a reflective wedge [4]:

$$Att_{dif} = 20 \log \left| \zeta \sum_{i=1}^4 G_i \xi_i 10^{\frac{\Delta_{dif}(N_i \gamma_i)}{20}} \right| \quad (7)$$

where $\zeta = d/(a+b)$, $\xi_i = [1 + \sin(\alpha_i/2)]/2$, $\gamma_i = (a+b+d)/[2(a+b)]$

$d_1 = d = SR$, $d_2 = S'R$, $d_3 = SR'$, $d_4 = S'R'$,

$\alpha_1 = \theta_R - \theta_S$, $\alpha_2 = \theta_R + \theta_S$, $\alpha_3 = -(\theta_R + \theta_S)$, $\alpha_4 = -(\theta_R - \theta_S)$.

N_i is the Fresnel number relative to the i th path ($i=1$ to 4) appearing in the UTD formulation. Notations relative to these paths are explained in Fig.7.

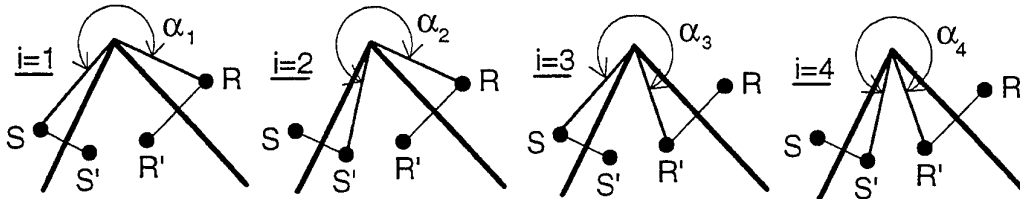


Fig.7. Definition of the four elementary paths.

The function Δ_{dif} is calculated from Eq.(5). Effect of impedance on wedge faces may be introduced heuristically in the same way as for UTD [10]. One must notice that Eq.(7) is simplifiable in many traffic noise problems when ζ , ξ_i and γ_i are reduced to 1.

Diffraction by a truncated wedge can be expressed as the product of two wedge diffractions [11]. Thus, Eq.(7) can be easily applied to such a case [12].

3. Complete model in homogeneous atmosphere

Expression of the MAPB-H

The combination of ground and diffraction effects are carried out by the use of a classical geometrical method. Two more hypotheses are made: the spherical reflexion coefficient is replaced by $(10^{\text{Att}_{grd}/20} - 1)$ and each elementary diffracted field referred to the free field is replaced by $10^{\text{Att}_{dif}/20}$. Thus, the complete expression of the method in a homogeneous atmosphere (called MAPB-H) is given by:

$$\text{Att}_{tot}^{\text{MAPB-H}} = 20 \log \left[10^{\frac{\text{Att}_{dif}(S, R)}{20}} + \left(10^{\frac{\text{Att}_{sol}^{rig}}{20}} - 1 \right) 10^{\frac{\text{Att}_{dif}(S_i, R)}{20}} + \left(10^{\frac{\text{Att}_{sol}^{obs}}{20}} - 1 \right) 10^{\frac{\text{Att}_{dif}(S, R_i)}{20}} \right. \\ \left. + \left(10^{\frac{\text{Att}_{sol}^{rig}}{20}} - 1 \right) \left(10^{\frac{\text{Att}_{sol}^{obs}}{20}} - 1 \right) 10^{\frac{\text{Att}_{dif}(S_i, R_i)}{20}} \right] \quad (8)$$

where S_i (resp. R_i) is the image source (resp. image receiver) relatively to the source ground (resp. receiver ground).

Validation

Validation is carried out with the help of a BEM software developed at CSTB [13]. Fig.8 and Fig.9 show results obtained from BEM and MAPB-H for the cases of a screen and an embankment respectively. Ground flow resistivities are $\sigma_s = 20000 \text{ kPa.s.m}^2$ (asphalt on source side) et $\sigma_r = 200 \text{ kPa.s.m}^2$ (meadow on receiver side). Four receiver positions are considered [Fig.8a and Fig.9a]. The agreement between BEM and MAPB-H is good. The interference visible on Fig.8d at 2200 Hz (and Fig.9d at 2900 Hz) is the second interference between direct ray and reflected ray on receiver side, and is not modelized in the MAPB expression for absorbing ground attenuation [Eq.(3)]. In Tab.1 are shown results in $dB(A)$ obtained by the two methods for the previous cases and for a traffic noise at emission.

For a one hundred points spectrum, calculation times are tenths of second for the MAPB-H and several hours for the BEM (on HP 9000/735 work station - 112 Mo RAM, 3 Go disk, 22 Mflops)

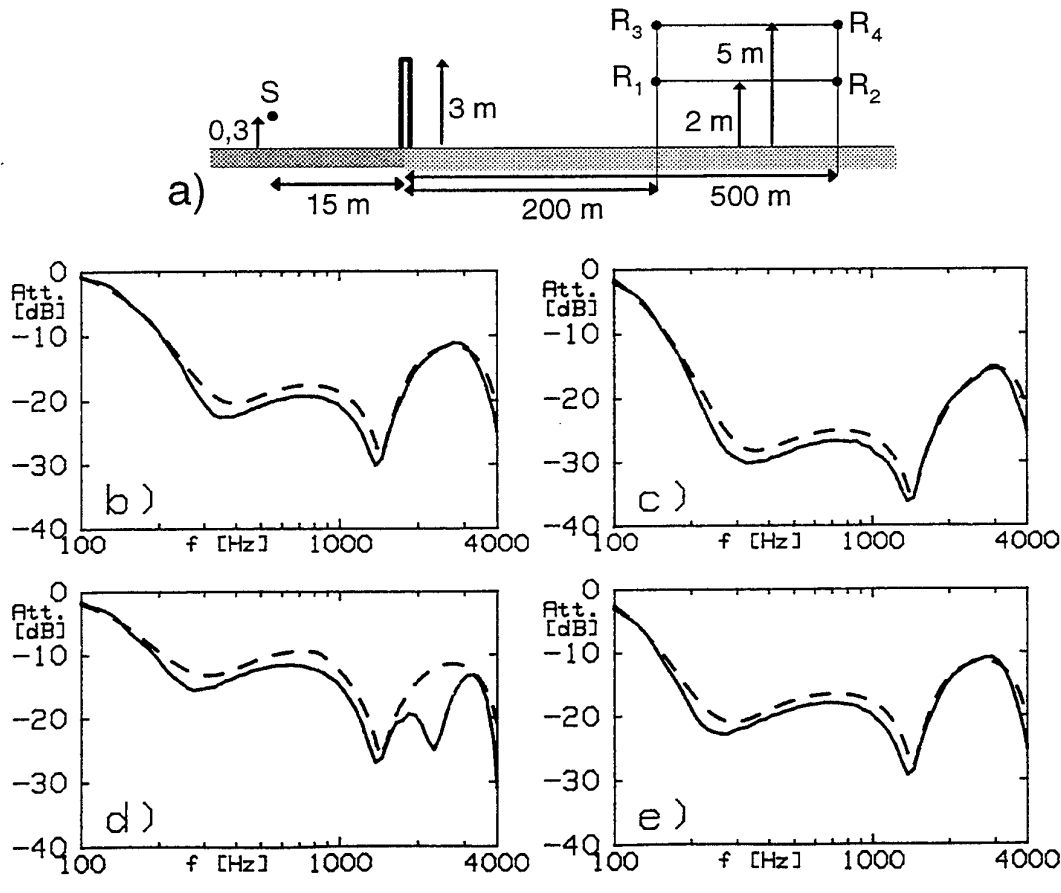


Fig.8. Case of a single screen. a) Geometry
Attenuation calculated at b) R_1 , c) R_2 , d) R_3 and e) R_4
BEM ———, MAPB-H - - -

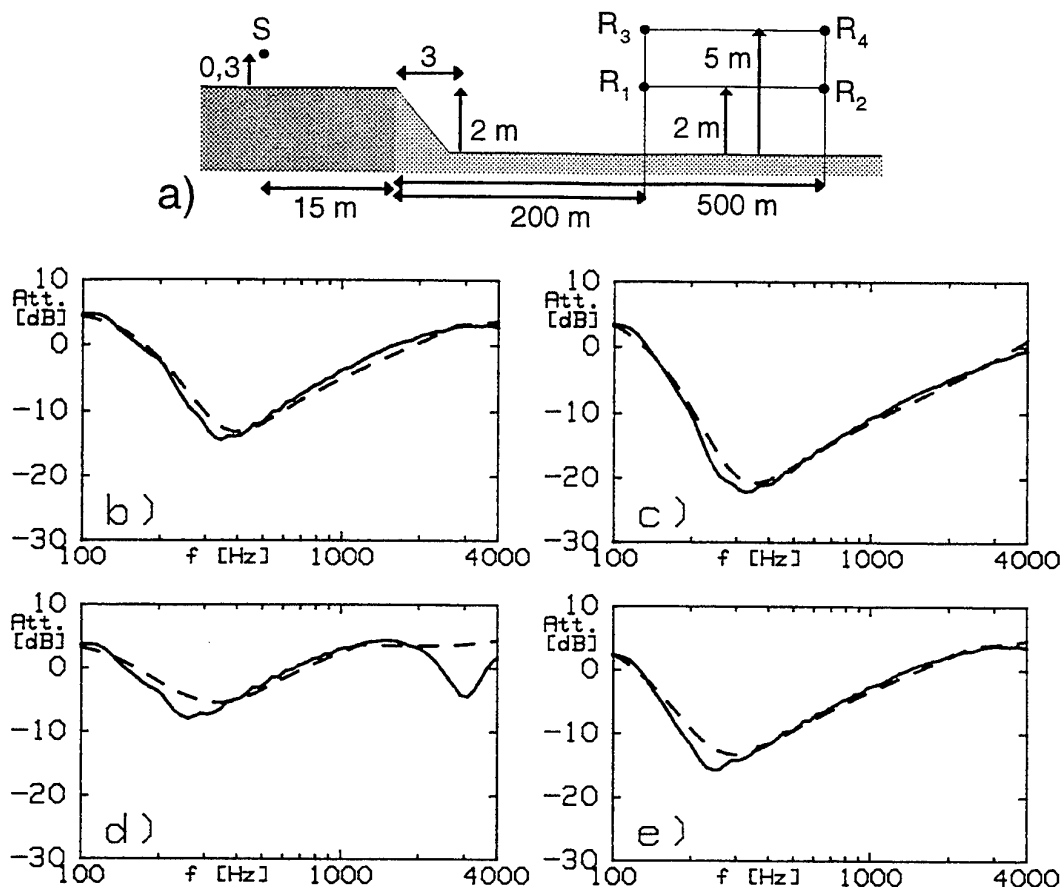


Fig.9. Case of an embankment. a) Geometry
Attenuation calculated at b) R1, c) R2, d) R3 and e) R4
BEM ———, MAPB-H - - -

case	method	R1 (b)	R2 (c)	R3 (d)	R4 (e)
screen (Fig.7)	BEM	-14.3	-17.8	-13.4	-15.9
	MAPB-H	-13.9	-17.5	-11.5	-15.2
embankment (Fig.8)	BEM	-1.4	-6.4	1.9	-0.8
	MAPB-H	-2.5	-6.3	0.8	-1.8

Tab.1. Attenuation in dB(A) obtained by the two methods for the eight previous cases and for a traffic noise at emission

4. Complete model in an atmosphere with a linear celerity gradient

Ground effect expression

In the case of an atmosphere with a linear celerity gradient a_0 , celerity $c(z)$ is given by:

$$c(z) = c_0(1 + a_0 z) \quad (9)$$

For small values of $|a_0|$, Brekhovskikh has shown that rays are circular with a radius of curvature nearly equals to $|a_0|^{-1}$ [14]. In the case of a single reflexion above a plane, an analogy *flat ground + curved rays / curved ground + straight rays* can be carried out [15]. This approximation is available for $a_0 > 0$ [Fig.10a] as well as for $a_0 < 0$ [Fig.10b].

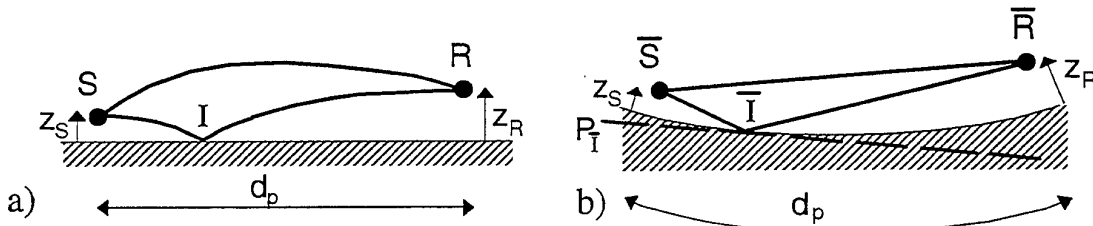


*Fig.10a. Ground effect with a positive celerity gradient
Representation : a) flat ground + curved rays, b) curved ground + straight rays*

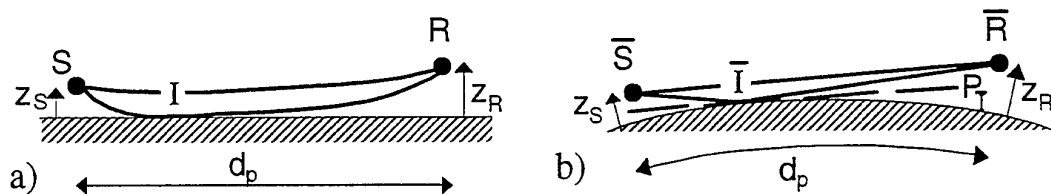


*Fig.10b. Ground effect with a negative celerity gradient
Representation : a) flat ground + curved rays, b) curved ground + straight rays*

The notations for the new problem (curved ground + straight rays) are the same with a bar above. The reflexion is considered to occur at the point \bar{I} above a fictitious plane $P_{\bar{I}}$ tangential to the curved surface at \bar{I} . Thus, Eq.(2) and Eq.(3) are usable with new variables \bar{z}_S , \bar{z}_R and \bar{d}_p given by:

$$\bar{d}_p^2 = d_p^2 - (\delta d_p)^2$$

$$\bar{z}_{S,R} = z_{S,R} + \delta z_{S,R}$$

(10)

δd_p (length correction) et de $\delta z_{S,R}$ (height correction) are written as [4]:

$$\boxed{\begin{aligned}\delta d_p &= a_0 \left| \frac{z_R - z_S}{z_R + z_S} \right| \frac{d_p^2}{2} \\ \delta z_{S,R} &= a_0 \left[\frac{z_{S,R}}{z_S + z_R} \right]^2 \frac{d_p^2}{2}\end{aligned}} \quad (11)$$

One may notice that δd_p is often negligible.

Diffraction effect expression

The diffraction effect expression is obtained as ground effects are not taken into account. If one considers Fresnel ellipsoid in the case of a screen in a homogeneous atmosphere [Fig.11a], this ellipsoid becomes curved in presence of a linear velocity gradient [Fig.11b].

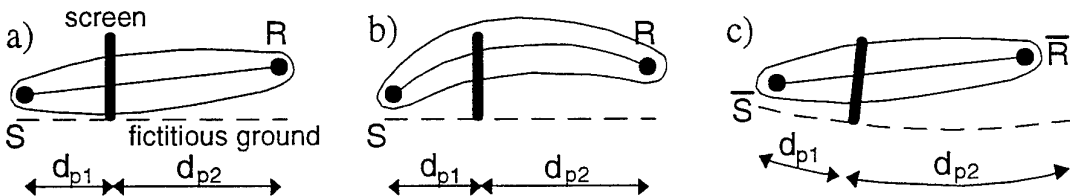


Fig.11. Diffraction effect with a positive celerity gradient

a) configuration with homogeneous atmosphere, b) and c) configurations with gradient
Representation : b) flat ground + curved rays, c) curved ground + straight rays

In the *curved ground + straight rays* representation, the ellipsoid is not curved anymore [Fig.11c] but the screen is more (for $a_0 < 0$) or less (for $a_0 > 0$) elevated of a quantity δh_e (in relation to the line $\bar{S}\bar{R}$) compared with the homogeneous case. For $d_p \ll |a_0|^{-1}$, δh_e is given by [4]:

$$\delta h_e = a_0 \frac{d_{p1} d_{p2}}{2} \quad (12)$$

MAPB-F and MAPB-D expressions

Complete formulations of the MAPB-F (for $a_0 > 0$) and MAPB-D (for $a_0 < 0$) are obtained from these previous results by using the MAPB-H complete expression, that is:

$$\text{Att}_{tot}^{MAPB-F,D} = 20 \log \left[10^{\frac{\text{Att}'_{dif}(S,R)}{20}} + \left(10^{\frac{\text{Att}'_{refl}}{20}} - 1 \right) 10^{\frac{\text{Att}'_{dif}(S_i,R)}{20}} + \left(10^{\frac{\text{Att}'_{abs}}{20}} - 1 \right) 10^{\frac{\text{Att}'_{dif}(S,R_i)}{20}} \right. \\ \left. + \left(10^{\frac{\text{Att}'_{refl}}{20}} - 1 \right) \left(10^{\frac{\text{Att}'_{abs}}{20}} - 1 \right) 10^{\frac{\text{Att}'_{dif}(S_i,R_i)}{20}} \right] \quad (13a)$$

where: $\text{Att}'_{refl} = \text{Att}_{refl}^{refl} \left(z_S + \delta z_S, z_e + \delta z_e, \sqrt{d_{p1}^2 - (\delta d_{p1})^2} \right)$

$$\text{Att}'_{abs} = \text{Att}_{abs}^{abs} \left(z_e + \delta z_e, z_R + \delta z_R, \sqrt{d_{p2}^2 - (\delta d_{p2})^2} \right) \quad (13b)$$

$$\text{Att}'_{dif} = \text{Att}_{dif} (z_S, z_R, z_e - \delta h_e)$$

Validity

The MAPB-F expression is valid as long as there are no multi-reflexion phenomena between screen and receiver, that is as long as (z_e being the height of the screen referred to receiver ground):

$$d_{p2} < 4 \sqrt{\frac{z_e + z_R}{a_0}} \quad (14)$$

The MAPB-D expression is applicable as long as the receiver is outside the shadow zone (delimited by the curved ray tangential to the flat ground), that is as long as:

$$d_{p2} < \sqrt{\frac{2z_e}{|a_0|}} + \sqrt{\frac{2z_R}{|a_0|}} \quad (15)$$

Validation

The validation of MAPB-F,D is performed by using a numerical method based on the works of Rasmussen [16] and Brekhovskikh [14]. The case of a screen in an atmosphere with a positive celerity gradient is considered here.

Attenuation at R has the form [16]:

$$Att_{tot} = 20 \log \left| \frac{d_p d_{p2} \sqrt{8\pi k_0}}{4\pi} \int_{z_e}^{\infty} \left[\frac{e^{j2\pi f(\tau_1 + \tau_3)}}{s_3 \sqrt{s_1 s_3 (s_1 + s_3)}} + \frac{\Omega_1' e^{j2\pi f(\tau_2 + \tau_3)}}{s_3 \sqrt{s_2 s_3 (s_2 + s_3)}} \right. \right. \\ \left. \left. + \frac{\Omega_2' e^{j2\pi f(\tau_1 + \tau_4)}}{s_4 \sqrt{s_1 s_4 (s_1 + s_4)}} + \frac{\Omega_1' \Omega_2' e^{j2\pi f(\tau_2 + \tau_4)}}{s_4 \sqrt{s_2 s_4 (s_2 + s_4)}} \right] dz \right| \quad (16)$$

where k_0 is the wavenumber at $z=0$, s_i and τ_i are respectively the curvilinear length and the traveling time relative to the i th elementary path [Fig.12], and Ω_1' and Ω_2' are calculated from Eq.(1b) with $\Omega_1' = \Omega(\theta_1', s_2, \beta_1, k_0)$ and $\Omega_2' = \Omega(\theta_2', s_4, \beta_2, k_0)$.

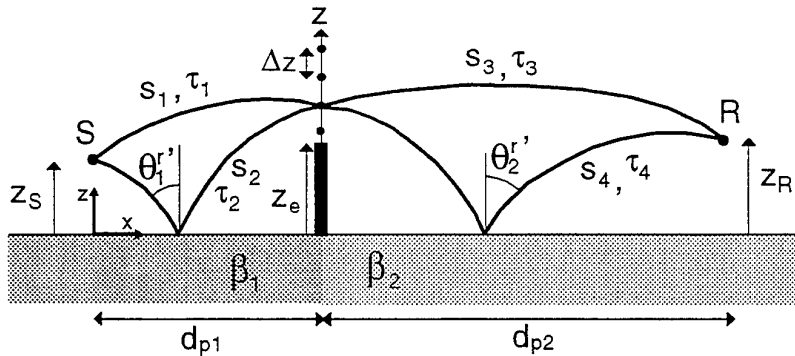


Fig.12. Geometry for the Rasmussen-Brekhovskikh solution in an atmosphere with a constant positive celerity gradient

An example is given in Fig.13 for the case of the screen. Different values of the (positive) celerity gradients are considered. Ground resistivities are $\sigma_s = 50000 \text{ kPa.s.m}^2$ (on source side) et $\sigma_r = 100 \text{ kPa.s.m}^2$ (on receiver side). The agreement between numerical method and MAPB-F is good. The interference visible on Fig.13b at 2900 Hz is, as in the homogeneous case, the second interference between curved direct ray and curved reflected ray on receiver side, and is not modelized in the MAPB expression for absorbing ground attenuation [Eq.(3)]

For a one hundred points spectrum, calculation times are tenths of second for the MAPB-H and several minutes for the Rasmussen-Brekhovskikh method (on HP 9000/735 work station - 112 Mo RAM, 3 Go disk, 22 Mflops)

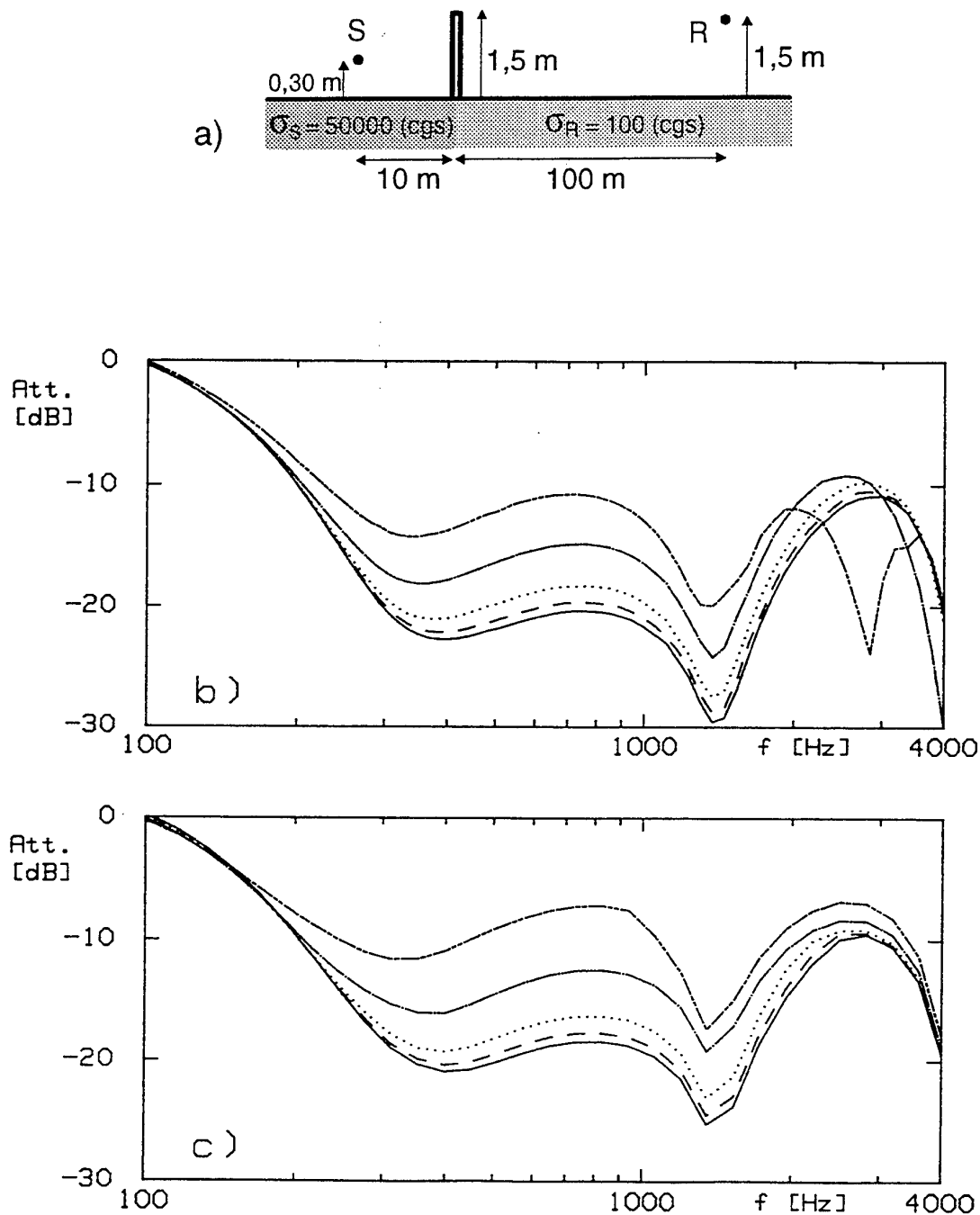


Fig.13. Attenuations for the configuration given in a)
calculated with : b) Rasmussen-Brekhovskikh , c) MAPB-F
for values of celerity gradient a_0 (in m^{-1}):
 10^{-5} ———, 5.10^{-5} - - - - , 10^{-4} - - - - - , 2.10^{-4} - - - - - , 5.10^{-4} - - - - -

Conclusion

An analytical method for traffic noise prediction (called MAPB) has been presented, and new expressions for ground and diffraction effects have been explained. This method can be used in the case of a homogeneous atmosphere as well as an atmosphere with a constant (positive or negative) celerity gradient. Comparisons with numerical methods have shown good agreement. MAPB is a simple and fast tool: no numerical integration is needed. Its calculations are transparent: each term of its formulation has a physical meaning. Moreover, it is evolutionary: new analytical diffraction expressions for more complex barriers could be developed and easily inserted in it.

Acknowledgements

The authors would like to thank the French Road Administration, the Environment Ministry and the French Environment and Energy Agency (A.D.E.M.E.) for their financial support.

References

- [1] DELANY M. E., BAZLEY E. N., *Acoustical properties of fibrous absorbent materials*, Appl. Acoust. 3, pp. 105-116, (1970)
- [2] CHIEN C. F., SOROKA W. W., *Sound propagation along an impedance plane*, J. Sound Vib. 43(1), pp. 9-20, (1975)
- [3] CHIEN C. F., SOROKA W. W., *A note on the calculation of sound propagation along an impedance surface*, J. Sound Vib. 69(2), pp. 340-343, (1980)
- [4] DEFRENCE J., *Analytical method for the calculation of outdoors sound propagation*, Ph.D. Dissertation, Université du Maine , 180 p. (1996)
- [5] SCHREIDEN A., DE MULLEWIE G., *Traitements pratiques de la diffraction et des problèmes connexes*, Bulletin d'Acoustique 13, pp. 9-33, (1992)
- [6] MACDONALD H. M., *Diffraction at a straight edge*, Proceed. London Math. Soc. 2, pp. 103-105, (1915)
- [7] DEYGOUT J., *Évaluation de l'affaiblissement de propagation des ondes décimétriques en zone rurale*, L'Onde Électrique 72(3), pp. 56-63, (1992)
- [8] MILLINGTON G., HEWITT R., IMMIRZI F. S., *Double knife-edge diffraction in field strength prediction*, Inst. Elec. Eng. Monograph 507E, pp. 419-429, (1962)
- [9] KOUYOUMJAN R. G., PATHAK P. H., *A uniform geometrical theory of diffraction for an edge in a perfectly conducting surface*, proc. IEEE 62, pp; 1448-1461, (1974)
- [10] KOERS P., *Diffraction by an absorbing barrier or by an impedance transition*, Proceed. Inter-Noise 83, pp.311-314
- [11] KAWAI T., *Sound diffraction by many-sided barrier or pillar*, J. Sound Vib. 79(2), pp. 229-242, (1981)
- [12] DEFRENCE J., GABILLET Y., *New analytical expressions for predicting outdoor sound propagation over a complex terrain*, proceed. Inter-Noise 96, pp. 3113-3116, (1996)
- [13] JEAN P., GABILLET Y., *A boundary element method program to study 2D noise barriers with ground effects*, proceed. Euro-Noise 95, pp. 251-256, (1995)
- [14] HIDAKA T., KAGEYAMA K., MASUDA S., *Sound propagation in the rest atmosphere with linear sound velocity profile*, J. Acoust. Soc. Jpn 6(2), pp. 117-125, (1986)
- [15] ALMGREN M., *Simulation by using a curved ground scale model outdoor sound propagation under the influence of a constant sound speed gradient*, J. Sound Vib. 118(2), pp. 335-370, (1987)
- [16] RASMUSSEN K. B., *A note on the calculation of sound propagation over impedance jumps and screens*, J. Sound Vib. 84(4), pp. 598-602, (1982)

**On the analogy between sound propagation over a rough surface
and sound propagation over a smooth surface with modified surface impedance**

Yves H. BERTHELOT

School of Mechanical Engineering

Georgia Institute of Technology

Atlanta, GA 30332, USA

FAX: (404) 894-7790

e-mail: yves.berthelot@me.gatech.edu

James P. CHAMBERS

National Center for Physical Acoustics

University, MS,38677 USA

Abstract:

The propagation of sound at grazing incidence over a rigid, rough surface can be modeled by introducing a *complex roughness parameter* ϵ whose magnitude is the standard roughness parameter discussed by Tolstoy and Medwin, and whose phase accounts for the attenuation of the boundary wave with distance by incoherent scattering. With this complex roughness ϵ , the analogy between a flat impedance boundary condition and a rough, rigid boundary condition is $\beta \rightarrow -ik\epsilon$, where β is the normalized surface admittance and k the wavenumber. This analogy has been successfully used to predict the sound field behind a curved, rigid surface at several frequencies, successively on the surface, along the line of sight, and along a vertical axis starting in the deep shadow, by computing the creeping wave series with a modified surface parameter $q = i(kl)\beta = (kl)(k\epsilon)$, where the phase of ϵ varies as $f^{3.3}$.

I. Background

A classical result concerning the reflection of sound from randomly rough surfaces is that incoherent scattering by the surface irregularities causes the reflection coefficient to decrease by a factor of the order $e^{-2k_z^2 d^2}$, where d is a characteristic length scale of the roughness and k_z is the wavenumber component normal to the surface.¹ This incoherent scattering is a second order effect in kd . However, Biot and Tolstoy have shown that the coherent part of the scattered field is a first order perturbation in kd which leads to more important effects, especially near the rough boundary.²⁻⁶ Specifically, the coherently scattered field appears in the form of a *boundary wave* localized near the rough surface. This boundary wave can be very substantial at large distances

in outdoor sound propagation near a rough ground. Methods based on perturbation techniques, for instance, cannot predict this first order effect because these methods are intrinsically second-order methods. The strength of the Biot-Tolstoy approach is that it is a first order theory, it is valid for steep-slope, densely packed scatterers, it includes de facto multiple scattering and back-scattering, and it is valid at grazing incidence. In addition, it is also valid in principle for non-isotropic roughness, and even for space-dependent surface statistics. All these elements are common occurrence on long range sound propagation.

In a nutshell, the Biot-Tolstoy approach consists in replacing the rough boundary by a distribution of monopoles and dipoles whose scattering coefficients depend on the geometry of the boundary. If the scatterers are smaller than a wavelength, their strength can be calculated from Rayleigh scattering theory. In the case of isotropic roughness, the Biot-Tolstoy boundary condition is written as:³

$$\phi_z + \epsilon(k^2\phi + \sigma\phi_{zz}) = 0 \quad (1)$$

where ϕ is the acoustic velocity potential, the z -axis is normal to the surface baseline, k is the acoustic wavenumber in the upper fluid, and ϵ and σ are two parameters directly related to the geometry of the rough surface.^{3,7} For the purpose of this paper, and for the discussion below, the scatterers are assumed to be perfectly rigid, although this is not a limitation of the Biot-Tolstoy approach.^{4,8}

When $|\sigma\phi_{zz}| \ll |k^2\phi|$, i.e., when $\sigma \sin^2 \theta \ll 1$, where θ is the grazing angle, the boundary condition (1) is approximated by:

$$\phi_z + \epsilon k^2 \phi = 0. \quad (2)$$

This approximate boundary condition is therefore appropriate at near grazing sound propagation and/or for sparse scatterers. This boundary condition at a rough interface is in the form of a standard impedance boundary condition at a flat plane (with the $e^{-i\omega t}$ convention):

$$\phi_z + \eta\phi = 0. \quad (3)$$

where $\eta = ik\beta$, and $\beta = \rho c/Z_s$, is the normalized surface admittance, ρc being the characteristic impedance of the upper fluid. By comparing boundary conditions (2) and (3), it appears that there is a formal analogy between sound propagation near a flat impedance plane and near a randomly rough, rigid plane, if $\eta = k^2\epsilon$, i.e., if

$$\beta = -ik\epsilon \quad (4)$$

This analogy has been suggested by several authors, and it has also been discussed in the context of non-rigid rough surfaces.^{4,8,9} With this analogy, the Biot-Tolstoy boundary

wave that propagates along a rough surface is formally equivalent to Wenzel's trapped surface wave¹⁰ near an impedance plane with large reactance. Indeed, Wenzel's eq. (20) in Ref. 10 is exactly the same as Tolstoy's equation (13) in Ref. 6 if $\eta = k^2\epsilon$ and κ , the wavenumber of the boundary mode, is $\sqrt{k^2 + \eta^2}$. Both boundary modes (surface wave or boundary wave) are confined to an exponential layer near the boundary with $1/e$ height $(\epsilon k^2)^{-1}$ (or $1/\eta$), both modes are slightly subsonic, but the deviation from the free field sound speed is a second order effect and it can be safely ignored. (The analogy turns out to be exact for hemispherical scatterers).

II. Complex roughness parameter

The analogy represented by eq. (4) is appealing but it must be taken cautiously. In fact it is easy to show that, because ϵ is a real number, the equivalent surface impedance is purely imaginary and there is no corresponding attenuation of the boundary wave, an unphysical attribute. Clearly, one has to introduce a *complex roughness parameter* ϵ to account for the attenuation $e^{-\delta r}$ of the boundary wave with distance r along the boundary.

Let $\epsilon = |\epsilon|e^{im}$, where $|\epsilon|$ is the usual roughness parameter discussed extensively by Tolstoy, Medwin, and, recently, Attenborough.^{3,7,8} The phase of ϵ can be found from the attenuation coefficient δ , which has also been extensively discussed by Tolstoy and Medwin. It can be shown that m is related to δ by :

$$\cos(2m) = \frac{1}{A}(-\delta + \sqrt{A^2 - k^2}) \quad (5)$$

where $A = k^4|\epsilon|^2/(2\delta)$. Conversely, one can express the attenuation of the boundary wave in terms of the phase of the roughness parameter ϵ , according to:

$$\delta = \left[\frac{-C_2 + \sqrt{C_2^2 + 4C_1}}{2} \right]^{1/2} \quad (6)$$

where $C_1 = (k^8|\epsilon|^4/4)\sin^2(2m)$ and $C_2 = k^2 + |\epsilon|^2k^4\cos(2m)$. In the rest of the paper, the analogy between the rough plane boundary condition the impedance plane boundary condition is tested with the complex roughness parameter ϵ in an attempt to predict the data reported by Chambers and Berthelot¹¹ in the case of the sound field in the shadow zone of a curved, rigid, rough surface.

III. Diffraction of sound by a curved, rigid, rough surface

The sound field behind a curved, smooth, boundary of finite normalized admittance β is accurately modeled by a creeping wave series (CWS) which depends on a parameter

q that includes both the effect of curvature and the finite impedance of the surface.¹² In fact, q is defined by

$$q = i(kl)\beta \quad (7)$$

where l is the Fock diffraction length defined by $l = (kR/2)^{1/3}$, k being the acoustic wavenumber and R , the radius of curvature of the hill ($kR >> 1$). Following the analogy $\beta \rightarrow -ik\epsilon$, (see eq. (4)), one can model the sound field behind a curved, rough, rigid, surface with the creeping wave series in which the surface parameter q is replaced by $(kl)(k\epsilon)$, where ϵ must be complex to account for the attenuation of the boundary wave through incoherent scattering.

This model was tested against the experimental data reported in Ref. 11. Because the attenuation coefficient for a boundary wave along a curved surface is not known, the problem was reformulated as follows: is there any complex coefficient q (i.e., any complex roughness parameter ϵ) that can be used in the creeping wave series to model accurately the data reported in Ref. 11?

1. Optimum parameter q

The optimum value of q was found by a least-square minimization of the difference between the model (CWS) and the data, successively at 5, 6, 8, 10 and 12 kHz. For each frequency, all three geometries reported in Ref. 11 were used: on the surface, along the line of sight, and along a vertical axis starting from the surface in the shadow zone. The radius of curvature was approximately 2.5 m, the data on the surface was taken from -0.2 to +1.0 m, the data along the line of sight was taken from 0 to 1.4 m, and the data along the vertical axis, at an arc radius of 1.00 m behind the apex, ranged from the surface ($z = 0$ m) to 0.40 m, and it crossed the line of sight at 0.20 m.

The quantity that was minimized is the standard deviation, $\bar{\sigma}$, between the theoretical and experimental values of the sound pressure levels relative to free field.

$$\bar{\sigma} = \left[\frac{1}{N} \sum_{i=1}^N (L_{\text{theo}} - L_{\text{data}})^2 \right]^{1/2} \quad (8)$$

where the summation is over the N data points at that frequency for the three geometries discussed above. The results are given in Table 1.

2. Results

The results are shown in Figures 1 to 4 at 5, 8, 10, and 12 kHz, respectively. Each figure contains 3 plots of the relative sound pressure level versus (a) arclength s along the surface ($s = 0$ being the apex), (b) horizontal distance x along the line of sight ($x = 0$ being the apex), and (c) the vertical axis that starts at $s = 1$ m in the deep shadow behind the apex. In Figures 1 to 4, the circles are the data points (curved, rough, rigid

surface), the solid line represents the creeping wave series with the optimum value of q (see Table 1). To illustrate the importance of the roughness effects, the theory for $q = 0$, i.e., for a rigid, smooth surface is plotted with a dashed line. The dotted line corresponds to the analogy (equation 4) in which ϵ is taken to be a real quantity. For convenience, this will be referred to as the "standard analogy".

Clearly, at each frequency, there is a complex q , or alternatively, a complex ϵ , that can be used to model accurately the sound field behind the curved, rigid, rough surface. The analogy [Eq. (4)], appears to be indeed a powerful modeling tool, provided that one allows for a complex value of the roughness parameter. The analogy fails when the roughness parameter is purely real.

3. Dependence of $|q|$ on $k|\epsilon|$

If the analogy described by eq. (4) holds, the ratio $|q|/kl$ should be equal to $k|\epsilon|$. The results are shown in Table 2, where the roughness parameter $|\epsilon|$ was taken to be about 1 mm (ref. 11). It appears that, indeed, the ratio of $|q|/kl$ to $k|\epsilon|$ is nearly equal to unity at all frequencies, thus confirming the validity of the analogy, at least with respect to the modulus of the roughness parameter.

4. Dependence of the phase of q , and of the attenuation δ on $k|\epsilon|$

The results are shown in Table 3. At those frequencies, the phase of the optimum value of q is between 0.2 and 0.3 radian (11° to 17°). According to eq. (6), this corresponds to an attenuation δ that varies nonlinearly with $k|\epsilon|$. A least-square fit shows that the attenuation varies as:

$$\delta = \Gamma(k|\epsilon|)^p \quad (9)$$

where $\Gamma = 407$ and $p = 3.3$. This is in contrast with the k^6 dependence of the attenuation of the boundary wave on a flat, rough surface.⁶ This confirms that the attenuation of boundary waves that creep in the shadow zone is not as strong as the attenuation of the same boundary wave, if it were to propagate on a flat, rough surface. This also confirms that the effect of surface roughness can be rather substantial in a shadow zone. At this point, it is not clear why the attenuation of the boundary wave in the shadow zone follows a $f^{3.3}$ dependence.

5. Empirical model

Based on the results discussed above, it is possible to predict the sound field in the shadow zone, behind a curved, rigid, rough surface, from only the frequency, f , the radius of curvature R of the hill, and the magnitude of the roughness parameter $|\epsilon|$. The model consists in using the creeping wave series¹² in which the surface parameter

q is such that its modulus is $(kl)(k|\epsilon|)$, where $l = (kR/2)^{1/3}$, and where the phase of q is found from eq. (5) above in which the attenuation δ is computed from eq. (9). Note that the phase of q is also the phase of ϵ , since $q = (kl)(k\epsilon)$ in the proposed analogy. The results of this prediction scheme are shown in Figures 5-8 in which the circles are the measured values of the relative sound pressure level and the solid line is the proposed model. The agreement is quite acceptable.

IV. Summary and conclusions

The propagation of sound over a curved, rigid, rough surface can be accurately modeled by introducing a complex roughness parameter ϵ whose magnitude is the standard roughness parameter discussed by Tolstoy and Medwin, and whose phase accounts for the attenuation of the boundary wave with distance. With this complex roughness ϵ , the analogy between a flat impedance boundary condition and a rough, rigid boundary condition is $\beta \rightarrow -ik\epsilon$, where β is the normalized surface admittance and k the wavenumber.

This analogy has been successfully used to predict the sound field behind a curved, rigid surface at several frequencies, successively on the surface, along the line of sight, and along a vertical axis starting in the deep shadow, by computing the creeping wave series with a modified surface parameter $q = i(kl)\beta = (kl)(k\epsilon)$.

The validity of such an analogy is very appealing for prediction purposes in long range sound propagation, either over natural hills covered with individual scatterers (assumed to be smaller than the wavelength), or in the case where the shadow zone is caused by sound refraction in the atmosphere.

References:

- [1] J. A. Ogilvy, *Theory of wave scattering from random surfaces*, Adam Hilger, New York, 1991.
- [2] M. A. Biot, "Generalized boundary condition for multiple scatter in acoustic reflection," *J. Acoust. Soc. Am.* **44**, 1616-1622 (1968)
- [3] I. Tolstoy, "Scattering of spherical pulses by rough surfaces," *J. Acoust. Soc. Am.* **66**(4), 1135-1145 (1979)
- [4] I. Tolstoy, "Energy transmission into shadow zone by rough surface boundary wave," *J. Acoust. Soc. Am.* **69**(5), 1290-1298 (1981)
- [5] I. Tolstoy, "Smoothed boundary conditions, coherent low frequency scatter, and boundary modes," *J. Acoust. Soc. Am.* **75**(5), 1-22 (1984)
- [6] I. Tolstoy, "Rough surface boundary wave attenuation due to incoherent scatter," *J. Acoust. Soc. Am.* **77**(2), 482-491 (1985)

- [7] K. Attenborough and S. Taherzadeh, "Propagation from a point source over a rough finite impedance boundary," J. Acoust. Soc. Am. **98**(3), 1717-1722 (1995)
- [8] H. Medwin and G. D'Spain, "Near-grazing, low frequency propagation over randomly rough rigid surfaces," J. Acoust. Soc. Am., **79**(3), 657-665 (1986)
- [9] M. S. Howe, "On the long range propagation of sound over irregular terrain," J. Sound and Vib., **98**, 83-94 (1985)
- [10] A. R. Wenzel, J. Acoust. Soc. Am. **55**(5), 956-963 (1974)
- [11] J. P. Chambers and Y. H. Berthelot, J. Acoust. Soc. Am. **95**(5), part 2 , (1995)
- [12] A. Berry and G. A. Daigle, J. Acoust. Soc. Am. **83**(6), 2047-2058 (1988)

f (kHz)	$ q $	phase of q	rms-error (dB)
5	0.48	0.25	0.25
6	0.61	0.22	0.35
8	0.81	0.23	0.60
10	1.10	0.27	1.0
12	1.49	0.29	1.7

Table 1: Optimum values of q

f (kHz)	$ q $	kl	$ q / kl$	$k \epsilon $	$(q /kl) / k \epsilon $
5	0.48	4.85	0.099	0.091	1.08
6	0.61	5.15	0.118	0.109	1.08
8	0.81	5.67	0.143	0.145	0.98
10	1.10	6.11	0.180	0.183	0.99
12	1.49	6.49	0.230	0.219	1.05

Table 2: Dependence of $|q|/ (kl)$ on $k|\epsilon|$.

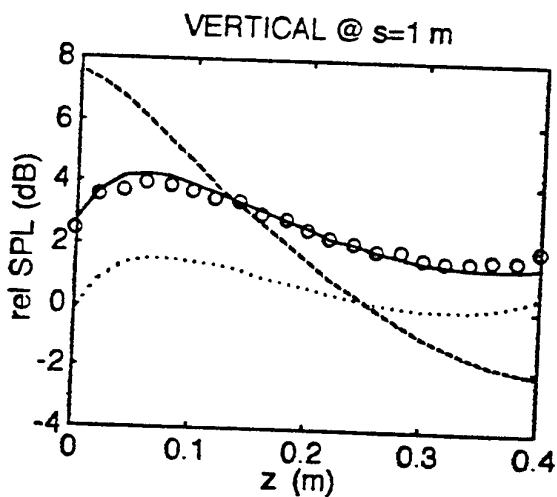
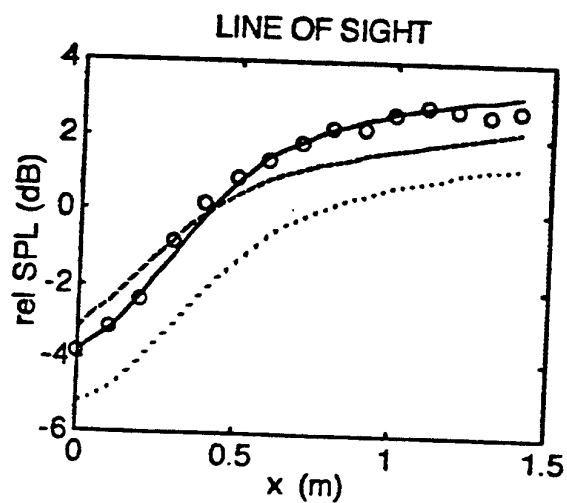
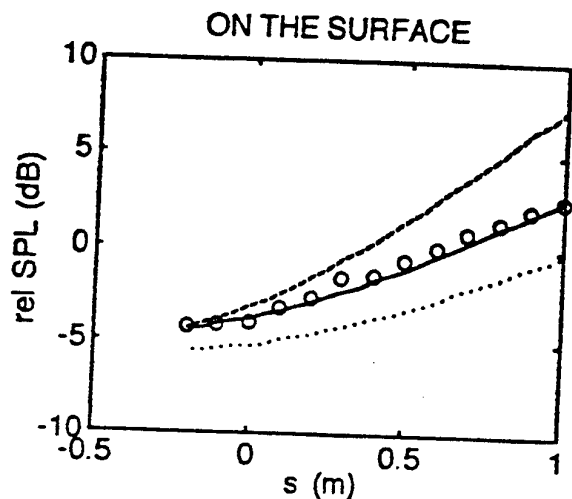
f (kHz)	phase of q	$ \epsilon $	δ	$k \epsilon $
5	0.25	1.0	0.182	0.091
6	0.22	1.0	0.279	0.109
8	0.23	1.0	0.686	0.145
10	0.27	1.0	1.544	0.183
12	0.29	1.0	2.828	0.219

Table 3: Dependence of the phase of q , and of the attenuation δ on $k|\epsilon|$

Sound Pressure Levels Relative to Free Field

$f = 5 \text{ kHz}$

$$(k|\epsilon| = 0.09, kR = 228, kl = (kR/2)^{1/3} = 4.85)$$



- : experimental data
- : CWS with optimum $q = 0.48 e^{i(0.25)}$
- - - : smooth surface (theory). ($q = 0$)
- : standard analogy ($\beta = -ik|\epsilon|$)

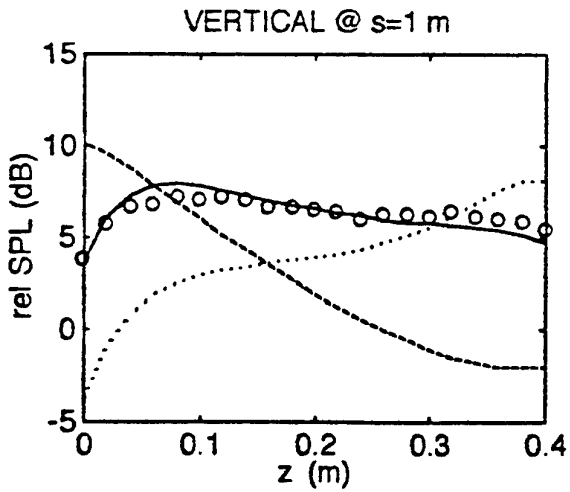
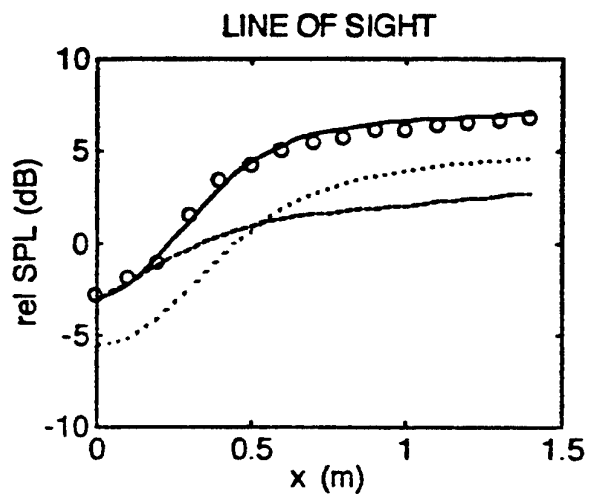
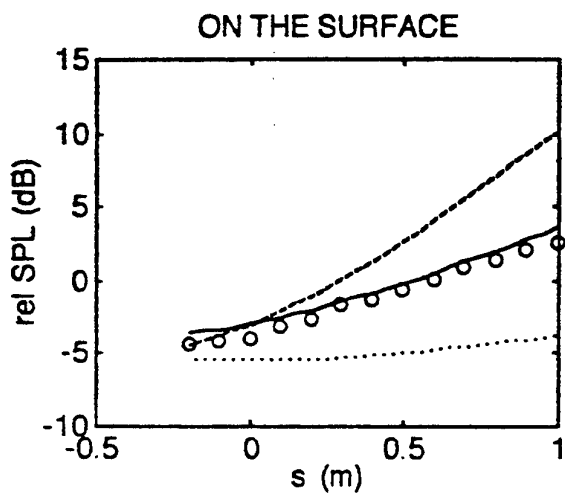
standard deviation: 0.25 dB

Figure 1

Sound Pressure Levels Relative to Free Field

$f = 8 \text{ kHz}$

$$(k|\epsilon| = 0.145, kR = 365, kl = (kR/2)^{1/3} = 5.67)$$



- : experimental data
- : CWS with optimum $q = 0.81 e^{i(0.23)}$
- - - : smooth surface (theory). ($q = 0$)
- : standard analogy ($\beta = -ik|\epsilon|$)

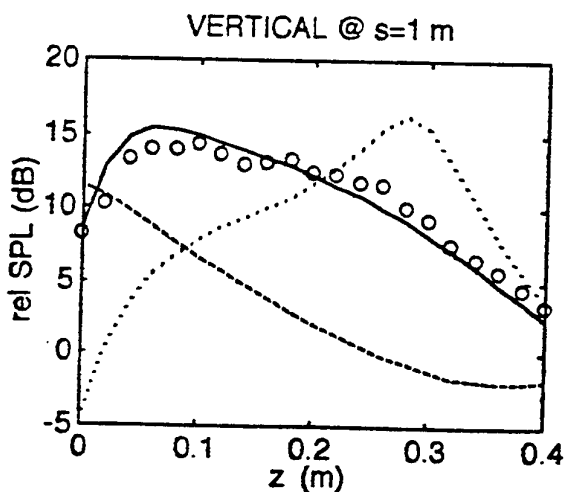
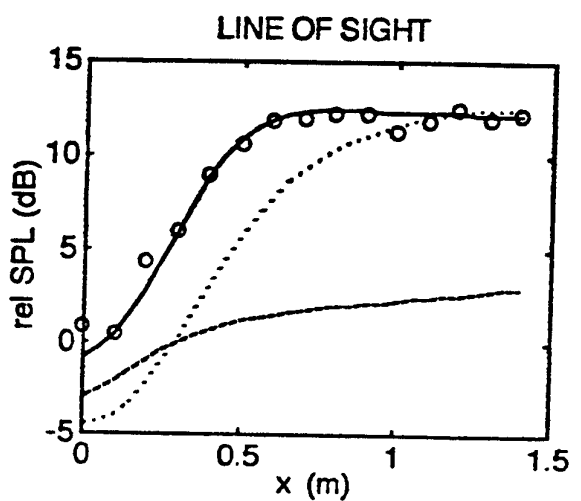
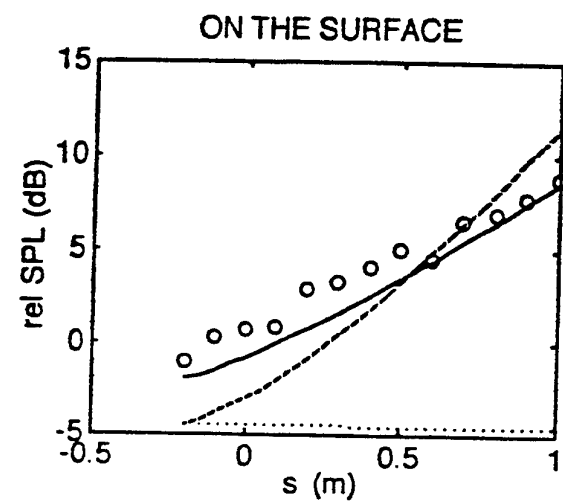
standard deviation: 0.6 dB

Figure 2

Sound Pressure Levels Relative to Free Field

$f = 10 \text{ kHz}$

$$(k|\epsilon| = 0.183, kR = 457, kl = (kR/2)^{1/3} = 6.11)$$



- : experimental data
- : CWS with optimum $q = 1.10 e^{i(0.27)}$
- - - : smooth surface (theory). ($q = 0$)
- : standard analogy ($\beta = -ik|\epsilon|$)

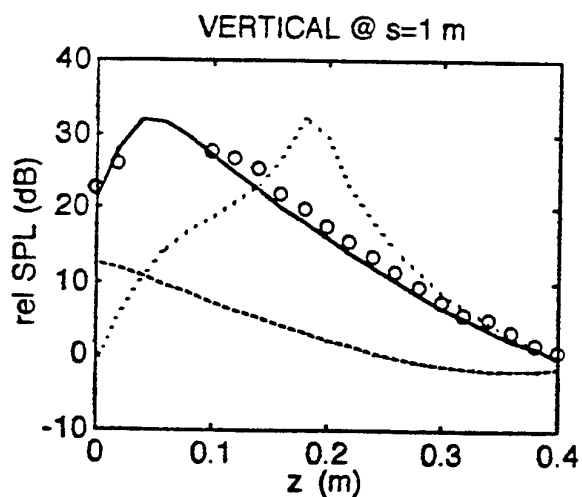
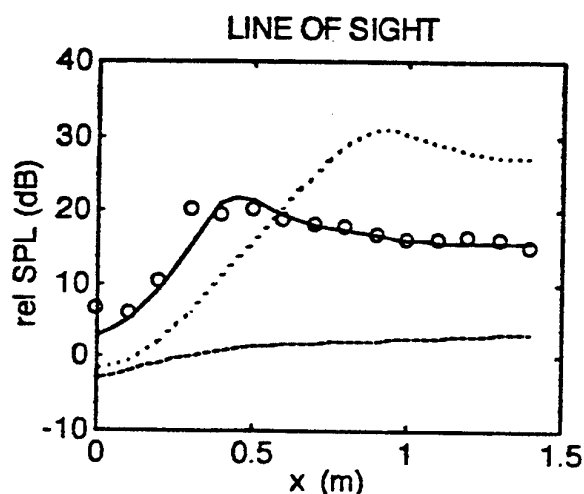
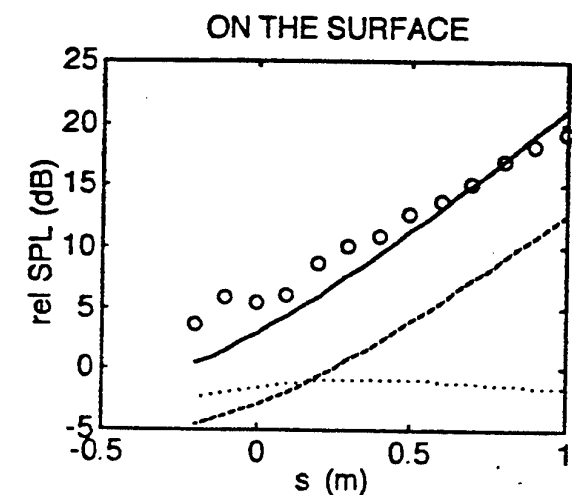
standard deviation: 1.0 dB

Figure 3

Sound Pressure Levels Relative to Free Field

$f = 12 \text{ kHz}$

$$(k|\epsilon| = 0.219, kR = 548, kl = (kR/2)^{1/3} = 6.49)$$



- : experimental data
- : CWS with optimum $q = 1.49 e^{i(0.29)}$
- - - : smooth surface (theory). ($q = 0$)
- : standard analogy ($\beta = -ik|\epsilon|$)

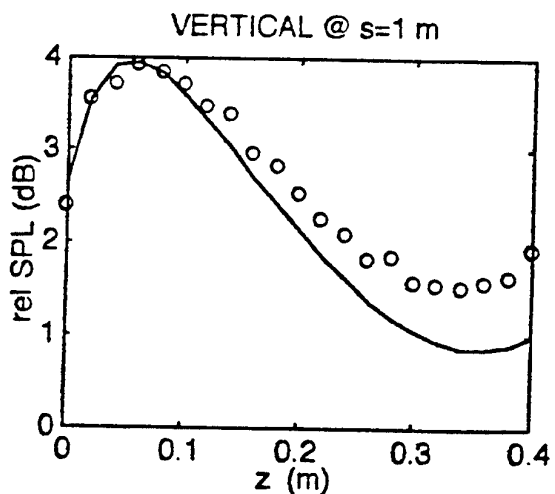
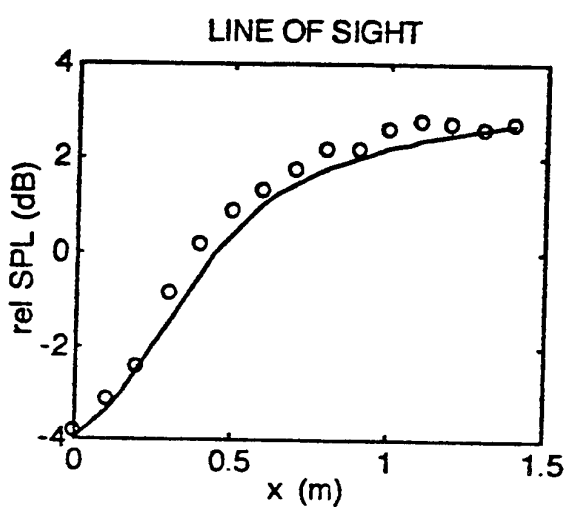
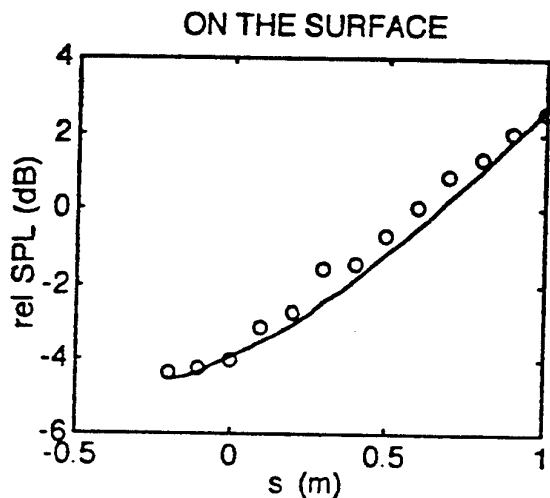
standard deviation: 1.7 dB

Figure 4

Sound Pressure Levels Relative to Free Field

$f = 5 \text{ kHz}$

$$(k|\epsilon| = 0.09, kR = 228, kl = (kR/2)^{1/3} = 4.85)$$



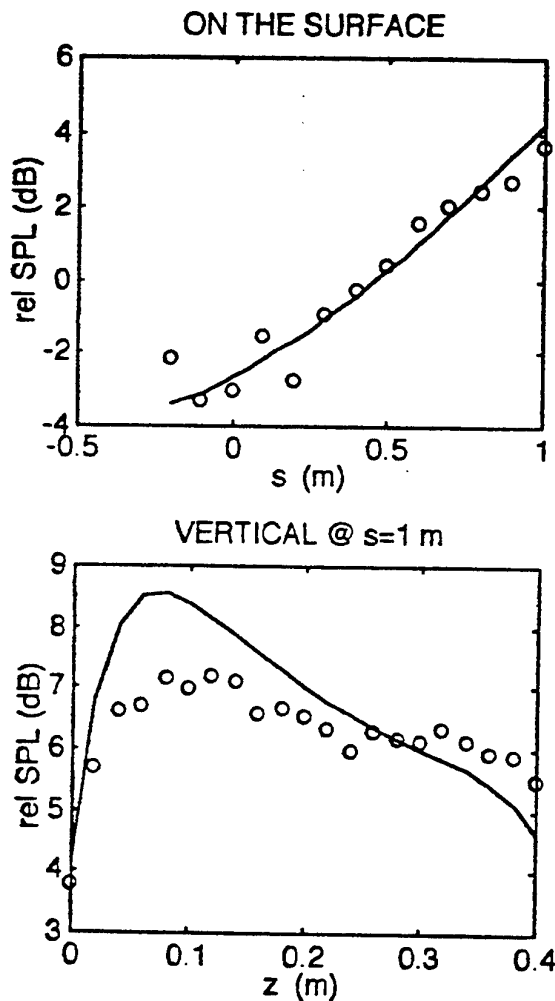
- : experimental data
- : CWS with $q = (kl) k\epsilon$
with $\epsilon = |\epsilon| e^{im}$, and m found from
eq (5) and eq. (9).

Figure 5

Sound Pressure Levels Relative to Free Field

$f = 8 \text{ kHz}$

$$(k|\epsilon| = 0.145, kR = 365, kl = (kR/2)^{1/3} = 5.67)$$



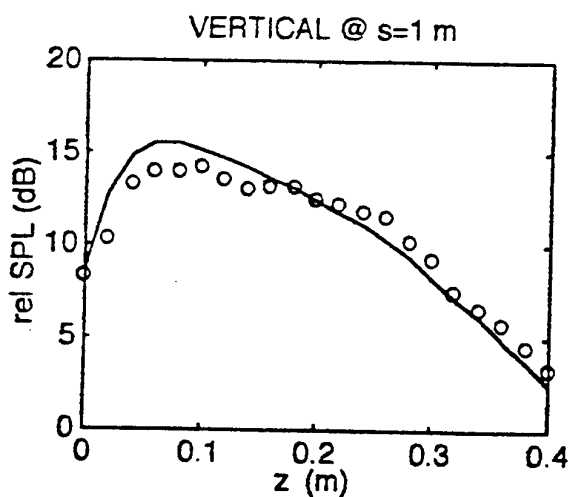
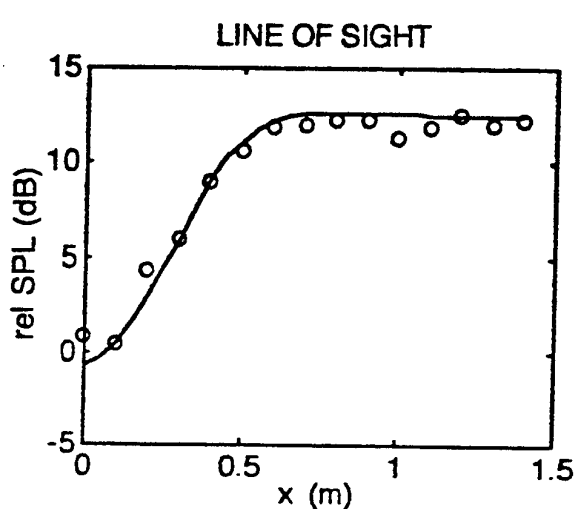
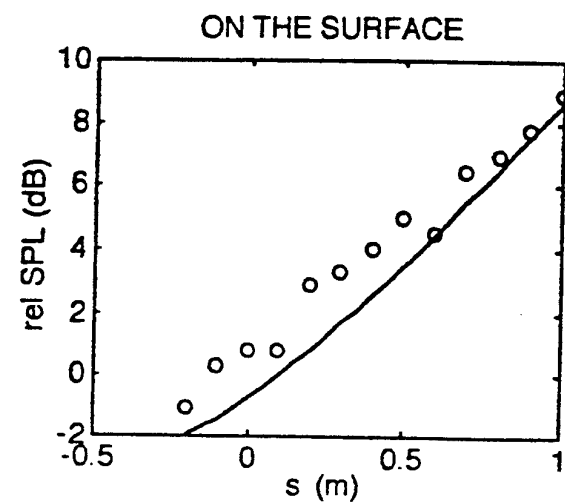
○ : experimental data
 — : CWS with $q = (kl) k\epsilon$
 with $\epsilon = |\epsilon| e^{im}$, and m found from
 eq (5) and eq. (9).

Figure 6

Sound Pressure Levels Relative to Free Field

$f = 10 \text{ kHz}$

$$(k|\epsilon| = 0.183, kR = 457, kl = (kR/2)^{1/3} = 6.11)$$



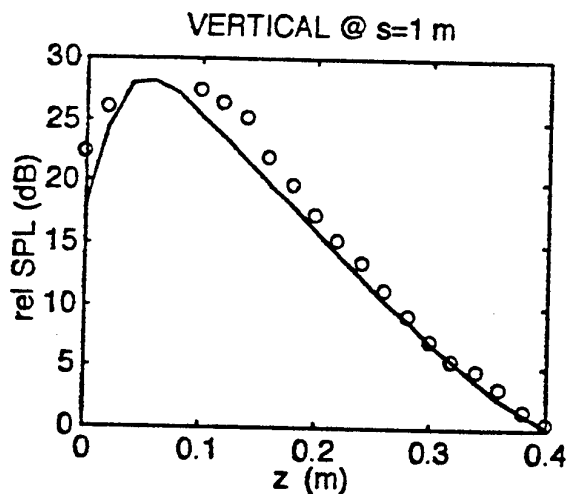
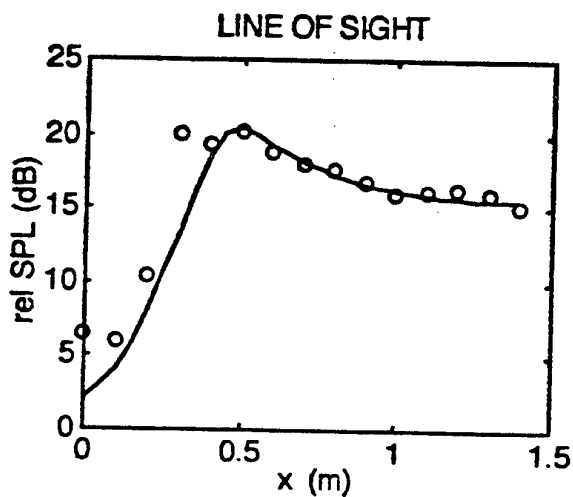
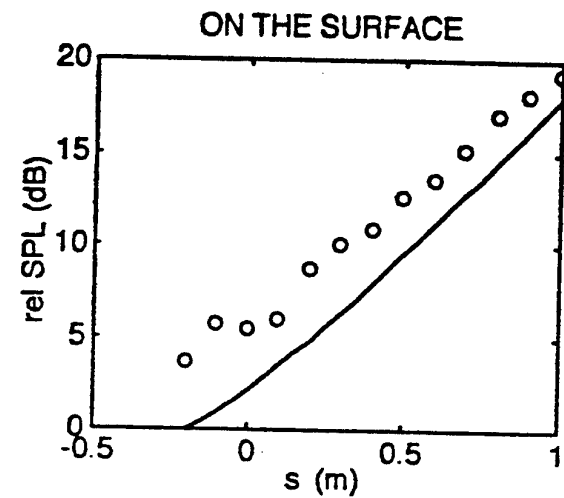
- : experimental data
- : CWS with $q = (kl) k\epsilon$
with $\epsilon = |\epsilon| e^{im}$, and m found from
eq (5) and eq. (9).

Figure 7

Sound Pressure Levels Relative to Free Field

$f = 12 \text{ kHz}$

$$(k|\epsilon| = 0.219, kR = 548, kl = (kR/2)^{1/3} = 6.49)$$



- : experimental data
- : CWS with $q = (kl) k\epsilon$
with $\epsilon = |\epsilon| e^{im}$, and m found from
eq (5) and eq. (9).

Figure 8

The prediction of sound field above a curved surface

Q. WANG and K. M. LI

*Engineering Mechanics Discipline, The Open University
Walton Hall, Milton Keynes MK7 6AA, United Kingdom
FAX (44) 1908 652 192*

Abstract

Experimental and theoretical investigations have been conducted to study the propagation of sound from a point source above a curved surface. The experiments were carried out in an anechoic chamber with the source located above a rigid and a finite impedance curved surface. Measurements were made for the receiver placed along the curved surface, the line of sight and a vertical distance across the shadow zone. A monopole source and a dipole source were used in the experiments. The experimental measurements agree reasonably well with theoretical predictions where they are based on the residue series solution and the theory of geometrical acoustics. The theoretical study has suggested that the sound field due to a dipole source above a curved surface is quite similar to that due to a point monopole source.

I. Introduction

The problem of predicting the diffraction of sound in the shadow zone and in the penumbra region is a subject of considerable interest in the past decade for atmospheric acoustics.¹ There are two wide classes of closely related problems that can be modeled by the same mathematical technique. The first class of problems is the normal refraction problem where the index of refraction increases with height above an impedance ground. The second wide class of problems is the diffraction of sound by convex surfaces. Both classes of problems are of practical importance.

The present investigation is primarily concerned with the problem where the radius of curvature of the curved surface is much longer than the wavelength of interest. There has been extensive literature for the research into the scattering and diffraction of electromagnetic waves by convex surfaces between the forties and sixties.² This work was motivated by the need for terrestrial and spatial communications as well as the advent of radar as a means of target detection. The analogy between these two classes of problems was identified and most of the theoretical formulas were derived during this period.³ Although most of these analyses were developed in the context of electromagnetic wave theory, the underlying principle had been applied to underwater acoustics⁴, and in the context of general linear acoustics.^{5,6}

The purpose of the present investigation is to re-examine the link between these two class of problems from the theoretical and experimental viewpoints. In Sec. I, the residue series solution and the geometrical acoustics solution are reviewed, and the residue series solution is extended for a horizontal dipole and a vertical dipole. Section II gives a general description of the experimental technique employed in the study. In Sec. III, a comparison of the residue series solution and the geometrical acoustics solution in the insonified regions is presented. Section IV demonstrates that the sound field due to a dipole above the convex surface is quite similar to that due to a point monopole source.

II. Theory

1. Residue series solution for a monopole source

In this section, we consider the diffraction of sound in a homogeneous medium near a spherical surface of large radius. It is convenient to use a spherical polar coordinate system, (R, θ, ψ) , in this problem. A point source is located at (R_s, θ_s, ψ_s) . We treat the sphere as a locally reacting surface. Let the radius, and normalized admittance of the sphere be R_c , and β respectively. The boundary condition at the surface of sphere is

$$\frac{\partial p}{\partial R} + ik_0 \beta p = 0 \quad (1)$$

There is no loss of generality by assuming $R_s > R$. It is because the reciprocity theorem allows one to swap the source and receiver position if $R > R_s$. The solution for the scattering of sound by a spherical surface is well-known^{2,7} and the details of the analysis will be omitted here. Rather, a brief description of the method in obtaining the solution is outlined as follows.

The direct wave p^i due to a monopole source can be expanded, with the use of Eqs. (10.1.45) and (10.1.46) of Ref. 8, as a series of Legendre polynomials:

$$p^i = S_0 \frac{e^{ik_0 R_d}}{k_0 R_d} = -iS_0 \sum_{n=0}^{\infty} (2n+1) h_n^{(1)}(k_0 R_s) j_n(k_0 R) P_n(\cos \Theta) \quad (2)$$

$$\text{where } R_d = \sqrt{R^2 + R_s^2 - 2RR_s \cos \Theta},$$

$$\text{and } \cos \Theta = \sin \theta \sin \theta_s \cos(\psi - \psi_s) + \cos \theta \cos \theta_s,$$

where S_0 is the source strength of the monopole. Here, in Eq. (2), the functions, $h_n(\cdot)$ and $j_n(\cdot)$ are n th order spherical Bessel functions and $P_n(\cdot)$ is the Legendre polynomial of degree n . Likewise, the reflected sound can be expressed in a similar form as

$$p^r = -iS_0 \sum_{n=0}^{\infty} V_n (2n+1) h_n^{(1)}(k_0 R_s) h_n^{(1)}(k_0 R) P_n(\cos \Theta), \quad (3)$$

where the coefficients V_n are to be determined according to the impedance boundary condition given in Eq. (1). The total sound field for $R_s > R > a$, can then be written as

$$\begin{aligned} p &= p^i + p^r \\ &= -iS_0 \sum_{n=0}^{\infty} (2n+1) \{ j_n(k_0 R) + V_n h_n^{(1)}(k_0 R) \} h_n^{(1)}(k_0 R_s) P_n(\cos \Theta) \end{aligned} \quad (4)$$

$$\text{where } V_n = -\frac{j'_n(k_0 R_c) + i\beta j_n(k_0 R_c)}{h_n^{(1)}(k_0 R_c) + i\beta h_n^{(1)}(k_0 R_c)} \quad (5)$$

and the primes denote the derivative of the spherical Bessel functions with respect to their arguments.

Following the procedures as detailed in Ref. 7, and using the asymptotic approximations⁸ for the Legendre polynomials, we can approximate the total sound field [*cf* Eq.(4)] by its integral representation as

$$p \approx S_0 \frac{\exp\left[i\left(k_1 R_c \Theta + \frac{\pi}{4}\right)\right]}{\sqrt{\frac{1}{2}\pi \sin \Theta}} \int_{-\infty}^{\infty} \frac{(\zeta - \frac{1}{2})!}{(\zeta - 1)!} \exp(\frac{1}{2}ik_0 R_c \mu \Theta) \{J_\zeta(k_0 R) + V_\zeta H_\zeta^{(1)}(k_0 R)\} H_\zeta^{(1)}(k_0 R_s) d\mu \quad (6)$$

where $\zeta = k_0 R_c \left(1 + \frac{\mu}{2}\right)$, $R = R_c + z$, $R_s = R_c + z_s$, $\quad (7)$

$R_c \gg \max(z, z_s)$ and higher powers of μ are ignored. With the identification of $r = R_c \Theta$, the sound field near a large spherical surface can be approximated by the corresponding sound field in a vertically-stratified medium with a bilinear sound speed profile and the radius of curvature of rays propagating in the medium is R_c . Figure 1 illustrates the connection between the parameters for a spherical surface and those for a stratified medium over a flat ground. It is possible to show that we can approximate Eq. (6) by

$$p \approx \sqrt{\Theta / \sin \Theta} p_m \quad (8)$$

where p_m is the residue series solution for the analogous situation of the sound field above a flat ground with the sound speed gradient varying according to the so-called bilinear profile. In the case of the bilinear profile, the speed of sound varies with height as

$$1/c^2(z) = [1/c^2(0)](1 + 2z/R_c)$$

where $R_c = c(0)/|dc/dz|$

and $c(z)$ is speed of sound which is a function of the vertical distance, z above the flat ground. The sound field, p_m can be found straightforwardly as follows^{1,9}

$$p_m(r, z) = \frac{\pi e^{ip/6}}{l} S_0 \sum_n H_0^1(k_n r) \frac{\text{Ai}[b_n - (h_s/l)e^{2ip/3}] \text{Ai}[b_n - (z/l)e^{2ip/3}]}{[\text{Ai}'(b_n)]^2 - b_n [\text{Ai}(b_n)]^2}, \quad (9)$$

where $b_n = \tau_n e^{2i\pi/3} = (k_n^2 - k_0^2)l^2 e^{2i\pi/3}$ $\quad (10)$

are the zeros of

$$\text{Ai}'(b_n) + q e^{i\pi/3} \text{Ai}(b_n) = 0, \quad (11)$$

H_0^1 is the Hankel function of the first kind and of order zero, Ai and Ai' are the Airy function and its derivative with respect to their arguments, Θ is the total angle between source and receiver, see Fig. 1, and

$$a = R_c^{-1} , \quad (12)$$

$$q = ik_0 \beta l , \quad (13)$$

$$l = (2ak_0^2)^{-1/3} , \quad (14)$$

$$k_0 = \omega/c(0) , \quad (15)$$

and $\tau_n = (k_n^2 - k_0^2)l^2 . \quad (16)$

It is obvious that the amplitude of the sound field above a large spherical surface is different from the corresponding situation of an upward refracting medium by a factor of $\sqrt{\Theta/\sin \Theta}$, where Θ is the total angle between the source and receiver, see Fig. 1 for the notation. As shown in Fig. 2, the correction factor renders a small term to the total sound field and it is only important at large Θ , i.e. for source deep in the shadow zone.

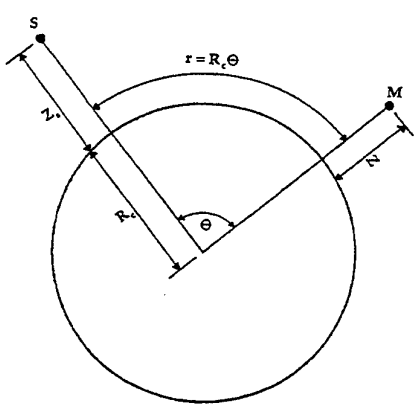


Fig. 1 : Illustration of the connection between the parameters for a spherical surface and those for a stratified medium over a plane boundary.

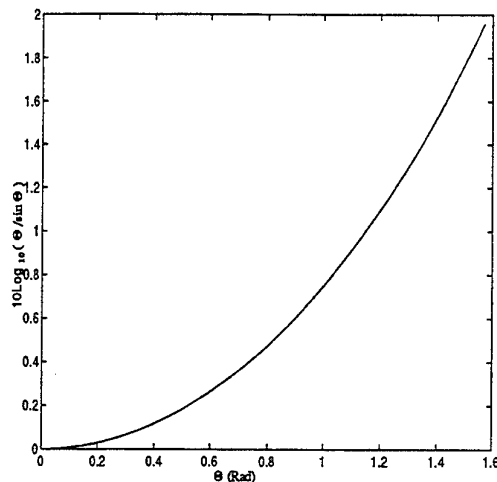


Fig. 2 : The correction factor, $\sqrt{\Theta/\sin \Theta}$ vs. the total angle Θ .

2. Geometrical acoustics

If R_c is large compared to the wavelength, and the receiver is in a bright zone above the curved surface, the acoustic pressure may conveniently be described by the geometrical acoustics solution¹. The solution for a point monopole source is

$$p_m(r, z) = S_0 \left\{ \frac{e^{ik_0 d}}{d} + \frac{Q e^{ik_0(d_1+d_2)}}{d_1 \sqrt{(1+d_2/d_1)(1+d_2/d_1 + 2d_2/R \cos \theta)}} \right\} , \quad (17)$$

where

$$\theta = \alpha_1 + \alpha_2, \quad (18a)$$

$$\alpha = \sin^{-1}[(R/d_1) \sin \alpha_2], \quad (18b)$$

$$d = \sqrt{(h_s + R)^2 + (z + R)^2 - 2(h_s + R)(z + R) \cos(r/R)}, \quad (18c)$$

$$d_1 = \sqrt{(h_s + R)^2 + R^2 - 2R(h_s + R) \cos \alpha_2}, \quad (18d)$$

$$d_2 = \sqrt{(z + R)^2 + R^2 - 2R(z + R) \cos(r/R - \alpha_2)}, \quad (18e)$$

$$[\sin(r/R - \alpha_2)][\sin \alpha_2]^{-1} = (d_2/d_1)(h_s + R)/(z + R). \quad (18f)$$

The variable Q is known as the spherical wave reflection coefficient given by

$$Q = R_p + (1 - R_p)F(w), \quad (19a)$$

where

$$R_p = \frac{\cos \theta - \beta}{\cos \theta + \beta} \quad (19b)$$

$$F(w) = 1 + i\sqrt{\pi} w \exp(-w^2) \operatorname{erfc}(-iw) \quad (19c)$$

and

$$w^2 = (ik_0 d_2/2)(\cos \theta + \beta)^2. \quad (19d)$$

3. Residue series solution for a dipole

In view of the fact that the range and height dependent factors are not coupled in the residue series solution for a monopole source, the complex acoustic pressure due to a horizontal dipole and a vertical dipole above a convex curved surface is given, respectively, by

$$p_h(r, z) \approx -\frac{\pi e^{i\pi/6}}{l} \sqrt{\frac{\Theta}{\sin \Theta}} S_d \sum_n \frac{k_n H_1^1(k_n r) \operatorname{Ai}\left(b_n - \frac{h_s}{l} e^{2i\pi/3}\right) \operatorname{Ai}\left(b_n - \frac{z}{l} e^{2i\pi/3}\right)}{\left[\operatorname{Ai}'(b_n)\right]^2 - b_n [\operatorname{Ai}(b_n)]^2} \quad (20)$$

$$p_v(r, z) = \frac{\pi e^{-i\pi/6}}{l^2} \sqrt{\frac{\Theta}{\sin \Theta}} S_d \sum_n \frac{H_0^1(k_n r) \operatorname{Ai}\left(b_n - \frac{h_s}{l} e^{2i\pi/3}\right) \operatorname{Ai}\left(b_n - \frac{z}{l} e^{2i\pi/3}\right)}{\left[\operatorname{Ai}'(b_n)\right]^2 - b_n [\operatorname{Ai}(b_n)]^2}, \quad (21)$$

where $S_d = 2bS_m$ is the source amplitude of the dipole which comprises two out-of phase monopoles separated by a distance, and H_1^1 is the Hankel function of the first kind and of order one.

II. Experimental technique

A series of indoor experiments was conducted to measure the sound field above a convex cylinder in an anechoic chamber. A tannoy driver with a 3 cm internal diameter long tube was

used as the point monopole source. A group of piezo speakers were introduced as the dipole sources for various frequency ranges. The signals were received by a 1/2 in. B&K condenser microphone fitted with a preamplifier. A PC-based system analyzer (MLSSA) was employed both as the signal generator for the speakers and as the analyzer for subsequent signal processing. In all cases, the results were given in terms of either excess attenuation (EA) or transmission loss (TL). The following definitions were used:

$$EA = 20 \log_{10} \left| \frac{p_t}{p_i} \right| \quad (22)$$

$$TL = 20 \log_{10} \left| \frac{p_t}{p_i} \right|, \quad (23)$$

where p_t and p_i are the total and direct acoustic pressures at a field point and p_i is the sound pressure of direct sound field at 1 m from the source.

The measurements were performed for a rigid boundary and a finite impedance surface. The receiver positions included the areas along the surface, along the line of sight, above the limiting ray, and across the shadow zone for various source heights. The rigid curved surface was a cross section of a cylinder and had a radius of curvature 2.5m and was constructed out of rigid masonite sheets. The finite impedance surface was a felt-covered surface. In the case of the finite impedance surface, a two-parameter locally reacting model¹⁰ was used to estimate the acoustic impedance of the absorbing boundary. The best agreement was found with the effective flow resistivity at the surface $\sigma_e = 38000$ MKS units, and the effective rate of change of porosity with depth $\alpha_e = 15 \text{ m}^{-1}$ for the flat felt-covered surface. The solid line in Fig. 3 indicates the excess attenuation measured above the flat felt-covered surface with the point monopole source at the height of 0.05 m and receiver at a height of 0.15 m separated by a distance of 2.0 m and the dashdot line indicates the theoretically predicted result.

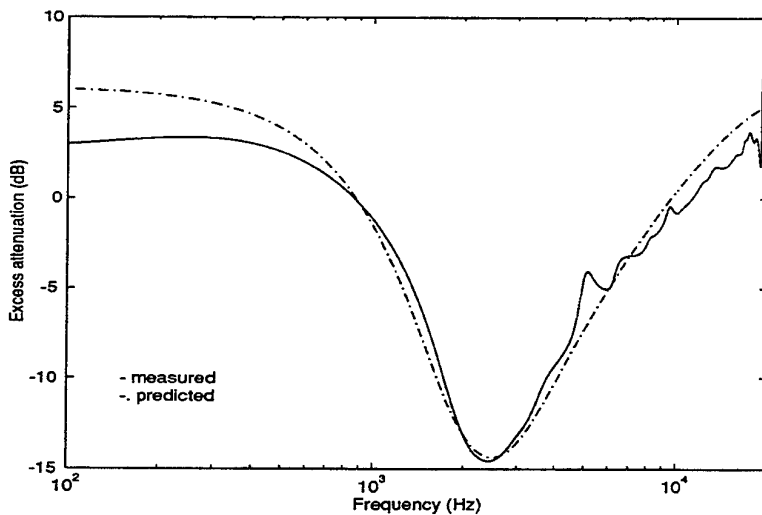


Fig. 3 : Excess attenuation above a flat felt-covered surface, with $h_s = 0.05 \text{ m}$, $z = 0.15 \text{ m}$, $r = 2.0 \text{ m}$.

III. Comparison of the residue series solution and the geometrical acoustics solution

In the case of a receiver situated in the illuminated zone above a curved surface, the geometrical acoustics solution expressed by Eq. (17) gives reasonable agreement with the measurements, as shown in Figs. 4 and 5. In this insonified region, the residue series solution [cf Eq.(8)] is valid provided that $z \ll R$. In Fig. 6, the solid curve is the excess attenuation measured over the rigid surface with the heights of the source and receiver both at 0.15m. The dash line is the prediction of the geometrical acoustics solution and the dashdot line is the prediction of the residue series solution using 40 terms. As the receiver height is increased, the residue series becomes a poorly convergent sum of many small terms. The dashdot lines in Figs.(21) and (22) are the predictions of residue series solution, with a source height of 0.2m and a receiver height of 0.5m using 55 terms, above the rigid surface and the felt-covered surface, respectively. It can be seen that the two versions of theory agree with the measured results only when the receiver was placed close to the surface, and the discrepancies become significant at the higher frequencies as the receiver height is increased above the surface.

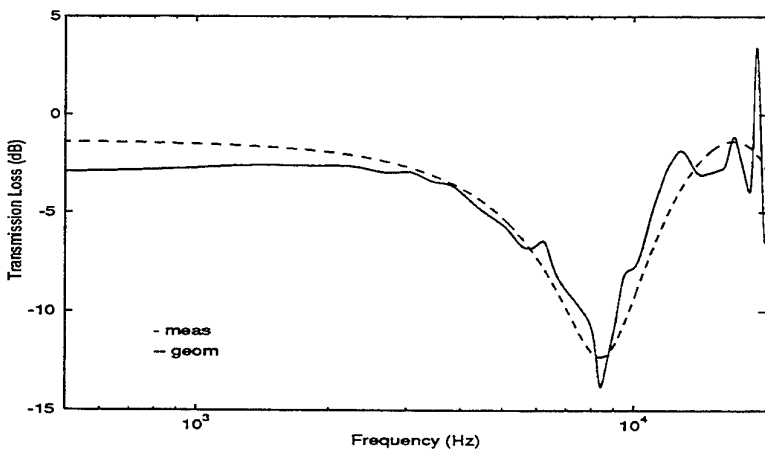


Fig. 4: Transmission loss above the rigid surface, $h_s = 0.2$ m, $z = 0.4$ m, and $r = 1.65$ m.

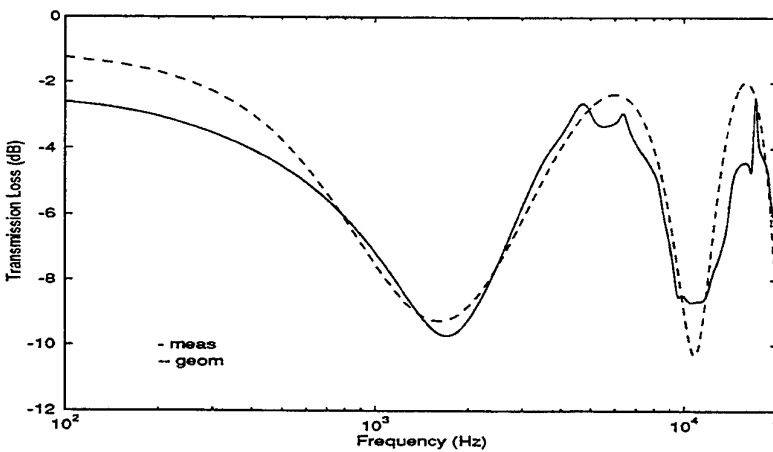


Fig. 5: Transmission loss above the felt-covered surface, with $h_s = 0.2$ m, $z = 0.5$ m, and $r = 1.62$ m.

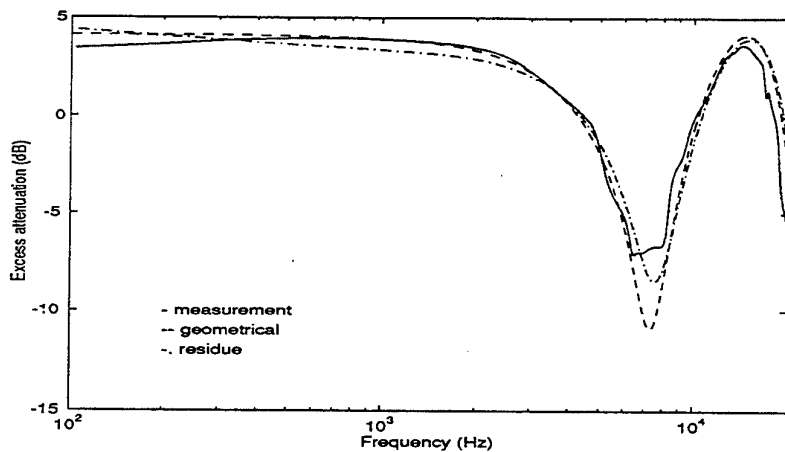


Fig. 6: Excess attenuation above the rigid surface with $h_s = z = 0.15 \text{ m}$ and $r = 0.92 \text{ m}$.

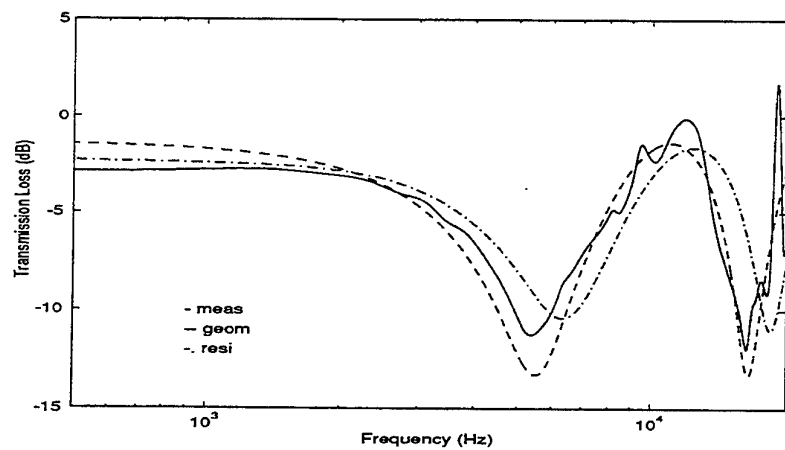


Fig. 7: Transmission loss above the rigid surface, with $h_s = 0.2 \text{ m}$, $z = 0.5 \text{ m}$, and $r = 1.65 \text{ m}$.

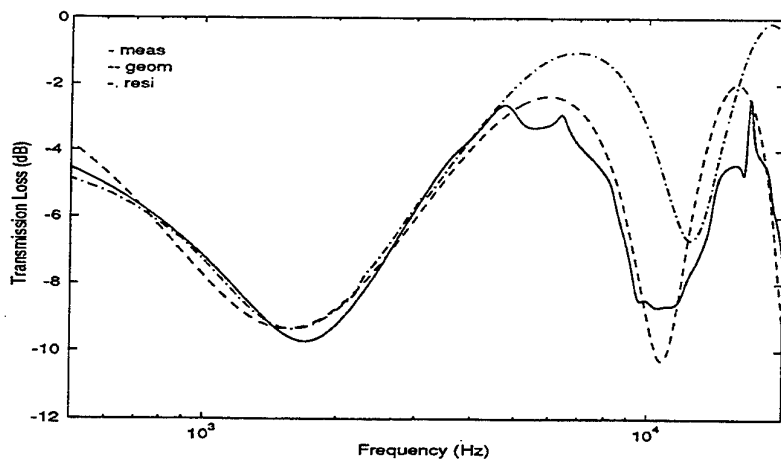


Fig. 8: Excess attenuation above the felt-covered surface, $h_s = 0.2 \text{ m}$, $z = 0.5 \text{ m}$, and $r = 1.62 \text{ m}$.

IV. Dipole sound field

Experiments above a curved surface using a point dipole source were designed to study the dipole sound field described by Eqs. (20) and (21). All the experimental results of the dipole source above the rigid and the felt-covered curved surfaces are presented in terms of transmission loss relative to the sound pressure of the direct sound field at 1.0m from the horizontal dipole source. Generally, a tolerable agreement has been achieved between the residue series solution extended for a horizontal dipole [*cf* Eq. (20)] or a vertical dipole [*cf* Eq. (21)] and measurements.

1. Vertical dipole

Similar to those of the monopole field, in the illuminated area close to the source along the surface, the residue series theory for a vertical dipole failed to give a converged result at the frequency of 2.9 kHz. Figures 9-11 show the transmission loss obtained with the vertical dipole fixed at a height of 0.24 m above the rigid and felt covered surfaces, labeled *rigid* and *felt*, as the receiver was at positioned various heights. The circles and crosses indicate the measurements, the solid lines are the predictions of Eq.(16).

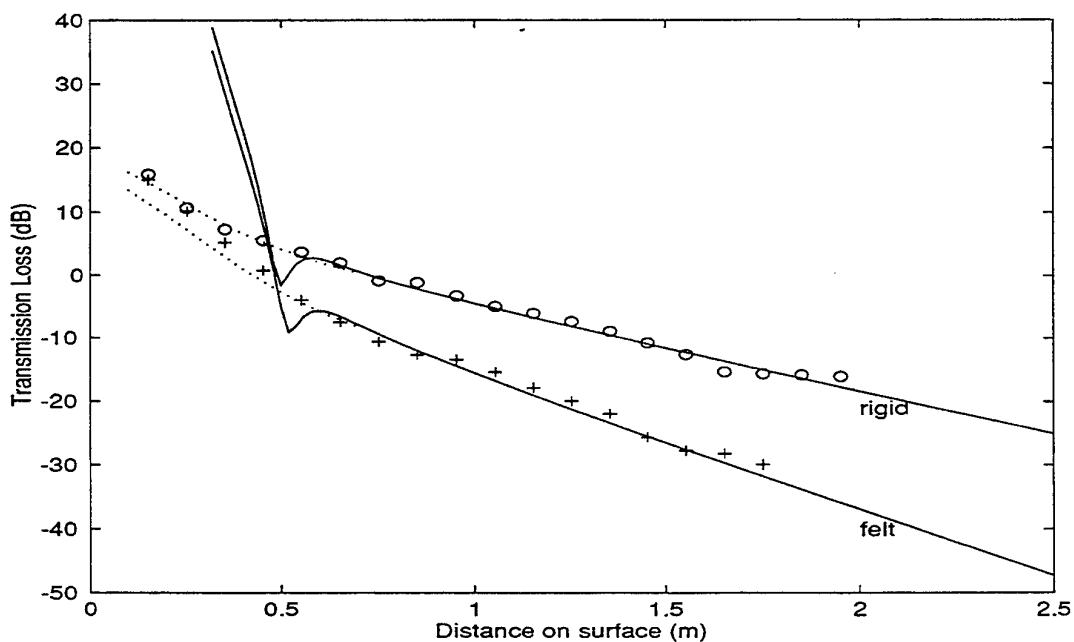


Fig. 9: Transmission loss at 2.9 kHz with a vertical dipole along the rigid and felt covered convex surfaces with $h_s = 0.24$ m. The circles and crosses indicate the measured data, and the solid lines are the predictions. The dotted lines are the predictions of the geometrical acoustics solution with two out-of phase monopoles.

In Fig. 9, we show the results when the receiver is on the surface with an arc distance from the source, the dotted lines are the calculations of the geometrical acoustics solution with two out-of phase monopoles. Figure 10 displays the results when the receiver is along the limiting ray, with direct distances from the apex of the convex cylinder. Figure 11 presents the results when the receiver is located along a vertical distance starting at an arc length of 1.95 m from the source on the surface.

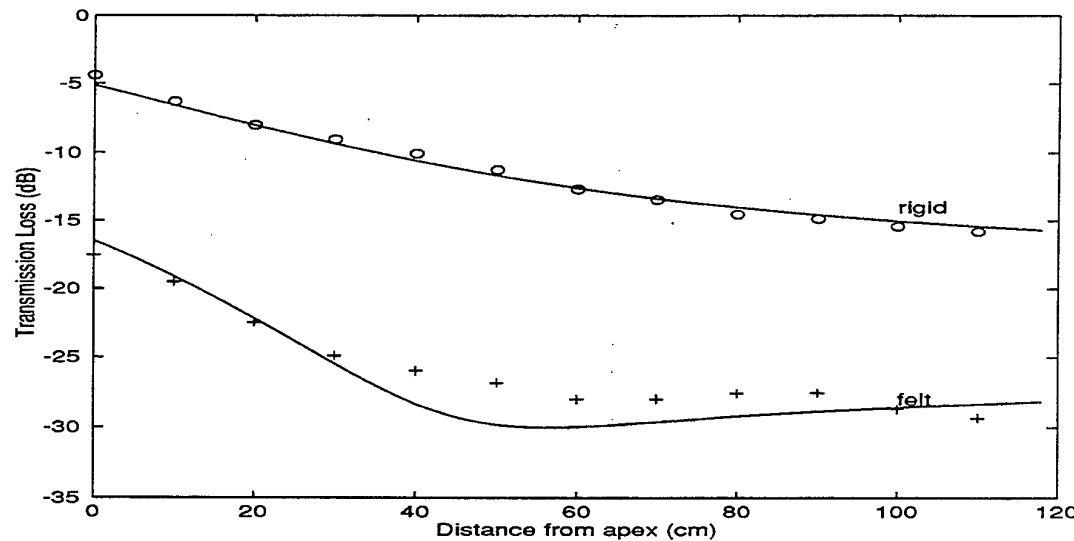


Fig. 10: Transmission loss at 2.9 kHz with a vertical dipole along the limiting ray above the rigid and felt-covered convex surfaces with $h_s = 0.24$ m. The circles and crosses indicate the measured data, and the solid lines are the predictions.

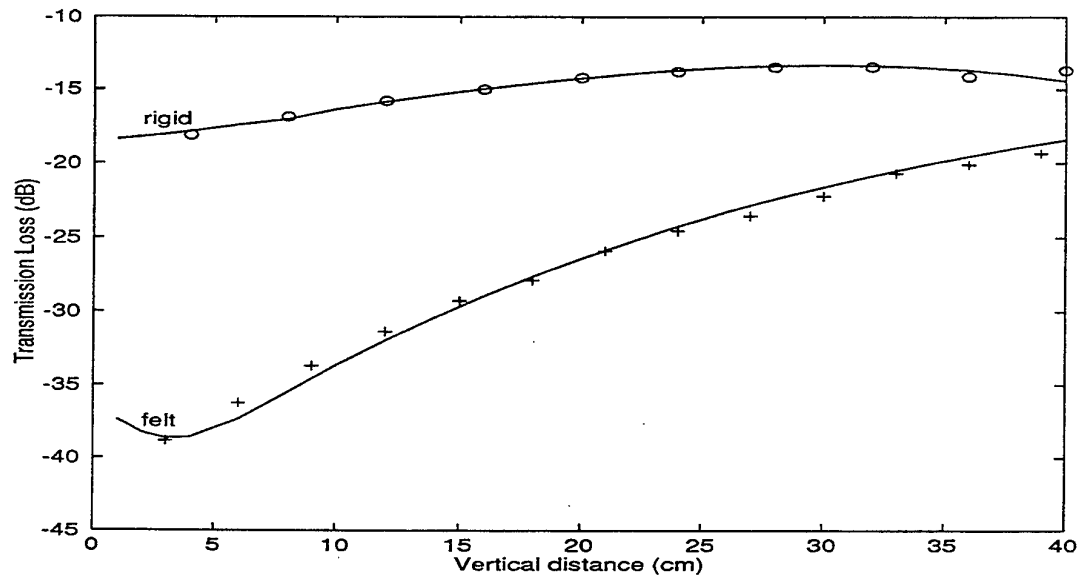


Fig. 11: Transmission loss obtained at 2.9 kHz with the vertical dipole across vertically the shadow zone above the rigid and felt-covered convex surfaces with $h_s = 0.24$ m and $z = 0$ m. The circles and crosses indicate the measured data, and the solid lines are the predictions.

2. Comparison of dipole and monopole

For a convenient comparison, a series of measurements was taken under the same condition using the monopole source, the horizontal and vertical dipole sources in sequence. The following figures show the results at a frequency of 2.9 kHz, with a source height of 0.24 m above the rigid and the felt-covered convex surface respectively. It is evident that the

horizontal dipole sound field is very close to that produced by the monopole source, and the vertical dipole sound field is quite similar to the monopole sound field.

A. Comparison of horizontal dipole and monopole

In Figs. 12-14, we show the calculated the transmission loss of the horizontal dipole source and the monopole source above the rigid and felt-covered surface. The measured results

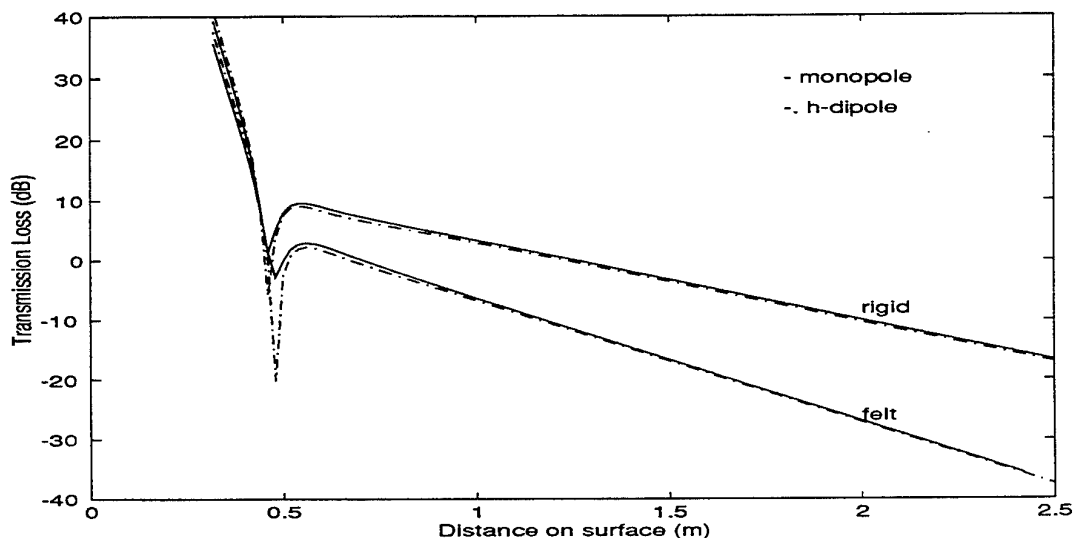


Fig. 12: Transmission loss due to a monopole source and a horizontal dipole source calculated at 2.9 kHz along the curved surface with $h_s = 0.24$ m and $z = 0$ m.

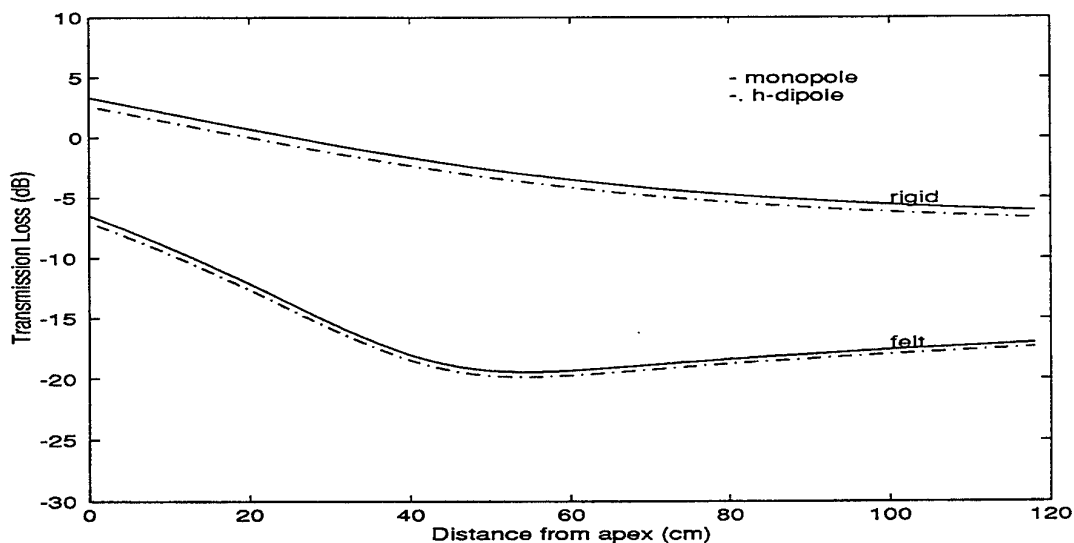


Fig. 13: Transmission loss due to a monopole source and a horizontal dipole source calculated at 2.9 kHz along the line of sight with $h_s = 0.24$ m.

originated from the horizontal dipole source are indistinguishable from those obtained by using the monopole source. The differences in the amplitude of transmission loss between them are predicted and measured to be less than 1 dB.

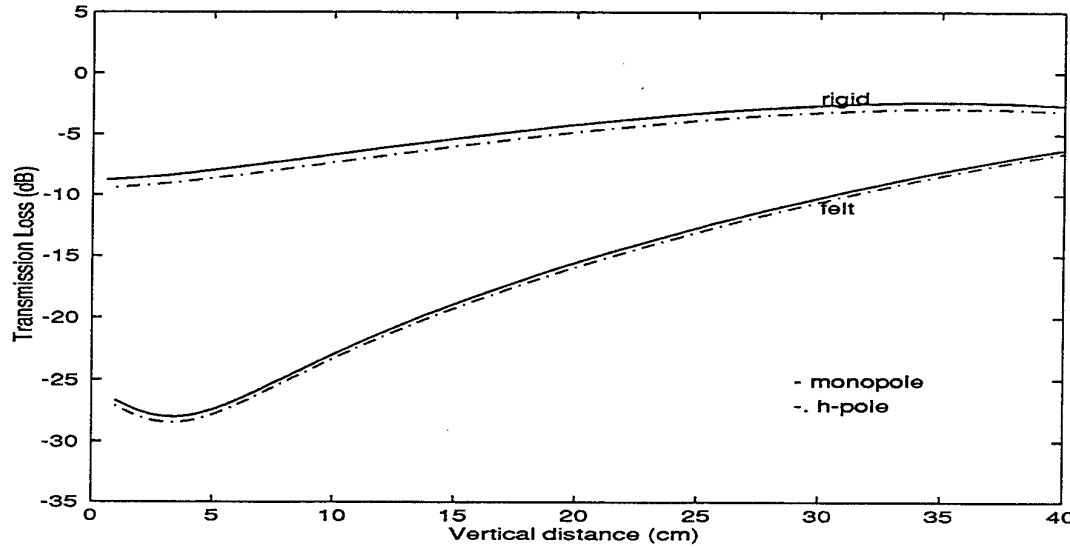


Fig. 14: Transmission loss due to a monopole source and a horizontal dipole source calculated at 2.9 kHz across the shadow zone, $h_s = 0.24$ m, and $z = 0$ m when $r = 1.95$ m.

B. Comparison of vertical dipole and monopole

In Figs. 15-20, the solid lines are the predictions for the monopole source and the vertical dipole source labeled by *mono* and *v-dipole*, separately, the corresponding measured results are

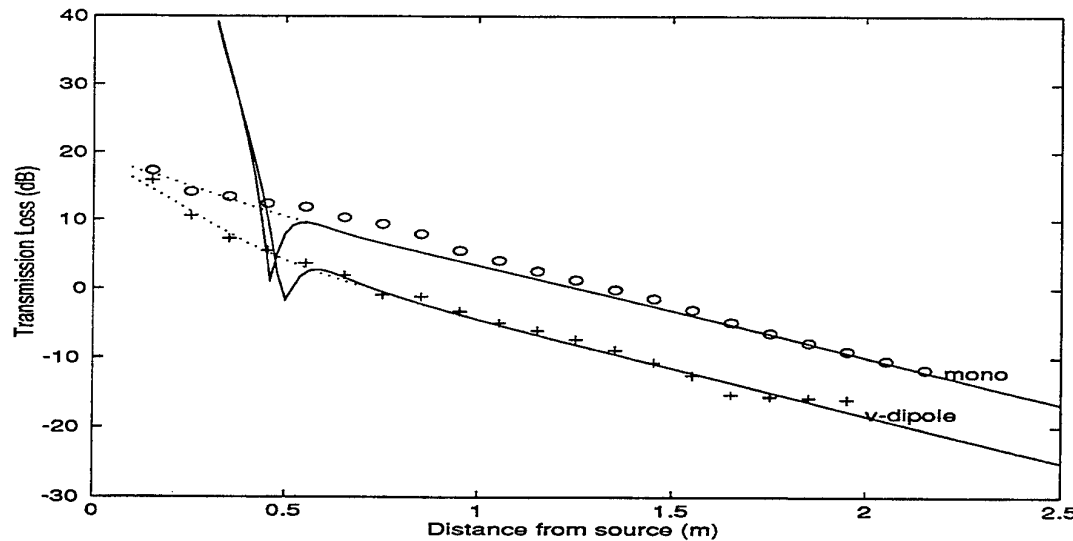


Fig. 15: Transmission loss due to a monopole and a vertical dipole, obtained along the rigid convex surface at 2915 Hz with $h_s = 0.24$ m, and $z = 0$ m. The circles and crosses indicate the measured data, and the solid lines are the predictions. The dotted lines are the predictions of the geometrical acoustics solution with two out-of-phase monopoles.

given by the circles and crosses respectively. In the near field, the geometrical acoustics theory was used to predict the sound pressure levels and is indicated by the dotted lines.

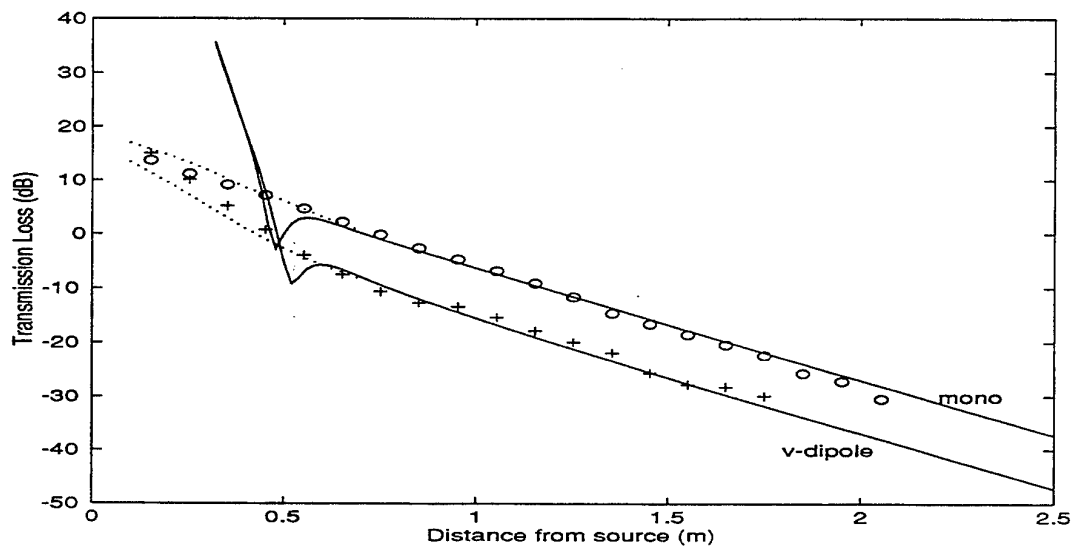


Fig. 16: Transmission loss due to a monopole and a vertical dipole, obtained along the felt-covered convex surface at 2915 Hz, with $h_s = 0.24$ m, and $z = 0$ m. The circles and crosses indicate the measured data, and the solid lines are the predictions. The dotted lines are the predictions of the geometrical acoustics solution with two out-of phase monopoles.

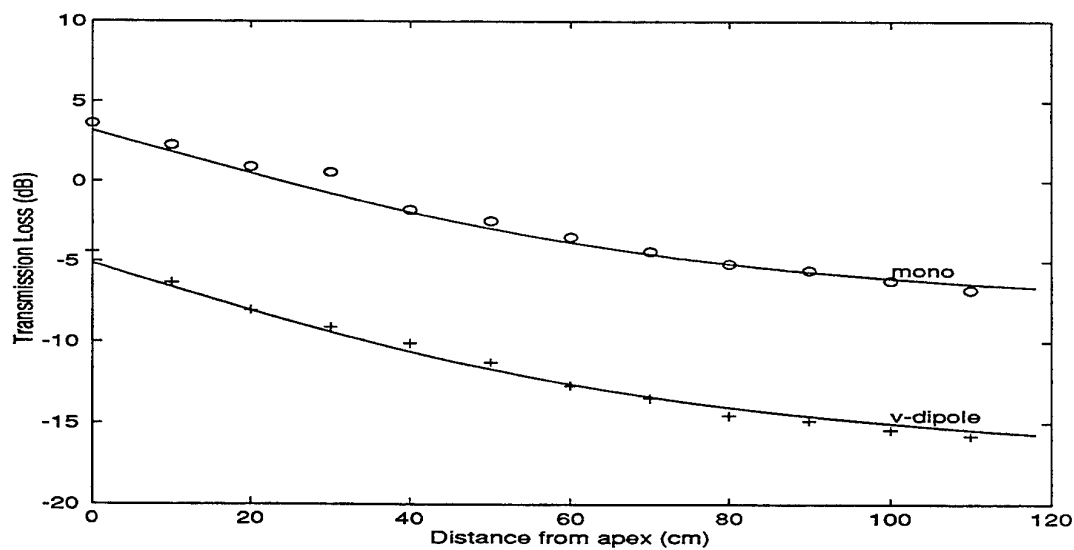


Fig. 17: Transmission loss due to a monopole and a vertical dipole, obtained along the line of sight over the rigid convex surface at 2915 Hz, with $h_s = 0.24$ m. The circles and crosses indicate the measured data, and the solid lines are the predictions.

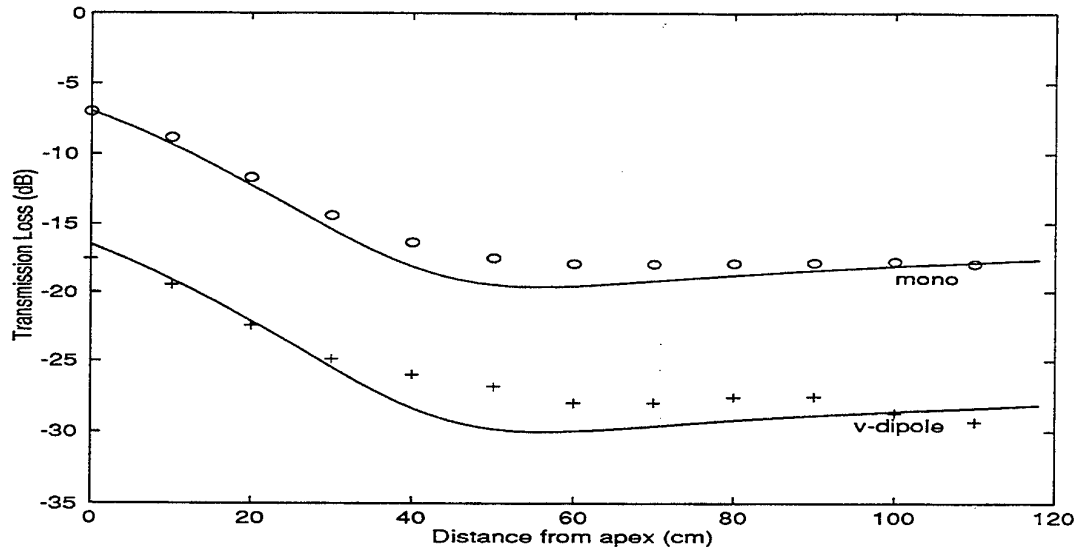


Fig. 18: Transmission loss due to a monopole and a vertical dipole, obtained along the line of sight over the felt-covered convex surface at 2915 Hz, with $h_s = 0.24$ m. The circles and crosses indicate the measured data, and the solid lines are the predictions.

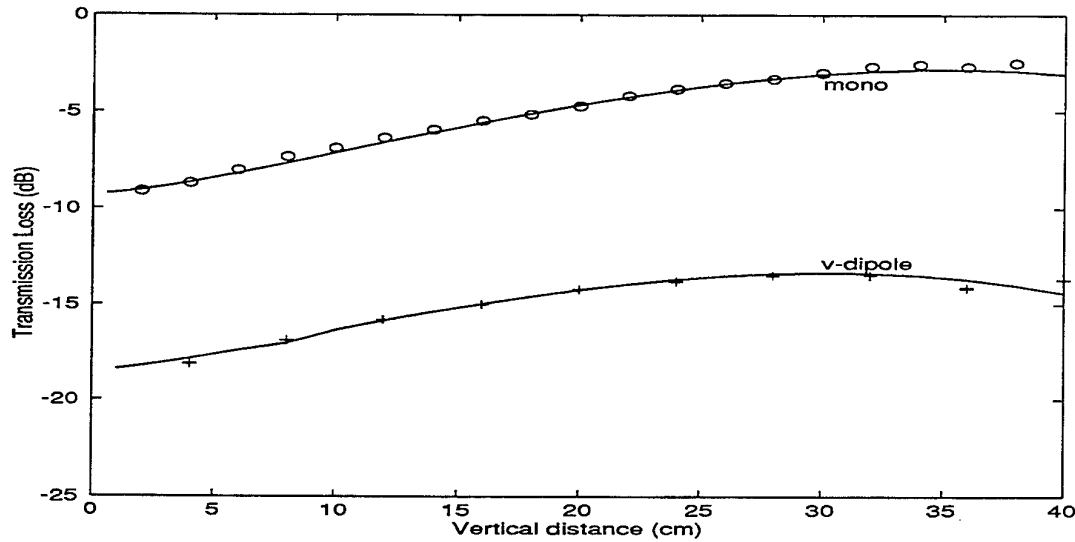


Fig. 19: Transmission loss due to a monopole and a vertical dipole, obtained vertically across the shadow zone over the rigid convex surface at 2915 Hz, with $h_s = 0.24$ m, $z = 0$ m and $r = 1.95$ m. The circles and crosses indicate the measured data, and the solid lines are the predictions.

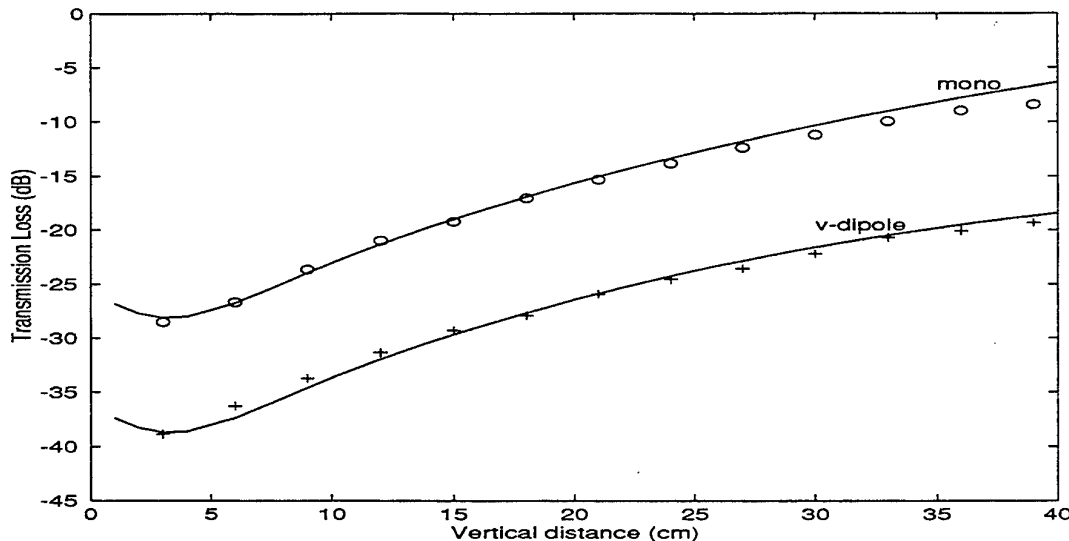


Fig. 20: Transmission loss due to a monopole and a vertical dipole, obtained vertically across the shadow zone over the felt-covered convex surface at 2915 Hz, with $h_s = 0.24 \text{ m}$, $z = 0 \text{ m}$ and $r = 1.95 \text{ m}$. The circles and crosses indicate the measured data, and the solid lines are the predictions.

V Conclusions

A more accurate approximation for the calculation of sound propagation from a point monopole source above a curved surface has been described and analysed. The approximation is in contrast with the previous analyses by including a correction term which is important when the receiver is situated deep in the shadow zone. The approximation has also been extended to include the prediction of sound fields for horizontal and vertical dipoles. Extensive experiments have been conducted to validate theoretical results. It has been demonstrated that theoretical predictions agree tolerably well with experimental measurements.

Acknowledgments

QW is supported by the Open University Research Studentship. KML wishes to thank Daniel Juvé, Henry Bass and Keith Attenborough for a travel grant to attend the 7th Long Range Sound Propagation Symposium.

References

1. A Berry and G A Daigle, *J. Acoust. Soc. Am.* **83**, 2047-2058 (1988).
2. R E Langer(Ed.), *Electromagnetic waves* (The Univ. of Wisconsin Press, Madison, 1962).
3. N A Logan and K. S. Yee, in Ref. 2, pp. 139-180.
4. C L Perkeris, *J. Acoust. Soc. Am.* **18**, 295-315 (1946).
5. B D Seckler and J. B. Keller, *J. Acoust. Soc. Am.* **31**, 192-205 (1959)
6. B D Seckler and J. B. Keller, *J. Acoust. Soc. Am.* **31**, 206-216 (1959)
7. D S Jones, *Acoustics and Electromagnetic Waves* (Clarendon Press, Oxford, 1986).
8. M Abramowitz and I Stegun, *Handbook of mathematical functions*, (Dover Publications, New York, 1970).
9. R Raspet, G E Baird and W Wu, *J. Acoust. Soc. Am.* **89**, 107-114 (1991).
10. K Attenborough, *J. Sound Vib.* **99**, 521-544 (1985).

Meteorology

A brief tutorial on atmospheric boundary-layer turbulence for acousticians

D. K. Wilson

U. S. Army Research Laboratory

ATTN: AMSRL-IS-EE

2800 Powder Mill Road

Adelphi, MD 20783 USA

Introduction

Atmospheric boundary layer structure and turbulence can dramatically affect sound levels by refracting and scattering acoustic energy. The importance of atmospheric phenomena is evident from the increasing number of papers dedicated to this subject during the past few Long Range Sound Propagation Symposia. Progress in the area of atmospheric effects on propagation will be most rapid, of course, if the acoustical community can integrate and guide its work with the best theoretical and computational models developed by boundary-layer meteorologists in recent decades.

This paper provides a brief tutorial on atmospheric turbulence and the boundary layer for acousticians. It is loosely formatted as a sequence of questions and answers, and miscellaneous topics. The paper is not meant to be a complete, self-contained course; it focuses instead on issues relevant to acoustics. Some misconceptions and misnomers that arise with varying frequency in the acoustics research community are discussed. After this "crash course" I certainly hope the reader eventually has a chance to read Stull (1988), Wyngaard (1992), or some of the other references listed at the end of the paper.

What is the atmospheric *boundary layer* ?

In meteorological usage, the boundary layer is normally defined as that part of the atmosphere whose structure changes directly in response to radiative heating and cooling of the ground, as occurs during the course of a day/night cycle. The boundary layer is generally between several hundred and several thousand meters thick, extending from the ground up to the *free troposphere*. (See Figure 1.) The interface between the boundary layer and the free troposphere is often marked by stratocumulus (puffy, flattened clouds) in fair weather conditions, although in other weather conditions the interface is not always so readily identifiable. The boundary layer thickness varies dynamically, growing over the course of a sunny day.

The atmospheric boundary layer is normally turbulent. Characteristic Reynolds numbers are huge: for a boundary-layer thickness of 1500 m and wind speed of 10 m/s, the Reynolds number would be about 10^9 ! However, situations do sometimes develop, particularly at night, where cold, dense air near the ground underlies relatively warmer air. If the density contrast between the air masses is sharp enough, turbulence will be cut off. Air motions can still occur in this situation, but they are normally *gravity waves*, not turbulence.

The lowermost part (usually the lowest tenth, by definition) of the boundary layer is called the *surface layer*. It is in this layer where the sharpest gradients in mean wind speed and temperature occur. The region above the surface layer is called the *mixed layer*.

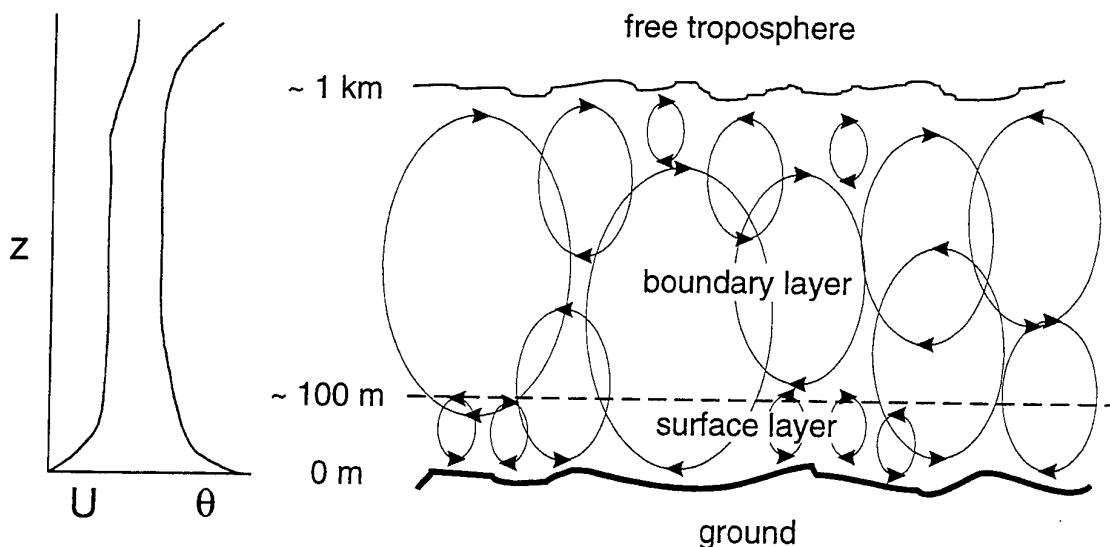


Figure 1. Schematic of the daytime atmospheric boundary layer. The plot on the left shows the mean wind speed (U) and potential temperature (θ) profiles.
 $(\theta = T + \gamma_d z$, where $\gamma_d = 0.098^\circ \text{C} / \text{km}$ is the dry adiabatic lapse rate, and T is the temperature.)

What is a *neutral* atmosphere?

Among atmospheric scientists *statically neutral* means that if an air parcel is displaced vertically, it will experience no buoyant acceleration. Because atmospheric pressure decreases with height, air will naturally expand and cool when it rises, and be compressed and heated when it sinks. If the air does not contain liquid water vapor, this expansion can be shown to cause a decrease of about 1 deg C per 100 m change in altitude, called the dry adiabatic lapse rate. If the mean temperature gradient is greater than the adiabatic lapse rate, a parcel would be decelerated, and conditions are termed *statically stable*. Gradients less than the adiabatic lapse rate would cause a parcel to be accelerated, and hence are called *statically unstable*.

Stable conditions tend to form at night, as a result of radiative cooling of the ground, whereas unstable conditions tend to form during the day, as a result of radiative heating. It is frequently the case during stable conditions that the near-surface winds are light, but the temperature gradients are very strong.

Acousticians frequently use *neutral atmosphere* to describe a situation where the mean sound speed is independent of height, hence resulting in no refraction of sound waves. Since the speed of sound is proportional to the square root of temperature, it actually decreases with height when conditions are statically neutral. Hence, neglecting the effect of wind shear, there will be upward refraction in what atmospheric scientists call a neutral atmosphere.

What are *mechanical* and *thermal* turbulence?

There are two types of instability responsible for the generation of turbulent kinetic energy: shear and buoyancy. To atmospheric scientists, *mechanical turbulence* suggests turbulence

generated primarily by shear instabilities, whereas *thermal* or *convective turbulence* suggests turbulence generated primarily by buoyant instabilities (statically unstable temperature gradients). High-wind conditions and a small temperature difference between the air and ground result in the generation of predominantly mechanical turbulence. Convective turbulence prevails when the ground is much warmer than the overlying air, as on a sunny day. Hence when atmospheric scientists speak of mechanical vs. convective turbulence, they are referring to the *source* of the dominant turbulent instability.

In the acoustics community, however, *mechanical turbulence* normally refers to velocity fluctuations, while *thermal turbulence* refers to temperature fluctuations. This usage describes the *effect* of the turbulence on the acoustic wave, rather than its source, as in the preceding paragraph. Even when the primary source of turbulence is shear instability, there can still be strong temperature fluctuations present. This is often the case at night. Likewise, when buoyant production predominates, there can still be strong velocity fluctuations (e.g., on a sunny day or in a rapidly boiling pot).

Correlations between horizontal velocity fluctuations and temperature.

When acoustic waves propagate nearly horizontally, the effective index-of-refraction variance is approximately

$$\langle \mu^2 \rangle \approx \frac{\langle u'^2 \rangle}{c_0^2} \cos^2 \phi + \frac{\langle v'^2 \rangle}{c_0^2} \sin^2 \phi + \frac{\langle u' T \rangle}{c_0 T_0} \cos \phi + \frac{\langle T^2 \rangle}{4T_0^2},$$

in which T , u' , and v' are the fluctuations in the temperature, horizontal wind speed parallel to the mean wind, and horizontal wind speed perpendicular to the mean wind, and ϕ is the angle between the wind and wavefront normal. The third term, representing velocity/temperature correlation, is usually neglected in propagation work. During daytime conditions, however, there is normally a high degree of correlation between horizontal velocity and temperature. This is because updrafts originating at the surface tend to transport relatively warm, slow-moving, air. Using surface-layer scaling methods, the effective index-of-refraction variance is given approximately by (Wilson and Thomson 1994)

$$\langle \mu^2 \rangle \approx \frac{5u_*^2}{c_0^2} + \frac{2.5u_* T_*}{c_0 T_0} \cos \phi + \frac{T_*^2}{T_0^2},$$

where u_* is the friction velocity and $T_* = -Q/u_*$, Q being the surface temperature flux. (Away from the surface, or during highly convective conditions, we must switch to turbulence parameterizations involving the "mixed-layer scales," w_* and θ_* . (Stull 1988).) We see that when the ratio $(u_*/c_0)/(T_*/T_0)$ is large, as is most often the case, the velocity variance term is the most important, the covariance term is second most important, and the temperature variance term is least important. Hence, if one neglects the covariance term, to an even better degree of approximation the temperature variance term can be neglected.

Relative contributions of temperature and velocity fluctuations to scattering during the day

During the daytime, the velocity term in the effective index of refraction nearly always dominates the temperature term. This is true even on very sunny days when buoyant production of turbulence dominates shear production. Although one can indeed expect higher temperature variance on sunny days, strong buoyant instabilities also have the effect of creating vigorous motions in the air. Hence *both* the temperature and velocity terms increase under such conditions. This is demonstrated in Fig. 2, which shows the ratio of the temperature variance term to the velocity variance term for propagation downwind. Even for extremely large values of the surface temperature flux ($Q = 0.5 \text{ K m/s}$), such as might occur around midday during the summer, the velocity variance term is still an order of magnitude larger than the temperature term at $z = 2 \text{ m}$. The formulas used to calculate the velocity and temperature variances were (e.g., Wilson and Thomson 1994; Stull 1988)

$$\langle u^2 \rangle = 5.4u_*^2 + 0.2w_*^2 ,$$

$$\langle T^2 \rangle = T_*^2 \left(0.25 + 1.1 \left(-\frac{z}{L} \right)^{2/3} \right)^{-1}$$

Relative contributions of temperature and velocity fluctuations to scattering at night

Situations where temperature fluctuations have a more significant effect on acoustic scattering than velocity fluctuations most often occur at night. In a very stable nocturnal boundary layer, such as occurs on clear, still nights, turbulent mixing is suppressed and strong positive temperature gradients develop. In the presence of such temperature contrasts, even very slight motions in the air generate high temperature variances at a fixed point. The source of these motions is generally gravity waves, not turbulence. (In the oceanographic community these are known as internal waves.) However, it should also be pointed out that intermittent episodes of turbulent mixing are known to occur in stable boundary layers, at intervals varying from 15 minutes to several hours. During these episodes velocity fluctuations doubtless play a significant role in scattering.

Turbules vs. eddies.

According to the dictionary an *eddy* is a rotating fluid parcel. The term is used quite generically in the turbulence literature, referring to virtually any turbulent motion. [See for example pp. 258–259 in Tennekes and Lumley (1972).] After all turbulence is, by nature, rotational. Other terms are used for specific types of coherent motions, such as *longitudinal roll vortices* and *horseshoe vortices*. Therefore the term *turbule*, apparently coined by researchers in the wave propagation community to mean a turbulent object, is not much different from what the turbulence research community calls an *eddy*.

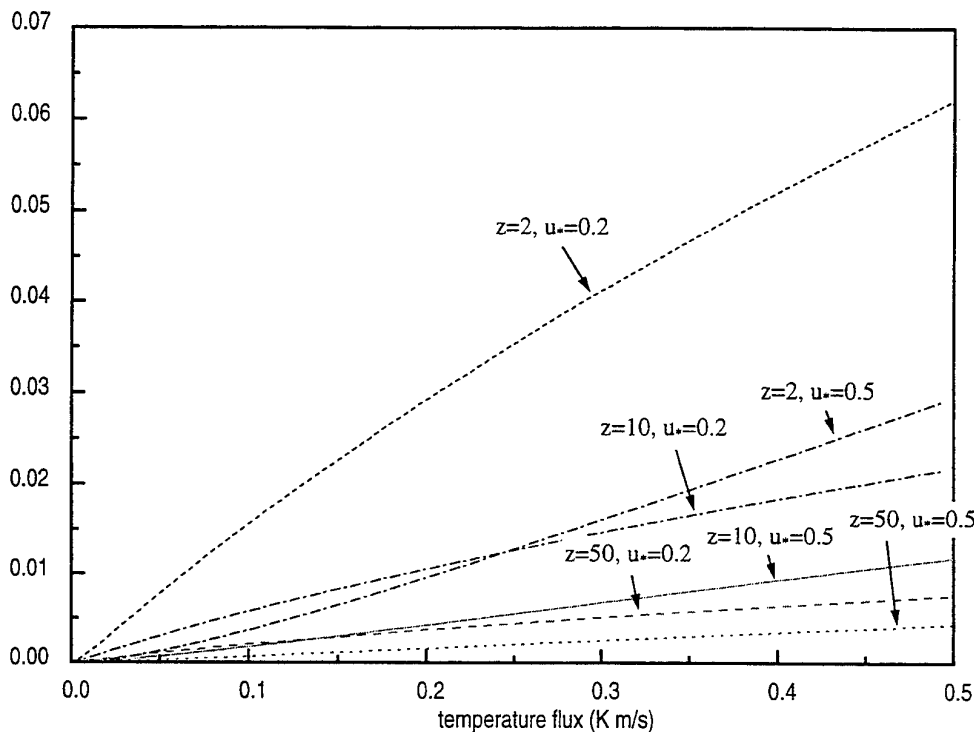


Figure 2. Ratio of the temperature variance and velocity variance contributions to the effective acoustic index of refraction, as a function of the surface temperature flux (equal to the surface heat flux divided by ρC_p). Several heights z are shown (m), along with several values for the friction velocity u_* (m/s).

What is *homogeneity*?

In turbulence theory *homogeneity* is applied in a statistical sense: it means that turbulent fluctuation statistics do not vary with position. For example, a consequence of homogeneity would be that the variance in the sound speed is everywhere constant. Homogeneity in this sense is the spatial analog of stationarity in time. Acousticians, on the other hand, often use the word to mean that there are no spatial variations in the sound speed or wind velocity (i.e., the sound speed and wind velocity, and not just their statistics, are everywhere constant.) Atmospheric scientists would simply describe this state of affairs as non-turbulent. Although the two usages of *homogeneity* are equally valid, acousticians should be aware of this difference in terminology.

Isotropy of the velocity field

Isotropy of a scalar field is straightforward concept. The word means that correlations and other statistical quantities, such as spatial correlations, are independent of a rotation of the coordinate axes. For a scalar quantity this implies that the correlation function depends only on the magnitude of the displacement vector. But isotropy of a vector field, such as velocity, is a somewhat more difficult concept, and the term is often misused in this context. This point has been made previously by Juvé *et al.* (1994)

The root of the confusion is this: stating that correlations of a vector field are independent of coordinate rotations does not imply a dependence only on the magnitude of the displacement. One must also account for the orientation of the velocity components being correlated. For example, consider the autocorrelations shown in Fig. 3. The top, left part of the drawing is for the autocorrelation of the velocity component u_1 , with the displacement (magnitude r) along the x_1 -axis. Notationally we indicate this as $R_{11}(r,0,0)$. By rotating the coordinate axes we can obtain the autocorrelations $R_{22}(0,r,0)$ (shown top right) and $R_{33}(0,0,r)$, but there is possible rotation from which we can obtain the autocorrelation in the bottom right of the figure, $R_{22}(r,0,0)$. The functions $R_{11}(r,0,0)$, $R_{22}(0,r,0)$, and $R_{33}(0,0,r)$ are termed *longitudinal* autocorrelations, whereas $R_{22}(r,0,0)$ is an example of a *transverse* autocorrelation. All of the transverse autocorrelations (there are five others) can be obtained by rotating $R_{22}(r,0,0)$. Most generally, for an isotropic vector field, the correlation function has the following form (Batchelor 1952):

$$R_{ij}(\mathbf{r}) = \sigma^2 \left(\frac{f(r) - g(r)}{r^2} r_i r_j + g(r) \delta_{ij} \right),$$

in which $f(r)$ and $g(r)$ are the normalized longitudinal and lateral autocorrelations, respectively, $\mathbf{r} = (r_1, r_2, r_3)$, $r = |\mathbf{r}|$, and σ^2 is the variance. One can determine $g(r)$ in terms of $f(r)$ by assuming incompressibility of the flow, with the result (Batchelor 1952)

$$g(r) = f(r) + \frac{r}{2} f'(r).$$

Similarly, isotropy of vector fields does not imply that the spectrum of a velocity component depends only on the magnitude of the wavenumber. Hence one cannot simply divide the turbulent kinetic energy spectrum $E(\kappa)$ by three to obtain the spectrum for an individual velocity component. The general relationship is (Batchelor 1952)

$$\Phi_{ij}(\kappa) = \frac{E(\kappa)}{4\pi\kappa^2} \left(\delta_{ij} - \frac{\kappa_i \kappa_j}{\kappa^2} \right),$$

where $\Phi_{ij}(\kappa)$ is the three-dimensional cross-spectral density of u_i and u_j , $\kappa = (\kappa_1, \kappa_2, \kappa_3)$, and $\kappa = |\kappa|$.

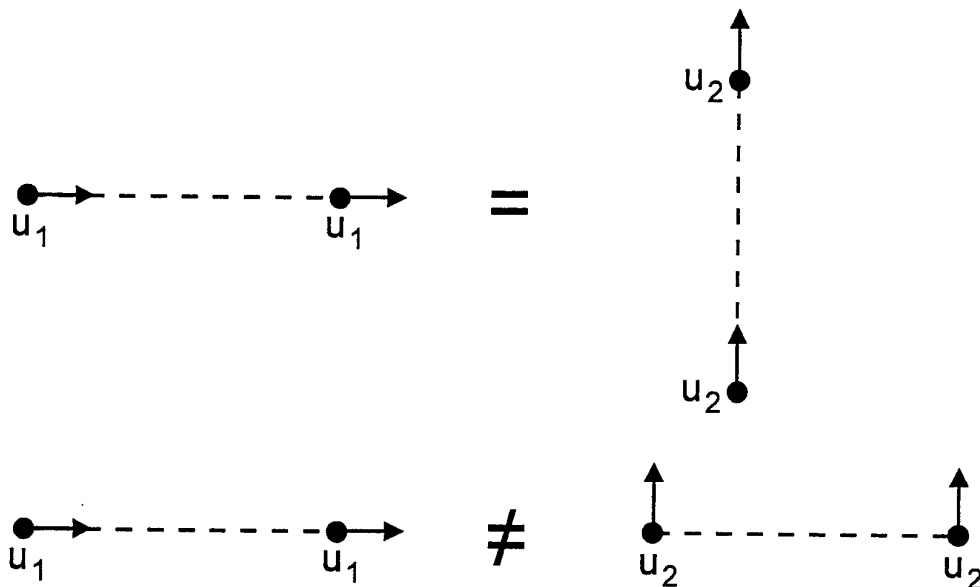


Figure 3. Top: Two cases of longitudinal autocorrelations in a vector field. If the vector field is isotropic, the two autocorrelations are described by the same function, since the one on the right can be reproduced from the one on the left by rotating the coordinate axes. Bottom: The autocorrelation on the left is longitudinal, whereas the one on the right is transverse. Isotropy does *not* imply equivalence of the two, since the transverse correlation cannot be obtained by the longitudinal one by a coordinate axes rotation.

What are the *outer* and *inner scales*?

According to Tennekes and Lumley (1972), *outer scale* means the same thing as *integral length scale*. The source of the former term is a literal translation from the Russian turbulence literature. The definition is

$$L = \frac{1}{\sigma^2} \int_0^\infty \langle u_i'(r) u_i'(0) \rangle dr,$$

in which σ^2 is the variance, u_i' is the fluctuation in a velocity component, and the angle brackets indicate the ensemble average. Since the most energetic eddies in a turbulent field are the large ones, the integral length scale is representative of the largest eddies in the flow. For the atmosphere the largest eddies are comparable in size to the boundary-layer thickness, typically 1–2 km on a sunny afternoon.

Actually, there is an ambiguity regarding definition of the integral length scale in homogeneous, isotropic turbulence. As can be surmised from the discussion above on isotropy, there must be two such scales: one when the displacement is taken in the same

direction as the velocity components, called the *longitudinal integral length scale*, and the other when the displacement is perpendicular to the velocity, called the *transverse scale*. It can be shown that the longitudinal scale is twice the transverse in homogeneous, isotropic turbulence (e.g., Batchelor, 1953).

Similarly, instead of *inner scale*, the preferred English-language term is *Kolmogorov microscale*. This is the length scale at which viscous dissipation processes begin to dominate:

$$\eta = \left(\frac{\nu^3}{\varepsilon} \right)^{1/4},$$

where ν is the kinematic viscosity and ε the dissipation rate of turbulent kinetic energy, per unit mass. For atmospheric turbulence, $\varepsilon \approx 10^{-3} \text{ m}^2/\text{s}^3$, implying $\eta \approx 1.4 \text{ mm}$. There is also a *Taylor microscale*, which is defined through a series expansion of the correlation function.

We see that atmospheric turbulence spans a vast range of spatial scales, from about 1 mm to 1 km.

Time and length scales for atmospheric turbulence.

Quite frequently in the outdoor sound propagation literature, 1 m is used as a typical length scale for the effective index of refraction. Under most atmospheric conditions the length scale is actually much larger. (Table I in Wilson and Thomson (1994) provides a summary of atmospheric length scale measurements.) Furthermore, index-of-refraction variances in the acoustics literature are normally reported in the range 10^{-6} to 2×10^{-6} , whereas values determined by field measurements described in the boundary-layer meteorology literature, and by similarity scaling methods, are an order of magnitude larger.

One might ask why, if the length scale used by acoustical studies is often too short, and the index-of-refraction variance too small, have researchers in outdoor propagation been able to obtain reasonable agreement between their models and acoustic scattering data. The reason apparently is that if the scattering comes from a narrow range of eddy sizes, one can simply choose a length scale characteristic of this range, and a variance representing only the energy in this range. This view is supported by the fact that most acoustical studies have set the turbulent length scale on the order of the acoustic wavelength; in large-angle scattering problems most of the scattering comes from eddy sizes comparable to the wavelength.

Figure 4 compares a one-dimensional von Karman spectrum to a pair of Gaussian spectra. The von Karman spectrum, known to work reasonably well for high Reynolds number turbulence, is given by

$$\hat{f}_K(\kappa) = \frac{\Gamma(5/6)}{\sqrt{\pi}\Gamma(1/3)} \frac{\sigma^2 \ell_K}{\left(1 + \kappa^2 \ell_K^2\right)^{5/6}},$$

where σ^2 is the variance, and $L = \ell_K \sqrt{\pi} \Gamma(5/6) / \Gamma(1/3)$ is the integral length scale. The Gaussian spectrum is

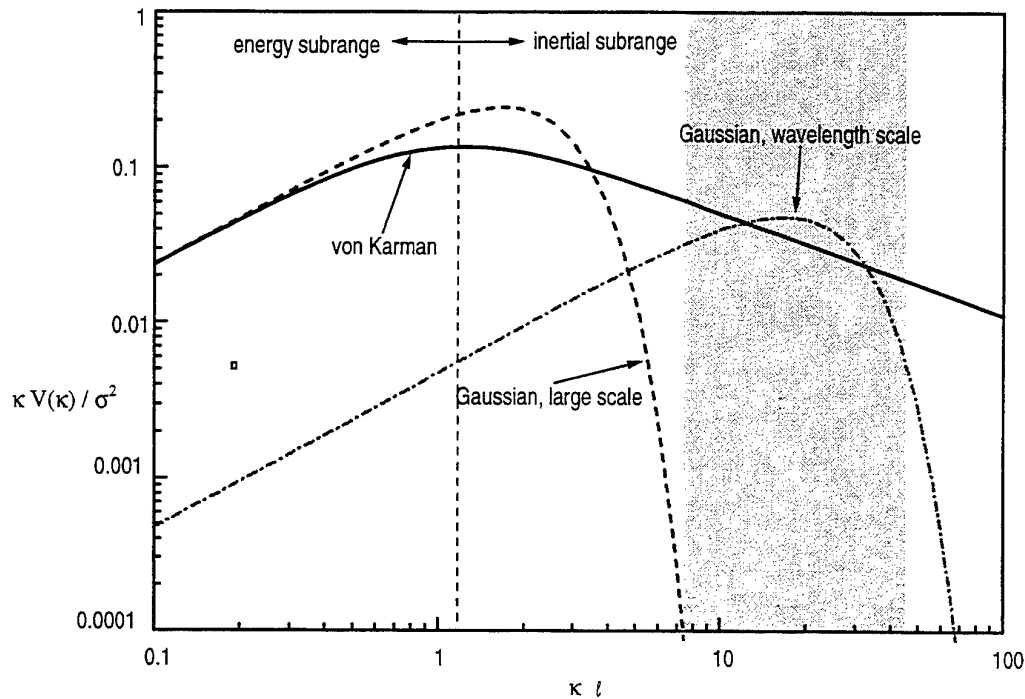


Figure 4. Comparison of the von Karman spectrum (solid line) to Gaussian spectra. The dashed line is a Gaussian spectrum with variance and integral length scales chosen to match the von Karman spectrum. The dash-dot line is a Gaussian spectrum whose integral length scale is one-tenth, and whose variance is one-fifth, the values used for the von Karman spectrum. The shaded region is meant to indicate the wavenumbers that are most important in a hypothetical scattering experiment, where the latter Gaussian spectrum may be satisfactory.

$$\hat{f}_G(\kappa) = \frac{\sigma^2 \ell_G}{2\sqrt{\pi}} \exp\left(-\frac{\kappa^2 \ell_G^2}{4}\right),$$

for which the integral length scale is $L = \ell_G \sqrt{\pi} / 2$. One of the Gaussian spectra in Fig. 4 was determined by setting the variance and integral length scales to the same values used for the von Karman spectrum. This version of the Gaussian spectrum fits the von Karman spectrum exactly at low wavenumbers, and reasonably well around the spectral peak. Past the spectral peak, at high wavenumbers (the *inertial subrange*), however, the Gaussian spectrum decays far too rapidly. Therefore we conclude that with variance and integral length scale parameters rigorously chosen, the Gaussian spectrum works reasonably well for large-scale turbulence,

but not well at all within the inertial subrange. The second version of the Gaussian spectrum in Fig. 4 has a length scale one-tenth, and variance equal to one-fifth, the values used for the von Karman spectrum. Over a certain range of wavenumbers, indicated by shading, the Gaussian spectrum approximates the von Karman spectrum reasonably well. If this happens to be the wavenumber range of interest in a scattering problem, then, a Gaussian spectrum may be satisfactory. (Although one could never hope to predict frequency-dependence of scattering successfully using a Gaussian spectrum.)

Averaging times in experiments.

In order to obtain accurate estimates of turbulence statistics in the atmospheric boundary layer, a sufficiently long averaging time must be used. Most acoustical work has relied on averaging times of just a few minutes, which turns out to be far too short. The r.m.s. error in the measurement of a statistical quantity f is given by (Lumley and Panofsky 1964)

$$\epsilon = \sqrt{\frac{2\tau \langle (f - \langle f \rangle)^2 \rangle}{T}},$$

where the angle brackets indicate the ensemble average, τ is the integral time scale, and T is the averaging time. For example, if one is measuring the mean wind speed the formula becomes

$$\epsilon = \sigma \sqrt{\frac{2\tau}{T}},$$

where σ is the standard deviation of the wind speed. Under daytime conditions τ is on the order of a minute. If $T = 5$ min, the r.m.s. error in the estimation of the mean is about 63% of the standard deviation. Even with an averaging time $T = 1$ hour, the error is about 18%. The situation is even worse for higher order statistics (Wyngaard 1992).

Unfortunately atmospheric stationarity can be a poor approximation over the time scales required to obtain accurate statistics, and so there is a trade-off between the need for long averaging times and non-stationarity. One of the best case scenarios is that of a well developed convective boundary layer, such as would occur in the afternoon on a sunny day. In this case reasonably stationary conditions might be present for just one to a few hours. This partially explains why there is so much scatter in measurements of atmospheric boundary-layer turbulence statistics.

Acknowledgements

I am indebted to J. Brasseur for presenting this paper in Lyon due to my absence at the LRSP. He and H. Auvermann read this paper and made many helpful suggestions. Several of the ideas in this paper resulted from discussions with J. Wyngaard, D. Thomson, and K. Gilbert. I thank them for sharing their knowledge of atmospheric turbulence and acoustic propagation.

References

- Arya, S. P. S., 1988: *Introduction to Micrometeorology*. Academic Press, San Diego, Calif.
- Batchelor, G. K., 1953: *The Theory of Homogeneous Turbulence*. Cambridge University Press, Cambridge, England.
- Juvé, D., Blanc-Benon, P., and Chevret, P., 1994: Sound propagation through a turbulent atmosphere: influence of the turbulence model. In *Proceedings of the Sixth International Symposium on Long-Range Sound Propagation*, Havelock, D. I., and Stinson, M. R., eds. Ottawa, Canada.
- Kaimal, J. C., and Finnigan, J. J., 1994: *Atmospheric Boundary Layer Flows: Their Structure and Measurement*. Oxford University Press, New York.
- Lumley, J. L., and Panofsky, H. A., 1964: *The Structure of Atmospheric Turbulence*. Wiley Interscience, New York.
- Stull, R. B., 1988: *An Introduction to Boundary-Layer Meteorology*. Kluwer, Dordrecht.
- Tennekes, H., and Lumley, J. L., 1972: *A First Course in Turbulence*. MIT Press, Cambridge, Mass.
- Wilson, D. K., and Thomson, D. W., 1994: Acoustic propagation through anisotropic, surface-layer turbulence. *J. Acoust. Soc. Am.* **96**, 1080–1095.
- Wyngaard, J. C., 1992: Atmospheric turbulence. *Annu. Rev. Fluid Mech.* **24**, 205–233.

Estimating long-term microclimatic conditions for long-range sound propagation studies

Y. BRUNET⁽¹⁾, J.P. LAGOUARDE⁽¹⁾ and V. ZOUBOFF⁽²⁾

⁽¹⁾ INRA-Bioclimatologie, BP 81, 33883 Villenave d'Ornon cedex (France)

⁽²⁾ Laboratoire Régional des Ponts et Chaussées d'Angers, BP 69, 49136 Les Ponts de Cé cedex (France)

ABSTRACT

Sound propagation in the lower atmosphere strongly depends on the wind direction and the vertical gradients in the speed of sound. The latter depends in turn on the vertical gradients of wind velocity and temperature. Because of the natural space and time fluctuations in microclimatic conditions, the acoustic level at a large distance from the source must be considered as a random variable. Therefore, knowing the statistical characteristics of the fluctuations in microclimatic conditions is of great importance for estimating the accuracy of a measurement or a calculation of long-range acoustic levels.

We describe a method based on a heat and mass transfer simulation model, for estimating hourly variations in local wind and temperature profiles. Two types of inputs are required:

- site descriptors (soil and vegetation parameters acting on the surface energy and water balances: albedo, roughness length, soil type...);
- standard climatic data provided by the meteorological network (insolation, wind velocity and direction, air temperature and humidity, precipitation...).

Using long-term (i.e., several years) climatic data files, it is possible to calculate statistical distributions of the vertical wind and temperature gradients at some height above the surface, as well as the distribution of the vertical sound velocity gradient. For a given source-receiver configuration, the corresponding distribution function of sound levels can then be deduced.

The method is illustrated by a case study performed with a 30 year climatic file for a typical rural site in France. As an example, we calculated the fraction of time during which the sound level exceeded a prescribed threshold, for one particular source-receiver configuration.

1. INTRODUCTION

Knowledge of the statistical properties of the sound pressure level is very important from a practical point of view. Sound propagation in the lower atmosphere strongly depends on the wind direction and the vertical gradients in the speed of sound. The latter depends in turn on the vertical gradients of wind velocity and temperature. Because of the natural space and time fluctuations in microclimatic conditions, the acoustic level at a large distance from

the source must be considered as a random variable. Therefore, knowing the statistical characteristics of the fluctuations in microclimatic conditions on a given site is of great importance for estimating the accuracy of a measurement or a calculation of long-range acoustic levels.

The vertical gradients in horizontal wind velocity and air temperature cannot be determined on the sole basis of the climatic data given by meteorological networks. Temperature gradients (and wind speed gradients, through the influence of stability forces) strongly depend on the partition of radiative energy into sensible and latent heat fluxes. This partition is determined to a large extent by the amount of water present in the top soil layers. As this variable is never measured routinely, the only way to address the problem is to simulate the soil water budget and the surface fluxes with the help of a model that can be integrated on a hourly basis over time scales of months or years.

This model must be simple, with as few parameters as possible. It must be able to accept standard meteorological data as inputs, and carry out a soil water budget. Such a model is presented here, along with some validation results. It is further shown, on an example, how it can be used to estimate the spread in sound levels (expressed here in terms of mean energy value L_{Aeq}) produced by long-term meteorological parameters, or the fraction of time during which a given sound pressure level is reached or exceeded, on a statistical basis.

2. THE SIMULATION MODEL

The model chosen is derived from the original model of Choisnel (1977), that was subsequently improved in many respects. It was primarily designed for agrometeorological purposes. The model simulates coupled energy and water transfer between the soil and the atmosphere. The vegetation is considered as a 'big-leaf' type surface layer. Convective fluxes (sensible and latent heat) are computed using the standard Monin-Obukhov similarity laws for turbulent transfer in the atmospheric boundary surface layer. Soil heat flux and temperature profiles are computed using the Fourier equation. A soil water balance is carried out at each time step, to estimate the amount of water that is available for the evaporation process.

The model is designed to be driven by standard meteorological data, and only requires a few easily available soil parameters. It runs on an hourly time step. The surface temperature T_s is computed by solving the energy budget equation. We first present the equations used for computing the surface fluxes. We then describe the water budget model and its coupling with surface processes.

2.1 Surface fluxes

2.1.1 *The radiative budget*

Net radiation R_n is computed as:

$$R_n = (1 - \alpha) R_s + \epsilon (R_a - \sigma T_s^4)$$

where R_s is the global radiation, R_a the atmospheric longwave radiation, T_s the radiative surface temperature and σ the Stefan-Boltzman constant.

R_s is estimated statistically from the daily sunshine fraction N (the ratio between the astronomical day length and the sunshine duration measured in meteorological networks). Computation of R_s first involves estimating the daily global radiation R_{sj} by an Angström type formula:

$$R_{sj} = R_{s0} (a_0 + b_0 N)$$

where R_{s0} is the extra-terrestrial radiation and a_0 and b_0 seasonal coefficients that depend on the location. Assuming that the fraction of diffuse solar radiation only depends on cloudiness, the daily diffuse radiation R_{dj} is computed in a similar way as:

$$R_{dj} = R_{s0} (a_1 + b_1 N)$$

The hourly values of direct ($R_i = R_s - R_d$) and diffuse (R_d) radiation are then estimated by weighting the daily values ($R_{sj} - R_{dj}$ and R_{dj} , respectively) by some function of solar elevation. This amounts to assuming that N is evenly distributed over the day. The hourly global radiation is finally estimated as $R_s = R_i + R_d$.

The atmospheric downward longwave radiation R_a is statistically estimated from the air temperature T_a and vapor pressure e_a :

$$R_a = \sigma [T_a - (33.5 - 18 \ln(e_a) + 1.7 e_a^{1/2})^4 + 70 fneb]$$

with e_a expressed in mbar. The second term on the right hand side is a correction to account for the possible contribution of clouds. It involves the cloud fraction $fneb$, estimated from N through empirical relationships with coefficients depending on the season.

All the empirical coefficients used here have been established for oceanic climate in France (Choisnel, 1977).

The albedo a is computed using the model proposed by Baret et al. (1988), that simulates its hourly variation and accounts for the effect of surface characteristics on solar radiation absorption. It requires input parameters describing the vegetation structure (such as Leaf Area Index LAI, mean leaf inclination angle, optical properties of leaves and soil). Arbitrary values are assigned to the emissivity ϵ , according to the vegetation type.

2.1.2 Soil heat transfer

In the version of the model used here the soil is divided into four layers, with lower limits set at 10, 30, 50 and 100 cm, respectively. At the present stage only three main classes of soils (sand, loam, clay) are distinguished in the model (Table 1). The thermal characteristics are assumed to be homogeneous, with a uniform water content estimated from the available water stored (see further). The heat capacity c_s is computed by weighting linearly the heat capacity of each of the components (mineral, organic matter, air, water) by their

concentration (De Vries, 1963). The thermal conductivity λ_s is also determined from the type of soil and its mean water content (De Vries, 1963). For computing the soil temperature profile, the heat conservation equation and the Fourier law are solved in each soil layer:

$$\frac{\partial T}{\partial t} = - \left(1 / c_s \right) \frac{\partial G_z}{\partial z} \quad \text{and} \quad G_z = - \lambda_s \frac{\partial T}{\partial z}$$

G_z is the soil heat flux at depth z . The boundary conditions are given (1) at the bottom ($z = 1$ m) by a yearly sinusoidal variation of temperature, and (2) at the surface by a flux condition.

soil type	% mineral	wilting point	field capacity	s_u (mm/cm)
loamy	0.55	0.13	0.28	1.5
clay	0.50	0.27	0.45	2.2
sandy	0.55	0.05	0.15	1.0

Table 1. Characteristics of the soil types (mineral matter content, water content at wilting point and field capacity, unit storage capacity in mm water by cm soil)

Temperature T_1 computed at 10 cm is then used for estimating the ground heat flux G_0 at the surface by the Fourier equation. Following several authors (e.g., Shuttleworth and Wallace, 1985), we introduce a correction to account for the attenuation by the vegetation, assumed to be similar to the exponential attenuation of radiation under the vegetation layer:

$$G_0 = (\lambda_s / \Delta z) (T_s - T_1) \exp(-K LAI)$$

A value of 0.2 is assumed for the attenuation coefficient K .

2.1.3 Turbulent fluxes

Standard surface layer equations are used to compute sensible (H) and latent (LE) heat fluxes. H is given by:

$$H = \rho c_p (T_s - T_a) / r_a$$

where ρ and c_p are the air density and specific heat of air at constant pressure, respectively. T_a is the air temperature at height z , and r_a the aerodynamic resistance defined as:

$$r_a = \left\{ \ln[(z-d) / z_{0m}] - \Psi_m [(z-d) / L] \right\} \left\{ \ln[(z-d) / z_{0h}] + \Psi_h [(z-d) / L] \right\} / k^2 U$$

where U is the mean wind speed at height z and k the von Karman constant ($k = 0.4$). The parameters z_{0m} and d are the momentum roughness length and displacement height, respectively. They are estimated from crop height h_c using the common approximation $z_{0m} = 0.13 h_c$ and $d = 0.66 h_c$ (Brutsaert, 1982). The ratio z_{0h}/z_{0m} (z_{0h} being the thermal roughness length) may vary with the structure (density, height...) of the vegetation (Brutsaert, 1982). It can be prescribed in the model, but a value of 0.1 corresponding to a dense 'close' crop is often used. L is the Monin-Obukhov length defined as:

$$L = - \rho c_p T_a u_*^3 / k g H$$

where g is the acceleration due to gravity and u_* the friction velocity defined as:

$$u_* = k U \left\{ \ln[(z-d) / z_{0m}] - \Psi_m [(z-d) / L] \right\}^{-1}$$

Ψ_m and Ψ_h are the common atmospheric stability functions, that can be found in Brutsaert (1982). A modification has been brought to the standard formulation that fails for very stable atmospheric conditions: an arbitrary threshold value of -5 has been set to avoid unrealistic values in this case.

The evapotranspiration at the soil-plant-atmosphere interface is estimated using the 'big-leaf' assumption (see Monteith, 1975):

$$LE = (\rho c_p / \gamma) [e_s(T_s) - e_a] / (r_a + r_*)$$

where γ is the psychrometric constant ($\gamma \approx 0.66 \text{ hPa K}^{-1}$), e_a and $e_s(T_s)$ the air vapour pressure and the saturated vapour pressure at temperature T_s , respectively; r_* is the bulk surface resistance, computed following Katerji and Perrier (1985) who distinguish soil and canopy resistances in the following manner:

$$r_*^{-1} = (r_{0g} + r_g)^{-1} + (r_0 + r_s)^{-1}$$

r_{0g} is the resistance due to the vegetation structure. It is defined as (Katerji and Perrier 1985):

$$r_{0g} = 340 \text{ LAI}$$

r_g is the resistance of the soil layer to water transfer; it depends on the soil water content. It is a function of the ratio between the actual and maximum soil water availability. r_0 is a resistance to water vapor transfer through the canopy due to its structure; it varies from 5 to 10 s m^{-1} for meadow, from 10 to 20 s m^{-1} for wheat (Katerji and Perrier 1985). The stomatal resistance r_s is computed according to a model adapted from Noilhan and Planton (1989):

$$r_s = r_{s \min} / (LAI F_1 F_2 F_3 F_4)$$

$r_{s \min}$ is the minimum value of resistance in the absence of water stress (around 50 s m^{-1}). F_1 , F_2 , F_3 and F_4 are factors varying from 0 to 1, and are taken from Jacquemin and Noilhan (1990).

F_1 accounts for the influence of solar radiation and is parameterized after Dickinson (1984):

$$F_1 = (1 + f) / (f + r_{s \min} / r_{s \max})$$

with

$$f = (\text{PAR} / R_{s1}) (2 / \text{LAI})$$

$r_{s\max}$ is the maximum crop stomatal resistance (set at 5000 s m^{-1}). PAR is the photosynthetically active solar radiation ($\approx 0.55 R_s$). For the limit solar radiation R_{s1} , Noilhan and Planton (1989) propose a value of 100 W m^{-2} .

F_2 characterises the effect of soil water stress on stomatal regulation. It depends on the availability of water for extraction by the roots. It allows surface fluxes to depend on the soil water budget. Its parameterization is described in the next section.

F_3 accounts for the influence of air vapor pressure deficit (Jarvis, 1976):

$$F_3 = 1 - g_e (e_s(T_s) - e_a)$$

with $g_e = 0.025 \text{ hPa}^{-1}$ (Noilhan and Planton, 1989).

Finally, the effect of air temperature is introduced by the way of a F_4 factor (Dickinson, 1984):

$$F_4 = 1.0 - 0.0016 (298 - T_a)^2$$

Finally, surface temperature and fluxes are simultaneously computed at each time step by solving the non-linear energy budget equation:

$$R_n(T_s) + G_0(T_s) + H(T_s) + LE(T_s) = 0$$

2.2 Soil water budget

Soil water transfer is simulated by a two-reservoir system (Jacquart and Choisnel, 1995). The maximum available amount of water R_{\max} that can be extracted by the plants from the soil is defined as the difference between the soil water content at field capacity and at the wilting point. It may be prescribed from measurements, or estimated from soil maps (see Mori, 1982, for France). It depends on the thickness d_{\max} of the cultivated soil layer and on the type of soil which characterizes the unit storage capacity s_u (see Table 1):

$$R_{\max} = s_u d_{\max}$$

The knowledge of s_u allows losses (evapotranspiration) and gains (rainfall, dew...) to be converted into an equivalent wetted soil thickness, which is then used for modifying the depths of the reservoirs at each time step.

The simulations are initialized at a date when the soil is saturated with water, in which case there is only one single reservoir (Figure 1a). The sequence of evaporation and rain phases lead to one- (Figure 1b) or two- (Figures 1c and 1d) reservoir systems, depending on the climatic conditions. At each time step rain is added on top of the soil. If the maximum available water limit is reached, excess rain is removed and converted into a runoff term - in the one-reservoir configuration -, or added to the lower part of the top reservoir - when there is one. In the latter case, the top reservoir may finally be filled up and a single-reservoir configuration is obtained again. Evaporated water is always extracted from the upper limit of

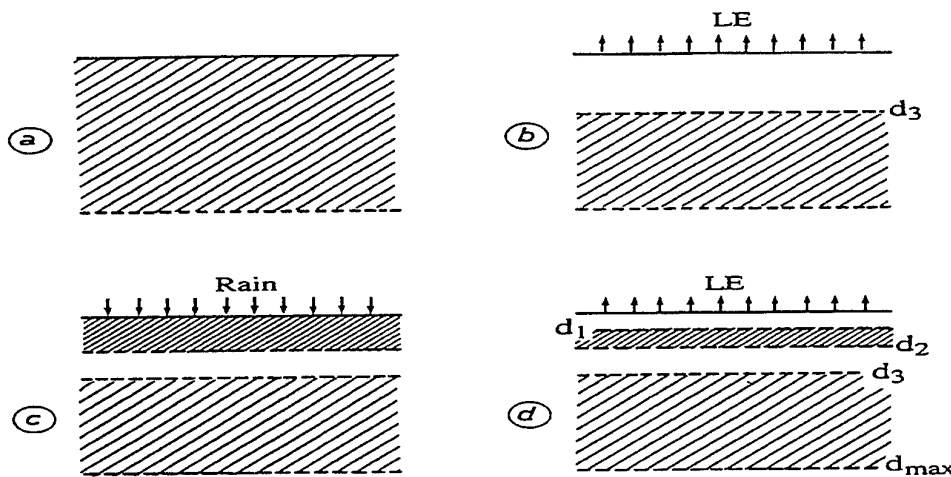


Figure 1. Soil water budget model: an evaporation phase after initialisation (a) leads to a one-reservoir configuration (b). Sequences of rain and evaporation are simulated by a top reservoir (c, d).

the top reservoir, until this surface reservoir completely dries out. Water is then extracted from the deep reservoir, which may dry out in turn, during long rain-free periods. The depths corresponding to the limits of the two reservoirs in the general case are d_1 and d_2 (top and bottom of the surface reservoir) and d_3 (top of the deep reservoir).

It has to be pointed out again that this model does not simulate a realistic water profile in the soil, but provides a good indicator of water availability at the surface. In particular the upper reservoir allows one to simulate events such as short periods of evaporation after rains occurring in dry conditions (summer rains for instance).

Defining d_4 as the depth of the reservoir nearest the surface ($d_4 = d_1$ or $d_4 = d_3$ in the one- and two-reservoir configurations respectively), the ratio d_4 / d_{max} is used for parameterizing the above mentioned F_2 factor that characterises the soil water stress: $F_2 = d_4 / d_{max}$.

The total amount of water in the soil at a given time is evaluated at each time step for computing the soil thermal characteristics. It corresponds to the sum of the water that cannot be extracted by evaporation (corresponding here to wilting point moisture), and of the remaining part of R_{max} that can be estimated as $R = s_u (d_{max} - d_3 + d_2 - d_1)$.

Two additional reservoirs have been introduced to account for dew (when evapotranspiration is negative) and interception of rain by vegetation. The amount of water I is accumulated in a reservoir (Calvet, 1990) whose maximum size I_x is defined by Dickinson (1984) as:

$$I_x = 0.2 \text{ LAI}$$

When it rains, this interception reservoir is filled first. If rainfall is greater than I_x , the excess water is distributed in the previous two soil reservoirs. As long as it exists, water is evaporated from the interception reservoir. Dew is accumulated in a fourth reservoir which is managed exactly as the interception reservoir. As long as intercepted rain or dew exist, a proportion d of surface covered by water is estimated following Noihlan and Planton (1989) as:

$$d = (I / I_x)^{2/3}$$

This factor appears in the computation of actual evapotranspiration LE , as a weighting term between potential evapotranspiration PET - corresponding to cases when the water remaining on leaf surfaces evaporates with no resistance - and the evapotranspiration of the canopy itself ET_c that is submitted to the stomatal regulation processes:

$$LE = d PET + (1 - d) ET_c$$

3. MODEL INPUTS AND OUTPUTS

3.1 Input meteorological data

Hourly air temperature T_a (h) and relative humidity Rh (h) are built from the minimum (T_{aN} and Rh_{N} , respectively) and maximum (T_{aX} and Rh_X , respectively) daily values using the following equations:

$$T_a (h) = T_{aN} + K_T(h) (T_{aX} - T_{aN})$$

$$Rh (h) = Rh_N + K_H(h) (Rh_X - Rh_N)$$

The coefficients $K_T(h)$ and $K_H(h)$ depend on the season and have been determined statistically. The hourly vapor pressure is then:

$$e_a = Rh (h) e_s(T_a)$$

In some cases, the only available information on air humidity is dew point temperature at 9:00 UT. The vapor pressure computed at this time is then considered as constant throughout the day.

As mentioned above, sunshine duration allows the hourly components of the solar radiation, and finally the net radiation, to be estimated. Windspeed is assumed to be constant all day long. This a rather strong assumption, and more realistic simulations would require time variations of this variable to be accounted for (particularly a day - night modulation). The daily rainfall is uniformly distributed over 24 hours.

3.2 Vegetation parameters

Mechanical and thermal roughness lengths are prescribed independently. The computation of the albedo with the model proposed by Baret et al. (1988) requires the type of

crop, the LAI and the mean leaf inclination angle to be prescribed. The emissivity value must also be known.

3.3 Soil parameters

The soil is assumed to be homogeneous. For the present time, three types of soil are defined in the model: loam, clay and sand. The soil composition, the thermal characteristics and the unit storage capacity s_u result from the choice of the soil type. Knowledge of the maximum available water amount is necessary. Soil minimum and maximum temperatures at 1 m, as well as the date of one of the extrema, are used to build the sinusoidal wave temperature required as a lower boundary condition for heat transfer computations.

3.4 Model outputs

The various surface fluxes and components of the radiative budget are computed every hour. The soil temperature profile and the soil water budget (configuration of the soil reservoirs, budget of the interception and dew reservoirs). The surface temperature is also an important output of the model. All these simulated data are synthetized for providing statistics (average values, extrema...) at daily and ten-day scales.

For the purpose of the present study the vertical gradients of mean horizontal wind speed and air temperature are calculated every hour from the standard Monin-Obukhov similarity laws:

$$\frac{\partial U}{\partial z} = [u_* / k (z_g - d)] \Phi_m [(z_g - d) / L]$$

$$\frac{\partial T}{\partial z} = [\theta_* / k (z_g - d)] \Phi_h [(z_g - d) / L]$$

where z_g is the desired height. The temperature scale θ_* is equal to $-H / (\rho c_p u_*)$ and the similarity functions are defined as:

$$\begin{array}{ll} \zeta \leq 0 & \Phi_m^2 = \Phi_h = (1 - 16 \zeta)^{-1/2} \\ 0 < \zeta < 1 & \Phi_m = \Phi_h = 1 + 5 \zeta \\ 1 < \zeta & \Phi_m = \Phi_h = 6 \end{array}$$

In order to get the wind vector gradient, the mean wind speed gradient is projected onto the source - receiver direction.

4. MODEL VALIDATION

The model has not been extensively validated against a long-term dataset. Such data are missing at the present time, but will be available in the next future in the framework of the Alpilles/reSeDA experiment planned for 1997 in the South-East of France. Accordingly the model has been validated only for some outputs and for some experiments performed in particular climatic conditions.

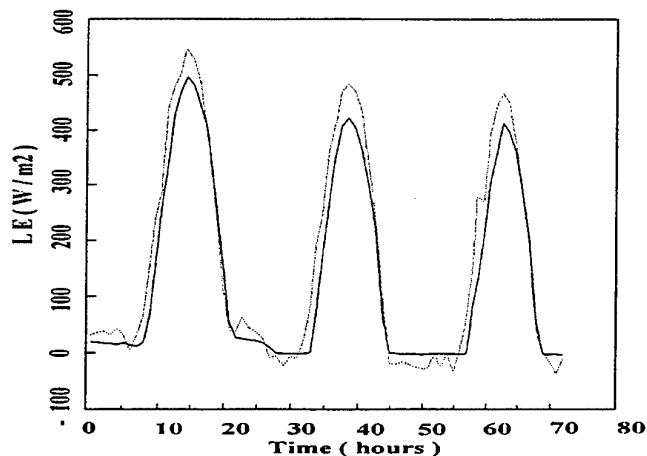


Figure 2. Comparison between simulated (solid line) and measured (dotted line) latent heat flux over a soybean crop (Avignon, 18-20 August 1989).

Figure 2 displays a comparison between actual evapotranspiration simulated with the model, and that measured over an irrigated soybean field, in Avignon. The overall agreement is satisfactory. It has to be pointed out that as the simulation is performed for maximum water availability, the coarse soil water budget model has not much effect here. For periods displaying both stressed and non-stressed conditions, we only present a comparison on surface temperatures (Figure 3). They have been recorded over a grass surface at Caumont airport (near Avignon) during an experiment performed over a seven month period (April to October 1986). Simulations have been performed using meteorological data recorded three kilometers away at an INRA station. The comparisons at the hourly scale (Figure 3a) and for

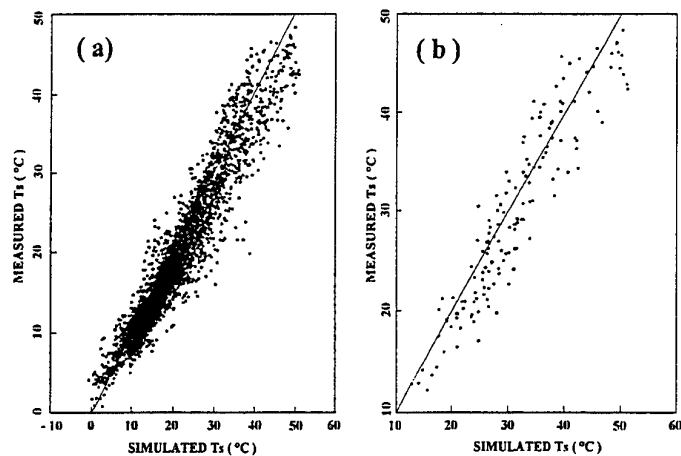


Figure 3. Comparison between hourly (a) and maximum (b) simulated and measured surface temperature over a grass field (Avignon, April-October 1986)

maximum daily temperatures (Figure 3b) are satisfactory. The scatter can primarily be related to the coarse assumption of a mean daily windspeed, and to possible discrepancies between simulated and actual soil water status which may induce differences at a few day scale. Nevertheless, we can think that the overall agreement observed in Figures 3a and 3b for surface temperature also implies a good agreement on surface fluxes.

The model was primarily designed for agrometeorological purposes and for long-term monitoring of surface water budget. The few previous examples of validation show that the simulated fluxes and surface temperatures agree rather well with the few available measurements. The model is not quite well suited for simulations at the hourly time scale for several reasons. First, the forcing variables are smoothed out because they are statistically rebuilt from daily meteorological data. Secondly the windspeed - that is responsible for large fluctuations in surface conditions and fluxes - is considered as constant, a rather severe assumption. Third, the coarse modelling of soil water budget makes it impossible to describe short time variations possibly related to rapid changes occurring in the top layers of soil. We must also mention that no coupling with a vegetation growth model exists at the present time: such a model would provide more realistic simulations throughout the year by introducing a link between the vegetation and the fluxes; as a matter of fact, plant development strongly depends on meteorological conditions (water status, drought for instance), and in return the plants determine the surface characteristics (structure, albedo, roughness...). Despite these limitations, the model seems realistic enough and appears as a good tool when only a statistical characterization of surface conditions over long periods is sought.

5. AN ILLUSTRATIVE CASE STUDY

We used this model to estimate the micrometeorological parameters needed to compute long-range sound propagation. In this context the hourly determination of these factors allows the random fluctuations of this propagation to be taken into account. The principle of the methodology can be summarized as follows.

The chosen site is located in Angers, in the Loire valley (France). The necessary meteorological information was obtained from the standard meteorological network. In order to insure a statistically correct distribution, a 30 year period was selected. The climatic data was taken every 3 hours, in order to improve the representativity of the wind direction and velocity.

The climatic data set, along with local ground and vegetation parameters are used to feed the micrometeorological model. The latter enables us to obtain, at a given height and for given time intervals, the hourly values of the vertical air temperature and wind velocity gradients. Defining a particular source - receiver geometry, the wind vector gradient can then be computed, along with the vertical sound speed gradient and L_{Aeq} (using an appropriate acoustical model based on vertical sound gradients).

The calculations were performed for the particular case of a receiver located above a homogeneous flat grassy surface 320 m away from a point source. The heights of the receiver and the source are respectively 1.5 m and 6 m above the ground. The source is assumed to be located exactly to the North of the receiver.

As an example, Figure 4 shows the frequency distribution of the vertical sound speed gradient obtained at the mean height between the source and the receiver, i.e. $z_g = 3.75$ m.

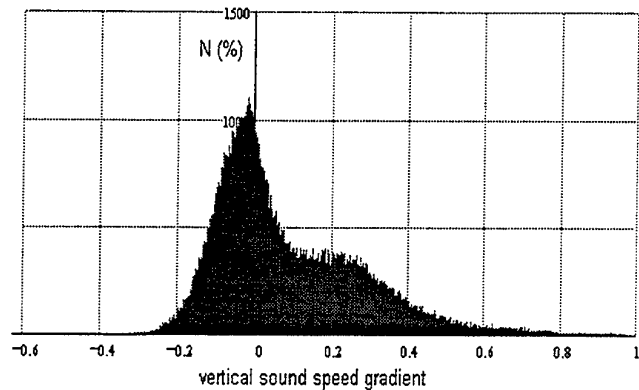


Figure 4. Frequency distribution of the vertical sound speed gradient obtained at $z_g = 3.75$ m over the 30 year climatic series.

In order to estimate L_{Aeq} (6 h - 22 h), we used the theoretical model described by Bérengier (1996) for positive sound speed gradients. For negative gradients, a set of experimental data were fitted to ensure a better accuracy in the shadow zone (Zouboff et al., 1994). Figure 5 shows the cumulative frequency distribution of L_{Aeq} (6 h - 22 h) over the 30 year period. As absolute values of L_{Aeq} depends on the power of the point source, the values given on the graph are not important per se.

This kind of chart can be very useful from a practical point of view: it allows one to

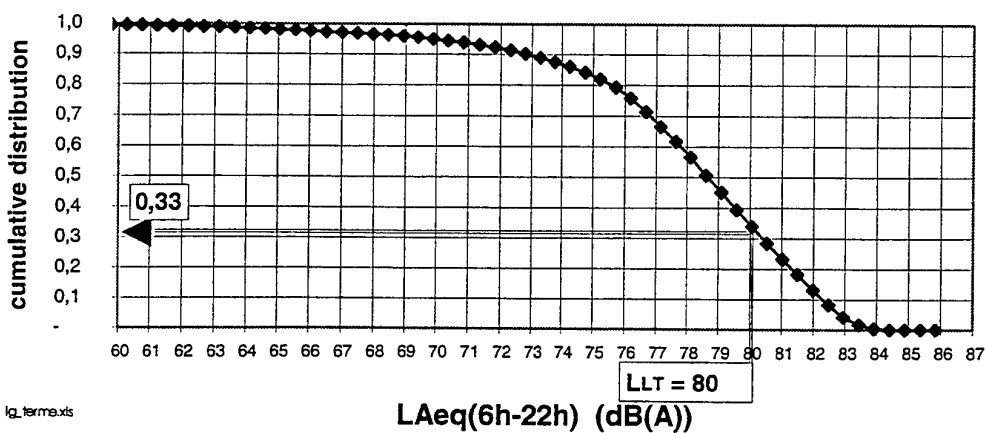


Figure 5. Cumulative frequency distribution of L_{Aeq} (6 h - 22 h) obtained over the 30 year period, for the configuration described in the text.

estimate the percentage of time during which a given acoustical value is reached or exceeded. For instance, using a practical method of calculation, we obtained a long-term L_{Aeq} level of 80 dB(A) for the same geometrical conditions as those described earlier. In Figure 5 it can be seen that this value can be reached or exceeded during about 33 % of the time.

6. CONCLUSION

The model presented here appears as a valuable tool for providing long-term statistical information on the microclimatic factors responsible for the propagation of sound in the lowest layers of the atmosphere. As the model was not primarily designed for this purpose, and as it was written about ten years ago, some improvements have to be made. In particular the parameterisation of the various resistances to the transfer of water has to be revised in the light of more recent studies. The treatment of heat and water transfer in the soil should also be improved. This is planned for the next future.

The model only allows the statistical properties of the sound pressure level to be estimated close to the meteorological measurements. In order to make this approach more general a methodology should be designed to provide a way of using the climatic data recorded by the meteorological network for estimating micrometeorological variables at locations not necessarily close to a particular station of this network. This is the subject of current research.

REFERENCES

- Baret, F., Guyot, G., Teres, J.M., Rigal, D., 1988. Un modèle simplifié de réflectance et d'absorptance d'un couvert végétal. Proceedings of the 4th International colloquium on Spectral Signatures of Objects in Remote Sensing. ESA SP 287, Aussois, 18-22 January 1988, 93-98.
- Bérengier, M.C., 1996. Influence of propagating effects on the acoustical classification of road pavements. Internoise 96, Liverpool, 639-644.
- Brutsaert, W.H., 1982. Evaporation into the atmosphere. Theory, history and applications. D. Reidel Publishing Company, London, England, pp. 299.
- Calvet, J.C., 1990. Adaptation d'un modèle agrométéorologique au cas des couverts hétérogènes (vignes-vergers). DEA Astrophysique, Géophysique et Techniques Spatiales. Université Paul Sabatier et Ecole de la Météorologie, Toulouse, pp. 43.
- Choisnel, E., 1977. Le bilan d'énergie et le bilan hydrique du sol. La Météorologie, numéro spécial Evapotranspiration, VI, 11, 103-133.
- De Vries, D.A., 1963. Thermal properties of soils. In W.R. van Wijk (ed.) Physics of the Plant Environment, North Holland, Amsterdam, 210-235.
- Dickinson, R.E., 1984. Modeling evapotranspiration from three-dimensional global climate models. In: Climate Processes and Climate Sensitivity, Geophys. Monogr., 29, 58-72.
- Jacquart, C., Choisnel, E., 1995. Un modèle de bilan hydrique simplifié à deux réservoirs utilisable en agrométéorologie. La Météorologie, 8, 29-43.
- Jacquemin, B., Noilhan, J., 1990. Sensitivity study and validation of land surface parametrization using the Hapex-Mobilhy data set. Boundary Layer Meteorol., 52, 93-134.

- Katerji, N., Perrier, A., 1985.** Détermination de la résistance globale d'un couvert végétal à la diffusion de vapeur d'eau et de ses différentes composantes. Approche théorique et vérification expérimentale sur une culture de luzerne. Agric. For. Meteorol., 34, 105-120.
- Monteith, J.L., 1975.** Vegetation and the Atmosphere. Vol 1: Principles. Academic Press, New York, pp. 278.
- Mori, A., 1982.** Carte de France des réserves en eau des sols. Service d'Etude des Sols et de la Carte Pédologique de France, INRA, pp. 53 + 2 cartes.
- Noilhan, J., Planton, S., 1989.** A simple parametrization of land surface processes for meteorological models. Mon. Weather. Rev., 117, 536-549.
- Shuttleworth, W.J., Wallace, J.S., 1985.** Evaporation from sparse crops. An energy combination theory. Quart. J. Met. Soc., 111, 839-855.
- Webb, E.K., 1970.** Profile relationships: the log linear range and extension to strong stability. Quart. J. R. Met. Soc., 96, 67-90.
- Zouboff, V., Brunet, Y., Bérengier, M., Séchet, E., 1994.** A qualitative approach of atmospheric effects on long-range sound propagation. Sixth International Symposium on Long Range Sound Propagation, Ottawa, Canada, 12-14 June 1994, pp. 1 (summary).

Meteorological measurements for use in sound propagation calculations

M. STINSON and G. DAIGLE

Institute for Microstructural Sciences
National Research Council, Ottawa, Ontario K1A 0R6, Canada

FAX (1) 613 952 3670

INTRODUCTION

Predictions of outdoor sound propagation require accurate knowledge of the meteorological conditions. Mean temperature and wind speed profiles control the upward or downward refraction characteristics. The stochastic fluctuations of wind speed and temperature, determine the scattering by turbulence. Measurements of both profiles and spectra have been obtained over the last couple of years at an airfield near Ottawa using a 10 m instrumented tower. From these data, it is becoming clear that the simple theoretical forms often assumed for these quantities are insufficient. Experimental results will be presented here and the implications for propagation modelling discussed.

A situation of particular interest is sketched in Fig. 1. For upward refraction conditions (sound speed decreasing with height, due to upwind propagation and/or thermal lapse conditions), sound rays curve upwards. The acoustic shadow formed contains no sound energy in this geometrical acoustics picture. Early measurements¹, though, demonstrated that there is significant sound energy in the shadow, much more than can be accounted for by diffraction. It is generally accepted that scattering of acoustic energy from turbulence accounts for the measured sound pressure levels.

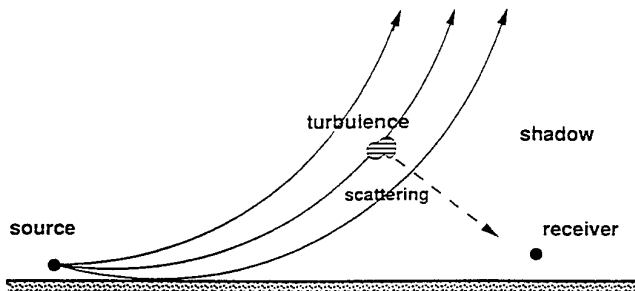


Figure 1. Sketch showing scattering of sound by turbulence into an acoustic shadow region formed by upward refraction conditions.

Clearly, to predict sound pressure levels in the shadow, both the refractive profile and the spectrum of turbulence responsible for scattering must be determined.

EXPERIMENTAL

The acoustical and meteorological measurements take place at an airfield about 50 km east of Ottawa in farmland. This airfield is used by a glider club so, except for the occasional tow plane, the site is relatively quiet. The layout of the site is shown in Fig. 2. The meteorological

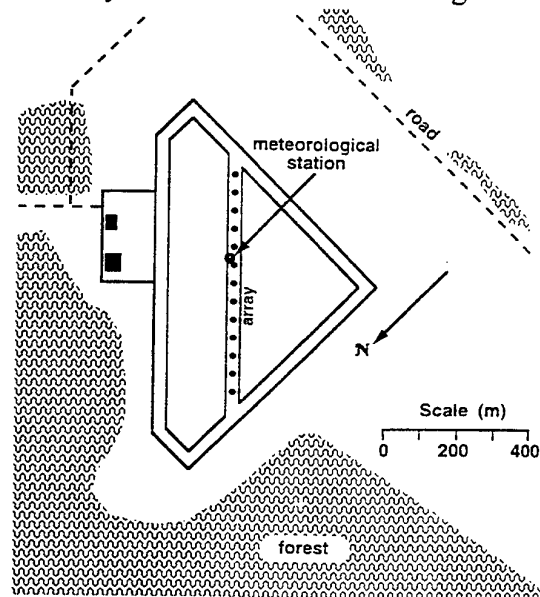


Figure 2. Plan view of airfield at which meteorological measurements were obtained.

tower is located partway along the unused, center runway. This runway is 30 m wide and composed of asphalt with some small shrubs breaking through. On either side of the runway, crops have been planted. The plants were about 1 m high during the measurements. The nearest buildings are over 300 m away from the tower while the nearest trees are more than 400 m away.

An important parameter for the application of theoretical forms for the refractive profile is the surface roughness. Independent measurements have been made during neutral conditions to establish this parameter. It was found that a surface roughness $z_0=0.05$ cm is appropriate for the runway itself; for the crop land beside the runway, a value of $z_0=0.5$ cm is estimated. In most cases, the winds reaching the meteorological sensors have travelled over the runway for only a short stretch and the profile will not have had time to adjust to the runway roughness². Hence, in the following analysis, we will simply assume a surface roughness of 0.5 cm.

The 10 m meteorological tower is sketched in Fig. 3. It is located approximately 3 m from the edge of the runway. The mean wind speeds are measured using Qualimetrics three-cup anemometers. An anemometer and a vane are located at the 10 m height; an additional sensor pair is located 0.3 m above the ground surface. Mean temperatures are determined using platinum resistance thermometers mounted in aspirated radiation shields. Temperatures are determined at heights of 8.7 m, 2.0 m, and 0.5 m. The electrical output signals from wind and temperature sensors are brought to our remote measurement trailer for display and recording. Measured values are recorded every two seconds.

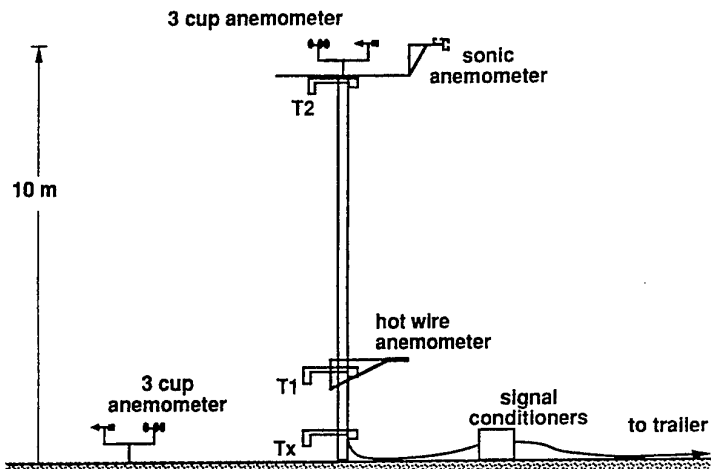


Figure 3. Sketch of the 10 m meteorological tower showing location of various thermal and wind sensors.

The turbulence spectra are determined using faster response devices. The primary tool is a pair of TSI hot wire anemometers, one configured to monitor wind speed fluctuations and the other, temperature fluctuations. These sensors are mounted at a height of 2 m. A sonic anemometer (on loan from ARL, WSMR) was also used on a few occasions to measure both temperature and wind speed variations; it was mounted at the 10 m height for one series of measurements and at 1.2 m for the next.

REFRACTIVE PROFILES - THEORY

When measured refractive profiles are not available, it is necessary to assume a theoretical form. Various forms have been used in the literature. The simplest is the linear profile for which the sound speed varies linearly with height. As will be seen, this does not provide a particularly good match to measured profiles. A better approximation is the logarithmic profile:

$$c(z) = \begin{cases} c(z_o) + a \ln(z/z_o), & z \geq z_o, \\ c(z_o) & , z < z_o. \end{cases} \quad (1)$$

To avoid a singularity at $z=0$, the sound speed is set constant below a height z_o , the surface roughness length. The parameter a is a measure of the strength of refraction for the profile.

An alternative profile can be generated through similarity scaling theory³. The sound speed profile in a given propagation direction is due to contributions from both the temperature profile $T(z)$ and the wind speed profile $u(z)$. For the wind speed profile, we take

$$u(z) = \frac{u^*}{\kappa_a} [\ln(z/z_o) - \psi_m(z/L) + \psi_m(z_o/L)] \quad (2)$$

with

$$\begin{aligned}\psi_m &= -5z/L & , \quad L > 0 \\ \psi_m &= \ln[(1+x^2)(1+x)^2/8] - 2\arctan x + \pi/2 & , \quad L < 0\end{aligned}\quad (3)$$

and

$$x = (1 - 16z/L)^{1/4} . \quad (4)$$

For the temperature profile, we have

$$T(z) = T_o + \frac{T^*}{\kappa_a} [\ln(z/z_o) - \psi_h(z/L) + \psi_h(z_o/L)] , \quad (5)$$

with

$$\begin{aligned}\psi_h &= -5z/L & , \quad L > 0 \\ \psi_h &= 2 \ln \left[\frac{1}{2} (1 + \sqrt{1 - 16z/L}) \right] & , \quad L < 0\end{aligned}\quad (6)$$

The wind and temperature profiles are not independent. From similarity scaling theory, the constants T^* and u^* and the Monin-Obukhov length L are related⁴ according to

$$\kappa_a g L T^* = T_s u^{*2} . \quad (7)$$

(In our calculations, we assume values of $\kappa_a=0.4$, $T_s=300$ K, and $g=9.81$ ms⁻².) From these profiles an effective sound speed profile is calculated according to

$$c(z) = c_o \sqrt{1 + T(z)/273} + u(z) \cos \psi \quad (8)$$

where $T(z)$ is specified in degrees Celcius, c_o is the sound speed at 0°C and ψ is the angle between wind and propagation directions.

REFRACTIVE PROFILES - MEASUREMENT

The profiles determined for one warm summer afternoon (21 June 1995) are shown in Fig. 4. Sensor data obtained during the 50 minutes of acquisition were averaged to give mean temperatures and wind speeds. These mean values have been plotted as solid circles against the corresponding sensor heights. The temperature is seen to be greater close to the ground so that a thermal lapse condition was in effect.

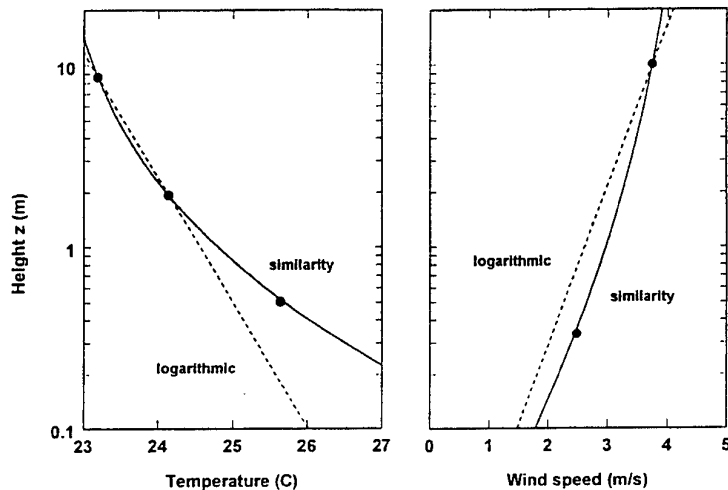


Figure 4. Mean temperature and wind speed profiles, measured and predicted, from data record METLOG.119 obtained 21 June 1995.

These measurements can be used to test the various theoretical forms for wind and temeprature profiles. Calculated curves are also presented in Fig. 4. Assuming a logarithmic variation of temperature with height, the measured temperatures at heights of 8.7 m (T_2) and 2 m (T_1) can be used to predict the temperature at all other heights; the calculated temperature profile is shown as the dashed curve in the left panel of Fig. 4. Similarly, assuming a logarithmic variation of wind speed with height, using the measured wind speed at the 10 m height (u) and setting the speed equal to zero at a height z_o , the calculated wind speed profile is obtained, shown as the dashed curve in the right panel. An alternate prediction is obtained by applying the similarity equations given in the previous section. The three quantities T_1 , T_2 and u are used as input and the iterative scheme describe by L'Espérance *et al.*⁴ followed to obtain the unknowns (u^* , T^* and T_o). Both the temperature and wind speed profiles are thus determined simultaneously. The results of this similarity-based calculation are shown as the solid curves in Fig. 4.

It is clear that similarity does a good job of predicting both temperature and wind speed at the lower heights (T_x and u_x , respectively) for this data set. The predictions made assuming logarithmic profiles are not so good, being low by about 0.5°C in the prediction of T_x and low by 10% in the prediction of u_x . It is noted that the thermal lapse was well-developed for these measurements. The difference in temperature between top and bottom thermometers was approximately 2.5°C .

Similar analyses have been applied to data obtained on a different days and a consistent trend has been observed. The similarity-based profiles agree well with the measured profiles whenever there is a well-developed thermal lapse, one for which the difference between lower and upper temperatures is greater than 1.7°C . When the temperature difference is less than this, neither similarity nor logarithmic profiles predict T_x correctly. However, in *all* cases, the similarity-based profile is superior to the logarithmic profile.

Although the empirical forms for the similarity equations were originally derived from data averaged over long time periods (1 hour or more), it is of interest to examine how well similarity works over shorter time periods. In Fig. 5, the solid curves show the temperatures measured at three different heights as functions of time. The responses have been smoothed using a 50 second averaging time. In Fig. 6, the measured wind speeds, at two heights, are shown. Predictions for the temperature T_x and the wind speed u_x can be computed using the same approach discussed last page. The predicted profiles obtained applying the similarity equations are shown in both Figs. 5 and 6 as the dashed curves. These calculated refractive profiles are in reasonable agreement with the measured profiles over the whole time record. Similarity, for this data set, works fairly well even with relatively short averaging times. The dot-dashed curves in Figs. 5 and 6 have been calculated assuming logarithmic variations of temperature and wind speed; they are not in as good agreement with the measured data.

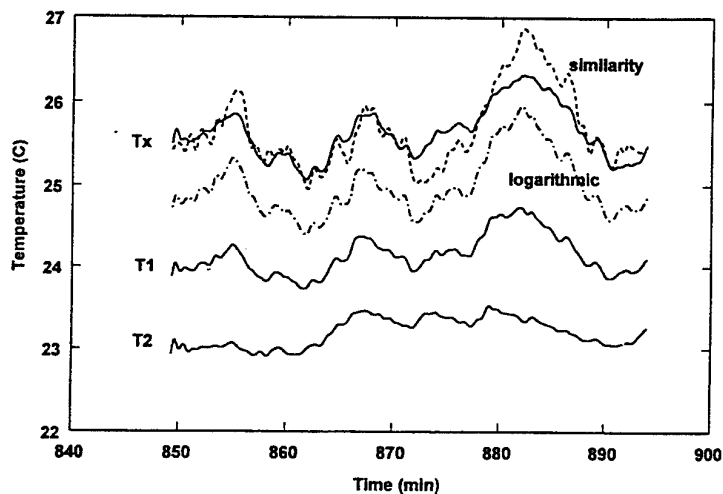


Figure 5. Measured temperatures at heights of 8.7 m (T_2), 2 m (T_1) and 0.5 m (T_x), from data record METLOG.119 obtained 21 June 1995. This same data record was used for Fig. 4.

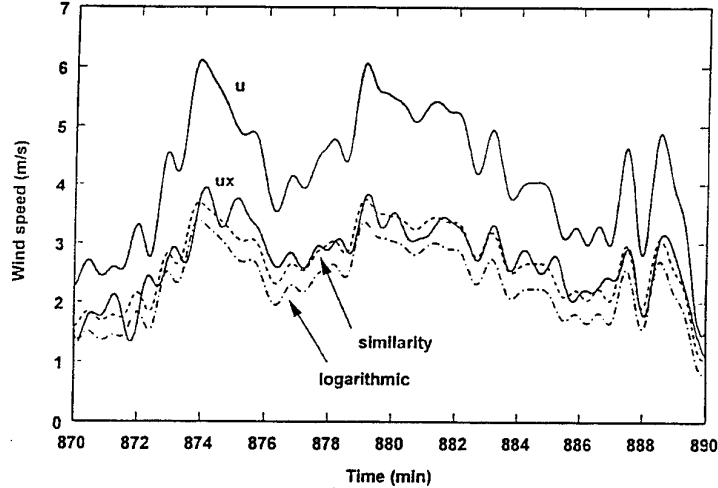


Figure 6. Measured wind speeds at heights of 10 m (u) and 0.3 m (u_x), from data record METLOG.119.

The importance of using the correct sound speed profile can be assessed by inputting the various profiles into a Fast-PE calculation⁵⁻⁷. Figure 7 shows the predicted sound pressure levels (relative to free field) obtained as a function of range for a 500 Hz tone; sound speed profiles obtained from similarity (solid curve) and a logarithmic assumption (dashed curve) have been used. A Gaussian spectrum for turbulence ($\langle u^2 \rangle = 2 \times 10^{-6}$, $L=1.1$ m) has been assumed. For these calculations, the sound source is 0.3 m above the ground and the receiver is on the ground. For ranges greater than 200 m, there is a significant difference between the two predictions, about 5 dB.

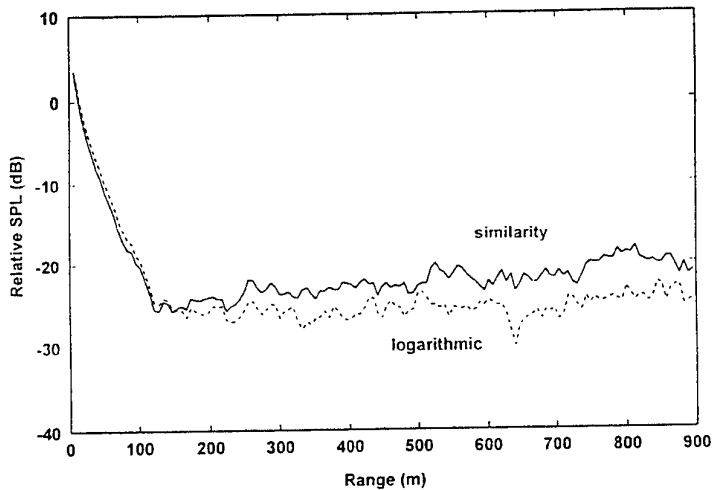


Figure 7. Predicted sound field for 500 Hz acoustical signals propagating in the similarity-based refractive profile (solid curve) and the logarithmic profile (dashed curve). A Gaussian spectrum of turbulence has been assumed.

TURBULENCE SPECTRA

The spatial variations in wind speed and temperature are responsible for scattering into the acoustic shadow region. We assess the variations through examination of the temporal fluctuations at fixed sensor positions (a one-to-one correspondence between temporal and spatial fluctuations is often assumed⁸). For example, the time histories at two anemometer positions, one 10 m above the ground, the other, 0.3 m, are shown in Fig. 8. Both long term and short term fluctuations are evident.

A quantitative estimate of the relative contributions of different frequency components is given by the power spectrum of the time series. In Fig. 9, the power spectra corresponding to the two sets of data in Fig. 8 are plotted together. The two spectra are in close agreement over most of the wind turbulence frequencies. The differences between the two curves occur at frequencies below 0.02 Hz, corresponding to long-term fluctuations (more than 50 seconds). The similarity of spectra measured at different heights was noted in all other data sets. The sonic anemometer data (1 November 1995) shown in Fig. 10 provides another example. For these measurements the same anemometer was used, first at the 10 m height, then immediately after at the 1.2 m height. Again, significant differences arise only at turbulence frequencies below 0.02 Hz.

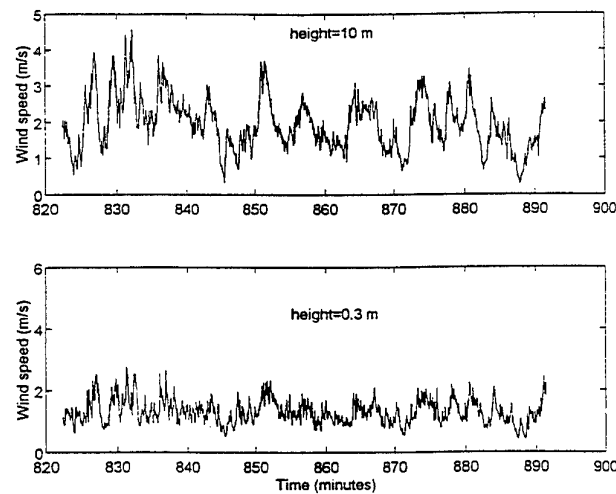


Figure 8. Three cup anemometer data obtained 27 July 1995 (METLOG.139).

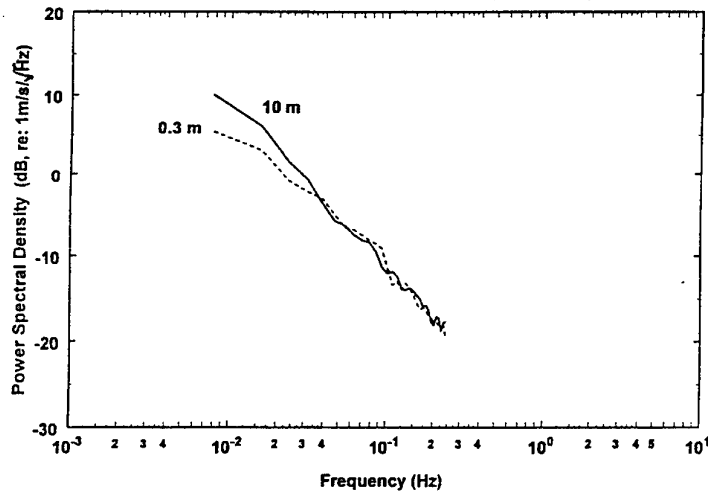


Figure 9. Wind turbulence spectra corresponding to the time series in Fig. 8.

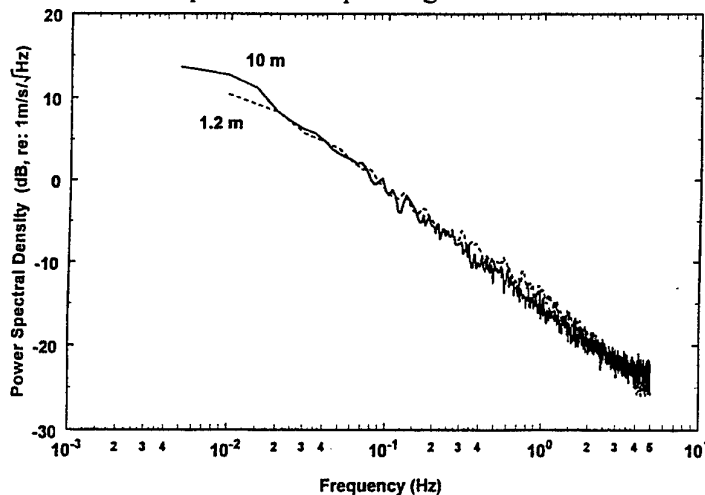


Figure 10. Wind turbulence spectra obtained at two heights using a sonic anemometer.

The important turbulence frequencies for scattering into acoustic shadows can be estimated using a Bragg scattering criterion⁶. For acoustic frequencies of 50 Hz and higher, the important turbulence frequencies are found to be greater than 0.03 Hz. Hence, we may assume that the wind spectra obtained are effectively insensitive to the height at which measurements are taken, at least over the 10 m range in heights available with our tower.

To assess the reliability of the spectral estimates, we show in Figure 11 the wind turbulence spectra measured using three different instruments. The three cup anemometer data were recorded every 2 seconds so that the maximum (Nyquist) frequency is 0.25 Hz. Sonic anemometer data give spectra up to 5 Hz. The hot wire anemometer data give spectra up to 100 Hz or more. It is seen in this figure that the three instruments agree well over the frequency ranges for which there is overlap.

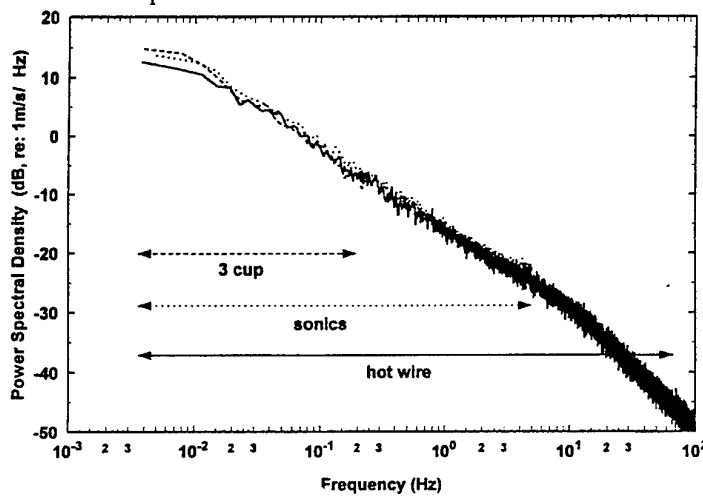


Figure 11. Wind turbulence spectrum obtained 1 November 1995 using three different anemometers.

In sound field calculations, an appropriate spectrum needs to be assumed if predictions are to be accurate. A wind turbulence spectrum measured during near-neutral conditions is shown in Fig. 12 by the solid curve. This spectrum is compared to several theoretical forms, shown as dashed curves. The Kolmogorov spectrum is characterized by a power spectral density ψ (power per unit frequency) that varies with turbulence frequency f as

$$\psi \propto f^{-5/3} \quad (9)$$

The dashed line labelled "Kolmogorov" on Fig. 12 has been matched to the data at high frequencies. The Gaussian spectrum has been widely used in the past because of its ease of implementation. The power spectrum for the Gaussian spectrum takes the form

$$\psi \propto e^{-\pi^2 f^2 \tau^2}, \quad (10)$$

where τ is the correlation length ($L=1.1$ m) divided by the mean wind speed (2 m/s). A curve with

this form has been matched to the data so as to give the same total power. Although this spectrum clearly does not follow the data, it is of interest that in a key region for scattering, between 0.03 Hz and 1 Hz say, it is off by no more than 10 dB. Juvé *et al.*⁹ have shown that quite different qualitative results are obtained if a Von Karmen spectrum is assumed. Højstrup¹⁰ has analyzed data reported by Kaimal *et al.*¹¹ and developed a model that accounts for both buoyancy-produced and shear-produced inputs. From his model spectra (his Fig. 11) for neutral conditions, we obtain the prediction of wind turbulence spectrum labelled "Højstrup" on Fig. 12. It has been scaled vertically to match the high frequency data. This spectrum seems to provide a better match to the data than either of the other estimates.

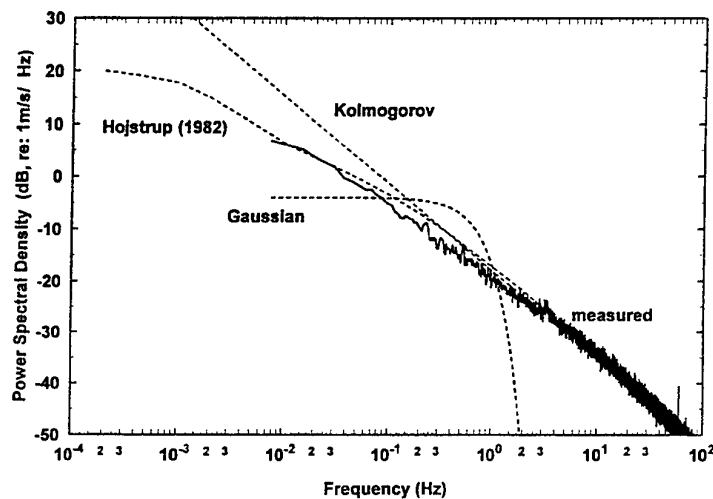


Figure 12. Comparison between measured wind turbulence spectrum (11 September 1995) and three theoretical forms.

CONCLUSION

Both mean sound speed profiles and turbulence spectra need to be specified before accurate predictions of sound fields can be expected.

Refractive profiles in the lower part of the planetary boundary layer can be estimated from point measurements at just a few heights. An appropriate theoretical form is necessary, though. For measurement periods with well-developed thermal lapses, similarity theory has been found to work quite well, predicting both temperature and wind speed profiles. Using logarithmic functions to describe the temperature and wind profiles does not work as well, leading to differences in typical sound field calculations of 5 dB. Linear functions to describe the profiles do not match measured profiles (although an "effective" linear profile can be designed to give acoustical predictions¹²).

Measured wind turbulence spectra show good agreement with either the Kolmogorov spectrum or the Højstrup spectrum over a wide frequency range. The measured spectra also illustrate the limitations of a Gaussian approximation. The height of anemometer has been found not to be critical over the 0.3 m to 10 m range.

REFERENCES

- ¹ F.M. Wiener and D.N. Kiest, "Experimental study of the propagation of sound over ground," *J. Acoust. Soc. Am.* **31**, 724-733 (1959).
- ² W.P. Elliott, "The growth of the atmospheric internal boundary layer", *Trans. Amer. Geophys. Union* **39**, 1048-1054 (1958).
- ³ H.A. Panofsky and J.A. Dutton, *Atmospheric Turbulence. Models and Methods for Engineering Application*, Wiley-Interscience (1984).
- ⁴ A. L'Espérance, J. Nicolas, D.K. Wilson, D.W. Thomson, Y. Gabillet and G. Daigle, "Sound propagation in the atmospheric surface layer: Comparison of experiment with FFP predictions," *Applied Acoustics* **40**, 325-346 (1993).
- ⁵ X. Di and K.E. Gilbert, "A phase screen approach to sound propagation through small-scale turbulence", *J. Acoust. Soc. Am.* **92**, 2405 (A) (1992).
- ⁶ M.R. Stinson, G.A. Daigle and D.I. Havelock, "Simulation of scattering by turbulence into a shadow region using the GF-PE method", *Proc. 6th Int. Symp. on Long Range Sound Propagation*, Ottawa, Canada (1994).
- ⁷ D.I. Havelock, X. Di, G.A. Daigle and M.R. Stinson, "Spatial coherence of a sound field in a refractive shadow: Comparison of simulation and experiment", *J. Acoust. Soc. Am.* **98**, 2289-2302 (1995).
- ⁸ G.I. Taylor, "The spectrum of turbulence", *Proc. R. Soc. London Ser. A* **164**, 476-490 (1938).
- ⁹ D. Juvé, Ph. Blanc-Benon and P. Chevret, "Sound propagation through a turbulent atmosphere: Influence of the turbulence model", *Proc. 6th Int. Symp. on Long Range Sound Propagation*, Ottawa, Canada (1994).
- ¹⁰ J. Højstrup, "Velocity spectra in the unstable planetary boundary layer", *Journal of Atmospheric Sciences* **39**, 2239-2248 (1982).
- ¹¹ J.C. Kaimal, J.C. Wyngaard, D.A. Haugen, O.R. Coté, Y. Izumi, S.J. Caughey and C.J. Readings, "Turbulence structure in the convective boundary layer", *J. Atmos. Sci.* **33**, 2152-2169 (1976).
- ¹² A. L'Espérance, G.A. Daigle and Y. Gabillet, "Estimation of linear sound speed gradients associated to general meteorological conditions", *Proc. 6th Int. Symp. on Long Range Sound Propagation*, Ottawa, Canada (1994).

Temporal Coherence of a Soundfield in the Turbulent Atmosphere Near the Ground

Marta Galindo

National Research Council, Ottawa Canada

Technical University of Denmark, Lyngby Denmark

David I. Havelock

National Research Council, Ottawa Canada

ABSTRACT

A soundfield propagating through the atmosphere changes with time due to the dynamics of the inhomogeneous medium. The coherence time, defined as the time lag beyond which the autocorrelation is less than $1/e$, is a time scale for dynamics of the medium as well as a design criterion for coherent processing of received signals. Example coherence data are presented and their characteristic interpreted. The experimental data consist of continuous tone signals, between 400 Hz and 1000 Hz, received simultaneously over 5 minute intervals at ranges up to 700 m. The data are processed to estimate the temporal coherence for individual tones at various ranges. The source and the receivers were positioned near the ground. Both upward and downward refracting conditions are considered. The characteristics of the data observed during the different conditions are related to simple models of the corresponding propagation mechanisms. Good agreement is found between the theory and measurements.

INTRODUCTION

Theoretical predictions of the statistical characteristics of a sound field in the turbulent atmosphere near the ground, as can be found in [Tatarskii 1971, Lee and Harp 1969] for example, have evolved from the analysis of electromagnetic propagation in the atmosphere and have had limited experimental verification. Many of the experiments in support of the propagation theories were conducted at frequencies well beyond 1 kHz, which are primarily of interest for short propagation ranges. Measurements to support noise propagation codes in the lower audio ranges have been made with an emphasis on the determination of sound pressure levels. Other statistics have been measured outdoors, as reported by [Wilken 1986, Daigle *et al.* 1986, Bass *et al.* 1991, Noble 1992, Havelock *et al.* 1995, Havelock 1996] for example, and examined with model experiments and simulations, as reported in [Blanc-Benon *et al.* 1986, Karweit *et al.* 1991] for example, but a detailed investigation of temporal coherence has

not been previously reported. Recent advances in propagation codes allow the prediction of complex soundfields in "realistic" turbulent atmospheres in the presence of complex ground impedance and refractive shadows. The development of these codes highlights the need for further experimental measurement of soundfields to provide (i) improved data quality, (ii) examination of statistical quantities other than sound pressure levels, and (iii) inter-comparison of independent measurement results.

A series of measurements and analysis have been conducted at a small airport near Ottawa [Havelock *et al.* 1995, Havelock 1996] to examine the spatial, frequency and temporal coherence of sound propagating near the ground, particularly during upward refraction conditions, in the frequency range of 100 Hz to 1000 Hz and at propagation distances up to 700 m. Example results for temporal coherence are reported here and are compared to theory.

1.0 EXPERIMENT SETUP AND SIGNAL PROCESSING

The experiments were conducted on an unused runway surface at a private glider airport near Ottawa. The runway surface is porous asphalt which is broken in places, with some plants protuding. The runway is approximately 700 m long and 30 m wide, with surrounding cultivated fields and trees in the distance.

The acoustic source consisted of four speakers placed on the ground at one end of the runway in a line transverse to the long axis of the runway. The center of the speakers was about 30 cm above the ground and on the runway axis. The test signal consisted of six simultaneous tones with frequencies 400, 500, 600, 700, 820, and 940 Hz.

There were 32 microphones in the receiving array. Each was fitted with a 9 cm wind-screen and placed on the ground. The array was in a "T" formation. The nominal spacing between microphones was 25 m along the longitudinal axis, which extended from 50 m in front of the source to a range of 675 m. The short, transverse axis of the array consisted of 5 unequally spaced microphones, spanning 12 m, at a range of 675 m.

Signals from the microphones were amplified and transmitted by cable to an equipment trailer where they were filtered and then digitized at 8000 samples/s with 12 bits resolution. The signal to noise ratio at the array was generally much better than 10 dB at all ranges and frequencies. The data was recorded in 15 minute segments but only about 5 minutes of each segment was used for analysis.

Two sets of data are considered, one being representative of upwind conditions and the other being representative of downwind conditions. For both cases, the mean wind speed was 4 m/s at a height of about 10 m, at an angle about 30° off of the runway. The mean temperature was about 20 °C with a weak negative gradient (less than 0.5 degrees between 2 m and 10 m heights). In both cases, it is assumed that turbulence is dominated by wind velocity fluctuations. The meteorological data was obtained from an instrumented 10 m tower similar to that described in [Stinson and Daigle., 1996].

The recorded signals were filtered to select each of the composite signal tones. The narrowband filters had a bandwidth of 100 Hz and were followed by a Hilbert transform, bandshifting, and decimation to obtain a complex signal with a reduced sampling rate of 400

Hz (and correspondingly reduced data volume). The complex autocorrelation function $C(\tau)$ was computed using a single-block 131072 point fast Fourier transform,

$$\begin{aligned} C(\tau) &= \langle x^*(t+\tau)x(t) \rangle, \\ &= \text{IFFT}\left\{\left[\text{FFT}\{x(t)\}\right]^2\right\}(\tau). \end{aligned} \quad (1)$$

The magnitude of the autocorrelation function was used to define the coherence time t_0 of the received signal, such that

$$|C(t_0)| = e^{-1}. \quad (2)$$

The coherence times, computed at all available ranges and frequencies, were then compared to the coherence times predicted by theory.

2.0 THEORY

2.1 Upwind Model

At ranges beyond a few hundred metres, upward refraction results in a strong acoustic shadow region near the ground. Within the shadow region, the received energy is predominantly due to scattering from turbulence in the ensonified region above the shadow. Following the development for scattering in a turbulent atmosphere developed in [Tatarskii, 1971; §29] we find that the power spectrum of the (envelope of the) scattered sound field has a Gaussian form,

$$|X(\omega)|^2 \propto \exp\left\{\frac{-(\omega + \vec{K} \cdot \vec{V}_0)^2}{2K^2\sigma^2/3}\right\} \quad (3)$$

where \vec{V}_0 is the mean wind velocity, σ_v is the standard deviation of the wind speed, and \vec{K} is the scattering vector defined as the difference between the scattered and the incident signal wavevectors.

A simple interpretation of this Gaussian form is as follows. Consider the turbulence to be locally frozen so that a volume of turbulent air moves with a random velocity \vec{V} and mean velocity \vec{V}_0 . Scattering from the frozen turbulence is dominated by a small region in the wavenumber space of the turbulence, and so is well approximated by a single horizontal grating. This grating satisfies the Bragg scattering condition and has a vertical spatial wavevector \vec{K} . Only the vertical component of \vec{V} contributes to variations in the scattered field, with a vertical component V_v resulting in a Doppler shift of KV_v ; hence, the variance in the received spectrum is just $K^2\sigma_v^2$, where σ_v^2 is the variance of V_v . Assuming that \vec{V} is isotropic, so that its variance is $\sigma^2 = 3\sigma_v^2$, we obtain the spectral variance in Eq. (3) above. It has been assumed that the distance to the scattering volume is sufficiently large that plane wave scattering is a reasonable approximation. Furthermore, it is assumed that the velocity variations within the frozen turbule provide only a small contribution to the variance of the wind speed. Within the limitations of these assumptions, this moving grating interpretation provides a simple working model.

The mean wind velocity \bar{V}_0 causes a Doppler shift which displaces the peak of the power spectrum by $\bar{K} \cdot \bar{V}_0$. In our case, this shift should be zero since the wind velocity is horizontal and the scattering vector is vertical. The variance of the Gaussian form of the power spectrum, which is the bandwidth about the center frequency, is equal to the reciprocal of the variance of the Gaussian form of the corresponding autocorrelation function. Consequently, the coherence time t_0 can be estimated from $1/\omega_0$, where $|X(\omega_0)|^2 = 1/e$, using

$$t_0 = \sqrt{6}/2k_0\sigma \sin\theta \quad (4)$$

where σ is the standard deviation of the wind speed fluctuations and the Bragg condition is $K = 2k_0 \sin(\theta)$ with k_0 being the signal wavenumber and θ half the scattering angle.

The scattering volume is considered to be near the shadow boundary mid-way between the source and receiver [Gilbert, 1990]. In this case, the scattering angle is twice the angle of upward refraction. The angle of refraction changes only slightly with range and so this model predicts that the change in coherence time with range will be small. It also predicts an inverse relationship between the coherence time and the wavenumber of the source signal.

Using a similarity relationship for the vertical profile of the speed of sound and a ray tracing model, it is found that $\sin(\theta) \approx 0.15$ for the upwind dataset. With t_0 experimentally determined, this leaves only σ undetermined. Although σ is not known, it is expected to be on the order of $V_0/3$, where V_0 is the mean wind speed at the scattering height. Accordingly, we can express σ as a function of the other variables and examine whether the results based on measurements follow the expected relationship

$$\sigma = \sqrt{6}/2k_0 t_0 \sin\theta. \quad (5)$$

2.2 Downwind Model

For downwind propagation we treat the turbulence as a frozen structure moving with the mean velocity \bar{V}_0 of the wind. As the turbulence traverses the propagation path, the received signal fluctuates. The received signal at a single point \bar{x} at times, t_1 and t_2 , are essentially the same as the signal received simultaneously at the two points $x_1 = \bar{x}$ and $x_2 = \bar{x} - (t_1 - t_2)\bar{V}_0$ at time t_1 . This simple model neglects the downward refraction of sound and treats the sound propagation as though it were direct line-of-sight propagation. The effects of multiple path interference and ground surface irregularities are not accounted for.

Following the development in [Tatarskii, §47, §57], the variance in the phase difference between the received signals at times separated by τ is

$$\begin{aligned} \sigma_s^2(\tau) &= D_s(\tau V_\perp) \\ &= 1.5 C_n^2 k_0^2 R(\tau V_\perp)^{5/3} \end{aligned} \quad (6)$$

where C_n^2 is the turbulence structure function (which is of the order of 10^{-6}), R is the propagation range, and V_\perp is the component of the wind velocity across the propagation path (which is about 2 m/s).

To a good approximation, the phase fluctuations dominate over amplitude fluctuations in determining the autocorrelation statistics of the received sound field. Furthermore, the phase fluctuations follow a Gaussian distribution, hence it can be shown that the coherence time t_0 for downward refraction with this model is

$$t_0 = (0.75 C_n^2 k_0^2 R)^{-3/5} / V_{\perp}. \quad (7)$$

As with the upward refraction model, we can express the transverse wind speed in terms of the other parameters and examine how the estimates based on the measured values compare with an estimate based on meteorological measurements.

3.0 MEASUREMENTS AND OBSERVATIONS

3.1 Typical Autocorrelation Measurements

Examples of the autocorrelation function for a 500 Hz signal received at various ranges are shown in Fig. 1 for the upwind case and in Fig. 2 for the downwind case. In the upwind case, at short ranges, the received signal is not dominated by scattered acoustic energy and contains considerable diffracted energy. This situation has not been considered in the theory here and is not examined further. At longer ranges, for upwind propagation, the autocorrelation function drops off rapidly with lag time, giving correlation times less than 0.5 seconds. In contrast, the correlation curves for the downwind case show correlation times which exceed 10 seconds.

This distinction is further illustrated in Fig. 3 where the coherence times for upward and downward refraction of a 500 Hz tone are compared at all ranges. (There is a prominent bump in the downward refraction data of Fig. 3 at about 200 m; the reason for this deviation has not been determined.)

3.2 Upwind

A plot of the coherence time for all the signal tones as a function of range for upwind conditions is shown in Fig. 4. Notice that the coherence time is essentially independent of range, beyond a few hundred metres, for all of the signal frequencies. Furthermore, the coherence time decreases with increasing frequency, in qualitative agreement with Eq.(4).

Estimates of σ from the measured coherence times, using $\sin(\theta) = 0.15$, are shown in Fig. 5. Except for a few deviant values (occurring in the higher frequency signal) the results are quite constant, predicting an averaged value of 2.5-3.0 for σ_v . This suggests a mean wind speed of 7-9 m/s, which is slightly higher than might be expected at the height where scattering takes place (about 50 m).

A doppler shift $\vec{K} \cdot \vec{V}_0$ is predicted by Eq. (3). Inspection of the power spectra of the received signals (not illustrated) does not reveal a shift in the spectral peak, suggesting that the scattering vector and the mean wind velocity are orthogonal.

3.3 Downwind

The coherence times for all of the signal frequencies for the downwind case are plotted as a function of range in Fig. 6. As was the case for upwind propagation, the coherence time decreases with increasing frequency, however a distinct range dependence can also be seen. (The anomalous bump in the vicinity of 200 m range is visible at most frequencies and the peak occurs at slightly shorter ranges for the higher frequencies.)

As was done for the upwind case, estimates of the wind speed, in this case the transverse component V_{\perp} of the wind velocity, are plotted in Fig. 7. The estimates are based on the measured values of t_0 and a nominal value of 10^{-6} for C_n^2 . The estimates for V_{\perp} vary between 0.5 m/s and 2.5 m/s, and are generally increasing with range and frequency.

These estimates are quantitatively reasonable, as they are close to the expected value of $V_{\perp} = 2.0$ m/s, particularly in consideration of the approximate value used for C_n^2 . The consistent trend in the data, however, suggest that the formulated dependance on range and frequency may not accurate. There are a number of possible contributing factors for this discrepancy. The importance of multipath interference and ground surface roughness would both be expected to cause an increase in the estimate of V_{\perp} with increasing frequency and with range, consistent with the observations.

SUMMARY

The autocorrelation function of the soundfield near the ground has been examined at ranges from 75 m to 675 m, at frequencies from 400 Hz to 940 Hz, and for upwind and downwind conditions. The observed coherence times have been compared to theoretical predictions through estimates of wind speed parameters. Agreement is quantitatively good in both cases but a distinct trend is observed in the downwind case. The observed trend may be due to multipath interference or ground surface roughness which are not accounted for in the downwind propagation model.

The specific characteristics which are predicted and observed are itemized below.

- The coherence time is dramatically longer for downwind propagation than it is within the refractive shadow during upwind propagation. Coherence times exceed 10 s for downwind propagation and are shorter than 0.5 s within the refractive shadow region.
- For upwind propagation the coherence time is governed by Eq. (4) to a very good approximation. This relationship features a k_0^{-1} dependence and an independence of range R . The relationship involves σ (the wind speed standard deviation) and θ (half the scattering angle, or the upward refraction angle).
- For downwind propagation the coherence time is governed by Eq. (7), although a residual trend exists. The relationship features a $k_0^{-6/5}$ and $R^{-3/5}$ dependence, which are not inconsistent with measurements but the exact exponent values are not verified experimentally. The relationship relies on the environmental parameters V_{\perp} (transverse component of the wind velocity) and C_n (turbulence structure function constant).

ACKNOWLEDGEMENTS

The field work for this and related studies was achieve through the contributed efforts of (alphabetically) Nicole Brien, Mark Bruehner, Gilles A. Daigle, Rene St. Denis, Xiao Di, Marta Galindo, Kenneth E. Gilbert, Scott D. Hansen, David I. Havelock, John Quaroni, Michael R. Stinson. The meteorological data was prepared by Michael R. Stinson.

REFERENCES

- H. E. Bass, L. N. Bolen, R. Raspert, W. McBride, and J. Noble, "Acoustic propagation through a turbulent atmosphere: Experimental characterization," *J. Acoust. Soc. Am.* **90**, pp. 3307-3313, 1991.
- P. Blanc-Benon, S. Chaize, and D. Juvé, "Coherence aspects of acoustic wave transmision through a medium with temperature fluctuation," *Aero- and hydro-acoustics IUTAM Symp. LYON*, (Springer-Verlag, Berlin), pp.217-226, 1986.
- G.A. Daigle, T. F. W. Embleton, and J. E. Piercy, "Propagation of sound in the presence of gradients and turbulence near the ground," *J. Acoust. Soc. Am.*, **79**(3), pp. 613-627, 1986.
- K.E. Gilbert, X. Di, and L.Wang, "Distored-wave Born approximation calculations for turbulence scattering in an upward-refracting atmosphere," proc. 4th International Symp. on Long Range Sound Propagation, Langley Research Center, Hampton VA, 16-17 May, 1990.
- D. I. Havelock, X. Di, G. A. Daigle, and M. R. Stinson, "Spatial coherence of a sound field in a refractive shadow: Comparison of simulation and experiment," *J. Acoust. Soc. Am.*, **98**(4), pp 2289-2302, 1995.
- D. I. Havelock, "Measurements of the two-frequency mutual coherence function for sound propagation through a turbulent atmosphere," submitted to *J. Acoust. Soc. Am.*, 1996
- M. Karweit, Ph. Blanc-Benon, D. Juvé, and G. Comte-Bellot, "Simulation of the propagation of an acoustic wave through a turbulent velocity field: A study of phase variance," *J. Acoust. Soc. Am.*, **89**(1), pp. 52-62, 1991.
- R. W. Lee and J. C. Harp, "Weak scattering in random media, with applications to remote probing," *Proc. IEEE*, Vol. 57, No. 4, pp. 375-406, April 1969
- J. M. Noble, "The effects of large-scale atmospheric inhomogeneities on acoustic propagation," *J. Acoust. Soc. Am.* **92**, pp.1040-1046, 1992.
- M. R. Stinson and G. A. Daigle, "Meteorological measurements for use in sound propagation calculations," proc. of the 7th International Symp. on Long Range Sound Propagation, Lyon France, 24-26 July, 1996.
- V. I. Tatarskii, *The effects of the Turbulent Atmosphere on Wave Propagation* (Keter, Jerusalem, 1971).
- W. Wilken, "Experimental study of the influence of varying atmospheric conditions on sound propagation close to the ground," *Acustica*, Vol. 62, pp.55-65, 1986.

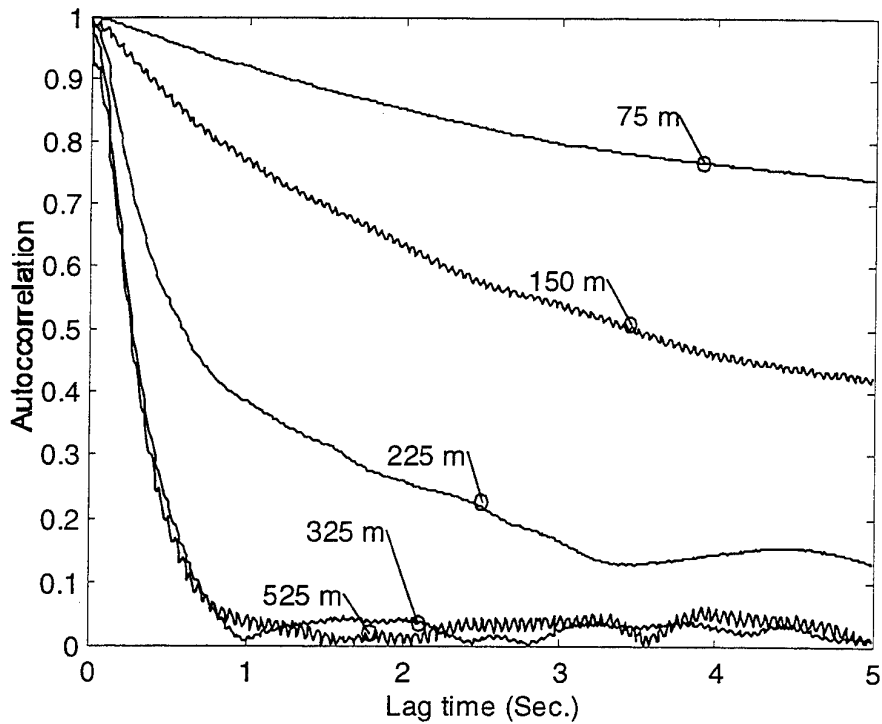


Figure 1 Autocorrelation of a 500 Hz signal at various ranges during upwind propagation.

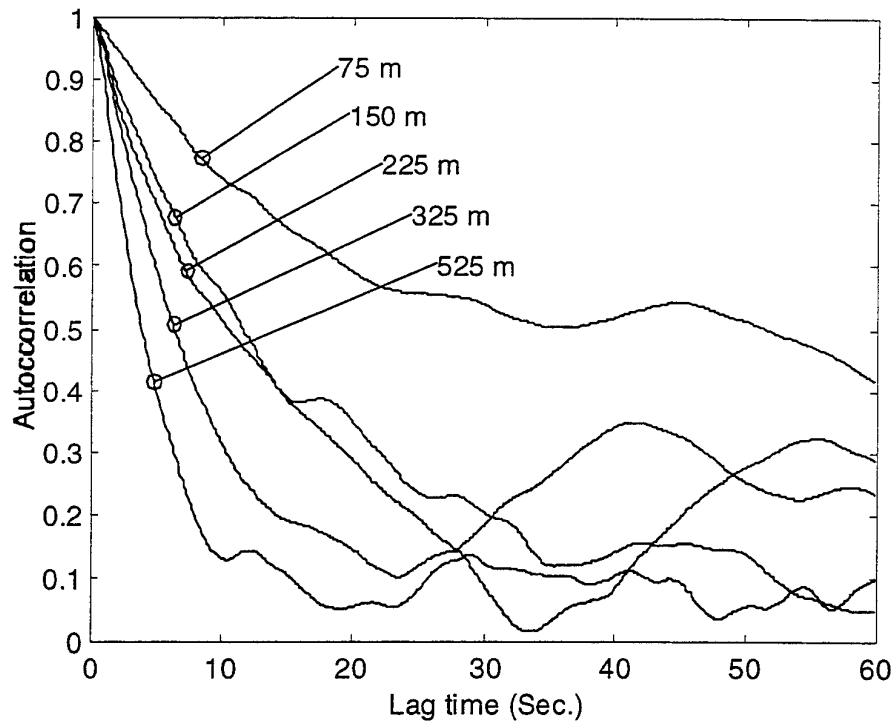


Figure 2 Autocorrelation for a 500 Hz signal at various ranges during downwind propagation.

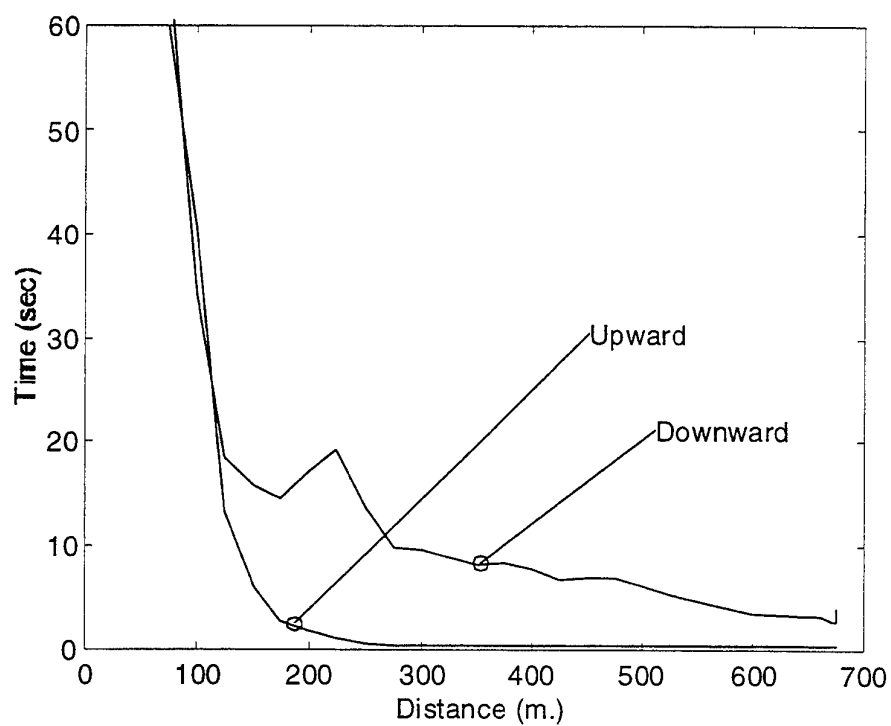


Figure 3 Coherence times for a 500 Hz signal, as a function of range, compared for upward and downward refraction conditions.

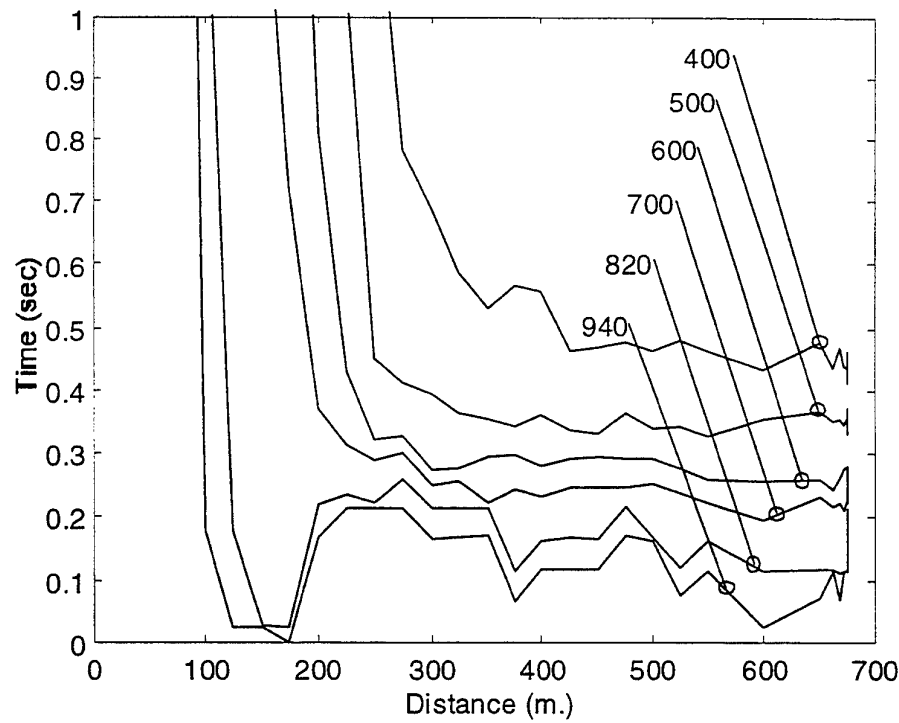


Figure 4 Coherence times as a function of propagation distance for various test frequencies during upwind propagation.

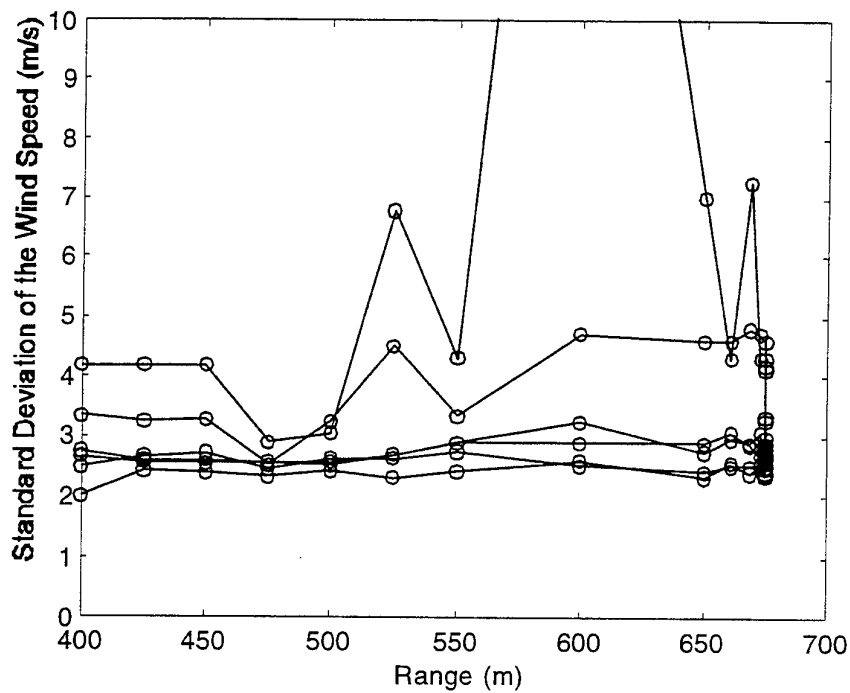


Figure 5 Estimates for the wind speed standard deviation based on the coherence time data for all frequencies.

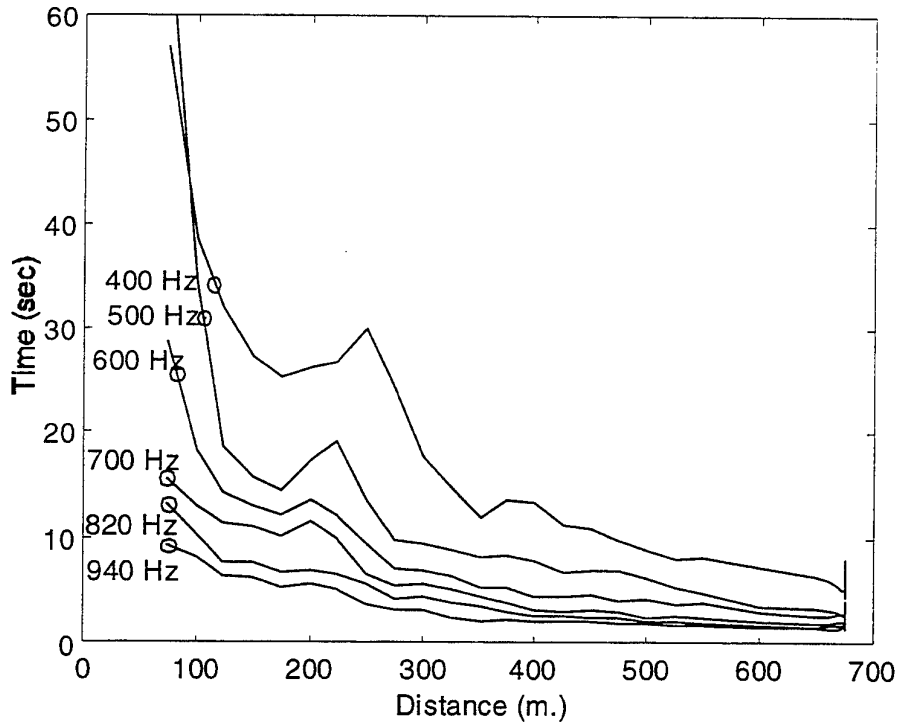


Figure 6 Coherence time as a function of distance for various frequencies during downwind propagation.

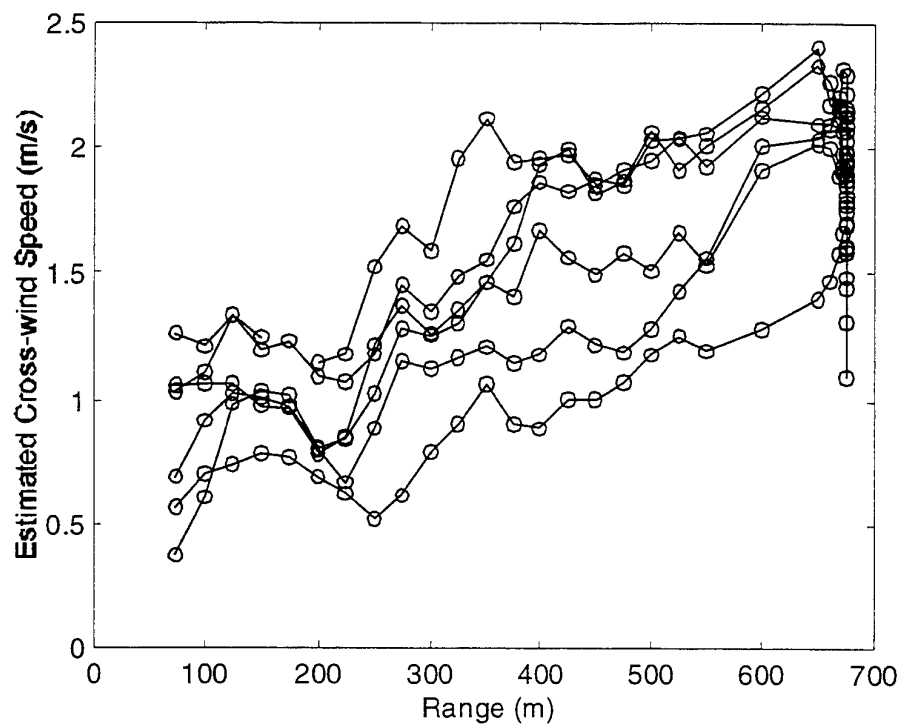


Figure 7 Estimated cross-wind speed based on coherence time data.

COMPARISON OF COHERENT SUMMATION TO INCOHERENT SUMMATION OF ACOUSTIC SIGNALS SCATTERED FROM TURBULENCE

by

Harry J. Auvermann
Army Research Laboratory, Battlefield Environment Directorate
White Sands Missile Range, New Mexico

ABSTRACT

The Turbule Ensemble Model (TEM) is employed to represent a turbulent atmospheric region from which the acoustic scattering is determined for an experiment sized geometry. In the first step, the Effective Scattering Volume (ESV) is calculated for the turbulence which is represented as an isotropic homogeneous continuous size distribution with an upper bound. The scattering pattern of individual turbules limits the volume of the region from which scattered signals must be accumulated and so serves to define the ESV. ESV is a function of turbule size. The ESV is further reduced by a wind induced shadow zone boundary here represented by a limit ray surface. The ESV so calculated is used in the second step to define an extended volume from which turbules are advected into the ESV by the wind assuming Taylor's Frozen Turbulence hypothesis holds for the duration of the experiment. In step three, the continuous distribution is discarded for a discrete distribution of isotropic turbules. This discrete distribution is implemented by placement of turbules at random locations within the extended volume for each size class. Incoherent summation of the signal scattered from the ESV using the scattering cross section of each turbule is followed as the ensemble passes through. Step four proceeds by populating the extended volume with randomly oriented individual turbules. A coherent sum of the scattered signal is followed using the scattering amplitude of the individual turbules vice the scattering cross section employed in the previous step. The results from steps three and four for representative turbule sizes will be shown.

1. INTRODUCTION

In a paper presented at the previous conference¹, the Turbule Ensemble Model (TEM) of turbulence was defined as well as the term turbule. A number of characteristics of turbules were derived including the scattering amplitude and the scattering cross section. Additionally, scaling parameters for the size classes in TEM were developed that insure the spectrum matches the Kolmogorov spectrum. In this paper TEM is used to calculate turbulence scattering for an experiment sized geometry. The calculation scenario includes a uniform gradient wind induced shadow zone above flat ground modeled as a limit ray surface. Ground reflections have not been included in the calculation and only velocity turbules are considered.

The purpose of the calculation is to show the difference between results obtained with an incoherent algorithm and results obtained with a coherent algorithm. The first step in the calculation is to determine the scattering volume for the chosen scenario. This step is described in section 3 where the concept of the Effective Scattering Volume (ESV) is defined

and ESV dimensions are calculated for a representative turbule size class. Step 2 is described in section 4, where ESV dimensions from step 2 are used to define an extended volume. The properties of the size classes including the number concentrations are defined, and the method to be used populate the extended volumes is explained. Step 3 involves an incoherent summation of the power scattered from each turbule. The scattered power is calculated from an orientation averaged cross section, and so the result represents incoherent scattering from an isotropic ensemble. The scattered power at the detector location is calculated as a function of time while the ensemble in the extended volume advects through the ESV assuming that Taylor's Frozen Turbulence hypothesis holds for the time of the experiment. Step 3 is covered in section 5. In step 4, the orientation averaged cross section of step 3 is replaced by the scattering amplitude for randomly oriented turbules and the summation carried out taking account of the phase of the signal from each turbule. This step is carried out in section 6. The results in section 6 show a coherent calculation of the scattered signal as a function of time which can be compared to the incoherent calculation of section 5. Section 7 contains a summary of the results and concluding remarks. Section 2 contains definitions of most of the symbols used in the equations. Remaining symbols are defined where they are first used.

2. NOTATION

a	= turbule characteristic size, m
a_l	= size of largest turbule = 10 m
c_∞	= asymptotic acoustic wave speed = $344 \text{ m}\cdot\text{s}^{-1}$
E	= exitance ($\text{watt}\cdot\text{m}^{-2}$)
E_s	= isotropic source exitance at a distance of R_s
E_p	= source signal at point $P = E_s (R_s/R_{sp})^2$
$E_D^{v(1)}(a, \psi)$	= scattered exitance at detector at scattering angle ψ for a single velocity turbule of size $a = E_p \sigma_v(a, \psi) R_{pd}^{-2}$
E_D^v	= exitance at detector after integration over a , y , and z
$e_D^v(\Xi_n, y_m, z_m)$	= signal amplitude at the detector
e_s	= source amplitude at a distance of R_s
$g(0)$	= wind field velocity gradient in the x - z plane = $-0.344 \text{ m}\cdot\text{s}^{-1}/\text{m}$
h_d	= detector height = 1.0 m
h_s	= source height = 1.5 m
$\phi(y, z)$	= angular extent of a ring in the volume integration
\mathbf{k}	= incident wave propagation vector at P , m^{-1}
k	= magnitude of $\mathbf{k} = \omega/c_\infty$
l	= ratio of turbule average spacing to characteristic size = $(N_1 a_l)^{-3}$
λ	= wavelength, m = $c_\infty/f = 0.688$ m
μ	= turbule distribution function size increment parameter
N_1	= largest turbule concentration, m^{-3}
$N_a(a)$	= number concentration distribution function as a function of a
$N_x(\chi)$	= number concentration distribution function as a function of χ $= (\lambda/2\pi) N_a(a)$

r	= radial vector from scatterer to detector
\hat{r}	= radial unit vector from scatterer to detector
R_{SP}	= source-(point P) distance
R_{PD}	= (point P)-detector distance
$\sigma_v(a, \vec{k}, \hat{r})$	= velocity turbule scattering cross section as a function of a , \vec{k} and \hat{r}
$\sigma_v(\chi, \psi_P)$	= velocity turbule scattering cross section as a function of χ and ψ_P
$T(a_\alpha)$	= kinetic energy of turbule of characteristic size a_α
x_d	= detector shadow zone height, m
x_s	= source shadow zone height, m
χ	= size parameter = ka
X_m	= maximum in the size parameter integration
X_n	= minimum in the size parameter integration
X_u	= largest turbule size parameter = 91.325367
v	= characteristic velocity for turbule of size a , $m \cdot s^{-1}$
v_1	= characteristic velocity for largest turbule = $3.44 \text{ m} \cdot \text{s}^{-1}$
v_w	= wind velocity at 10 m height = $3.44 \text{ m} \cdot \text{s}^{-1}$
ψ_P	= scattering angle between \vec{k} and \hat{r} at the point P
Z_{SD}	= source-detector distance = 320 m

3. DETERMINATION OF SCATTERING VOLUME

The equations for determining Effective Scattering Volume (ESV) will be set up relative to the geometry of figure 1. The ESV is defined to be the region of space and the turbule size

CALCULATION GEOMETRY

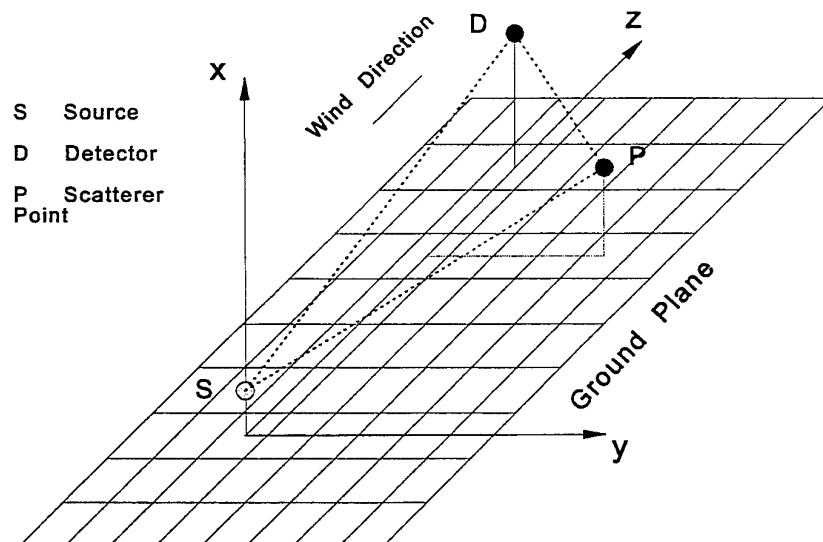


Figure 1. Calculation geometry

range from which significant scattering occurs. . The desire is to define a four-dimensional (three space dimensions and a size dimension) space for which the scattered signal is a prescribed fraction of the signal from all space. To avoid complications associated with very large scattering entities, the upper size limit will be set as if the turbulence was that of a region whose height above the ground was 10 meters. Thus the largest turbule size (a_1 in the notation table) is 10 meters. The source frequency is 500 hz and the average sound speed is $344 \text{ m}\cdot\text{s}^{-1}$ so that the wavelength is 0.688 mIn the figure, the coordinate system origin is on the ground beneath the source S with the z-axis directed towards the detector location D where the accumulated scattered signal will be determined. The direct signal at the point D will be ignored. The x-axis is up and the y-axis is to the right when looking from the source towards the detector. The source height

is h_S , set to 1.0 m, and the detector height is h_D , set to 1.5 m. The point P denotes a location where a turbule center is located. For the ESV calculation, the turbulence will be assumed to be homogeneous and isotropic so that the scattered signal from P will be the same for all locations on a circle centered on the S-D line. A wind field with a decreasing uniform velocity gradient flows in the direction from detector to source. This wind field is assumed to have a velocity of v_w at a height of 10 m so that the gradient g is $-0.344 \text{ m}\cdot\text{s}^{-1}/\text{m}$.

3.1 Detector Signal Equations

The single turbule orientation averaged cross-section is² for the previously defined

$$\sigma_v(\chi, \psi_p) = \left(\frac{\pi}{3} \right) \left(\frac{v \chi^4}{4 k c_\infty} \right)^2 [\sin(\psi_p) \cos(\psi_p)]^2 \exp\{-\chi^2[1 - \cos(\psi_p)]\} \quad (1)$$

velocity distribution. The single turbule scattering exitance at detector is

$$E_D^{v(1)}(\chi, \psi_p) = \left(\frac{\pi E_s}{12} \right) \left(\frac{v R_s \chi^4}{4 R_{sp} R_{pd} k c_\infty} \right)^2 [\sin(2\psi_p)]^2 \exp\{-2[\chi \sin(\psi_p/2)]^2\} \quad (2)$$

The variables (ψ_p , R_{sp} , R_{pd}) are all functions of (x_p y_p , z_p), the position coordinates of the point P and χ is a function of the turbule size a.

To sum over a scattering volume and a size distribution, the number concentration of turbules is the starting point. The following power laws for fractal scaling have been determined¹:

$$\frac{N_\alpha}{N_1} = \left(\frac{a_\alpha}{a_1} \right)^{-3}, \quad \frac{v_\alpha}{v_1} = \left(\frac{a_\alpha}{a_1} \right)^{1/3}, \quad \frac{a_\alpha}{a_{\alpha+1}} = e^{-\mu}, \quad v_\alpha = \Omega_\alpha a_\alpha \quad (3)$$

The meaning of eq. (3) is as follows. The largest turbules, identified by the subscript 1, have

the concentration N_1 . Their characteristic size is a_1 . The largest velocity turbules have characteristic velocities v_1 . Other sized turbules are identified by the index α . Ω_α is the angular velocity of turbules of size class α . The exponents have been chosen so that a homogeneous isotropic ensemble of turbules matches the Kolmogorov spectrum. The relationship between the sizes of adjacent classes is fractal with the parameter μ controlling the relative spacing. There are N_s size classes. The desired quantity is the number concentration in a differential extent da of the a variable. For this, a continuous function must be fashioned for integration whereas eq. (3) has been written for a discrete spectrum. The result¹ is shown in eq. (4).

$$N_a(a_\alpha) = \frac{N_1 a_1^3 e^\mu}{a_\alpha^4 (e^\mu - 1)} \quad N_\chi(\chi_\alpha) = \frac{N_1 \chi_1^3 e^\mu}{\chi_\alpha^4 (e^\mu - 1)} \quad (4)$$

It is now possible to write the size parameter dependence of the scattered exitance for each size of turbules. Multiplying eq. (2) by N_a from eq. (4) and substituting for v_α from eq. (3) yields the exitance per unit volume per unit size parameter for size parameter χ_α (size a_α). Dropping the subscripts P and α , the result is in eq. (5).

$$\frac{d E_D^v(\chi, \psi)}{d \chi} = \left(\frac{\pi N_1 E_S \chi_1^{7/3} e^\mu}{192(e^\mu - 1)} \right) \left(\frac{v_1 R_S}{k c_\infty R_{SP} R_{PD}} \right)^2 \chi^{14/3} [\sin(2\psi)]^2 \exp\{-2[\chi \sin(\psi / 2)]^2\} \quad (5)$$

Equation (6) below derived from eq. (5) gives the specific mathematical form for the total velocity turbule ensemble scattering exitance at the detector.

$$E_D^v = \left(\frac{\pi N_1 E_S \chi_1^{7/3} e^\mu}{96(e^\mu - 1)} \right) \left(\frac{v_1 R_S}{k c_\infty} \right)^2 \int_0^{x_u} d\chi \int_{-\infty}^{+\infty} dz \int_0^{+\infty} dy \int_0^{+\infty} dx \left[\frac{\sin(2\psi)}{R_{SP} R_{PD}} \right]^2 \chi^{14/3} \exp\{-2[\chi \sin(\psi / 2)]^2\} \quad (6)$$

3.2 Shadow Zone Boundary Equations

The equations for the shadow zone boundary surface were developed in an earlier paper³. The sound speed gradient is related to the component of the wind velocity in the launch plane or $g(\beta) = g(0) \cos(\beta)$ where β is the angle a ray makes with the x-z plane. The shadow zone boundary (SZB) is the limit ray circle which contains the source point and is tangent to the ground. For $\beta = 0$, the equation of this circle is given in the following. The last form in eq. (7) is the useful one since the height of the SZB at a variable source distance z_s will

$$(x_s - r_{c0})^2 + (z_s - z_{c0})^2 = r_{c0}^2; \quad r_{c0} = c_\infty / g(0); \quad z_{c0} = (2r_{c0}h_s - h_s^2)^{1/2}$$

$$x_s = \{r_{c0} - [r_{c0}^2 - (z_s - z_{c0})^2]^{1/2}\} \quad (7)$$

later on determine a limit for an integral. The parameter r_{c0} is the circle radius and the parameter z_{c0} is the distance to the ground intersection. For the circle in a plane at an angle β with the x-z plane, in eq. (7) replace $g(0)$ with $g(\beta)$ and (z_s, z_{c0}) by an analogous distances, say $(\rho_\beta, \rho_{c\beta})$. Then, replace $\cos(\beta)$ and $(\rho_\beta, \rho_{c\beta})$ with the appropriate functions of the variable coordinates (y, z) . This is done in the next equation.

$$(x_s - r_{c\beta})^2 + (\rho_\beta - \rho_{c\beta})^2 = r_{c\beta}^2; \quad \rho_\beta = (y^2 + z^2)^{1/2}; \quad \cos(\beta) = z/\rho_\beta$$

$$r_{c\beta} = c_\infty / (g(0)\cos(\beta)); \quad \rho_{c\beta} = (2r_{c\beta}h_s - h_s^2)^{1/2}$$

$$x_s = \{r_{c\beta} - [r_{c\beta}^2 - (\rho_\beta - \rho_{c\beta})^2]^{1/2}\}, \quad z > 0$$

$$= 0, \quad z \leq 0 \quad (8)$$

The last expression for x_s where z is less than or equal to 0 recognizes the fact that propagation in the negative direction (down wind) will not experience a shadow zone. This is unimportant except for algorithm purposes. There is also a SZB associated with the detector. Signal scattered from turbules below the detector SZB will not reach the detector. This boundary will be of the same form except that the z_s coordinate will turn to $-z_d$, and then the z_d will be replaced by $(Z_{SD} - z)$ as shown in the next equation.

$$(x_d - r_{c\alpha})^2 + (\rho_\alpha - \rho_{c\alpha})^2 = r_{c\alpha}^2; \quad \rho_\alpha = [y^2 + (Z_{SD} - z)^2]^{1/2}; \quad \cos(\alpha) = (Z_{SD} - z)/\rho_\alpha$$

$$r_{c\alpha} = c_\infty / (g(0)\cos(\alpha)); \quad \rho_{c\alpha} = (2r_{c\alpha}h_D - h_D^2)^{1/2}$$

$$x_d = \{r_{c\alpha} - [r_{c\alpha}^2 - (\rho_\alpha - \rho_{c\alpha})^2]^{1/2}\}, \quad z < Z_{SD}$$

$$= 0, \quad z \geq Z_{SD} \quad (9)$$

The integral limit mentioned above will be determined for a y-z plane point (y, z) by choice of the larger of x_s or x_d . The larger of x_s or x_d is referred to as SZB or x_{SZ} hereafter.

3.3 Scattering Volume Results

As mentioned previously, the assumption of isotropic homogeneous turbulence permits the replacement of the x integration of eq. (6) with the length of the circular arc. This is reflected in eq. (10) where the differential volume has been changed to the ring

$$E_D^v = \left(\frac{\pi N_1 E_S \chi^{7/3} e^\mu}{96(e^\mu - 1)} \right) \left(\frac{v_i R_S}{k c_\infty} \right)^2 \cos(\gamma) \\ \int_0^{X_u} d\chi \int_{-\infty}^{+\infty} dz \int_0^{+\infty} dy r_r(y, z) \phi(y, z) \left[\frac{\sin(2\psi)}{R_{SP} R_{PD}} \right]^2 \chi^{14/3} \exp\{-2[\chi \sin(\psi/2)]^2\} \quad (10)$$

$r_r(y, z) \phi(y, z) dz dy$ with r_r the radius of the ring and $\phi(y, z)$ the angle between the x-z plane and the SZB intersection. The geometry is such that there is symmetry with respect to the x-z plane so that the y integration only need extend from zero to infinity. The $\cos(\gamma)$ factor accounts for the inclination of the S-D line where $\tan(\gamma) = (h_D - h_S)/Z_{SD}$.

The Effective Scattering Volume is to be defined by placing suitable limits on the integrals in eq. (10) such that the value of the integral is a large fraction (say 0.99) of the value of the integral with the limits shown. Thus, the constant in front of the integral can be dispensed with and the

$$J(X_n, X_m, Z_n, Z_m, Y_m) = \int_{X_n}^{X_m} d\chi \int_{Z_n}^{Z_m} dz \int_0^{Y_m} dy r_r(y, z) \phi(y, z) \left[\frac{\sin(2\psi)}{R_{SP} R_{PD}} \right]^2 \chi^{14/3} \exp\{-2[\chi \sin(\psi/2)]^2\} \\ \Sigma = \left(\frac{J(X_n, X_m, Z_n, Z_m, Y_m)}{J(0, X_u, -\infty, +\infty, \infty)} \right) = 0.99 \\ \Sigma(X_n) = \left(\frac{J(X_n, X_u, -\infty, +\infty, \infty)}{J(0, X_u, -\infty, +\infty, \infty)} \right) = 0.998 \quad (11)$$

significance criteria Σ defined as in eq. (11).

The problem is to determine the numbers X_n , X_m , and the functions $Z_n(\chi)$, $Z_m(\chi)$, $Y_m(\chi, z)$ such that the second line in eq. (11) is true. This has been done by allotting the separate determinations of the five limits equal portions of the total error (0.01 in the above). An example of this allotment is shown in the third line of eq. (11). The result of the ESV determination is summarized below.

$$X_n = 1.43 \quad Z_n(16.667) = 95.56 \quad Y_m(16.667, 160) = 25.00 \\ X_m = 51.80 \quad Z_m(16.667) = 221.94$$

The values are for a particular choice of size parameter χ , namely that of the size class used later in the paper.

4. POPULATION OF THE EXTENDED VOLUME

The basic parameters for the turbule distribution function, the second expression in eq. (4),

are μ and l which have been determined previously³. The size increment parameter will be determined by energy conservation considerations assuming no energy loss when a turbule of one size class breaks up into two turbules of the next lower class. The result is

$$\frac{T(a_1)}{T(a_2)} = \left(\frac{v_1^2 a_1^3}{v_2^2 a_2^3} \right) = \left(\frac{a_1}{a_2} \right)^{11/3} = [\exp(\mu)]^{11/3} = 2; \quad \mu = (3/11) \ln(2) = 0.1890 \quad (12)$$

There are 49 size classes in this distribution starting from the largest at 10 m. and continuing to the smallest at 1.146 mm which is in the dissipation size range. To calculate l , the expression⁴ for the velocity structure constant was used. This expression is

$$C_v^2 = \left(\frac{0.69}{\mu} \right) \left(\frac{N_1 a_1^3}{V_s} \right) \left(\frac{v_1}{a_1^{1/3}} \right)^2 J_{14/3}^v(0, \infty) \quad (13)$$

$$J_{14/3}^v(0, \infty) = \int_0^\infty dy y^{14/3} \exp(-y^2/2) = 2^{11/6} \Gamma(17/6, 0, \infty) = 6.1455$$

A value for the structure parameter of $0.1111 \text{ m}^{4/3} \cdot \text{s}^{-2}$ was obtained from the literature⁴ so that the turbule spacing parameter can be calculated to be

$$l = \left(\frac{0.69 v_1^2 J_{14/3}^v(0, \infty)}{C_v^2 \mu a_1^{2/3}} \right)^{1/3} = \left(\frac{(0.69)(3.44)^2 (6.1455)}{(0.1111)(0.1890)(10)^{2/3}} \right)^{1/3} = 8.0148 \quad (14)$$

If the centers of vortices are closer than 2.8 times the diameter of an individual vortex, the mutual distortion can be expected to cause the vortices to disintegrate⁵ (eq. (13), page 468). This number of 2.8 would translate into a value of 5.6 if the spacing were compared to the vortex radius. Thus, the value of 8 from eq. (14) is reasonable although the exact relation of the vortex diameter to a is not yet known.

4.1 Determination of Turbule Distribution Parameters

The turbule distribution parameters for the 49 size classes were determined starting with the assumed size and characteristic velocity of the largest class which has class index 1. The size was taken to be the "center" of a size parameter interval. The interval (upper limit, lower limit) was calculated to be $(e^{+\mu/2}, e^{-\mu/2})$ times the center size parameter. The concentration for class 1 was calculated as if one turbule was in a volume of $(l a_1)^3$. The distribution function was then calculated from eq. (4). The turbule concentration is this distribution function times the size parameter interval. Values calculated for a few size classes are reproduced in Table 1. The data of this report have been generated using only class 10 whose parameters have been included in the table. This class was chosen because it was the largest contributor to the detector signal.

Table 1. TURBULE ENSEMBLE CHARACTERISTICS

Cl. In- dex	Center Size, m	Center Size Parameter	Charac- teristic Velocity, m· s ⁻¹	Size Parameter Interval	Concen- tration Distribution Funct., m ⁻³	Number Concen- tration, m ⁻³
α	a_α	χ_α	v_α	$\Delta\chi_\alpha$	$N_x(\chi_\alpha)$	$N_x(\chi_\alpha) \Delta\chi_\alpha$
1	1.00e+01	9.132e+01	3.44e+00	1.729e+01	1.235e-07	2.135e-06
10	1.83e+00	1.666e+01	1.95e+00	3.150e+00	1.113e-04	3.512e-04
21	2.28e-01	2.084e+00	9.75e-01	3.945e-01	4.552e-01	1.796e-01
42	4.31e-03	3.937e-02	2.59e-01	7.453e-03	3.573e+06	2.663e+04
49	1.14e-03	1.0488e-02	1.67e-01	1.985e-03	7.101e+08	1.410e+06

4.2 Turbule Location Strategy

To generate a discrete set of turbules, an extended scattering volume was selected. This volume was a rectangular parallelepiped whose x dimension was the maximum height of the ESV and whose y dimension was the width of the ESV at the center of the experimental zone.

The length of the parallelepiped was the source-detector distance plus the wind speed times the time interval of the experiment. The latter was chosen to be 100 s. Multiplying this volume by the concentration in the last column of Table 1 gives the expected number of turbules to be placed in the extended volume. A list of turbule locations for about 10% more than the number so indicated was formed by random number generation in the three coordinate directions. The list was then sorted in ascending z. The purpose of the next step was to spread the spacing in the z direction so that nearest neighbors were no closer than $3 a_{10}$ apart. Those locations that were beyond the end of the extended volume were then discarded. Still, there remained a few too many. Some of those whose spacing was exactly $3 a_{10}$ were also discarded to arrive at the indicated mean concentration. Finally, those turbules that were outside of the cylinder generated by the circle of the ESV at the experiment center were discarded. The total number remaining was 162.

5. TIME HISTORY OF INCOHERENTLY SUMMED SIGNAL

The results for the entire 100 seconds are shown in Fig. 2 below. The total exitance of the signal at the detector was the sum of the contributions calculated by eq. (2) from each

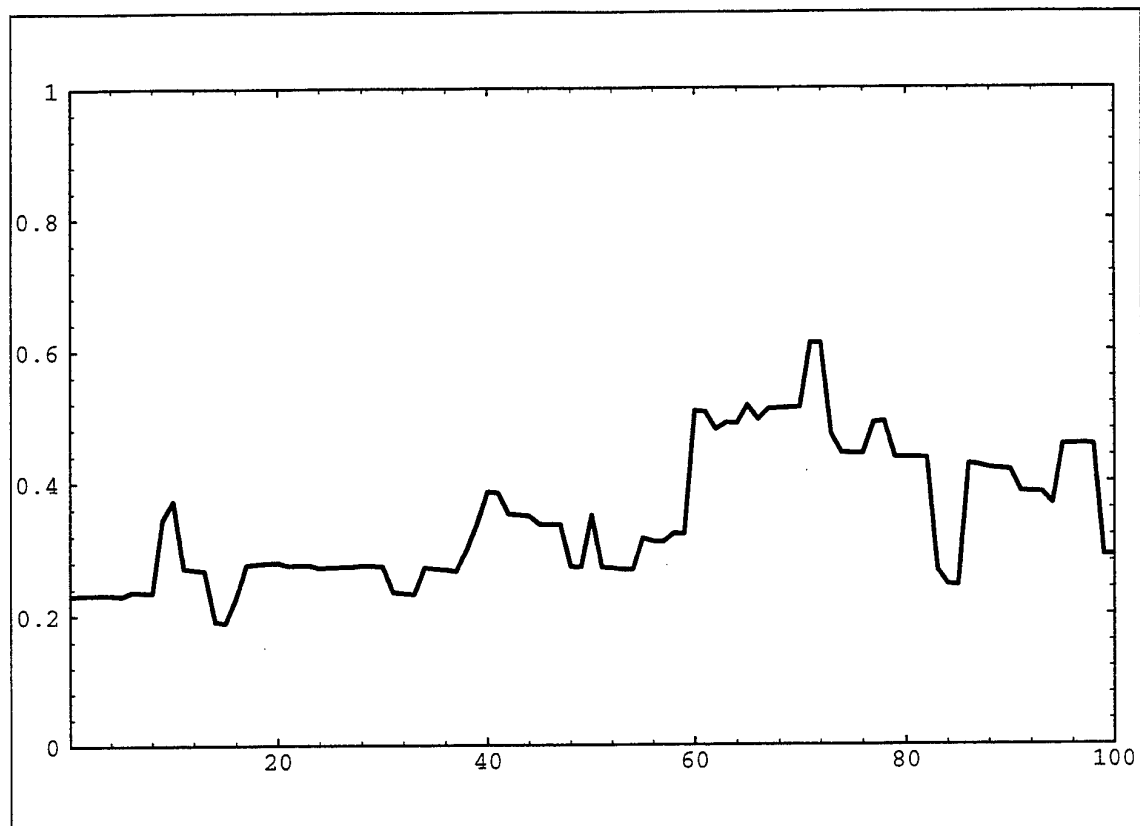


Figure 2. Time history of the incoherently summed signal magnitude.

turbule within the minimum z and the maximum z of the ESV at any given time instant. The number of effective scatterers was of the order of 25 for the 101 time instants at 1 second intervals. The calculation was made at $t = 0$, and then all the turbules were moved a distance of v_w times one second towards smaller z . The calculation was repeated for these new locations to give the exitance at $t = 1$ s. The quantity plotted is the square root of the exitance representing the relative sound pressure level. The horizontal scale in the remaining figures is time in seconds.

6. TIME HISTORY OF COHERENTLY SUMMED SIGNAL

To arrive at the time history of the coherently summed signal, several changes in the previous procedure were necessary. The first change was to use the scattering amplitude rather than the scattering cross section. This quantity changes the scattered pressure and the phase of the scattered sine wave with respect to the sine wave incident upon each scatterer. Thus, it is necessary to sum complex numbers at each time instant. Furthermore, the orientation average of the scattering amplitude is zero. It is therefore necessary to include the turbule orientation in the calculation. To do this, a list of 162 randomly orientated unit vectors was generated using a uniformly oriented distribution function. This list was paired with the location list previously obtained and the complex sum at each time instant calculated. The results are

presented in the next two figures. In Figure 3, the in- and out-of-phase components of the scattered signal are plotted. In Figure 4, the magnitude of the signal is shown.

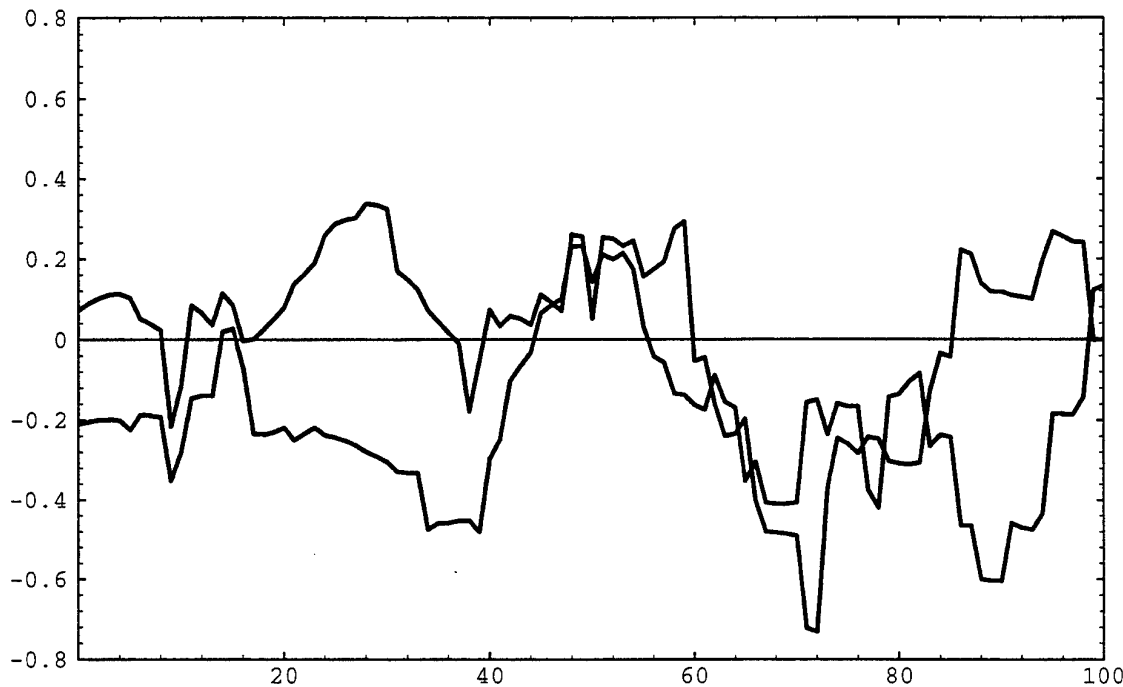


Figure 3. Coherently summed in- and out-of-phase scattered signal components

7. SUMMARY OF RESULTS AND CONCLUSIONS

Comparison of incoherently summed magnitude (Figure 2) with coherently summed magnitude (Figure 4) reveals the important role phase relations play in calculation of signals scattered by an ensemble of turbules. The maximum:minimum ratio is very much larger in the coherent case and the variations are much faster. Comparison of the data of this paper (Figure 4) with the experimental data⁶ shows that the experimental data (Figure 7 of that paper) varies more rapidly yet and the maximum:minimum ratio is greater in the latter. This ratio is about 19 here whereas it is about 200 there. It is quite possible that inclusion of smaller turbules or that finer time resolution here would enhance this ratio by making deeper minima possible. Yet, the message of this comparison is that something is inconsistent. Perhaps the assumption of uniform distribution of turbules is at fault. Accounting for intermittency may increase the maximum:minimum ratio but predicting a more rapid rate of variation may depend upon selection of a more self consistent set of geometric parameters leading to more accurate shadow zone boundary and dimensions for the ESV.

Much the same analysis as recorded in the previous paragraph were apparent at the time of the

previous paper⁶. This paper has made several improvements in the methodology compared to

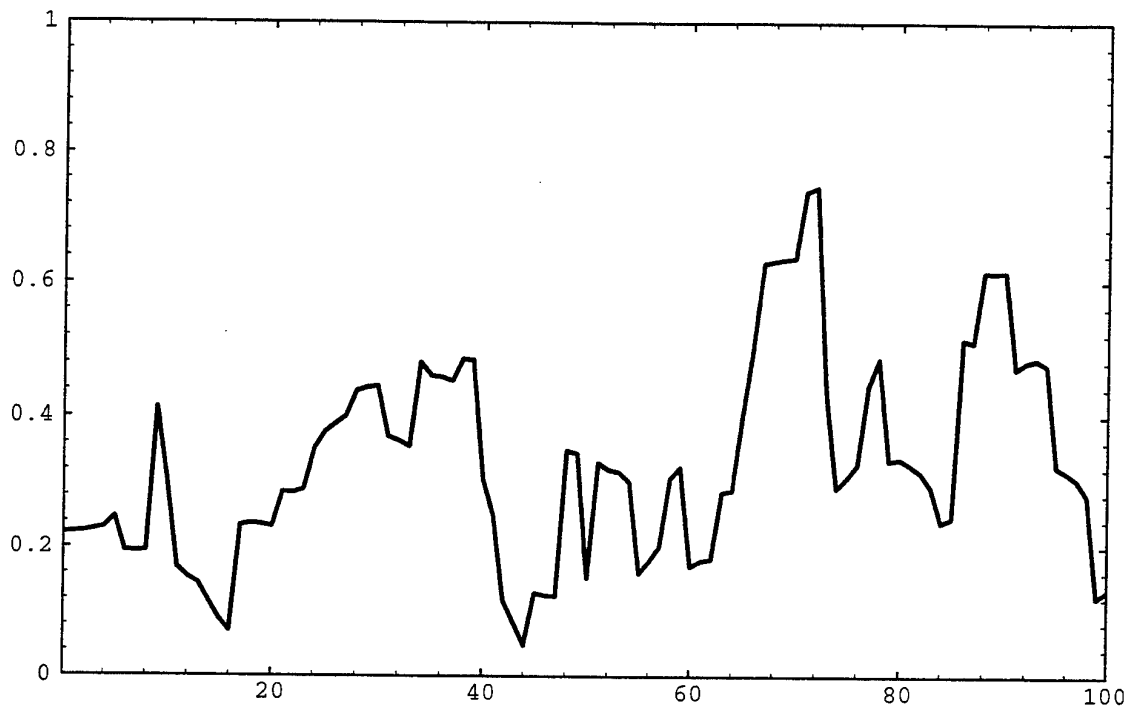


Figure 4. Coherently summed scattered signal magnitude.

the former. These improvements are listed below.

- The use of an Effective Scattering Volume (ESV), a volume delineated by the scattering pattern of the scatterers, has allowed the scattering volume to be defined in relation to the geometry of the experiment.
- The ESV concept has allowed determination of the contributing turbule size interval.
- Inclusion of a shadow zone boundary has shown how the influence of large turbules is reduced.
- A turbule size distribution was proposed that is based upon known characteristics of turbulence.
- The derived turbule scattering amplitude, rather than an assumed one, was used for the coherent calculation along with variable turbule orientation.

- The previous analysis included simultaneous vertical and cross-wind motion of turbules whereas the present does not.

Future work will require comparison with a data set that has a more complete set of environmental parameters so that a better shadow zone model can be incorporated. After this is done, summing the contributions of all of the relevant turbule size classes will be appropriate.

REFERENCES

1. Auvermann, H. J., G. H. Goedecke and M. D. DeAntonio, 1994, "Conclusions Pertinent to Acoustical Scattering by Atmospheric Turbulence Using a Turbule Ensemble Model, Proceedings of the Sixth International Symposium on Long-Range Sound Propagation, Ottawa, Canada, 12 - 14 June, 1994, pp 357-370.
2. Goedecke, G. H., 1992, "Scattering of Acoustical Waves by a Spinning Atmospheric Turbule," CR-92-0001-2, U. S. Army Research Laboratory, White Sands Missile Range, NM 88002-5501.
3. Auvermann, H. J., and G. H. Goedecke, 1995, "Shadow Zone Boundary Limitation of the Effective Acoustical Turbulence Scattering Volume Using the Turbule Ensemble Model," Proceedings of the 1995 Battlefield Atmospherics Conference, 5 - 7 Dec., 1995, White Sands Missile Range, New Mexico.
4. Brown, E. H. , and S. F. Clifford, 1976, "On the attenuation of sound by turbulence," Journal of the Acoustical Society of America, vol. 60, pp 788 - 794.
5. Moore, D. W. and P. G. Saffman, 1975, Journal of Fluid Mechanics, vol. 69, part 3.
6. Auvermann, H. J., G. H. Goedecke and M. D. DeAntonio, 1993, "Fluctuations of Acoustic Signals Scattered by an Ensemble of Turbule," Proceedings of the 1993 Battlefield Atmospherics Conference, 30 Nov. - 2 Dec., 1993, White Sands Missile Range, New Mexico.

Non Linear Propagation

Sonic boom research at Applied Research Laboratories

David T. Blackstock
Applied Research Laboratories,
and Mechanical Engineering Department,
The University of Texas at Austin,
Austin, TX 78712-1063, U.S.A.

A review is presented of sonic boom research done at Applied Research Laboratories during the period 1991-95. B. Lipkens performed a model experiment to investigate the effect of atmospheric turbulence on sonic boom propagation. The model N wave was generated by an electric spark, the model turbulence by a plane jet. R. O. Cleveland carried out theoretical studies of sonic boom propagation in a quiet (but stratified) atmosphere to answer the following two questions: (1) Does the sonic boom waveform freeze, i.e., does it attain an asymptotic shape, before the boom reaches the ground? (2) Are dissipation and nonlinear distortion in balance in sonic boom shocks, i.e., do steady state conditions prevail in sonic boom shocks? Partly to answer the second question, Cleveland developed a propagation algorithm (THOR) that includes nonlinear distortion, atmospheric absorption and dispersion, stratification, and geometrical spreading. The final task was to enter THOR in a NASA exercise to compare various sonic boom computer programs. [Work supported by NASA]

Influence of molecular relaxation on the rise time of sonic booms

François COULOUVRAT, Thierry AUGER

*Laboratoire de Modélisation en Mécanique
 Université Pierre et Marie Curie & C.N.R.S. (URA n° 229)
 case 162, 4 place Jussieu, F75252 Paris Cedex 05, France
 Tél : (33) 01 44 27 51 46 - Fax : (33) 01 44 27 52 59*

INTRODUCTION

Sonic boom is the acoustic noise resulting from aircrafts flying at supersonic speeds. Typical sonic boom waveforms are "N" waves of duration 0.1 - 0.2 s, with a peak overpressure of a few tens of Pa (Figure 1). This waveform is a consequence of nonlinear effects altering the waveform during its propagation from the aircraft down to the ground, and leading to shock waves formation [for reviews over the sonic boom problem, see Plotkin, 1989, or Maglieri and Plotkin, 1995]. Sonic boom waveforms can be predicted within the frame of geometric acoustics, solving a modified Burgers equation along each acoustic ray emanating from the airplane (Hayes, Haefeli and Kulsrud, 1969).

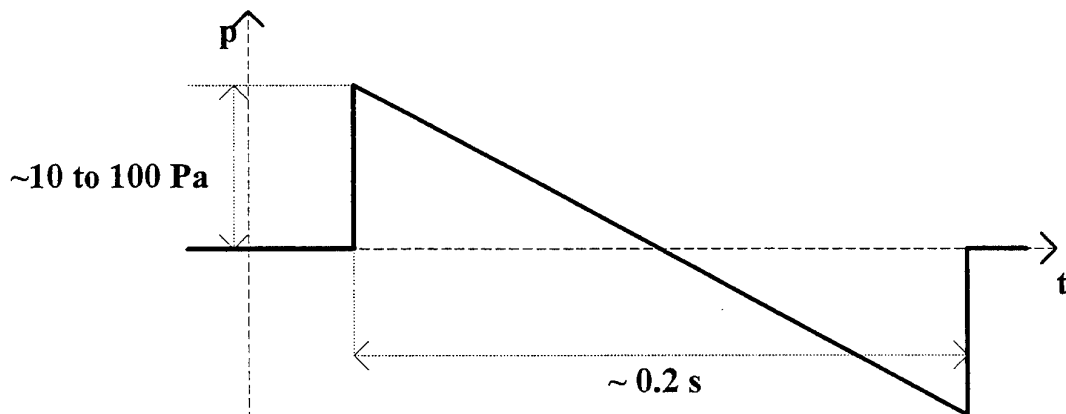


Figure 1: "N" wave

However, observed shock waves are not perfectly steep : the peak overpressure is reached only after a small but finite time. This is the so-called "rise time" (Figure 2). Typical values for the rise time are a few milliseconds, but experimental measurement values show a very large dispersion (Parmentier *et al.*, 1973). Only shock waves contribute to the subjective sensation of sonic boom loudness. Early experiments (Zepler and Harel, 1965) have shown that the sonic boom is perceived the louder as the rise time is shorter. In order to properly estimate the acoustic disturbance of sonic booms, a fine description of the shock structure would be useful. Finite rise times associated to shock structures are known for long (Taylor, 1910) to result from a local balance between nonlinear and thermoviscous effects. However, in the case of sonic booms, classical thermoviscous absorption would lead to rise times several orders of

magnitude smaller than observed values. As a consequence, two mechanisms have been suggested for explaining measured values.

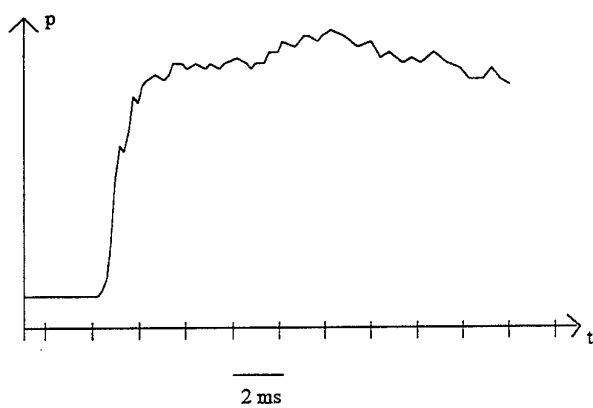


Figure 2 : schematic view of a sonic boom front shock wave

The first one is atmospheric turbulence. The detailed mechanism through which turbulence influences the rise time of sonic booms has been the subject of some controversy and the question still remains open, though recent progress has been made on this question (Lipkens, 1993, Lipkens and Blanc-Benon, 1995).

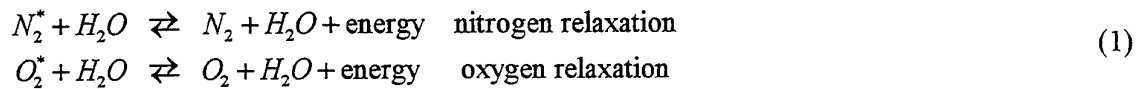
The second mechanism is molecular relaxation of nitrogen and oxygen molecules in air, as suggested by Hodgson (1973). First studies on the influence of molecular relaxation on the propagation of finite amplitude sound waves date back from the pioneering works of Lighthill (1956) and Polyakova, Soluyan and Khokhlov (1962). They showed that a single relaxation mechanism could "absorb" only shock waves whose amplitude is smaller than a critical value. For higher amplitude shock waves, the shock structure itself is discontinuous. It is then necessary to introduce an additional absorption mechanism to make it continuous again, such as thermoviscous absorption as studied by Crighton and Scott (1979).

For the particular case of a sonic boom propagating in the atmosphere, a generalized Burgers equation ("BGH equation") taking into account all absorption mechanisms can be derived. Two ways of estimating the influence of molecular relaxation have been suggested. The first one is to solve numerically the BGH equation all over the acoustic ray (Bass, Ezell and Raspert, 1983, Cleveland, 1995). The second one is less numerically intensive. It makes the assumption of a shock structure, in which a local balance between nonlinear and absorption effects always takes place (Hodgson, 1973, Crighton and Scott, 1979, Pierce and Kang, 1990). This assumption implies i) that the rise time is short enough compared to the signal total duration – which is well verified for most sonic booms signals –, ii) that the signal has travelled over a sufficiently long distance so that it has reached some steady state and the history of the signal travelling can be ignored. This last assumption has been questioned by Bass and Raspert (1992) or Cleveland (1995). Comparisons between the two methods indicate some differences depending on the atmospheric state. Though the rise time magnitude order is the same, numerical integration of the BGH equation leads to rise times slightly shorter than the shock structure method. However, due to the uncertainty about experimental results, the shock structure method still appears sufficient for the time being.

1. SONIC BOOM PROPAGATION

1.1 Molecular relaxation in air

In the atmosphere, vibrational molecular relaxation is a major mechanism for sound absorption. As air in the lower atmosphere layers (thermosphere and stratosphere) is composed mainly of oxygen and nitrogen molecules, it is sufficient to consider only the relaxation of these two molecules. Oxygen and nitrogen relaxation can be schematically represented as two independant chemical reactions :



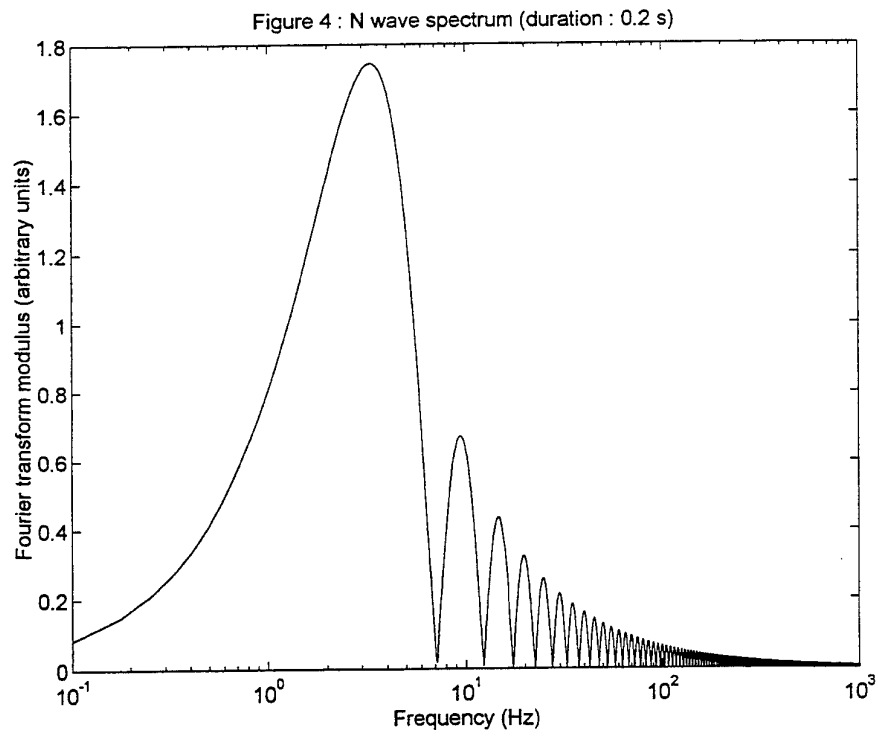
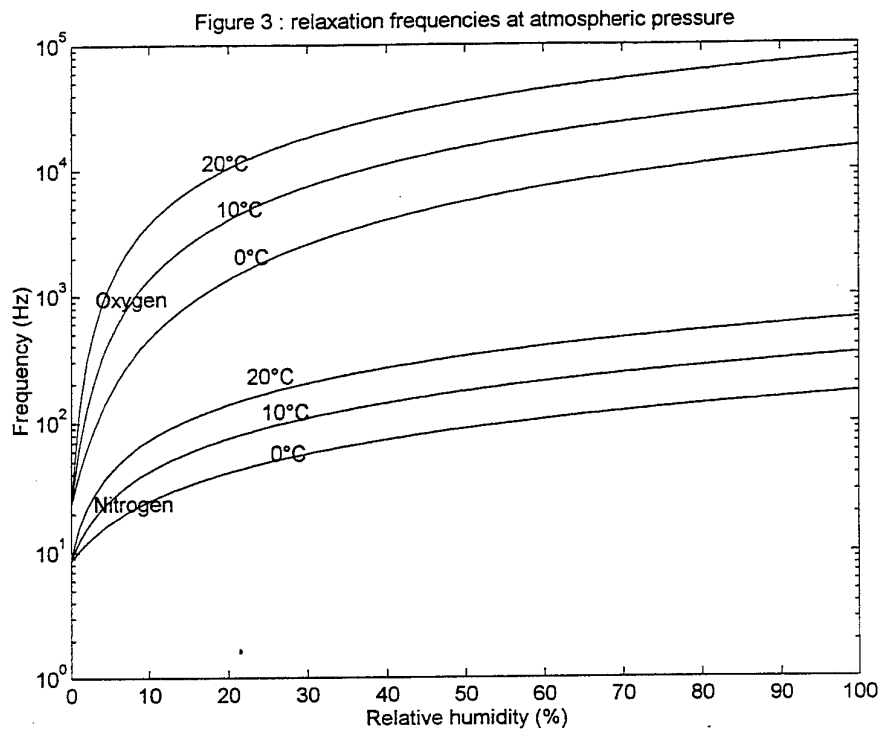
where * denotes a molecule whose internal vibrational mode is excited. Excited molecules return to thermodynamic equilibrium (unexcited internal vibrational mode) *via* collisions with water vapor molecules, a process through which energy is dissipated. Indeed, real relaxation mechanisms involve several chemical reactions. In particular, there is also relaxation in a dry atmosphere (Bass *et al.*, 1984). However, from an acoustical point of view, this model is sufficient to correctly describe sound absorption.

Introducing two internal variable ξ_1 and ξ_2 "measuring" the advancement of each chemical reaction, the state equation of the fluid relates its specific internal energy e to its specific entropy s , its density ρ and these two internal variables : $e = e(s, \rho, \xi_1, \xi_2)$. The relaxation times $\tau_{R,1}$ and $\tau_{R,2}$ are characteristic times of the kinetics of each reaction. These relaxation times are dependant on wator vapor concentration : the more wator vapor, the fastest the reaction. Relaxation times also decrease with increasing temperatures. Relaxation frequencies as given by standard ISO 9613-1 (1993) are plotted on Fig. 3 versus relative humidity at different temperatures.

In a relaxing atmosphere, sound propagation is slightly dispersive, as sound velocity depends on the thermodynamic state. At frequencies much below relaxation frequencies, acoustic perturbations are slow enough so that the fluid can be considered at thermodynamic equilibrium, and the sound velocity is c_0 . At frequencies much beyond relaxation frequencies, acoustic perturbation are fast enough so that the chemical reactions seem to be "frozen". Consequently, it is possible to define the two following velocities : $c_{\alpha,\infty}$ ($\alpha = 1, 2$) which are the high frequency sound velocities when the i th chemical reaction is frozen, the other one being at equilibrium. For stability reasons, $c_{\alpha,\infty}$ is always higher than c_0 . However, in air, dispersion resulting from relaxation is very small. It can be measured by the two parameters $m_\alpha = (c_{\alpha,\infty}^2 - c_0^2) / c_0^2$. These two parameters are small. They are mostly temperature dependant, and do not depend on humidity.

1.2 The generalized nonlinear wave equation in an inhomogeneous and absorbing fluid

Sonic boom is a finite amplitude sound wave which propagates in the inhomogeneous atmosphere. To describe this propagation, thermoviscous absorption and molecular relaxation effects must also be taken into account. The following generalized nonlinear wave equation takes into account all these mechanisms (Coulouvrat, 1996) :



$$\frac{\partial^2 p_a}{\partial t^2} - c_0^2 \Delta p_a = -\frac{c_0^2}{\rho_0} \operatorname{grad} p_a \cdot \operatorname{grad} \rho_0 + c_0^2 \tau_\nu \frac{\partial \Delta p_a}{\partial t} + \rho_0 \sum_{\alpha=1}^2 \frac{\partial^2 \zeta_\alpha}{\partial t^2} + \frac{\beta}{\rho_0 c_0^2} \frac{\partial^2 (p_a^2)}{\partial t^2} \\ \rho_0 \left(1 + \tau_{R,\alpha} \frac{\partial}{\partial t} \right) \frac{\partial \zeta_\alpha}{\partial t} = c_0^2 m_\alpha \tau_{R,\alpha} \Delta p_a \quad (1 \leq \alpha \leq 2). \quad (2)$$

The acoustic pressure is denoted p_a , while ρ_0 and c_0 are respectively the ambient fluid density and sound velocity. According to classical notations, β is equal to $1 + B/2A$ where $B/2A$ is the nonlinear parameter. The time τ_ν is a characteristic time for thermoviscous absorption and is equal to : $\tau_\nu = \frac{1}{\rho_0 c_0^2} [\eta + 4\mu/3 + \chi(\gamma - 1)/c_{p0}]$ with μ the fluid shear viscosity, η its bulk viscosity, χ its thermal conductivity, c_{p0} its specific heat at constant pressure and γ the ratio of its specific heats ($= 7/5$ for a diatomic gas). The quantities ζ_1 and ζ_2 in Eq.(2) are the acoustic perturbation of the two internal variables ξ_1 and ξ_2 .

1.3 Geometric acoustics approximation : the "BGH" equation

Typical sonic boom duration is about 0.1-0.2 s, which corresponds to a main frequency of 5 to 10 Hz, and a wavelength of 30 m (yet, because of shock waves, sonic booms are extremely broadband, see Fig. 4). However, sonic booms propagate over very long distances of several tens of kilometers. As a consequence, it appears beyond today numerical means to solve the 3D generalized wave equation. In order to reduce the problem size, it is necessary to work within the frame of the geometric acoustics approximation. Geometric acoustics assumes that, locally, the acoustic perturbation propagates as a plane wave. This approximation is valid only if the main wavelength is small compared to all others characteristic distances. For the sonic boom, this approximation is verified, as the largest wavelength (about 30 m) is much smaller than :

- the shock formation distance (several hundred meters for a supersonic transport aircraft such as "Concorde" flying at Mach 2);
- the characteristic distance for atmosphere stratification (30 kms for standard atmosphere);
- the characteristic distances for sound absorption (several tens of kilometers at 10 Hz).

Introducing the eikonal function $\psi(\bar{x}) = \psi_0 + \int_0^l \frac{dl}{c_0(\bar{x}_{ray})}$ measuring the travelling time between the source and the receiver along one specified ray, acoustic pressure can be written as :

$$p_a(\bar{x}, t) = \hat{p}_a(\bar{x}, \tau = t - \psi(\bar{x})). \quad (3)$$

Geometric acoustics approximation assumes that amplitude pressure variations are small compared to phase variations :

$$|\operatorname{grad} \hat{p}_a| \ll \left| \frac{\partial \hat{p}_a}{\partial \tau} \operatorname{grad} \psi \right|. \quad (4)$$

Substituting expressions (3-4) into Eq.(2) and keeping only dominant terms lead to a nonlinear one-dimensional equation governing pressure amplitude evolution along each ray :

$$\frac{\partial \hat{p}_a}{\partial l} + \frac{\hat{p}_a}{2} \left(\frac{1}{S} \frac{dS}{dl} - \frac{1}{c_0} \frac{dc_0}{dl} - \frac{1}{\rho_0} \frac{dp_0}{dl} \right) = \frac{\tau_\nu}{2c_0} \frac{\partial^2 \hat{p}_a}{\partial \tau^2} + \frac{\rho_0}{2c_0} \sum_{\alpha=1}^N \frac{\partial \hat{\zeta}_\alpha}{\partial \tau} + \frac{\beta}{\rho_0 c_0^3} \hat{p}_a \frac{\partial \hat{p}_a}{\partial \tau} \\ \rho_0 \left(1 + \tau_{R,\alpha} \frac{\partial}{\partial \tau} \right) \hat{\zeta}_\alpha = m_\alpha \tau_{R,\alpha} \frac{\partial \hat{p}_a}{\partial \tau} \quad (1 \leq \alpha \leq N). \quad (5)$$

In Eq. (5), l is the distance from the source measured along the selected ray, while $S(l)$ is the infinitesimal ray tube cross section.

Eq.(5) can be written in a dimensionless form by introducing the following variables :

$$\hat{P}(\sigma, \theta) = \sqrt{\frac{S(l)\rho_0(0)c_0(0)}{S(0)\rho_0(l)c_0(l)}} \frac{\hat{p}_a(l, \tau)}{\rho_0(0)c_0(0)U_{ac}} \\ \hat{Z}_\alpha(\sigma, \theta) = \frac{\hat{\zeta}_\alpha}{c_0(l)m_\alpha(l)\tau_{r,\alpha}(l)\omega_{ac}U_{ac}} \sqrt{\frac{S(l)\rho_0(l)c_0(l)}{S(0)\rho_0(0)c_0(0)}} \\ \hat{\theta} = \omega_{ac}\tau \\ \hat{\sigma} = U_{ac}\omega_{ac} \int_0^l \frac{\beta(l')}{c_0^2(l')} \sqrt{\frac{S(0)\rho_0(0)c_0(0)}{S(l')\rho_0(l')c_0(l')}} dl' \quad (6)$$

where U_{ac} is a typical value of the acoustic velocity magnitude, and ω_{ac} a characteristic signal frequency. This leads to the following generalized Burgers' equation

$$\frac{\partial \hat{P}}{\partial \hat{\sigma}} - \hat{P} \frac{\partial \hat{P}}{\partial \hat{\theta}} = \hat{\varepsilon}_\nu(\hat{\sigma}) \frac{\partial^2 \hat{P}}{\partial \hat{\theta}^2} + \sum_{\alpha=1}^2 \hat{\varepsilon}_\alpha(\hat{\sigma}) \frac{\partial \hat{Z}_\alpha}{\partial \hat{\theta}} \\ \left(1 + \hat{\Omega}_\alpha(\hat{\sigma}) \frac{\partial}{\partial \hat{\theta}} \right) \hat{Z}_\alpha = \frac{\partial \hat{P}}{\partial \hat{\theta}} \quad (1 \leq \alpha \leq N). \quad (7)$$

The several parameters of Eq.(7) are defined as follows :

$$\hat{\varepsilon}_\nu(\hat{\sigma}) = \frac{\omega_{ac}\tau_\nu(l)c_0(l)}{2\beta(l)U_{ac}} \sqrt{\frac{S(l)\rho_0(l)c_0(l)}{S(0)\rho_0(0)c_0(0)}} \\ \hat{\varepsilon}_\alpha(\hat{\sigma}) = \frac{\omega_{ac}\tau_{R,\alpha}(l)m_\alpha(l)c_0(l)}{2\beta(l)U_{ac}} \sqrt{\frac{S(l)\rho_0(l)c_0(l)}{S(0)\rho_0(0)c_0(0)}} \quad (1 \leq \alpha \leq 2) \\ \hat{\Omega}_\alpha(\hat{\sigma}) = \omega_{ac}\tau_{R,\alpha}(l) \quad (1 \leq \alpha \leq 2). \quad (8)$$

Due to stratification, all parameters depend on the slow $\hat{\sigma}$ variable. When relaxation is omitted, this equation is the one derived by Guiraud (1965) and Hayes *et al.* (1969). For this reason, we suggest to call it the "Burgers - Guiraud - Hayes" equation (BGH equation).

2. THE SHOCK STRUCTURE

2.1 Shock waves

The BGH equation (7) involves 5 parameters. For the typical duration and amplitude of a sonic boom signal created by a supersonic transporter, all these five parameters are small. This means that, at first order, thermoviscous absorption and relaxation can be ignored. Then, the BGH equation reduces to the classical inviscid Burgers' equation, whose solutions are known under implicit form:

$$\hat{P}_{fp}(\hat{\sigma}, \hat{\theta}) = F(\phi) \quad \text{with} \quad \hat{\theta} = \phi - \hat{\sigma}F(\phi). \quad (9)$$

It is well known that, after some propagation, solutions (9) exhibit shock waves. A shock wave of amplitude $\hat{H}(\hat{\sigma}) = \hat{P}_+(\hat{\sigma}) - \hat{P}_-(\hat{\sigma})$ happening at time $\hat{\theta}_c(\hat{\sigma})$ verifies the law of equal areas : $\hat{W}(\hat{\sigma}) = d\hat{\theta}_c / d\hat{\sigma} = -(\hat{P}_-(\hat{\sigma}) + \hat{P}_+(\hat{\sigma})) / 2$.

2.2 The shock structure

In reality, shock waves are regions of fast variations of the pressure field, with high frequency components for which absorption and relaxation effects cannot be neglected anymore. A local study of the shock structure can be made by rescaling the BGH equation around the shock wave. With this in view, we introduce the small parameter : $\hat{\varepsilon}(\hat{\sigma}) = \min(\hat{\varepsilon}_\nu(\hat{\sigma}), \hat{\varepsilon}_{1,2}(\hat{\sigma}), \hat{\Omega}_{1,2})$, and the new scaling :

$$\begin{aligned} \bar{\theta} &= (\hat{\theta} - \hat{\theta}_c(\hat{\sigma})) / \hat{\varepsilon}(\hat{\sigma}) \\ \bar{Q}(\hat{\sigma}, \bar{\theta}) &= \hat{P}(\hat{\sigma}, \hat{\theta}) - \hat{P}_-(\hat{\sigma}) \\ \bar{Z}(\hat{\sigma}, \bar{\theta}) &= \hat{\varepsilon}(\hat{\sigma}) \hat{Z}(\hat{\sigma}, \hat{\theta}). \end{aligned} \quad (10)$$

Introducing these new variables into Eq.(7), keeping only leading orders terms and integrating once leads to the differential system governing the shock structure :

$$\begin{aligned} 2\bar{\varepsilon}_\nu \frac{\partial \bar{Q}}{\partial \bar{\theta}} + \bar{Q}^2 - \hat{H}(\hat{\sigma}) \bar{Q} + 2 \sum_{\alpha=1}^2 \bar{\varepsilon}_\alpha \bar{Z}_\alpha &= 0 \\ -\frac{\partial \bar{Q}}{\partial \bar{\theta}} + \left(1 + \bar{\Omega}_\alpha \frac{\partial}{\partial \bar{\theta}} \right) \bar{Z}_\alpha &= 0 \quad (\alpha = 1, 2) \\ \lim_{\bar{\theta} \rightarrow -\infty} \bar{Q} &= \lim_{\bar{\theta} \rightarrow -\infty} \bar{Z}_1 = \lim_{\bar{\theta} \rightarrow -\infty} \bar{Z}_2 = 0. \end{aligned} \quad (11)$$

(The law of equal areas has been used in order to cancel the integration constant in Eq.(11).) Parameters are $\bar{\varepsilon}_\nu = \hat{\varepsilon}_\nu / \hat{\varepsilon}$, $\bar{\varepsilon}_{1,2} = \hat{\varepsilon}_{1,2} / \hat{\varepsilon}$, $\bar{\Omega}_{1,2} = \hat{\Omega}_{1,2} / \hat{\varepsilon}$. Boundary conditions are necessarily specified at $-\infty$, as the shock structure equations must be solved with increasing time and entropy, according to the second law of thermodynamic. It must be noticed that system (11) is invariant under time translation.

2.3 Influence of the different absorption mechanisms

According to a method suggested by Pierce and Kang (1990), it is useful to study the local behaviour of solutions of Eq.(11) at $-\infty$. As all quantities vanish, it is possible to neglect nonlinear terms there. Solutions are then locally proportional to $\exp[r(\sigma)\tilde{\theta}]$, where $r(\sigma)$ is one root of the following third degree polynomial :

$$2\bar{\varepsilon}_\nu \bar{\Omega}_1 \bar{\Omega}_2 r^3 + [2(\bar{\varepsilon}_1 \bar{\Omega}_2 + \bar{\varepsilon}_2 \bar{\Omega}_1 + \bar{\varepsilon}_\nu (\bar{\Omega}_1 + \bar{\Omega}_2)) - H \bar{\Omega}_1 \bar{\Omega}_2] r^2 + [2(\bar{\varepsilon}_1 + \bar{\varepsilon}_2 + \bar{\varepsilon}_\nu) - H(\bar{\Omega}_1 + \bar{\Omega}_2)] r - H. \quad (12)$$

It is easy to prove (Coulouvrat, 1996) that there exists one and only one root with a positive real part (this root being indeed real), the two others having a negative real part. Only the real positive root can match the boundary condition at $-\infty$, which "proves" the uniqueness of the solution. A similar study at $+\infty$ could have lead to several possible solutions. This confirms that the correct boundary conditions must indeed be specified at $-\infty$.

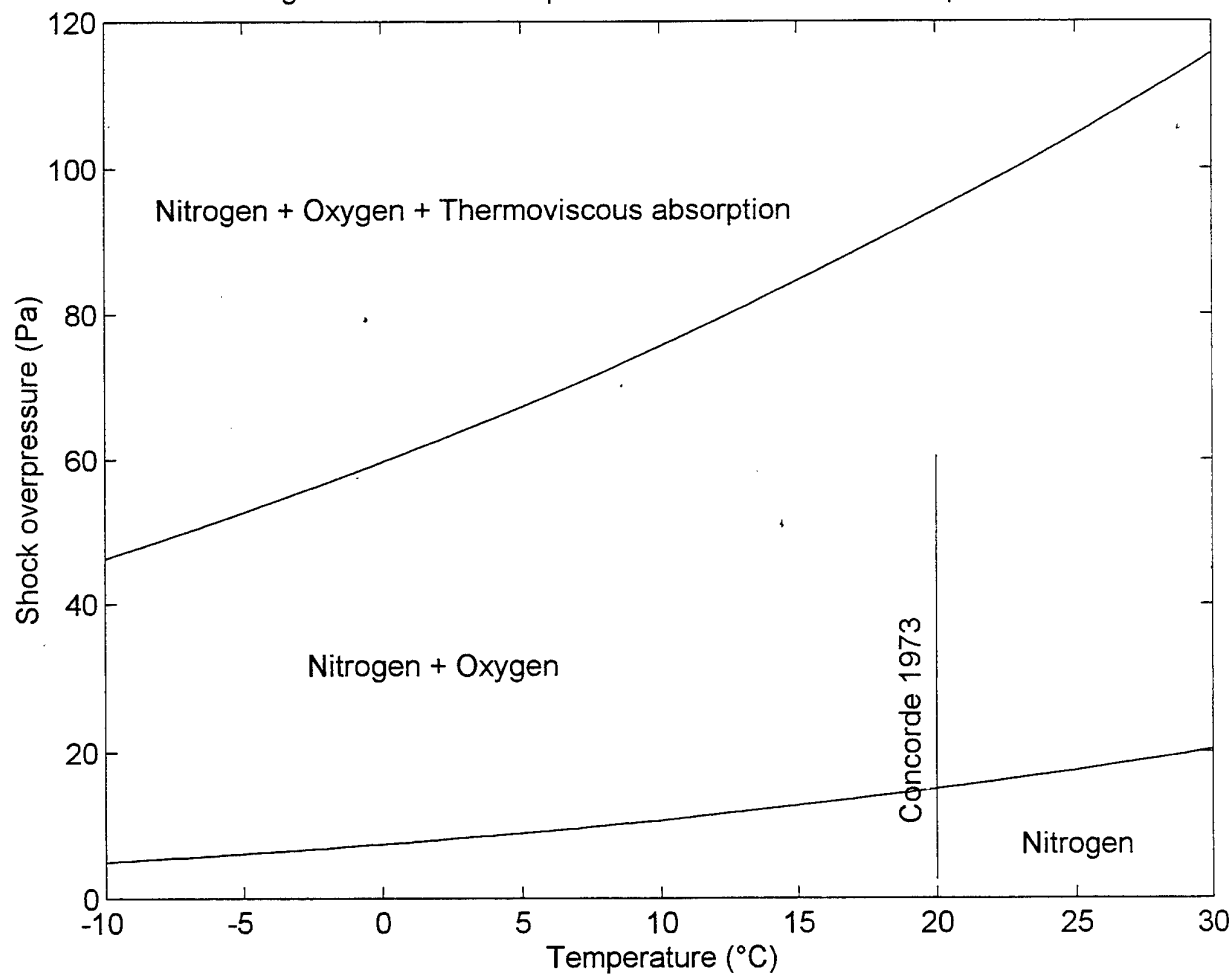
However, when thermoviscous absorption is omitted ($\bar{\varepsilon}_\nu = 0$), the polynomial is only a second degree one, and there exists an acceptable root (one with a positive real part) only if the shock amplitude is smaller than a given value. This means that for high amplitude shock waves, there exists no continuous shock structure matching the left and right pressure values. This generalizes for two relaxations the case of a partly dispersed shock studied by Lighthill (1956) for a single relaxation. The condition for which two relaxations are sufficient for a fully dispersed shock is: $[p_a] < [p_1] + [p_2] = p_0 c_0^2 (m_1 + m_2) / \beta$.

This last result underlines the role played by the several absorption mechanisms. As the main frequency of a sonic boom signal is very low, one expects nitrogen relaxation to be the dominant one. However, according to the results of Lighthill (1956) and Polyakova *et al.* (1962), nitrogen relaxation can "absorb" only shock waves of relatively low amplitude $[p_a] < [p_N] = p_0 c_0^2 m_N / \beta$. Most sonic booms are beyond this value and would correspond to partly dispersed shocks. In this case, it is necessary to take also into account oxygen relaxation in order to correctly describe their structure. This explains the particular shape of many sonic boom shock waves, with a first steep increase dominated by oxygen relaxation, followed by a more progressive rise phase in which nitrogen relaxation only is dominant. Finally, for extremely high amplitude shock waves, there would also be a first, very sharp rise dominated only by thermoviscous absorption. However, usual sonic booms amplitude are not beyond this last critical value. Critical values separating the three different types of shock structures are plotted versus temperature on Fig. 5 for a 1 atm pressure (the critical values are independant of humidity). On the same figure has been reported the widest range of shock pressure values measured during Concorde experiments (Parmentier *et al.*, 1973).

2.4 The composite solution

The shock structure solution is valid only in the vicinity of shock waves, while the inviscid fluid solution is valid far from them. Moreover, the shock structure is invariant under any translation: any function $\bar{Q}(\sigma, \bar{\theta} - \bar{\theta}_0(\sigma))$ is also a solution of the inner problem, whatever $\bar{\theta}_0(\sigma)$. In order to build a uniform approximate solution and to determine the value of $\bar{\theta}_0(\sigma)$, one defines the composite solution by :

Figure 5 : critical overpressures as a function of temperature



shock lefthand ($\theta \leq \theta_c(\sigma)$) :

$$P(\sigma, \theta) = P_{fp}(\sigma, \theta) + \bar{P}(\sigma, \bar{\theta}(\sigma, \theta) - \bar{\theta}_0(\sigma)) - P_-(\sigma) = P_{fp}(\sigma, \theta) + \bar{Q}(\sigma, \bar{\theta}(\sigma, \theta) - \bar{\theta}_0(\sigma))$$

shock righthand ($\theta \geq \theta_c(\sigma)$) :

$$P(\sigma, \theta) = P_{fp}(\sigma, \theta) + \bar{P}(\sigma, \bar{\theta}(\sigma, \theta) - \bar{\theta}_0(\sigma)) - P_+(\sigma) = P_{fp}(\sigma, \theta) + \bar{Q}(\sigma, \bar{\theta}(\sigma, \theta) - \bar{\theta}_0(\sigma)) - H(\sigma). \quad (13)$$

It is easy to check that the composite solution is a continuous function which is equivalent to the inviscid solution far from the shock wave, and to the shock structure close to it. Integrating the BGH equation over the interval $-\infty \leq \theta \leq +\infty$ yields the following condition that must be verified by the exact solution :

$$\int_{-\infty}^{+\infty} P(\sigma, \theta) d\theta = Cte. \quad (14)$$

As this condition is already fulfilled by the inviscid fluid solution (it is an other formulation of the law of equal areas), it finally leads to a condition about the inner solution :

$$\int_{-\infty}^{-\theta_0(\sigma)} \bar{Q}(\sigma, u) du + \int_{-\theta_0(\sigma)}^{+\infty} [\bar{Q}(\sigma, u) - H(\sigma)] du = 0, \quad (15)$$

which provides an expression for the only undetermined quantity :

$$\bar{\theta}_0(\sigma) = \lim_{\bar{\theta} \rightarrow +\infty} \left(\int_{-\infty}^{\bar{\theta}} \frac{\bar{Q}(\sigma, u)}{H(\sigma)} du - \bar{\theta} \right), \quad (16)$$

and achieves to determine the composite solution.

A schematic view of the composite solution is given by Fig. 6.

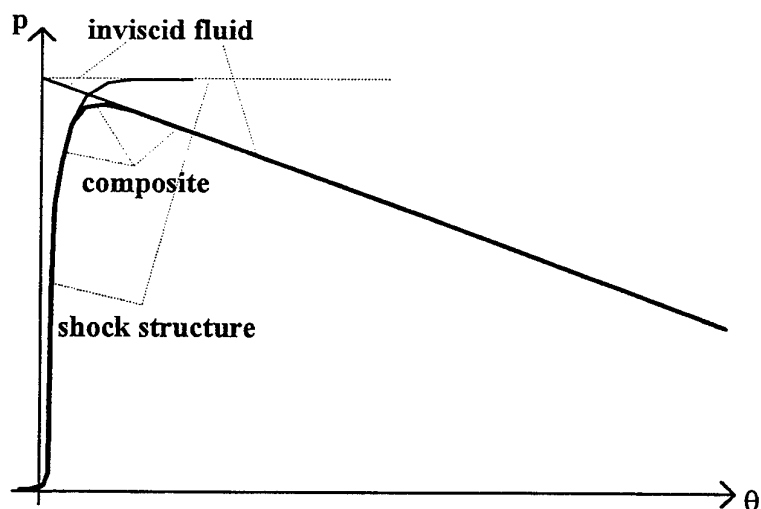


Figure 6 : schematic view of the composite solution

One can see that it leads to a slight rounding of the pressure field around its peak value, which is itself reduced compared to the inviscid value, and also to a small decrease of the rise time compared to the value deduced from the shock structure only. These effects are more pronounced for a relatively short signal than for a long one. This is, at least qualitatively, in agreement with observations from Bass and Raspé (1992) and Cleveland (1995), who noticed that the shock structure method gave less satisfying results (too long rise times) for short signals (fighter aircrafts or low altitude flights) or long rise times (dry atmosphere). The composite solution appears to be able to correct, at least partially, this drawback.

3. NUMERICAL RESULTS

3.1 Numerical simulations

Numerical simulations of sonic boom waveforms and shock structures were performed by Auger (1996) who augmented the Hayes, Haefeli and Kulsrud sonic boom simulation code (1969) with a shock structure treatment. The shock structure differential equations (11) were solved numerically by standard integration procedures, using NAG® Fortran library.

Fig. 7 displays computed shock structures at four different relative humidities ranging from 25 % to 100 %, for a shock amplitude of 15 Pa and an ambient temperature of 20 °C. Obviously, as humidity increases, relaxation frequencies increase (see Fig. 3) and the peak pressure is reached faster. Also, an increase of the shock wave amplitude would lead to a decrease of the rise time. The respective role of the two relaxation mechanisms is presented on Fig. 8, for which calculations have been done with nitrogen relaxation only, oxygen relaxation only and both relaxations (shock amplitude : 15 Pa, temperature 20 °C, relative humidity 50 %). It is clear on the figure that the beginning of the rise phase is dominated by oxygen relaxation, while the end is by nitrogen relaxation. Thus are confirmed numerically the results expected from theory as explained in section 2.3.

That vibrational molecular relaxation is dominant over thermoviscous absorption is illustrated by Table I, in which are compared the rise times computed with and without relaxation for two different shock amplitudes (relative humidity 50 %, temperature 20 °C). Here, the rise time is defined as the time needed for the pressure to jump from 1 % to 99 % of its peak value.

rise time (1 → 99 %)		
shock amplitude : 15 Pa	without relaxation	1,56 µs
	with relaxation	0,944 ms
shock amplitude : 20 Pa	without relaxation	0,857 µs
	with relaxation	0,643 ms

Table I : computed rise time with thermoviscous absorption only and with relaxation

Figures 9 and 10 show an example of a computed sonic boom waveform with molecular relaxation included (composite solution) in the case of "Concorde" supersonic transporter flying at Mach 1.99, with a 59 % relative humidity and a ground temperature of 22.9 °C. Fig. 9 is the whole time signal, on which the influence of absorption looks very weak, and Fig. 10 is a "zoom" on the first front shock. On this last figure, the rounding and small decrease of the peak pressure zone, the slight displacement of the shock time and the characteristic shape of the shock structure are clearly observable.

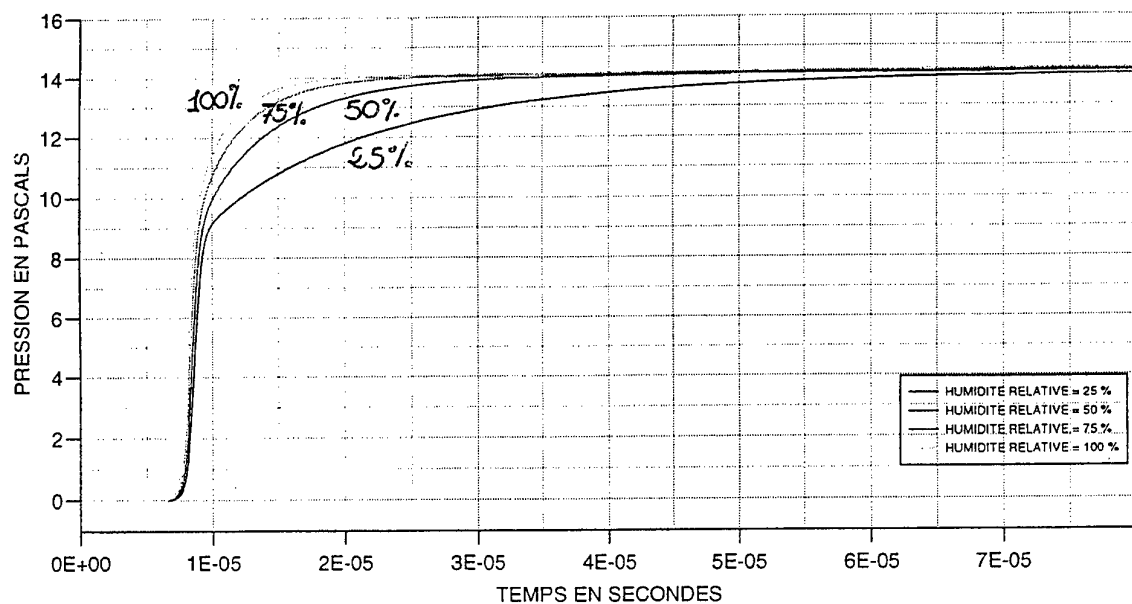


Figure 7 : shock structure (pressure in Pascal versus time in seconds) for a 15 Pa amplitude shock wave at atmospheric pressure, 20 °C temperature and various relative humidities ranging from 25 % to 100 %.

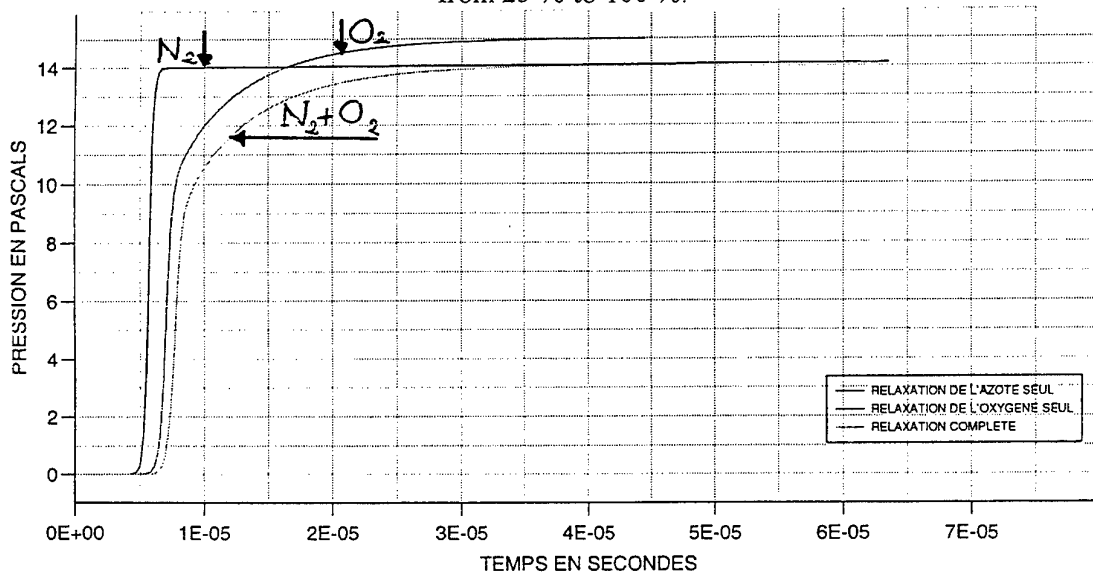


Figure 8 : shock structure (pressure in Pascal versus time in seconds) for a 15 Pa amplitude shock wave at atmospheric pressure, 20 °C temperature and 50 % relative humidity. Thick curve : nitrogen relaxation and thermoviscous absorption only. Medium curve : oxygen relaxation and thermoviscous absorption only. Thin curve : nitrogen relaxation, oxygen relaxation and thermoviscous absorption.

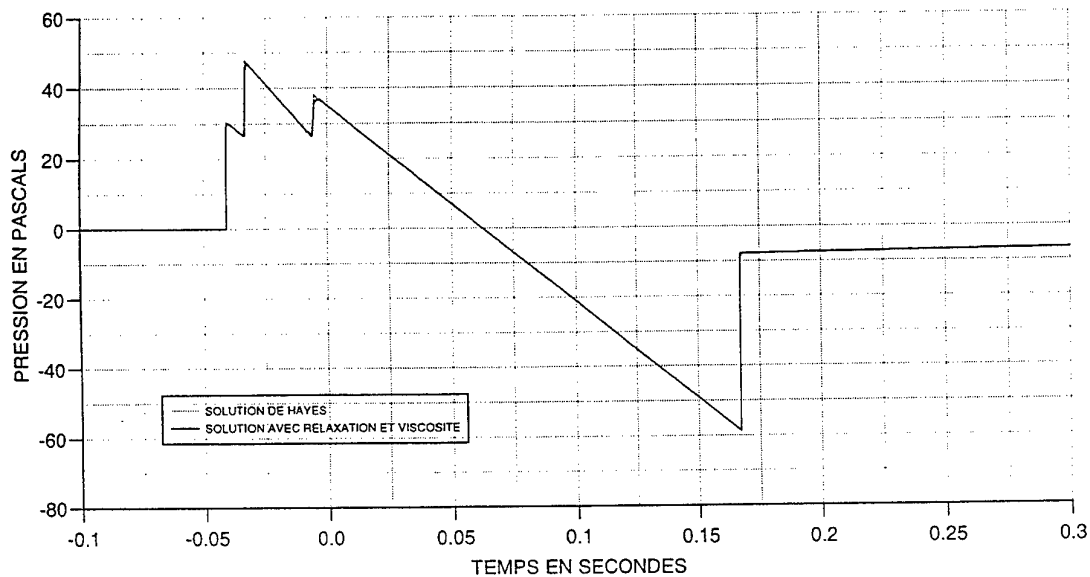


Figure 9 : computed « Concorde » sonic boom waveform (Mach = 1.99, ground temperature = 22.9 °C, ground relative humidity = 59 %). Thin curve : inviscid solution. Thick curve : composite solution with molecular and thermoviscous absorption included.

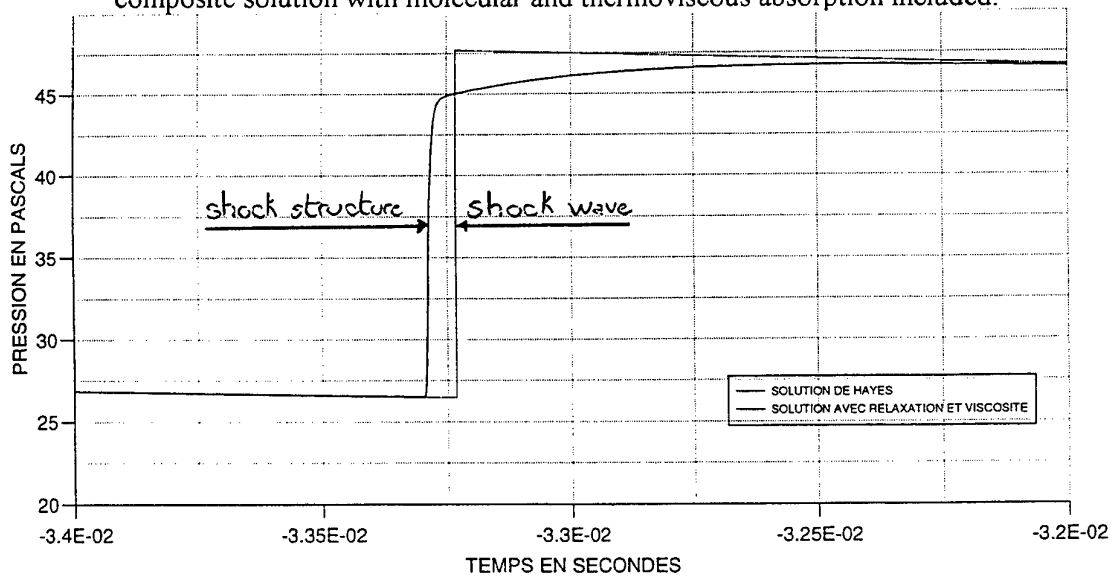


Figure 10 : computed « Concorde » sonic boom waveform (Mach = 1.99, ground temperature = 22.9 °C, ground relative humidity = 59 %). Thin curve : inviscid solution. Thick curve : composite solution with molecular and thermoviscous absorption included. Detail of the first shock wave.

3.2 Comparisons with "Concorde" experiments

Comparisons have been made with numerous measurements made during several "Concorde" test flights in Biscarrosse along the Atlantic French Coast on June 14 and 15, 1973 (Parmentier *et al.*, 1973). However, the collection of observed rise times shows considerable scattering, though there is nevertheless a "mean" trend of decreasing rise time with increasing shock amplitude, as predicted by the shock structure theory. Comparisons indicate that theory provides a lower bound for the rise time. This lower bound is reached or almost reached for several high amplitude shock waves (more than 40 Pa after reflection). On the contrary, for low amplitude shock waves, the observed rise times are much longer than predicted. Two reasons can be suggested for explaining the disagreement for low amplitude shock waves. First, as these ones were measured at the largest lateral distances off the aircraft trajectory, they correspond to acoustic rays that crossed the atmospheric turbulent boundary layer over the longest distances, and thus were more affected by turbulence. The other reason may be that some measurement points were near or even beyond the sonic boom carpet boundaries, in the shadow zone where geometric acoustics does not apply anymore. Finally, it must be noticed that the present results do not lead exactly to the same conclusion as Pierce and Kang, according to whom the shock structure yields a mean value rather than a lower bound for the rise time. One possible explanation could be the fact that the 1973 French experiments were done in a much more humid atmosphere and with a longer aircraft than US experiments, conditions under which the shock structure theory is expected to give better results (see discussion at the end of section 2).

ACKNOWLEDGMENTS

This work was supported by Aérospatiale Avions (Toulouse), contract n° 95/106. The authors are grateful to R. Etchevest and J. Carla (Aérospatiale) for initiating this study and for helpful discussions on the topic.

REFERENCES

- Auger, Th. (1996). "Propagation de la détonation balistique : influence de la relaxation sur la structure de choc", mémoire de stage du D.E.A. de Mécanique, Université Pierre et Marie Curie (Paris VI) & Aérospatiale Aéronautique (in French)
- Bass, H. E., Ezell, J., Raspert, R. (1983). "Effect of vibrational relaxation on rise times of shock waves in the atmosphere", *J. Acoust. Soc. Am.*, **74**, 1514-1517
- Bass, H. E., Raspert, R. (1992). "Comparison of sonic boom rise time prediction techniques", *J. Acoust. Soc. Am.*, **91**, 1767-1768
- Bass, H. E., Sutherland L. C., Piercy, J., Evans, L. (1984). "Absorption of Sound by the Atmosphere", in "Physical Acoustics : Principles and Methods", eds. Mason, W. P., Thurston, R. N. (Academic Press, Orlando), Vol. XVII, 145-232
- Cleveland, R. O. (1995). "Propagation of sonic booms through a real, stratified atmosphere", Ph.D. dissertation, The University of Texas at Austin
- Coulouvrat, F. (1996). "Influence de la relaxation moléculaire sur le temps de montée d'un bang sonique", Université Pierre et Marie Curie, rapport final contrat Aérospatiale Avions n° 95/106 (in French, limited diffusion)
- Crighton, D. G., Scott, J. F. (1979). "Asymptotic solutions of model equations in nonlinear acoustics", *Philos. Trans. R. Soc. Lond.*, **A292**, 101-134

- Guiraud, J.-P. (1965). "Acoustique géométrique, bruit balistique des avions supersoniques et focalisation", *Journal de Mécanique*, 4, 215-267 (in French)
- Hayes, W. D., Haefeli, R. C., Kulsrud, H. E. (1969). "Sonic boom propagation in a stratified atmosphere with computer program", NASA Contractor Report CR-1299, National Aeronautics and Space Administration (Washington)
- Hodgson, J. P. (1973). "Vibrational relaxation effects in weak shock waves in air and the structure of sonic bangs", *J. Fluid Mech.*, 58, 187-196
- ISO 9613-1 (1993). "Acoustics - Attenuation of sound during propagation outdoors - Part 1: Calculation of the absorption of sound by the atmosphere" (International Organization for Standardization, Genève)
- Lighthill, M. J. (1956). "Viscosity effects in sound waves of finite amplitude", in "*Surveys in Mechanics*", eds. Batchelor, G. K., Davies, R. M., (Cambridge University Press, Cambridge), 250-351
- Lipkens, B. (1993). "Experimental and theoretical study of the propagation of N waves through a turbulent medium", Ph.D. dissertation, The University of Texas at Austin
- Lipkens, B., Blanc-Benon, Ph. (1995). "Propagation of finite amplitude sound through turbulence : a geometric acoustics approach", *C. R. Acad. Sci. Paris*, t. 320, Série II b, 477-484
- Maglieri, D. J., Plotkin, K. J. (1995). "Sonic Boom", in "*Aeroacoustics of Flight Vehicles*", Vol. 1 ("Noise Sources"), ed. Hubbard H. H., Acoustical Society of America, 519-561
- Parmentier, G., Mathieu, G., Schaffar, M., Johe, Ch. (1973). "Bang sonique de Concorde. Enregistrement hors trace des variations de pression au sol. Centre d'Essais des Landes ; 13 au 15 juin 1973", Rapport Technique RT 19/73, Institut Franco-Allemand de Recherches de Saint-Louis (ISL) (in French)
- Pierce, A. D., Kang, J. (1990). "Molecular relaxation effects on sonic boom waveforms", in "*Frontiers of Nonlinear Acoustics : Proceedings of the 12th ISNA*", eds. Hamilton, M. F., Blackstock, D. T., (Elsevier, London), 165-170
- Plotkin, K. J. (1989). "Review of sonic boom theory", AIAA 12th Aeroacoustics Conference, San Antonio (USA), April 10-12, 1989, AIAA-89-1105
- Polyakova, A. L., Soluyan, S. I., Khokhlov, R. V. (1962). "Propagation of finite disturbances in a relaxing medium", *Sov. Phys. Acoust.*, 8, 78-82
- Taylor, G. I. (1910). "The conditions necessary for discontinuous motion in gases", *Proc. Roy. Soc. Lond.*, A84, 371-377
- Zepler, E. E., Harel, F. R. P. (1965). "The loudness of sonic booms and other impulsive sounds", *J. Sound Vib.*, 2, 249-256

Sonic boom scattering from anisotropic turbules

MARK KELLY, RICHARD RASPET, AND HENRY E. BASS

National Center for Physical Acoustics, University of Mississippi, University, MS 38677

INTRODUCTION

Sonic boom flight tests performed over the last three decades provide an opportunity to gain insight into the characteristics of atmospheric turbulence. Turbulence in the atmosphere causes random fluctuations in the index of refraction, both temporally and spatially. Early analysis demonstrated that boom rise times are anomalously large compared to predictions which take into account viscosity, thermal conductivity, and molecular diffusion, for planar shocks in a homogeneous atmosphere.¹ Vibrational relaxation absorption may be taken into account to further increase predicted rise times. When included in a non steady calculations which also account for spherical spreading and dispersion in a layered atmosphere, including relaxation, it gives a realistic lower limit for predicted rise times.² This still does not account for the large rise times which have been measured; it has been postulated that turbulence produces these longer rise times.³

Recent sonic boom experiments provide the data for analysis and comparisons undertaken in this work. The experiments, whose objective was to study the influence of atmospheric turbulence on sonic boom propagation, were conducted in 1991 at the White Sands Missile Range as a follow up to a NATO program. These tests, titled the Joint Acoustic Propagation Experiments (JAPE) and (JAPE-2), involved the collection of acoustic data below the flight path of supersonic aircraft.⁴ A linear array of microphone systems recorded the acoustic data, while an extensive system of meteorological equipment recorded temperature and wind data.

Modeling the turbulent atmosphere with a single-scatter, spherical turbule model has produced boom statistics which are somewhat consistent with the JAPE data, but which still underpredict the rise times.⁵ Evidence from the atmospheric sciences literature⁶⁻⁹ suggests that turbules are elongated in different manners, depending upon conditions and altitude. The extension of the realistic turbulent atmospheric model to include asymmetric turbules is the next logical step in modeling the turbulent atmosphere, and is the basis of this paper.

I. SINGLE SCATTER, CENTER-BASED TURBULES

Before looking at the use of many turbules to represent sound propagation through a turbulent atmosphere, it is prudent to first examine the effect one turbule has on an incident boom. A turbule may be understood as a local fluctuation in the index of refraction of a medium, whose center is the point of maximum local fluctuation. deWolf¹⁰ first characterized a turbule as a spherically symmetric Gaussian entity with the following profile:

$$\mu(r,s) = q_i e^{-(\frac{r}{s})^2}, \quad (1)$$

where μ is the deviation of the index of refraction from unity ($|\mu| < 1$), q_i is the strength of the turbule, r is the radial distance from the center of the turbule, and s is the radius of the $1/e$ contour of the turbule. These parameters will be related to meteorological theory in the next section. A turbule characterized by the aforementioned profile has an index of refraction ($1+\mu$) at its center, and will scatter incident sound; the effect of one turbule upon the incident wave may be modeled as a scattered wave emanating from the turbule center. The scattered wave amplitude may be calculated via the use of a first Born approximation, which, in closed form, is time-efficient in a

computer simulation. The scattering contribution from one turbule may be written as

$$\bar{\Psi}_1^B = \frac{k^2 q \sqrt{\pi}}{2} \frac{e^{ik(r_{st} + r_{tr})}}{r_{st} r_{tr}} \frac{s^3}{1 - ia} e^{-\frac{1}{4} C_d k^2 s^2}, \quad (2)$$

and is derived in McBride, et. al.¹¹

An asymmetric, ellipsoidally shaped turbule may also be modeled as a center-based scatterer to represent anisotropic turbulence. It is useful to describe such a scatterer in Cartesian coordinates, with the turbule center at the origin. Then the turbule profile may be written as

$$\mu(x, y, z, s_x, s_y, s_z) = q_i e^{-(x/s_x)^2 - (y/s_y)^2 - (z/s_z)^2}, \quad (3)$$

where the characteristic turbule radius s is replaced by three ellipsoidal axis lengths (s_x, s_y, s_z). The scattering contribution from such an asymmetric scatterer may also be obtained in a closed form using the first Born approximation. This scattered wave has a form similar to that of the

$$\text{spherical turbule's contribution: } \bar{\Psi}_1^B = \frac{k^2 q \sqrt{\pi}}{2} \frac{e^{ik(r_{st} + r_{tr})}}{r_{st} r_{tr}} \frac{1}{s_1 s_2 s_3} e^{-\frac{1}{4} C_d k^2 (s_1 s_2 s_3)^{-2}}, \quad (4)$$

where r_{st} is the distance between source and turbule, r_{tr} the distance between turbule and receiver, k is the wave number, and q is the turbule strength. $C_d, s_1, s_2, \text{ and } s_3$ are constants based on the turbule shape and its position relative to the source and receiver. The derivation of these quantities and evaluation of the Born scattering integral follow in the appendix. The complex pressure at the receiver may generally be written as $p(\mathbf{r}) = \bar{p}_0(\mathbf{r}) + \bar{\Psi}_1^B$ for a first Born approximation, with $\bar{p}_0(\mathbf{r})$ denoting the complex pressure due to the direct wave, and \mathbf{r} being the vector coordinate of the receiver with respect to the source. The scattered wave from the turbule center should be out of phase with the direct wave due to the path length difference, and its amplitude will be much smaller than that of the direct wave. In addition, the scattered wave amplitude will also depend on the scattering angle, Θ_0 . This brings up a point of note. The spherical case Born integral evaluation involves an approximation of the polar angle Θ by the scattering angle Θ_0 . This occurs in the second order approximation of the geometric term $|\vec{r}'| + |\vec{r} - \vec{r}'|$ which is substituted into an exponent in the Born scattering integral (see appendix). The ellipsoidal case uses a Cartesian coordinate system to evaluate the integral, and avoids such an approximation. Thus the ellipsoidal model may be slightly more accurate than the spherical turbule representation, if not more realistic.

The ellipsoidal model was applied to simulated booms originating from a T-38 flying at an altitude of 10,000 m. A single 30*10*10 turbule was placed (in the planetary boundary layer) directly below the aircraft, with the receiver on the ground at various positions. Pressure fields and rise times were calculated for a receiver located between 0 and roughly 120 m off-axis. The calculation of rise times used the definition forwarded by Willshire, et. al.¹²

$$rt = \frac{0.9 p_{max} - 0.1 p_{max}}{(dp/dt)_{max}}, \quad (5)$$

with $(dp/dt)_{max} \approx$ the slope from 0.4 to 0.6 p_{max} . The results of these calculations generally showed slightly higher rise times off-axis than for spherical turbule simulations. Figure 1 shows a comparison of off-axis rise times in one direction for two turbules, of size 30*10*10 and 10*10*10. Similar results were produced comparing the same ellipsoidal turbule with a spherical one of equal volume ($s=14.22$ m).

Another feature of the ellipsoidal model is that it accounts for different rise times at receiver positions which are the same distance off-axis, but at different angular positions with respect to the major turbule axis (or mean wind flow). This is displayed in figure 2. To further inspect (and check) the angular dependent behavior of this single-scatter asymmetric model, calculations of rise time were also made with the T-38 at positions other than directly above the turbule. An example is presented in figure 3; this displays the rise times due to a 30*10*10 eddy,

with the boom approaching at a 45° angle relative to the mean wind direction (major axis). The overall trend observed was a slight increase in rise times, with directional dependence. This promising result logically leads to this model's use in more developed atmospheric simulations.⁵ These multiple turbule calculations are discussed in the following two sections.

II. SELECTION OF TURBULE PARAMETERS USING METEOROLOGICAL DATA

The purpose of this section is to explain the connections between actual meteorological data and the aforementioned variables which describe a singular turbule; this will serve as a bridge to describing the atmosphere as an agglomeration of discrete turbules. Starting again with deWolf's representation of an isotropic, nearly transparent medium, we have $\mu(r,s) = q_i e^{-(\gamma s)^2}$. To relate most simply, it can be said that s and q_i may be given in terms of two independently measured micrometeorological variables, namely $\langle \mu^2 \rangle$ and L . These can be obtained in various manners. A scale length L may be found using an autocorrelation analysis, in conjunction with Taylor's hypothesis (assuming the atmosphere is changing slowly). For windy conditions where the temperature variance is much smaller than the wind velocity variance, the index of refraction fluctuation may be approximated or estimated by $\langle \mu^2 \rangle \approx \frac{\sigma_w^2}{c_0^2}$.

The value of $\langle \mu^2 \rangle$ may also be obtained in terms of the individual meteorological fluctuations in T , u , v , and w . Indirectly, s may be obtained in the form of a density of scatters $n(s)$. This density of scatters (or "turbule number density spectrum") may be found through the fit of a von Karman spectrum to the spectrum of index of refraction fluctuations, or to the wind speed fluctuation spectrum.⁵ The von Karman spectrum has the form

$$\Phi(\mathbf{k}) = \frac{\gamma C_n^2}{(k \cdot k + L_0^2)^{11/6}} e^{-(k \cdot k \ell_m^2)} \quad (6)$$

in terms of wave vectors; it may also be rewritten in terms of frequency. The microscale ℓ_m^2 is quite small (typically 1 mm) and thus the exponential term is usually ignored. Fitting the von Karman spectrum to the measured spectra mentioned above gives values of C_n^2 and L_0^2 which allow a calculation of the density of scatters:

$$n(s) = \frac{2^{-5/6} \gamma}{q^2 \pi^3 \Gamma(5/6)} C_n^2 s^{-10/3} e^{-(s^2/2L_0^2)}. \quad (7)$$

If a Gaussian refractivity spectrum is observed¹³, then only one turbule size exists;

$$\Phi_n(k) = \frac{q^2}{8} \int_0^\infty s^6 n(s) e^{-k^2 s^2/2} \quad (8)$$

gives the spectrum in terms of the number density, showing that $n(s)$ must be a delta function in order to produce a Gaussian refractivity spectrum. In this case we can write

$$\Phi_n(k) = \frac{\langle \mu^2 \rangle L_0^2}{8 \pi^{3/2}} e^{-k^2 L^2/4}, \quad (9)$$

and obtain q_i to match $\langle \mu^2 \rangle$ for a given number turbules per volume (or vice-versa). This is merely an example of the use of the von Karman spectrum; Boulanger, *et. al.*⁵ showed that a single scale simulation involving random positioning of eddies did not give boom characteristics consistent with JAPE-2 observations.

The concept of many spherical turbules may be extended to a simulation involving ellipsoidal turbules. The von Karman spectrum may be rewritten in terms of frequency as mentioned above, but cannot be done conveniently without assuming isotropic turbulence. This assumption does not, however, rule out the use of ellipsoidal turbules. It holds reasonably well for ellipsoidal turbules as long as no axis is much larger than another. The von Karman fit may

be used to give an ellipsoidal turbule distribution, and is reasonable as long as turbule volume is preserved.

The simulated shapes of asymmetric turbules follows from theory forwarded by D. K. Wilson, *et. al.*¹⁴, and is height dependent. Atmospheric sciences literature suggests that eddies may be horizontally elongated (in the direction of the mean wind) when shearing mechanisms dominate turbulence production, and vertically elongated when convective conditions dominate. Wilson, *et. al.* use a stretching matrix \mathbf{S} to model the elongation of turbules. The matrix is diagonal, with each element representing the stretch in its direction, with respect to the vertical element. The forms suggested for this stretching are

$$\mathbf{L}^{-2} = L_z^{-2} \mathbf{S}, \quad (10)$$

where

$$\mathbf{L}^{-2} = \begin{bmatrix} L_x^{-2} & 0 & 0 \\ 0 & L_y^{-2} & 0 \\ 0 & 0 & L_z^{-2} \end{bmatrix}, \quad \text{and} \quad \mathbf{S}(\zeta) = \begin{bmatrix} f_x(\zeta) & 0 & 0 \\ 0 & f_y(\zeta) & 0 \\ 0 & 0 & 1 \end{bmatrix} \quad (11)$$

with

$$f_x(\zeta) = \begin{cases} 1/\kappa^2, & \delta \geq 1/\kappa^2 \\ \delta, & 1/\kappa_{fc}^2 < \delta < 1/\kappa^2 \\ 1/\kappa_{fc}^2, & \delta \leq 1/\kappa_{fc}^2 \end{cases}, \quad f_y(\zeta) = \begin{cases} 1, & \delta \geq 1 \\ \delta, & 1/\kappa_{fc}^2 < \delta < 1 \\ 1/\kappa_{fc}^2, & \delta \leq 1/\kappa_{fc}^2 \end{cases} \quad (12), (13)$$

and where $\delta \equiv (-\zeta)^{-\frac{3}{2}}$ and $\zeta = \frac{z}{L_{mo}}$. The Monin-Obukhov length is L_{mo} , and serves as the surface-layer length scale. It is negative for statistically unstable conditions, and was on the order of -30m in our simulations and (due to) the JAPE-2 data. The von Karman constant is $\kappa=0.4$, and the free convection von Karman constant has a value given by $\kappa_{fc}^{-2} = 0.7$. Hence the stretching matrix produces turbules which are stretched horizontally by a factor of about 6 near the ground, and compressed by 0.7 in the mixed layer (the mixed layer begins at roughly one tenth the inversion height, or about 100m for our data and calculations).

The literature also suggests that for windy conditions, such as those present in the JAPE-2 data, there is no definite height dependence for the scale of turbulence (turbule size). Thus ellipsoidal turbules in the simulations are of quasi-random sizes (depending on $n(s)$), and are stretched according to height using the stretching matrix. The turbule strengths, however, show a dependence on altitude; the strengths were assigned in different manners depending upon the atmospheric model being tested and thus will be treated in the next section.

III. DIFFERENT MODELS OF THE ATMOSPHERE

Three different schemes for ellipsoidal turbule placement and characterization have been tested. All three were single-scatter center based models which involved the random placement of eddies in a simulated atmosphere. All three were repeated for spherical turbules and ellipsoidal turbules (spherical turbules stretched according to stretching matrix). All elliptical turbules were stretched such that their volume was the same as their corresponding (unstretched) sphere's volume. All calculations had the same input, a boom from a T-38 traveling at Mach 1.2. The Mach cone apex angle was accounted for geometrically. For each atmospheric model, four cases were tested: the case of spherical eddies, and the cases of ellipsoidal turbules with angles of 0°, 45°, and 90° between flight trajectory and mean wind direction.

The input to the calculations was a simulated T-38 boom which was propagated through the first 9000m of atmosphere using an improved Anderson algorithm.¹⁵ This input wave is shown in figure 4. The point of input of this wave, or 'top' of the atmospheric turbulence, was the height Z_i of the planetary boundary layer (about 1000m).

A. SINGLE SCALE SIMULATION

The first simulation uses only one size for turbules. This approach has already been described as ineffective in terms of predicting boom rise time distributions⁵, but was nonetheless used as a preliminary means of comparing spherical and ellipsoidal results. From (9), and considering that $\int_0^\infty n(s)ds = \frac{N}{V}$, one may obtain the strength for single scale turbulence:

$$q^2 = \frac{8}{\pi^{3/2}} \frac{V}{N} \frac{\langle \mu^2 \rangle}{L^3}, \quad (14)$$

where N is the total number of turbules in the simulation volume V . Simulations were run with different numbers N of turbules in a box shaped atmosphere. The number of turbules N was chosen from the simulation which provided the closest match to $\langle \mu^2 \rangle$ and $\langle \mu^4 \rangle$ determined from the JAPE-2 data. The simulation was then repeated many times (with the best N and aforementioned q); the rise time from each run was recorded as well as the output waveform. Rise time distributions and a sample output waveform for this calculation are found in figs. 5; a 5 m base radius (before stretching) was assumed for all turbules. The rise time distributions produced by the spherical and ellipsoidal simulations were similar, with a peak in the distribution around 1 ms (Again, note that this model is a preliminary benchmark, for sake of comparing ellipsoidal and spherical results). One significant result of this single scale simulation is the evidence of an angular rise time dependence. Comparing figs. 5c, 5e and 5g, one observes higher rise times when the approach angle is in a direction other than that of the mean wind. Another important observation are the short rise times predicted by all cases here. The predicted lower limit on rise times is somewhat compromised by the algorithm used to compute rise times from a waveform. That is, spikes in the waveform 'confused' the rise time algorithm. Because of these spikes, the rise time was calculated using the average slope between 10% and 90% of the maximum pressure, instead of the slope between 0.4 and 0.6 p_{max} . This did not really bias the results toward increased rise times, as the spikes were generally of short duration. In fact, some of these spikes may be non-physical, having characteristic frequencies considerably higher than the sampling frequency; spikes of more reasonable duration may be caused by large turbules whose center is on axis with the source and receiver. Future work will remedy this problem, as described later. An additional point worth mentioning concerns the number of total simulations. Due to computer time limitations, this single scale model was simulated 50 to 100 times (depending on which case) instead of the number originally intended (at least 500 times). This may cause some gaps in the rise time distributions, but does not significantly obscure the trends shown.

B. RANGE OF SCALE SIZES SIMULATION

This model used a von Karman spectrum fit to get $n(s)$ (equation 7). This spectrum was then used to determine the proportion of turbules of six different discrete sizes (centered in different non-overlapping ranges of scale size) to be placed into a box-shaped atmosphere. The 'top' of the box was again 1000m. The total range of sizes was from 1 to 300m, before stretching. As in the single scale model, a single q was chosen to match both the second and fourth moments of the index of refraction fluctuations. The total number of turbules in the box, or percent volume occupancy, was determined iteratively.¹⁶ Multiple simulations were run, each with the same turbule population proportions but with different total numbers of turbules. Averages of $\langle \mu^2 \rangle$ and $\langle \mu^4 \rangle$ were calculated along several vertical lines in the simulated box; the percent volume occupancy to be used in the model was chosen from the simulation which gave best agreement between measured and calculated $\langle \mu^2 \rangle$ and $\langle \mu^4 \rangle$. After the turbule strength and the number of turbules were chosen, multiple runs, or 'realizations,' for that atmospheric model were accomplished. A different random spatial eddy distribution was calculated for each realization (one realization may be thought of as a 'snapshot' of the atmosphere at an instant in

time). The output waveform and rise times of each realization were recorded. The distribution of predicted rise times from 500 realizations is given in figures 6 along with a sample waveform for one of the four different cases tested (all four produced similar waveforms). The histograms of rise time shown in figs. 6 show two interesting trends. The first is that a larger number of short rise times are predicted by the ellipsoidal model than by the spherical. This may be somewhat suspect, as the rise time algorithm used again was 'misled' by some spikes in the waveform. Inspection of individual waveforms verifies this. A second trend is the higher number of rise times above 2.5 ms produced in the ellipsoidal cases. A comparison between cross-wind and parallel to wind approaches shows that the cross-wind and off-angle cases may produce more rise times between 2 and 3 ms, which is the peak time range of the measured distribution. These results justified the development of a continuous scale size distribution model, offered in the following section.

C. CONTINUOUS SCALE SIZE (MONTE CARLO) DISTRIBUTION

This model utilizes the same method as the previous one to determine $n(s)$, but uses a continuous distribution of scale sizes. The assignment of eddy sizes follows from the method developed by Boulanger¹⁶ for spherical turbules. The turbules are assigned a radius using a Monte Carlo method, as well as random positions. They are then stretched (or compressed) using the previously mentioned stretching matrix. The sizes are assigned with the relation

$$s = (1 - Ran)^{-\frac{1}{3}}, \quad (15)$$

where Ran is a randomly generated number between 0 and one. This size distribution conforms to the previously calculated turbule size distribution (six scales); it is also derived from $n(s)$.

Instead of a single turbule strength being chosen, as in the above models, this model used a height dependent q^2 . The height dependence of q^2 was based upon the theoretical altitude dependence of the von Karman spectrum in the planetary boundary layer.⁵ This turbule strength can be summarized as

$$q^2(z) = \begin{cases} q^2(30), & z \leq 30m \\ q^2(30)(z/30)^{-4/3}, & 30 < z < Z_i/10 \\ q^2(30)(Z_i/10/30)^{-4/3} & z \geq Z_i/10 \end{cases} \quad (16)$$

where $q^2(30)$ is the strength at 30 m. The value for $q^2(30)$ was chosen using the same method as the two earlier models, matching $\langle u^2 \rangle$ and $\langle u^4 \rangle$.

The box shape used to simulate the atmosphere was replaced with a cylinder; this was done to reduce computing time. The volume of the cylinder is roughly the same as the boxes used in the earlier models. The number of turbules chosen to fill the cylinder used the same criteria as the previous model; i.e., the best percent volume occupancy to fit the measured variances was used.

Due to computing time constraints, only 50 realizations of the atmosphere were performed, instead of 500. As with the single scale model, this is due to the large number of turbules used in each simulation (over 138000 for this model). From the data obtained, several observations may still be made. An immediately noticeable trait of the rise time distributions (figs. 7) is that there are some gaps (see above statements). Another phenomenon noticed is a wider distribution in rise times. The upper limit of predicted rise times (fig. 8) is higher for the ellipsoidal cases than for the spherical case, around 15 ms. This agrees quite well with measured data (fig. 9: rise times measured using 10%-90% peak criteria), but the peak of the distribution seems to possibly be a bit too high. This peak depends on the angle between the mean wind and the T-38 velocity (approach direction), and seems to vary from 2 to 5 ms. This is promising, and would agree well with data taken using the 0.4 to 0.6 p_{max} criteria. As mentioned in earlier sections, a removal of or accounting for drastic spikes in the waveform would help clarify these rise time distributions and their interpretation, as would a larger number of simulations.

IV. CONCLUSIONS

The extension of existing spherical single scatter models of the turbulent atmosphere to allow for ellipsoidal turbules has produced promising results. The ellipsoidal turbulence generally results in a wider distribution in predicted rise times, conforming better to measured data. The distributions are limited, though in the number of tests which they represent. Gaps in the distributions will be remedied by continuing work which is producing a larger number of results. The lower limits on rise times in the distributions are somewhat suspect due to the presence of spikes in the waveform, and the limits of the algorithms used to compute the rise time. Future work will incorporate "smarter" rise time algorithms, as well as some correction of very short duration spikes via the use of the Anderson algorithm for the propagation between turbule and receiver.

The angular dependence of rise times displayed by the ellipsoidal model also appears promising. This dependence helps account more for fluctuations occurring in the measured data. Future work will investigate this angular dependence, with the production of more simulation results at different approach angles relative to the mean wind.

Additional work will focus on the size distributions and scales used, and their initial determination from meteorological data. The turbule sizes used in the ellipsoidal model were based on spherical size distributions; the ellipsoidal turbules were created by stretching a given sphere, depending upon the turbule altitude. The scale lengths used in the spherical modeling were, in turn, derived from correlation analyses of wind velocity in the direction of mean wind flow. Because the direction of mean wind flow is the direction of the major axis of ellipsoidal turbules (near the ground), it is apparent that the size and volume of turbules used in the spherical models was too large. In order to still fit von Karman spectra to the meteorological data, conservation of turbule volume which was adhered to, producing oversized ellipsoidal turbules as well. The overall effect of these larger volumes is a shift in turbule number density to higher sizes. Future work will investigate the scales of turbulence in directions other than the mean wind flow to better represent individual turbules.

APPENDIX: EVALUATION OF THE BORN SCATTERING INTEGRAL

The wave equation for an inhomogeneous medium having index of refraction fluctuations $|\mu| \ll 1$ can be converted into an integral equation for p :

$$p(\mathbf{r}) = p_0(\mathbf{r}) + 2k \int_V G(\mathbf{r} - \mathbf{r}') \mu(\mathbf{r}') p(\mathbf{r}') dV', \quad (A1)$$

with $\mu(\mathbf{r}) = \mu(x, y, z) = q_i e^{-(x/s_x)^2 - (y/s_y)^2 - (z/s_z)^2}$ and $G(\mathbf{r} - \mathbf{r}') = \frac{e^{ik|\mathbf{r} - \mathbf{r}'|}}{4\pi|\mathbf{r} - \mathbf{r}'|}$. These give us

$$p(\mathbf{r}) = p_0(\mathbf{r}) + \frac{q_i k^2}{2\pi} \int_V \frac{e^{ik|\mathbf{r} - \mathbf{r}'|}}{|\mathbf{r} - \mathbf{r}'|} e^{-(x/s_x)^2 - (y/s_y)^2 - (z/s_z)^2} p(\mathbf{r}') dx dy dz. \quad (A2)$$

The first Born approximation consists of replacing $p(\mathbf{r}')$ in the integral with $p_0(\mathbf{r}') = \frac{e^{ik|\mathbf{r}'|}}{|\mathbf{r}'|}$. Now we have

$$p(\mathbf{r}) = p_0(\mathbf{r}) + \frac{q_i k^2}{2\pi} \int_V \frac{e^{ik(|\mathbf{r} - \mathbf{r}'| + |\mathbf{r}'|)}}{|\mathbf{r}'||\mathbf{r} - \mathbf{r}'|} e^{-(x/s_x)^2 - (y/s_y)^2 - (z/s_z)^2} dx dy dz. \quad (A3)$$

We can safely approximate $|\mathbf{r}'||\mathbf{r} - \mathbf{r}'| \approx r_{st} r_{tr}$, and now we must express $|\mathbf{r} - \mathbf{r}'| + |\mathbf{r}'|$ in terms of x, y , and z . Since $|\mathbf{r}'| \approx r_{st}$ and $|\mathbf{r} - \mathbf{r}'| \approx r_{tr}$, we can expand around r_{st} and r_{tr} , respectively, by means of a Taylor expansion. Using $|\mathbf{r} - \mathbf{r}'| = \sqrt{(x_r - x)^2 + (y_r - y)^2 + (z_r - z)^2}$ and

$|\mathbf{r}'| = \sqrt{(x_s - x)^2 + (y_s - y)^2 + (z_s - z)^2}$, and taking derivatives, we have to second order:
 $|\mathbf{r} - \mathbf{r}'| + |\mathbf{r}'| = r_{st} + r_{tr} + A^2 x^2 + By + Cz - 2Dxy - 2Exz - 2Fyz - Gx - Hy - Iz$, (A4)

with $A^2 = \frac{Y_s^2 + Z_s^2}{2r_{st}^2} + \frac{Y_t^2 + Z_t^2}{2r_{tr}^2}$, $B^2 = \frac{X_s^2 + Z_s^2}{2r_{st}^2} + \frac{X_t^2 + Z_t^2}{2r_{tr}^2}$, $C^2 = \frac{X_s^2 + Y_s^2}{2r_{st}^2} + \frac{X_t^2 + Y_t^2}{2r_{tr}^2}$,
 $D = \frac{X_s + Y_s}{2r_{st}} + \frac{X_t + Y_t}{2r_{tr}}$, $E = \frac{X_s + Z_s}{2r_{st}} + \frac{X_t + Z_t}{2r_{tr}}$, $F = \frac{Y_s + Z_s}{2r_{st}} + \frac{Y_t + Z_t}{2r_{tr}}$, $G = \frac{X_s}{r_{st}} + \frac{X_t}{r_{tr}}$, $H = \frac{Y_s}{r_{st}} + \frac{Y_t}{r_{tr}}$, $I = \frac{Z_s}{r_{st}} + \frac{Z_t}{r_{tr}}$.

This gives us

$$\bar{\Psi}_1^B = \frac{k^2 q \sqrt{\pi}}{2} \frac{e^{ik(r_{st} + r_{tr})}}{r_{st} r_{tr} s_1 s_2 s_3} e^{-\frac{1}{4} C_{el} k^2 (s_1 s_2 s_3)^{-2}}, \quad (A5)$$

with $C_{el} = k^2 (2DEHI + 2DFGI + 2EFGH - (DI)^2 - (EH)^2 - (FG)^2) + 2ik(DGH\gamma^2 + EGI\beta^2 + FHI\alpha^2) - (G\beta\gamma)^2 - (H\alpha\gamma)^2 - (I\alpha\beta)^2$,

$$s_1 = \alpha, \quad s_2 = \sqrt{\beta^2 + (kD/s_1)^2}, \quad s_3 = \sqrt{\gamma^2 + k^2((E/s_1)^2 + (F/s_2)^2 - 2ikDEFs_1^2 s_2^2) - (k^2 DES_1^2 s_2^2)^2},$$

$$s_1 s_2 s_3 = \sqrt{(\alpha\beta\gamma)^2 + k^2((D\gamma)^2 + (E\beta)^2 + (F\alpha)^2 - 2ikDEF)}, \text{ and } \alpha = \sqrt{s_x^2 - ikA^2}, \quad \beta = \sqrt{s_y^2 - ikB^2}, \quad \gamma = \sqrt{s_z^2 - ikC^2}.$$

¹A. D. Pierce, "Statistical theory of atmospheric turbulence effects on sonic-boom rise times," J. Acoust. Soc. Am. **49**, 906-924 (1971).

²H. E. Bass, J. Ezell, and R. Raspet, "Effect of vibrational relaxation on rise times and shock waves in the atmosphere," J. Acoust. Soc. Am. **74**, 1514-1517 (1983).

³A. D. Pierce, "Molecular relaxation effects on sonic boom waveforms: A tutorial survey," J. Acoust. Soc. Am. **92**, 2329(A) (1992).

⁴B. W. Kennedy, R. O. Olsen, J. R. Fox, and G. M. Mitchler, "Joint Acoustic Propagation Experiment Project Summary," The Bionetic Corporations, Las Cruces, NM (September 1991).

⁵P. Boulanger, R. Raspet, and H.E. Bass, "Sonic boom propagation through a realistic turbulent atmosphere," J. Acoust. Soc. Am. **98**, 3412-3417 (1995).

⁶W. Wilken, "Experimental study of the influence of varying atmospheric conditions on sound propagation close to the ground," Acustica **62**, 55-65 (1986)

⁷W. Wilken, "Korrelation lokaler Schallpegelschwankungen bei der Scallausbreitung in der bodennahen Grenzschicht," Acustica **66**, 104-108 (1988).

⁸H. E. Cramer, "Measurements of turbulence structure near the ground within the frequency range from 0.5 to 0.1 cycles/sec," Adv. Geophys. **6**, 75-96 (1959).

⁹H. A. Panofsky, "Scale analysis of atmospheric turbulence at 2 m," Q. J. R. Meteorol. Soc. **88**, 57-69 (1962).

¹⁰D.A. de Wolf, "A random-motion model of fluctuations in a nearly transparent medium," Radio Sci. **18**(2), 138-142 (1975)

¹¹W.E. McBride, H.E. Bass, R. Raspet, and K.E. Gilbert, "Scattering of sound by atmospheric turbulence: A numerical simulation above a complex impedance boundary," J. Acoust. Soc. Am. **90**, 3314-3325 (1991).

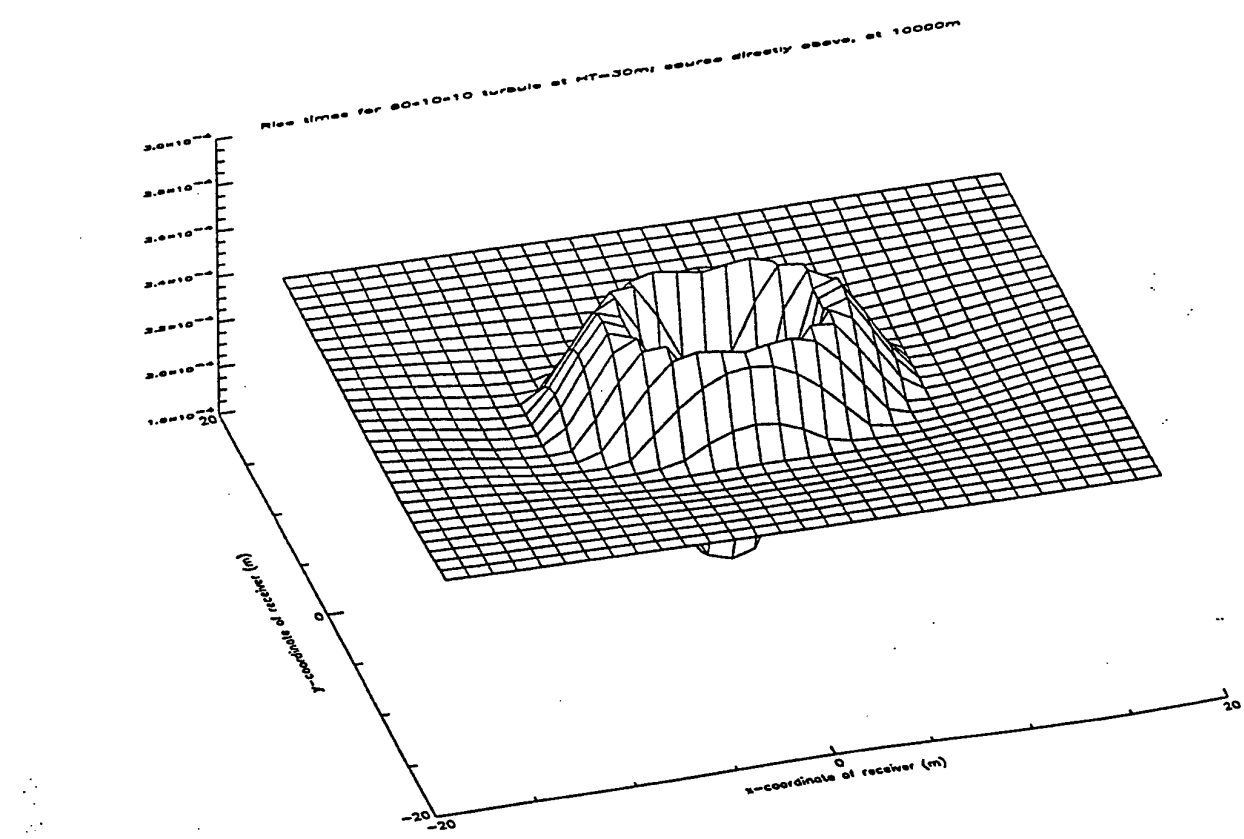
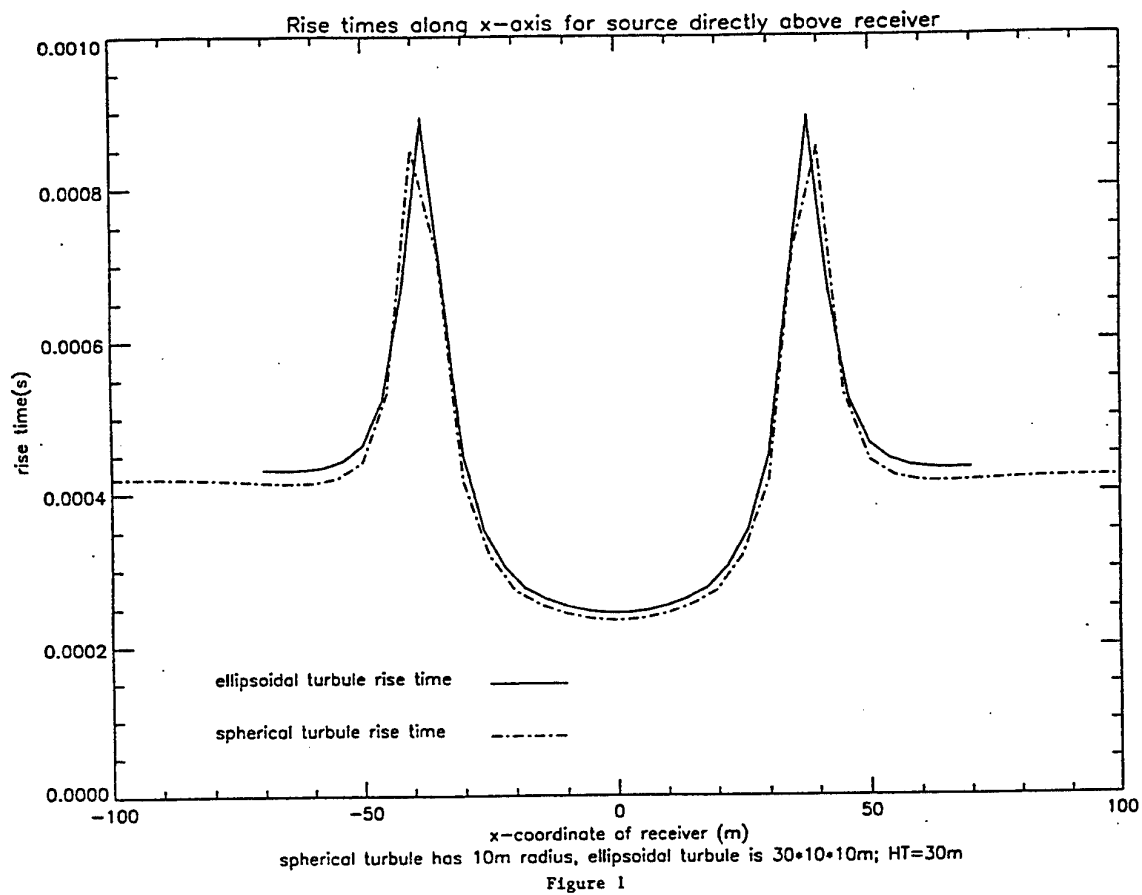
¹²W. L. Willshire, Jr., D. P. Garber, and D.W. deVilbiss, "The effect of turbulence on the propagation of sonic booms," Proceedings of the Fifth International Symposium on Long Range Sound Propagation, The Open University, Milton Keynes, England (May 1992).

¹³G. A. Daigle, J. E. Piercy, and T. F. W. Embleton, "Line-of-sight propagation through atmospheric turbulence near the ground," J. Acoust. Soc. Am. **74**, 1505-1513 (1983).

¹⁴D. K. Wilson, D. W. Thomson, "Acoustic propagation through anisotropic, surface-layer turbulence," J. Acoust. Soc. Am. **96**, 1080-1095 (1994).

¹⁵M. O. Anderson, "The propagation of a spherical N wave in an absorbing medium and its diffraction by a circular aperture," Appl. Res. Lab. Tech. Rep. No. 77-5 (ARL-TR-74-25), AD 787878 Applied Research Laboratories, The University of Texas, Austin, TX (August 1974).

¹⁶P. Boulanger, "Sonic boom propagation through a realistic turbulent atmosphere," Ph.D. thesis, Graduate Program in Physics, The University of Mississippi (1994).



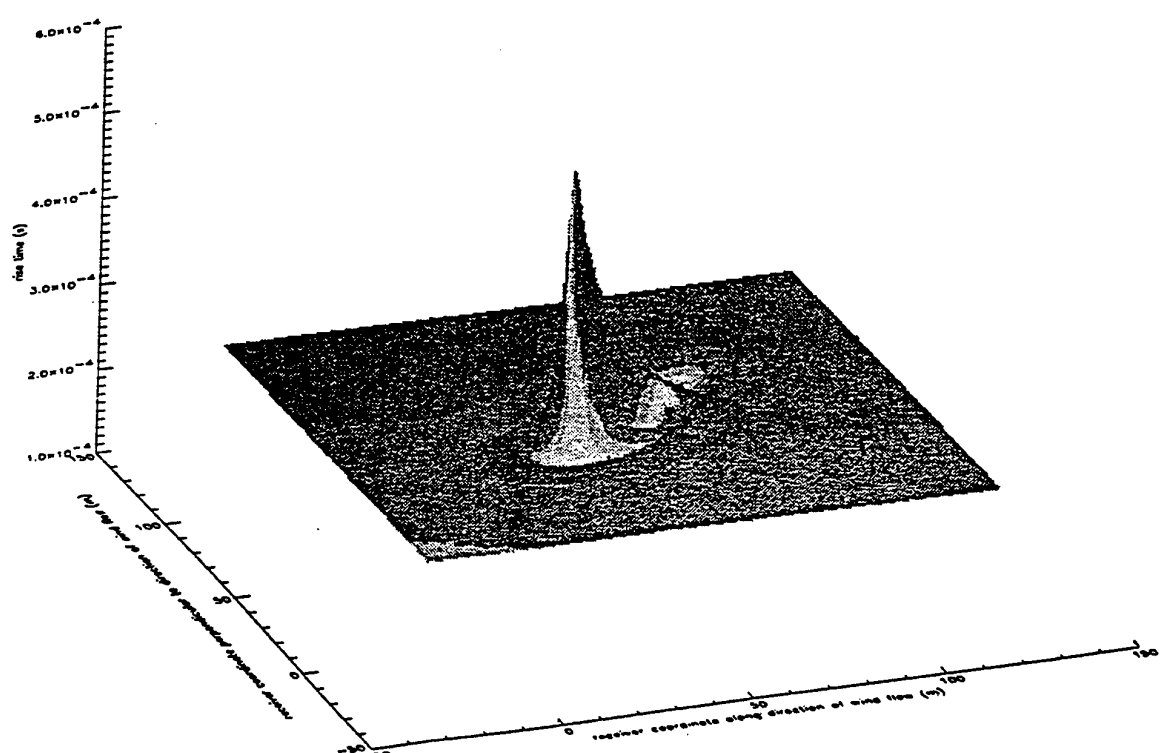
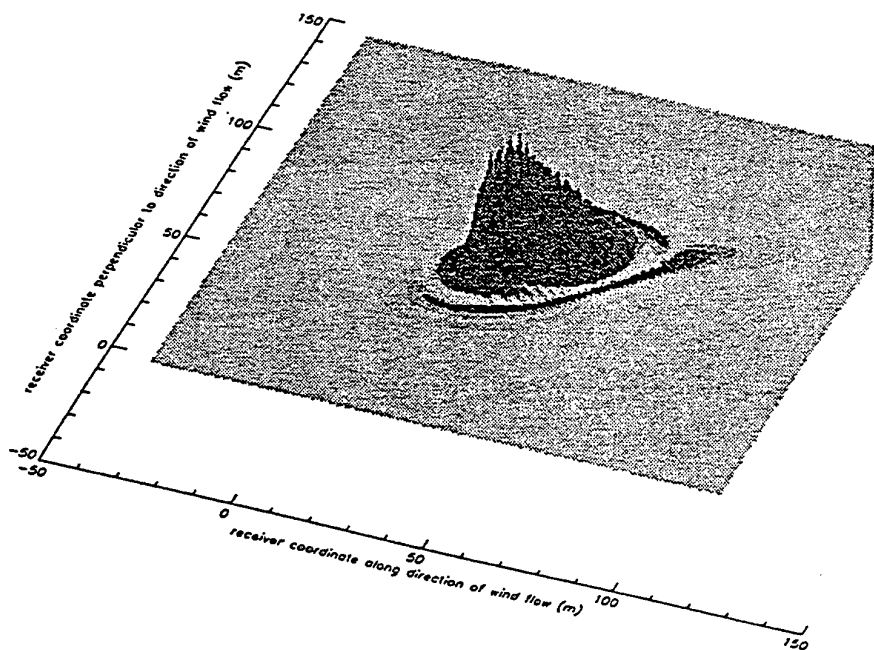


Figure 3. Rise times due to $30 \times 10 \times 10$ turbule. Source altitude is 10,000 m, turbule altitude is 30 m, and has a positive q . Mean wind is in x-direction; source is travelling at a 45° angle to mean wind.

Figure 5h. Output waveform, single scale: (5m) ellipsoidal simulation; wave approach perpendicular to mean wind.

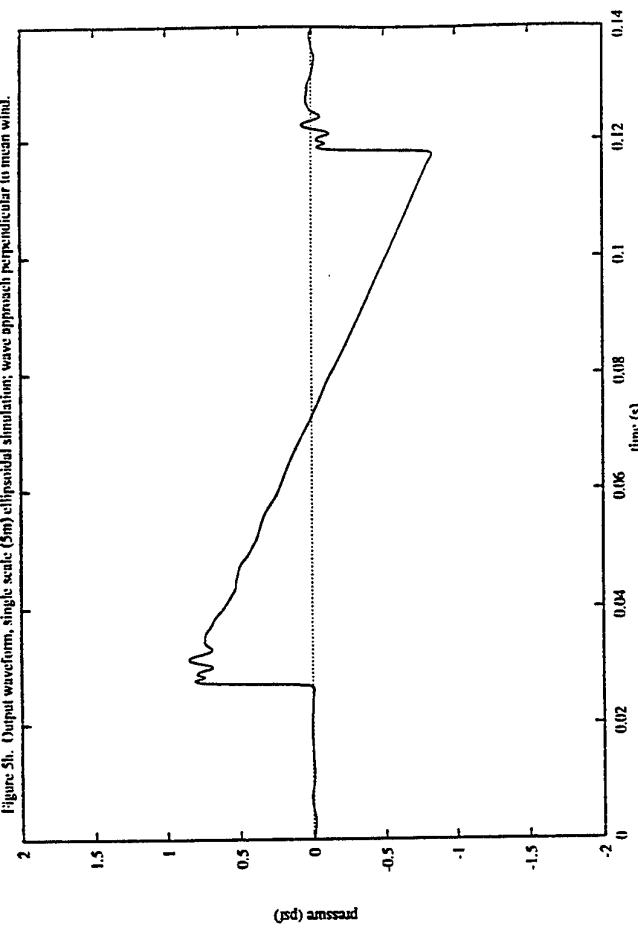


Figure 7h. Output waveform, ellipsoidal Monte Carlo model; wave approach perpendicular to mean wind.

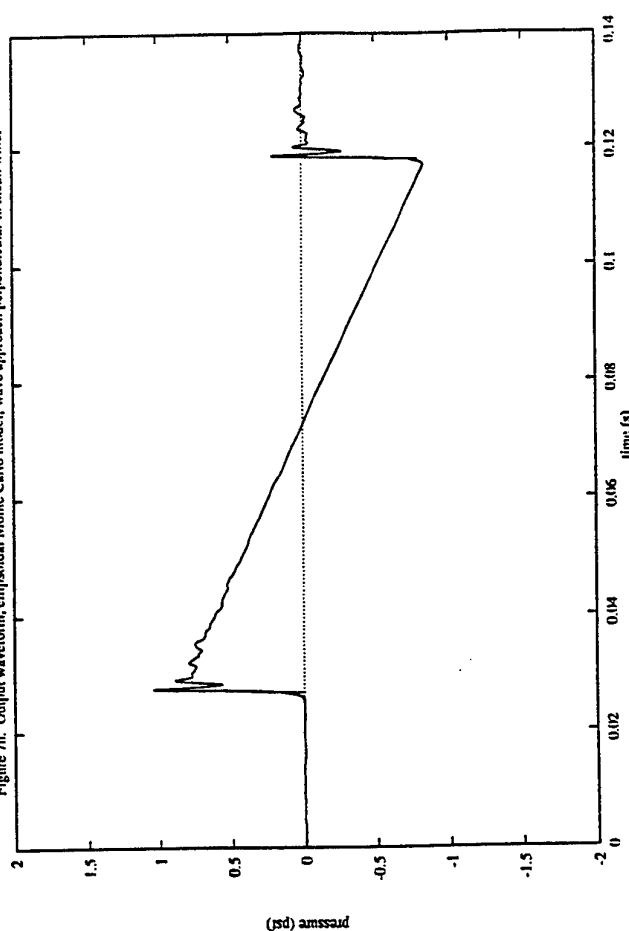


Figure 4. N-wave predicted by Anderson algorithm.

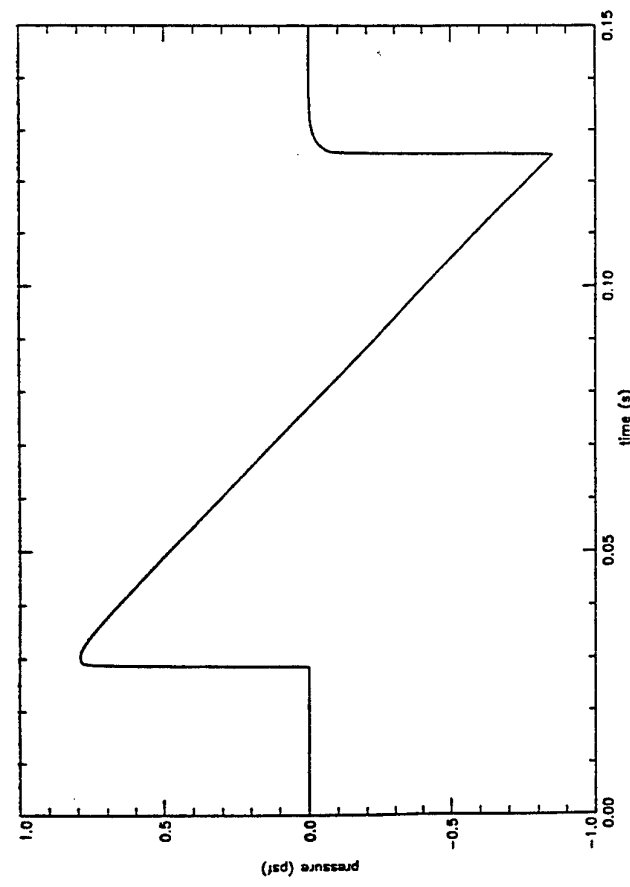


Figure 6h. Output waveform, ellipsoidal f-scale model; wave approach perpendicular to mean wind.

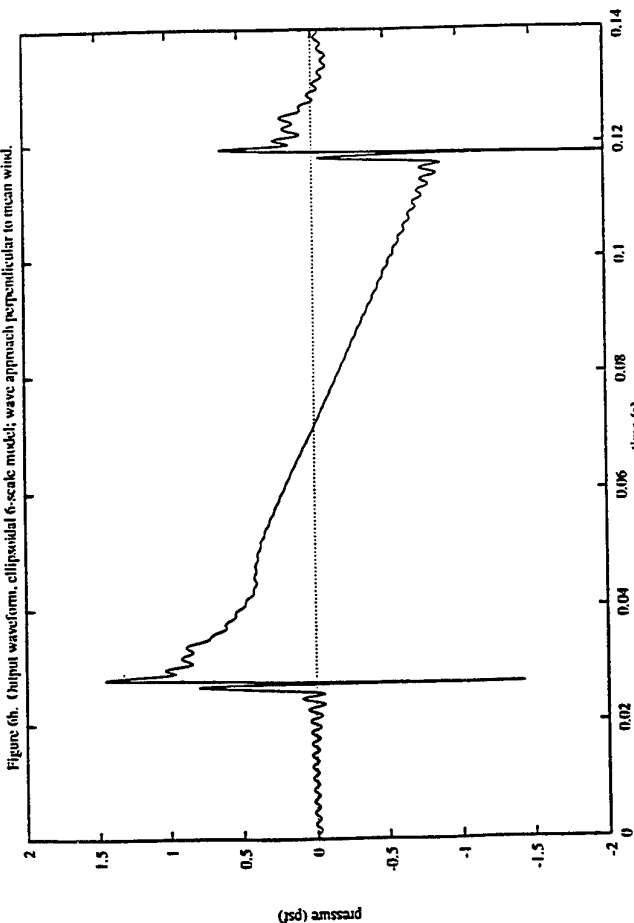


Figure 5c. Rise time distribution for single scale (5m) ellipsoidal model; wave approach at 45 deg. to mean wind.

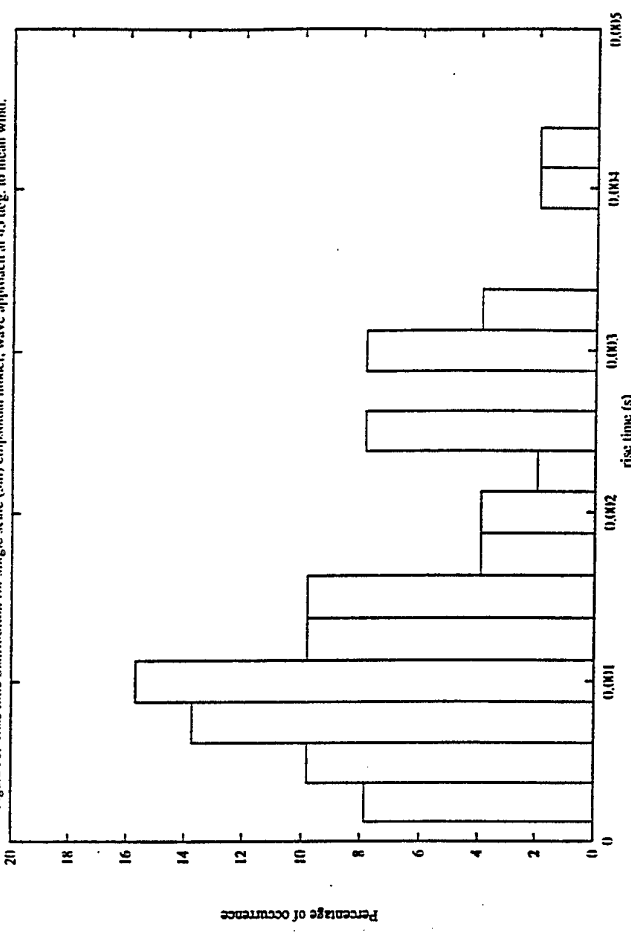


Figure 5g. Rise time distribution for single scale (5m) ellipsoidal model; wave approach perpendicular to mean wind.

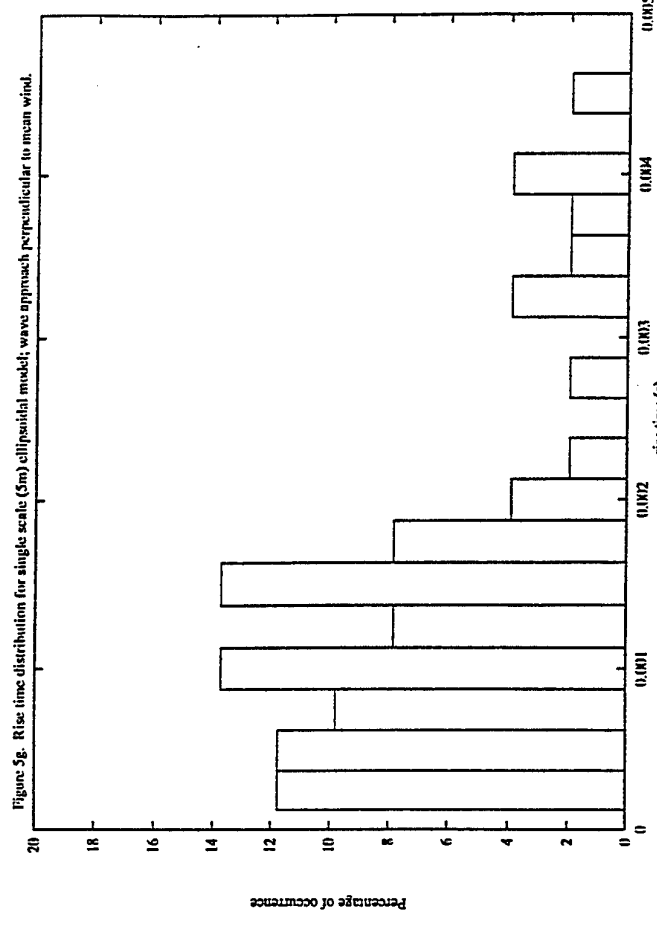


Figure 5a. Rise time distribution for single scale (5m) spherical model; wave approach perpendicular to mean wind.

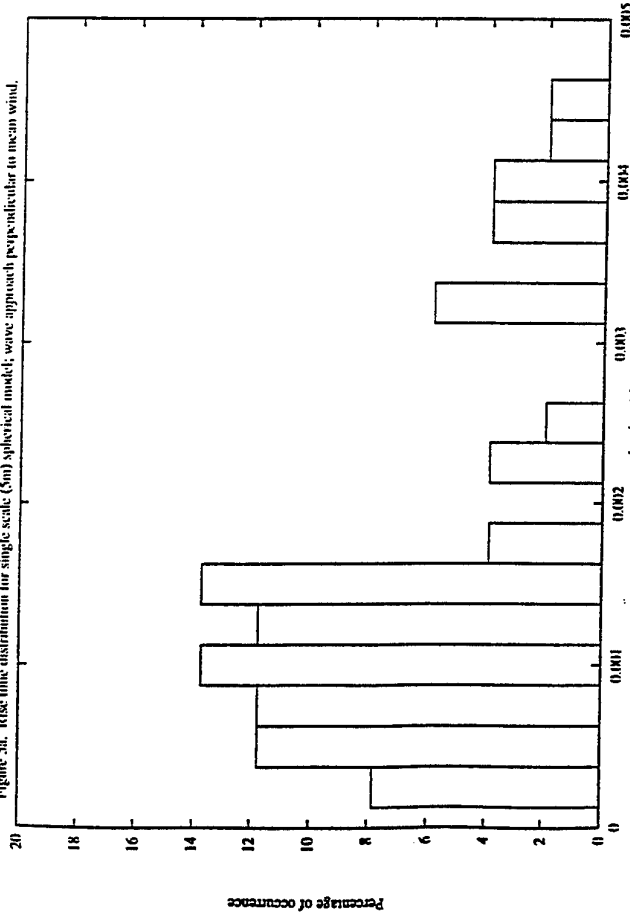


Figure 5c. Rise time distribution for single scale (5m) ellipsoidal model; wave approach parallel to mean wind.

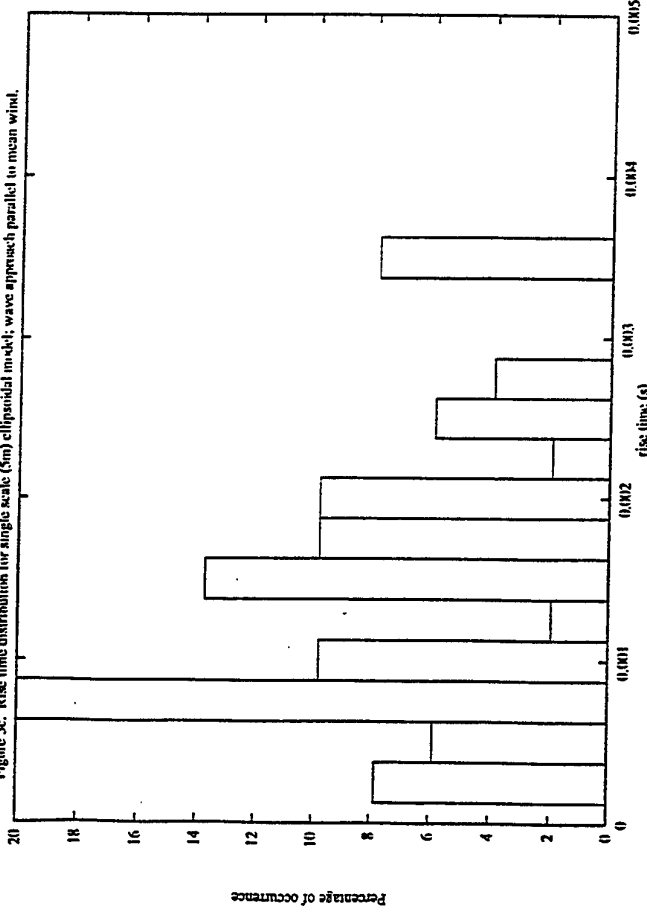


Figure 6c. Rise time distribution from ellipsoidal 6-scale model; wave approach parallel to mean wind.

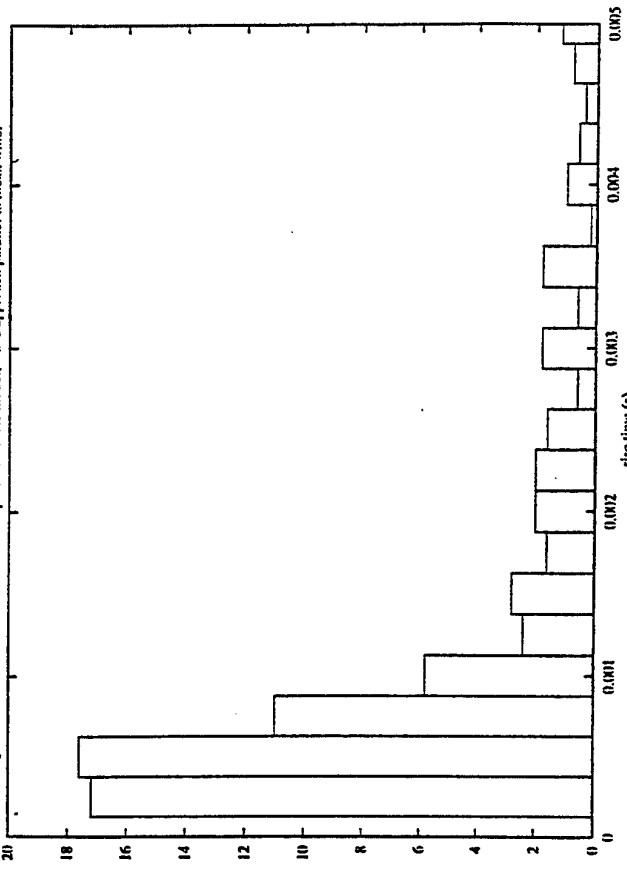


Figure 6a. Rise time distribution from spherical 6-scale model; wave approach perpendicular to mean wind.

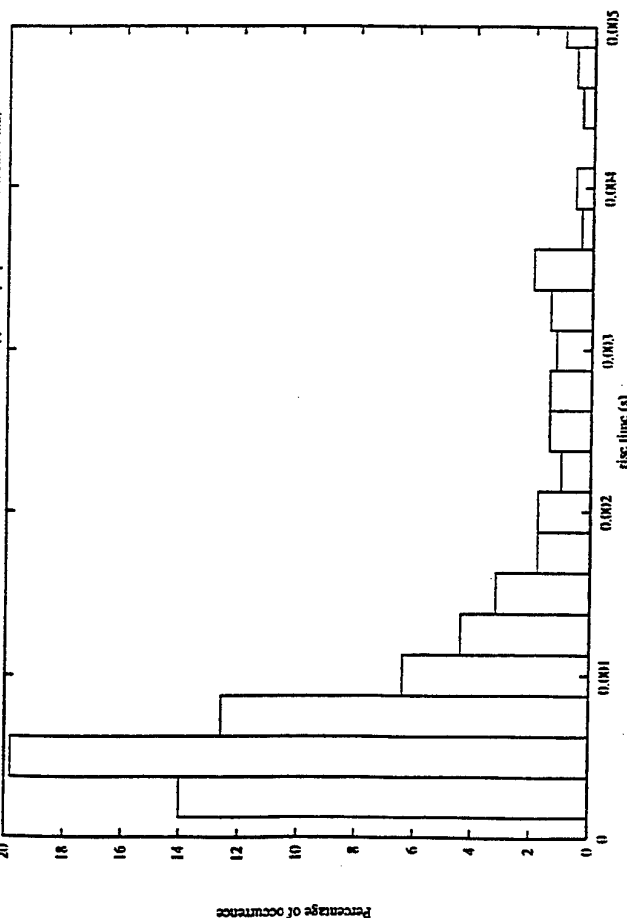


Figure 6b. Rise time distribution from ellipsoidal 6-scale model; wave approach perpendicular to mean wind.

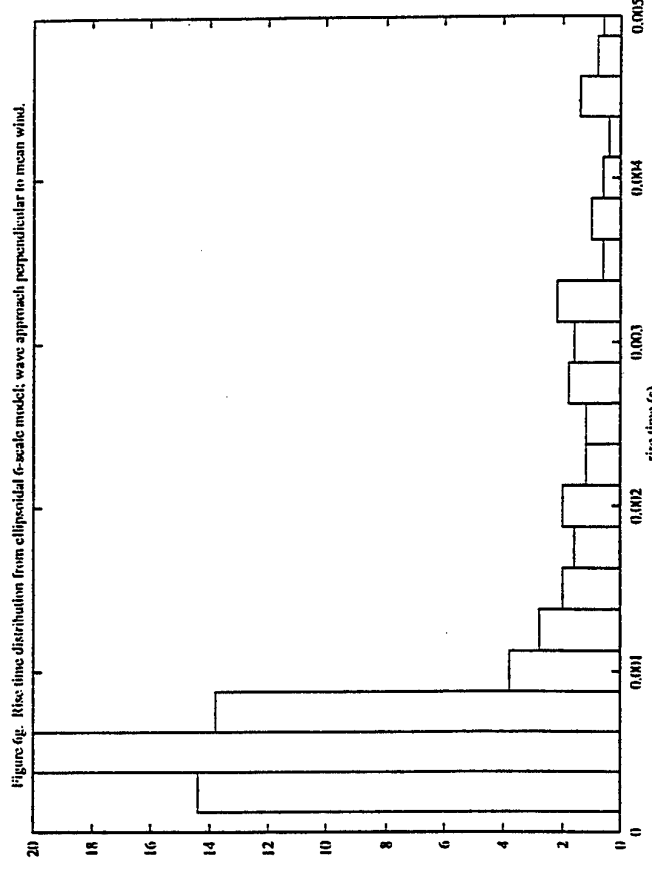


Figure 6c. Rise time distribution from ellipsoidal 6-scale model; wave approach @ 45 deg to mean wind.

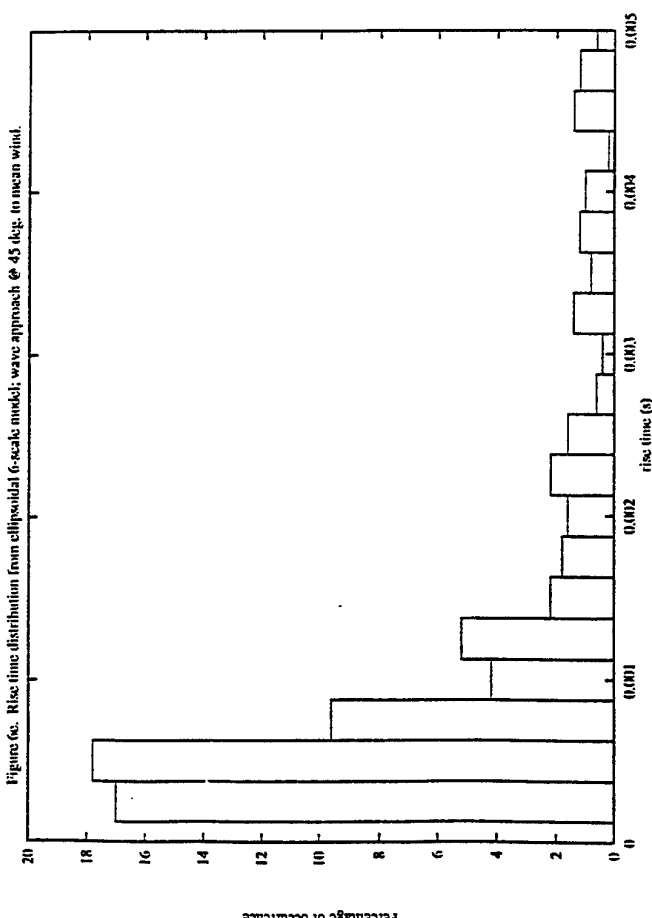


Figure 7e. Rise time distribution for ellipsoidal Monte Carlo model; wave approach parallel to mean wind.

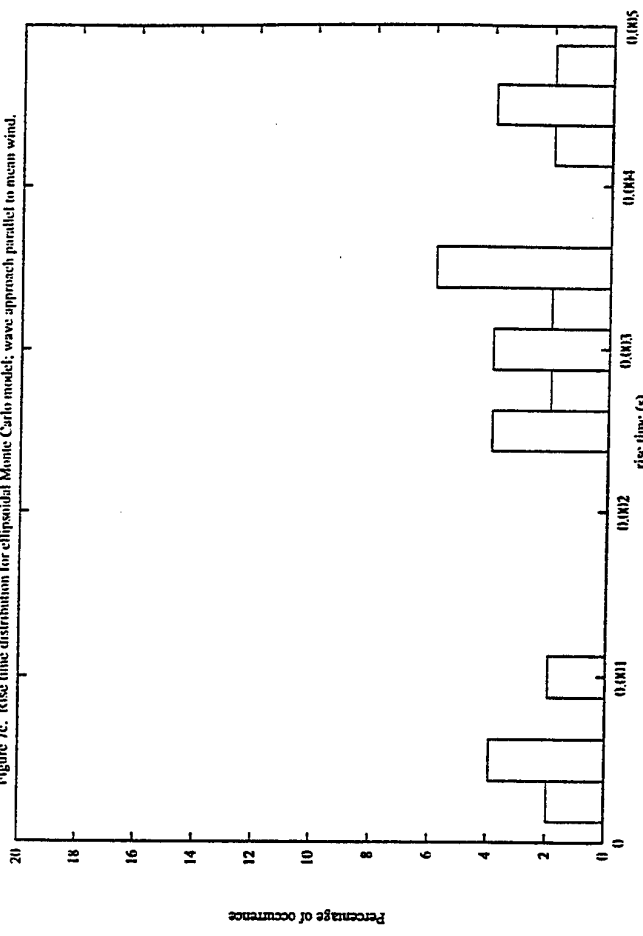


Figure 7e. Rise time distribution for ellipsoidal Monte Carlo model; wave approach parallel to mean wind.

Percentage of occurrences

20

18

16

14

12

10

8

6

4

2

0

Percentage of occurrences

20

18

16

14

12

10

8

6

4

2

0

0.1N1

0.1N2

0.1N3

0.1N4

1.0N1

1.0N2

1.0N3

1.0N4

2.0N1

2.0N2

2.0N3

2.0N4

3.0N1

3.0N2

3.0N3

3.0N4

4.0N1

4.0N2

4.0N3

4.0N4

5.0N1

5.0N2

5.0N3

5.0N4

6.0N1

6.0N2

6.0N3

6.0N4

7.0N1

7.0N2

7.0N3

7.0N4

8.0N1

8.0N2

8.0N3

8.0N4

9.0N1

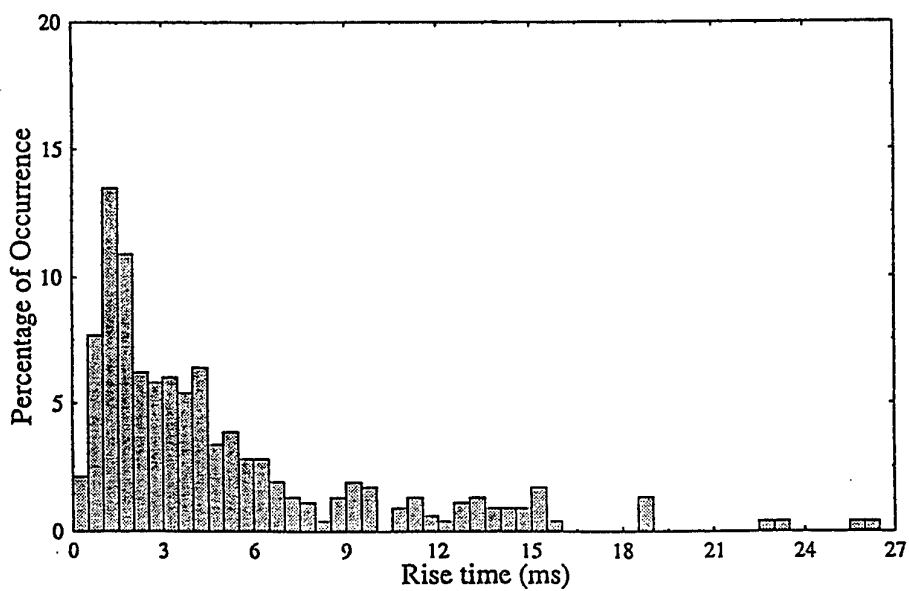
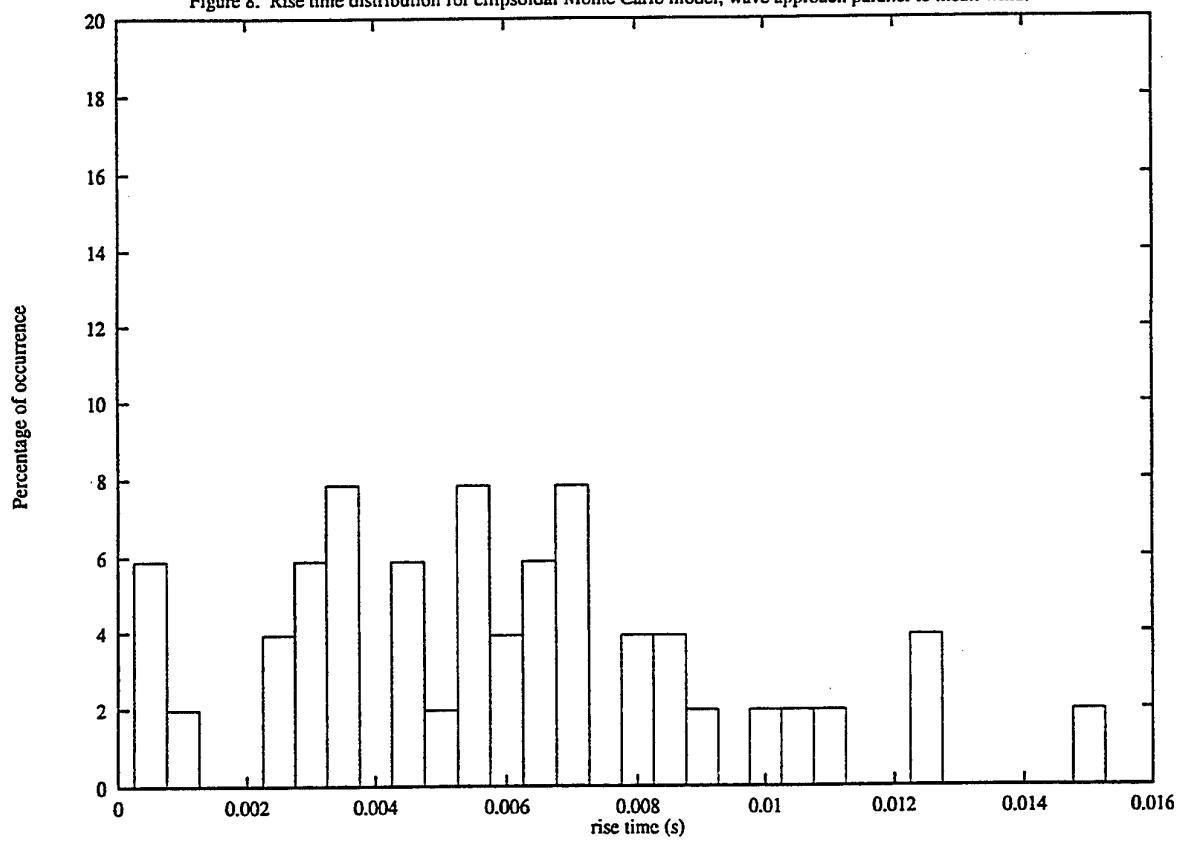
9.0N2

9.0N3

9.0N4

1

Figure 8. Rise time distribution for ellipsoidal Monte Carlo model; wave approach parallel to mean wind.

Figure 9. Measurement of a rise time distribution for the T-38 aircraft using the points $0.1 p_{\max}$ and $0.9 p_{\max}$ (low turbulence case).

**DESCRIPTION of ACOUSTICAL CHANNELS
LINEAR and NONLINEAR APPROXIMATE METHODS**

R. Burvigt

THOMSON-CSF APPLICATIONS RADAR

6 rue Nieuport - B.P 86 - 78143 VELIZY-VILLACOUBLAY CEDEX

1 INTRODUCTION

For description of acoustical channels, computations methods are here mentioned. The first one is based on the use of LUDWIG uniform asymptotic developments [1] and allows field evaluations in caustic vicinities. Since the field is expressed with the help of geometrical optics solution, this later shall be defined in shadow areas by taking into account complex rays. These complex rays are analytical prolongations of the usual real rays. For being able to perform these prolongations, approximate analytical expressions for the rays are introduced [2].

One also evocates an alternative computing principle which is derived from consideration of a modified geometrical optics. A somewhat different eikonal equation can be employed at the first step of the asymptotic development.

Considering nearly progressive waves and nonlinear effects, the method in which a nonlinear functional can be taken into account for propagation descriptions in an inhomogeneous medium.

These methods were formulated for underwater acoustics. They could be transposed to atmospheric sound studies. They are in great part analytical and manageable numerically.

2 USE OF LUDWIG DEVELOPMENTS

2.1. Method principle

The Ludwig's uniform asymptotic developments [1] are considered for the description of underwater channels. The field is then formulated with the help of an integral which is derived from geometrical optics solutions.

Directive point sources and range independent channels are considered here.

By taking into account the results of [1] Helmholtz solution can be written as :

$$u = \int_C G(\vec{x}, \zeta, k) e^{ik\varphi(\vec{x}, \zeta)} d\zeta \quad (1)$$

where, if n rays are passing at the observation point, φ and G are respectively polynomial of order $n + 1$ and $n - 1$. The values of φ at the saddle points of (1) form a set which is identical, versus permutations, with the set of geometrical optics phase values associated with the n rays. C is an integration contour.

We write :

$$\varphi(\vec{x}, \zeta) = \varphi_o(\vec{x}) + \sum_{l=1}^{n-1} (-1)^l \frac{\zeta^l}{l} \varphi_l(\vec{x}) + (-1)^n \frac{\zeta^{n+1}}{n+1} \quad (2-1)$$

$$G(\vec{x}, \zeta, k) = \sum_{l=0}^{n-1} G_l(\vec{x}, k) \zeta^l \quad (2-2)$$

In (2-2) G_n are k decending power series.

The approximation that consists of keeping just the first term of this series is retained here.

Then :

$$G \approx g(\vec{x}, \zeta) = \sum_{l=0}^{n-1} g_n(\vec{x}) \zeta^l \quad (3)$$

From this approximation (3) one obtains approached values for the field u which do not diverge at the caustics (cf [1,2]) and appear to estimate precisely this field when $k \gg 1$. u is depending upon the coefficients ϕ_0, ρ_l et g_l . These laters satisfy the relations :

$$\varphi(\vec{x}, \zeta_n) = \phi_n \quad (4-1)$$

$$\frac{\partial \varphi}{\partial \zeta}(\vec{x}, \zeta = \zeta_n) = 0 \quad (4-2)$$

$$g(\vec{x}, \zeta_n) = \sqrt{\varphi_{\zeta\zeta}(\vec{x}, \zeta_n)} A_n \quad (5)$$

where ϕ_n and A_n are respectively the phase and the amplitude associated with one ray (number n).

We know how to solve the system (4) when $1 \leq n \leq 3$. It will be shown in the following that computations can be performed when $n > 3$.

Evaluations of u consist in the developments that are effectuated in two steps.

First a determination of geometrical optics solutions is needed. These solutions will be taken into account in the illuminated areas and also in the shadow areas under the form of an analytical prolongation. This prolongation correspond to complex rays which are emitted on the source under complex angles.

Determination of these complex angles can practically be done if the geometrical optics solutions are analytically derived.

When the index profil is arbitrary, an approached form for this kind of solution can be introduced by considering Fourier series.

Rays being calculated at every points (real and complex rays), in a second time an evaluation of the field can be developed with the help of incomplet functions.

2.2. Rays expressed in terms of FOURIER series

We consider a set of discret values θ_i ef θ . The depth of a ray emited under a given angle θ_i can be, versus the range dependant variable r , written as :

$$z = \sum_{m=0}^M A_{i,m} \cos m(\omega_i r + l_i)$$

Here the coefficients $A_{i,m}$ ω_i and l_i can be computed after having for example, represented the index profil as a sum of small segments where the index is approximatevely a linear function of z .

At each θ_i corespond values $A_{i,m}$, ω_i and l_i . It is possible to build functions $A_m(\theta)$, $\omega(\theta)$ and $l(\theta)$ (with for example the help of the least square method) which take approximatively the $A_{i,m}$, ω_i and l_i values for $\theta = \theta_i$ and interpolation values for $\theta_i < \theta < \theta_{i+1}$.

Then for every θ it is possible to track rays by taking into account the expression :

$$z = \sum_{m=0}^M A_m(\theta) \cos m(\omega(\theta) r + l(\theta)) \quad (6)$$

It was shown that (6) can be used for an accurate representation of rays when realist undersea index profil are retained.

This expression (6) is analytical in θ . It can be employed in an analytical prolongation for complex values of θ .

At a point (r, z) a θ complex value which satisfy (6) correspond to a complex ray. Then (6) can then be used in the determination of these complex rays in shadow areas of caustics. Thereafter values of ϕ_i and A_i figuring in (4-1) and (5) can be derived for points in these areas.

2.3 Field expression in terms of incomplet functions

Concerning the integration contour in (1) can be chosen as the real axis in the ζ complex plan. To a real ray can be associated a real saddle point and, to a couple of complex saddle points, an inflexion point of $\phi(\zeta)$ whens $(\zeta \in \mathbb{R})$. This real axis can be cut into several intervals each of which containing (i) one, two or three saddle points or (ii) one saddle point and one inflexion point or (iii) one inflexion point.

There is a slight degree at freedom in the definition of these intervals.

This consideration allows to write down the field u as :

$$u = \sum_{p=1}^P u_p$$

where p is the interval number ($p = 1, \dots, P$).

Terms u_p can be expressed with (i) Fresnel functions (one saddle point belongs to the interval p) (ii) incomplet Airy function (two saddle points or one inflexion point exist) (iii) incomplet pearcey function (three saddle points or one saddle point and one inflexion point exist).

The incomplet functions are introduced after changing the integration variable and performing approximations of small importance versus the amplitude term

$$g(\vec{x}, \zeta)$$

3 ALTERNATIVE METHOD FOR DESCRIBING CAUSTICS VICINITIES IN CHANNELS - MODIFIED GEOMETRICAL OPTICS -

3.1 Generalities

A method which consist in a modification of geometrical optics can be also taken into account for describing acoustical channels. In this method a somewhat different eikonal equation is considered at first stage of asymptotic development. It allows caustics vicinities descriptions. This method looks like the perturbation method for rays presented in [3] but the computational principle differs here. Geometrical optics developments allow to construct asymptotic evaluation of Helmholtz equation solution on points where are passing rays defined from eikonal equation.

These developments can indeed only be used in illuminated regions of space (or far from the caustic in the shadow areas when complex rays are retained) and they fail near caustics.

Rays constitute curvilinear axis along which field description can be elaborated at high frequencies. One may attempt to formulate similar developments on different curvilinear axis than those derived from the classical geometrical optics (CGO). This way for deriving mathematical developments has already been effectuated by some authors.

Michaeli [4] for example takes into account a particular curvilinear coordinates system for elaborating diffraction description on convex objects. These coordinates are linked to the shape of the diffracting surface. Here we point out another way in the determination of curvilinear system. The chosen systems of coordinates present a slight difference from those of CGO. Analysis mentioned in the following concerns propagation effects in acoustical channels. It could be extended to acoustical diffusion but a mention of that will be done in the future.

Asymptotic developments of the CGO type are considered here but in the first stage a different eikonal equation is retained which makes them different. We formulate rays existing in CGO shadow areas and asymptotic computation principle. It is supposed here that the acoustical field can be described with the help of the following two dimensional Helmholtz equation :

$$\frac{\partial^2 u}{\partial r^2} + \frac{1}{r} \frac{\partial u}{\partial r} + \frac{\partial^2 u}{\partial z^2} + k^2 n^2(r, z) u = 0 ,$$

where k is a reference wave number which can be large, r and z are respectively the horizontal and vertical coordinates, $n^2(r, z)$ is the squared index by which an acoustical channel can exist.

We suppose that sound is generated by a point source situated in the channel.

3.2 Formal developments derived by considering a modified eikonal equation.

The geometrical optics asymptotic solution is obtained by writing :

$$u = e^{ik\varphi} \sum_{n=0}^N g_n(r, z) \frac{1}{k^n} \quad (7)$$

where $N \geq 0$ and the phase φ is solution of eikonal equation :

$$\vec{\nabla}\varphi^2 = n^2(r, z), \quad (8)$$

and $g_n(r, z)$ satisfy the transport equations :

$$2\vec{\nabla}\varphi \cdot \vec{\nabla}g_n + \nabla\varphi g_n = \frac{i}{k} \nabla g_{n-1} \quad (9)$$

with $g_{-1} = 0$ and $n = 0, \dots, N$

Instead of (8), the following modified equation can be used :

$$\vec{\nabla}^2\varphi = n^2(r, z) + \frac{1}{k^\mu} \eta(r, z) \quad (10)$$

where $\mu > 0$ and η is a function whose choice determinates the shape of modified rays ($\eta = 0$ (1)). Indication about possible choices will be given otherwise. (10) being taken into account we can obtain the new transport equations :

$$2 \frac{\partial g_n}{\partial \sigma} + (\Delta\varphi + ik^{1-\mu}\eta) g_n = \frac{i}{k} \Delta g_{n-1} \quad (11)$$

Here σ is a curvilinear coordinate along the rays determined from (10) ($\sigma = 0$ on the point source).

By choosing : $\mu = \frac{1}{3}$, and :

$$v_1 = \int_0^\sigma \eta d\sigma, \quad v_2 = \int_0^\sigma \vec{\nabla}^2 v_1 d\sigma \quad (12-1)$$

$$\zeta_1 = i(\vec{\nabla}v_1 \cdot \vec{\nabla}v_2 - \frac{1}{k^{1/3}} \vec{\nabla}^2 v_2 - \frac{1}{k^{1/3}} \Delta v_1 - \frac{1}{k^{2/3}} \Delta v_2) \quad (12-2)$$

$$\zeta_2 = v_1 + \frac{1}{k^{1/3}} v_2 \quad (12-3)$$

$$g_n = e^{\frac{-ik^{2/3}\zeta_2}{2}} l_n(x, z) \quad (12-4)$$

Equations (11) leads to following equations :

$$2 \frac{\partial l_n}{\partial \sigma} + (\Delta \varphi + \zeta_1) l_n - \frac{1}{k^{1/3}} \vec{\nabla} \zeta_2 \cdot \vec{\nabla} l_n = \frac{i}{k} \Delta l_{n-1} \quad (13)$$

where k does figure with a negative exponent.

Transport equations (13) can be more suitable than (11) for performing approached computations when $k \gg 1$. Terms which depend upon k are small if the computed points do not reside near the new caustics. If (10) and (13) are solved, asymptotic development for u can be written as :

$$u = e^{ik\varphi - ik^{2/3}\zeta_2} \sum_{n=0}^N l_n \frac{1}{k^n} \quad (14)$$

IF the choice of η in (10) determinates rays passing in CGO shadow areas, (14) gives approximated values for the field on points belonging to these areas.

For simplifying the discussion a range independant channel is now considered. The index is then only depending upon z . This kind of channel does exist when the function $n^2(z)$ admits at least one maximum versus z .

The point source being situated in the channel, rays emitted on it, are periodic curves which form caustics.

A convenient description seems to be possible if, after retaining as previously

$\mu = \frac{1}{3}$ the function η appearing in (10) is noted as :

$$\eta(x, z) = k^{1/3} (n^2(z + \frac{\alpha}{k^{1/3}}) - n^2(z)) + \beta x \quad (15)$$

It can be shown, that, taking (15) into account, the modified rays (calculated from (5)) may be deduced from CGO rays by one vertical translation and one horizontal shift (shift directions are depending upon the sign of α and β). After obtaining shifted rays, caustics appear also shifted.

In fact, present development is an algorithm choice. A somewhat arbitrariness resides in the choice of η but it allows computations at given points. It influences the algorithm convergence but computations results will not depend upon it precisely. In these computations, the approximate analytical expressions for rays in term of Fourier series previously presented can be employed if (15) is retained.

Caustics vicinities are problematic when easy computations are wanted in field descriptions.

Methods do exist, but we point out here an alternative way for computing the field which could be advantageous.

4 ON NONLINEAR PROPAGATION

When considering slightly inhomogeneous fluids at rest, small acoustical Mach numbers (M) and nearly progressive waves, it was shown [5] that the nonlinear wave equation :

$$\begin{aligned} \varphi_{tt} - c^2 \Delta \varphi + \beta \frac{\partial}{\partial t} (\varphi_t^2) + \zeta \frac{\partial}{\partial t} (\varphi_t^3) = \\ \mu \varphi_{ttt} + \mu' \varphi_{tttt} + \mu'' \frac{\partial^2}{\partial t^2} (\varphi_t^2) + \mu''' \varphi_{ttt}^2 + O(M\varepsilon_d) \end{aligned} \quad (16)$$

can be derived. Here : $\beta = O(M)$; μ is a relevant dissipation effects number (β/μ is the Gol'dberg number), $\zeta = O(M^2)$, $\mu' = O(\mu^2)$, $\mu'' = O(M\mu)$, $\mu''' = O(M\mu)$, ε_d scales the beam divergence. We assumed that terms of magnitude up to $(|\nabla c| M)$ can be neglected. If $c = 1$ and $\zeta = \mu' = \mu'' = \mu''' = 0$, (16) is similar to the KUZNETSOV equation [6].

This last equation is relative to irrotational fluid movements.

In temporal cases analytical calculus can be developed by introduction of the non linear functional :

$$F_1 = - \frac{1}{ib} \int_0^\infty e^{-pt} (e^{-ib\varphi_t} - 1) dt, \quad (17)$$

where real $(p) > 0$ and $b \in \mathbb{R}$.

Then if F_1 is calculated, φ is obtained as :

$$\varphi = L^{-1} \left(\frac{1}{p} F_1(b=0, p) \right) \quad (18)$$

where L^{-1} represents an inverse Laplace transform application ($p \rightarrow t$).

In fact, If at $t=0$: $\varphi_t = \varphi_{tt} = \varphi_{ttt} = 0$, it can be shown [1] that F_1 verifies the equation (when : $\mu' \approx 0, \mu'' \approx 0, \mu''' \approx 0$) :

$$(p^2 - \mu p^3) F_1 - c^2 \Delta F + 2i\beta p^2 \frac{\partial F_1}{\partial b} - 3\zeta p^2 \frac{\partial^2 F_1}{\partial b^2} = ibH \quad (19)$$

with $H = 0(\gamma) + 0(\mu) + 0(\varepsilon_d)$.

In this new equation, partial derivatives approximate the nonlinearities.

This new method is up to now not well achieved and not far tested.

CONCLUSION

Three methods concerning propagation effects descriptions have been described here. In the first one, which is the most achieved, the Ludwig developments are used. The principle of the second indicates easy computation possibilities for caustics vicinities descriptions. About nonlinear effects we indicate that linear differential forms can be taken into account.

These methods specially initialized for underwater acoustical propagation can be extended to other domains such as aero acoustics and radiowave for example.

REFERENCES

- [1] D. LUDWIG, "Uniform Asymptotic Expansions at a caustic", Comm. Pure Appl. Math. 19 (1966) 215 - 250.
- [2] R. BURVINGT, "Formulation du champ dans un chenal acoustique sous-marin à l'aide des développements de LUDWIG", 3rd French Congrès on acoustics, journal de physique, (C.5 - 1133 / 1994).
- [3] Yu..A. KRAVTSOV, Yu. I. ORLOV, "Geometrical Optics of inhomogeneous media", Springer-Verlag (1990).
- [4] MICHAELI A. (1993) "High-Frequency Electromagnetic Fields Near a Smooth Convex Surface in the Shadow Region", Journal of Electromagnetic Waves and Applications, Vol. 7, No 4, 533-546.
- [5] R. BURVINGT, "Transformation in an approximate linear form of a nonlinear third order equation for nearly progressive waves", 13^e ISNA (BERGEN), Advances in nonlinear acoustics, World Scientific.
- [6] V.P. KUZNETSOV, Equations of nonlinear acoustics, Sov. Phys. Acoust. 16 (1971) 467-470.

Computational models

Towards a Multiazimuth Field Prediction Algorithm Based on a New Fast PE which Includes Turbulence

M. WEST

*The Telford Institute of Acoustics, Department of Acoustics
and Audio Engineering, University of Salford, Salford M5 4WT, UK*

1. Introduction

There is an urgent requirement for a reliable field prediction model for use on UK military test ranges. The model should be capable of producing peak SPL contours out to 30 km for an explosive source, the calculation being completed within a few minutes. Firing would be curtailed if the contours show there is a risk of creating noise levels at dwellings which would be expected to provoke complaint.

Currently a ray based "hybrid" model¹ is in use at most UK ranges. This model includes algorithms which give approximate peak SPL predictions when there is a full or partial shadow zone present (and hence no ray information). These algorithms were derived from measured data together with parameterised predictions obtained with our Crank-Nicholson parabolic equation (CN-PE) model.² The CN-PE model though reliable and robust runs far too slowly on a desk top PC to be capable of meeting the above requirement.

The PE model is however ideal for the above purpose since it can take proper account of

ground reflection
meteorological refraction and
atmospheric turbulence

because of its use of a range dependent solution procedure. We therefore require a very fast PE (or PE like) algorithm. The Green's Function 'PE' (GF-PE³) was the first algorithm of this type offering a very high speed range dependent solution. Typically the GF-PE runs two orders faster than the CN-PE. Unfortunately there is a "cost" in terms of greatly increased numerical errors at the low frequencies of interest here [10 - 50 Hz]. At higher frequencies the GF-PE's errors are much smaller and lie within the bounds of acceptability.

In order to produce a fast PE we need to be able to use range steps typically 2 orders greater than the $\lambda/5$ of the CN-PE (20λ). This can only be done if errors implicit in the CN-PE formulation can be minimised. Leaving aside the errors stemming from the choice of starter and choice and implementation of upper and lower boundary conditions, which are common to all PE models, the main causes of error are

- (i) errors resulting from the paraxial approximation
- (ii) errors from discrete x
- (iii) errors from discrete z

Other PE's⁴ have attempted to reduce *some but not all* of these errors. The LP-PE⁵ was the first to attempt to simultaneously reduce all of these errors to very small values. The LP-PE is used as the "engine" for our multiazimuth program. In this paper the emphasis is on the implementation of the multiazimuth program - a short review of the LP-PE model is presented first.

2. The LP-PE

We follow the procedure used in reference 5 of factorizing the potential Ψ into a rapidly varying exponential carrier and a slowly varying modulator, φ

$$\Psi(x, z) = e^{ik_0 x} \varphi(x, z) \quad (1)$$

k_0 is a reference wavenumber.

Substitution of Ψ into the 2D Helmholtz equation gives the "Modulator Wave Equation (MWE)"

$$\frac{\partial^2 \varphi}{\partial x^2} + P \frac{\partial \varphi}{\partial x} + R \varphi = 0 \quad (2)$$

with

$$P = 2ik_0, \quad R = \frac{\partial^2}{\partial z^2} - k_0^2 + k^2 \quad (3)$$

Rewriting (2) with the operator $\partial/\partial x$ treated as scalar λ

$$\lambda \varphi = (b + \epsilon \lambda^2) \varphi \quad (4a)$$

$$\text{or} \quad \lambda = b + \epsilon \lambda^2 \quad (4b)$$

$$\text{with} \quad \epsilon = -1/P \quad (4c)$$

Note that we do not attempt to remove the term $\partial^2 \varphi / \partial z^2$ or even approximate it as in reference 6. Approximations or neglection of this term are responsible for the paraxial errors.

The exact solution of (2) at range step $x+h$ can be given in terms of the solution at range step x

$$\varphi(x + h, z) = \exp(h\lambda) \varphi(x, z) \quad (5)$$

where λ must satisfy equation (4a).

We treat λ as a variable and expand the term $\exp(h\lambda)$ as a Lagrange series.⁵

$$e^{h\lambda} = e^{hb} + \sum_{n=1}^{\infty} \frac{\epsilon^n}{n!} h \frac{d^{n-1}}{db^{n-1}} [b^{2n} e^{hb}] \quad (6)$$

Expanding

$$\exp(h\lambda) = \sum_{n=0}^{\infty} \sum_{m=0}^{\infty} C_{nm} \epsilon^n h^m b^{n+m} \quad (7)$$

where

$$\left. \begin{aligned} C_{00} &= 1 ; \quad C_{n0} = 0 && (n > 0) \\ C_{nm} &= \frac{(2n + m - 1)!}{n! (m - 1)! (m + n)!} && (m > 0) \end{aligned} \right\} \quad (8)$$

For our problem we need the exponential in (7) as a power series in b

$$\exp(h\lambda) = \sum_{N=0}^{\infty} W_N b^N \quad (9)$$

The W_N are homogeneous power series in h and ϵ of degree N . All the W_N can be found from the first few W 's:

$$W_0 = 1, \quad W_1 = h, \quad W_2 = \epsilon h + h^2/2 \quad (10)$$

and the recurrence relations for C_{nm} and W_N (both obtained from the C_{nm} recurrence relation) given in reference 5.

Table 1 shows the C_{nm} coefficients for $n = 1$ to 5, $m = 1$ to 5. We can assemble W_N from this table simply by working our way along the diagonal line of elements joining $m = N$ to $n = N$.

$$W_N = C_{0,N} \epsilon^0 h^N + C_{1,N-1} \epsilon^1 h^{N-1} + C_{2,N-2} \epsilon^2 h^{N-2} + \dots + C_{N,0} \epsilon^N h^0 \quad (11)$$

Table 1
Coefficients, $C_{n,m}$, in the Expansion for $\exp(h\lambda)$

		m					
		0	1	2	3	4	5
n	0	1	1	1/2	1/6	1/24	1/120
	1	0	1	1	1/2	1/6	1/24
	2	0	2	5/2	3/2	7/12	1/6
	3	0	5	7	14/3	2	5/8
	4	0	14	21	15	55/8	55/24
	5	0	42	66	99/2	143/6	1001/120

We now expand (9) in Padé approximant form. The first stage is to represent (9) as a quotient of two polynomials

$$\sum W_N b^N = \frac{U_{LM}(b)}{V_{LM}(b)} = \frac{1 + \sum_{\ell=1}^L \alpha_\ell b^\ell}{1 + \sum_{m=1}^M \beta_m b^m} + O(b^{L+M+1}) \quad (12)$$

We keep the degree of the polynomials the same ($L \leq M$ for stability). The coefficients α_ℓ and β_m in the polynomials U_{LM} and V_{LM} are obtained by numerical solution of the $2M$ sets of linear equations obtained from (12).

Provided b and ϵ are pure imaginary (which is the case if air absorption is ignored) we can show (reference 5) that

$$U_{MM}(\epsilon, h) = V_{MM}^*(\epsilon, h) \quad (13)$$

This produces a substantial simplification of (12) as well as ensuring that U and V have the same modulus which is expected for exponentials with a purely imaginary argument.

We now factorize the denominator into linear terms to provide a split step formulation

$$V_{MM}(b) = \prod_{i=1}^M (1 + \rho_i b) \quad (14)$$

The coefficients ρ_i are obtained by a Newton Raphson iterative solution of $V_{MM}(b) = 0$. Equation (12) can now be written⁵

$$\frac{U_{MM}}{V_{MM}} = \prod_i \frac{(1 + \rho_i b)^*}{1 + \rho_i b} \quad (15)$$

The ρ_i can be found prior to the range dependent part of the solution. A further modification is to rewrite (15) with new coefficients $\hat{\rho}_i$ which depend only on $\epsilon/h = 1/(2ik_0 \Delta x)$

$$\frac{U_{MM}}{V_{MM}} = \prod_i \frac{(1 + \hat{\rho}_i hb)^*}{1 + \hat{\rho}_i hb} \quad (16)$$

Coefficients $\hat{\rho}_i$ are given in reference 5 for Padé approximant orders up to 4.

3. Implementation of the Core Algorithm

The solution procedure is identical to that used in other split operator methods.⁴ Each operator L_i is used to obtain a partial solution which must not be assigned to a physical location within the interval h . The solutions only exist at the beginning and end of the interval. A partial solution step would be

$$\varphi^{(i)} = L_i \varphi^{(i-1)}, \quad L_i = \frac{(1 + \hat{\rho}_i hb)^*}{(1 + \hat{\rho}_i hb)} \quad (17)$$

At the start of the range step h the $\varphi^{(i-1)}$ on the right hand side is $\varphi(x)$ and at the end of the range step the $\varphi^{(i)}$ on the left hand side is the required $\varphi(x+h)$. This split step procedure has been examined in some depth⁴ and it is clear that provided a partial step solution is itself stable the combined solution from the repeated application of the partial solutions must also be stable.

The numerator and denominator of the L_i are configured as tridiagonal matrices² with the elements along any row being determined using the central finite difference form for $\partial^2/\partial z^2$

$$\frac{\partial^2 \varphi_m}{\partial z^2} = \frac{\varphi_{m+1} - 2\varphi_m + \varphi_{m-1}}{\Delta z^2} \quad (18)$$

We do of course still require a small Δz interval which is typically $\lambda/5$ even though we are now able to use very large Δx values ($10-20\lambda$).

4 Modifications for the Ground and Upper Boundary Conditions

The second order ground boundary condition² is

$$\varphi_0 = Z_{\text{cons}} (4\varphi_1 - \varphi_2) \quad (19)$$

where

$$Z_{\text{cons}} = 1 / \left(3 - 2i\omega\rho \Delta z / Z_{\text{GND}} \right)$$

with Z_{GND} as the ground impedance. We incorporate this condition by appropriate modification of the first row in each of the two tridiagonal matrices.

An upper boundary condition which guarantees Sommerfeld radiation conditions has been described in reference 7 and implemented here by modifying the last row of each of the two tridiagonal matrices in accordance with the boundary condition

$$\Phi_{M+1} = 2f\Phi_M - f^2\Phi_{M-1} \quad (20)$$

where

$$f = \exp \left\{ ik_M \Delta z \sin \theta \right\}$$

where θ is the angle of ray incidence on the upper boundary and k_M is the wave number at $z = z_M$. Experiments with the Sommerfeld Upper Boundary Condition (SUBC) were disappointing. Unlike the Wide Angle Crank-Nicholson (WACN) algorithm there were unexpectedly large numerical errors produced close to the source resulting from spurious reflections from the upper boundary. The LP-PE though stable is close to the limit of stability whereas the WACN-PE is (by virtue of the simple relationships between the operator coefficients) much more stable and hence less susceptible to these upper boundary effects.

As a temporary measure we had to reluctantly use an Artificial Absorbing Layer (AAL) at the top of the computational atmosphere in place of the SUBC³. Typically the AAL requires a 30% increase in atmospheric depth and a proportionate run time reduction.

5. Subrange Configuration

The LP-PE using a range step of 10λ with 4 Padé terms gives results at the calculation points identical to those obtained with the WACN-PE.⁵ However close to the upper boundary (as observed in the last section) or close to the source we often get spurious spikes in the results which we believe to be due to the proximity to the limit of numerical stability. We have found that the upper boundary errors

are best reduced with an AAL and the near source errors by using one Padé factor at first and then increasing the number of Padé factors up to 4 over the first 2.5 km.

The case $M = 1$ is equivalent to the standard WACN-PE and gives a high degree of stability in the region close to the source. The speed is of course the same as the original WACN-PE algorithm. The subrange configuration used was in 4 zones, $M = 1$ for 10 - 800m, $M = 2$ for 800 - 1400m, $M = 3$ for 1400 - 2500m and $M = 4$ for > 2500 m, the corresponding range steps being $\lambda/5$, $4\lambda/5$, 3λ and 10λ .

The LP-PE predictions have been tested against the published benchmark cases at 10 Hz and 100 Hz. The agreement was found to be excellent.⁵

6. Turbulent Realisation of the Atmosphere

Synthetic atmospheric realisations have been generated for our WACN-PE using the isoturbulent model described in reference 8. This is satisfactory when we are using small $\lambda/5$ range steps where the PE's range step picks up the physically relevant turbulent effects. However for the LP-PE where we are using 10λ range steps at the lower frequencies, within one range step we jump over relevant turbulent changes in perturbed sound speed. Because the partial solutions cannot be allocated to physical locations it would appear that the high speed - large range step solution is not capable of including turbulent effects.

An ingenious solution to this problem has been given by Di and Gilbert³ who implemented a phase screen method. The screen is evaluated over each large range step as a phase shift $\Phi(z)$ by integrating the refractive index over the step h at each vertical mesh height z

$$\Phi(z) = k_0 \int_x^{x+h} \mu(x, z) dx \approx k_0 \sum_{i=1}^M \mu_i(z) \Delta x_T$$

The turbulent effects are then incorporated in a single factor $\exp[i\Phi(z)]$ which is applied after the solution at range step $x+h$ has been found. Δx_T is the x sampling interval for the turbulent atmosphere which should be identical to Δz ($\lambda/5$). The phase screen factors are precomputed for each atmospheric realisation and stored on disk ready to be picked up as the range calculation proceeds. Di and Gilbert have shown that the phase screen does not introduce errors for range step sizes up to 25λ .

7. Multiazimuth Configuration

Our operational requirement is to produce peak SPL contours over a range of 30 km within a few minutes on a powerful desk top PC. This is *just* possible with the LP-PE producing predictions along azimuthal paths in 15° intervals. In order to keep run times to a minimum it is essential that for a given azimuth the atmospheric depth is kept as small as possible. A ray trace is performed to ensure that all landing rays are included in the selected atmospheric depth. For "true" upwind cases the atmospheric depth can be drastically reduced to as little as 1 - 2% of the range.

For upwind azimuths (or azimuths where some upward refraction occurs) we must use a turbulent realisation of the atmosphere. At least 5 realisations are needed to give a sensible mean prediction. Each "upwind" azimuth prediction therefore takes 5 times as long as its downwind counterpart. We have investigated the possibility of taking a smoothed prediction for a *single* realisation instead of the 5 averaged predictions (which must still be smoothed). The predictions so obtained can be in error by 4 - 6 dB particularly at the larger ranges, which is not acceptable. As a compromise we are currently using 3 realisations with errors of

2 - 4 dB at the larger ranges. Experiments have shown that we only need use a turbulent atmosphere solution when we have "strong" upward refraction (where rays are turned away from the ground). We can often cut down the number of azimuths were we require the turbulent solution to only 6.

References

1. M. West, J. D. Turton and G. Kerry. A New Package for Blast Noise Prediction at UK Artillery and Testing Ranges. *Applied Acoustics*, 48(2), 133-154 (1996).
2. M. West, K. E. Gilbert and R. A. Sack. A Tutorial on the Parabolic Equation (PE) Model Used for Long Range Sound Propagation in the Atmosphere. *Applied Acoustics*, 37, 31-49 (1992).
3. K. E. Gilbert and X. Di. A Fast Green's Function Method for One-Way Sound Propagation in the Atmosphere. *J. Acoust. Soc. Amer.*, 93, 712-714 (1992).
4. M. D. Collins. Applications and Time Domain Solution of Higher-Order Parabolic Equations in Underwater Acoustics. *J. Acoust. Soc. Amer.*, 86(3), 1097-1102 (1989).
5. R. A. Sack and M. West. The Lagrange Padé Parabolic Equation (LP-PE) for the Prediction of Long Range Sound Propagation in the Atmosphere. *Applied Acoustics*, 49(2), 105-125 (1996).
6. R. A. Sack and M. West. Representation of Elliptic by Parabolic Partial Differential Equations with an Application to Axially Symmetric Sound Propagation. *Applied Acoustics*, 37, 141-149 (1992).

7. M. West and R. A. Sack. Development of an Algorithm for Prediction of the Sound Field from a Spherical Acoustic Source Using the Parabolic Approximation. Proceedings of the 5th International Symposium on Long Range Sound Propagation. The Open University, Milton Keynes, 115-127 (1992).
8. K. E. Gilbert, R. Raspot, X. Di. Calculation of Turbulence Effects in an Upward Refracting Atmosphere. J. Acoust. Soc. Amer. 87, 2428-37 (1990).

Acknowledgements

The author wishes to thank the UK Ministry of Defence (Directorate of Health and Safety) for their financial support.

The author also wishes to thank Professor R A Sack for his assistance in preparing this paper.

APPROXIMATIONS IN THE PE METHOD.

PHASE AND LEVEL ERRORS IN A DOWNWARD REFRACTING ATMOSPHERE.

Marta Galindo

Department of Acoustic Technology
Technical University of Denmark
DK-2800 Lyngby, Denmark

ABSTRACT

Two different sources of errors may occur in the implementation of the PE method; a phase error introduced in the approximation of a pseudo-differential operator and an amplitude error generated from the starting field. First, the inherent phase errors introduced in the solution are analyzed for a case where the normal mode solution to the wave equation is valid, when the sound is propagated in a downward refracting atmosphere. The angular limitations for the different parabolic approximations are deduced and calculations showing shifts in the interference pattern for long distance propagation in downward refraction are presented. The starter as the second source of error is investigated. Numerical and analytical starters are compared for source locations close to the ground. The spectral properties of several starters are presented.

1. INTRODUCTION

Since 1989, when K.E. Gilbert and M.J. White¹ presented an application of the parabolic equation method for sound propagation through the atmosphere, several PE methods have been developed for specific outdoor propagation problems, as; propagation over large ridge², propagation over ground with impedance variations^{3,4} and diffraction by a screens⁵. In the last years, the new PE codes⁶⁻⁹ maximize the potential of the method to handle inhomogeneous media, with special focus on the study of sound propagation through a turbulent atmosphere. A huge effort has been made to understand and exploit the parabolic wave equations when they are applied to outdoor sound propagation. The study of the inherent errors in the parabolic approximations is a step further in this understanding of the PE method. Two errors of different nature are dealt with in this work. First, the phase error created in the numerical implementation of the different parabolic equations is evaluated. An example of the phase shift in the calculations using two different parabolic equations is shown for a downward propagating atmosphere. Second, several starters are investigated. Calculations with different starting fields are compared for source positions close to the lower boundary. The spectral properties of the starters are determined for two parabolic equations. An example of the level error in the calculations using two different starters is shown for a downward refracting atmosphere.

2. PHASE ERROR AND ANGULAR LIMITATIONS OF THE PARABOLIC EQUATIONS.

The starting point of any model based on the parabolic approximation is the family of outgoing parabolic wave equations¹⁰,

$$\frac{\partial \phi}{\partial r} = ik_0 \left(\sqrt{n^2 + \frac{1}{k_0^2} \frac{\partial^2}{\partial z^2}} - 1 \right) \phi . \quad (1)$$

Defining the two operators P and Q as

$$P = \frac{\partial}{\partial r} , \quad Q = \sqrt{n^2 + \frac{1}{k_0^2} \frac{\partial^2}{\partial z^2}} , \quad (2)$$

the family of outgoing parabolic wave equations, Eq(1), is rewritten in operational form as,

$$P \phi = ik_0 (Q - 1) \phi . \quad (3)$$

The numerical solution of Eq(3) involves the approximation of the pseudo-differential operator Q that limits the convergence to the exact solution. The number of terms in the series expansion of the square-root operator generates the different parabolic equations. This approximation introduces a phase error in the calculations and limits the angular spectrum of the solution. Therefore, a certain limit angle is always associated to each of the parabolic equations. This angle represents the angular interval from the horizontal, where forward propagating plane waves are treated accurately by the parabolic equations. Depending on how wide is this angular interval, the parabolic equations can be classified as narrow or wide.

The Tappert¹⁰ equation, the first one applied to sound propagation, includes in its development the paraxial approximation. It is also called the standard PE or narrow PE and can be classified as a 15°-20° parabolic equation. The Tappert equation uses the two-term Taylor series expansion of the pseudo differential operator. To obtain wider PE the rational function representation for the operator $Q = (1+q)^{1/2}$ is introduced in the PE models. Using the general form of the rational linear approximation, the operator Q is rewritten as

$$Q = \sqrt{1+q} \approx \frac{a_0 + a_1 q}{b_0 + b_1 q} . \quad (4)$$

Each set of coefficients selected, (a_0, a_1, b_0, b_1) , gives a different parabolic wave equation which different angle properties in the solution. Table 1 shows the expansion coefficients of the operator Q associated with each of the parabolic equations involved in the study.

$a_0=1, a_1=0.5$ $b_0=1, b_1=0$	$\sqrt{1+q} \approx 1 + 0.5q$	Tappert
$a_0=1, a_1=0.75$ $b_0=1, b_1=0.25$	$\sqrt{1+q} = \frac{1+0.75q}{1+0.25q}$	Claerbout ¹¹ , Padé(1)
$a_0=0.99987, a_1=0.79624,$ $b_0=1, b_1=0.30102$	$\sqrt{1+q} = \frac{0.99987 + 0.79624q}{1 + 0.30102q}$	Greene ¹²
$\sqrt{1+q} \approx 1 + \frac{0.1382q}{1 + 0.65451q} + \frac{0.36180q}{1 + 0.09549q}$		Padé(2) ¹³

Table 1 Scheme of different parabolic equations. At the left column the selected set of coefficients in the expansion of the pseudo-differential operator Q and at the right column the name associated with each of the approximations.

2.1 Theory

In this section, the inherent phase errors introduced in the Claerbout¹¹ rational approximation are analysed for a case where the normal mode solution to the wave equation is valid. The conclusions are extended for all the parabolic equations presented above, associating a limit angle

to each of them. These phase error analysis follow closely the one by Jensen¹⁴, based in the propagation of a single normal mode in the parabolic approximation developed by McDaniel¹⁵. This phase error study is applied for sound propagation in a downward refracting atmosphere with no range variations, $n(z)=k(z)/k_0$, over a complex impedance ground surface. Under these conditions both equations, the elliptic Helmholtz equation and the parabolic wave equation have closed solutions, and can be solved using the normal mode method. This theory has been successfully applied to outdoor sound propagation under downward refraction conditions by Raspet *et al.*¹⁶. These results are compared with the phase and the amplitude with which a normal mode propagates under the Claerbout parabolic approximation.

Starting from an explicit differential form of the Claerbout equation,

$$(k^2(z) + 3k_0^2 + \frac{\partial^2}{\partial z^2}) \frac{\partial \phi}{\partial r} = 2ik_0(k^2(z) - k_0^2 + \frac{\partial^2}{\partial z^2}) \phi , \quad (5)$$

and using the method of separation of variables, $\phi(r,z)=\Phi(r)\Psi(z)$, the two separated differential equations are calculated.

The height dependent differential equation is

$$\frac{d^2\Psi}{dz^2} + [k^2(z) - k_n^2] \Psi = 0 , \quad (6)$$

and radial equation is

$$\frac{d^2\Phi}{dr^2} - ik_0 \frac{2k_n^2 - 2k_0^2}{3k_0^2 + k_n^2} \Phi = 0 , \quad (7)$$

where k_n is the separation constant for each of the n th-modes.

Eq (6) is similar to the height separated part of the homogeneous Helmholtz equation, presented by Pierce¹⁷. A normal mode under a downward refracting atmosphere is propagated in the Claerbout parabolic approximation with the correct amplitude and mode shape. This is a general result for all PE's based on the rational linear approximation¹⁴.

The phase with which a normal mode propagates in the Claerbout parabolic approximation is determined solving the radial differential equation, Eq (7). The general solution can be written as,

$$\Phi(r) = \Phi(r_0) \exp \left[ik_0 \left(\frac{2k_n^2 - 2k_0^2}{3k_0^2 + k_n^2} \right) (r - r_0) \right]. \quad (8)$$

Making use of the initial factorization in the development of the family of parabolic wave equations, where the pressure field is separated in two componentes¹,

$$p(r,z) = \frac{1}{\sqrt{r}} \phi(r,z) e^{ik_0 r}, \quad (9)$$

and adding the modulated carrier wave, $\exp(i k_0 r)$, into Eq(8), the pressure for the n th-mode is expressed as

$$p(r,z) = p(r_0, z) \sqrt{\frac{r_0}{r}} \exp \left[ik_0 \left(\frac{k_0^2 + 3k_n^2}{3k_0^2 + k_n^2} \right) (r - r_0) \right]. \quad (10)$$

The general expression for the pressure calculated above is compared with the solution of the Helmholtz equation using the normal-mode theory for the particular case of a linear sound speed profile of the form,

$$c(z) = \frac{c(0)}{\sqrt{1 - 2z/R}}, \quad (11)$$

where $R = c(0)/|dc/dz|_{z=0}$ is the radius of curvature of the ray initially propagating horizontally from the source. Following Raspot et al.¹⁶, the height separated Helmholtz equation has solutions given in terms of Airy functions Ai and their derivatives Ai' . Using the residual theory to integrate, the discrete modes are calculated and $H_0^{-1}(k_n r)$ determines the decay of the n th-mode with horizontal distance. Including the far field approximation for the Hankel function, the correct phase for the n th-mode is expressed as,

$$e^{ik_n(r-r_0)}, \quad (12)$$

where $k_n = \sqrt{k_0^2 + \frac{\tau_n}{l^2}}$, $l = \left(\frac{R}{2k_0^2} \right)^{1/3}$, and τ_n is calculated from the polo condition.

The n th-mode will decay cylindrically with the distance if k_n is a pure real number and if is complex, the mode will under go an exponential decay with argument $-\text{Im}(k_n)(r-r_0)$.

When the radial part of the parabolic equation, Eq(7), is compared with the correct modal phase for a cylindrical decay, $\exp[i k_n(r-r_0)]$, is clear that there is a phase error in the Claerbout equation. The error is dependent on the choice of k_0 in Eq(9). Thus, the n th-mode can always be propagated with the right phase, selecting $k_0=k_n$, but all the other modes will propagate with slightly wrong phases. Only one unique mode can be propagated with the right phase.

Relating the phase error with the propagation angles is of major interest to characterize the angle interval where each of the parabolic equations provides a good solution. Therefore, the identity¹⁶

$$\text{Re}(k_n) = k_0 \cos \theta_{n_0} , \quad (13)$$

is introduced, where θ_{n_0} is the horizontal propagation angle at the ground for the n th-mode. Selecting $k_0=1$, the phase for the n th-mode in the Helmholtz equation is given by $\cos\theta_{n_0}$ and in the Claerbout equation is,

$$\varphi = \frac{1 + 3 \cos^2 \theta_{n_0}}{3 + \cos^2 \theta_{n_0}} . \quad (14)$$

To find simplify expressions for the modal phases, the angles are expressed in terms of $\sin^2 \theta$ and the subindexes n_0 are dropped. Now, the correct modal phase can be written as

$$\varphi = \sqrt{1 - \sin^2 \theta} , \quad (15)$$

and the Claerbout as

$$\varphi = \frac{1 - 0.75 \sin^2 \theta}{1 - 0.25 \sin^2 \theta} . \quad (16)$$

Comparing the two equations, is clear that Eq(16) is the rational-function approximation of the Eq(15) in $\sin^2 \theta$. This result can be extrapolated to the study of the expansion of the square-root operator Q in Eq(4). Thus, each of the parabolic approximations can be associated with a limit propagation angle. Table 2 presents the different phase angles for each of the parabolic equations.

$\varphi = \sqrt{1 - \sin^2 \theta}$	Helmholtz
$\varphi_1 = 1 - \frac{\sin^2 \theta}{2}$	Tappert
$\varphi_2 = \frac{1 - 0.75 \sin^2 \theta}{1 - 0.25 \sin^2 \theta}$	Claerbout, Padé(1)
$\varphi_3 = \frac{0.99987 - 0.79624 \sin^2 \theta}{1 - 0.30102 \sin^2 \theta}$	Greene
$\varphi_4 = 1 - \frac{0.13820 \sin^2 \theta}{1 - 0.65451 \sin^2 \theta} - \frac{0.36180 \sin^2 \theta}{1 - 0.09549 \sin^2 \theta}$	Padé(2)

Table 2 Phases associated with each of the Parabolic Equations.

The phase errors for the different parabolic approximations are defined as $|\varphi - \varphi_i| \leq e_i$, where e_i is an arbitrary value for the accepted error in a specific application. Figure 1 shows the errors as a function of the angles for the parabolic approximations presented above. One parabolic approximation can have several angles associated with it, depending on how restrictive is the problem to be solved. In Figure 1, two sets of angles are associated with the different PE approximations. Due to the exponential behaviour of the error functions, the angular properties of the different parabolic equations stay in a close interval as long as the acceptable error, e_i , is in the same order of magnitude. Thus, the Trappert equation is associated with angles between 15° - 20° and defined as a 15° - 20° equation, the Claerbout is a 30° - 37° equation, the Greene is a 40° - 45° equation and the Padé(2) is a 50° - 56° equation. It is important to remark that the coefficients used in Greene equation have been calculated for horizontal propagation, the same optimization procedure¹² can be used for different directions of propagation.

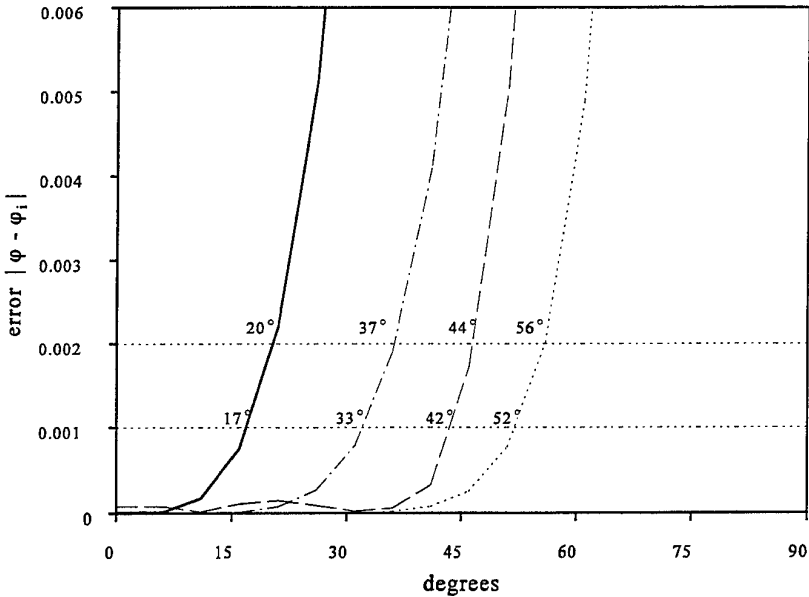


Figure 1 Phase error versus propagation angle for different parabolic equations, where the solid line (—) represents the Tappert Eq., the solid-dotted line (---) represents the Claerbout Eq., the dashed line (--) represents the Greene Eq. and the dotted line (...) represents the Padè(2) Eq. Two sets of limited angles, for $e_l = 0.002$ and $e_l = 0.001$, are displayed in the graph. From Jensen et al. ²⁰.

2.2 PE calculations in a downward refracting atmosphere.

As an example of the phase error introduced in the calculations, the Case III in the normal mode study, presented by Raspet et al.¹⁷, is implemented for the Tappert Eq. and for the Claerbout Eq. The source height is 1.00 m, the receiver height is 1.05 m and the ground is a porous surface. The complex impedance ground surface is modelled using Attenborough's low-frequency/high flow resistivity expression¹⁸. The sound speed profile is

$$c(z) = \begin{cases} \frac{c(0)}{\sqrt{1-2z/R}} & z < z_t, \\ \frac{c(0)}{\sqrt{1-2z_t/R}} & z \geq z_t. \end{cases} \quad (17)$$

of the form of Eq(9), but truncated at $z_t=67.7$, and the value for the radius of curvature is $R=1000$ m. The normal modes solution for the truncated problem includes the first 10 propagation modes. Making use of the mode wave numbers in Table III, Ref.17., and the identity Eq(11), the propagation angles are calculated. The propagation angle interval for the 10th modes goes from

$4,64^\circ$ to $21,15^\circ$. Looking at the position of source and receiver above the ground, the propagation is almost horizontal, but due to the gradient in the sound speed profile, the narrow PE introduce an error in the phase, while the wide-Claerbout PE gives the right solution. Figure 2 shows the SPL relative to a free field for both approximations along the first kilometre. In the calculations, the 10th-mode is the one selected to propagate with the right phase. In a truncate sound speed profile is the last mode the one with a minimum attenuation and determines the behaviour of the solutions at long ranges. The phase error increases with the distance, when the last modes with higher angles dominate the solution. In this example, the sound speed profile is truncated at $z_t=67.7$ m, and the solution includes 10 modes.

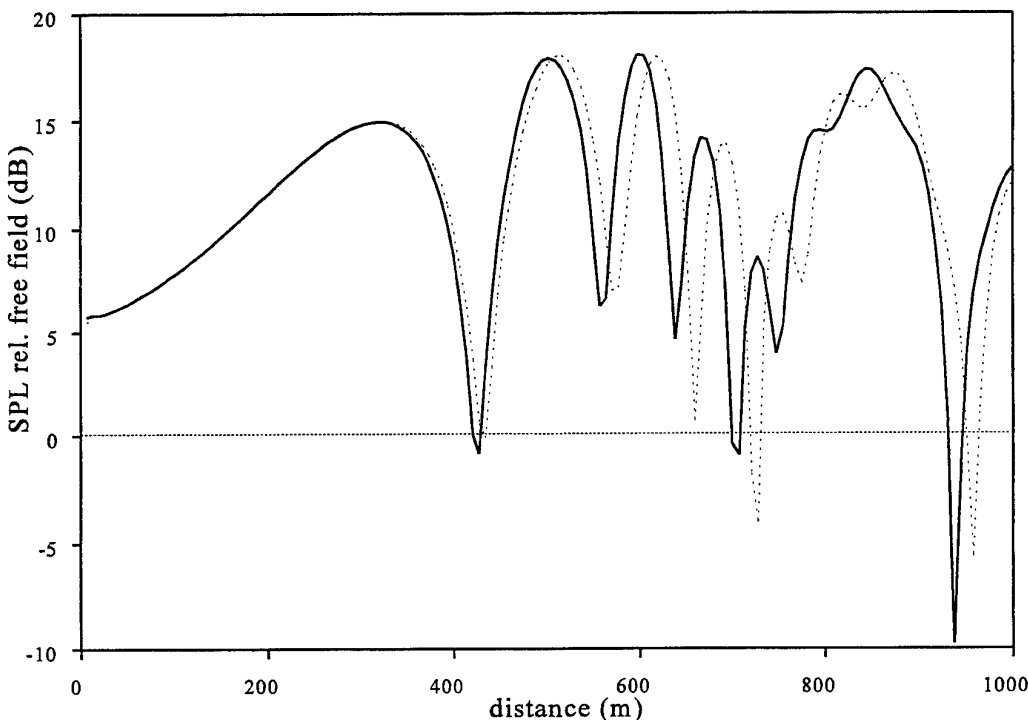


Figure 2 Sound pressure level relative to a free field versus range. Source height, $h_s=1$ m, receiver height, $h_r=1,05$ m, porous ground¹⁸, $\sigma_{eff}=3 \cdot 10^6$, the sound speed profile is as Eq(15). The solid line are calculations with the Claerbout Eq. and the dotted line are calculations with the Tappert Eq.

The full solution of this problem includes 196 modes. It is the 107th mode, the one with the minimum attenuation and with a major contribution in the long distance solution. The propagation angle associated with the 107th mode is $54,86^\circ$. The Clearboult Eq. introduces a phase error for the full solution, and wider equations have to be used as; Padé(5), with small phase error for angles within $\pm 60^\circ$. The propagation angle associated with the minimum attenuation mode is directly proportional to the sound speed gradient. Therefore, for long distance calculations under stronger downward refracting atmosphere, the very-wide-angle PE base on the Padé expansion¹³ are needed to avoid phase errors.

3. STARTING FIELDS.

The transformation from the elliptic Helmholtz equation into the parabolic wave equation introduces the advantage of solving the PE one-way wave equation by a range-marching technique. The marching technique requires an initial solution to start the calculations. A set of complex pressure values over the height (r_0, z) has to be spaced at the starting range. As long as the environment is range-independent, a far field approximate solution can be used as starting field. The position of the starting field is determined by each specific problem. When the field is propagated in a homogeneous medium, the starting range can be located near the discontinuities of the boundaries. In most of the cases, when an inhomogeneous medium is considered, the interest is to model a point source at the origin. The ideal is to generate a beam-limited source with an aperture that is compatible with the angular limitation of the PE approximation used. The initial field can be created using numerical or analytical solutions of the problem.

3.1 Analytical Starters.

The analytical starters are based on Gaussian distributions of the field at the initial position r_0 . They are designed to closely match the far field pattern generated from a point source that is propagating in a homogeneous medium. The advantage of the analytical starters is, that the initial field is created with a minimum computational effort. The first analytical starter, proposed by Tappert¹⁰, is a Gaussian function of the form:

$$\phi(0, z) = \sqrt{k_0} e^{-\frac{k_0^2}{2}(z - z_s)^2}, \quad (18)$$

where z_s is the source height. This starter is known as the Gaussian source. The development includes the paraxial approximation, therefore it can only be used for almost horizontal propagation. The Gaussian source is the starter used for narrow angle parabolic calculations. Several improvements have been made to solve the angular restriction. Greene¹² presents a weighed Gaussian source with better wide angle properties

$$\phi(0, z) = \sqrt{k_0} [1.4467 - 0.4201 k_0^2 (z - z_s)^2] e^{-\frac{k_0^2 (z - z_s)^2}{3.0512}}, \quad (19)$$

These two analytical sources have been modelled as a point source in a free field. It is a good approximation, whenever the source is placed several wavelengths over the ground. For the situations where the source is close to the ground, the starter field should include the ground boundary condition. The Graph 3 shows the predictions of sound pressure levels relative to a free field versus distance for a case where the source is located close to the ground at 0.25m and the receiver is at 1.5m. height. The propagation frequency is 100Hz, and source and receiver are located over a porous ground.

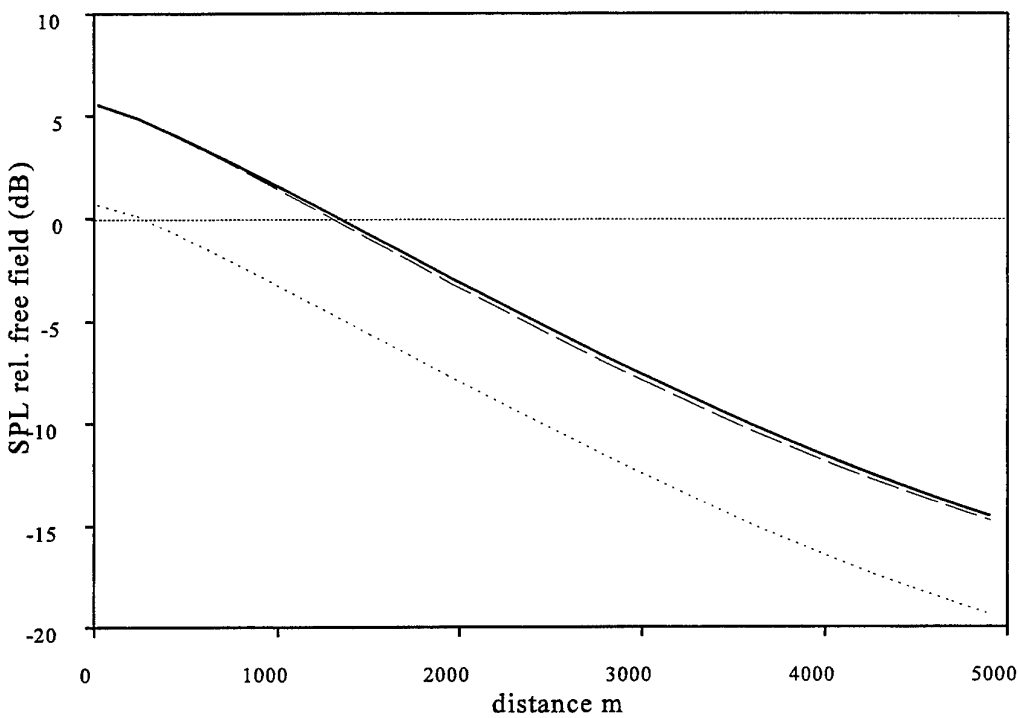


Figure 3 Sound pressure levels relative to a free field versus distance for $h_s=0.25m$, $h_r=1.5m$, $f=100Hz$ over a porous ground $\sigma=200\text{ Nsm}^{-4}$, — C&S solution, - - Back PE starter, . . . Gauss starter.

The Gaussian starter does not include the presence of the ground and predicts an extra attenuation of 5dB. The back propagator is a numerical starter, presented later, that corrects this error. The example shows the importance of including the ground boundary condition inside the starter field. The error is a level error and stays constant along the distance. Numerical tests indicate that the level of the error is a function of the characteristic impedance of the boundary and the distance of the source to the ground.

X.Di *et al.*⁶ has presented a Gaussian-shaped starter that models the source and its image at the ground. The amplitude of the image Gaussian is modulated by the plane wave reflection coefficient for vertical incidence on the ground,

$$\phi(0,z)=\sqrt{k_0/2} \left[e^{-\frac{k_0^2}{4}(z-z_i)^2} + \frac{Z^*-1}{Z^*+1} e^{-\frac{k_0^2}{4}(z+z_i)^2} \right], \quad (20)$$

where Z^* is the characteristic impedance of the ground. This starter is further called the image starter.

3.2 Numerical Starters.

Basically all different numerical methods - i.e. ray tracing, Fast Field models, or close solutions for the wave equation- may be used to generate the starting field. The aim is to generate a good numerical starter without increasing the complexity of the PE model. When the sound propagates through a homogeneous medium, the complex pressure generated from a point source over the ground can be calculated using the first order approximate solution of Chein and Soroka¹⁹, where the solution includes the reflection of spherical waves from a locally reacting plane surface. The starter field is generated over the height for a certain starting range r_0 ,

$$\phi(r_0, z) = \sum_{j=0}^n \phi(r_0, z_j) = \sum_{j=0}^n \sqrt{r_0} \left[\frac{e^{ik_0 d_{j-}}}{d_{j-}} + Q_j \frac{e^{ik_0 d_{j+}}}{d_{j+}} \right], \quad (21)$$

where $d_{j\pm} = \sqrt{r_0^2 + (z_j \pm z_s)^2}$, and Q_j is the spherical waves reflection coefficient,

$$Q_j = R_p(\theta_j) + B[1 - R_p(\theta_j)]F(w_j), \quad (22)$$

and R_j is the plane wave reflection coefficient, $F(w_j)$ is the boundary loss function, and B is a constant close to one. Figure 4 shows the different geometrical parameters used to generate the ground PE starter. The ground PE starter can be used to initialize the PE models for propagation in a homogeneous medium without any angle limitations. In these cases the initial range, r_0 , is chosen at the first ground discontinuity. In this way, the computation time can be reduced significantly.

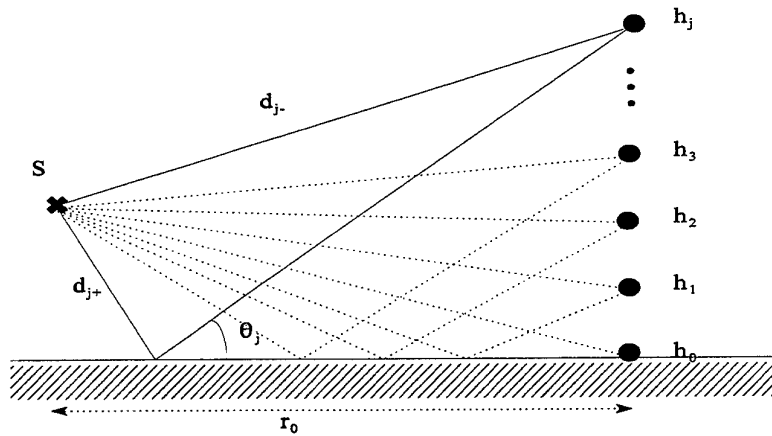


Figure 4 Scheme of the ground PE starter.

One of the major advantages of the PE method applied to outdoor sound propagation is the flexibility for propagating sound waves through inhomogeneous medium, making possible to model sound propagation through a turbulent atmosphere. The ground PE starter can not be used in these cases. A good numerical starter, including the boundary condition, should be generated at the source position $r_0=0$.

To solve the problem, a back propagated PE starter²⁰ is constructed by back propagating the ground PE starter from $r=r_0$ to $r=0$. The same parabolic equation, Eq (1), is used to back propagate the field. In the PE marching algorithm, the field located at $r=r'$ is known, and the field at $r=r'+\Delta r$ is calculated. In the back propagator algorithm, the known field is located at $r=r'-\Delta r$, and the field at $r=r'$ is calculated. Using this method, the ground PE starter, generated several wavelengths from the source, is back propagated to the source position, always through a homogenous medium. The back PE starter includes the boundary condition, and because it is located at the source, it can be used for calculations through inhomogeneous media.

3.3 Comparison between different starters.

Using the Cranck-Nicholson Parabolic Equation model, CNPE, based on the Claerbout approximation, the four starters presented above are compared. The error in the calculations due to the starting field is a level error along the distance. In the next calculations the distance is a fix parameter, $d=500m$. The following graphs represent the SPL relative to a free field versus the deviation angle from horizontal propagation. In the first case, Figure 5, the SPL is calculated for a frequency of 100 Hz, at a source height of 0.5m. The solid line represents the Chien and Soroka¹⁹ reference solution, the dashed lines show the calculations using analytical starters and the symbol * represents the calculations using the back PE starter. The source is located at $1/6 \lambda$ from the ground. At this height the initial fields generated with the analytical starters have not decayed to zero and interact with the interface. The image starter includes the boundary condition and shows the best behaviour for horizontal propagation among the analytical starter fields. At bigger deviation angles, the prediction error increases, with errors over 3 dB for angles bigger than 25° . This error will determine the spectral properties of the starter and it will be analysed in the next section. The Greene starter shows a constant error of 2 dB from the horizontal propagation to a deviation angle of 40° . The calculations with a Gauss starter predict an extra attenuation of 3dB for horizontal propagation that increases with the deviation angle. The errors seem to be inversely proportional to the beamwidth of the Gaussian function used as starter. The back PE starter predictions are close to the solution, less than 0.5 dB, from horizontal propagation to a deviation angle of 40° .

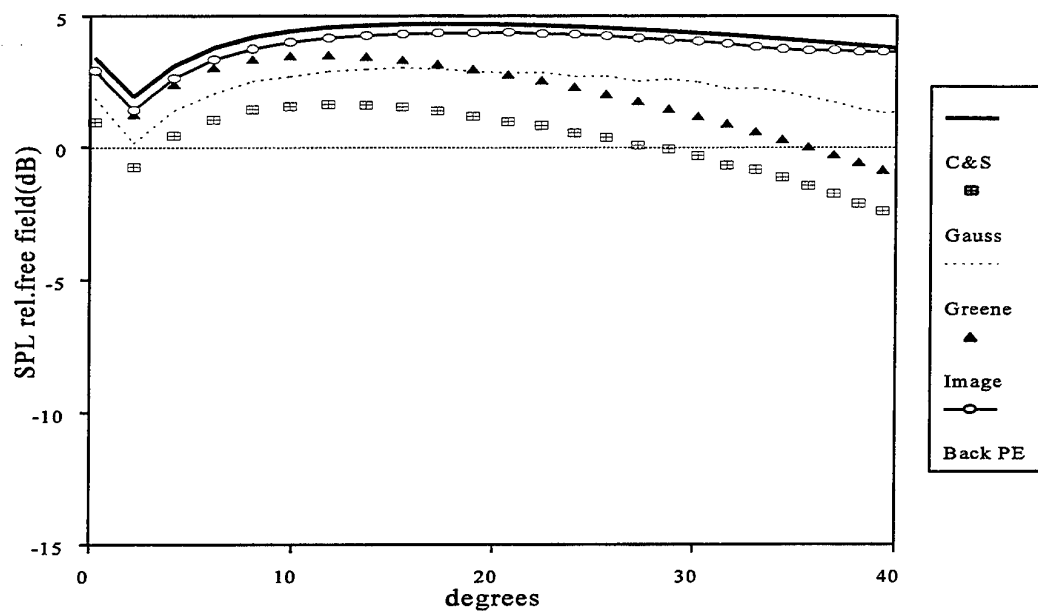


Figure 5 Sound pressure levels relative to a free field versus the deviation angle from horizontal propagation, $d=500m$, $h_s=0.5m$, soft ground $\sigma=200 \text{ Nsm}^{-4}$, $f=100\text{Hz}$.

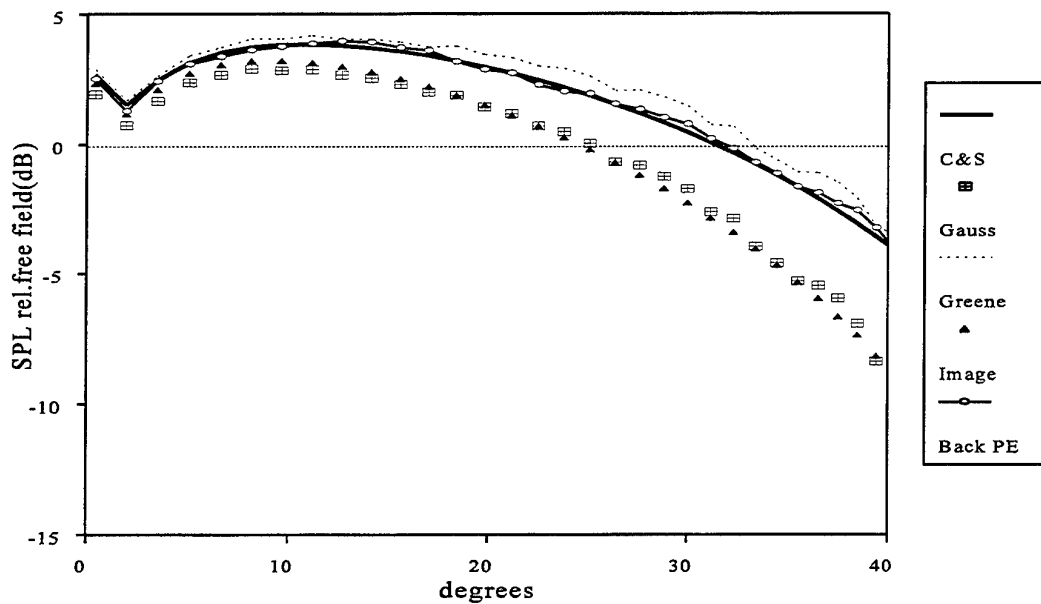


Figure 6 Sound pressure levels relative to a free field versus angle from horizontal propagation, $d=500m$, $h_s=1m$, soft ground $\sigma=200 \text{ Nsm}^{-4}$, $f=100\text{Hz}$.

Figure 6 shows the same calculations for a higher source, at 1m over the ground. The frequency is 100Hz, the source is located at $1/3 \lambda$ over the interface. At this height, all the analytical fields decay to zero and the errors are significantly reduced. At this frequency, the Greene starter predicts a constant error of less than 1 dB from 0 to 40 degrees. The image source generates good results in a short range of angles from 0 to 10. When the source is located higher than $1/3\lambda$, the error due to the boundary condition becomes insignificant.

Similar behaviour is shown in Figure 7, for higher frequencies, $f = 250$ Hz, at a source height of 0.5m. For this geometrical configuration, the source is at $1/3\lambda$ over the ground, and the errors are less than 1 dB. Therefore, the three analytical starters can be used for horizontal propagation at source positions higher than $1/3\lambda$ above the ground. For lower positions of the source and horizontal propagation, among the analytical starters, the image source is a good starter. For higher positions of source or receiver, when the propagation is not horizontal, the analytical starter has to be studied in relation with each of the parabolic equations to determine the spectral properties of the source. The numerical starters introduced above, include the boundary condition, and do not present any problem with the position of the source and the propagation angle. The ground starter can be used through a homogeneous medium, and the back PE starter through an inhomogeneous medium.

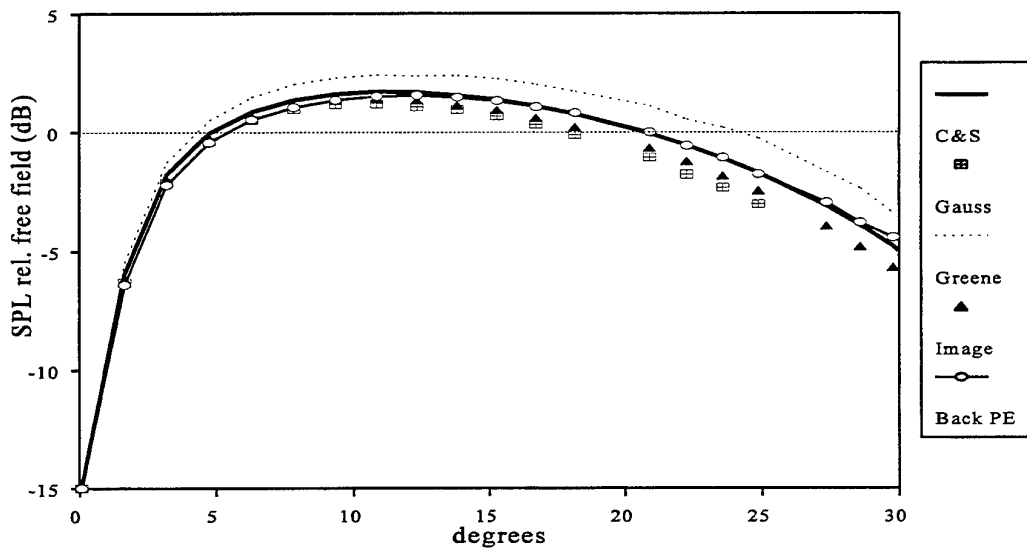


Figure 7 Sound pressure levels relative to a free field versus the deviation angle from horizontal propagation, $d=500$ m, $hs=0.5$ m, soft ground $\sigma=Nsm^{-4}$ c.g.s., $f=250$ Hz.

3.4 Spectral Properties of the Analytical Sources

Each of the parabolic equations- i.e. Tappert Eq, Claerbout Eq, Padè Eq- is developed from the family of parabolic wave equations, Eq (1), using different numerical approximations for the pseudo differential operator. Depending on the angular limitation of the parabolic wave equations, each one leads to a different farfield radiation pattern for the same starting field. Thus, it is not possible to define a source beamwidth without specifying the wave equation used to propagate the field.

In the first case for the narrow-angle Tappert equation, the effective beamwidth of the sources in a homogeneous medium is calculated. The position of the source is 2m above a porous ground, the distance between source and receiver is 100m and the frequency is 100Hz. For this geometry the three analytical starters give the correct predictions in near horizontal propagation. The beamwidth of the source is arbitrarily selected as the angle interval with prediction errors less than 3 dB compared to the Chien and Soroka¹⁹ reference solution. Looking at Figure 8, for the narrow angle PE, the image source has a beamwidth of approximately 40°, and shows the best behaviour of the three starters. The Gauss starter, created for this parabolic equation, shows good predictions with a beamwidth of 35°, and the Greene starter has the narrowest beamwidth 27°.

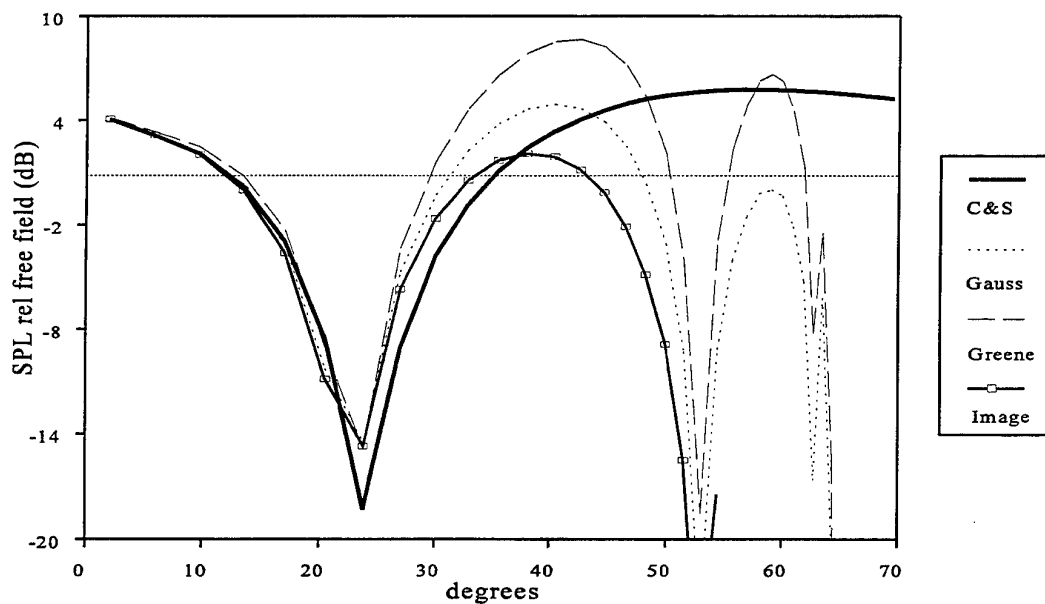


Figure 8 Calculation using the Tappert parabolic equation of sound pressure levels relative to a free field versus angle from horizontal propagation, $d=100m$, $hs=2m$, soft ground $\sigma=200 Nsm^{-4}$, $f=100Hz$.

Figure 9 shows the Claerbout Eq calculations for these three starters using the parameters above. The Greene starter is specially designed for a wide PE, in this case the beamwidth is approximate 65°. The Gauss and image starters have narrower beamwidth, 40° and 30° respectively

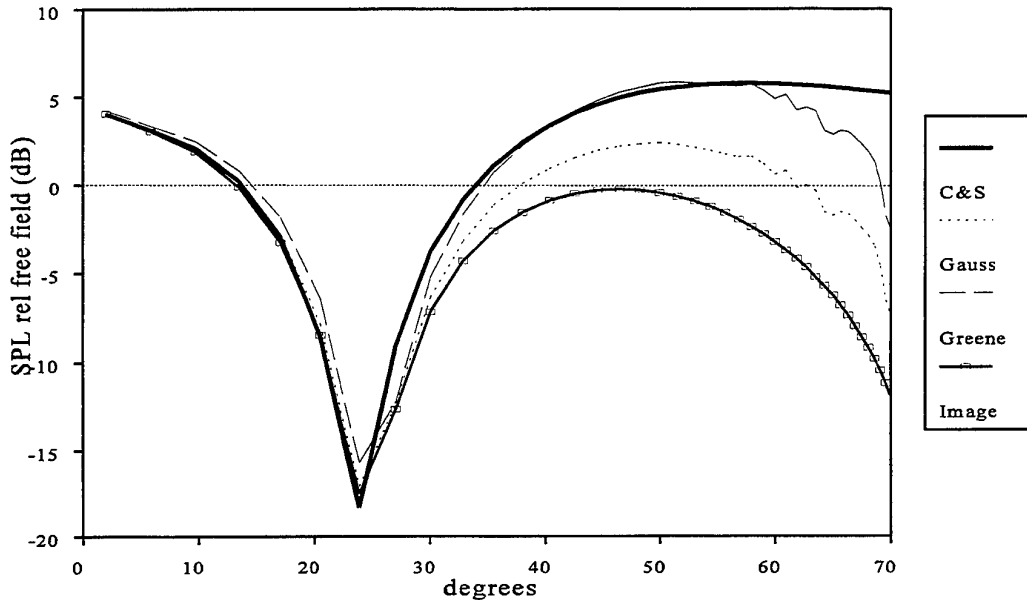


Figure 9 Calculations using the Claerbout parabolic equation of sound pressure levels relative to a free field versus angle from horizontal propagation, $d=100m$, $hs=2m$, soft ground $\sigma=200 \text{ Nsm}^{-4}$, $f=100\text{Hz}$.

Therefore, for source positions higher than $1/3\lambda$ each of the parabolic equations has associated one analytical starter with wider beamwidth. For the Claerbout approximation the Greene source is the optimal choice and for the Tappert Eq is the image starter. Special considerations has to be made for source positions close to the ground, using numerical starters or the image source.

3.5 PE calculations in a downward refracting atmosphere.

The level error introduced in the PE calculations due to the starters is studied for the same downward condition as the phase shift above. Figure 10 shows the CNPE calculations, based on the rational linear approximation, using the Gauss starter, the Greene starter and the Back PE starter. The propagation angle interval for this problem goes from $4,64^\circ$ to $21,15^\circ$. At these angles the Greene source has an aperture that is compatible with the Claerbout approximation, giving the right SPL. The Back PE converges to the Greene starter solution. A lever error of 1 dB is predicted with the Gauss starter. The CNPE calculations with the Image starter gives a 0.5 dB error under this atmospheric conditions.

For sound propagation in a downward refracting atmosphere the beamwidth of the starting field has to fulfill the angular limitation of the parabolic equation selected for the calculations. Using an starter with smaller beamwidth than the one required introduces a level error.

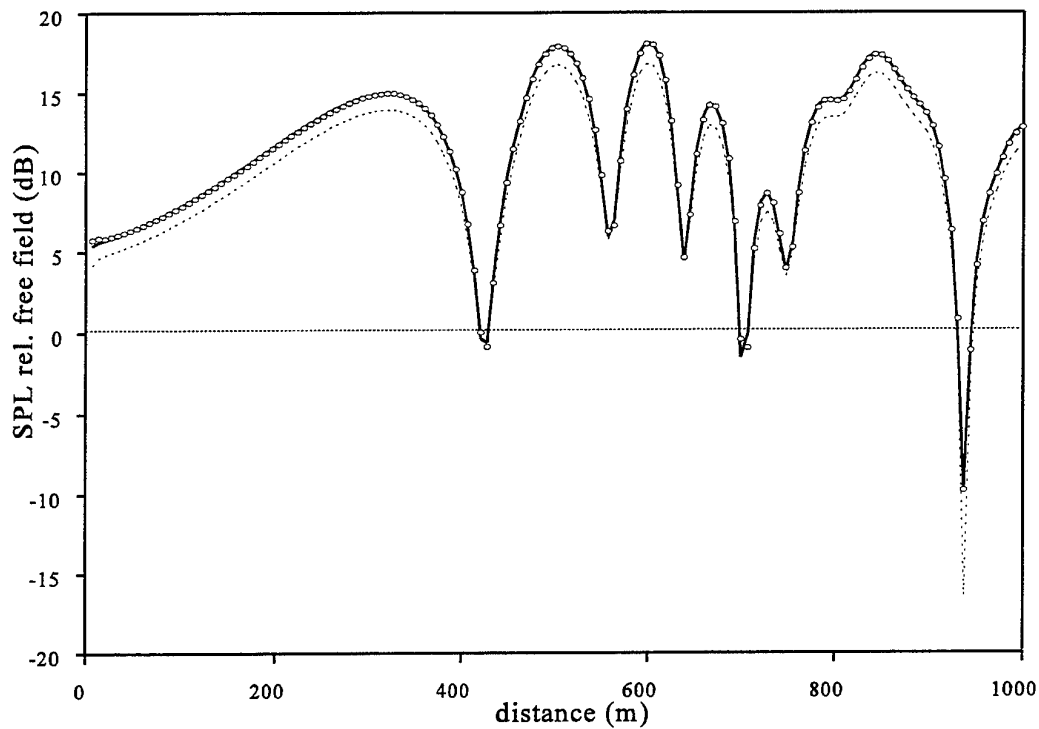


Figure 10 Sound pressure level relative to a free field versus range. Source height, $h_s = 1$ m, receiver height, $h_r = 1,05$ m, porous ground^{d/8}, $\sigma_{eff} = 3 \cdot 10^6$, the sound speed profile is as Eq(15). The solid line are calculations with the Greene starter, the markers (○) are calculations with the back PE starter and the dotted line are calculations with the Gauss starter.

4. CONCLUSION

Two sources of errors in the implementation of the PE model have been investigated. A phase error introduced in the approximation of the pseudo-differential operator and a level error introduced in the implementation of the starting field.

The angle associated with different parabolic equations are deduced, characterizing the different parabolic equations as narrow or wide. The angle associated with each of the parabolic equations represents the angular interval from the horizontal where forward propagating plane waves are treated accurately. The Claerbout equation is solved and compared with the normal mode solution of the Helmholtz equation in a downward refracting atmosphere. A normal mode in the Claerbout equation is propagated with the correct amplitude and mode shape. Only one unique mode can be propagated with the right phase. The propagation angle associated with the minimum attenuation mode is directly proportional to the sound speed gradient. Therefore, for long distance calculations under stronger downward refracting atmosphere, the very-wide angle PE base on the Padé expansion is needed to avoid phase error.

A level error is introduced in the parabolic calculations with the analytical starting fields under some special conditions; when the source is close to the ground or when the beamwidth of the starter does not fulfill the needs of the problem.

When the source is located close to the ground, less than $1/3 \lambda$, the analytical starters interact with the ground and introduce a level error that stays constant with the distance. Numerical test indicates that the level of error is a function of the characteristic impedance of the boundary and the distance source to the ground. The ground PE starter is a numerical starting field proposed in this work for a homogeneous atmosphere that includes the impedance boundary condition. For inhomogeneous atmosphere a back propagator PE is presented. These numerical starter do not present any problem with the source position and the propagation angle.

The spectral properties of the analytical starters have been calculated for two different parabolic equations for a fixed position of the source and ground impedance. In this case, for the Tappert equation the image starter has a beamwidth of 40° and for the Claerbout equation the Greene starter has a beamwidth of 65° . In the case of downward propagation the beamwidth of the starter and the angular limitation of the parabolic equation has to be wide enough to include the angle interval of the propagation modes.

5. REFERENCES

- [1] K.E. Gilbert and M. White "Application of the parabolic equation to sound propagation in a refracting atmosphere". J.Acoust.Soc.Am.85 (1989), 630-637.
- [2] J.S. Robertson, M. J. Jacobson, W.L. Siegmann and D.P. Santandrea, "Acoustical effects of a large rigide on low frequency sound propagation in stationary and moving atmospheres," RPI Math. Rep. No 181, Dept. Of Mathematical Sciences, Rensselear Polytechnic Institute, Troy, NY 12180-3590 (1989).
- [3] J.N. Craddock and M.J. White , "Sound propagation over surface with a varying impedance: A parabolic equation approach", J. Acoust. Soc. Am. 91 (1992), 3184-3191.
- [4] M. Galindo, "Application of the parabolic approximation method to sound propagation above ground with impedance variations", Procidings of the Sixth International Symposium on Longe-Range Sound Propagation, (1994), 394-407.
- [5] E.M. Salomons, "Diffraction by screen in downwind sound propagation: A parabolic-equation approach". J.Acoust. Soc. Am, 95, (1994), 3109-3117.
- [6] X. Di and K. Gilbert, "Applications of the Fast Green's function method to long range sound propagation in the atmosphere", Proceedings of the Fifth International Symposium on Long Range Sound Propagation, 128-145, (1992).
- [7] K.E. Gilbert and X. Di, "A Fast Green's function method for one-way sound propagation in the atmosphere," J. Acoust, Soc. Am. 93, (1992), 714-720.
- [8] K.E. Gilbert, R.Raspet and X. Di, "Calculation of turbulence effects in an upward refracting atmosphere" J. Acoust, Soc. Am. 87, (1990), 2428-2437.
- [9] J.M. Noble, H.E. Bass and R.Raspet , "Effects of large-scale wind driven turbulence on sound propagation".J. Acoust, Soc. Am. 87, S149.
- [10] F.D. Tappert "The parabolic approximation method" in Wave Propagation and Underwater Acoustics, edited by J.B. Keller and J.S. Papadakis (Springer, Heidelberg, 1977) Lecture Notes in Physics, Vol 70.
- [11] J.F. Claerbout, "Fundamentals of Geophysical Data Processing" (McGraw-Hill, New York, 1976).
- [12] R.R. Greene, "The rational approximation to the acoustic wave equation with bottom interaction," J. Acoust.Soc.Am. 76, 1764-1773 (1984).
- [13] M.Collins, "Applications and time domain solution of higher-order parabolics equations in underwater acoustics"m J.Acoust.Soc:Am. 86, (1989) 1097-1102.

- [14] F. Jensen, W. Kuperman, M. Porter and H. Schmidt, " Computational Ocean Acoustics", AIP SERIES in modern Acoustics and Signal Processing ,New York, 1994.
- [15] S.McDaniel,"Propagation of a normal mode in the parabolic approximation", J.Acoust.Soc.Am.57 (1975), 307-311.
- [16] R.Raspet, G.Baird and W. Wu, " Normal mode solution for low frequency sound propagation in a downward refracting atmosphere above a complex impedance plane" J. Acoust. Soc.Am. 91, 1341-1352 (1991).
- [17] A. Pierce "Acoustics. An introduction to its physical principles and Applications". American Institute of Physics, New York, 1991, pp.472.
- [18] K. Attenborough, "Acoustical impedance models for outdoor ground surfaces" J. Sound Vib. 99, 501-544 (1985).
- [19] C. Chien and W.Soroka " A note on the calculation of sound propagation along an impedance surface" J.Sound and Vibr., 69 (1980) , 340-343.
- [20] M. Collins and E.K. Westwood " A higher- order energy-conserving parabolic equation for range-dependent ocean depth, sound speed, and density", J. Acoust. Soc. Am. 89 (1991), 1068-1075 .

Atmospheric Sound Propagation Using the Wide-angle Parabolic Equation

P. MALBEQUI

*Office National d'Etudes et de Recherches Aérospatiales,
B.P. 72, 92322 Châtillon Cedex, France
FAX (33) 1 46 73 41 48*

The wide-angle parabolic equation proposed by Claerbout is applied to atmospheric sound propagation. Comparisons with experimental results are detailed in this paper. In 1991, the NATO JAPE 91 (Joint Acoustic Propagation Experiments) experimental campaign on outdoor propagation over a sandy ground, including meteorological measurements, were carried out using microphones of the French-German Institute of Saint Louis (ISL). Under almost non-turbulent atmosphere, the PE calculations are in a very good agreement with the experiment over a distance of 1.6 km from the electroacoustic source at frequencies 80 and 200 Hz. For higher frequencies (500 Hz), computations confirm that the transmission loss strongly depends on the wind and temperature gradients. Comparisons with JAPE 91 results for a helicopter in hover flight above a hill are also considered. Again, the computation of the sound pressure in the shadow zone of the hill is in good agreement with experiment in the frequency range 10-400 Hz.

I. Introduction

ONERA has developed a code based on the so-called parabolic equation (PE) for the prediction of sound propagation above the ground [1]. A number of validations with two other numerical methods have shown the capabilities of the two-dimensional 2DPE code : ray method developed by Institut de Saint Louis [2] and gaussian beam due to Centre Scientifique et Technique du Bâtiment (CSTB) [3]. Comparisons with tunnel experiment at CSTB [4] and long range sound propagation experiment in the Beauce country of central France were also performed [5]. A three-dimensional PE has also been implemented at ONERA to take into account 3D effects due to scattering by obstacles of finite dimension and wind speed variations with respect to the azimuth [6]. The main results were presented during the Vth Symposium on Long Range Sound Propagation [7].

More recently, benchmarks cases were defined by Attenborough *et al.* [8] to validate and to point out the advantages and the limitations of many prediction models applied to outdoor propagation. The ONERA PE software was checked with these benchmarks cases and gives results similar to those obtained by other PE's implementations. Moreover, experimental results obtained by ISL during JAPE 91 for electroacoustic source and helicopter in hover flight above a hill are available. The soil characteristics, speed and direction of the wind, and temperature gradients were also recorded during the JAPE 91 to enable one accurate comparisons with the PE model.

The objective of this paper is to show the capabilities of the Claerbout 2DPE applied to JAPE 91 configurations.

This paper starts with a brief presentation of the Claerbout PE. In particular, it is shown that when using the Thomson and Chapman approach, the Claerbout approximation

gives more accurate results than the standard PE and other PE's. Comparisons with experiments are subsequently discussed.

II. Formulation

The Claerbout equation

The Claerbout PE is based on the approximation of the square root operator \mathcal{Q} with a rational function. Assuming an homogeneous medium and a plane wave in the θ direction with respect to the horizontal, it has been established that the Claerbout PE provides a good approximation of the Helmholtz equation for θ less than 40 degrees.

It is shown here that the approach of Thomson and Chapman [9] also enables a comparison of the Claerbout PE with the standard PE (the 15 degrees approximation), the Thomson and Chapman PE and the Tappert PE. Derivation of the Claerbout PE is now briefly presented with usual notations.

Consider the two-dimensional Helmholtz Equation (2DHE) in cylindrical co-ordinates

$$\left[\frac{\partial^2}{\partial r^2} + \frac{1}{r} \frac{\partial^2}{\partial r \partial z} + \frac{\partial^2}{\partial z^2} + k_0^2 n^2 \right] p = 0 \quad (1)$$

where r is the range and z the height. $n = c_0/c$ is the index of refraction, where c_0 is a reference sound speed and c the local sound speed; k_0 represents a reference wave number.

The time dependence $\exp(-i\omega t)$ is omitted.

The acoustic pressure p is written in the form

$$p(r, z) = \frac{u(r, z)}{\sqrt{r}} \quad (2)$$

where u designates the envelope function.

Applying the farfield approximation ($k_0 r \gg 1$), Eq. (1) becomes

$$\left[\frac{\partial^2}{\partial r^2} + \frac{\partial^2}{\partial z^2} + k_0^2 n^2 \right] u = 0 \quad (3)$$

The following linear partial differential operators are now introduced

$$P = \frac{\partial}{\partial r} \quad (4)$$

and

$$\mathcal{Q} = [I + \varepsilon + \mu]^{1/2} \quad (5)$$

where

$$\varepsilon = n^2 - 1 \quad (6)$$

and

$$\mu = \frac{1}{k_0^2} \frac{\partial^2}{\partial z^2} \quad (7)$$

After substitutions, Eq. (3) is rewritten

$$[P^2 + k_0^2 \mathcal{Q}^2] u = 0 \quad (8)$$

Assuming that the dependence of the index of refraction with the range is small, Eq. (8) can be transformed into the product of two operators

$$[P - ik_0 Q][P + ik_0 Q]u = 0 \quad (9)$$

the first one corresponding to forward propagation and the second one to backward propagation.

According to the parabolic approximation (neglecting the backscattered field with respect to the forward field), Eq. (9) is reduced to

$$[P]u = [ik_0 Q]u \quad (10)$$

Let us define a slow varying function

$$\psi = u \exp(-ik_0 r) \quad (11)$$

According to the approximations for the Q operator, many PE's have been proposed in the literature.

$$Q_1 = I + \frac{\varepsilon}{2} + \frac{\mu}{2} \quad (12)$$

gives the standard PE

$$\frac{\partial \psi}{\partial r} = ik_0 \left[\frac{\varepsilon + \mu}{2} \right] \psi \quad (13)$$

proposed by Hardin and Tappert [10].

$$Q_2 = [I + \mu]^{1/2} + \frac{I}{2} \varepsilon \quad (14)$$

has been derived by Tappert [11].

$$Q_3 = [I + \mu]^{1/2} + [(I + \varepsilon)^{1/2} - I] \quad (15)$$

has been presented by Thomson and Chapman.

Using the following rational function approximation

$$Q_4 = \frac{1 + \frac{3\varepsilon}{4} + \frac{3\mu}{4}}{1 + \frac{\varepsilon}{4} + \frac{\mu}{4}} \quad (16)$$

the Claerbout PE is obtained

$$\left[I + \frac{\varepsilon + \mu}{4} \right] \frac{\partial \psi}{\partial r} = ik_0 \left[\frac{\varepsilon + \mu}{2} \right] \psi \quad (17)$$

It was originally developed for seismic predictions [12] and has also been applied to underwater [13] and atmospheric sound propagation [14]. The advantages of these approximations have been examined in the past. It should be remembered that the Claerbout PE allows, like the standard PE, a straightforward finite difference implementation. Thus, it is well-suited to atmospheric propagation problem where the reflection by the ground has to be properly modelled.

Error between the Helmholtz and the PE's solutions

Following the Thomson and Chapman method, we set the error measured

$$E_i = Q_i^2 - Q^2, \quad i = 1, 2, 3 \text{ and } 4 \quad (18)$$

An homogeneous medium for the index of refraction

$$n = 1 + \delta n \quad (19)$$

and a plane wave propagation are assumed

$$u = \exp[ik_0(r \cos \theta + z \sin \theta)] \quad (20)$$

For this configuration, where no backscattered field occurs, a solution to Eq. (10) also represents an exact solution to the Helmholtz equation (Eq. (3)). As a result, E_i gives the error between Helmholtz and PE's solutions.

Using (19) and (20), one obtains

$$|\mu| = \sin^2 \theta \quad (21)$$

and

$$|\varepsilon| \leq |\delta n|(2 + |\delta n|) \quad (22)$$

Thomson and Chapman derived errors bounds for the operators Q_1 , Q_2 , and Q_3 . For instance, with Q_1 , the error is

$$|E_1| \leq \frac{1}{4} [|\delta n|(2 + |\delta n|) + \sin^2 \theta]^2 \quad (23)$$

After some algebraic manipulations, we easily showed that the error bounds for the Claerbout operator is given by

$$|E_4| \leq \frac{[|\delta n|(2 + |\delta n|) + \sin^2 \theta]^3}{[4 - |\delta n|(2 + |\delta n|) - \sin^2 \theta]^2} \quad (24)$$

Errors E_i performed with a fixed $\theta = 20$ degrees and for $0 < \delta n < 0.2$ are plotted on Fig. 1a. E_i with a fixed $\delta n = 0.1$ and θ in the range 0-40 degrees are plotted on Fig. 1b.

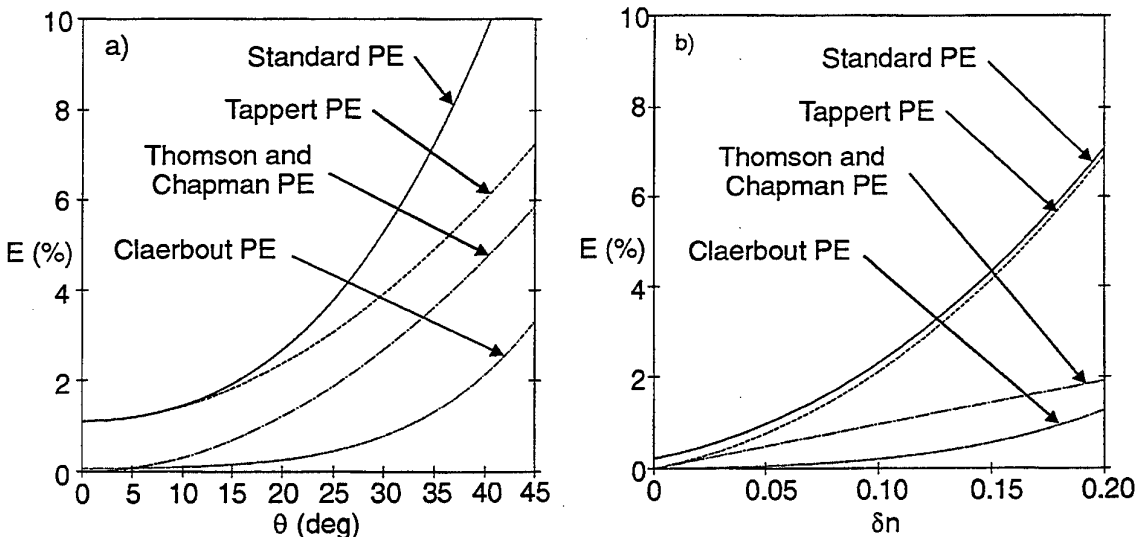


Fig. 1 - Error E_i between Helmholtz and parabolic equations;
a) fixed index of refraction : $\delta n = 0.1$. b) fixed direction of propagation : $\theta = 20$ deg.

It appears that, for this homogeneous case, the Q_4 curve remains below the others, so that the Claerbout PE provides more accurate results. In the underwater community, other PE's have also been proposed. For instance, based on the rational fraction approximation for Q , Knightly *et al.* [15] proposed a 67 degrees approximation. Nevertheless, the 40 degrees approximation is excellent for sound propagation at low altitude, as shown below.

III. Numerical implementation and boundary conditions

In the ONERA code, the standard PE and Claerbout are classically solved using an implicit finite difference (IFD) scheme. The $\frac{\partial^2 \psi}{\partial z^2}$ derivative is estimated with central differences of order $O(\Delta z^2)$. Stability of the IFD is ensured according to the naïve Von Neumann stability method.

The initial condition at range r_0 corresponds to the sound pressure due to a point source above a plane. On the ground, an impedance condition is applied. The locally reacting impedance is here deduced from the Attenborough model [16] depending on both effective flow resistivity and porosity. On the top of the mesh, at $z = z_{Max}$, a non-reflecting condition is required. Usually, to avoid numerical reflections, an artificial attenuation in the upper part of the mesh is added, so that the amplitude of reflected waves are greatly reduced. Instead of this technique, a radiation boundary condition directly derived from the wave impedance in homogeneous medium is here considered. To obtain the wave impedance at $z = z_{Max}$, the pressure and acoustical velocity are analytically computed from the solution of a point source above an absorbing ground in homogeneous medium. Numerical tests have shown that this technique is also efficient under downward and upward refractions. It avoids to mesh the fluid in the absorbing layers and reduces CPU time.

IV. Comparison between the standard PE and the Claerbout PE

The homogeneous medium test discussed above demonstrates the accuracy of the Claerbout PE and allows comparisons with many PE's. However, it does not take into account the boundary conditions and the sound speed profiles in air. For this purpose, an application to a benchmark case defined in [8] is now presented, where the standard PE and the Claerbout PE are integrated by the IFD method.

The linear sound speed, corresponding to downward refraction, is $c(z) = 344 + 0.1 z$ (m/s). The point source is located at $r = 0$ and $z = 5$ m above a rigid surface and its frequency is 10 Hz. The sound pressure level is plotted in dB and referenced to 0 dB at 1 m from the source.

Fig. 2 displays the comparison between standard PE and Claerbout PE as contour plots. As expected, the two PE's are in a good agreement near the ground. At higher altitude, where the 15 degrees approximation is no more valid, significant differences appear. For instance, for z greater than 200 m, about 10 dB difference is observed between the two PE's. Wiggles also appear for the standard PE computation which do not occur with Claerbout PE. They may be attributed to phase errors in the small angle approximation.

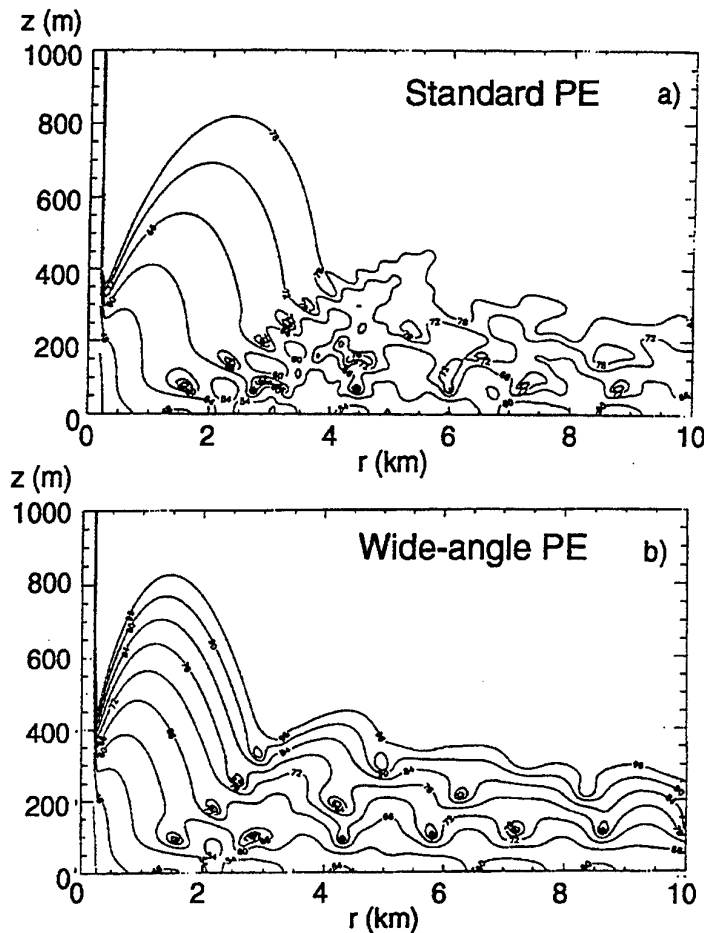


*Fig. 2 - Benchmark case of downward sound propagation above a rigid ground, $f = 10$ Hz.
a) standard PE ; b) Claerbout PE.*

V. Sound propagation above a sandy ground

Experimental Set-up

During JAPE 91, the ISL team recorded the sound pressure produced by a loudspeaker located above a flat sandy ground over a range of 1.6 km from the acoustical source. The experiments have been carried out in the White Sands Missile Range in New Mexico with the contribution of 15 teams during summer 1991. Extensive meteorological characterisations as well as ground measurements were also made along with the acoustic experiments. Some experimental results are presented in [17]. The parameters were the source height, the frequency emission and meteorological conditions. Meteorological measurements of temperature gradients, speed and direction of the wind allow the derivation of the vertical profiles of sound velocity up to 500 m height in the source-receiver direction. From among the many runs realised during JAPE 91, ISL run 005102 recorded on 11th July, at 10:20 pm with loudspeakers located on the North tower at 2 m above the ground is investigated. ISL instrumentation is summarised on Fig. 3.

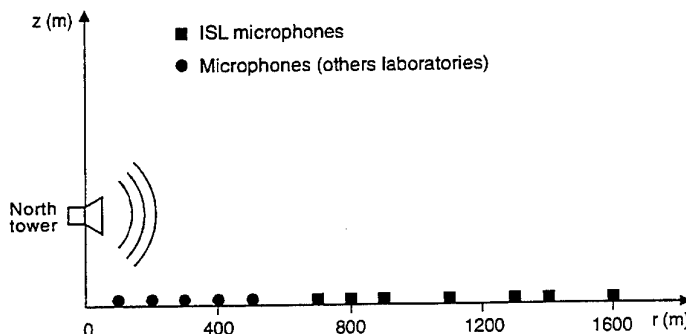


Fig. 3 - Experimental set-up for sound propagation above a sandy ground during JAPE 91.

Meteorological conditions were measured the same day at 9:10 and 11:10 pm. Sound velocities are plotted on Fig. 4a and Fig. 4b; the average sound velocity of the two previous profiles is also displayed on Fig. 4c. During this run, the atmosphere was non-turbulent and almost homogeneous, so that only weak amplitude variations in the range 342-348 m/s are observed for the sound speed. Notice that close to the ground, the sound speed gradients measured at 9:10 and at 11:10 pm differ. The soil characteristics are 44% porosity and 10^6 rayls MKS for the flow resistivity. They are introduced with the vertical sound profiles in the Claerbout model.

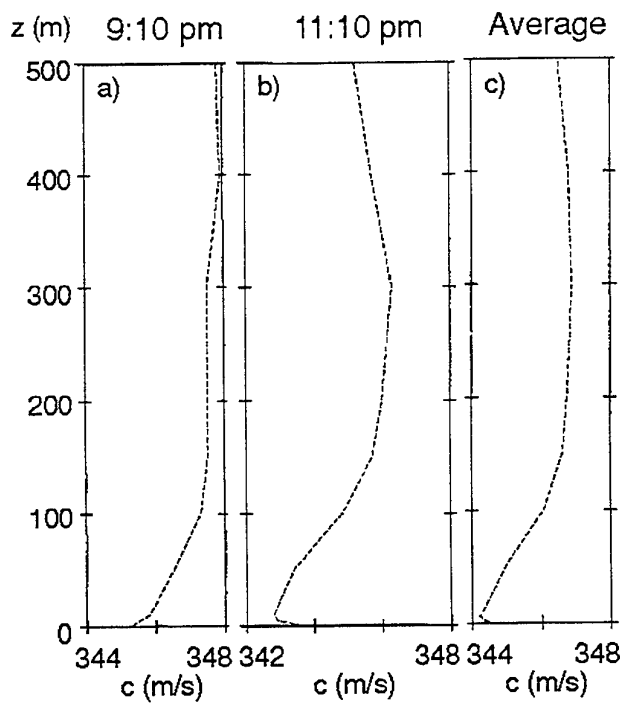


Fig. 4 - Vertical profiles of sound velocity recorded in July 11, during JAPE 91; a) 9: 10 pm; b) 11: 10 pm ; c) average of profiles a) and b).

Results

Comparisons between experiment and Claerbout PE computation for the sound pressure level are presented on Fig. 5, for the source frequencies 80, 200 and 400 Hz.

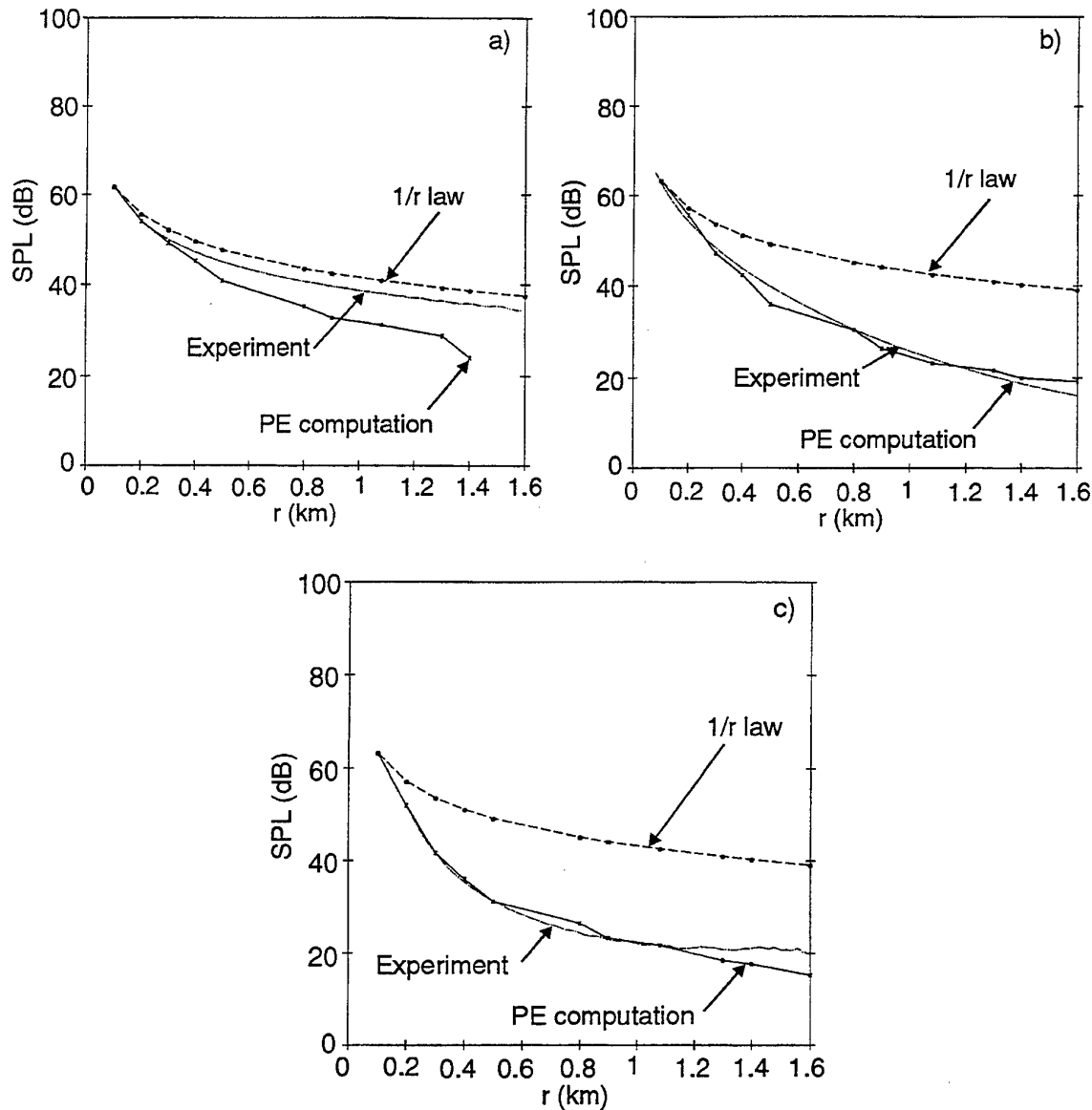


Fig. 5 - Sound propagation above a sandy ground, comparison between Claerbout computation and ISL experiment. a) $f = 80$ Hz; b) $f = 200$ Hz; c) $f = 500$ Hz

Computations are here performed with the average sound velocity of Fig. 4c. For the PE computation, the SPL is referenced to sound level measured on the microphone located at 100 m from the source. Notice that no corrections of absorption of sound by the atmosphere is introduced in the PE model; in the frequency range of interest, it remains below 2 decibels per kilometre. The $1/r$ law spreading is also plotted on Fig. 5. The agreement is good at 80 Hz and excellent at 200 and 500 Hz. In particular, the transmission loss is properly retrieved

using both the Claerbout PE and the Attenborough model. Classically, it is observed that attenuation is more intense for higher frequencies. At 500 Hz, 20 dB differences appear between computation/experiment and the $1/r$ law due to ground absorption and non-homogeneous medium.

Sensitivity of the computation to the meteorological conditions is also analysed on Fig. 6a and Fig. 6b for the frequencies 80 and 500 Hz.

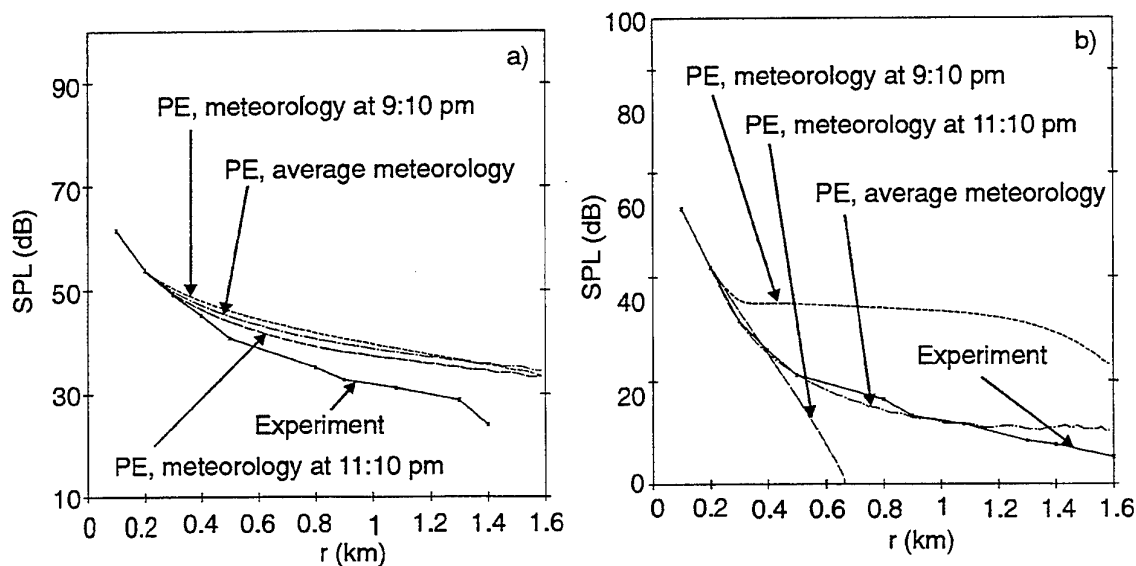


Fig. 6 - Sound propagation above a sandy ground, sensitivity of the Claerbout computation to the meteorological conditions: a) $f = 80$ Hz; b) $f = 500$ Hz.

The three sound velocity profiles plotted of Fig. 4 are now successively incorporated in the PE model. At 80 Hz, the SPL remains almost the same under the three meteorological environments. At 500 Hz, a significant deviation appears: for the 9:10 pm condition, the level falls off slowly with increasing range and at 11:10 pm a shadow zone is created where SPL is greatly reduced. Incorporating the average sound velocity profile gives a good agreement with the experiment. A ray tracing was also computed by ISL for both sound profiles at 9:10 and at 11:10 pm. On the ray tracing displayed on Fig. 7, the plot of interest corresponding to run 005102 is for negative range. According to previous PE prediction, it clearly shows that the 9:10 pm condition corresponds to a downward refraction and the 11:10 pm configuration create upward refraction associated with a shadow zone. These results confirm that, at high frequencies, the SPL strongly depends on the wind speed fluctuations.

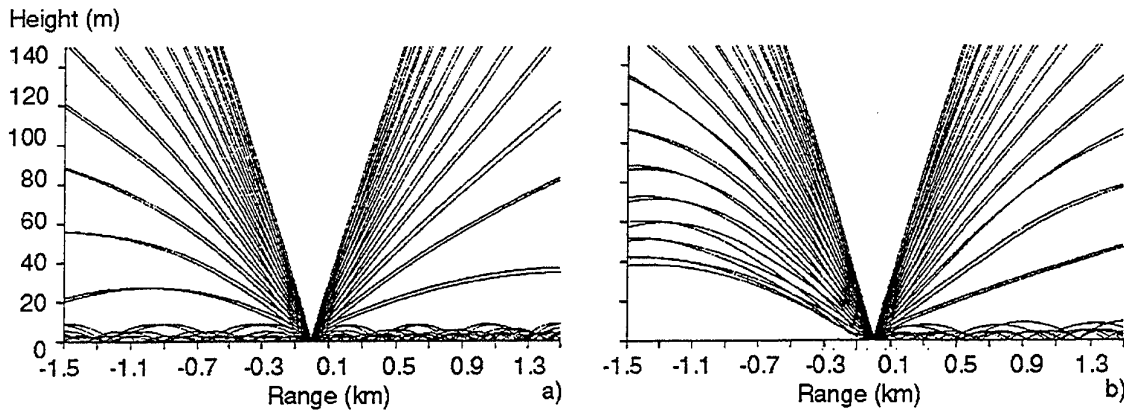


Fig. 7 - Sound propagation above a sandy ground, sensitivity of ray tracing to the meteorological conditions: a) 9:10 pm; b) 11:10 pm.

VI. Sound radiated by a helicopter above a hill

Capability of the PE model to take into account irregular topography have been examined in the past. Comparisons with experimental results validated PE software in case of propagation behind a screen [6]. The main difficulty arising in the implementation is the incorporation of the derivative operator P on the topography; it is detailed in [18]. The helicopter test now presented is obviously more realistic and particularly interesting for military purposes.

During the "terrain masking" experiment of the NATO JAPE 91, Atlas Electronik and ISL measured the pressure field due to a helicopter in hover flight above a small hill. Microphones were located on the shadow zone of the hill to study diffraction effects on the propagation and capability of detection systems. The experimental set-up and results are summarised in [19]. The height of the hill is about 60 m. The helicopter made hover flight at different height above the hill between 20 and 110 m. The 20 m height configuration, that produces the more intense shadow zone, is here analysed. The frequencies 10.5, 160 and 400 Hz emitted by the main rotor and the tail rotor are considered. Meteorological measurements show that the atmosphere was almost homogeneous and very quiet during the acoustic run. An homogeneous medium assumption is then made for PE prediction.

The hill profile, ISL microphones located along the hill profile and helicopter in hover flight on the left side of the hill are plotted on the lower part of Fig. 8. Range $r = 0$ m corresponds to the location of the helicopter behind the hill. The upper part of Fig. 8 displays comparison between experiment and computation. In the computation, the SPL is referenced to the one measured on microphone located at 600 m from the helicopter. As backscattered waves are neglected in the PE model, the sound pressure in the left side of the hill is no more valid, so that only computation of the SPL on the right side is plotted.

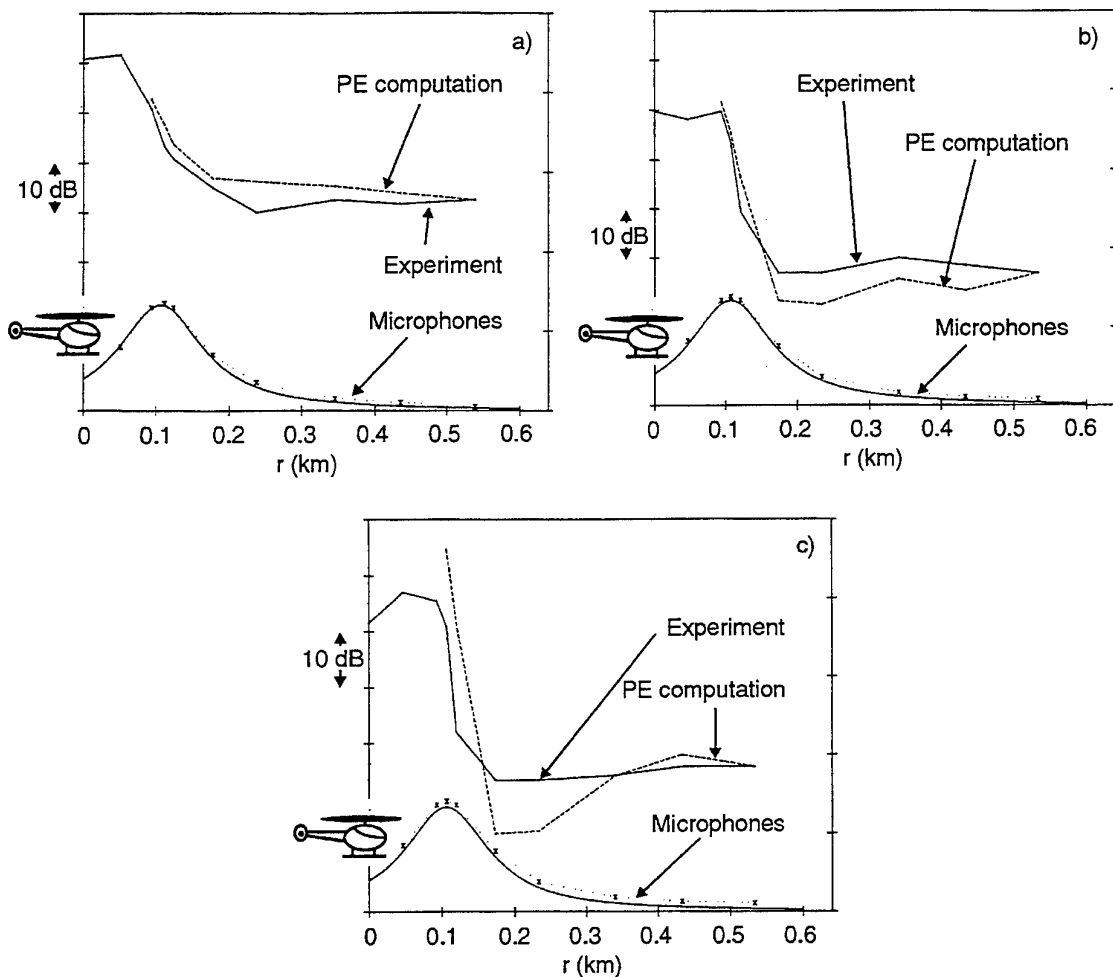


Fig. 8 - Sound radiated by a helicopter in hover flight behind a hill.
a) $f = 10.5$ Hz; b) $f = 160$ Hz; c) $f = 400$ Hz.

At 10.5 Hz, 20 dB attenuation with respect to sound pressure at the top of the hill is observed in the shadow zone. According to classical diffraction effects, the attenuation is greater at the foot of the hill ($r = 250$ m) and almost constant with increasing ranges. The same tendency applies at 160 Hz and 400 Hz but, masking effect is, as expected, more effective where 30 dB and 35 dB attenuation are observed, respectively. PE predictions and experimental results are in a good agreement. However, the computation predicted excess attenuation of about 5 to 10 dB on the foot of the hill at 160 Hz and 400 Hz. Such a difference can be explained with the homogeneous medium assumption in the PE computation. Downward propagation may bend the energy close to the foot of the hill and reduce attenuation.

VII. Summary

Many comparisons between Claerbout PE prediction using a code developed by ONERA and realistic experiments have been analysed in this paper. During JAPE 91, extensive acoustic transmission loss along with meteorological conditions were measured. The PE prediction is in good agreement with experimental results obtained for a loudspeaker emitting above a flat sandy ground and the "terrain masking" experiment with an helicopter in hover flight behind a hill. Future analysis may focus on upward propagation where the influence of the turbulent atmosphere has to be incorporated in the PE model to propagate the pressure field deep inside the shadow zone.

Acknowledgements

This work was supported by Direction de la Recherche et de la Technologie (DRET). The author would like to thank the ISL team for providing the experimental results of JAPE 91.

References

- [1] P. Malbéqui, F. Jouaillec, "Acoustic propagation over the ground using the parabolic approximation method", *Proceedings of the International Conference on Noise Control Engineering*, Vol. 3, pp. 1579-1582, 1988.
- [2] J. Vermorel, "La propagation acoustique dans la basse atmosphère", Doctoral thesis - Université du Maine, 1987.
- [3] Y. Gabillet, H. Schroeder, G.A. Daigle and A. l'Espérance, "Application of the Gaussian beam approach to sound propagation in the atmosphere: Theory and experiments", *J. Acoust. Soc. Am.*, Vol. 93, pp. 3105-3116, 1993.
- [4] P. Malbéqui, "Etude d'un réseau à pas variable et comparaison entre la méthode des rayons et l'équation parabolique dans le cadre de la propagation atmosphérique", ONERA Technical Report 12/3641 PY, 1989.
- [5] S. Canard, S. Léwy, J. Vermorel and G. Parmentier, "Long range sound propagation near the ground", *Noise Control Engineering Journal*, Vol. 34, pp. 111-119, 1990.
- [6] Y. Delrieux, "Analyse de la propagation acoustique à basse altitude par l'équation parabolique tridimensionnelle", Doctoral thesis, Ecole Centrale de Lyon, Nov. 1991.
- [7] Y. Delrieux and P. Malbéqui, "Atmospheric sound propagation using a three-dimensional parabolic equation", *Proceedings of the Vth Intern. Symp. on Long Range Sound Propagation*, London (UK), pp. 147-157, 1992.
- [8] K. Attenborough *et al.*, "Benchmark cases for outdoor sound propagation models", *J. Acoust. Soc. Am.*, Vol. 97, pp. 173-191, 1995.
- [9] D.J. Thomson, N. R. Chapman, "A wide angle Split-Step algorithm for the parabolic equation", *J. Acoust. Soc. Am.*, Vol. 74, pp. 1848-1854, 1983.
- [10] R. H. Hardin, F. D. Tappert, "Application of the Split-Step Fourier method to the resolution of non-linear and variable coefficient wave equations", SIAM, Rev. 15, 423, 1973.
- [11] F. D. Tappert, "The parabolic approximation method", in *Wave Propagation and Underwater Acoustics*, edited by J. B. Keller and J. S. Papadakis, Springer-Verlag, New York, Vol. 70, 1977.
- [12] J. F. Claerbout, *Fundamentals of geophysical data processing*, McGraw-Hill, New York, 1976.
- [13] D. Lee and S.T. McDaniel, *Ocean acoustic propagation by finite difference methods*, General Editor E. Y. Rodin, 1987.
- [14] K. E. Gilbert, M. J. White, "Application of the parabolic equation to sound propagation in a refracting atmosphere", *J. Acoust. Am.*, Vol. 85, pp. 630-637, 1989.

- [15] G. H. Knightly, D. Lee, Donald F. St. Mary, "A higher-order parabolic wave equation", *J. Acoust. Soc. Am.*, Vol. 82, pp. 580-587, 1987.
- [16] K. Attenborough, "Acoustical impedance models for outdoor ground surfaces", *J. Sound and Vib.*, Vol. 99, pp. 521-544, 1985.
- [17] P. Naz and G. Parmentier, "Some results of sound propagation experiments", to be published in *Proceedings of the VIIth Intern. Symp. on Long Range Sound Propagation*, Ecole Centrale de Lyon, France, 1996.
- [18] Y. Delrieux, "Propagation acoustique en présence d'une colline dans l'approximation parabolique", Colloque de Physique, supplément au N°7, Tome 51, C3-244, 1990.
- [19] P. Naz, "JAPE 91 : Influence of terrain masking on the acoustic propagation of helicopter noise", ISL Report PU317/93, JAPE91 Workshop, NASA Langley, Hampton/VA, USA, 1993.

Computational model for propagation of bullet noise

N A KINNEGING and F H A Van den BERG

TNO Institute of Applied Physics

Stieltjesweg 1, P.O.Box 155

2600 AD Delft

The Netherlands

1. INTRODUCTION

Shooting noise can often be heard at large distances from the shooting ranges. In order to predict the immission levels of shooting noise there is a need for reliable long-range propagation models. Shooting noise may have three components: muzzle noise, due to the explosion of the propulsive powder; bullet noise for supersonic bullets and detonation noise in case of a detonating charge. Van den Berg et al [1] give an overview of a method, that is being developed for the Dutch Ministry of Defence, to predict average propagation of shooting noise around shooting ranges. This paper will concentrate in more detail on the propagation model for bullet noise.

Due to the supersonic flight of the bullet a shock wave is generated (sonic boom). The form of the wave front is conical, where the cone is centered on the bullet path. The top angle α of the cone depends on the bullet speed v and the sound speed c by,

$$\alpha = 2 \arcsin\left(\frac{c}{v}\right) \quad (1)$$

For a bullet path of finite length the bullet noise is just audible in a restricted area, the Mach area. In figure 1 the Mach area is illustrated relative to the bullet path. Here a bullet path of finite length and from a decreasing bullet speed is displayed. Outside this area the level of the bullet noise is much lower than inside the Mach area.

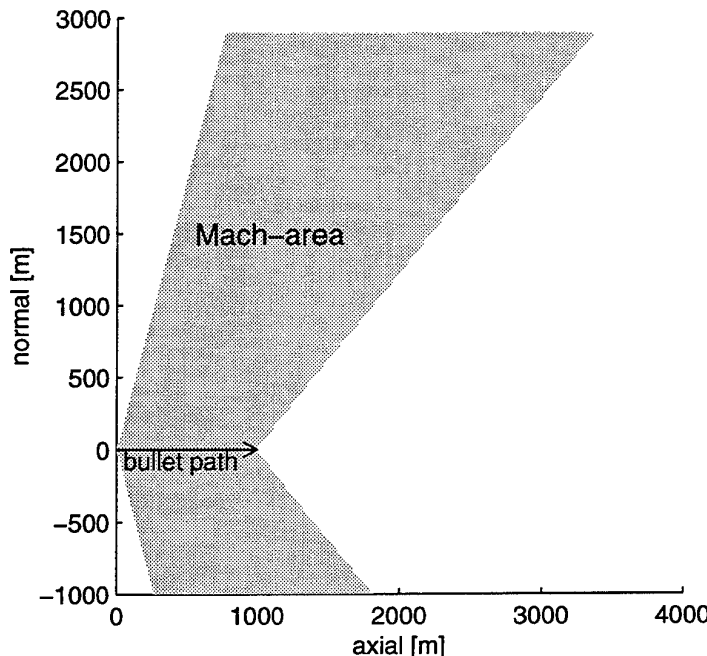


Figure 1: Illustration of the Mach area relative to the bullet path.

The wave propagation of bullet noise is non-linear. There exist analytical solutions for bullet noise [2], but these are restricted to idealised situations with bullet paths of infinite length and bullets of constant speed. Decreasing bullet speeds cannot be modelled. Also diffraction effects due to the finite length of the bullet paths cannot be handled.

In this paper we present a method to compute the propagation of bullet noise, which can also be used for bullet paths of finite length with decreasing bullet speed. The method can also correct for atmospheric absorption, meteorological effects and ground effects.

2. COMPUTATION SCHEME

The pulse of the bullet noise has the form of an N (an N-wave). The propagation of N-waves can be described by the weak shock theory. Using this theory the amplitude and pulse length of the N-waves can be calculated as a correction to amplitude and pulse length derived from linear acoustics. The atmospheric, meteorological and ground effects are incorporated as an excess attenuation to the non-linear free field parameters.

Therefore the global scheme consists of three steps:

1. computation of the linear wave propagation
2. non-linear correction of the amplitude and pulse length of the N-wave
3. application of atmospheric, meteorological and ground effects

Linear Modelling

For the modelling of the linear wave propagation we use Huygen's Principle. This principle states that a wave front can be seen as a number of point sources. The propagation of the total wave front is the sum of the contributions of all (secondary) point sources. For bullet noise the bullet path can be considered as a line source. Using Huygen's Principle this line source can be handled as a number of point sources. Each point source has a delay that corresponds to the time that the bullet passes that point. The strength of the sources is based on the bullet dimensions and the local bullet speed. The method of using Huygen's Principle is illustrated in figure

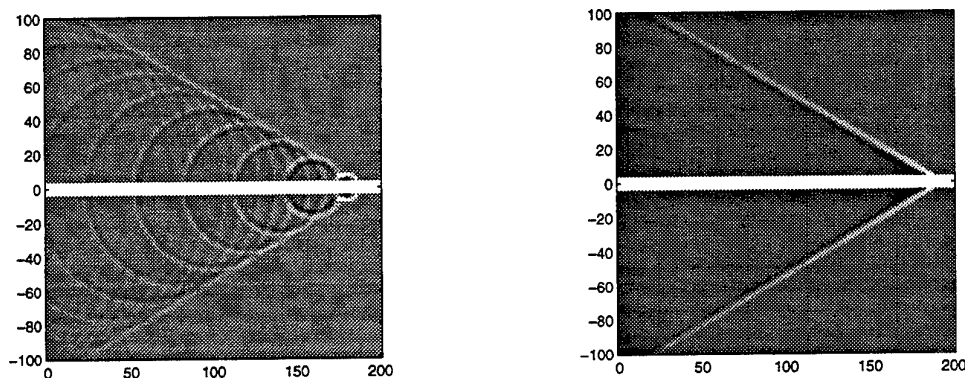


Figure 2: Illustration of the Huygen's Principle. In the left figure the sampling interval of the Huygens sources is coarse, such that the wave fronts of the individual secondary sources are visible. On the right figure a proper sampling of the Huygens sources is chosen. Now just the resulting wave front is present.

In this way it is possible to calculate the response of bullet paths of finite length with a decreasing bullet speed. In figure 3 an example is given of the wave fronts that are calculated for a decreasing bullet speed. The initial speed of the bullet was 650 m/s and after 150 m it has decreased to below the sound speed. The ray paths are indicated, which are normal to the wave fronts. Notice that the top angle of the conical wave front increases for a decreasing bullet speed according to equation (1). Beyond the point where the bullet speed decreases below the sound speed, the wave propagates in the same direction as the bullet direction.

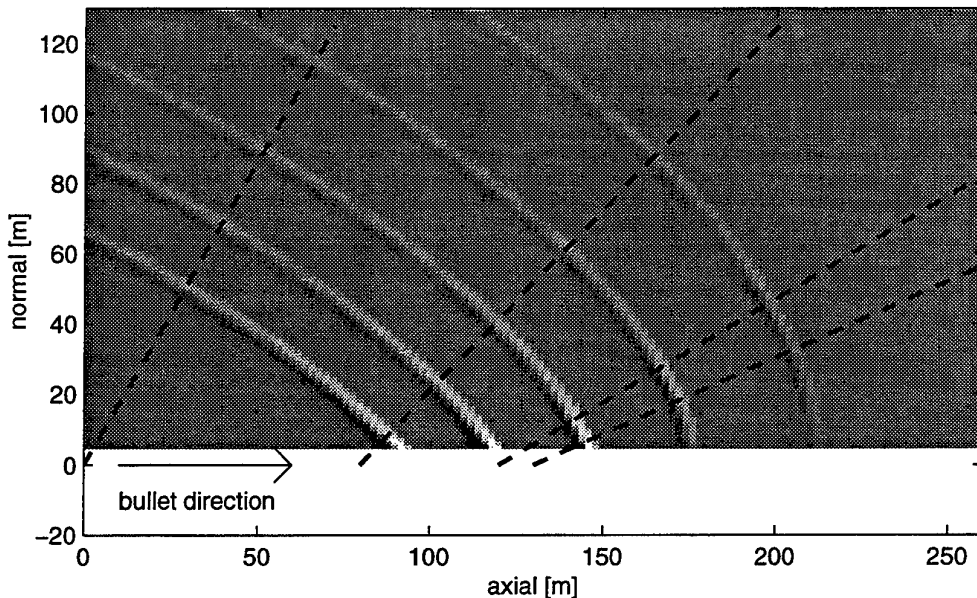


Figure 3: Wave fronts and rays calculated using linear modelling.

Non-Linear Corrections

For large sound pressures the propagation velocity of sound depends on the sound pressure itself. In the first order this can be described as,

$$c(p) = c_0 + \beta \frac{p}{\rho c_0} \quad (2)$$

where c_0 is the linear sound speed, p the sound pressure, β a non-linearity constant ($=1.2$ for air) and ρ the density of air.

The normalised amplitude factor $B(l)$ gives the linear amplitude at a distance l along the ray. At a reference point $l=0$ the amplitude factor equals 1. Using the weak shock theory the amplitude (P) and pulse length (T) of the N-wave can be calculated by,

$$P(\ell) = B(\ell)P(0) \left[1 + \frac{P(0)}{T(0)} \text{Age}(\ell) \right]^{-1/2} \quad (3a)$$

$$T(\ell) = T(0) \left[1 + \frac{P(0)}{T(0)} \text{Age}(\ell) \right]^{1/2} \quad (3b)$$

where the Age-function is defined as,

$$\text{Age}(\ell) = \frac{\beta}{\rho c_0^3} \int_0^\ell B(\ell^*) d\ell^* \quad (4)$$

From the linear wave field these non-linear parameters can be determined numerically. A description of the weak shock theory can be found at Pierce [2].

Using the weak shock theory for the special case of supersonic bullets expressions can be derived for the amplitude and pulse length of the N-wave, that is generated.

The overpressure P of the shock wave can be written as,

$$P(r) = \frac{\rho c_0^2 (M^2 - 1)^{1/8}}{2^{1/4} \beta^{1/2} r^{3/4}} \frac{S_{\max}^{1/2} K}{L^{1/4}} \quad (5)$$

and for the pulse length of the N-wave,

$$T(r) = \frac{2^{7/4} \beta^{1/2} M r^{1/4}}{c_0 (M^2 - 1)^{3/8}} \frac{S_{\max}^{1/2} K}{L^{1/4}} \quad (6)$$

where	ρ	the mass density of air
	c_0	the sound propagation velocity in air
	M	the Mach number
	β	the non-linearity constant (=1.2 for air)
	r	the distance to the bullet path
	S_{\max}	the maximum diameter of the bullet
	L	the effective length of the bullet
	K	a constant dependent on the shape of the bullet

It can be seen that due to the non-linear effects the pressure amplitude decreases with the distance to the bullet path as $r^{-3/4}$. Furthermore the pulse length increases as a function of the distance to the bullet path as $r^{1/4}$. This means that the sound exposure of an N-wave decreases with the distance to the bullet path as $r^{-5/4}$. The sound exposure level therefore decreases with $-12.5 \lg(r)$.

As a comparison the sound exposure levele decreases with $-10 \lg(r)$ if no non-linear effects were considered and for a point source the sound exposure level decreases with $-20 \lg(r)$.

Atmospheric, Meteorological and Ground Effects

From the first two steps in the scheme the non-linear wave field is calculated without the influence of absorption, meteorological (wind and temperature profile) and ground effects. Ideally these effects should be incorporated in the previous steps, because of the non-linear effects. These steps however prove to be of second order and can therefore be treated separately. The atmospheric absorption is calculated based on the spectrum, that is derived from the amplitude and pulse length at the immission location. The meteorological and ground effects are calculated using the Parabolic Equation (PE) method described by Salomons [3].

Coherence Loss

In the computation scheme described above we assumed that the different parts of the bullet path contributed coherently to the total wave field. However the noise from the different secondary sources has travelled along different paths in the atmosphere. During that propagation the coherence of the waves is gradually lost.

In the linear modelling this effect can be simulated by allowing small perturbations along the wave front. The total result of this coherence loss is a decrease of the amplitude of the wave front and therefore the non-linear effects on the wave propagation will be smaller. The amount of coherence loss will depend on the turbulence of the atmosphere.

3. RESULTS

Figure 4 shows the contours of equal sound exposure level around a certain bullet path with a length of 1000 m. Clearly the Mach area can be recognized. In the forward direction also bullet noise (at a much lower level) can be observed, due to the truncation of the bullet path at 1000 m. The bullet noise in the backward direction will usually coincide with the muzzle noise and cannot be observed in practice.

In figure 5 the spectrum of the bullet noise is displayed for a point at about 2 km from the bullet path. The solid line is the measured bullet noise. Below 125 Hz the measurements are dominated by wind noise.

The dashed line is the computed result when no coherence loss is introduced. The level is clearly too high and the central frequency too low. Including coherence loss gives the dash-dotted line, that corresponds very well with the measurements. For this case it proves that about 50 m of the bullet path contributes coherently to the wave front at 2 km distance.

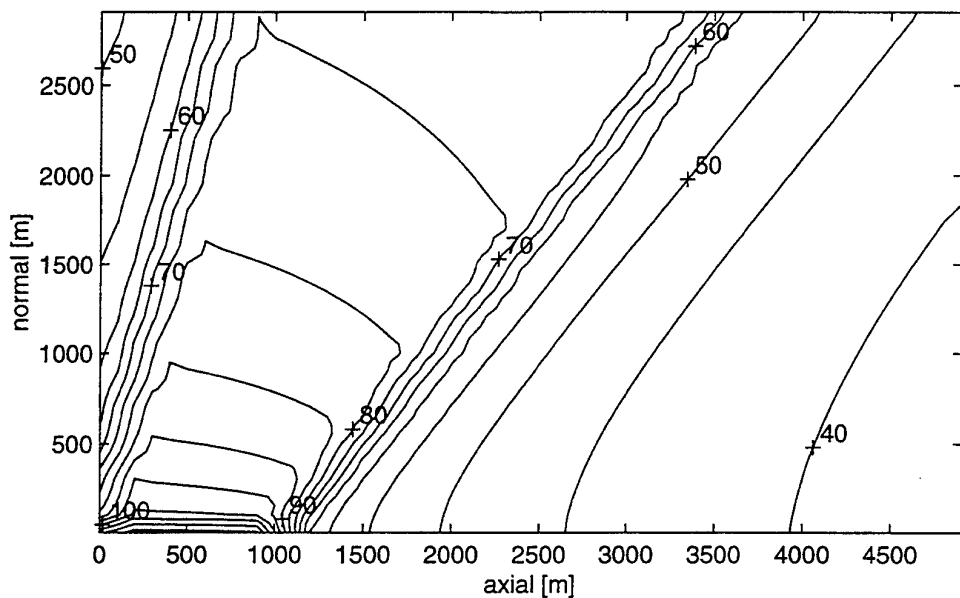


Figure 4: Contours of equal sound exposure level around a certain bullet path.

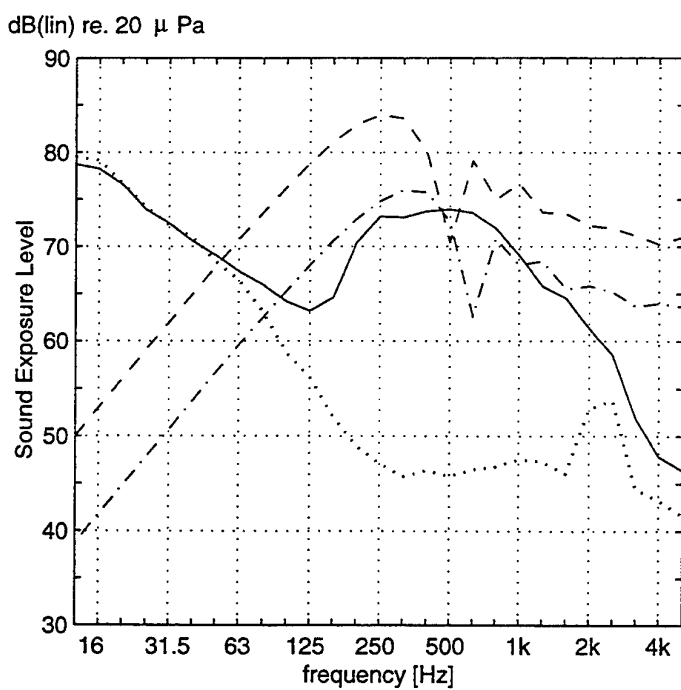


Figure 5: 1/3 octave band spectrum of measured data (solid line), computed without coherence loss (dashed line) and computed with coherence loss (dash-dotted line) and the background noise on the measurements (dotted line).

4. CONCLUSIONS

In this paper we have introduced a method to calculate the immission level of bullet noise around shooting ranges. With this method the noise can be calculated for finite bullet paths and decreasing bullet speeds. Also effects caused by the propagation through the atmosphere, like wind, turbulence and absorption, can be incorporated. Comparison to measurements of bullet noise at large distances from the shooting range show that the model corresponds very well with the measurements.

Acknowledgement

The research has been supported by the Dutch Ministry of Defence.

5. REFERENCES

- [1] FHA Van den Berg, NA Kinneging, EM Salomons, InterNoise96 (1996)
- [2] AD Pierce, Acoustics (Acoust. Soc. Am., New York, 1989)
- [3] EM Salomons, J. Acoust.Soc.Am., 95, 3109 (1994)

Ground effects

An efficient algorithm for predicting sound propagation at long range in the presence of wind and temperature gradients

K. M. LI, S. TAHERZADEH and K. ATTENBOROUGH

Engineering Mechanics Discipline, The Open University,

Walton Hall, Milton Keynes, MK7 6AA, United Kingdom

FAX (44) 1908 652192

Abstract

The propagation of low-frequency sound above an impedance plane in a vertically stratified medium is considered. The combined effects due to the vector wind and temperature gradients on sound propagation are studied. Recently, a WKB-type approximation has been combined with turning point theory and applied to the efficient computation of the height-dependent Green's function [J. Acoust. Soc. Am. **98** 3405-3411], which, in turn, has been used in the fast field program (FFP). Although this method is applied to a temperature-stratified medium, it leads to a significant reduction in the computational time for predicting sound propagation outdoors. The present paper examines on how one can extend the method of WKB-type approximation to include the vector wind velocity. Attention is focused on the development of efficient algorithms for numerical evaluation of the inverse Fourier transform and considerations of numerical stability. The limitations of the approximation are examined particularly for logarithmic profiles.

I. Introduction

The purpose of the present paper is twofold: first, to offer a formulation of fast field program (FFP) that includes the effect of vector wind explicitly and without resort to the use of effective sound speed gradient. We show that the effect of vector wind can be included easily with minor alterations of conventional FFP codes that assume cylindrical symmetry about a point source. Secondly, we investigate the use of airy functions to approximate the height-dependent Green's function that reduces the overall computational time in predicting the propagation of sound in the presence of wind and temperature gradients. We also address some practical issues regarding the computation of Airy functions and the integration path for automatic Gaussian quadrature when computing the phase function. We suggest methods for dealing with numerical stability as well as speeding up the computation of the Green's function. Finally, we highlight the limitations of the approximate method before offering some concluding remarks.

II. Theory

(a) The 'exact' sound field in the presence of wind and temperature gradients

An integral expression for the sound field due to a point monopole source, in a moving stratified atmosphere, is given by¹⁻³

$$p(x, y, z) = \frac{1}{4\pi^2} \int_{-\infty}^{\infty} \int_{-\infty}^{\infty} (\rho \omega_m)^{-1/2} P(z) \exp[i(k_x x + k_y y)] dk_x dk_y \quad (1)$$

where (x, y, z) is the rectangular coordinates of the field point, $\rho(z)$ is density of air, k_x and k_y are horizontal wave numbers resolved in the x and y directions respectively, and ω_m is the angular velocity of sound in the moving medium given by

$$\omega_m = \omega_s - k_x u_x - k_y u_y . \quad (2)$$

Here, the symbol $\omega_s \equiv 2\pi f/c$ denotes the reference angular velocity with f and c denoting the frequency and the speed of sound respectively. The symbol u denotes the wind velocity and the subscripts x and y denote the corresponding components in the x and y directions respectively. In addition, the height dependent Green's function $P(z)$ [see Eq. (1)] is the solution of

$$\frac{d^2 P}{dz^2} + k_z^2 P = i\sqrt{\rho} \delta(z - z_s) \quad (3)$$

where $k_z = +\sqrt{(\omega_m/c)^2 - k_x^2 - k_y^2 - (\rho''/2\rho) + (\rho'/2\rho)^2}$, (4)

and the primes denotes the derivative with respect to the vertical distance, z . In deriving the integral representation for the sound field, we ignore the effects of turbulence, non-linearity and gravity. We also assume that the variations of field properties are small in comparison with the sound pressure. In normal atmospheric conditions, the variation of air density can be ignored. Consequently, the terms involving ρ' and ρ'' can be neglected in Eq. (4).

The evaluation of the two-dimensional integral in Eq. (1) demands considerable computational resources. However, by using the method of stationary phase⁴ (or, alternatively, by noting the discrete/continuous Fourier transform pair⁵), we can simplify Eq. (1) to a one-dimensional integral that reduces the required computational time significantly. In this case, the sound field is given by

$$p(r, \theta, z) = \frac{1}{2\pi\sqrt{2i\pi r}} \int_0^\infty \sqrt{fk_r} P(z) \exp(ik_r r) dk_r, \quad (5a)$$

where $f = \rho\omega_m^2$, (5b)

(r, θ) is the receiver position expressed in the polar coordinate and $k_r \equiv \sqrt{k_x^2 + k_y^2}$. Furthermore, the angular velocity in the moving medium, ω_m and k_z in Eq. (4) can be rewritten, respectively, as

$$\omega_m = \omega_s - k_r u_r \cos(\theta - \psi_w) \quad (6)$$

and $k_z = +\sqrt{[(\omega_s - k_r u_r \cos(\theta - \psi_w))/c]^2 - k_r^2}$, (7)

where (u_r, ψ_w) is the vector wind expressed in the polar coordinate.

It is interesting to note that the integral of Eq. (5a) can be computed efficiently by the fast field (FFP) technique.⁶ However, the kernel of the integrand is modified by a factor of $(f)^{1/2}$ and the vertical wave number is replaced by Eq. (7). In the conventional FFP, the vertical wave number is given by

$$k_z = +\sqrt{\omega_s^2 / [c + u_r \cos(\theta - \psi_w)]^2 - k_r^2} , \quad (8)$$

where the effective sound speed profile is used to replace the presence of the vector wind. It is obvious that the conventional FFP can be modified easily to incorporate the effect of vector wind without a significant change in the computer programme. We have modified the fast field program⁶ accordingly to include the effect of vector wind. Figures 1 and 2 display plots of sound pressure levels (SPL) versus the horizontal range in the downwind direction with the source frequency of 100 Hz and the wind speed increases linearly with height at a rate of ± 0.1 s⁻¹, respectively. The parameters are chosen to coincide with that given in Ref. 4. These calculations serve to validate our FFP. The predictions agree extremely well with that computed by Li *et al.*⁴

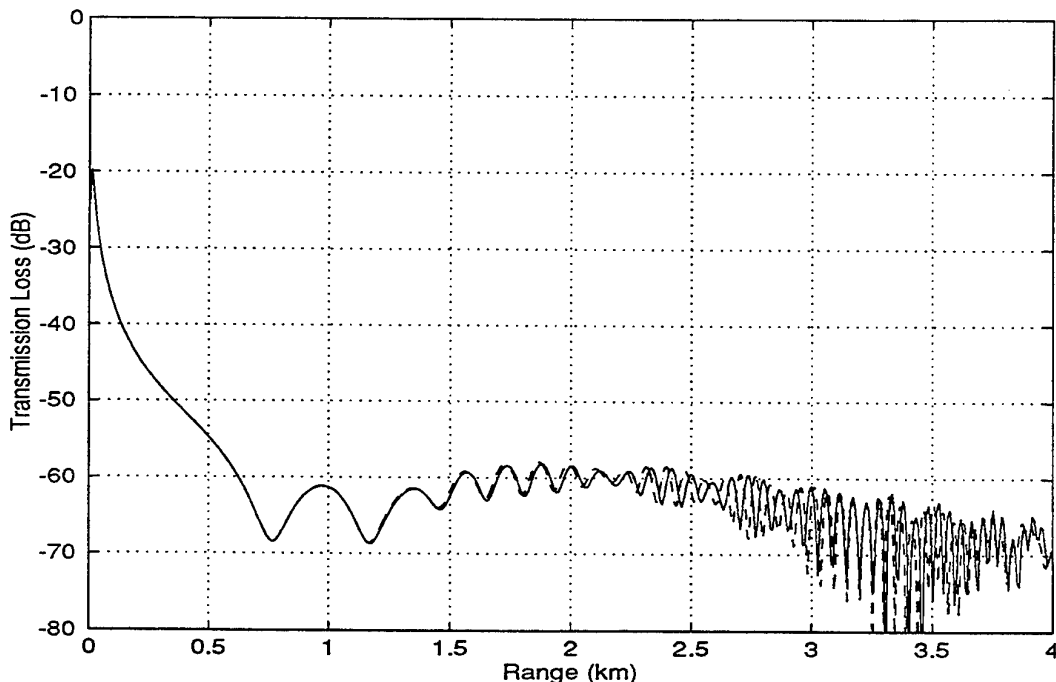


Figure 1 Plot of SPL vs. Range in the downwind direction. Solid line represents prediction of FFP modified to take the effect of vector wind into account, and dashed line represents predictions of FFP with an effective sound speed profile. Source and receiver heights are 5.0 and 1.0m respectively and the frequency is 100. Hz. The wind speed profile is linear with $du/dz=+0.1$ s⁻¹.

β is the specific admittance of the impedance ground, $\xi_s \equiv \xi(z_s)$, $\xi_> \equiv \xi(z_>)$ and z_u is the turning point such that $k_z(z_u) = 0$. The subscripts $>$, $<$, 0 and s represent the parameters to be evaluated at the heights $z_>$, $z_<$, z_s and 0 above the impedance ground. The symbols $z_>$ and $z_<$ denote

$$z_> = \max(z_s, z) \quad \text{and} \quad z_< = \min(z_s, z). \quad (13 \text{ a,b})$$

On the other hand, the approximate Green's function for a downward refracting medium (k_z decreases monotonically with height) is given by

$$P = \frac{2\pi e^{i\pi/6} \text{Ai}(-\zeta_>) g_> g_<}{\sqrt{f_s}} \left\{ \text{Ai}(-\zeta_< e^{i2\pi/3}) - \frac{\text{Ai}(-\zeta_<) [e^{i2\pi/3} \text{Ai}'(-\zeta_0 e^{i2\pi/3}) + q_d \text{Ai}(-\zeta_0 e^{i2\pi/3})]}{\text{Ai}'(-\zeta_0) + q_d \text{Ai}(-\zeta_0)} \right\} \quad (14)$$

where $g = (\zeta/k_z^2)^{1/4}$ (15)

$$\zeta(z) = \begin{cases} \left[\frac{3}{2} \int_z^{z_d} k_z dz' \right]^{2/3} & \text{if } z < z_d \\ - \left[\frac{3}{2} \int_{z_d}^z (-k_z^2)^{1/2} dz' \right]^{2/3} & \text{if } z > z_d \end{cases} \quad (16)$$

$$q = ik_0 \beta \sqrt{\zeta_0 / (k_0^2 - k_r^2)}, \quad (17)$$

and z_d is the corresponding turning point for the downward refracting medium.

To construct numerical solutions, a layered model is used in Sec. I (a) for the ‘exact’ sound field in the conventional implementation of the fast field program. However, an alternative approach is described by Li⁹ in which he considers a continuous sound speed profile that leads to an Airy function type solution as above. The use of Airy function leads to significant reductions in computing the total sound field with an acceptable numerical accuracy. Here, we extend Li’s analysis to include the effect of vector wind. We discuss some practical aspects of improving the efficiency of computation and removing the numerical instability in Sec. III and examining the limitation of this approach in Sec. IV.

III. Some practical issues

(a) Efficient computation of Airy functions

For a successful implementation of the numerical scheme detailed in Sec. II b, it is imperative to calculate the Airy functions accurately and efficiently. Although Pierce and Main¹⁰ have described an elaborate scheme in computing the Airy function of complex arguments more accurately, we find that the use of power series or asymptotic expansion is adequate for our purposes. We remark that Pierce and Main’s method involves the use of a numerical integration scheme at the expense of high computational time. Using a double precision

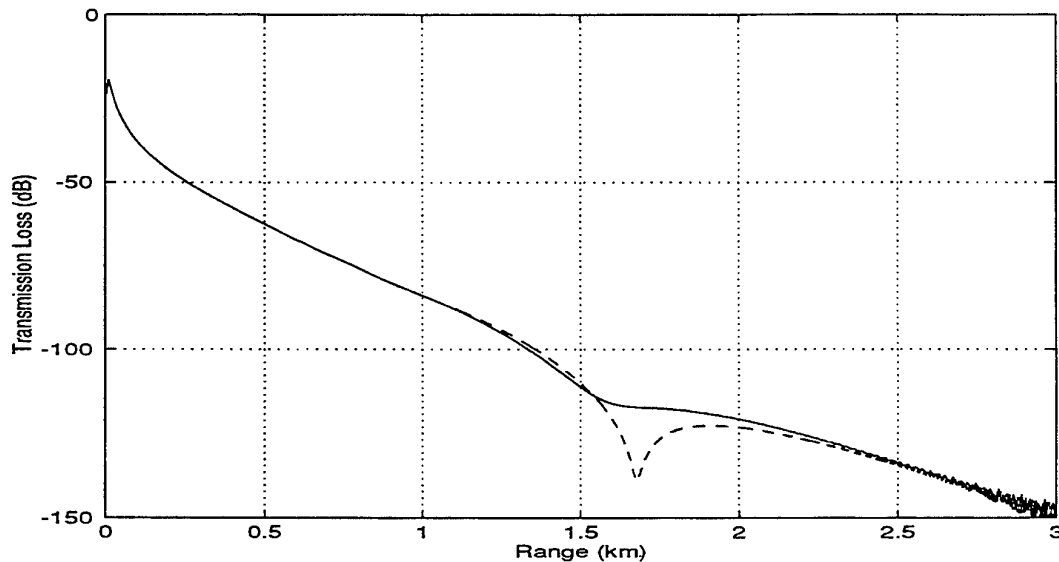


Figure 2 As in figure 1 but for upwind direction.

(b) An approximate sound field in the presence of wind and temperature gradients

To allow the computation of the total sound field, it is essential to determine the solution of the Green's function, $P(z)$. In general, there is no closed form analytical solution for the Green's function in the case of arbitrary sound and wind speed gradients. However, approximate solutions may be obtained for the situation where k_z varies slowly and monotonically (either increasing or decreasing) with height, z . The turning point theory⁷ may be applied to determine an approximate solution for $P(z)$ that involves the use of Airy functions. This method removes the restriction of the conventional WKB method and allows accurate solutions even in turning points. In an upward refracting medium (k_z increases monotonically with height), the Green's function can be approximated by⁸

$$P = \frac{2\pi e^{i\pi/6} \text{Ai}(-\xi_s e^{i2\pi/3}) h_s h_c}{\sqrt{f_s}} \left\{ \text{Ai}(-\xi_c) - \frac{\text{Ai}(-\xi_s e^{i2\pi/3}) [\text{Ai}'(-\xi_0) - q_u \text{Ai}(-\xi_0)]}{e^{i2\pi/3} \text{Ai}'(-\xi_0 e^{i2\pi/3}) - q_u \text{Ai}(-\xi_0 e^{i2\pi/3})} \right\} \quad (9)$$

$$\text{where } h = (\xi/k_z)^{1/4} \quad (10)$$

$$\xi(z) = \begin{cases} \left[\frac{3}{2} \int_{z_u}^z k_z dz' \right]^{2/3} & \text{if } z > z_u \\ \left[-\frac{3}{2} \int_z^{z_u} (-k_z^2)^{1/2} dz' \right]^{2/3} & \text{if } z < z_u \end{cases} \quad (11)$$

$$q_u = ik_0 \beta \sqrt{\xi_0 / (k_0^2 - k_r^2)} \quad (12)$$

(usually accurate to 16 significant figures in most language compilers) in summing the series, we find that the Airy functions are accurate to at least 8 significant figures.

In the implementation, we use the power series [Eq. 10.4.2 of Ref. 11] when the argument, $|z|$ is less than 6 and use the asymptotic series [Eq. 10.4.58-10.4.62 of Ref. 11] otherwise. We find that a maximum of 50 and 20 terms are required, respectively, for the power and asymptotic series. Effectively, we approximate the Airy function by a 50 term power series for $|z| < 6$ and a 20 term asymptotic series for $|z| \geq 6$. To save computational time further, we pre-compute and store all the constant terms of the series for subsequent computation of the Airy functions.

(b) Numerical integration of the phase function

The integrals in the calculation of the arguments for the Airy functions, Eqs. (11) and (16), must be performed numerically in general, although for certain profiles such as linear profile or the bilinear refractive index profile the integral can be evaluated analytically. We point out that the solution for P , and in particular, the functions g and h [see Eqs. (10) and (15)] remain finite even at the turning points. On the other hand, it is well known that the classical WKB method is unsatisfactory at the turning point because it predicts an infinite sound field. More importantly, the numerical evaluation of the integrals is relatively straightforward by using an automatic Gaussian quadrature which is both efficient and accurate.⁹ It is interesting to note that the turning point is a complex quantity because the horizontal wavenumber, k , is complex as a result of the implementation of FFP in order to remove singularities in the integrand. It is convenient to choose the integration path as shown in Fig. 3, for the evaluation of the phase functions.

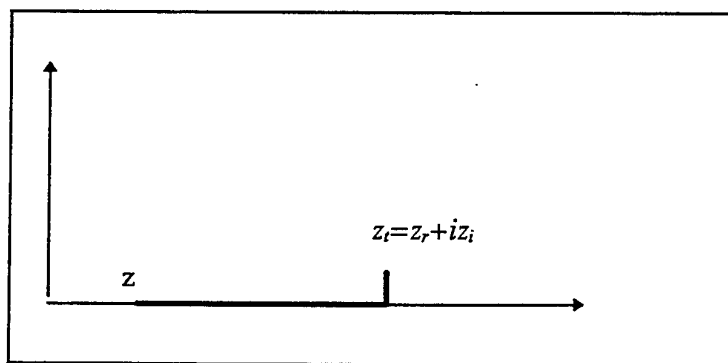


Figure 3 Path of integration for the phase function when the turning point is complex.

(c) Numerical instability

The height-dependent Green's function can be computed efficiently by using the approximate solution detailed in Sec. II b with due consideration of the practical aspects that we have discussed. However, the direct implementation is not sufficiently accurate, especially for the downward refracting case. Figure 4 shows the corresponding prediction for a bilinear profile with a sound speed gradient of 0.1 s^{-1} . A two-parameter ground impedance model¹² is used with effective flow resistivity of $30\,000 \text{ MKS rayl m}^{-1}$ and effective rate of change of porosity

of 20 m^{-1} (the same ground parameters will be used in the subsequent calculations). The source and receiver heights are 1.5m and 1.0 m, respectively, and the source frequency is 100 Hz. It is obvious that there is a significant numerical instability in the calculation that gives rise to some oscillations in the predicted sound field.

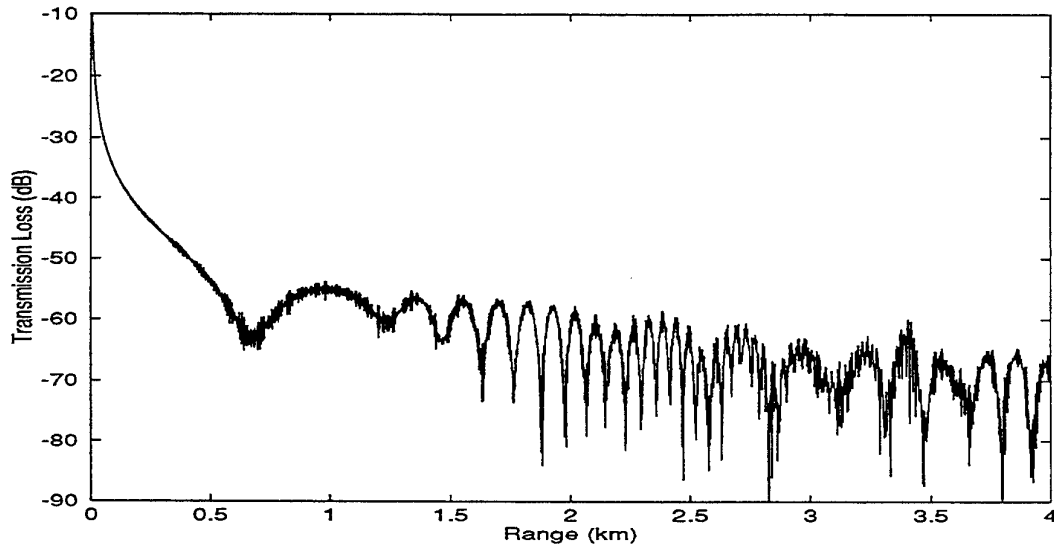


Figure 4: Prediction of unmodified implementation of WKB-Airy model for bilinear sound speed profile and $dc/dz=0.1 \text{ s}^{-1}$. Source and receiver heights are 1.5 and 1.0m respectively and the frequency is 100 Hz.

A close examination of the Green's function reveals that, for small values of k , corresponding to modes propagating vertically from the source, the kernel suffers from numerical instability problems mainly because of the oscillatory behaviour of $\text{Ai}(z)$ for large arguments, see Fig. 5.

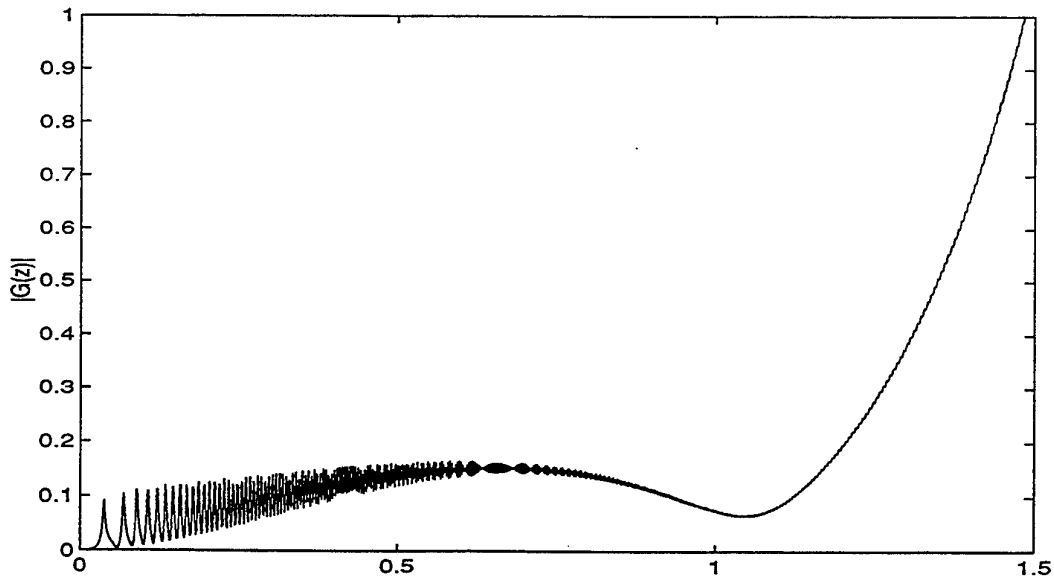


Figure 5 Part of the Green's function corresponding to figure 4

This is especially so for the downward refracting case. Rasmussen¹³ has suggested an appropriate remedy consistent with the fact that, near to the vertical, sound or wind speed gradients do not affect the propagation. Consequently, for k_r values less than one-half $\omega/c(0)$, the fluid is assumed to be homogeneous and the Green's function is calculated using the wave potential for homogeneous fluid;

$$\varphi_0 = \frac{1}{k_z} \left[e^{ik_r|z-h_s|} + \frac{k_z - k_0\beta}{k_z + k_0\beta} \cdot e^{ik_r(z+h_s)} \right]. \quad (18)$$

This approximation not only increases computation efficiency but also removes the artificial oscillatory behaviour for small k_r at the expense of small error at close range. Figures 6 shows a comparison of the approximate solution [see Sec. II b] with that of the conventional FFP formulation [see Sec. II a] at a frequency of 100 Hz. Figure 7 shows a plot of their corresponding Green's functions. In these plots, we have used a bilinear wind speed gradient of 0.1 s^{-1} instead of the sound speed gradient used in Fig. 4. It is obvious that the two calculations agree up to the thickness of the plot lines, except at the first one or two range grid points (very short distances).

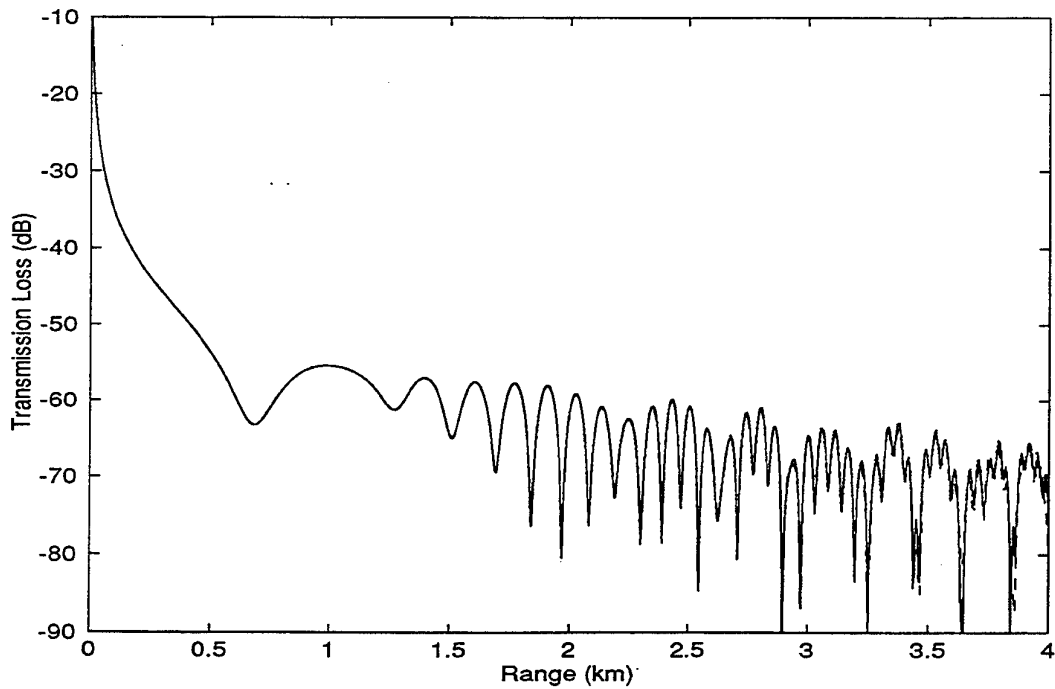


Figure 6 Comparison of calculations for 100 Hz using the conventional FFP formulation and the approximate method described in this paper. The lines are coincident up to 3500m. Source height 1.5m and receiver height 1.0m. In both cases a positive linear wind speed profile was used with $du/dz=0.1 \text{ s}^{-1}$

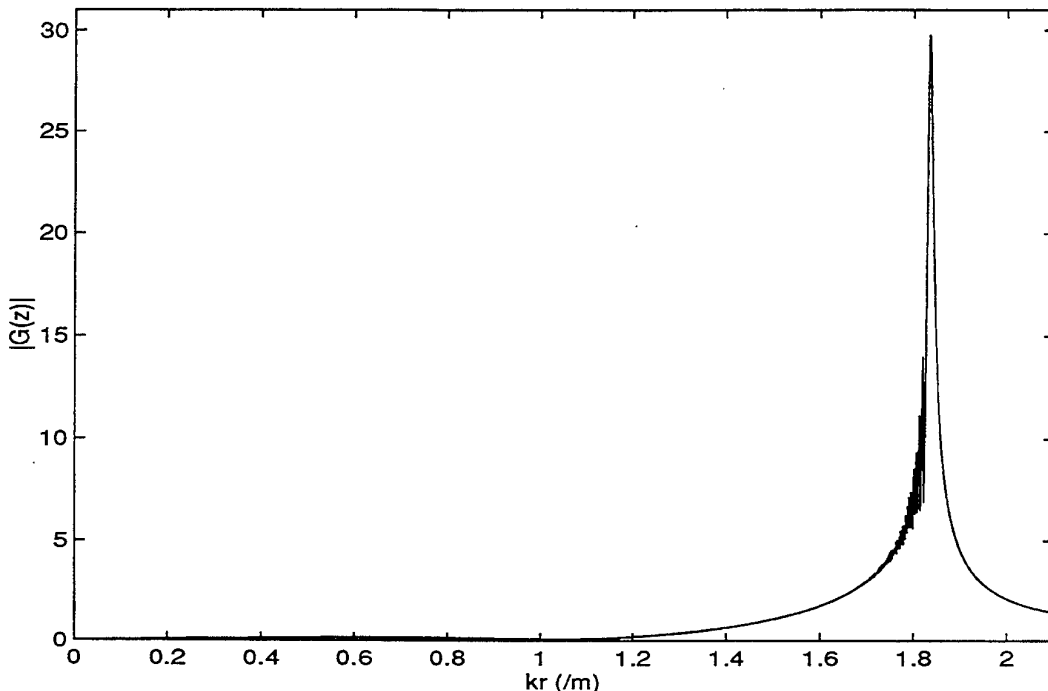


Figure 7 Green's functions corresponding to the cases shown in figure 6.

IV. Limitation of the model

With an appropriate modification, it appears that the approximate solution detailed in Sec. II b offers an attractive method to predict the sound propagation in the presence of wind and temperature gradients. However, it is important to point out the main limitation of the model. Turning point theory, and hence, the approximate solution, is only valid provided that⁷

- there is only one turning point, and
- the vertical wave number, k_z is a slowly varying function of z .

In terms of ray acoustics every positive turning point represents a direct ray from the source to receiver. An intriguing consequence of this observation is the proof that under certain circumstances there may be more than one direct ray present. Consider a logarithmic sound speed profile. This type of profile is very common in wind and sound speed profiles.

$$c(z) = c_0 [1 + a \ln(1 + bz)] \quad (19)$$

where a is positive for down-wind and negative for up-wind conditions. The turning point is the solution of $k_z(z_t) = 0$ which gives a turning height, z_t of

$$z_t = \frac{1}{\beta} \left\{ \exp \left[\frac{1}{a} \left(\pm \frac{1}{\sin \mu} - 1 \right) \right] - 1 \right\} \quad (20)$$

where $\sin \mu = k_r / k_0$ represents the incident angle of the ray which is real for downward refracting direct rays and complex for upward refracting ones (since they do not reach the ground). For real μ , $\sin \mu \leq 1$ and it is clear that there is only one turning point under downwind conditions because only the positive sign in the exponent gives a positive z . Upwind

(a is negative and $\sin\mu > 1$), both positive and negative signs give valid (i.e. positive) values for z which effectively means two direct rays. The fact that there are two turning points, renders the modified WKB method unsuitable for this important class of wind speed profiles. Neither is it valid for positive logarithmic gradients. This is because near the ground the rate of change of sound speed with height is large (typically of the order of 2.0 s^{-1}) and the condition that the parameters should change little within one wavelength is violated over a significant part of the audio frequency range. This is seen by comparing the results of the above method with those of an FFP program for downward refracting conditions.

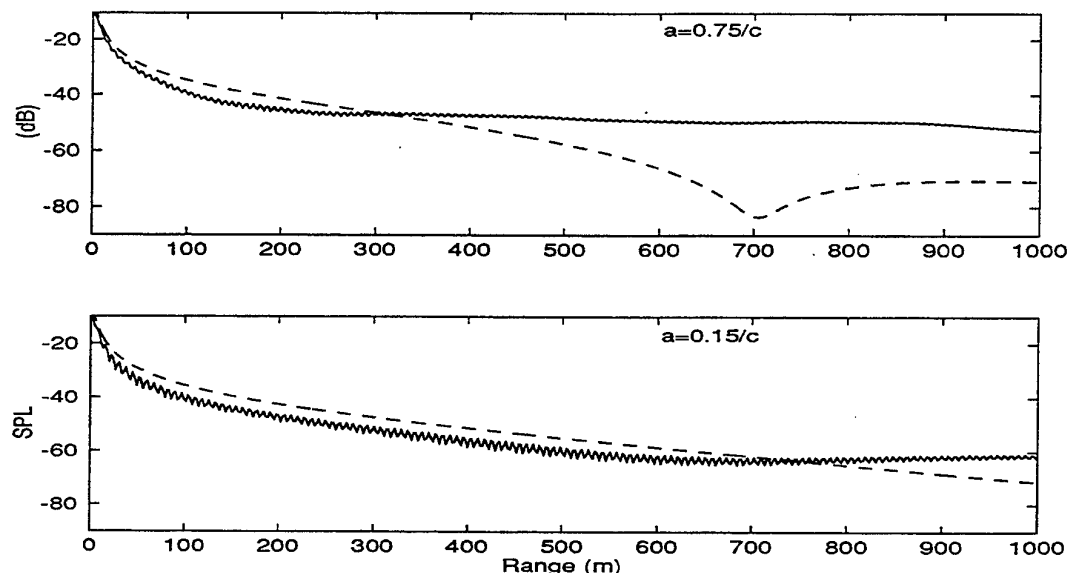


Figure 8 Predictions of FFP (dashed line) and WKB-Airy (solid line) under a positive logarithmic profile for two values of a . The frequency is 100 Hz and $b=2.5$.

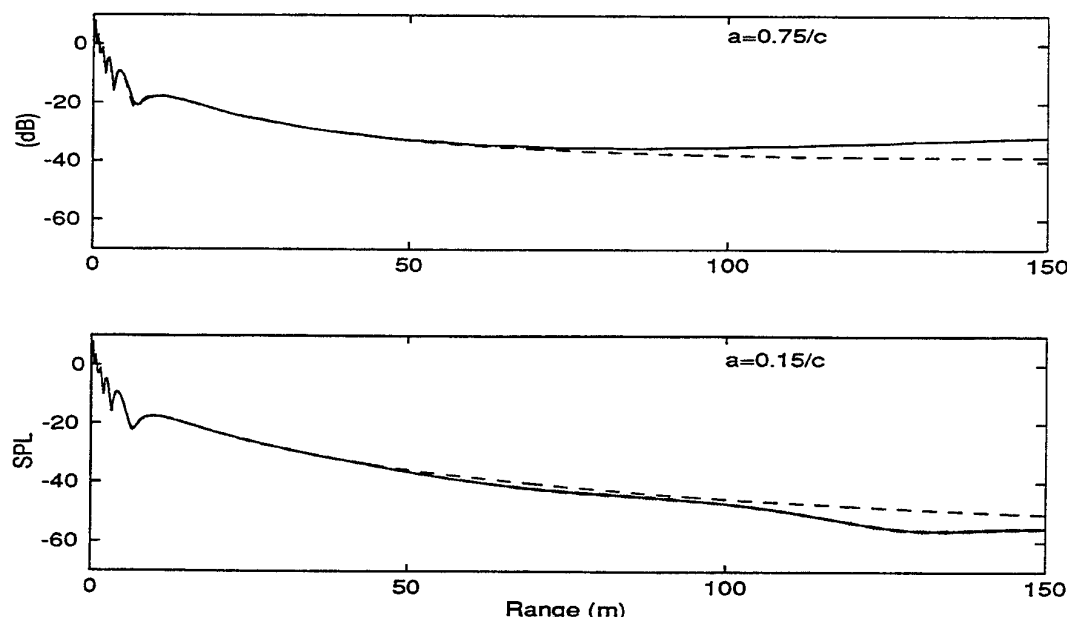


Figure 9 As in figure 8 but for $f=1000 \text{ Hz}$.

V. Conclusions

In this paper, we have investigated the numerical evaluation of the sound field in the presence of wind and temperature gradients. It has been shown that the conventional FFP can be modified to incorporate the effect of vector wind explicitly. The numerical results agree well with previous calculations based on a slightly different but analogous formulation. In addition, we have derived an approximate Green's function for efficient computation of the total sound field. It has been shown that, without modification, the use of the approximate Green's function in the fast field program, does not yield stable results because of the errors induced by the computation of Airy functions of large arguments. The deficiency can be remedied for small horizontal wave numbers by replacing the Airy function solution with the corresponding solution for a homogeneous fluid. Finally, we have demonstrated the inherent limitation of the approximate solution when used in the FFP formulation particularly for logarithm profiles.

Acknowledgments

This work was supported by a grant from EPSRC, UK.

Reference

1. K. M. Li, "A high frequency approximation of sound propagation in a stratified moving atmosphere above a porous ground surface," *J. Acoust. Soc. Am.* **95**, 1840-1852 (1994).
2. V. E. Ostashev, "On the discrete spectrum of a sound field in a stratified moving medium," *Sov. Phys. Acoust.* **39**, 522-529 (1993).
3. L. Nijs and Wapenaar, "The influence of wind and temperature gradients on sound propagation, calculated with the two-way wave equation," *J. Acoust. Soc. Am.* **87**, 1987-1998 (1990)
4. Y. L. Li *et al* "New fast field programs for anisotropic sound propagation through an atmosphere with a wind velocity profile," *J. Acoust. Soc. Am.* **95**, 718-726 (1994)
5. D. K. Wilson, "Sound field computations in a stratified, moving medium," *J. Acoust. Soc. Am.* **95**, 400-407 (1993).
6. S. Tooms *et al*, "Sound propagation in a refracting fluid above a layered fluid-saturated porous elastic material," *J. Acoust. Soc. Am.* **93**, 173-181 (1993).
7. F. W. J. Olver, "Asymptotics and special functions," (Academic Press, New York, 1974).
8. K. M. Li and Q. Wang, "Analytical solutions for outdoor sound propagation in the presence of wind," Submitted to *J. Acoust. Soc. Am.* (1996).
9. Y. L. Li, "Efficient computation of sound field above ground in horizontally stratified media using a Wentzel-Kramers-Brillouin-type approximation with Airy functions," *J. Acoust. Soc. Am.* **98** 3405-3411 (1995).
10. A. D. Pierce and G. L. Main, "Computational algorithm for the matched asymptotic expansion solution of high frequency acoustic wave diffraction by curved surfaces of finite impedance," Ed. R Vichnevetsky and R. S. Stepleman in *Advances in computer methods for partial differential equations VI*. 187-194 IMACS (1987).
11. M. Abramowitz and I. A. Stegun, "Handbook of mathematical functions," (Dover Publications, New York, 1970)
12. K. Attenborough, "Ground parameter information for propagation modelling," *J. Acoust. Soc. Am.* **92** 418-427 (1992).
13. K. B. Rasmussen, "Sound propagation over ground under the influence of a sound speed profile in the atmosphere," *J. Sound Vib.* **139**(1) 71-81 (1990)

**MODELS AND MEASUREMENTS OF SOUND
PROPAGATION FROM A POINT SOURCE OVER MIXED
IMPEDANCE GROUND†**

by

Patrice Boulanger, Tim Waters-Fuller, Keith Attenborough and Kai Ming Li, Engineering Mechanics, Faculty of Technology, the Open University, Milton Keynes, MK7 6AA, United Kingdom

INTRODUCTION

The propagation of sound above ground of mixed impedance is a subject of increasing interest for noise prediction and for exploitation of ground effect. A number of studies have been presented in the past in order to develop models for predicting the effect of mixed impedance on sound propagation over flat ground.

Naghieh and Hayek¹ have developed an analytical solution to the problem of noise propagation from a point source above two infinite half planes of different impedance. Their solution is based on wedge diffraction theory where the diffracted field of an impedance transition is calculated by taking it as a wedge with a top angle of 180° and different impedance on each side. The theory predicts the existence of two surface waves for the two half planes, however their solution is not straightforward and requires numerical computation. Enflo and Enflo² gave an exact solution for the singular integral equation obtained from the Helmholtz equation and the boundary condition when the source and receiver are close to the ground many wavelengths away from the impedance discontinuity. Naze Tjøtta³ found a simple analytical solution for a pure tone, a transient wave and for the impulse response and showed numerical results illustrating the structure of the sound field both in the nearfield and the farfield.

Apart from the theories presented above, the models developed to date can be classified into two categories. A first category is based on numerical methods. Durnin and Bertoni⁴ used two approaches based on Green's theorem and obtained excellent agreement between their predictions and measurements of the excess attenuation at 1 kHz over ground presenting various proportions of grass and concrete in the case of source and receiver located at ground level. Harriott et al.⁵ developed an approximate method for solving the boundary integral equations for propagation from a point source at a single frequency and predicted simple trends for a broad band A-weighted notional environmental noise source. A model developed by Rasmussen⁶ involves joining the two parts of the sound field calculated respectively over the two infinite half planes at the impedance discontinuity. The predictions of excess attenuation for traffic noise were in good agreement with the experiments. A wide-angle Parabolic Method (PE) in two dimensions was developed by Galindo⁷ for sound propagation through a homogeneous atmosphere over mixed impedance ground. The predictions of the model were compared with a model based on ray theory and with measurements made in a scale model. The results of the predictions showed that the PE method is a powerful tool to

† An extended version of this paper has been submitted for publication to the Journal of The Acoustical Society of America.

predict the sound pressure level in a range of frequencies between 100 Hz and 2.5 kHz when sound propagates over a porous strip in a hard surface. The NASA implicit finite-difference (NIFD) implementation of the parabolic equation was used by Robertson et al.⁸ to predict long-range, low frequency sound propagation over varying terrain. A pair of test problems demonstrated the accuracy of the implementation, and predictions of pure-tone signals were made for propagation paths including portions of a flat lake surface in both quiescent and windy atmospheres.

A second category of models is based on semi-empirical solutions. Koers⁹ presented a model based on Kirchoff diffraction theory where the diffracted field at an impedance transition is calculated by taking it as a wedge with a top angle of 180° and different impedance on each side. The results shown for two cases of proportion between hard and soft surfaces compare well with measurements. Daigle et al.¹⁰ compared indoor and outdoor measurements of excess attenuation to semi-empirical solutions and solutions from Green's theorem for few values of proportion between hard and soft surfaces for a given geometry and showed that the semi-empirical models fail when source and receiver are near the ground. More recently Hothersall and Harriot¹¹ have compared the approximate numerical method in solving the boundary integral equations to the semi-empirical method developed by De Jong¹² and to a third model where the boundary is simply related to the region around the specular reflection point defined by a Fresnel-zone condition. The result of their study performed for single or double discontinuity cases is presented for a few frequencies as graphs of excess attenuation versus the distance between source and impedance discontinuity. The agreement between the De Jong model and the boundary element method was generally good except near grazing. The Fresnel-zone method was adequate in describing the general trends in the results of the other methods.

This review of previous work on sound propagation above mixed impedance ground shows clearly that there is a need for validation of model predictions of excess attenuation spectra in the case of both single and multiple impedance discontinuities. The latter situation has received relatively little attention in the literature. Another point of interest is the investigation of the influence that various proportions of mixed impedance might have on ground effect (through variation in the frequency and phase of the first interference dip). Moreover, additional work should investigate both the very different theoretical cases of a single discontinuity impedance plane and a striped impedance plane. The objective of this paper is to contribute some of the necessary additional work.

Four models are investigated and compared to measured data. The Fresnel-zone model is the simplest. It incorporates a boundary simply related to the region around the specular reflection point defined by a Fresnel-zone condition. The method used in our work is an improvement on that of Hothersall and Harriot¹¹ who assume an excess attenuation dependent on the proportions of the different surfaces on the line representing the Fresnel-zone. In this work we assume that the excess attenuation is dependent on the proportion of the different surface areas inside the elliptical Fresnel-zone. A second improvement is the use of a new definition of the excess attenuation in mixed impedance cases. Instead of a linear interpolation between the predicted excess attenuation above uniform boundaries of each impedance¹¹, we use a linear interpolation between the pressure at the receiver relative to the free field above a surface of impedance Z_1 and the pressure at the receiver relative to the free field above a surface of impedance Z_2 . Predictions obtained by this modified model show a better agreement with the measured data than the results calculated from the previous model. The De Jong model¹² consists in using an empirical modification of the expression for

diffraction at a rigid half-plane that can be easily applied to single discontinuity and extended to multiple discontinuities. More recently, Nyberg¹³ presented a solution of the Helmholtz equation for multiple discontinuities using a Fourier transform technique. He showed that under certain conditions the ground effect due to mixed impedance may be determined from that predicted by using the area-averaged impedance. The fourth method was developed by Chandler-Wilde and Hothersall¹⁴ and relies on a numerical solution of the problem of propagation from a line source by use of a boundary element technique. It has the advantage of allowing any number of discontinuities. The impedance model incorporated into these four approaches assumes a microstructure of a log-normal size distribution of triangular pores¹⁵. The model has been simplified for the repetitive calculations necessary here by the use of Padé approximation techniques^{16,17}.

I. THEORIES

A. Theories of sound propagation over a single impedance discontinuity

1. The De Jong model

This model has been developed by De Jong¹² and uses an approximation of diffraction theory at a semi-infinite wedge. Taking the limit of zero angle for the wedge and obtaining a semi-infinite screen, De Jong presented a heuristic solution by analogy between the case of a semi-infinite screen, which can be regarded as an admittance step from an acoustically hard surface to air, with the case of an admittance step occurring at a transition between two types of ground.

In all further calculations the excess attenuation is obtained from

$$EA = 20 \log \left| \frac{P}{P_1} \right| \quad (1)$$

where:

$$P = P_0 \left[\frac{\exp(ikR_1)}{R_1} + Q \frac{\exp(ikR_2)}{R_2} \right] \quad (2)$$

is the total pressure at the receiver due to a point source above an homogeneous impedance plane and

$$P_1 = P_0 \frac{\exp(ikR_1)}{R_1} \quad (3)$$

is the pressure due to the direct wave from the source. The variable Q is the spherical wave reflection coefficient, R_1 is the direct path length from source to receiver, R_2 is the path length through the specular reflection point and R_3 is the path length through the impedance discontinuity (see Fig. 1). Note that according to this definition, attenuation is maximum at an excess attenuation minimum. De Jong's calculations give the following result for the pressure above a plane containing a single impedance discontinuity,

$$\frac{P}{P_1} = 1 + \frac{R_1}{R_2} Q_{1,2} \exp\{ik(R_2 - R_1)\} + (Q_2 - Q_1) \frac{\exp\left(\frac{-i\pi}{4}\right)}{\sqrt{\pi}} \frac{R_1}{R_3} \{F_{31} \pm F_{32} \exp\{ik(R_2 - R_1)\}\} \quad (4)$$

where Q_1 is the spherical wave reflection coefficient for the ground of impedance Z_1 used in conjunction with the plus sign in the right hand side bracket when the specular point falls on the ground of impedance Z_1 . If the specular point falls on the ground of impedance Z_2 , the spherical wave reflection coefficient Q_2 is used in conjunction with the minus sign. In the relation above

$$F_{31} \equiv F\left[\sqrt{k(R_3 - R_1)}\right] \quad (5)$$

and

$$F_{32} \equiv F\left[\sqrt{k(R_3 - R_2)}\right] \quad (6)$$

where

$$F(x) \equiv \int_x^{\infty} \exp(-iw^2) dw \quad (7)$$

is the Fresnel integral function.

For all cases investigated in this work, source and receiver are 0.1 m above the ground, and 1 m apart. The discontinuity between a finite impedance and a hard surface is perpendicular to the source receiver line. The source is situated above the hard surface, and the receiver above the sand surface.

The admittance of the hard surface is modelled by choosing a value equal to zero, and the sand is modelled using a rigid porous medium model. Following Attenborough¹⁷, a material of flow resistivity R_s and porosity Ω containing a log normal distribution of similarly-shaped pores of tortuosity T , has a complex density defined by

$$\rho_b(\omega) = \frac{T}{\Omega} \left[\rho_0 + \left(\frac{iR_s\Omega}{\omega T} \right) G_d(\omega) \right] = \frac{T}{\Omega} \rho_p(\omega) \quad (8)$$

and a complex compressibility defined by

$$C_b(\omega) = \frac{1}{\gamma P_0} \left[\gamma - \frac{(\gamma-1)\rho_0}{\rho_p(\omega \sqrt{N_{PR}})} \right] \quad (9)$$

where ρ_0 is the density of air, P_0 is the pressure at equilibrium, γ is the ratio of specific heats and N_{PR} is the Prandtl number for air. $G_d(\omega)$ is a two-parameter Padé approximation derived from small and large argument forms for a log-normal distribution of slits or equilateral triangular pores and is given by¹⁷

$$G_d(\omega) = \frac{1 + a_1 \epsilon + a_2 \epsilon^2}{1 + b_1 \epsilon} \quad (10)$$

where $\epsilon = \sqrt{\frac{-i\omega\rho_0}{\Omega R_s}}$, $a_1 = \frac{\theta_1}{\theta_2}$, $a_2 = \theta_1$, $b_1 = a_1$, and for equilateral triangular pores

$\theta_1 = \frac{10}{7} e^{4(\sigma \ln 2)^2} - 1$, and $\theta_2 = \sqrt{\frac{5}{3}} e^{\frac{3}{2}(\sigma \ln 2)^2}$. The variable σ is the standard deviation in ϕ units of

the log normal pore size distribution. The assumption of triangular pores is reasonable for sand if we assume that the sand grains are spherical. The bulk propagation constant may be evaluated by

$$k_b(\omega) = \omega \sqrt{\rho_b C_b} \quad (11)$$

and the characteristic impedance by

$$Z_b(\omega) = \frac{\omega \rho_b}{\rho_0 c_0 k_b} \quad (12)$$

where c_0 is the speed of sound.

The resulting model requires knowledge of four parameters R_s , Ω , T and σ . The flow resistivity of the sand used in the experiments was measured and the value was found to be $R_s=473000$ mks rayls/m. A common value of porosity for sand $\Omega=0.4$ was chosen, and tortuosity $T=1/\Omega$ was assumed. Measurements of the fraction by volume versus pore size in ϕ

unit for glass beads have been fitted by assumed log normal pore size distributions using the standard deviation as an adjustable parameter. Values in the range $0.7 < \sigma < 1.2$ were found appropriate for glass beads. Our study used the value $\sigma = 1.3$ giving the best visual fit between predictions and measurements of excess attenuation above sand.

2. The boundary element model

Chandler Wilde and Hothersall¹⁴ have developed a method based on the formulation of a boundary integral equation to evaluate the pressure at the receiver. A solution for the Helmholtz equation for the pressure at the receiver can be solved for a locally reacting boundary and gives for the case of a strip with impedance Z_2 imbedded in a plane of impedance Z_1

$$P(\bar{r}, \bar{r}_0) = P_i(\bar{r}, \bar{r}_0) - ik \left(\frac{1}{Z_2} - \frac{1}{Z_1} \right) \int_S G_{Z_2}(\bar{r}_s, \bar{r}) P(\bar{r}_s, \bar{r}_0) ds(\bar{r}_s) \quad (13)$$

where $P_i(\bar{r}, \bar{r}_0)$ would be the pressure at the receiver if the surface had the homogeneous impedance Z_1 and \bar{r}_0 , \bar{r} , \bar{r}_s are the position vectors of the source, the receiver and a point in the boundary respectively. $G_{Z_2}(\bar{r}_s, \bar{r})$ is the Green's function associated with propagation over a boundary of impedance Z_2 , and S is the surface of the strip. The integral can be calculated numerically by a standard boundary element technique once the pressure $P(\bar{r}_s, \bar{r}_0)$ is known at point \bar{r}_s in the strip. An equivalent two-dimensional problem can be solved in order to save computation time. Source receiver and specular point are in a vertical plane perpendicular to the impedance discontinuity, and a line integral is solved instead of a surface integral. The boundary element code is applied easily to predicting propagation of sound over multiple strips by including more discontinuity coordinates in the input file to the program.

3. The Fresnel-zone model

In order to evaluate the proportions of impedance of each type contributing significantly to the excess attenuation at the receiver, Slutsky and Bertoni¹⁸ suggested use of Fresnel diffraction theory. The method is applied by Hothersall and Harriott¹⁹ and is briefly summarised as follows.

Consider points P' (see Fig. 2) such that

$$S'P' + RP' - R_2 = F\lambda \quad (14)$$

where F is a constant, S is the source, R is the receiver, S' is the image source and λ is the wavelength. This consideration is based on the generalisation to all space of the definition of Fresnel-zones being regions in a surface over which ray paths from the source via reflection points to the receiver have path length in the range $n\lambda$ to $(n+1/2)\lambda$ where n is an integer. Hothersall and Harriott¹¹ have shown that path length differences between $\lambda/2$ and $\lambda/4$ are acceptable. Consequently, in the following work the value $F=1/3$ will be used. The set of all the possible positions P' defines an ellipsoid with foci S' and R . The major semi-axis of the ellipsoid along the line $S'R$ is given by

$$a = \frac{R_2 + F\lambda}{2} \quad (15)$$

and the minor semi-axis by

$$b = \sqrt{\frac{R_2 F \lambda}{2} + \left(\frac{F \lambda}{2} \right)^2} \quad (16)$$

The position of the points P' relevant to our study in terms of Fresnel-zones are inside the boundary, the goal being to assess the positions of the reflection points P' contributing significantly to the excess attenuation at the receiver. In order to do so, we need the intersection of the ellipsoid and the boundary. The form of this ellipse depends on the value of the constant F , the wavelength considered, and the geometry source receiver. The equation of the ellipse in the coordinate system shown in Fig. 3 is

$$\frac{x^2}{b^2} + \frac{(y \cos \theta - c)^2}{a^2} + \frac{y^2 \sin^2 \theta}{b^2} = 1 \quad (17)$$

where $c = \frac{R_2}{2} - SP$. It should be noted, in the Hothersall and Harriott¹⁹ expression of the equation of the ellipse the x and y variables are interchanged, and this is inconsistent with their notation as shown in Fig. 3. To compute the area of the ellipse we are interested in the boundary values $x_{1,2}$ and $y_{1,2}$ (see Fig. 3) and find

$$x_{1,2} = \pm b \sqrt{1 - \frac{(y_m \cos \theta - c)^2}{a^2} + \frac{y_m^2 \sin^2 \theta}{b^2}} \quad (18)$$

where

$$y_m = \frac{cb^2 \cos \theta}{a^2 \sin^2 \theta + b^2 \cos^2 \theta} \quad (19)$$

and

$$y_{1,2} = -\frac{B}{A} \pm \sqrt{\frac{1}{A} - \left(\frac{c \sin \theta}{Aab} \right)^2} \quad (20)$$

where $A = \left(\frac{\cos \theta}{a} \right)^2 + \left(\frac{\sin \theta}{b} \right)^2$ and $B = \frac{c \cos \theta}{a^2}$. It should be noted that the expression of $y_{1,2}$ given by Hothersall and Harriott¹⁹ does not have the dimension of a length.

Because the source and receiver are at identical heights above the ground, the specular reflection point is at mid-distance between source and receiver and $y_1 = y_2$.

The first modified Fresnel-zone model used in this study corresponds to that suggested by Hothersall and Harriott^{11,19}. Following their assumption, we evaluate the excess attenuation at the receiver for a given geometry from

$$EA = \mu 20 \log \left| 1 + \frac{R_1}{R_2} Q_1 \exp \{ik(R_2 - R_1)\} \right| + (1-\mu) 20 \log \left| 1 + \frac{R_1}{R_2} Q_2 \exp \{ik(R_2 - R_1)\} \right|. \quad (21)$$

In Hothersall and Harriott's work, μ is the proportion of the line representing the Fresnel-zone and intersecting with the area of impedance Z_1 . The line representing the Fresnel-zone is defined as the intersection between the elliptical Fresnel-zone and the vertical plane containing source, receiver and specular reflection point. The first term in Eq. (21) is the product of μ and the excess attenuation EA_1 above a uniform boundary of surface impedance Z_1 , and the second term is the product of $(1-\mu)$ and the excess attenuation EA_2 above a uniform boundary of surface impedance Z_2 .

An alternative is to assume that the excess attenuation is linearly dependent on the proportions of the different surface area inside the elliptical Fresnel-zone in the boundary. The coefficient μ needed to compute the excess attenuation from relation (21) is obtained by calculating the proportion of area having surface impedance Z_1 inside the elliptical Fresnel-zone. However, greater improvement in the model can be achieved by modifying the definition of the excess attenuation from that used in equation (21).

The second modified Fresnel-zone model proposed in this work is based on a new definition of the excess attenuation in mixed impedance cases. Instead of the linear interpolation between EA_1 and EA_2 shown in relation (21), we use a linear interpolation between the pressure at the receiver relative to the free field in the case of a surface of impedance Z_1 and the pressure at the receiver relative to the free field in the case of a surface of impedance Z_2 . The new expression proposed for the excess attenuation is

$$EA = 20 \log \left\{ \mu \left| 1 + \frac{R_1}{R_2} Q_1 \exp\{ik(R_2 - R_1)\} \right| + (1-\mu) \left| 1 + \frac{R_1}{R_2} Q_2 \exp\{ik(R_2 - R_1)\} \right| \right\}. \quad (22)$$

As previously, the coefficient μ is obtained by calculating the proportion of area having surface impedance Z_1 inside the elliptical Fresnel-zone.

We note that the Fresnel-zone model can be extended easily to multiple strips.

B. Nyberg's theory of sound propagation over a periodic impedance

In Ref. 13, Nyberg shows that the Helmholtz equation with the boundary condition for a point source above an infinite plane surface with striped impedance can be solved by using Cartesian coordinates and a Fourier transform technique.

If a point source has Cartesian coordinates $(0,0,z_0)$ above a flat surface with a specific acoustic admittance $\beta(y)$, the wave field at the point $R(x,y,z)$ can be found as the solution of a helmholtz equation

$$[\Delta + k^2] \Psi(x, y, z) = \delta(x) \delta(y) \delta(z - z_0) \quad (23)$$

and boundary condition

$$\left[\frac{\partial}{\partial z} + ik\beta(y) \right] \Psi(x, y, z) = 0, \quad z = 0_+. \quad (24)$$

Using the Fourier transform of Ψ , $F(\alpha, y, z) = \frac{1}{2\pi} \int_{-\infty}^{+\infty} e^{-i\alpha x} \Psi(x, y, z) dx$ one obtains:

$$\left[\frac{\partial^2}{\partial y^2} + \frac{\partial^2}{\partial z^2} + k^2 - \alpha^2 \right] F(\alpha, y, z) = \delta(y) \delta(z - z_0) \quad (25)$$

and

$$\left[\frac{\partial}{\partial z} + ik\beta(y) \right] F(\alpha, y, z) = 0, \quad z = 0_+. \quad (26)$$

The solution for an homogeneous surface with admittance β_0 is :

$$\Psi_0(x, y, z) = -\frac{e^{ikR_1}}{4\pi R_1} - \frac{e^{ikR_2}}{4\pi R_2} + \frac{\beta_0}{2\pi} \int_{-\infty}^{+\infty} L_0(\alpha, y, h) e^{i\alpha x} d\alpha \quad (27)$$

where

$$R_{1,2} = \sqrt{x^2 + y^2 + (z \pm z_0)} \quad (28)$$

$$h = z + z_0 \quad (29)$$

and

$$L_0(\alpha, y, h) = -\frac{k}{2\pi i} \int_{-\infty}^{+\infty} \frac{e^{i(ty + h\sqrt{k^2 - \alpha^2 - t^2})}}{\left(\sqrt{k^2 - \alpha^2 - t^2} + k\beta_0 \right) \sqrt{k^2 - \alpha^2 - t^2}} dt. \quad (30)$$

Consider the two-valued infinite periodic striped impedance shown in Fig. 4. If the term:

$$e^{-iy} H_0^{(1)} \left(\sqrt{k^2 - \alpha^2} \sqrt{y^2 + z_0^2} \right) \quad (31)$$

does not change appreciably over the distance $y=a+b$, then the solution of (26) and (27) can be written as¹³:

$$\Psi(x, y, z) = -\frac{e^{ikR_1}}{4\pi R_1} - \frac{e^{ikR_2}}{4\pi R_2} + \frac{1}{2\pi} \int_{-\infty}^{+\infty} L_0'(\alpha, y, h) e^{i\alpha x} d\alpha \quad (32)$$

where

$$L_0' = \frac{\beta_0 b + \beta_1 a}{a+b} L_0. \quad (33)$$

The ground effect due to a two-valued infinitely periodic striped impedance may be determined from that predicted by using the area-averaged impedance.

The approximation that the sum of the two periods must be small compared to the y -quasiperiod of the expression (32), translates into $a+b \ll \lambda$ in the particular geometry used in our experiment. This condition is satisfied for frequencies up to 1700 Hz when the proportion of hard surface equals 50% and up to 3400Hz in the case of 100% hard surface.

II. DESCRIPTION OF THE EXPERIMENTAL PROCEDURE

A. Experiments involving sound propagation over a single impedance discontinuity

The point source used in the experiment was a Tannoy driver fitted with a 1 m long tube, with a 3-cm internal diameter. It was suspended 0.1 m above the surface of the sand box in an anechoic chamber of dimensions 3 m x 3 m x 3 m. The receiver was a Brüel & Kjaer type 4311 1.3 cm diameter condenser microphone fitted with a preamplifier suspended 1 m away at the same height. Signal processing and signal generating were done using MLSSA, a maximum length sequence system analyser. Background noise effects were eliminated by analysing the microphone signal with respect to the known output sequence. In order to calculate the excess attenuation, a reference measurement was carried out by elevating source and receiver at the maximum height of 2 m allowed by the suspending cable above the floor of the anechoic chamber. A hardwood board measuring 1.1 m x 0.9 m x 0.03 m was set flush with the surface of the sand in a sand box measuring 2 m x 1.2 m x 0.3 m.

In this experiment the proportion of hard surface was varied, while trying to minimise edge effects, by either moving the source and receiver normal to the discontinuity or translating the board in the sand pit parallel to the source receiver axis.

B. Experiments involving sound propagation over a periodic impedance

The experimental procedure was very similar to the one previously used in measurements over a single discontinuity impedance case in that source and receiver heights and separation distances were kept identical. The main change is the use of a smaller sand box of size 1.0 m x 0.8 m x 0.08 m in which blocks of wood with rectangular cross-section 0.1 m x 0.08 m were moved along the source-receiver line perpendicularly to their axes inside the sand pit in order to achieve the various proportions of hard surface.

IV. COMPARISON BETWEEN EXPERIMENTAL RESULTS AND PREDICTIONS

A. Sound propagation over a single impedance discontinuity

In the work presented here and unless specified otherwise, for example, a 40% hard surface between source and receiver means that the discontinuity between sand and hard board is a horizontal distance of 0.4 m from the source. The excess attenuation spectra measured for proportions of hard surface 0%, 50%, 80% and 100% are shown as the dotted lines in Figs. 5(a)-5(d). Excess attenuation spectra predicted by the boundary element method and by the De Jong model which reduces to the classical Weyl-van der Pol expression for a

continuous sand surface are shown respectively as dashed line and solid line in Fig. 5(a). The excellent agreement between the measurements and the predictions supports the chosen four-parameter model for the acoustical properties of sand. Figures 5(b) and 5(c) display also the predictions using the second modified Fresnel-zone method shown as a dotted-dashed line, the predictions using the semi-empirical model shown as a solid line and the predictions using the boundary element code shown as a dashed line. Figure 5(d) uses the same line style convention but does not show the predictions from the second modified Fresnel-zone method because it reduces to the classical Weyl-van der Pol expression for a continuous hard surface and would give the same predictions as the semi-empirical model. The overall agreement between measurements and predictions of the depths and frequency positions of the excess attenuation spectra first dip is satisfactory.

The frequency of the minima of the first dip in measured excess attenuation spectra (ground effect) is seen to increase steadily from the cases of low percentage of hard surface to the cases of high percentage up to 70%. However, for values of the proportion of hard surface above 70%, the frequencies of the minima of the first dip are seen to decrease as the percentage of hard cover approaches 100%. In order to show clearer evidence of this phenomenon, more experimental data have been taken and are shown in Fig. 6 where the frequencies of the first dip minima are plotted versus the proportion of hard surface. The circles are obtained in part from the data presented in Figs. 5(a)-5(d), and the triangles are data taken in a second experiment involving more cases of various proportions of hard surface. The measurements show a lack of repeatability for the cases involving 70%, 80% and 90% of hard ground cover. The measured shift in dip frequency position can be reproduced in the predictions by a 7% variation in source and receiver heights. Therefore, slight variations in the location of the reflecting plane might be the cause of the lack of repeatability. Nevertheless, among the fourteen measurements taken for proportions of hard surface 60% and above, nine of them show a frequency position of the first dip above the expected maximum value of 8500 Hz. Figure 6 shows also the predictions from the improved Fresnel-zone method as a dotted-dashed line, the predictions from the semi-empirical model as a solid line and the predictions from the boundary element code as squares. The improved Fresnel-zone method shows a discontinuity in frequency around a value of horizontal distance source-discontinuity equal to 0.4 m. This discontinuity is expected from the definition of the excess attenuation given in Eq. (22) which shows a weighted sum of the excess attenuation spectra of a continuous sand surface and a continuous hard surface. However, this discontinuity is not displayed by the measurements and shows the limitation of the Fresnel zone method in predicting the exact frequency of the ground effect in excess attenuation spectra. The boundary element theory predicts a frequency maximum of 9600 Hz for proportions 60%-70% while the De Jong model shows a maximum frequency of 9300 Hz at a hard ground cover percentage of 65 % to be compared to the measured 10500 Hz at 70% hard ground cover. The existence of this maximum is certainly due to diffraction of the sound wave by the single discontinuity as shown in Figs. 7(a)-7(b) where the dotted line, dashed line and the solid line display the function $20\log(|1+A|-|D|)$, $20\log(|1+A|+|D|)$ and the excess attenuation spectrum $20\log|1+A+D|$ respectively. The term $1+A$ stands for the Weyl-van der Pol term [first two terms in equation (4)] and D stands for the diffraction term [last term in Eq. (4)]. Figure 7(a) shows the results in the case 65% of hard ground cover, percentage for which the predicted first dip presents the highest frequency position, and Fig. 7(b) shows the results in the case 80% of hard ground cover. We note that for the phenomenon to occur, the terms A and D need to have opposite phases for frequencies in the higher portion of the frequency range

where $1+A$ and D have comparable magnitudes (in this case $20\log(|1+A|-|D|)$ reaches its minimum region). Secondary maxima are observed in Fig. 6 for proportions of hard surface 89% and 95%. They are explained by the phase of the diffraction term varying more rapidly as the proportion of hard surface increases, and reaching a maximum rate of variation when the discontinuity is situated vertically beneath the receiver. Consequences are the presence of oscillations in the excess attenuation function when the receiver is close to the single discontinuity [See Fig. 5(d)].

Prediction of the excess attenuation spectra from the first modified and second modified Fresnel-zone model for a proportion of hard surface equal to 70% are shown as the solid line and the dotted-dashed line respectively in Fig. 8. The agreement between measurements and the prediction from the first modified Fresnel-zone model is poor. Indeed, the magnitude of the dip is over predicted by 20 dB. These results demonstrate that the first modified Fresnel-zone method is not satisfactory for predicting excess attenuation spectra. The agreement between the measured data and the predictions of the second modified model is good. Fig. 8 also establishes clearly the improvement of the predictions due to the introduction in Eq. (22) of a frequency dependent coefficient μ (as in the Fresnel-zone model) compared with predictions from a crude model (dashed line) where the excess attenuation is also given by Eq. (22) but the coefficients μ are frequency independent. For this crude model, a horizontal distance 0.7 m between source and discontinuity implies that 70% of the surface is covered with hard ground and thus $\mu=0.7$ for all frequencies. The crude model allows good predictions of the frequency position of the first dip, but the second modified Fresnel-zone model allows much better prediction of the magnitude of the dip.

B. Sound propagation over a periodic impedance

The measured excess attenuation spectra for proportions of hard surface 50%, 70% and 80% are shown as the dotted lines in Figs. 9(a)-9(c). In the case of 50% of hard ground cover, Fig. 9(a) shows two measurements. One measurement corresponds to a sand strip at the specular reflection point, and the other represents the case when a hard strip is at the specular reflection point. The two measured excess attenuation curves are slightly shifted with an increase in frequency of the minimum of the first dip in the case of the specular reflection point on the strip of wood as would be expected. The predictions using the second modified Fresnel-zone calculations and Nyberg's theory are shown as the dotted-dashed lines and dashed lines respectively. In Figs. 9(b)-9(c) the solid line is the prediction using the boundary element calculations.

The measured data show oscillations that could be mistaken for diffraction effects due to the array of strips. However, the oscillations are seen also in data obtained over continuous sand. The fluctuations in excess attenuation appear to be due to the reflections of sound at the edges of the sand box used for the experiments.

In Figs. 9(b) and 9(c) the agreement between measured data and the predictions of Nyberg's theory is satisfactory and appears even better for cases of higher percentage of hard surface. The prediction seems a good average of the two measured cases for either a wood or sand strip at the specular reflection point. For all percentage cases the agreement appears to be surprisingly good for values of frequency above a couple thousand Hertz although the approximation $a+b \ll \lambda$ might not be satisfied. A more detailed analysis of the quasi-period approximation condition given by Nyberg¹³ might be needed in order to verify if the validity of the approximation can be extended to higher frequencies or wider strips.

Figures 9(b) and 9(c) show very good agreement between the boundary element code predictions and the measured data. Figures 9(a)-9(c) show a qualitative agreement between the measured data and the predictions of the second modified Fresnel-zone model. The magnitude of the first dip is predicted correctly but discrepancies are found for the frequency position of the dip as the proportion of hard strips decreases.

6. Conclusions

Laboratory measurements of the excess attenuation of sound from a point source over a single discontinuity between an acoustically hard surface and a sand surface have been compared to (a) a diffraction based heuristic (De Jong) model, (b) a model whose boundary effect is simply related to the region around the specular reflection point defined by a Fresnel-zone condition and (c) a numerical solution using boundary element theory when the proportion of hard surface is varied systematically. The Fresnel-zone method used in our work is improved compared to previous models which assumed an excess attenuation dependent on the proportions of the different surfaces on the line representing the Fresnel-zone. In this work we assume that the excess attenuation is dependent on the proportion of the different surface-areas inside the elliptical Fresnel-zone, and we use a new definition of the excess attenuation in mixed impedance cases. Instead of a linear interpolation between the excess attenuation above each type of surface impedance, we use a linear interpolation between the pressures at the receiver relative to the free field for the two types of impedance. The results of the predictions obtained by this modified model show a better agreement with the measured data than that calculated from the previous model. The semi-empirical model and the boundary element code are found to give satisfactory agreement with the measurements but the Fresnel-zone model does not perform as well in predicting the frequency position of the first dip. In addition, due to diffraction effect, the frequency of the excess attenuation first dip is predicted to be highest at approximately 70% hard surface cover rather than the expected 100%.

Laboratory measurements of the excess attenuation of sound from a point source over a striped impedance with the source-receiver line perpendicular to the strips are compared to the semi-empirical model extended to the case of multiple impedance discontinuities and to the Fresnel-zone model. The results show that the Fresnel-zone model is not adequate to predict excess attenuation for all frequencies in the case of multiple impedance discontinuities. However, both the Fourier transform method and the boundary element method give good agreement with the measured results. The agreement between Nyberg's theory and the measurements shows that for the geometry used in the experiment, the ground effect due to striped impedance may be determined from that predicted by using the area-averaged impedance.

ACKNOWLEDGMENT

The authors gratefully acknowledge financial support from BBSRC (UK) through grant ref. no. CTE 02649.

REFERENCES

- ¹M. Naghieh and S. Hayek, "Diffraction of a point source by two impedance covered half-planes" *J. Acoust. Soc. Am.* **69**, 629-637 (1981).
- ²B. O. Enflo and P. H. Enflo, "Sound wave propagation from a point source over a homogeneous surface and over a surface with an impedance discontinuity" *J. Acoust. Soc. Am.* **82**, 2123-2134 (1987).

- ³J. Naze Tjøtta, "Reflection of an acoustic wave on a plane surface presenting an impedance discontinuity along a straight line" *Acta Acustica* **1**, 15-33 (1993).
- ⁴J. Durnin and H. Bertoni, "Acoustic propagation over ground having inhomogeneous surface impedance" *J. Acoust. Soc. Am.* **70**, 852-859 (1981).
- ⁵J. N. B. Harriott, S. N. Chandler-Wilde and D. C. Hothersall, "Long distance sound propagation over an impedance discontinuity" *J. Sound Vib.* **148**, 365-380 (1991).
- ⁶K. B. Rasmussen, "Propagation of road traffic noise over level terrain" *J. Sound Vib.* **82**, 51-61 (1982).
- ⁷M. Galindo, "Application of the parabolic approximation method to sound propagation above ground with impedance variations" *Proceedings of the Sixth International Symposium on Long-Range Sound Propagation*, 394-407 (1994).
- ⁸J. S. Robertson, P. J. Schlatter and W. L. Siegmann, "Sound propagation over impedance discontinuities with the parabolic approximation" *J. Acoust. Soc. Am.* **99**, 761-767 (1996).
- ⁹P. Koers, "Diffraction by an absorbing barrier or by an impedance transition" *Proceedings of Internoise*, 311-314 (1983).
- ¹⁰G. A. Daigle, J. Nicolas and J.-L. Berry, "Propagation of noise above ground having an impedance discontinuity" *J. Acoust. Soc. Am.* **77**, 127-138 (1985).
- ¹¹D.C. Hothersall and J. N. B. Harriott, "Approximate models for sound propagation above multi-impedance plane boundaries" *J. Acoust. Soc. Am.* **97**, 918-926 (1995).
- ¹²B. A. De Jong, A. Moerkerken and J. D. Van Der Toorn, "Propagation of sound over grassland and over an earth barrier" *J. Sound Vib.* **86**, 23-46 (1983).
- ¹³C. Nyberg "The sound field from a point source above a striped impedance boundary" *Acta Acustica* **3**, 315-322 (1995).
- ¹⁴S. N. Chandler-Wilde and D. C. Hothersall, "Sound propagation above an inhomogeneous impedance plane" *J. Sound Vib.* **98**, 475-491 (1985).
- ¹⁵K. Attenborough, "Models for the acoustical properties of air-saturated granular media", *Acta Acustica* **1**, 213-226 (1993).
- ¹⁶S. N. Chandler-Wilde and K. V. Horoshenkov, "Padé approximants for the acoustical characteristics of rigid frame porous media" *J. Acoust. Soc. Am.* **98**, 1119-1129 (1995).
- ¹⁷K. Attenborough, "Models for the acoustical properties of rigid-porous materials", *Proceedings of the 15th International Congress of Acoustics*, **2**, 365-368 (1995).
- ¹⁸S. Slutsky and H. L. Bertoni, "Analysis and programs for assessment of absorptive and tilted parallel barriers", *Transportation Research Record* 1176, *Transportation Research Record*, National Research Council, Washington DC, 13-22 (1987).
- ¹⁹D.C. Hothersall and J. N. B. Harriott, "A Fresnel zone approach to the prediction of sound propagation above a multi-impedance plane", *Proceedings of the Institute of Acoustics* **16**, 83-90 (1994).
- ²⁰M. R.Bassiouni, C. R. Minassian and B. Chang, "Prediction and experimental verification of far field sound propagation over varying ground surfaces" *Proceedings of Internoise*, 287-290 (1983).

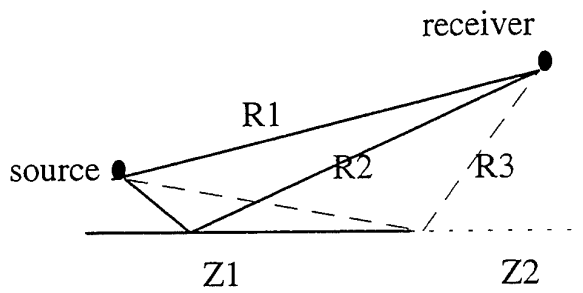


Figure 1 Definition of the various path lengths.

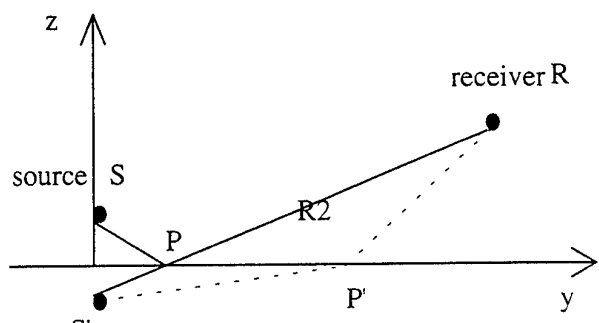


Figure 2 Source receiver geometry.

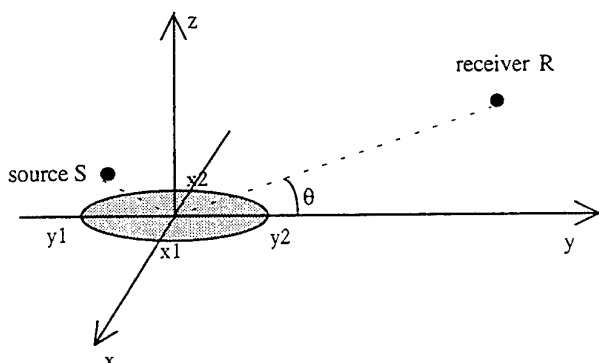


Figure 3 The elliptical Fresnel zone in the boundary.

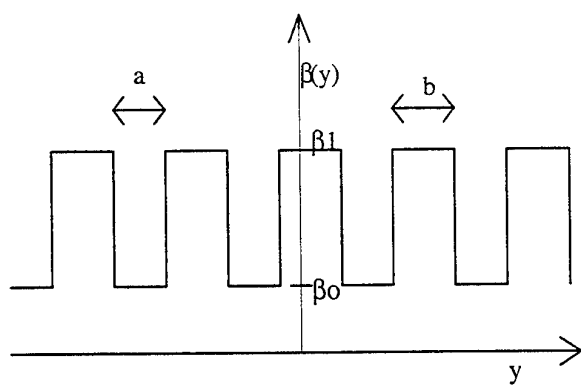


Figure 4 The periodic admittance used in Nyberg's theory.

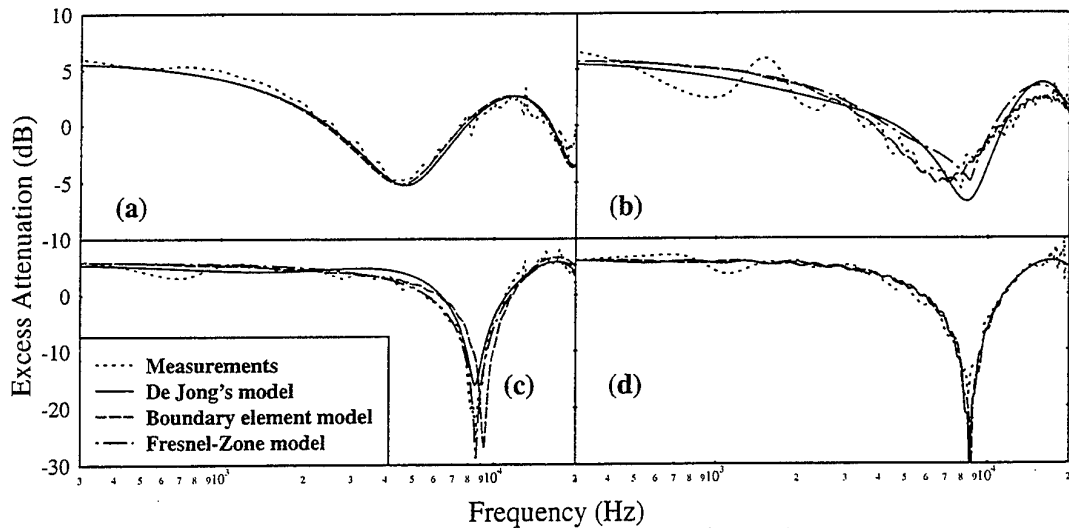


Figure 5: Excess attenuation spectra for (a) a continuous sand boundary, (b) a 50% hard boundary, (c) a 80% hard boundary, (d) a 100% hard boundary.

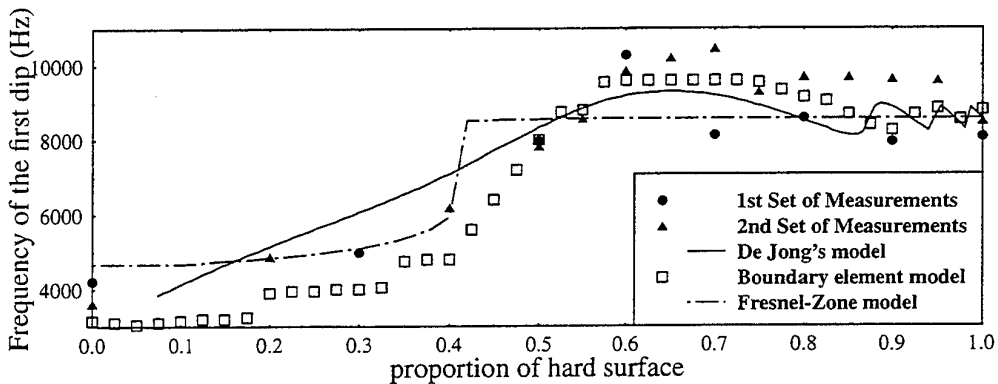


Figure 6: Frequency location of the first dip for the excess attenuation spectra in the case of varying proportions of hard surface.

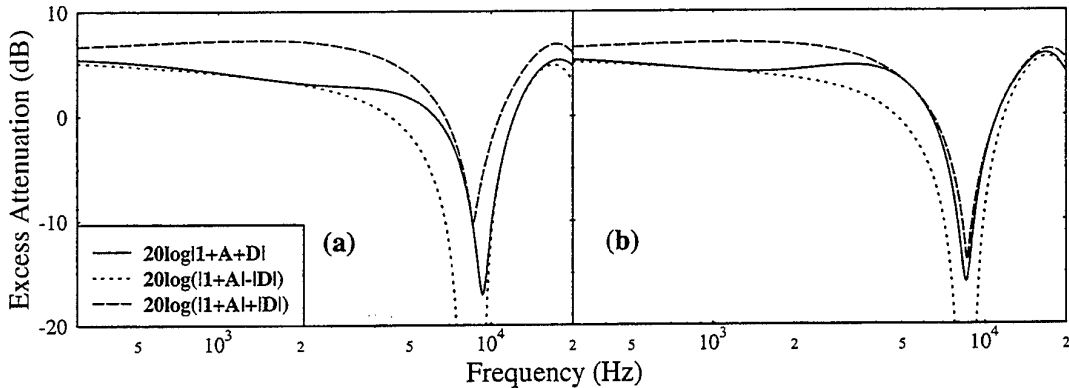


Figure 7: Excess attenuation spectra for (a) a 65% hard ground cover, (b) a 80% hard ground cover

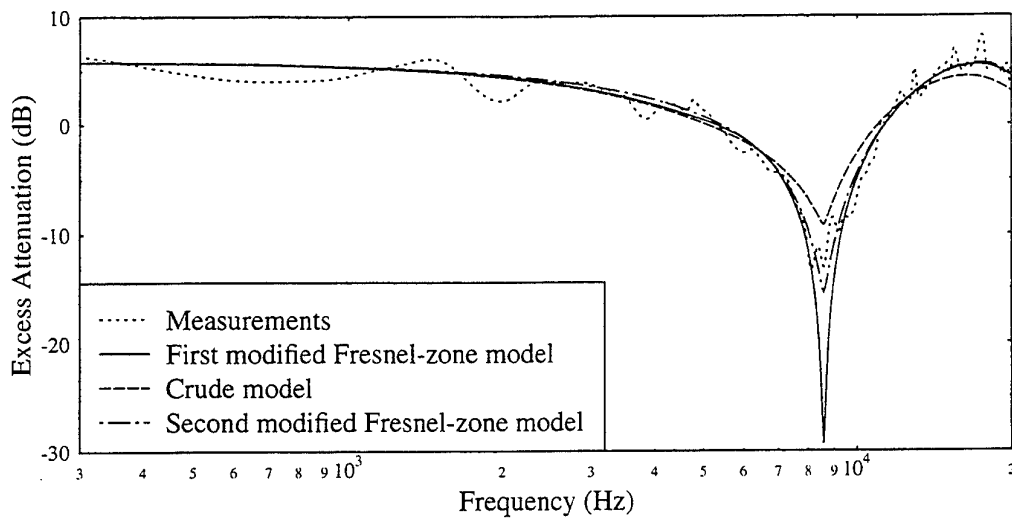


Figure 8: Excess attenuation spectra for a 70% hard ground cover.

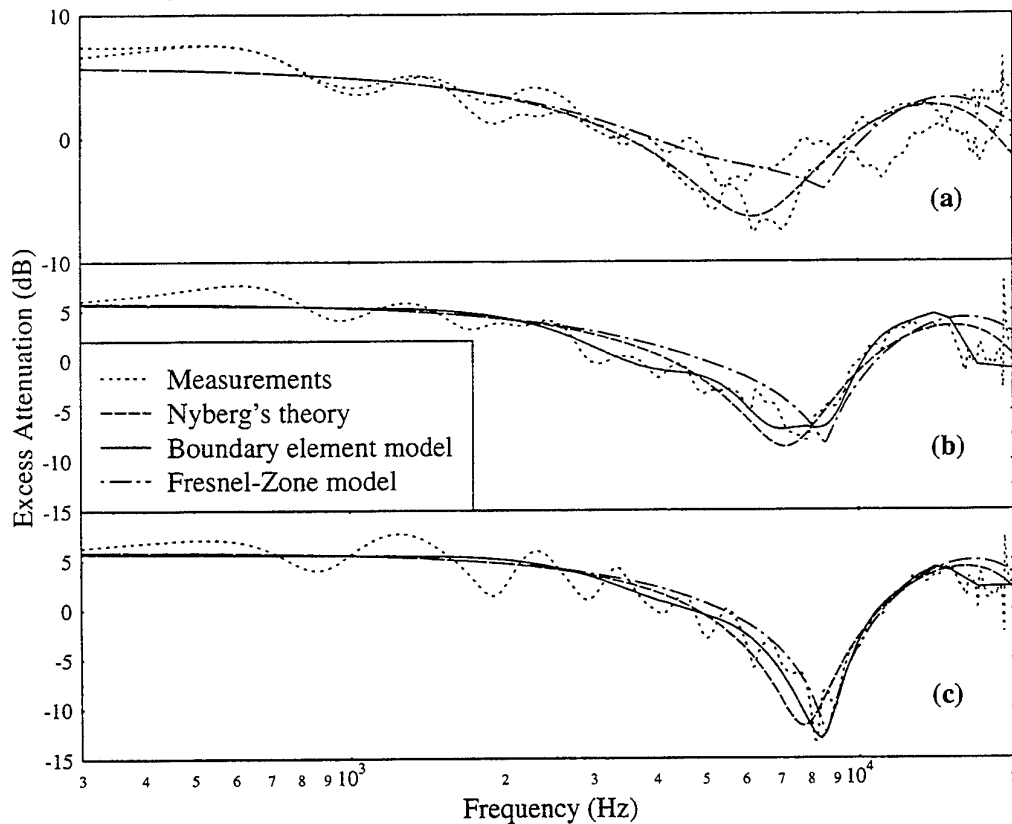


Figure 9: Excess attenuation spectra for (a) a 50% hard-strip boundary, (b) a 70% hard-strip boundary and (c) a 80% hard-strip boundary.

Computer cost of a 3D numerical model for noise barrier insertion loss

A.TEKATLIAN and E.PREMAT

Ecole Nationale des Travaux Publics de l'Etat

Département Génie Civil et Bâtiment URA CNRS 1652 - Laboratoire des Sciences de l'Habitat
1 rue Maurice Audin - 69518 Vaulx-en-Velin cedex - France
FAX (33) 72 04 70 41

The computer cost of a 3D diffraction model is studied both in terms of CPU time and memory size. Some order of magnitude of these costs are given. The CPU time necessary to calculations is measured when changing the numerical schemes involved in these calculations. The results show that a large calculation time can be earned by the use of numerical schemes simple enough to be easily used by non specialists in mathematics. Then some other possible improvements to reduce the CPU time, the memory size or both of them are proposed and discussed. In this latter case, a set of further simulations are to be done to precise the model limitation in terms of frequency range or geometrical dimensions.

1. INTRODUCTION

Barriers are now widely used to reduce road traffic noise. However, there remains a need about the understanding of the diffraction around these barriers. A large number of works have been carried out in this aim, and some simulation models for noise barriers insertion loss are commonly used today. The reader might refer to Hothersall who made a recent review on this subject [1].

Most often during the past 10-15 years, models based on ray theory are used and developed for rather realistic cases [2], [3]. Although they provide rapid and accurate results for 2D and even 3D configurations, only simple shaped or infinite barriers, flat ground, with a few possibilities to describe the barrier and ground absorption can be studied. Moreover, it is difficult to assess the accuracy of this kind of models in some propagation domain zones and for low frequencies of the traffic noise spectrum.

A second type of mathematical modelling of the performances of barriers is called Boundary Element Methods (BEM). This denomination corresponds actually rather to the numerical technique used to solve the problem than to the general modelling approach, based on integral formulation. This approach consists in searching a wave equation solution, most often in the frequency domain, using a numerical technique of subdivision of the propagation domain boundary and approximation of the unknowns by piecewise functions defined on these subdivisions [4], [5], [6], [7]. These methods can deal with arbitrary shape and absorption properties of barriers and ground provided that the boundary subdivisions size is small enough to provide a sufficient accuracy of the numerical resolution. Although recent studies based on this kind of modelling apply to noise barriers, most of them focus on simplified cases or are concerned only with simplified cases like flat ground, 2D configurations, or very low frequencies [8], [9], [10]. These limitations come from the numerical technique complexity which constitutes the major method drawback. However, such a 3D model would be useful, for example to study the combined diffraction of vertical and horizontal edges, or the influence of several type and location of sources. Moreover, a worthwhile application of the model is the understanding of phenomena or the set up of approximations which would help to apply simpler models, such as ray path modelling or 2D BEM ones, to 3D realistic configurations.

We have developed a computer code, named BEMAS3D (Boundary Element Model for Acoustic Scattering in 3 Dimensions), which corresponds to this kind of modelling. To keep

the possibility to deal with various shapes and absorption characteristics of the barrier and ground, neither symmetry nor any other idealisation restriction has been taken into account. The algorithm is built with a principle of modularity : For example, the impedance model used can be changed with another one without having to modify a large part of the algorithm. For all these reasons, this model leads to high computer costs if any simple numerical technique is used, and the necessary memory size prevents us from simulations within the whole traffic noise spectrum on a workstation. We have then to precise what are the orders of magnitude and limits in terms of computer cost, as well as possible improvements of the computer code, which has been implemented using the most simple numerical techniques. We examine the possibility to introduce some improvements in the code, which can be performed by engineers and researchers not specialised in mathematics or computer science. It could be a way to transform the original heavy model to provide informations within at least the low frequency range of traffic noise.

The next part presents the model. The analytical formulation leads to an exact solution while its transformation into a suitable automatic calculation form leads to numerical approximations. What we call computing cost is then commented, and some order of magnitude are presented. Improvement possibilities are then tested for some of them, commented for some others. The implied idea is always to try to provide results which are sufficiently accurate for engineering uses, and corrects anywhere in the propagation domain and for any parameter configurations.

2. THE MATHEMATICAL MODEL

The mathematical model is based on choosing an a priori form of the acoustic pressure in the propagation medium which verify the propagation problem. Including this expression in the boundary condition leads evaluate this acoustic pressure.

2.1 ANALYTICAL FORMULATION

Let S be a point source situated in the semi-infinite homogeneous propagation domain Ω (Fig. 1). The ground and barrier surface constitute this domain boundary σ . The signal is supposed to be harmonic, with temporal dependency $\exp(-i\omega t)$, where ω is the angular frequency.

We remain within the bounds of the linear acoustics' assumptions. The total acoustic pressure p_t in Ω can thus be expressed as the sum of pressure p_i radiated by the point source S as if it were alone in an infinite medium and the pressure p_s scattered by the boundary σ :

$$p_t = p_i + p_s$$

The boundary value problem can be represented by the system :

$$\left\{ \begin{aligned} & (\Delta + k^2) p_i(M) = \delta_S \quad , \quad M \in \Omega \\ & (\Delta + k^2) p_s(M) = 0 \quad , \quad M \in \Omega \end{aligned} \right. \quad (1)$$

$$\left\{ \begin{aligned} & \lim_{M \in \Omega \rightarrow P' \in \sigma} \left[\partial_{\bar{n}}(P') p_t(M) - ik \frac{\rho c}{Z_n} p_t(M) \right] = 0 \quad , \quad P' \in \sigma \end{aligned} \right. \quad (2)$$

$$\left\{ \begin{aligned} & \lim_{M \in \Omega \rightarrow P' \in \sigma} \left[\partial_{\bar{n}}(P') p_t(M) - ik \frac{\rho c}{Z_n} p_t(M) \right] = 0 \quad , \quad P' \in \sigma \end{aligned} \right. \quad (3)$$

$$\left. \begin{aligned} & \text{Sommerfeld conditions for } p_i \text{ and } p_s \end{aligned} \right. \quad (4)$$



Fig. 1. Symbols used

where ρ is the air density, $k = \omega/c$ is the wave number, c the speed of sound in the air, Z_n is the normal acoustic impedance of the boundary σ , supposed to be a locally reacting infinite

surface. $\partial_{\bar{n}(P')} p_t(M) = \bar{n}(P') \cdot \nabla [p_t(M)]$ is the $p_t(M)$ normal derivative. The normal vector is assumed to point out the propagation domain.

Equations (1) and (4) yield to the pressure radiated at a receiver M by a point source in an infinite medium :

$$p_i = -\frac{\exp(ikr(M, S))}{4\pi r(M, S)}$$

It has been shown that the pressure p_s , solution of equations (2), (3), (4), can be expressed as a linear combination of simple and double layer potentials [11]. It is simply written here as a simple layer potential :

$$p_s(M) = \int_{\sigma} \mu(P) G(M, P) \sigma(P) , \quad M \in \Omega \quad (5)$$

where G is the free space Green's function for the Helmholtz equation (1), which has the same form than p_i . Thus, the layer potential density function μ characterizes entirely the scattered acoustic pressure.

The introduction of p_t in the boundary condition (3) leads to the following boundary integral equation :

$$\begin{aligned} & \frac{\exp(ikr(P', S))}{4\pi r(P', S)} \left[ik \frac{\rho c}{Z_n} - \left(ik - \frac{1}{r(P', S)} \right) \bar{n}(P') \nabla_{P'} r(P', S) \right] \\ & - \frac{\mu(P')}{2} + \int_{\sigma} \mu(P) \partial_{\bar{n}}(P') G(P', P) d\sigma(P) - ik \frac{\rho c}{Z_n} \int_{\sigma} \mu(P) G(P', P) d\sigma(P) = 0 \quad (6) \end{aligned}$$

where $\nabla_{P'}$ is the gradient operator taken with respect to P' coordinates.

In this equation, every term is a data of the boundary problem, except the μ function, which appears to be an intermediate unknown. Indeed, the BEM used here is called indirect, because μ has to be determined in a first step to lead to the acoustic pressure by the equation (5).

The direct and indirect methods are the two major BEM families [6].

The mathematical method presented here is exact, and the pressure solution of the boundary value problem is unique provided that both the propagation medium and its complementary are infinite.

2.2 NUMERICAL FORMULATION AND TECHNIQUE

The resolution of the integral equations is performed using a simple classical discrete formulation. It is based on subdividing the boundary σ into plane rectangular elements on the center of which a collocation point is located [12]. The complex layer density μ is approximated by a piecewise constant function defined upon these elements :

$$\begin{cases} \mu(P) = \sum_{j=1}^N \mu_j f_j(P) \\ f_j(P) = 0 \quad \text{if } P \notin \sigma_j \\ f_j(P) = 1 \quad \text{if } P \in \sigma_j \end{cases},$$

where N is the subdivisions (and then the collocation points) number.

The boundary equation (6) is written for each collocation point P'_i :

$$\begin{aligned} & \frac{\exp(ikr(P'_i, S))}{r(P'_i, S)} \left[ik \frac{\rho c}{Z_n} - \left(ik - \frac{1}{r(P'_i, S)} \right) \bar{n}(P'_i) \nabla_{P'_i} r(P'_i, S) \right] \\ & - 2\pi \delta_i^j - \sum_{j=1}^N \mu_j \int_{\sigma_j} \frac{\exp(ikr(P'_i, P))}{r(P'_i, P)} \left(ik - \frac{1}{r(P'_i, P)} \right) \bar{n}(P'_i) \nabla_{P'_i} r(P'_i, P) d\sigma(P) \\ & + ik \frac{\rho c}{Z_n} \sum_{j=1}^N \mu_j \int_{\sigma_j} \frac{\exp(ikr(P'_i, P))}{r(P'_i, P)} d\sigma(P) = 0 \quad , \quad P'_i \in \sigma_i \quad (7i) \end{aligned}$$

This leads to a linear algebraic (N, N) square system which unknown vector is composed by the complex μ_j numbers. If $i=j$, the simple layer and its normal derivative light singularities have to be treated. It is a classical problem which does not constitute a main difficulty [5]. It has to be noticed that the terms related to the source are only situated in the system second member, which lies on the first part of eq.(7i).

Once the density layer approximation is known, the scattered acoustic pressure is calculated at each receiver R_m by a discretised form of equation (5) :

$$p_s(R_m) = - \sum_{j=1}^N \mu_j \int_{\sigma} \frac{\exp(ikr(R_m, P))}{4\pi r(R_m, P)} d\sigma(P) \quad (8)$$

then the total pressure at each receiver can be known.

The total pressure at each receiver is calculated on one hand when the propagation domain boundary considered is only the ground, on the other hand when the boundary is the barrier lying on the ground. Finally, the difference between the total acoustic pressure level with and without the barrier give the so-called barrier insertion loss.

Algorithm structure

To comment upon computing topics, it is useful to present roughly the algorithm structure. The propagation domain boundary, that is to say the barrier lying on the ground or the ground alone, is divided into plane rectangular subdivisions. Every subdivision σ_k is defined by the three coordinates of the four points $A_{lk}, l \in \{1, 2, 3, 4\}$ located on its corners. The writing order of this coordinates in the meshing file enables us to define a coordinate system $(A_{lk}, \xi_{1k}, \xi_{2k}, \xi_{3k})$ related to this subdivision σ_k . It also defines a normal vector, chosen here to point out of the propagation domain. When meshing the boundary, a group number is associated to each subdivision. This group number corresponds to a ground physical property, for example its flow resistivity. The meshing is performed with MAX, which is a part of the CESAR-LCPC code [13].

In the algorithm, three coordinate systems are taken into account (cf. Fig. 2). The first one, $(o, \bar{i}, \bar{j}, \bar{k})$, is the arbitrary reference chosen when meshing the boundary. The two other ones are related to the meshing plane subdivisions. The system $(A_{1j}, \bar{\xi}_{1j}, \bar{\xi}_{2j}, \bar{\xi}_{3j})$ is related to the subdivision σ_j on which are performed the double integrations. The system $(A_{1i}, \bar{\xi}_{1i}, \bar{\xi}_{2i}, \bar{\xi}_{3i})$ is related to the subdivision on the center of which lies the collocation point P_i . When calculating the matrix elements to solve the linear system, each subdivision represents one time an integration surface, and one time a collocation surface (the surface where lies the collocation point).

The coding is organised so that part of it can easily be modified (cf. Fig. 3). Three major steps are to be distinguished. The first one is the calculation of each element A_{ij} of the matrix corresponding to the system to solve (see eq. 7_i) :

$$A_{ij} = -2\pi \delta_i^j - \alpha_{ij} + ik \frac{\rho c}{Z_n} \beta_{ij} ,$$

$$\alpha_{ij} = \int_{\sigma_j} \frac{\exp(ikr(P'_i, P))}{r(P'_i, P)} \left(ik - \frac{1}{r(P'_i, P)} \right) \bar{n}(P'_i) \nabla_{P'_i} r(P'_i, P) d\sigma(P) , \quad (9)$$

$$\beta_{ij} = \int_{\sigma_j} \frac{\exp(ikr(P'_i, P))}{r(P'_i, P)} d\sigma(P) , \quad (10)$$

and the calculation of the second member.

The second step is the linear system resolution which provides us with the μ_j intermediate unknowns N values. Then, in a third step, the scattered acoustic pressure $p_s(R_m)$ is calculated for each receiver R_m by the product between the complex vector μ_j and the one made of the integrals shown in eq. (8), for which no problems of singularity occurs.

The double numerical integrations are performed in the integration surface coordinate system $(A_{1j}, \bar{\xi}_{1j}, \bar{\xi}_{2j}, \bar{\xi}_{3j})$. So the lower limits are always equal to zero. The upper limits, corresponding to subdivision sizes, have to be calculated for each integration, since it is not necessarily always the same. The functions to be integrated appear in eq. (9) and (10), taking into account the related jacobians (see [14] p 179-191 for example).

The data input consists mainly in the meshing file, the source and receivers coordinates, the frequency, and the flow resistivity values, which are located in a vector whose size is as large as the boundary subdivisions number.

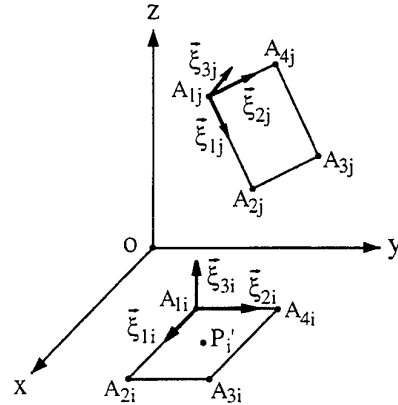


Fig. 2. Three coordinate system used

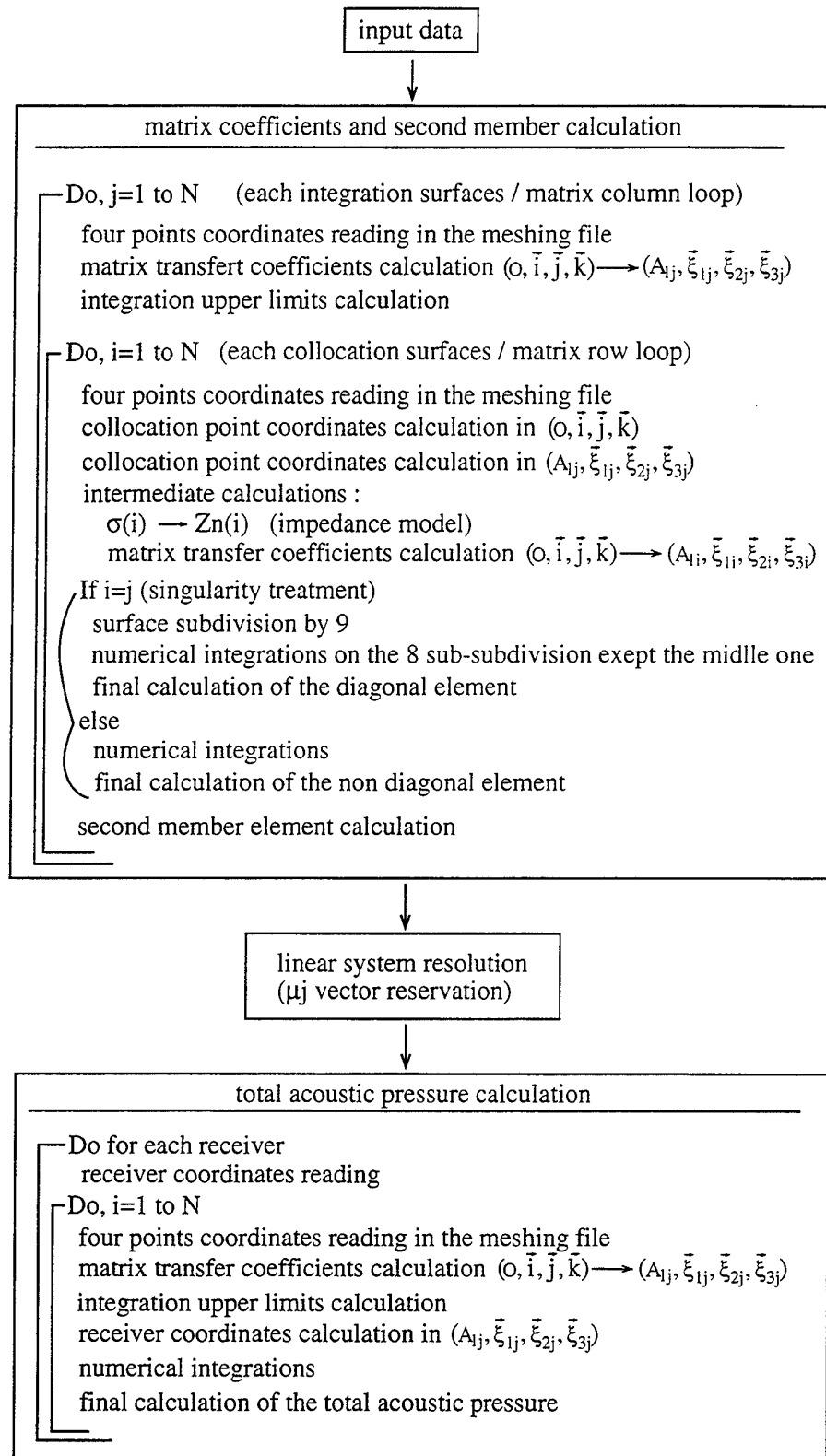


Fig. 3. Structure algorithm

3. COMPUTING COST

Among the three major parts of the algorithm that are detailed above, the one related to the acoustic pressure calculation at receivers is of negligible computing cost. Indeed, considering 30 to 50 receiver points in the examples used in this paper, this calculation stage corresponds to much less than about 1% of the total CPU calculation time. Thus, our comments focus on the matrix generation and the linear system resolution processes.

A lot of assumptions have been made about computing costs of numerical implementations of BEM. They sometimes seem to disagree totally, mainly because the contexts are not comparable. There after, we use commonly accepted numerical rules that are not prohibitive for non specialists in mathematics. Besides, our results are all based on real numerical experimentations to get an idea and provide some precise examples.

3.1 WHAT IS EXPENSIVE AND WHAT KIND OF COMPUTING COST

We deal here after with two kinds of computing cost: the calculation CPU time and the memory storage size. In the first part of the code, every element of the linear square system matrix is calculated, performing surface integrations. Depending on the number of matrix elements, this may lead to large calculation times. Then the system has to be solved. In the general case, the matrix is not symmetric nor multi-diagonal. The most classical numerical schemes involve keeping the entire matrix in the computer memory. This step generally leads to both large calculation time and large memory storage size.

Memory Size

The limitations in terms of memory size is related to the size of the linear system matrix. This size is directly related to the number of boundary subdivisions. When the function μ is approximated by a piecewise constant or a linear one, the size of each subdivision has to be no larger than about the sixth of the acoustic signal wavelength [5], [8]. This numerical convergence criteria is the result of previous numerical experiments and is widely used. It means for example that for a harmonic signal of frequency 1 kHz, each dimension of the subdivision has to be no larger than 0.06 m. The table 1 gives some ideas of the size of the matrix we would have to keep in memory space for low frequencies of traffic noise spectrum and some ground dimensions. Each complex element needs 8 bytes of memory when calculations are performed using single precision.

frequency	dimensions	10 m * 10 m	20 m * 20 m
125 Hz		230 000 / 1.8 Mo	4 000 000 / 32 Mo
250 Hz		3 700 000 / 29.6 Mo	68 000 000 / 544 Mo

Tab. 1. Minimum number of elements of the matrix / memory size (Mo)

This example shows that it is not possible to model realistic configurations using a workstation and considering the traffic noise spectrum without improvement of the technique.

The memory size of a computer can be virtually extended using the hard disc. In this case, a part of the disc is definitely devoted to this task (swap space), no file can be written there, so the quantity of files that can be saved on the disc is reduced. Moreover, this task consists in reading and writing often on the disc : this may be very costly as regards to the calculation time. Thus, this solution has to be chosen only when there is no other way to deal with a large memory size, more often for high frequencies.

Calculation Time

One part of the calculation time corresponds to the calculation of each element of the matrix. The major numerical schemes involved in this step are the numerical integrations. The other

major part of the time is consumed by the linear system resolution. Authors often agree to say that if the square linear system is characterised by a size N then the time cost for the first stage is aN^2 elementary operations, and that of the second one is bN^3 for direct methods with $a \gg b$ [15], [16]. So for small systems the matrix elements calculation step is more costly than the system resolution, but when the frequency increases - and therefore the system size - the calculation time for the system resolution becomes prohibitive. We illustrate this idea by giving some order of magnitude in a further paragraph.

3.2 COMPARISON SET OF EXAMPLES

To improve our code in terms of computing cost, we have to use a set of reference configurations. The three examples commented here after are called "ex1", "ex2" and "ex3". The kind of meshing is described in Fig. 4.

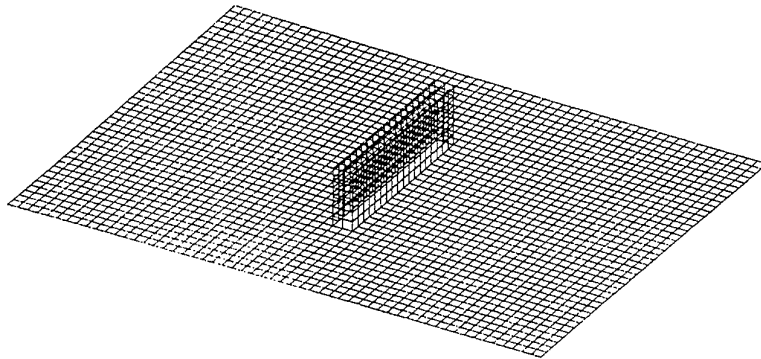


Fig. 4. Kind of meshing used in the reference configurations

These reference configurations differ in the ground and barrier dimensions, the frequency of interest, and the flow resistivity taken as input data. The number N of boundary subdivisions (which is also the size of the square system), depends on the geometrical dimensions and the frequency, since the $\lambda/6$ criteria presented above is respected. The related values are given in Tab. 2.

	frequency (Hz)	ground dimensions (m*m)	barrier dimensions (m*m)	subdivisions number	RAM (Mo)	flow resistivity (rayls cgs)
ex1	100	19.25*11	5.5*3.3*1.1	700 844	3.9 5.7	ground: 150 barrier: 150
ex2	100	30.25*22	9.9*3.3*1.1	2200 2440	38.7 47.6	ground: 300 barrier: 100 000
ex3	250	12*10	1.2*0.4*0.2	3000 3025	72 73.3	ground: 200 000 barrier: 200 000

Tab. 2. set of examples description

Since the number of receivers does not influence the total calculation time, it is not precised here for each case. The storage memory (RAM, for Random Access Memory) is calculated for

the number N^2 of the square matrix elements, considering 8 bytes for each single precision defined complex element. The visual controls when the program is running show that the total real memory size never exceeds this value more than about 5% of it. Each calculation is performed once considering the ground alone, and once considering the ground and the barrier. That is why two elements numbers are given. The question of the validity of the approximation of the infinite ground by a finite dimension one has to be treated in a further stage. Indeed, it is usually assumed that the ground can be described with finite dimensions provided that these are "sufficiently" large. This last condition has to be quantified. Like many authors, and taking into account the wavelength and the source and receivers positions, we assume in this study that the ground dimensions are sufficiently large not to affect the accuracy of our results.

3.3 CALCULATION TIMES AND FIRST IMPROVEMENTS

All calculations are performed on a HP 715/75 MHz workstation (RAM : 128 Mo). In order to be able to generalise reasonably our conclusions, we had to perform a large number of calculations. To get rather quickly a set of results, we chose to work first as regards numerical schemes which would help to improve our calculation time rather than deal with the storage memory problem at high frequencies. So, for each of our reference configurations, among which are the three ones described above, some simple numerical schemes are used and the calculation times are compared. Numerical details like precisions for stop or cut-off tests are adjusted to lead to negligible discrepancies in acoustic levels at each receiver (always smaller than about 0.01 dB), every parameter being the same for each comparison.

The goal of this study is then first to have a look at numerical methods used in the acoustical literature and then to choose among the many existing numerical schemes the most appropriate ones. Two numerical scheme families have been dealt with. The first one is devoted to surface integrations, involved in the matrix generation step, the second one is devoted to the system resolution. The latter concerns only direct linear system resolution methods for the moment.

Matrix elements calculation stage

We have got to calculate two integrals: α_{ij} and β_{ij} (cf eqs 9 and 10)

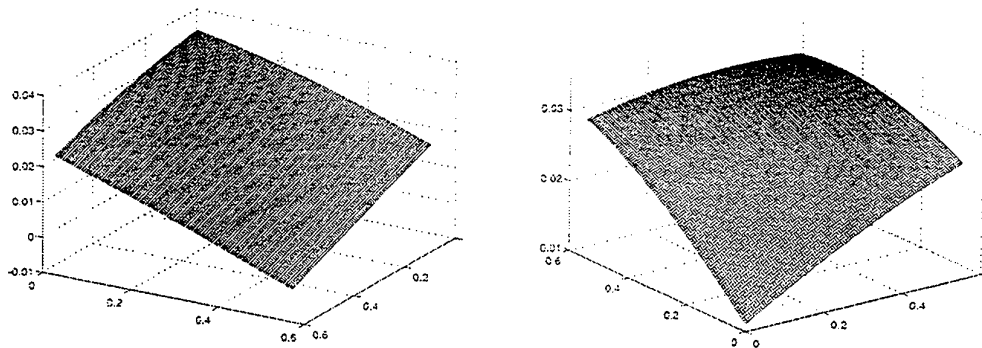


Fig. 5. Function to integrate for α_{ij} . Left handside: real part. Right handside: imaginary part. $(i,j)=(1,844)$ corresponding to the case "ground and barrier" of ex1 (844 matrix elements). Both imaginary and real part of this function are equal to 0 for $(i,j)=(1,1)$ and $(i,j)=(1,422)$

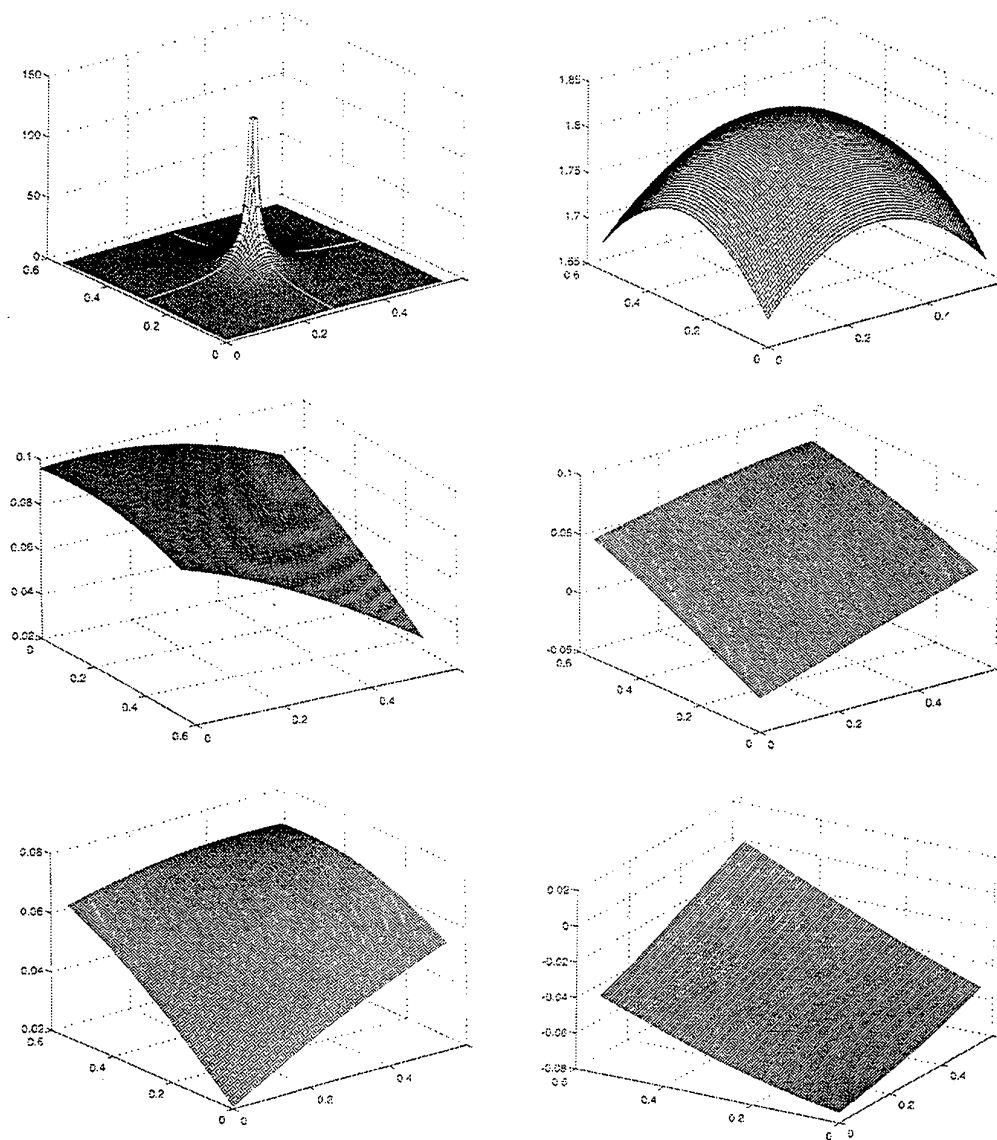


Fig. 6. Function to integrate for β_{ij} . Left handside: real part. Right handside: imaginary part. Top to bottom : $(i,j)=(1,1)$, $(i,j)=(1,422)$, $(i,j)=(1,844)$ corresponding to the case "ground and barrier" of ex1 (844 matrix elements).

These integrals are regular except when $i=j$. To calculate these regular integrals, when the functions to integrate are smooth enough and do not present too high peaks or discrepancies, a so-called Gauss quadrature appears to be very efficient ([17]) and particularly much less costly than a simple product of Simpson rules : "For smooth, nonsingular problems, nothing beats Gaussian quadrature..." ([18] p.783). Nevertheless these quadrature methods have a drawback ([18] p.784): there is no other simple way to obtain an estimate of the error in the result than to increase the number of the points involved in the quadrature and to use the difference between the two successive values as a rough estimate of the error of the last term.

Since the functions to integrate (except for the discontinuity) are "good-looking" (see Fig. 5 and Fig. 6) we use a Gauss-Legendre quadrature to calculate α_{ij} and β_{ij} :

$$\int_{\sigma} f(x, y) dx dy = \sum_{i=1}^n \sum_{j=1}^n \omega_i \omega_j f(x_i, y_j) \text{ where } x_i \text{ and } y_j \text{ are zeros of the Legendre polynomials and}$$

ω_i, ω_j are the corresponding weights ([19] p.892).

The question is then : how many points must we take into account? Amini and Wilton ([17] p59) use a 3*3 product rule of Gauss-Legendre for which they state that "*Extensive experience (...) has shown that the choice of a 3*3 point product Gauss-Legendre rule (...) is the most efficient for a moderate number of collocation points...*"

Our own experience led us to find out that the best thing to do for the regular integrals ($i \neq j$) is to divide each elementary collocation surface σ_i into four parts and to use then a 3*3 product Gauss-Legendre rule. Concerning the singular elements ($i=j$), in order to calculate α_{ii} and β_{ii} we divided the elementary collocation surface into 9 parts. In the middle part we took $\alpha_{ii} = -2\pi$ taking into account the simple layer normal derivative discontinuity and we divided again each of the remaining parts into four elements on which we used the 3*3 Gauss-Legendre product rule.

Linear system resolution stage

For solving a linear system there are two different classical approaches : direct methods and iterative methods.

The latter are based either on an appropriate splitting of the matrix (Jacobi, Gauss-Seidel, Successive Over Relaxation -SOR- methods...) or use alternate directions techniques, descent methods particularly efficient but usually valid in the cases where the matrix has got particular "good-looking" properties such as symmetry, definite positive symmetry (gradient, conjugate gradient methods...)

We chose to focus our attention at first to direct methods : Gauss-Jordan inversion, Gauss elimination, Lower Upper (LU) decomposition, Choleski method, Householder method...

In the general case of a full nonsymmetric linear system matrix the less costly direct method seems to be the LU decomposition [18]. Besides, comparing to Gauss elimination, this method has the same operation cost and becomes much less costly when you have got to solve the same linear system with several different second members (the LU decomposition is still valid) which is very interesting when you want to solve an acoustic problem with several sources. The LU decomposition is the most commonly used direct method for matrices having no particular property ([20] and [21] p.26...). We chose this well-known numerical scheme keeping in mind we could still improve this linear system resolution stage in a near future (see § 3.4 : other improvement possibilities).

First improvements

	Simpson / GJ	Gauss9 / GJ	Simpson / LU	Gauss9 / LU
ex1 ground alone	41mn	36mn	14mn	11mn
	1h10mn	1h03mn	25mn	20mn
ex2 ground alone	18h50mn			3h50mn
	27h30mn			5h17mn
ex3 ground alone	48h45mn			9h
	52h15mn			9h43mn

Tab. 3. Total CPU calculation times versus different numerical schemes

Some calculation times of our simulations are precised in Tab. 3.

Each reference configuration has been modelled, when different numerical schemes are used. Two calculation times are given, the first corresponding to the case where the boundary is the ground alone, the second one concerns the ground plus the barrier. The numerical schemes used for surface integrations are the Simpson's rule and the 9 points Gauss' rule (Gauss9). The ones used for the system resolution are the optimised Gauss-Jordan's rule (GJ) and the LU decomposition. The results show clearly such simple improvements usefulness.

What has to be noticed is the proportion between the calculation time devoted to the matrix generation step and the one necessary to the resolution step. Fig. 7 shows some order of magnitude for the examples given above, when the Gauss9 / LU numerical schemes are used and the boundary contains the barrier. This proportion has been observed on all of our simulations.

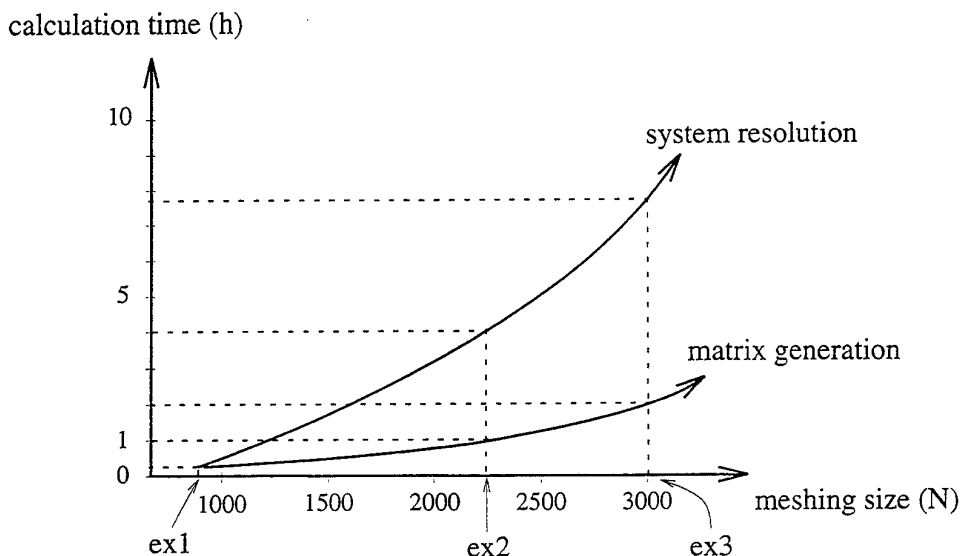


Fig. 7. Calculation time devoted to the two major steps of calculation

This leads to encourage to improve the numerical technique devoted to the system resolution, since to apply the model to the whole traffic noise spectrum implies increasing the meshing size.

3.4 OTHER IMPROVEMENT POSSIBILITIES

The problem is to improve with the best compromise both the calculation time and the memory size. We have to keep in mind that if a large calculation time is an obvious practical drawback, it does not impeach to perform the calculations. On the other hand, if the memory size necessary to store the matrix is too large, the simulation is simply impossible on a workstation. This first version of the computer code is useful when the harmonic signal frequency is no larger than some hundred Hz for realistic ground dimensions. It is possible, and rather often done, to work for larger frequencies using a swap space (§ 3.4), but this alternative extends the calculation time and leads to a (larger) frequency limitation. So it would be worth finding a mean to reduce the size of the matrix.

Some improvements are to be taken into account. Part of them are definitely worthwhile, but only for one or the other of the calculation time or memory size aspect. So they have to be tested to verify that the gain in terms of memory size does not increase significantly the

calculation time. The improvements proposed here below stay enough simple not to be reserved to numerical methods specialists.

Numerical technique

The numerical schemes used can be improved or changed.

In the past fifteen years a few generalizations of the above methods ([22] for instance) for solving a linear system were applied to any kind of matrix, yet all these iterative methods are actually efficient for big sparse matrices. That is why recent studies have tried to obtain such good-looking matrices requiring wavelets for instance (see e.g [23]) or modifying classical moment methods [21].

Following these ideas we could try to use more adapted basis functions to localise the weight of the interacting elements or modify the existing matrix with matrix operations like F.X. Canning in [21] in order to get a sparse matrix.

We also want to test the efficiency of the Generalized Minimal Residual algorithm for solving non-symmetric linear systems (GMRES [22]) which seems to be rather interesting for dealing with big matrices.

In another way the layer density function numerical approximation (which defines the boundary element type) can be modified. Indeed, to deal with a piecewise constant approximation corresponds to the collocation technique simpler form, but some other approximations are now widely used. The function μ can be approximated for example by a quadratic one. In this case, each dimension of the boundary subdivisions can be extended to the quarter of the harmonic signal wavelength λ . The values involved in the Tab.1. are then greatly modified, see Tab.3.

frequency	dimensions	10 m * 10 m	20 m * 20 m
125 Hz		1.8 Mo / 0.3 Mo	32 Mo / 4.9 Mo
250 Hz		29.6 Mo / 5.6 Mo	544 Mo / 90 Mo

Tab.3. Size of the minimum memory with the $\lambda/6$ criteria / $\lambda/4$ criteria

One can see that it is then possible to apply the model to a realistic part of the traffic noise spectrum with a workstation. The gain in terms of calculation time has then to be examined to conclude to this improvement opportunity.

Idealisation approximations

The most important idealisation approximation used in the numerical model is the fact that the ground is numerically of finite dimensions, while the idealised model considers a finite dimensions ground. Usually, with the help of practice and experience, larger dimensions than what could be sufficient is used to be sure that this approximation does not affect the results accuracy. The minimum boundary size to get the desired accuracy depends on the signal wavelength and the source, barrier and receivers positions. If it could be possible to define an order of magnitude of the minimum boundary size, versus these above parameters, the memory size necessary to the simulations, related directly to the number of the subdivisions, that is to say the boundary size, could be also minimised. This order of magnitude can be defined by the mean of numerical experimentations performed on a large number of well chosen geometrical configurations and frequencies..

Another way to decrease the number of subdivisions is to increase this size. The idea is to try to extend the ' $\lambda/4$ (or $\lambda/6$) criteria' for large ground dimensions. Physically, to model the scattered acoustic pressure by a simple layer potential is to represent the scattered field by a set of monopoles situated on the propagation medium boundary. So it seems reasonable to consider that the boudary part close to the source, barrier and receivers has to be well

described, while the boundary part far from these specific points does not contribute for a large part to the results accuracy. We could then use a non regular meshing, as the one on Fig. 8. This idea has also to be defined by numerical experimentations. Moreover, the scattered acoustic pressure could be represented by a linear combination of simple and double layer potential (§2.1). Physically, this representation corresponds to a set of monopoles and dipoles (normal to the boundary) lying on the propagation medium boundary, more precise than a simple layer potential. It seems reasonable to think that this latter form of scattered acoustic pressure representation could allow to use more larger subdivisions on the boundary edges.

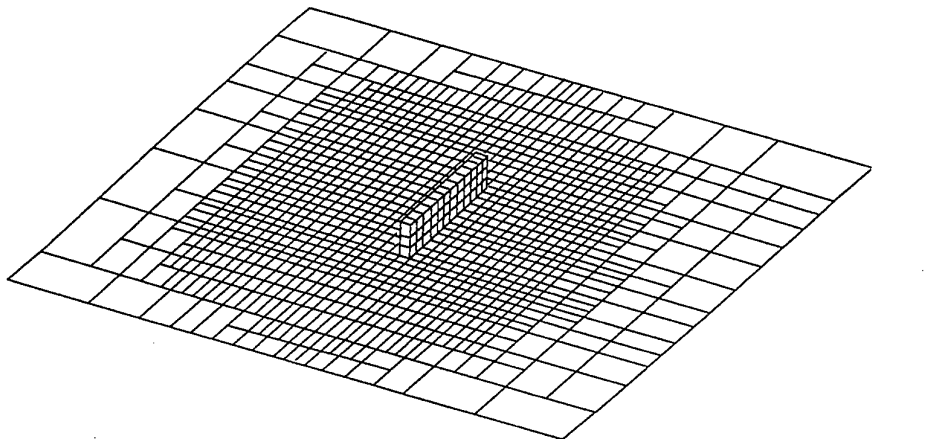


Fig. 8. Example of a non regular meshing.

Following the same idea, we could go back to the method itself : the acoustic pressure could be modelled by a hybrid formulation. An integral one, for instance the one used in this paper, could be applied to a propagation subdomain close to the source, the receivers and the barrier. The field corresponding to the other infinite subdomain could be evaluated by an asymptotic development for which a set of virtual sources would be located on the boundary between the two subdomains.

4. CONCLUSION AND PERSPECTIVES

A 3D diffraction model has been presented, which allows to take into account various shapes and absorption of barriers and ground. The model computer cost orders of magnitude and first improvements show together the limitations to low frequencies or dimensions, and the opportunity to use it for applications which others models cannot deal with. To select carefully the numerical schemes leads to sensible improvements in terms of calculation time and memory size. A set of further improvements are yet to be tested, some of them being definitely worthwhile. However, this model can be used in its first form for complex configurations in the low part of the traffic noise spectrum, for which it is difficult to obtain precise results by the ray theory models. Some problems of interest, like combined diffraction by the barrier vertical and horizontal edges, or array of incoherent sources, can be examined. The results could be compared to other models for which only 2-D calculations or high frequencies have been taken into account.

REFERENCES

1. Hothersall D.C., *The mathematical modelling of the performance of noise barriers.* Building Acoustics, 1(2), p. 91-104, 1995.

2. Isei T., Embleton T.F.W., and Piercy J.E., *Noise reduction by barriers on finite impedance ground.* J. A. S. A., **67**(1), p. 46-58, 1980.
3. Nicolas J., Embleton T.F.W., and Piercy E., *Precise model measurements versus theoretical prediction of barrier insertion loss in presence of the ground.* J.A.S.A., **73**(1), 1983.
4. Schenck H.A., *Improved integral formulation for acoustic radiation problems.* J.A.S.A., **44**(1), 1968, p. 41-58.
5. Terai T., *On calculation of sound fields around three dimensional objects by integral equations methods.* J.A.S.A., **69**(1), 1980, p. 71-100.
6. Sayhi, M.N., Ousset Y., and Verchery G., *Solution of radiation problems by collocation of integral formulations in terms of simple and double layer potentials.* J.S.V., **74**(2), 1981, p. 187-204.
7. Ciskowski R.D. and Brebbia C.A., ed. *Boundary element methods in acoustics.* International series on computational engineering, ed. C.A. Brebbia. 1991, Computational mechanics publications, Elsevier applied science, Southampton, Boston, London, New York.
8. Sezne, R., *Diffraction of sound around barriers : use of the boundary element technique.* Journal of Sound and Vibration, **73**(2), 1980.
9. Antes H., *Applications in environmental noise,* in *Boundary Element Methods in Acoustics*, C.a. Brebbia, Editor, 1991, Elsevier Applied Sciences, Elsevier Applied Sciences, London New York.
10. Hothersall D.C., Chandler-Wilde S.N., and Hajmirzae M.N., *Efficiency of single noise barriers.* Journal of Sound and Vibration, **146**(2), 1991, p. 303-322.
11. Filippi P.J.T., *Layer potential and acoustic diffraction.* Journal of Sound and Vibration, **54**(4), 1977, p. 473-500.
12. Tekatlian A., Filippi P., and Habault D., *Détermination des caractéristiques vibratoires de sources de bruit par résolution d'un problème inverse de rayonnement.* Acustica-Acta Acustica, **82**, 1996, p. 91-101.
13. Dubouchet A., *développement d'un pôle de calcul CESAR-LCPC.* Bull. liaison Labo P. et Ch., **178**, (ref.3632), p. 77-84, 1992.
14. Banerjee B., *BEM in Engineering Sciences.* 1981, U.K.: Mac graw Hill Book Company limited.
15. Rosen E.M., Canning F.X., and Couchman L.S., *A sparse integral equation method for acoustic scattering.* J.A.S.A., **98**(1), 1995.
16. Amini S., Ke C., and Harris P.J., *Iterative solution of boundary element equations for the exterior acoustic problem.* Journal of Vibrations and Acoustics, **112**, 1990.
17. Amini S. and Wilton D.T., *An investigation of boundary element method for the exterior acoustic problem.* Computer Methods in Applied Mechanics and Engineering, **54**, 1986.
18. Press W.H., et al., *Numerical recipes in Fortran.* Cambridge ed. 1994, 2nd Edition.
19. Abramowitz M. and Stegun I.A., *Handbook of mathematical functions with formulas, graphs, and mathematical tables.* 1964, Washington DC: US Government Printing Office.
20. *NAG Fortran Library Manual.* Mark 14. ed. 1st edition. 1990.
21. Canning F.X., *The impedance matrix localisation (IML) Method for Moment-Method calculations.* IEEE Antennas and Propagation Magazine, october 1990.
22. Yale University / DSC. *GMRES A Generalized Minimal Residual algorithm for solving nonsymmetric linear systems.* 1983.
23. Wagner R.L., *A study of wavelets for the solution of electromagnetic integral equations.* IEEE Transactions on Antennas and Propagation, **43**(8), 1995.

**Lamb waves from airborne explosion sources:
Viscous effects and comparisons to ducted acoustic arrivals**

D. O. REVELLE and R. W. WHITAKER

*Earth and Environmental Sciences - 5,
Los Alamos National Laboratory
Los Alamos, New Mexico 87545
(505) 665-3687 FAX*

Observations of large explosions in the atmosphere at long range are dominated by a leading pulse of large amplitude and long period that is often followed by a series of higher frequency impulses usually of smaller amplitude. This description can be interpreted using linearized acoustic-gravity wave theory in terms of a Lamb wave arrival followed by ducted acoustic and/or gravity waves. This pattern of arrivals is not the same at all ranges nor is it independent of the source energy or of the altitude of the source. Earlier, Pierce (1963), using an isothermal, windless atmospheric model, theoretically formulated the distances beyond which the Lamb wave would just be discernible and also where it would dominate the arriving signals for a specified explosion source. In this work we have evaluated these distances for the cases of both an inviscid and a viscous fluid (using a Rayleigh friction approach) for the source energies of interest to the CTBT (Comprehensive Test Ban Treaty) R&D work at Los Alamos. Although the inviscid results are analytic, the fully viscous solutions are iterative. For the inviscid solutions, we find that the Lamb wave domination distance is proportional to wave frequency at frequencies large with respect to the acoustic waveguide cut-off frequency. Under similar conditions we also find that the computed distances are linearly proportional to the source height. At 1 Hz for example, the Lamb wave must propagate about 200 km before having a significant amplitude (for a source elevation of 100 m). This is equivalent to the predicted behavior of a 0.1 Hz wave detonated at an elevation of 1 km. For a viscous fluid we found slight increases in the distances compared to an inviscid fluid with the lower frequencies, near the acoustic cut-off frequency, exhibiting the greatest changes.

During the period from 1981-1994 at Los Alamos, we have also observed infrasound from eight point source, near-surface ANFO explosions at White Sands Missile Range (24 to 4880 tons) at ranges from about 250 to 5300 km. In many cases Lamb waves were not observed from these events even though the ducted acoustic waves were observed. In this work, we will compare the current theory against some of these observations.

I. Introduction and Overview

In an earlier report ReVelle (1996b) reported on analytic, inviscid calculations of Lamb wave development from airborne explosions in a hydrostatic, isothermal, windless model of the atmosphere. In this paper we will determine the corresponding results for viscous propagation in an isothermal, windless atmosphere utilizing an iterative technique while using a Rayleigh friction parameter approach suggested by Pierce (1963).

Pierce's solution was accomplished using the method of stationary phase (an energetics approach) in the complex plane. The Lamb wave satisfies the identical lower boundary condition that is also satisfied separately by the sum of the arriving direct and ground reflected blast wave (acoustical signal), namely that the vertical velocity should vanish at the lower boundary. As noted in ReVelle (1996b), this condition is easily satisfied for long period Lamb waves from large explosions, but is increasingly more difficult to satisfy for mesoscale and microscale atmospheric

motions that do not simultaneously satisfy a state of geostrophic and hydrostatic balance. Finite ground impedance effects were explicitly ignored in our analysis, which seems reasonable based on the modeling of Attenborough as summarized in Embleton (1996) for frequencies > about 100 Hz. Standard acoustic reflection coefficients using the acoustic impedance of air and of typical soils yield values of > about 99 %, i.e., only < 1 % of the acoustic wave energy penetrates into the ground (see for example, Cox, 1958).

II. Airborne Lamb Wave Generation and Propagation

A. Review of Earlier Work

The key parameters identified in ReVelle (1996b), for the high frequency, infrasound limit, were respectively:

$$r_0 = \text{abs}[\beta\mu/(B\omega)]^2 h \quad (1)$$

$$r_1 = \{\text{abs}[\beta\mu/(2\pi\omega)]^2 h \exp(2Bh)\}^{1/3} \quad (2)$$

If: $r_1 \gg r_2 = \text{abs}[\mu]^2 h/(B\omega)^2$ (3a)

or: $r_1 \gg r_3 = \text{abs}[\mu]h/\omega$ (3b)

$$\omega_{bv} = (\gamma-1)^{1/2} (g/c_s) \quad (4)$$

$$\omega_{ac} = \gamma g / (2c_s) \quad (5)$$

where

ω = Dimensionless angular frequency of the wave
(in units of c_s/H_p)

ω = Dimensional angular wave frequency

h = z/H_p = Dimensionless vertical height of the source

$H_p = c_s/(\gamma g)$ = Atmospheric pressure scale height

γ = Ratio of specific heat at constant pressure to that at constant volume = 1.4 for an ideal diatomic gas

c_s = Adiabatic phase speed of acoustical waves

g = Acceleration due to gravity

r_0 = Minimum formation distance for the Lamb wave

r_1 = Lamb wave domination distance

r_2 = Distance scale that r_1 must exceed to be meaningful

r_3 = Distance scale that r_1 must exceed to be meaningful

ω_{bv} = Brunt-Vaisalla (Buoyancy) angular frequency

ω_{bv} = Nondimensional Buoyancy frequency = A

ω_{ac} = Acoustic Waveguide angular cut-off frequency

ω_{ac} = Nondimensional acoustic cut-off frequency = 1/2

and

$$A = \frac{(\gamma-1)}{\gamma}^2 = 0.2041 \quad (i)$$

$$\beta = \Omega^{-1/4} \quad (ii)$$

$$\mu = \Omega^2 - A \quad (iii)$$

$$\Omega^2 = \omega(\omega + i\varepsilon) \quad (iv)$$

$$|\Omega| = \sqrt{\omega\{\omega + \varepsilon\}}^{2/2} = 0.5 \quad (v)$$

$$B = (1/\gamma)^2 - (1/2)^2 = 0.2143 \quad (vi)$$

ε = Dimensionless Rayleigh friction constant (vii)

$$\varepsilon = \varepsilon^*/(c_s/H_p)$$

ε^* = Rayleigh friction parameter with units of 1/sec

Note that to convert r_1 and r_0 to actual distances the latter must be multiplied by the scale height and the former by the scale height to the 2/3 power. It should also be noted that although Pierce's approach for making the scaled frequency complex is quite valid, it is more common that the phase speed of the waves is decomposed into real and imaginary parts (Holton, 1992). In this latter approach it is the imaginary part of the phase speed that is identified with the dissipation of wave energy just as it is the imaginary part of the scaled angular wave frequency in our current approach which is identified with wave energy removal processes.

The following additional necessary restrictions are also applicable for the accuracy of the r_i distances ($i = 0, 1, 2, 3$) listed above (ReVelle, 1996b):

$$\bar{\omega} \gg f \quad (ix)$$

$$r_i < R_e \quad (x)$$

since Pierce's original solution was derived using Cartesian geometry in a non-rotating fluid.

where

R_e = Radius of the Earth

f = Coriolis parameter (= inertial frequency)

B. Distances for the Development of Lamb Waves: Inviscid Results

At very high and very low angular frequencies, in the inviscid limit, the earlier results apply respectively for Lamb wave development:

$$1) \bar{\omega} \gg \bar{\omega}_{ac}: r_1 \propto \omega \cdot h$$

$$2) \bar{\omega} \ll \bar{\omega}_{bv}: r_1 \propto (1/\omega) \cdot h$$

Thus, we can say that at high frequencies compared to the acoustic waveguide-cutoff frequency that r_1 becomes progressively larger as either the scaled source height or scaled wave

frequency increases. This is also predicted to be the case at very low frequencies that are small with respect to the Brunt-Vaisalla frequency as well, but the distances are not symmetric about the Brunt-Vaisalla frequency, i.e., the distances are predicted to increase far more rapidly at the very high frequencies than at the lower frequencies. Also, if the angular wave frequency is between ω_{bv} and ω_{ac} , there is no minimum distance restriction predicted regarding the presence of the Lamb wave from a point source explosion.

In a strictly isothermal atmosphere the Lamb wave is non-dispersive so that ω (or its dimensional counterpart) does not change with range from the source. Thus the ω value can readily be interpreted as that observed in an isothermal medium. In a real temperature and wind stratified atmosphere this is no longer the case as discussed later.

If the inviscid formation/dominance distances for Lamb waves are further analyzed, we can attempt to understand their physical meaning more clearly. If the various distances at high frequencies ($>> \omega_{ac}$) are reinterpreted as times instead of as distances, we can interpret them in either of two ways, i.e., either as a build-up time locally or as a propagation delay time for the passage of the Lamb wave relative to the observer's location. If we examine (1) (or (2)) in this way in the high frequency limit, we can divide the dimensional form of the right hand side of (1) by the adiabatic phase velocity and re-interpret the new expression as a time parameter (for small amplitude waves if the wind speed is sufficiently small compared to c_s , i.e., not allowing for Doppler shifting of the signal). The resulting dimensional Lamb wave delay time expression is:

2

$$\Delta t^* = r_0^*/c_s = (\{\bar{\omega}/(c_s/H_p)\}/c_s) \cdot h \cdot H_p = (k/c_s) h \cdot H_p = (k/c_s) z \cdot H_p \quad (6a)$$

$$\Delta t^* = 2\pi \cdot (z/\lambda) \cdot (H_p/c_s) \quad (6b)$$

where

Δt^* = Dimensional form of the Lamb wave time delay

r_0^* = Dimensional form of Lamb wave formation length

" = $2\pi(z/\lambda) \cdot H_p$

k = $2\pi/\lambda$ = Total acoustic wavenumber

c_s = $\bar{\omega}/k$

z = Dimensional explosion height above the ground

Thus, we can now interpret the formation/dominance time in terms of the height of the explosion above the ground in comparison to the wavelength of the Lamb waves, with $\lambda >> z$ producing progressively smaller time delays (and shorter formation distances). Thus, for near-surface sources, for Lamb waves with very large wavelengths as produced by great explosions, its presence will be felt over a large region almost instantaneously. If however $\lambda << z$, the waves need a longer time to propagate to the observer. Thus, there is a constructive interference effect for $\lambda >> z$ and if $\lambda << z$, a destructive interference effect must be evident.

III. Viscous Effects on Lamb Wave Development

A. Iterative Procedure for Viscous Lamb Wave Calculations

In contrast to the inviscid solutions presented in ReVelle (1996b), the viscous solutions are of necessity iterative. We first assume a small seed value of the Rayleigh friction parameter, next appropriately non-dimensionalize it by dividing by c_s/H_p and then calculate r_0 . We cannot use r_1 as the characteristic scale for the dominance of the Lamb wave since it normally does not exceed r_2 .

or even r_0 as discussed earlier in ReVelle (1996b), except at sufficiently large source altitudes. Note that both r_0 and r_1 have an identical scaled angular frequency behavior at sufficiently low or high frequencies however, so using r_0 is not of great concern except that the "true" dominance distance is likely to be about 2 - 10 times greater than r_0 (ReVelle, 1996b).

In order to accommodate the fact that the true dominance distance exceeds r_0 , we have introduced two integral length scales, namely m and n , which are defined as:

$m = \text{Integral multiple of } r_0 \text{ for defining the source energy}$
 $(= 1, 2, 3, \text{ etc.}); \text{ see equation (10) below.}$

$n = \text{Integral multiple of } r_0 \text{ for defining the viscous attenuation}$
 $\text{length scale } (= 1, 2, 3, \text{ etc.})$

Thus $m \cdot r_0$ is used only to define E_s in (11) below, whereas $n \cdot r_0$ is used to compare the computed Lamb wave domination distance against the viscous length scale inherent in (7b) below. The immediate question becomes what values should be used for (m, n) and are they equal, etc.? In our current work we have used $m = 2$ and $n = 2$ and $m = 2$ and $n = 10$ for computation purposes. The first case corresponds to an amplitude removal of approximately $1/e$ or a reduction of about 60 % of the initial pressure amplitude whereas the latter case corresponds to about a 8-15 % pressure amplitude reduction. The dominance distances as a function of frequency computed in this way are not greatly sensitive to this procedure (as compared to the exact, inviscid, analytic case presented in ReVelle (1996b)), but unfortunately the source energy values as a function of frequency are reasonably sensitive to this procedure. This will be discussed in more detail below.

Using the assumed values of m and of n , if the computed dominance distance value is comparable to the distance scale inherent in ϵ^* , then the calculation is halted. If not an iterative procedure is performed until convergence of the two length scales is achieved.

We started with a seed value of the Rayleigh friction parameter of $3.4 \cdot 10(-3)/\text{sec}$. This value corresponded to a typical high frequency Lamb wave speed divided by a range of 100 km or $0.34 \text{ km/sec}/100 \text{ km}$. If we assume that the wave speed is roughly a constant and that only the range varies significantly between the source and the observer, then when the dimensional Rayleigh friction parameter is normalized by c_s/H_p , it can be adjusted solely by varying the range. Thus, we started with $3.4 \cdot 10(-3)/\text{sec}$ divided by c_s/H_p ($= 0.34 \text{ km/s}/8.0 \text{ km} = 4.25 \cdot 10(-2)/\text{s}$) or $8.0 \cdot 10(-2)$ at 100 km range decreasing by an order of magnitude at 1000 km range, etc. In the numerical routine we began with the above approach and then iterated ϵ^* until the deduced distance values converged so that the Rayleigh friction parameter viscous length (in (7b)) closely matched with the range computed using n times the distance scale in (1) above computed at each wave frequency. The relevant inverse viscous length scale is given by $\{\epsilon^*/(c_s/H_p)\}/H_p = \epsilon^*/c_s$.

The above Rayleigh friction parameter, ϵ^* is equivalent to the more familiar form by dividing it by the adiabatic sound speed so that the decay can be modeled using inverse distance rather than using inverse time (Kuchlikov, 1987). In this way we can express the amplitude decay in the form:

$$\Delta p / \Delta p_0 (\%) = 100 \cdot \{1 - \exp[R_v \cdot n \cdot r_0]\} \quad (7a)$$

$$1/R_v = c_s/\epsilon^* = n \cdot r_0 = \text{Rayleigh viscous length scale} \quad (7b)$$

We iterated ε^* until $1/R_V$ was within a small increment of $n \cdot r_0$ for the specified set of (m, n) values as discussed above, i.e., until a self-consistent solution for $n \cdot r_0$ was determined. The quantity, ε^*/c_S , represents the decay coefficient per km, which is perhaps more commonly used in acoustics than is ε^* (which has been used more commonly in atmospheric dynamics for zeroth order viscous decay studies of mesoscale circulation patterns due to the presence of gravity waves, etc.; see for example, Holton, 1992). In addition to a length scale associated with absorption effects, similar length scales can also be defined for dispersion, for nonlinearity effects, etc. (ReVelle, 1976). The process with the shortest associated length scale is the one which will ultimately control the behavior of the signal during its propagation.

B. Results of Viscous Calculations

The magnitude of Ω in a viscous fluid depends on the magnitude of the Rayleigh friction constant, ε^* . For the case of a viscous fluid, using the Rayleigh friction parameter the tendency of the predicted results are clear. The development distances for Lamb waves should increase compared to the inviscid case, with the lower scaled frequencies showing the greatest relative increase for $\varepsilon^* \neq 0$. More specifically the predicted dip in the formation distance near the Brunt-Vaisalla period should be nearly absent with viscous effects included. It is also clear why the viscous case produces longer formation distances and longer time delays at progressively higher frequencies. This occurs partly because Ω is now larger due to the imaginary part of the scaled angular wave frequency, i.e., due to ε^* .

The results of the calculations briefly outlined above are presented in Figure 1. below. Briefly, the major differences in the viscous versus the inviscid results in ReVelle (1996b) are the slight increases in r_0 , etc. in the region for periods from 50 to 300 seconds, with the lowest frequencies exhibiting the greatest relative increase in the Lamb wave dominance distance. In this period range the distances can increase from 30 to 90 % over the values computed assuming inviscid conditions. Thus, the predicted minimum in the Lamb wave formation distance near the acoustic cut-off frequency nearly disappears due to the presence of viscous forces which we have allowed for using the simple Rayleigh friction parameterization. For the case $m = n$, amplitude reductions of about 60 % were evident (nearly e-folding conditions). Secondly, for $n = 5$ to 10 times m , much smaller amplitude reductions, on the order of 8-15 %, were computed. The computed formation and Lamb wave domination distances were not very sensitive to this change except at quite low frequencies again in the 50-300 second period range. Thirdly, for very low frequencies (\ll the Brunt-Vaisalla frequency), our iterative viscous modeling approach was not successful, i.e., distance convergence could not be achieved. However from about 10(3) to 10(4) seconds period, the procedure was again successful.

The final iterated values of the Rayleigh friction parameter ranged from about 0.4/km at a period of 100 seconds to a minimum of about 10(-4)/km at a period of 0.01 sec (100 Hz). Expressed in alternative units this corresponds to a value of about 0.6/sec at a period of 10 seconds decreasing to about 10(-3)/sec at a period of 0.01 sec. Between these period limits the predicted behavior of the final value of the Rayleigh friction parameter is changing nearly linearly with wave frequency. This nearly linear dependence of the Rayleigh friction parameter is a direct consequence of the approximately linear dependence of the minimum formation distance and the Lamb wave domination distance with frequency at sufficiently high wave frequencies.

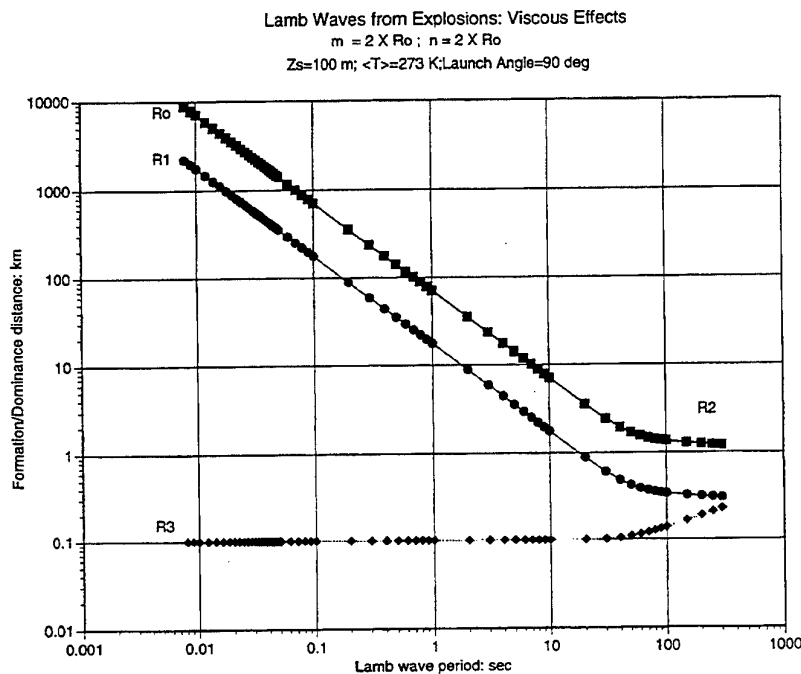


Figure 1. Viscous development of Lamb waves from airborne explosive sources using an iterative Rayleigh friction parameter approach. Lamb wave dominance distance as a function of the angular wave frequency of the propagating Lamb wave in an isothermal, windless atmosphere (using $2 \cdot r_0$ as the criterion for Lamb wave dominance).

The cause of the unsuccessful iterative calculation from 300 to 500 seconds can be seen by examining equations (v) or (vi). The ϵ values associated with the short formation/dominance distances for the Lamb wave were all sufficiently large so that the value of the magnitude of Ω was changed dramatically. It could be changed so significantly that a wave far outside the frequency band between the Brunt-Vaisala and the acoustic cut-off frequency could be put within the band by changes in Ω due to a self-consistent value of ϵ (so that the distance scale implied by ϵ^* was consistent with the distance r_0 computed using the dependence of Ω on ϵ). At very high frequencies or at very low frequencies all values of ϵ are so small that almost no changes were evident compared to the inviscid case. Successful solutions could also be found from 300-1000 seconds period if m and n were increased substantially, for example using m and n in the range from 100-1000. As m and n were allowed to become larger with all other factors remaining the same the inviscid limit computed in ReVelle (1996b) was approached asymptotically.

C. Source Energy Relations

In order to interpret the results in terms of source energy, E_S , we have made use of two approximate expressions which are an attempt to bound the possible wave period-source energy relationship. One is a long period approach due to Pierce and Posey (1971), combined with the semi-empirical approach of Whitaker et. al. (1990) and the other is a short period approach relating

the source energy to the period of the blast wave itself. These relations can be written respectively in the limiting forms:

Blast wave approach:

$$E_S = (4/3)\pi p_0 \cdot \exp[-z_S/H_p] R_S^3 = k \cdot \exp[-z_S/H_p] \{c_s \cdot \tau / 2.21\}^{1/3} \quad (8a)$$

$$R_S = \{E_S / \{(4/3)\pi p_0(z_S)\}\} \quad (8b)$$

$$\tau = \{2.21 R_S\} / c_s \quad (8c)$$

where

E_S = source energy in Joules

k = constant ($= (4/3) \cdot \pi \cdot p_0$)

p_0 = surface atmospheric pressure

$p(z) = p_0 \exp(-z_S/H_p)$ for a hydrostatic, isothermal atmosphere

z_S = source altitude

R_S = Blast wave relaxation radius (point source)

τ = Blast wave period at $x = 10$ ($R = 10 \cdot R_S$)

$x = R/R_S$ = scaled distance from the source

(Note that in order to convert from Joules to kt the results in (8a) must first be divided by $4.185 \cdot 10(12)$ J/kt).

Lamb wave approach:

$$E_S = K \Delta p (c_s \tau_L)^{3/2} \{R_e \sin(R/R_e)\}^{1/2} H_p \quad (9)$$

where

E_S = Source energy in ergs, with all quantities in CGS units

τ_L = Period of the arriving Lamb wave: sec

K = Constant numerical factor ($= 13$)

Δp = Total amplitude of the arriving Lamb wave (peak to trough value): μ bars

In addition to the above relations, we also have available the semi-empirical result developed by Whitaker et. al.(1990) that relates the ducted acoustic signal amplitude versus scaled range and the explosion source energy which is based on a regression of a number of known, relatively low yield (from about 0.02-4.9 kt), surface and near-surface DNA bursts. This relation can be written for the zero wind case, i.e. Spring/Fall, in the form (here we refer to the winds aloft near 40-60 km that act as a duct for surface sound sources):

$$\Delta p_{p-p} = 4.69 \cdot 10(4) \{R/W_S(\text{kt})\}^{0.5} \quad (10a)$$

where

W_S = Equivalent explosion charge weight in kilotons
 R = Range from the explosion in km
 Δp_{p-p} = Peak to peak pressure amplitude in μ bars

In addition however, unpublished results done by one of the authors (D.O.R.) indicates the following general relationship which can be derived from direct blast scaling of the explosion:

$$\Delta p = C \left(\frac{p_0}{p} \right)^{\frac{(q-3)}{3}} \cdot R^{\frac{q}{3}} \cdot W_S^{\frac{q}{3}} \quad (10b)$$

where

C = Constant
 q = Power law exponent for amplitude decay ($= q(R)$ in general)
 p_0 = Pressure at the source altitude
 $p(z)$ = Pressure at the altitude of the observation

Three regimes can be identified for the above equation in terms of q , namely: the near-field ($q = 3$), an intermediate field ($1.1 \leq q \leq 2$) and the far-field acoustic regime (linear region where $q = 1$).

Winds at 50 km can substantially influence the pressure versus range behavior, but their inclusion at present is beyond the scope of the current efforts, namely to find simple alternative expressions for source energy as a function of Lamb wave frequency. These wind effects will be examined in a future effort. At that time the Doppler shifting of the Lamb wave will also be examined as well, since such effects have already been incorporated into the computer code written to analyze the inviscid and Rayleigh friction viscous cases. In the latter case it is the near surface winds and not those at 50 km that are important to the full solution since the Lamb waves are guided primarily near the Earth's surface.

Unfortunately in order to utilize (9) the amplitude of the arriving Lamb wave signal must be explicitly known. We can however assume a doubled, ducted acoustic wave amplitude from (10a) above, since at these high frequencies the technique used by Pierce (1963), discussed in detail in ReVelle (1996b), allows for computation of the distance that the Lamb wave must travel in order to achieve a doubling of the ducted, ground reflected acoustic signal. An additional limitation however is that equation (9) was derived for long period waves, i.e. a composite of the lowest order acoustic and gravity modes of the infinite set of all possible normal modes (Pierce and Posey, 1971).

Assuming the long period Lamb wave result is valid up to a period of 0.1 seconds and formally including the doubling of the semi-empirical equation given in Whitaker et. al. (1990), we can write equation (9), after changing units, etc., in the desired form:

$$E_S (kt) = \{ A \cdot B^{0.55} \cdot (m \cdot R)^{-1.36} \cdot C_1^{0.5} \cdot H_p^{1.5} \cdot [c_s \tau L]^{-x} \} \quad (11)$$

where

$$A = 13 \cdot (2 \cdot (4.69 \cdot 10(4)) / 4.185 \cdot 10(19)) = 2.914 \cdot 10(-14) \text{ in CGS units}$$

$$B = (p_0 / p(z))$$

$$C_1 = R_e \sin(R/R_e)$$

and where $1.492 \leq x \leq 3.125$ (see below).

For frequencies below the Brunt-Vaisala frequency (which are not of direct concern to the CTBT program), this expression should be further modified to account for the fact that the computed signal is no longer doubled as it is in the high frequency acoustic limit, but could be 4-6 times the ducted gravity wave arrivals because of the computed reflection coefficient predicted in Pierce (1963) in this period regime. This may account for the unexplained decrease in the predicted relation between E_S and τ_L as shown in Figure 2 at very long periods. Also, the semi-empirical result itself (10a) is surely suspect in this low frequency and consequently, very high source energy regime since it was calibrated using much smaller associated source energies.

Equation (11) is the desired relationship between the source energy and the distance at which the Lamb wave has an amplitude double to that of the ducted acoustic, ground reflected arrivals. Thus, at a distance of m times r_0 at a known angular wave frequency (or equivalently at a known Lamb wave period), we can now assign an associated source energy as well as indicated in (11) above. The general relationship between wave period and source energy is indicated in Figure 2. below. As indicated in Figure 2., in general agreement with our earlier work (ReVelle, 1995), a Lamb wave frequency of about 0.7 Hz is indicative of a nominal source energy of 1 kt. If the blast wave scaling results, i.e., equations (8a)-(8c) are used similarly, the associated Lamb wave frequency estimate corresponding to a 1 kt source is somewhat lower as also indicated in Figure 2.

The precise value of x to use in the above equation depends critically on the form of the pressure-range dependence versus source energy. In (9) above the exponents of E_S and R were determined by empirical regression analyses of a number of kiloton class HE explosions. The formal solution for this case yields $x = 3.125$, but as seen earlier from (10b), this will approach 1.492 in the acoustic (small amplitude) propagation limit. The lower limit of x which we have used in this analysis comes from assuming $q = 1$ formally in (10b) above and then substituting that result into (10a) and (11) above. We have not yet formally changed the exponent of R from the nominal value of -1.36 to -1 in (11) however since we are still evaluating the above approach for its overall utility as a predictor of source energy versus Lamb wave period. As m and n are systematically increased for the curve labeled Lamb/acoustic in Figure 2., the energy versus period relationship shifts to the right and approaches the curve labeled AFTAC discussed directly below.

Other approaches (see for example, ReVelle, 1995) include the estimation by AFTAC (Air Force Technical Applications Center, Patrick Air Force Base, Florida) of the source energy by using the period at maximum amplitude of the ducted acoustic signal (for the 50 km Stratopause duct). Such methods relate the source energy in kt empirically to the observed period at maximum amplitude (at long range) to a power as a function of yield varying from 3.34 to 4.13, in direct contrast to the third power derived above at close range from numerical calculations of the fundamental hydrodynamic equations. These relations which are also plotted in Figure 2 below can be written in the form (ReVelle, 1995):

$$E_S = 2 \cdot (\tau_{ac}/5.922)^{3.34} ; E_S/2 > 40 \text{ kt} \quad (12a)$$

$$E_S = 2 \cdot (\tau_{ac}/7.44)^{4.13} ; E_S/2 < 100 \text{ kt} \quad (12b)$$

where

τ_{ac} = acoustic period at maximum signal amplitude

In (12a) and (12b) above, the changeover in the scaling for the power law exponent of the acoustic period at maximum amplitude occurs at about 20 seconds period (corresponding to a source energy of about 118 kt).

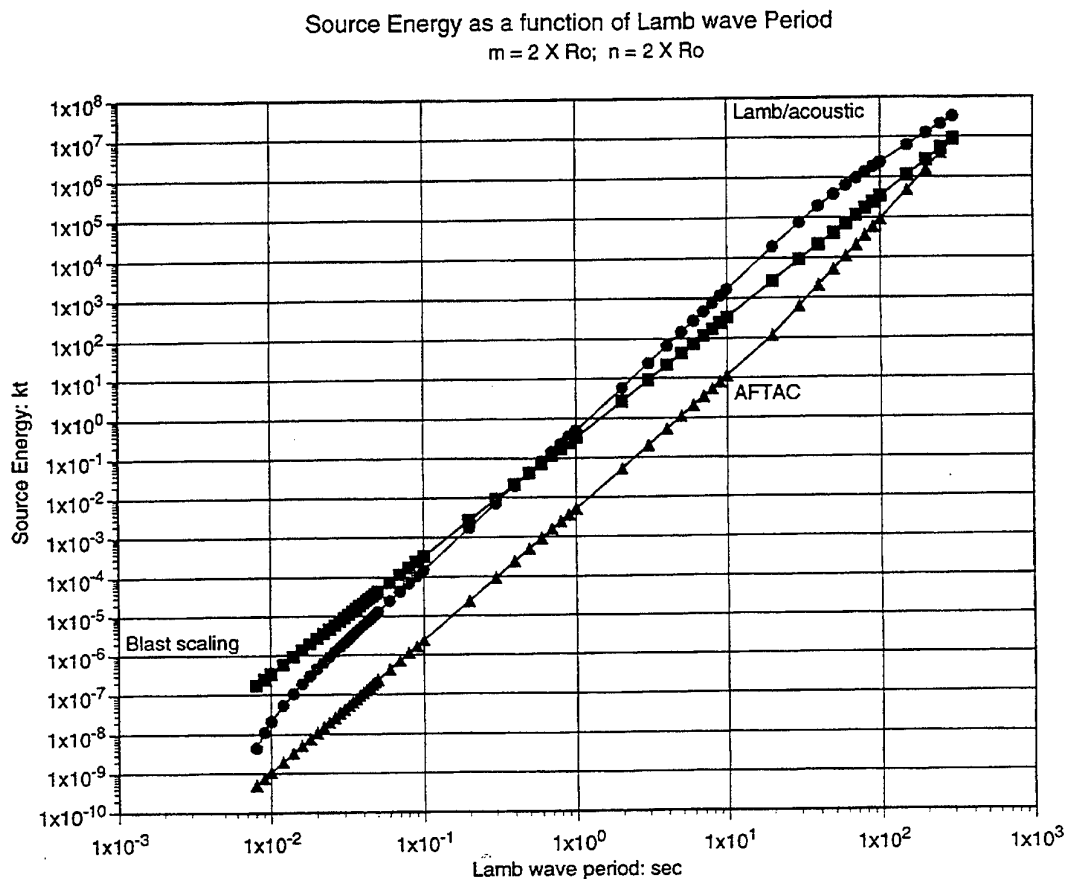


Figure 2. Lamb wave period as a function of the source energy in kt using equations (8a)-(8c) via near-field blast wave scaling laws and equation (11) using the Pierce-Posey-Kinney Lamb wave relation combined with the semi-empirical, neutral wind, ducted acoustic regression relation of Whitaker et. al. (1990).

In our approach above we have also neglected the small constant power law-logarithmic range dependence predicted in a homogeneous (constant density) atmosphere for blast waves (Groves, 1963; 1964) or the more general result for a density stratified medium involving a constant power law dependence of the exponential integral. The latter is justified by the propagation path for low altitude Lamb waves that can safely ignore the density stratification effects. We are not currently trying to precisely predict the source energy relationship with the wave period, but only to bound the limits. In the high frequency limit, the Lamb wave period should approach the blast wave period at least at sufficiently close range (ReVelle and Delinger, 1981). Values of the predicted source energy for a near-surface burst at a surface pressure of $1.0325 \cdot 10(5)$ Pa, a mean sound speed of 340 m/sec and a corresponding pressure scale height of 8 km for a Lamb wave period from 0.1 to 1.4 s range from about $3 \cdot 10(-3)$ kt to 1 kt respectively as indicated in Figure 2.

D. Comparisons between Los Alamos Infrasound Observations and Current Theory

On the basis of our earlier work at Los Alamos National Laboratory (LANL) and earlier work by AFTAC (ReVelle, 1995), we can predict the types of pressure wave returns and horizontal signal velocities to be expected at long range as a function of season from large, near-surface explosions, namely:

- a) L type: Lamb-surface wave; Signal velocity 0.33-0.34 km/s
- b) T type: Tropopause ducted; Signal velocity: 0.30-0.32 km/s
- c) S type: Stratopause ducted; Signal velocity: 0.28-0.31 km/s
- d) I type: Ionosphere ducted; Signal velocity: 0.22-0.24 km/s

We can now evaluate the development of Lamb waves from airborne, near-surface explosions conducted by DNA at White Sands Missile Range and monitored on a routine basis infrasonically at LANL from 1981-1994. The results are summarized below in Table 1. for two events, Misers Gold and Minor Uncle, both having $E_S = 2.44$ kt. From our work above (equations (8a)-(8c) and using the Lamb/acoustic curve in Figure 2 at 2.44 kt, i.e., equation (11)), this should correspond to a blast wave and a Lamb wave frequency of 0.52 Hz and 0.64 Hz respectively (at an assumed temperature of about 273 K) whereas the computed power spectrum analyses of the observational data indicated a spectral peak at frequencies from about 0.2 Hz to an upper limit of about 1 Hz, in reasonable agreement with the theory. In comparison, the AFTAC curve indicates a wave frequency of 0.16 Hz at this source energy. The current theory ignores nonlinear spreading and dispersive propagation effects as a function of range respectively, the former of which has recently been considered in Khmelevskaja-Plotnikova and Pavlov (1996).

For the Misers Gold event we have two possible detection's of Lamb waves whereas for Minor Uncle we also have two quite good detection's of Lamb waves. In contrast to the theory that insures higher frequency Lamb waves to develop progressively as distance from the source increases, for Misers Gold we have possible detection's at close range, but not for the most distant stations. If we strictly use a minimum Lamb wave signal velocity of 0.34 km/sec as a positive indicator of Lamb waves and not allow values as small as 0.32 km/sec (which may well be refracted signals from the Tropospheric wave duct associated with the Polar jet stream), most of the presumed Lamb wave detections are in fact not real. This is a systematic effect that can be explored in the future with our updated version of the Pierce-Posey-Kinney normal mode code and with our ray-tracing code (Whitaker et. al. 1990; 1994).

For the Minor Uncle event we also have detections at similar ranges from the source as were made for Misers Gold, but no observations were made at close range (at the Los Alamos array for example). This is somewhat surprising since both events have an identical source energy, etc.. This could be partly due to the effects of mesoscale meteorological processes on the weak vertical motion field of high frequency Lamb waves, unlike the strong hydrostatic control that is evident at much lower Lamb wave frequencies (ReVelle, 1996b). It could also be due to a combination of terrain effects and local/regional meteorology which we have not yet investigated. The current theory assumes flat terrain conditions throughout the propagation however.

Table 1. Evaluation of Lamb and ducted acoustic waves from two surface HE explosions at White Sands Missile Range (Davidson and Whitaker, 1992; Whitaker et. al., 1994).

Event, Date and Yield	Recording Array and Range to explosion: km	First Arrival-Signal Velocity: m/sec	Next Arrivals-Signal Velocity: m/sec	Lamb wave arrivals: Yes/No
Misers Gold, 6/1/1989: 2.44 kt				
250 km	Los Alamos, NM	339.2	225.5-298.0	Yes
517 km	Flagstaff, AZ	316.9	235.9-296.0	No
750 km	St. George, UT	324.9	273.4-309.9	?/ Yes
928 km	NTS, NV	316.1	272.8-303.2	? / No
1170 km	Crescent Valley, CA,	320.5	277.9-310.8	?/ No
1219 km	Huntington Lake, CA	300.1	286.4-291.9	No
1225 km	Reedley CA	312.5	278.4-303.2	No
1372 km	Murphy, ID	306.1	225.5-299.5	No
Minor Uncle, 6/10/1993: 2.44 kt				
250 km	Los Alamos, NM	0.291	0.223-0.230	No
750 km	St. George, UT	0.324	0.285-0.311	?/ Yes
928 km	NTS, NV	0.327	0.284-0.315	?/ Yes

In addition, reprocessing of the above data sets using a grid of say 100 X100 points in the slowness plane (currently we have used a 21X21 point matrix), will allow for a better evaluation of the signal trace velocity, assuming negligible surface winds ($= c_s/\cos q$, where q is the elevation arrival angle of the plane wave across the array). For the cases where the signal velocity is as low as 0.32 km/sec we may be able to find systematic non-horizontal elevation arrival angles by evaluating the trace velocity that confirm that these were in fact not Lamb waves, but instead ducted Tropospheric signals. A visual examination of the trace velocity plots for all the above events as displayed in Davidson and Whitaker (1992) and in Whitaker et. al. (1990; 1994) could not be used to conclusively distinguish whether or not the questionable cases identified above with moderately large signal velocity also had a systematically high trace velocity as well, i.e., signals with significant elevation arrival angles above the horizontal.) Future studies should explore both of these signal attributes as well as the overall signal structure when the Lamb wave mode is being conclusively identified for testing against theoretical models.

IV. Summary and Conclusions

A. Expectations for Airborne Lamb Wave Development

We have developed a predictive capability for the development of Lamb waves in an isothermal, windless atmosphere allowing in an approximate way for the expected effects of viscous forces using the Rayleigh friction parameter in an iterative self-consistent scheme. The results increase the development distances by about 30-90 % in the period band from about 50 to 300 seconds as compared to the inviscid results given earlier in ReVelle (1996b). The greatest relative increases in the Lamb wave domination distance occurred for the lowest frequencies within this frequency band.

At 1 Hz for a source at 100 m in elevation, we expect a minimum propagation distance of about 200 km for the dominance of the Lamb wave over the ducted acoustic arrivals. This range is equivalent to that predicted for a 0.1 Hz wave detonated from an explosion at a source height of 1 km. From our results in Figure 2., this Lamb wave frequency range corresponds to a source energy range from about 0.05-50 kt.

B. Future Work

Corrections are clearly needed for more realistic atmospheres. These and other effects that need to be considered include:

- 1) Direct radiation of Lamb waves by meteorological and other natural processes , i.e., geostrophic adjustment, volcanic eruptions, etc.
- 2) Influences of three-dimensional temperature and wind gradients, i.e., range-dependent propagation effects.
- 3) A physically based wave absorption prediction should be evaluated from the small amplitude hydrodynamic equations which should include molecular absorption due to viscous, thermal conductivity and molecular relaxation effects as well as those due to lower atmospheric turbulence. At least for the nocturnal boundary layer, this latter effect has been shown to be both spatially and temporally intermittent at times (see for example, ReVelle, 1993).
- 4) Effects of Stratopause winds on high altitude explosive sources and Doppler shifting of the Lamb wave should also be investigated.

Other effects such as finite ground impedance, irregular and mountainous terrain, terrain induced attenuation effects (Kulichkov, 1987), etc., should also be studied further. Future numerical work will also allow us to examine the Lamb wave behavior in greater detail using the normal mode code developed by Pierce and co-workers (1976) including a more realistic model atmosphere over "flat" terrain with time averaged vertical variations of both temperature and wind having been incorporated (for assumed range independent stratification conditions).

V. ACKNOWLEDGMENTS

This work was supported by the Department of Energy, Office of Nonproliferation and International Security, DOE HQ, NN-20.

VI. REFERENCES

- Cox, E.G., Sound Propagation in Air, Handbuch der Physik, Springer Verlag Pub. Co., Berlin, Vol. XLVIII, Chapter 22, 455-478, 1958.
- Davidson, M. and R.W. Whitaker, Miser's Gold, LA-12074-MS, UC-741, 28 pp., February, 1992.
- Embleton, T.F.W., Tutorial on Sound Propagation Outdoors, J. Acous. Soc. Amer., 100, 31-48, 1996.
- Groves, G.V., Initial Expansion to Ambient Pressure of Chemical Explosive Releases in the Upper Atmosphere, J. Geophys. Res., 68, 3033-3047, 1963
- Groves, G.V., Acoustic Pulse Characteristics of Explosive Releases in the Upper Atmosphere, Project Firefly (1962-3), AFCRL Report 364, 351, 1964.
- Holton, J.R., An Intro. to Dynam. Meteor.: Third Edition, Academic Press, Inc., New York, 507

- pp., 1992.
- Khmelevskaja-Plotnikova, G. and V. Pavlov, On transversal structure of finite amplitude Lamb waves in the atmosphere near the Earth's surface, *J. Acous. Soc. Amer.*, 100, 734-740, 1996.
- Kulichkov, S.N., On the propagation of Lamb waves in the atmosphere along the earth's surface, *Izv. Akad. Nauk SSSR, Atmos. and Ocean. Phys. (English Translation)*, 23, 1251-1261, 1987.
- Kulichkov, S.N., Long-Range Propagation of Sound in the Atmosphere, A Review, *Izv. Atmos. and Ocean. Phys.*, 28, 253-269, 1992.
- Pierce, A.D. and J.W. Posey, Theory of Excitation and Propagation of Lamb's Atmospheric Edge Mode from Nuclear Explosions, *Geophys. J. Roy. Astron. Soc.*, 26, 341-368, 1971.
- ReVelle, D.O., On Meteor-Generated Infrasound, *J. Geophys. Res.*, 81, 1217-1237, 1976.
- ReVelle, D.O. and W.G. Delinger, Passive Acoustic Remote Sensing of Infrasound of Natural Origin, Proceed. Internat. Sympos. Acoustic Remote Sensing of the Atmos. and the Oceans, Univ. of Calgary Press, Calgary, Alberta, Can., V-6 to V-15, 1981.
- ReVelle, D.O., Chaos and "Bursting" in the Planetary Boundary Layer, *J. Appl. Meteor.*, 32, 1169-1180, 1993.
- ReVelle, D.O., Historical Detection of Atmospheric Impacts by Large Bolides Using Acoustic-Gravity Waves, LA-UR-95-1263, Los Alamos National Laboratory, Los Alamos, New Mexico 87545, 26 pp., 1995; Also, New York Academy of Sciences, J.R. Remo Editor, Proceedings: International Conference on Near-Earth Objects, Explorer's Club, Sandia Nation. Lab. and the United Nations, New York, New York, April 1995, 26 pp., In Press, New York Academy of Sciences, 1996a.
- ReVelle, D.O., The Development and Propagation of Lamb Waves from Airborne Explosion Sources, LA-UR-96-881, 12 pp., 1996b.
- Whitaker, R.W., J.P. Mutschlecner, M. Davidson and S.D. Noel, Infrasonic Observations of Large-scale HE Events, Fourth Intern. Symp. on Long-Range Sound Propagation, NASA Conf. Pub. 3101, Compiled by W.L. Willshire, NASA Langley Res. Center, Hampton, Va., 133-141, 1990.
- Whitaker, R.W., S.D. Noel and W.R. Meadows, Infrasonic Observations and Modeling of the Minor Uncle High Explosive Event, Sixth Internat. Sympos. on Long-Range Sound Propagation, National Res. Coun. Canada, Compiled by D.I. Havelock and M.R. Stinson, Ottawa, Ontario, Canada, 480-497, 1994.

Turbulence and scattering

Line-of-sight sound propagation in the turbulent atmosphere with Gaussian correlation functions of temperature and wind velocity fluctuations.**V.E.OSTASHEV and G.GOEDECKE***Department of Physics, NMSU, Las Cruces, NM 88003-8001, U.S.A.***F.GERDES and R.WANDELT***Fachbereich Physik, Universität Oldenburg, Oldenburg D-26111, Germany***J.NOBLE***US Army Research Laboratory, 2800 Powder Mill Road, Adelphi, MD 20783-1155, U.S.A***Abstract**

Equations for the most widely used statistical moments of plane and spherical sound waves propagating in the turbulent atmosphere with arbitrary spectra of temperature and wind velocity fluctuations are presented. Among these moments are the following: the variances of phase and log-amplitude fluctuations; the correlation functions of phase and log-amplitude fluctuations; the mean sound field; and the coherence function of the sound field. These statistical moments are then calculated for the Gaussian correlation functions of temperature and wind velocity fluctuations. The relative contributions to the statistical moments of the sound field due to sound scattering by temperature and wind velocity fluctuations are studied. It is shown that these contributions can differ significantly.

1 Introduction

The presentation deals with the theory of line-of-sight sound propagation through the turbulent atmosphere. We shall assume that the sound wavelength λ is less than the scale L_l of largest inhomogeneities in the atmosphere, which affect sound field fluctuations. In this case, the sound wave is only scattered by fluctuations in the temperature \tilde{T} and wind velocity component v_x in the direction from a source to a receiver. This direction is chosen to be coincident with the x -axis. For line-of-sight sound propagation, the most widely used statistical moments of the sound field are the following: The variances of phase and log-amplitude fluctuations $\langle \phi^2 \rangle$ and $\langle \chi^2 \rangle$; the correlation functions of phase and log-amplitude fluctuations, $B_\phi(r)$ and $B_\chi(r)$; the mean sound field $\langle p \rangle$; and the coherence function of the sound field $\Gamma(r)$. Here, r is the separation between two points of observation in the yz -plane. The equations for these statistical moments were derived in electrodynamics. For the Gaussian correlation function of medium inhomogeneities, these equations contain the variance σ_ϵ of dielectric permittivity fluctuations. It was assumed

in the previous theories of sound propagation through the turbulent atmosphere that the equations for $\langle \phi^2 \rangle$, $\langle \chi^2 \rangle$, $B_\phi(r)$, $B_\chi(r)$, $\langle p \rangle$ and $\Gamma(r)$ can be obtained from equations for analogous statistical moments in electrodynamics if in the latter equations σ_ϵ is replaced by $\sigma_T^2/T_0^2 + 4\sigma_v^2/c_0^2$. Here, σ_T^2 and σ_v^2 are the variances of the random fields \tilde{T} and v_x , and T_0 and c_0 are the mean values of temperature and adiabatic sound speed. But it is shown in the review [3] that the statistical moments of the sound field cannot not be obtained by such a replacement and should be calculated anew.

The main goal of the presentation is to briefly review recently obtained equations for the aforementioned statistical moments of plane and spherical sound waves propagating in the turbulent atmosphere with the Gaussian correlation functions of temperature and wind velocity fluctuations. We shall also present equations for these statistical moments for arbitrary spectra of temperature and wind velocity fluctuations. The derivation and detailed analysis of both sets of equations will be published elsewhere. It is worthwhile to briefly list in here all these equations because they can be useful in further theoretical studies of sound propagation through the turbulent atmosphere. Furthermore, these equations are needed for comparison between the theory developed and proposed experiments, which will be a continuation of experiments discussed in [1].

2 Basic equations

In electrodynamics, equations for the statistical moments $\langle \phi^2 \rangle$, $\langle \chi^2 \rangle$, $B_\phi(r)$, $B_\chi(r)$, $\langle p \rangle$ and $\Gamma(r)$ contain the three-dimensional spectral density $\Phi_\epsilon(0, \kappa)$ of dielectric permittivity fluctuations. It is shown in [3] that if in these equations $\Phi_\epsilon(0, \kappa)$ is replaced by the effective spectral density

$$\Phi_{\text{eff}}(0, \kappa) = \frac{\Phi_T(0, \kappa)}{T_0^2} + \frac{4F(\kappa)}{c_0^2}, \quad (1)$$

one obtains equations for the analogous statistical moments of a sound field propagating in the turbulent atmosphere. In Eq. (1), $\Phi_T(0, \kappa)$ and $F(\kappa)$ are the three-dimensional spectral densities of temperature and wind velocity fluctuations. For the Gaussian correlation functions of temperature and wind velocity fluctuations, Eq. (1) reads [3]

$$\Phi_{\text{eff}}(0, \kappa) = \frac{l^3}{8\pi^{3/2}} \left(\frac{\sigma_T^2}{T_0^2} + \frac{\sigma_v^2 \kappa^2 l^2}{c_0^2} \right) e^{-\frac{\kappa^2 l^2}{4}}, \quad (2)$$

where l is the unique scale of inhomogeneities associated with a Gaussian correlation function.

Eqs. (1) and (2) and the equations for the involved statistical moments $\langle \phi^2 \rangle$, $\langle \chi^2 \rangle$, $B_\phi(r)$, $B_\chi(r)$, $\langle p \rangle$ and $\Gamma(r)$, known in electrodynamics, allow one to obtain statistical moments of plane and spherical sound waves propagating through the turbulent atmosphere.

3 Variances of log-amplitude and phase fluctuations

3.1 Plane wave

For the case of a plane electromagnetic wave propagating in a random medium, the equations for $\langle \phi^2 \rangle$ and $\langle \chi^2 \rangle$ are given in [4]. Replacing $\Phi_\epsilon(0, \kappa)$ in these equations by $\Phi_{\text{eff}}(0, \kappa)$ yields the equations for the variances of phase and log-amplitude fluctuations of a plane sound wave in the turbulent atmosphere

$$\langle \phi^2 \rangle = \frac{\pi^2 k^2 x}{2} \int_0^\infty d\kappa \kappa \Phi_{\text{eff}}(0, \kappa) \left[1 + \frac{\kappa_F^2}{\kappa^2} \sin \frac{\kappa^2}{\kappa_F^2} \right], \quad (3)$$

$$\langle \chi^2 \rangle = \frac{\pi^2 k^2 x}{2} \int_0^\infty d\kappa \kappa \Phi_{\text{eff}}(0, \kappa) \left[1 - \frac{\kappa_F^2}{\kappa^2} \sin \frac{\kappa^2}{\kappa_F^2} \right]. \quad (4)$$

Here, x is a distance from a source to a receiver, $k = 2\pi/\lambda$, and $\kappa_F = \sqrt{\frac{2\pi}{\lambda x}}$. Eqs. (3) and (4) are valid for arbitrary spectra of temperature and wind velocity fluctuations.

Substituting the value of $\Phi_{\text{eff}}(0, \kappa)$, given by Eq. (2), into these equations and calculating the integrals over κ , one obtains the equations for $\langle \phi^2 \rangle$ and $\langle \chi^2 \rangle$ for the plane sound wave propagating in the turbulent atmosphere with the Gaussian correlation functions of temperature and wind velocity fluctuations

$$\langle \phi^2 \rangle = \frac{\sqrt{\pi} k^2 l x}{8} \left[\left(1 + \frac{\arctan D}{D} \right) \frac{\sigma_T^2}{T_0^2} + \left(1 + \frac{1}{1+D^2} \right) \frac{4\sigma_v^2}{c_0^2} \right], \quad (5)$$

$$\langle \chi^2 \rangle = \frac{\sqrt{\pi} k^2 l x}{8} \left[\left(1 - \frac{\arctan D}{D} \right) \frac{\sigma_T^2}{T_0^2} + \left(1 - \frac{1}{1+D^2} \right) \frac{4\sigma_v^2}{c_0^2} \right]. \quad (6)$$

Here, $D = \frac{4}{\kappa_F^2 l^2}$ is the so-called wave parameter [4].

3.2 Spherical wave

The book [2] presents the equations for $\langle \phi^2 \rangle$ and $\langle \chi^2 \rangle$ for a spherical electromagnetic wave propagating in a random medium. Replacing $\Phi_\epsilon(0, \kappa)$ in these equations by $\Phi_{\text{eff}}(0, \kappa)$, one obtains equations for phase and log-amplitude fluctuations of a spherical sound wave in the turbulent atmosphere

$$\langle \phi^2 \rangle = \frac{\pi^2 k^2 x}{2} \int_0^1 dt \int_0^\infty d\kappa \kappa \Phi_{\text{eff}}(0, \kappa) \left[1 + \cos \left(\frac{\kappa^2 t(1-t)}{\kappa_F^2} \right) \right], \quad (7)$$

$$\langle \chi^2 \rangle = \frac{\pi^2 k^2 x}{2} \int_0^1 dt \int_0^\infty d\kappa \kappa \Phi_{\text{eff}}(0, \kappa) \left[1 - \cos \left(\frac{\kappa^2 t(1-t)}{\kappa_F^2} \right) \right]. \quad (8)$$

These equations are also valid for arbitrary spectra of temperature and wind velocity fluctuations.

Substituting $\Phi_{\text{eff}}(0, \kappa)$ from Eq. (2) into Eqs. (7) and (8) and then calculating the integrals over t and κ yields the equations for $\langle \phi^2 \rangle$ and $\langle \chi^2 \rangle$ for the spherical sound wave

in the turbulent atmosphere with the Gaussian correlation functions of temperature and wind velocity fluctuations

$$\langle \phi^2 \rangle = \frac{\sqrt{\pi} k^2 l x}{8} \left\{ [1 + F_1(D)] \frac{\sigma_T^2}{T_0^2} + [1 + F_2(D)] \frac{4\sigma_v^2}{c_0^2} \right\}, \quad (9)$$

$$\langle \chi^2 \rangle = \frac{\sqrt{\pi} k^2 l x}{8} \left\{ [1 - F_1(D)] \frac{\sigma_T^2}{T_0^2} + [1 - F_2(D)] \frac{4\sigma_v^2}{c_0^2} \right\}. \quad (10)$$

Here,

$$F_1(D) = \frac{\arctan \sqrt{\frac{2}{\Omega}} + \frac{\Omega\Delta}{2} \ln \frac{1+\Delta\sqrt{2\Omega}}{1-\Delta\sqrt{2\Omega}}}{\Delta^2(\Omega+1)\sqrt{8\Omega}},$$

$$F_2(D) = \frac{\Omega(\Omega+2)}{2(\Omega+1)^2} \left[1 + \frac{\sqrt{2\Omega}(\Omega+3) \arctan \sqrt{\frac{2}{\Omega}}}{4(\Omega+1)} \right. \\ \left. + \frac{\Delta\sqrt{2\Omega}(\Omega-1)(\Omega+2) \ln \frac{1+\Delta\sqrt{2\Omega}}{1-\Delta\sqrt{2\Omega}}}{8(\Omega+1)} \right],$$

where, $\Delta = D/4$, and $\Omega = \sqrt{1 + \Delta^{-2}} - 1$.

4 Correlation functions of log-amplitude and phase fluctuations

4.1 Plane wave

For the case of a plane electromagnetic wave propagating in a random medium, the equations for $B_\chi(r)$ and $B_\phi(r)$ can be found in [4]. Replacing $\Phi_\epsilon(0, \kappa)$ in these equations by $\Phi_{\text{eff}}(0, \kappa)$, one obtains the equations for the correlation functions of phase and log-amplitude fluctuations of a plane sound wave in the turbulent atmosphere with arbitrary spectra of temperature and wind velocity fluctuations

$$B_\phi(r) = \frac{\pi^2 k^2 x}{2} \int_0^\infty d\kappa \kappa J_0(\kappa r) \Phi_{\text{eff}}(0, \kappa) \left[1 + \frac{\kappa_F^2}{\kappa^2} \sin \frac{\kappa^2}{\kappa_F^2} \right], \quad (11)$$

$$B_\chi(r) = \frac{\pi^2 k^2 x}{2} \int_0^\infty d\kappa \kappa J_0(\kappa r) \Phi_{\text{eff}}(0, \kappa) \left[1 - \frac{\kappa_F^2}{\kappa^2} \sin \frac{\kappa^2}{\kappa_F^2} \right]. \quad (12)$$

In these equations, $J_0(\kappa r)$ is the Bessel function of zero order.

Substituting $\Phi_{\text{eff}}(0, \kappa)$ given by Eq. (2) into Eqs. (11) and (12) and calculating the integrals over κ yields the equations for $B_\phi(r)$ and $B_\chi(r)$ for the plane sound wave in the

turbulent atmosphere with the Gaussian correlation functions of the random fields \tilde{T} and v_x

$$B_\phi(r) = \frac{\sqrt{\pi}k^2lx}{8} \left\{ \left[e^{-r^2/l^2} - \frac{1}{D} \Im E_1 \left(\frac{r^2 e^{i \arctan D}}{l^2 \sqrt{1+D^2}} \right) \right] \frac{\sigma_T^2}{T_0^2} + \left[\left(1 - \frac{r^2}{l^2} \right) e^{-r^2/l^2} + \frac{\exp(-\frac{r^2}{l^2(1+D^2)})}{1+D^2} \left[\cos \left(\frac{r^2 D}{l^2(1+D^2)} \right) - \frac{1}{D} \sin \left(\frac{r^2 D}{l^2(1+D^2)} \right) \right] \right] \frac{4\sigma_v^2}{c_0^2} \right\}, \quad (13)$$

$$B_\chi(x, r) = \frac{\sqrt{\pi}k^2lx}{8} \left\{ \left[e^{-r^2/l^2} + \frac{1}{D} \Im E_1 \left(\frac{r^2 e^{i \arctan D}}{l^2 \sqrt{1+D^2}} \right) \right] \frac{\sigma_T^2}{T_0^2} + \left[\left(1 - \frac{r^2}{l^2} \right) e^{-r^2/l^2} - \frac{\exp(-\frac{r^2}{l^2(1+D^2)})}{1+D^2} \left[\cos \left(\frac{r^2 D}{l^2(1+D^2)} \right) - \frac{1}{D} \sin \left(\frac{r^2 D}{l^2(1+D^2)} \right) \right] \right] \frac{4\sigma_v^2}{c_0^2} \right\}. \quad (14)$$

Here, E_1 is the exponential-integral function, and

$$\Im E_1 \left(\frac{r^2 e^{i \arctan D}}{l^2 \sqrt{1+D^2}} \right) = - \int_{r^2/(l^2(1+D^2))}^{\infty} \frac{\sin(yD)}{ye^y} dy.$$

4.2 Spherical wave

The equations for $B_\phi(r)$ and $B_\chi(r)$ for a spherical electromagnetic wave propagating in a random medium are presented in [2]. Replacing $\Phi_\epsilon(0, \kappa)$ in these equations by $\Phi_{\text{eff}}(0, \kappa)$ yields the equations for the correlation functions of phase and log-amplitude fluctuations of a spherical sound wave in the turbulent atmosphere with arbitrary spectra of temperature and wind velocity fluctuations

$$B_\phi(x, r) = \frac{\pi^2 k^2 x}{2} \int_0^1 dt \int_0^\infty d\kappa \kappa J_0(\kappa r t) \Phi_{\text{eff}}(0, \kappa) \left[1 + \cos \left(\frac{\kappa^2 t(1-t)}{\kappa_F^2} \right) \right], \quad (15)$$

$$B_\chi(x, r) = \frac{\pi^2 k^2 x}{2} \int_0^1 dt \int_0^\infty d\kappa \kappa J_0(\kappa r t) \Phi_{\text{eff}}(0, \kappa) \left[1 - \cos \left(\frac{\kappa^2 t(1-t)}{\kappa_F^2} \right) \right]. \quad (16)$$

Replacing $\Phi_{\text{eff}}(0, \kappa)$ in these equations by its value given by Eq. (2) and then calculating the integrals over κ yields the equations for $B_\phi(r)$ and $B_\chi(r)$ for the spherical sound wave propagating in the turbulent atmosphere with the Gaussian correlation functions of the random fields \tilde{T} and v_x

$$B_\phi(x, r) = \frac{\sqrt{\pi}k^2lx}{8} \int_0^1 dt \left\{ \left[e^{-\rho^2} + \frac{e^{-\rho^2/d}}{d} \left[\cos \left(\frac{\rho^2 D \tau}{d} \right) + D \tau \sin \left(\frac{\rho^2 D \tau}{d} \right) \right] \right] \frac{\sigma_T^2}{T_0^2} + \left[(1 - \rho^2) e^{-\rho^2} + \frac{e^{-\rho^2/d}}{d^3} \left[(1 - D^4 \tau^4 + \rho^2(3d - 4)) \cos \left(\frac{\rho^2 D \tau}{d} \right) + D \tau (2d + \rho^2(d - 4)) \sin \left(\frac{\rho^2 D \tau}{d} \right) \right] \right] \frac{4\sigma_v^2}{c_0^2} \right\}, \quad (17)$$

$$\begin{aligned}
B_x(r) = & \frac{\sqrt{\pi}k^2lx}{8} \int_0^1 dt \left\{ \left[e^{-\rho^2} - \frac{e^{-\rho^2/d}}{d} \left[\cos\left(\frac{\rho^2 D\tau}{d}\right) + D\tau \sin\left(\frac{\rho^2 D\tau}{d}\right) \right] \right] \frac{\sigma_T^2}{T_0^2} \right. \\
& + \left[(1 - \rho^2)e^{-\rho^2} - \frac{e^{-\rho^2/d}}{d^3} \left[(1 - D^4\tau^4 + \rho^2(3d - 4)) \cos\left(\frac{\rho^2 D\tau}{d}\right) \right. \right. \\
& \left. \left. + D\tau(2d + \rho^2(d - 4)) \sin\left(\frac{\rho^2 D\tau}{d}\right) \right] \right] \frac{4\sigma_v^2}{c_0^2}. \quad (18)
\end{aligned}$$

Here, $\rho = rt/l$, $\tau = t(1 - t)$, and $d = 1 + D^2\tau^2$.

5 Mean sound field

For an electromagnetic wave propagating in a random medium, the equation for $\langle p \rangle$ can be found in [4]. Replacing $\Phi_\epsilon(0, \kappa)$ in this equation by $\Phi_{\text{eff}}(0, \kappa)$, one obtains the equation for a mean sound field in the turbulent atmosphere

$$\langle p(x, \mathbf{r}) \rangle = e^{-\gamma x} p_0(x, \mathbf{r}). \quad (19)$$

In this equation, $p_0(x, \mathbf{r})$ is the sound field in the atmosphere without turbulence, and γ is the extinction coefficient of the mean sound field, given by

$$\gamma = \frac{\pi^2 k^2}{2} \int_0^\infty d\kappa \kappa \Phi_{\text{eff}}(0, \kappa). \quad (20)$$

Eqs. (19) and (20) are valid for plane and spherical sound waves. For a plane wave, $p_0 = \exp(ikx)$, while for a spherical wave, $p_0 = e^{ikR}/R$. It follows from Eq. (19) that the mean sound field is exponentially attenuated with the distance x of sound propagation through the turbulent atmosphere.

Substituting $\Phi_{\text{eff}}(0, \kappa)$ given by Eq. (2) into Eq. (20) and calculating the integral over κ yields the equation for the extinction coefficient of the mean sound field propagating in the turbulent atmosphere with the Gaussian correlation functions of the random fields \tilde{T} and v_x

$$\gamma = \gamma_T + \gamma_v = \frac{\sqrt{\pi}k^2 l}{8} \left(\frac{\sigma_T^2}{T_0^2} + \frac{4\sigma_v^2}{c_0^2} \right). \quad (21)$$

In Eq. (21), the contributions to the extinction coefficient due to sound scattering by temperature and wind velocity fluctuations are denoted by γ_T and γ_v , respectively. These contributions are given by

$$\gamma_T = \frac{\sqrt{\pi}k^2 l}{8} \frac{\sigma_T^2}{T_0^2}, \quad \gamma_v = \frac{\sqrt{\pi}k^2 l}{2} \frac{\sigma_v^2}{c_0^2}. \quad (22)$$

6 Coherence function

6.1 Plane wave

The book [4] gives the equation for $\Gamma(r)$ for a plane electromagnetic wave propagating in a random medium. Replacing $\Phi_\epsilon(0, \kappa)$ in this equation by $\Phi_{\text{eff}}(0, \kappa)$, one obtains the equation for the coherence function of a plane sound wave in the turbulent atmosphere

$$\Gamma(r) = I_0 \exp \left\{ -\pi^2 k^2 x \int_0^\infty d\kappa \kappa \Phi_{\text{eff}}(0, \kappa) [1 - J_0(\kappa r)] \right\}. \quad (23)$$

Here, $I_0 = p_0 p_0^*$ is the intensity of the plane sound wave in the atmosphere without turbulence. Eq. (23) is valid for arbitrary spectra of temperature and wind velocity fluctuations.

Replacing $\Phi_{\text{eff}}(0, \kappa)$ in Eqs. (23) by its value given by Eq. (2) and then calculating the integral over κ , yields the equation for $\Gamma(r)$ for the plane sound wave in the turbulent atmosphere with the Gaussian correlation functions of temperature and wind velocity fluctuations

$$\Gamma(r) = I_0 \exp \left\{ -2\gamma_T x \left(1 - e^{-r^2/l^2} \right) - 2\gamma_v x \left[1 - \left(1 - \frac{r^2}{l^2} \right) e^{-r^2/l^2} \right] \right\}. \quad (24)$$

This equation can be represented in the form

$$\Gamma(r) = I_0 \Gamma_T(r) \Gamma_v(r), \quad (25)$$

where $\Gamma_T(r)$ and $\Gamma_v(r)$ are the contributions to the coherence function due to sound scattering by temperature and wind velocity fluctuations. It can be shown from Eqs. (24) and (25) that

$$\Gamma_T(r) = \exp \left\{ -2\gamma_T x \left(1 - e^{-r^2/l^2} \right) \right\}, \quad (26)$$

$$\Gamma_v(r) = \exp \left\{ -2\gamma_v x \left[1 - \left(1 - \frac{r^2}{l^2} \right) e^{-r^2/l^2} \right] \right\}. \quad (27)$$

The functions Γ_T and Γ_v versus r/l are plotted in figure 1 for $\gamma_T x = \gamma_v x = 1/2$. It is clearly seen from figure that the contributions to the coherence function due to sound scattering by temperature and wind velocity fluctuations have different dependence on the normalized distance r/l between the two points of observation.

It is worthwhile noting here that it follows from the equations presented above that the relative contributions to $\langle \phi^2 \rangle$, $\langle \chi^2 \rangle$, $B_\phi(r)$ and $B_\chi(r)$ due to sound scattering by temperature and wind velocity fluctuations also have different dependences on x , k , l and r .

6.2 Spherical wave

The equation for the coherence function of a spherical electromagnetic wave propagating in a random medium is presented in [2]. Replacing $\Phi_\epsilon(0, \kappa)$ in this equation by $\Phi_{\text{eff}}(0, \kappa)$

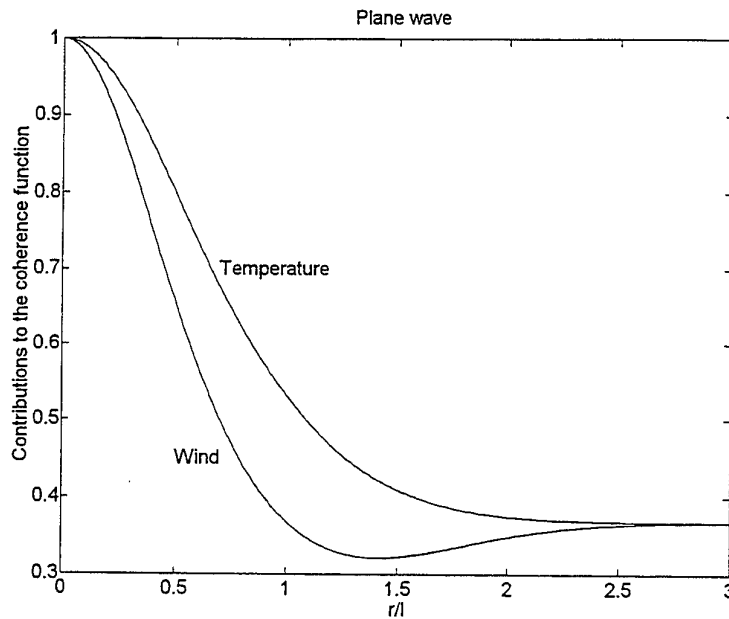


Figure 1: The contributions to the coherence function of the plane sound wave due to sound scattering by temperature and wind velocity fluctuations.

yields the equation for the coherence function of a spherical sound wave in the turbulent atmosphere

$$\Gamma(\mathbf{r}, \mathbf{r}_+) = \frac{\exp \left\{ \frac{i k \mathbf{r} \cdot \mathbf{r}_+}{x} - \pi^2 k^2 x \int_0^1 dt \int_0^\infty d\kappa \kappa \Phi_{\text{eff}}(0, \kappa) [1 - J_0(\kappa r t)] \right\}}{(4\pi x)^2}. \quad (28)$$

In this equation, $\mathbf{r} = \mathbf{r}_1 - \mathbf{r}_2$ and $\mathbf{r}_+ = (\mathbf{r}_1 + \mathbf{r}_2)/2$, where \mathbf{r}_1 and \mathbf{r}_2 are the coordinates of the two points of observation in the yz -plane. Eq. (28) is valid for arbitrary spectra of temperature and wind velocity fluctuations.

Substituting $\Phi_{\text{eff}}(0, \kappa)$ given by Eq. (2) into Eqs. (28) and calculating the integrals over t and κ , one obtains the equation for the coherence function of the spherical sound wave propagating in the turbulent atmosphere with the Gaussian correlation functions of temperature and wind velocity fluctuations:

$$\begin{aligned} \Gamma(\mathbf{r}, \mathbf{r}_+) = & (4\pi x)^{-2} \exp \left\{ \frac{i k \mathbf{r} \cdot \mathbf{r}_+}{x} - 2\gamma_T x \left[1 - \frac{\sqrt{\pi} l}{2r} \operatorname{erf} \left(\frac{r}{l} \right) \right] \right. \\ & \left. - 2\gamma_v x \left[1 - \frac{\sqrt{\pi} l}{4r} \operatorname{erf} \left(\frac{r}{l} \right) - \frac{1}{2} e^{-r^2/l^2} \right] \right\}. \end{aligned} \quad (29)$$

Here, $\operatorname{erf}(r/l)$ is the error-function. The coherence function Γ can be represented in the following form

$$\Gamma(\mathbf{r}, \mathbf{r}_+) = \frac{\exp \left\{ \frac{i k \mathbf{r} \cdot \mathbf{r}_+}{x} \right\}}{(4\pi x)^2} \Gamma_T(r) \Gamma_v(r), \quad (30)$$

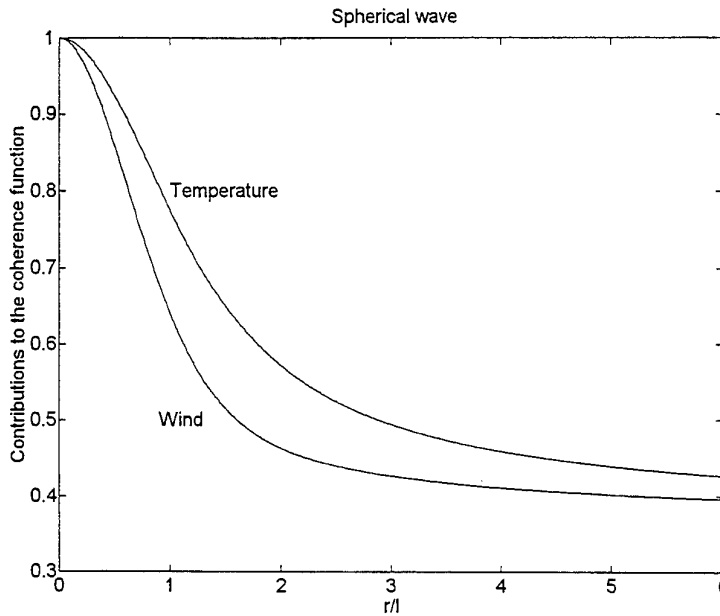


Figure 2: The contributions to the coherence function of the spherical sound wave due to sound scattering by temperature and wind velocity fluctuations.

In this equation, $\Gamma_T(r)$ and $\Gamma_v(r)$ are the contributions to the coherence function of the spherical wave due to sound scattering by temperature and wind velocity fluctuations, given by

$$\Gamma_T(r) = \exp \left\{ -2\gamma_T x \left[1 - \frac{\sqrt{\pi}l}{2r} \operatorname{erf} \left(\frac{r}{l} \right) \right] \right\}, \quad (31)$$

$$\Gamma_v(r) = \exp \left\{ -2\gamma_v x \left[1 - \frac{\sqrt{\pi}l}{4r} \operatorname{erf} \left(\frac{r}{l} \right) - \frac{1}{2} e^{-r^2/l^2} \right] \right\}. \quad (32)$$

The functions Γ_T and Γ_v versus r/l are plotted in figure 2 for $\gamma_T x = \gamma_v x = 1/2$. It is seen from this figure that these functions have different dependence on the normalized distance r/l between the two points of observation.

7 Conclusions

The equations for the most widely used statistical moments $\langle \phi^2 \rangle$, $\langle \chi^2 \rangle$, $B_\phi(r)$, $B_\chi(r)$, $\langle p \rangle$ and $\Gamma(r)$ of plane and spherical sound waves propagating in the turbulent atmosphere with arbitrary spectra of the random fields T and v_x are presented. The statistical moments are then calculated for Gaussian correlation functions of these random fields.

The most important result which can be drawn from the equations obtained is that the contributions to the statistical moments of the sound field due to sound scattering by temperature and wind velocity fluctuations can differ significantly. Furthermore, these

contributions have different dependences on the parameter of the problem: x , k , l and r . In the previous theories of sound propagation through the turbulent atmosphere, these contributions were assumed to be the same.

It should be noted here that the theory developed is quite general and can be applied for studying sound propagation in the turbulent ocean, in turbulent flows of gasses and liquids, etc.

Acknowledgments

This material is partly based upon work done by V.E.Ostashev and G.Goedecke that was supported by the U.S. Army Research Office under contract number DAAH04-95-1-0593.

References

- [1] G.A.Daigle, J.E.Piercy and T.F.W.Embleton, "Line-of-sight propagation through atmospheric turbulence near the ground," *J. Acoust. Soc. Am.*, **74** (5), 1505-1513 (1983).
- [2] A.Ishimaru, *Wave propagation and scattering in random media* (Academic, New York, 1978).
- [3] V.E.Ostashev, "Sound propagation and scattering in media with random inhomogeneities of sound speed, density and medium velocity (Review Article)," *Waves in Random Media* **4**, 403-428 (1994).
- [4] S.M.Rytov, Yu.A.Kravtzov and V.I.Tatarskii, *Principles of statistical radio physics. Part 4. Wave propagation trough random media* (Springer, Berlin, 1989).

Coherence functions of plane and spherical sound waves in the turbulent atmosphere with von Karman spectra of temperature and wind velocity fluctuations.

V.E.OSTASHEV and G.GOEDECKE

Department of Physics, NMSU, Las Cruces, NM 88003-8001, U.S.A.

B.BRÄHLER and V.MELLERT

Fachbereich Physik, Universität Oldenburg, Oldenburg D-26111, Germany

H.AUVERMANN

US Army Research Laboratory, 2800 Powder Mill Road, Adelphi, MD 20783-1155, U.S.A

Abstract

When calculating statistical moments of a sound field in the turbulent atmosphere, Kolmogorov and Gaussian spectra of temperature and wind velocity fluctuations have most widely been used in the literature. The Kolmogorov spectrum allows one to take into account the effects of inhomogeneities in the inertial subrange of locally homogeneous and isotropic turbulence on the statistical moments of the sound field. On the other hand, the Gaussian spectrum enables us to study the effects of the largest inhomogeneities in the atmosphere, which affect sound field fluctuations. The main goal of the presentation is to use von Karman spectra of temperature and wind velocity fluctuations for calculating the statistical moments of the sound field. It is shown that the von Karman spectrum can be considered as a "combination" of the Kolmogorov and Gaussian spectra. For this spectrum of atmospheric turbulence, the mean sound field and the coherence functions of plane and spherical sound waves are calculated. In limiting cases, the equations for the coherence functions coincide with those obtained for the Kolmogorov and Gaussian spectra. The contributions to the mean sound field and the coherence functions of plane and spherical waves due to sound scattering by temperature and wind velocity fluctuations are also studied.

1 Introduction

The presentation is a logical continuation of [3], where the theory of line-of-sight sound propagation through the turbulent atmosphere is considered. In [3], equations for the most widely used statistical moments of plane and spherical sound waves propagating in the turbulent atmosphere with arbitrary spectra of temperature and wind velocity fluctuations are presented. These statistical moments are then calculated for the Gaussian correlation functions of temperature and wind velocity fluctuations.

In this presentation, we calculate some of these statistical moments (namely, the mean sound field $\langle p \rangle$ and the coherence function Γ of the sound field) for the case of sound propagation through the turbulent atmosphere with the von Karman spectra of temperature and wind velocity fluctuations. We show that the von Karman spectrum can be considered as a "combination" of the Kolmogorov and Gaussian spectra. In the inertial subrange of locally homogeneous and isotropic turbulence, the von Karman spectrum becomes the Kolmogorov spectrum, while for large scale inhomogeneities it is similar to the Gaussian one.

2 Basic equations

The equation for the mean sound field propagating in the turbulent atmosphere with arbitrary spectra of temperature and wind velocity fluctuations is presented in [3] and is given by

$$\langle p(x, \mathbf{r}) \rangle = \exp(-\gamma x) p_0(x, \mathbf{r}). \quad (1)$$

Here, x and $\mathbf{r} = (y, z)$ are the Cartesian coordinates, and a source and receiver are located at the points $(x = 0, \mathbf{r} = 0)$ and (x, \mathbf{r}) , respectively. Furthermore, in Eq. (1) $p_0(x, \mathbf{r})$ is the sound field in the atmosphere without turbulence, and

$$\gamma = \frac{\pi^2 k^2}{2} \int_0^\infty d\kappa \kappa \Phi_{\text{eff}}(0, \kappa) \quad (2)$$

is the extinction coefficient of the mean sound field. Here, k is the wave number, and $\Phi_{\text{eff}}(0, \kappa)$ is the effective spectral density given by

$$\Phi_{\text{eff}}(0, \kappa) = \frac{\Phi_T(0, \kappa)}{T_0^2} + \frac{4F(\kappa)}{c_0^2}. \quad (3)$$

In this equation, $\Phi_T(0, \kappa)$ and $F(\kappa)$ are the three-dimensional spectral densities of temperature and wind velocity fluctuations, and T_0 and c_0 are the mean values of temperature and adiabatic sound speed.

Eqs. (1) and (2) are valid for a sound wave of any form, for instance, for a plane or spherical sound wave.

The equations for the coherence functions Γ of the plane and spherical sound waves propagating in the turbulent atmosphere with arbitrary spectra of temperature and wind velocity fluctuations are also presented in [3]. For the plane sound wave, Γ is given by

$$\Gamma(r) = I_0 \exp \left\{ -\pi^2 k^2 x \int_0^\infty d\kappa \kappa \Phi_{\text{eff}}(0, \kappa) [1 - J_0(\kappa r)] \right\}, \quad (4)$$

where r is the distance between two points of observation in the yz -plane, $I_0 = p_0 p_0^*$ is the intensity of the sound wave in the atmosphere without turbulence, and J_0 is the Bessel function of zero order.

For the spherical sound wave, the equation for the coherence function reads

$$\Gamma(\mathbf{r}, \mathbf{r}_+) = \frac{\exp \left\{ \frac{i\mathbf{k}\cdot\mathbf{r}_+}{x} - \pi^2 k^2 x \int_0^1 dt \int_0^\infty d\kappa \kappa \Phi_{\text{eff}}(0, \kappa) [1 - J_0(\kappa r t)] \right\}}{(4\pi x)^2}. \quad (5)$$

Here, $\mathbf{r} = \mathbf{r}_1 - \mathbf{r}_2$ and $\mathbf{r}_+ = (\mathbf{r}_1 + \mathbf{r}_2)/2$, where \mathbf{r}_1 and \mathbf{r}_2 are the coordinates of the two points of observation in the yz -plane.

Eqs. (2), (4) and (5) are valid for an arbitrary function $\Phi_{\text{eff}}(0, \kappa)$. We shall calculate $\langle p \rangle$, $\Gamma(r)$ and $\Gamma(\mathbf{r}, \mathbf{r}_+)$ for the von Karman spectra of temperature and wind velocity fluctuations, when $\Phi_{\text{eff}}(0, \kappa)$ is given by

$$\Phi_{\text{eff}}(0, \kappa) = \frac{A}{(\kappa^2 + \kappa_0^2)^{11/6}} \left(\frac{C_T^2}{T_0^2} + \frac{\kappa^2}{(\kappa^2 + \kappa_0^2)} \frac{22C_v^2}{3c_0^2} \right). \quad (6)$$

Here, C_T^2 and C_v^2 are the structure parameters of temperature and wind velocity fluctuations, $A = 0.033$, and $1/\kappa_0 \sim L_l$, where L_l is the scale of the largest inhomogeneities in the atmosphere, which affect fluctuations in the sound field.

3 Comparison between von Karman, Kolmogorov and Gaussian spectra

For the Kolmogorov spectra of temperature and wind velocity fluctuations, the effective spectral density is given by [2]

$$\Phi_{\text{eff}}(0, \kappa) = A \kappa^{-11/3} \left(\frac{C_T^2}{T_0^2} + \frac{22C_v^2}{3c_0^2} \right). \quad (7)$$

Comparison of Eqs. (6) and (7) reveals that the effective spectral densities $\Phi_{\text{eff}}(0, \kappa)$ for the von Karman and Kolmogorov spectra are the same if $\kappa \gg \kappa_0$.

For the Gaussian spectra of temperature and wind velocity fluctuations, the equation for the effective spectral density reads [2, 3]

$$\Phi_{\text{eff}}(0, \kappa) = \frac{l^3}{8\pi^{3/2}} \left(\frac{\sigma_T^2}{T_0^2} + \frac{\sigma_v^2 \kappa^2 l^2}{c_0^2} \right) e^{-\frac{\kappa^2 l^2}{4}}. \quad (8)$$

Here, σ_T^2 and σ_v^2 are the variances of temperature and wind velocity fluctuations, l is the unique scale associated with the Gaussian spectrum.

If $\kappa \ll \kappa_0$ in Eq. (6) and $\kappa \ll 1/l$ in Eq. (8), the effective spectral densities $\Phi_{\text{eff}}(0, \kappa)$ for the von Karman and Gaussian spectra show the same dependence on κ .

For the Gaussian spectrum of atmospheric turbulence, $\Phi_{\text{eff}}(0, \kappa)$ contains the following parameters: l , σ_T^2 and σ_v^2 . On the other hand, for the von Karman spectrum, $\Phi_{\text{eff}}(0, \kappa)$ contains other parameters: κ_0 , C_T^2 and C_v^2 . To be able to compare $\langle p \rangle$, $\Gamma(r)$ and $\Gamma(\mathbf{r}, \mathbf{r}_+)$ for the Gaussian and von Karman spectra, one needs to know the relationship between these parameters. This relationship can be obtained by comparing the correlation functions of temperature fluctuations $B_T(R)$ for the Gaussian and von Karman spectra, and by comparing the longitudinal correlation functions of wind velocity fluctuations $B_{RR}(R)$ for

these spectra. Here, R is the modulus of the vector $\mathbf{R} = (x, y, z)$. The functions $B_T(R)$ and $B_{RR}(R)$ can be expressed through $\Phi_T(0, \kappa)$ and $F(\kappa)$, respectively [1, 4]

$$B_T(R) = \frac{4\pi}{R} \int_0^\infty d\kappa \kappa \sin(\kappa R) \Phi_T(\kappa), \quad (9)$$

$$B_{RR}(R) = 4\pi \int_0^\infty d\kappa \cos(\kappa R) \int_\kappa^\infty d\kappa_1 \frac{\kappa_1^2 - \kappa^2}{\kappa_1} F(\kappa_1). \quad (10)$$

For the von Karman and Gaussian spectra, $\Phi_T(0, \kappa)$ and $F(\kappa)$ can easily be found by using Eqs. (3), (6) and (8). Substituting then these values of $\Phi_T(0, \kappa)$ and $F(\kappa)$ into Eqs. (9) and (10) and calculating the integrals over κ and κ_1 , one obtains the correlation functions of temperature fluctuations $B_T^{vK}(R)$ and $B_T^G(R)$ for the von Karman and Gaussian spectra, respectively, and the longitudinal correlation functions $B_{RR}^{vK}(R)$ and $B_{RR}^G(R)$ for these spectra.

We shall assume that for the von Karman and Gaussian spectra, the variances of temperature fluctuations are the same, and that the variances of wind velocity fluctuations are also the same:

$$B_T^{vK}(0) = B_T^G(0), \quad B_{RR}^{vK}(0) = B_{RR}^G(0). \quad (11)$$

Furthermore, we shall assume that for the von Karman and Gaussian spectra, the integral lengths of the normalised correlation functions of temperature fluctuations are the same, and that the integral lengths of the normalised longitudinal correlation functions of wind velocity fluctuations are also the same:

$$\int_0^\infty dR \frac{B_T^{vK}(R)}{B_T^{vK}(0)} = \int_0^\infty dR \frac{B_T^G(R)}{B_T^G(0)}, \quad \int_0^\infty dR \frac{B_{RR}^{vK}(R)}{B_{RR}^{vK}(0)} = \int_0^\infty dR \frac{B_{RR}^G(R)}{B_{RR}^G(0)}. \quad (12)$$

Substituting the values of $B_T^{vK}(R)$, $B_T^G(R)$, $B_{RR}^{vK}(R)$ and $B_{RR}^G(R)$ into Eqs. (11) and (12), one can obtain the desired relationship between parameters of the von Karman and Gaussian spectra

$$l = \frac{2\Gamma(5/6)}{\Gamma(1/3)} \frac{1}{\kappa_0}, \quad \sigma_T^2 = \frac{\Gamma^2(1/3)}{\pi 2^{4/3} \sqrt{3}} \frac{C_T^2}{\kappa_0^{2/3}}, \quad \sigma_v^2 = \frac{\Gamma^2(1/3)}{\pi 2^{4/3} \sqrt{3}} \frac{C_v^2}{\kappa_0^{2/3}}. \quad (13)$$

4 Mean sound field

It follows from Eq. (1) that the mean sound field in the turbulent atmosphere is exponentially attenuated with the distance x . The coefficient γ of such attenuation is given by Eq. (2). Substituting $\Phi_{\text{eff}}(0, \kappa)$ given by Eq. (6) into Eq. (2) and calculating the integral over κ yields the extinction coefficient γ for the case of the von Karman spectra of temperature and wind velocity fluctuations

$$\gamma = \gamma_T + \gamma_v. \quad (14)$$

Here, γ_T and γ_v are the contributions to γ due to sound scattering by temperature and wind velocity fluctuations, given by

$$\gamma_T = \pi^2 A \frac{3k^2}{10\kappa_0^{5/3}} \frac{C_T^2}{T_0^2}, \quad \gamma_v = \pi^2 A \frac{6k^2}{5\kappa_0^{5/3}} \frac{C_v^2}{c_0^2}. \quad (15)$$

When comparing the relative contributions to $\langle p \rangle$, $\Gamma(r)$ and $\Gamma(\mathbf{r}, \mathbf{r}_+)$ due to sound scattering by temperature and wind velocity fluctuations, we shall assume that

$$\frac{C_T^2}{T_0^2} = \frac{4C_v^2}{c_0^2}. \quad (16)$$

If this equality is valid, the temperature and wind velocity fluctuations make the same contributions to the variance of acoustic refractive index fluctuations. It can be easily shown from Eqs. (15) and (16) that $\gamma_T = \gamma_v$.

By using the relationships (13), it can also be shown that γ_T and γ_v , given by Eq. (15), exactly coincide with γ_T and γ_v for the Gaussian spectrum of turbulence [3]. This coincidence is a consequence of the assumed integral relationship (12).

5 Coherence function of the plane wave

Substituting $\Phi_{\text{eff}}(0, \kappa)$ from Eq. (6) into Eq. (4) and calculating the integral over κ in the equation obtained, yields the coherence function of the plane sound wave propagating in the turbulent atmosphere with the von Karman spectra of temperature and wind velocity fluctuations

$$\Gamma(r) = I_0 \Gamma_T(r) \Gamma_v(r). \quad (17)$$

Here, Γ_T and Γ_v are the contributions to the coherence function due to sound scattering by temperature and wind velocity fluctuations, given by

$$\Gamma_T(r) = \exp \left\{ -2\gamma_T x \left[1 - \frac{\Gamma(1/6)}{\pi 2^{5/6}} (\kappa_0 r)^{5/6} K_{5/6}(\kappa_0 r) \right] \right\}, \quad (18)$$

$$\Gamma_v(r) = \exp \left\{ -2\gamma_v x \left[1 - \frac{\Gamma(1/6)}{\pi 2^{5/6}} (\kappa_0 r)^{5/6} \left(K_{5/6}(\kappa_0 r) - \frac{1}{2} (\kappa_0 r) K_{1/6}(\kappa_0 r) \right) \right] \right\}. \quad (19)$$

Here, $\Gamma(1/6)$ is the gamma-function, and $K_{1/6}(\kappa_0 r)$ and $K_{5/6}(\kappa_0 r)$ are the modified Bessel functions. Comparison of Eqs. (18) and (19) reveals that $\Gamma_T(r) \neq \Gamma_v(r)$ even if the equality (16) is valid. In other words, the contribution to the coherence function due to sound scattering by temperature fluctuations is different from that due to wind velocity fluctuations.

The functions $\Gamma_T(r)$ and $\Gamma_v(r)$ versus the normalized distance $\kappa_0 r$ between the two points of observation are plotted in figure 1 for $\gamma_T x = \gamma_v x = 1/2$. It is seen from the figure that Γ_v is less than Γ_T for all values of $\kappa_0 r$.

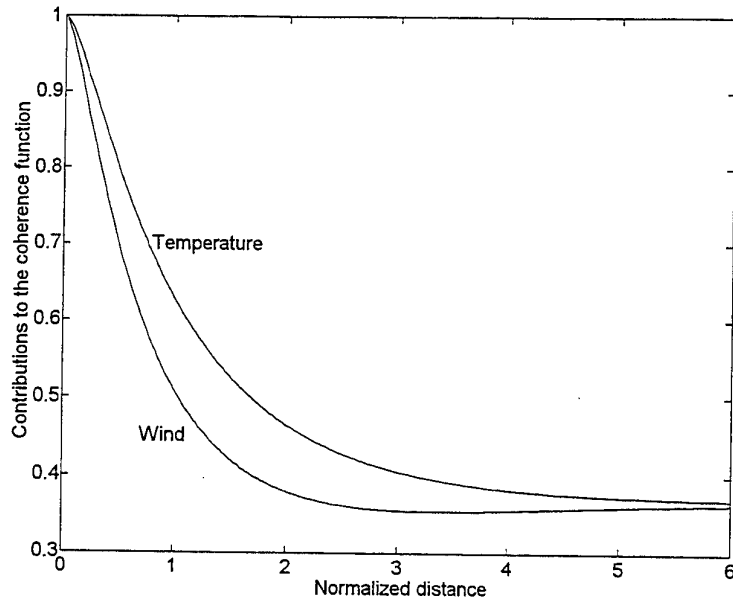


Figure 1: The contributions to the coherence function due to sound scattering by temperature and wind velocity fluctuations.

If $\kappa_0 r \ll 1$, $K_{1/6}(\kappa_0 r)$ and $K_{5/6}(\kappa_0 r)$ in Eqs. (18) and (19) can be developed as series in $\kappa_0 r$. Retaining first nonvanishing terms in the exponents in these equations and replacing γ_T and γ_v by their values given by Eq. (15), yields

$$\Gamma_T(r) = \exp \left\{ -B \frac{C_T^2}{T_0^2} k^2 r^{5/3} x \right\}, \quad (20)$$

$$\Gamma_v(r) = \exp \left\{ -B \frac{22}{3} \frac{C_v^2}{c_0^2} k^2 r^{5/3} x \right\}. \quad (21)$$

Here, $B = 0.364$. Eqs. (20) and (21) exactly coincide with the equations for coherence functions $\Gamma_T(r)$ and $\Gamma_v(r)$, calculated for the Kolmogorov spectra of temperature and wind velocity fluctuations. Thus, if $\kappa_0 r \ll 1$, as one would expect, the coherence functions $\Gamma_T(r)$ and $\Gamma_v(r)$, calculated for the von Karman spectrum, coincide with those calculated for the Kolmogorov spectrum.

For the opposite limiting case $\kappa_0 r \gg 1$, Eqs. (18) and (19) become

$$\Gamma_T(r) = \exp(-2\gamma_T x), \quad (22)$$

$$\Gamma_v(r) = \exp(-2\gamma_v x). \quad (23)$$

As one would expect, these equations coincide with the equations for the coherence functions $\Gamma_T(r)$ and $\Gamma_v(r)$, calculated for the Gaussian spectrum and presented in [3], if in the latter equations $r/l \gg 1$.

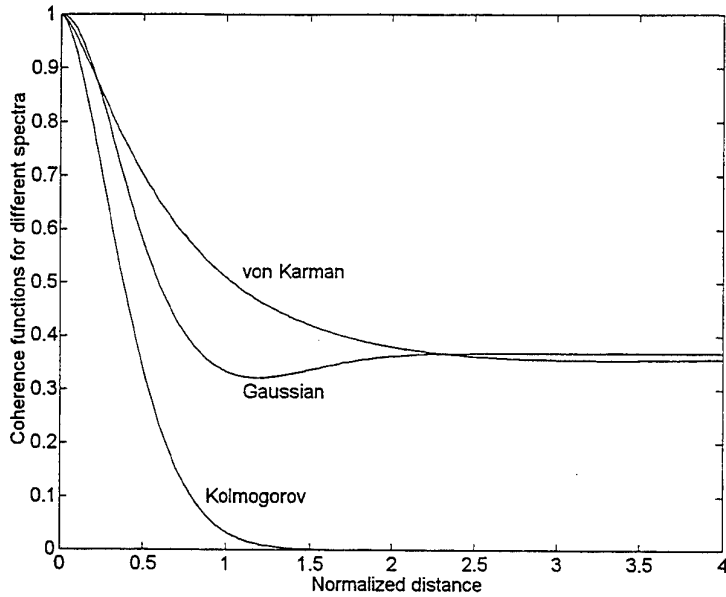


Figure 2: The coherence functions for the von Karman, Kolmogorov and Gaussian spectra versus the normalized distance for short range sound propagation.

The coherence functions $\Gamma_v(r)$ for the von Karman, Kolmogorov and Gaussian spectra of atmospheric turbulence versus the normalized distance $\kappa_0 r$ are plotted in figures 2 and 3. In figure 2, $x = 0.5\gamma_v^{-1}$, while in figure 3, $x = 150\gamma_v^{-1}$, so that these figures correspond to the cases of short and long ranges of sound propagation through the turbulent atmosphere, respectively. It follows from figure 2 that the coherence function $\Gamma_v(r)$ for the von Karman spectrum nearly coincides with that for the Gaussian spectrum if $\kappa_0 r > 2$. On the other hand, the coherence function $\Gamma_v(r)$ for the von Karman spectrum is nearly the same as that for the Kolmogorov spectrum if $\kappa_0 r < 0.04$, see figure 3. These conclusions are both in agreement with the analytical comparison between the coherence functions for the von Karman, Kolmogorov and Gaussian spectra, presented above.

6 Coherence function of the spherical wave

Substituting $\Phi_{\text{eff}}(0, \kappa)$ given by Eq. (6) into Eq. (5) and then calculating the integral over κ , one obtains the equation for the coherence function of the spherical sound wave in the turbulent atmosphere with the von Karman spectra of temperature and wind velocity fluctuations

$$\Gamma(\mathbf{r}, \mathbf{r}_+) = \frac{\exp\left\{\frac{i\mathbf{k}\cdot\mathbf{r}\cdot\mathbf{r}_+}{x}\right\}}{(4\pi x)^2} \Gamma_T^{sp}(r) \Gamma_v^{sp}(r), \quad (24)$$

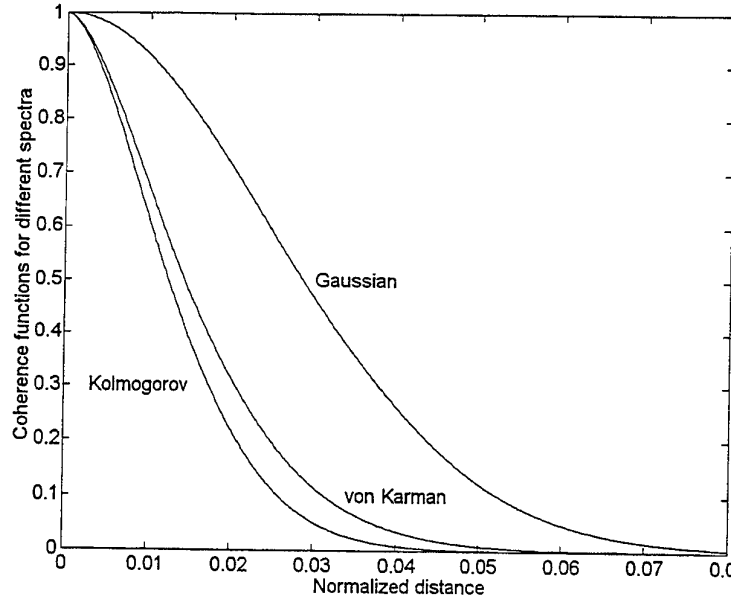


Figure 3: The coherence functions for the von Karman, Kolmogorov and Gaussian spectra versus the normalized distance for long range sound propagation.

Here, $\Gamma_T^{sp}(r)$ and $\Gamma_v^{sp}(r)$ are the contributions to $\Gamma(r, r_+)$ due to sound scattering by temperature and wind velocity fluctuations, given by

$$\Gamma_T^{sp}(r) = \exp \left\{ -\frac{2\gamma_T x}{\kappa_0 r} \int_0^{\kappa_0 r} dt \left[1 - \frac{2^{1/6} t^{5/6}}{\Gamma(5/6)} K_{5/6}(t) \right] \right\}. \quad (25)$$

$$\Gamma_v^{sp}(r) = \exp \left\{ -\frac{2\gamma_v x}{\kappa_0 r} \int_0^{\kappa_0 r} dt \left[1 - \frac{2^{1/6} t^{5/6}}{\Gamma(5/6)} \left(K_{5/6}(t) - \frac{1}{2} t K_{1/6}(t) \right) \right] \right\}. \quad (26)$$

Comparison of Eqs. (25) and (26) reveals that $\Gamma_T^{sp}(r)$ and $\Gamma_v^{sp}(r)$ have different dependence on r and κ_0 .

For the limiting case $\kappa_0 r \ll 1$, Eqs. (25) and (26) become

$$\Gamma_T^{sp}(r) = \exp \left\{ -B \frac{3}{8} \frac{C_T^2}{T_0^2} k^2 r^{5/3} x \right\}, \quad (27)$$

$$\Gamma_v^{sp}(r) = \exp \left\{ -B \frac{11}{4} \frac{C_v^2}{c_0^2} k^2 r^{5/3} x \right\}. \quad (28)$$

As one would expect, these equations coincide with the equations for $\Gamma_T^{sp}(r)$ and $\Gamma_v^{sp}(r)$ for the Kolmogorov spectrum.

For the opposite limiting case $\kappa_0 r \gg 1$, Eqs. (25) and (26) become

$$\Gamma_T^{sp}(r) = \exp(-2\gamma_T x), \quad (29)$$

$$\Gamma_v^{sp}(r) = \exp(-2\gamma_v r) . \quad (30)$$

These equations coincide with the equations for $\Gamma_T^{sp}(r)$ and $\Gamma_v^{sp}(r)$ for the Gaussian spectrum, presented in [3], if in the latter equations $r/l \gg 1$.

7 Conclusions

The mean sound field $\langle p \rangle$ and the coherence functions $\Gamma(r)$ and $\Gamma(\mathbf{r}, \mathbf{r}_+)$ of the plane and spherical sound waves propagating in the turbulent atmosphere with the von Karman spectra of temperature and wind velocity fluctuations are calculated. The contributions to these statistical moments of the sound field due to sound scattering by temperature and wind velocity fluctuations are compared provided that the equality (16) is valid. It is shown that temperature and wind velocity fluctuations make the same contributions to the extinction coefficient γ of the mean sound field $\langle p \rangle$. On the other hand, their contributions to the coherence functions $\Gamma(r)$ and $\Gamma(\mathbf{r}, \mathbf{r}_+)$ differ significantly.

The obtained equations for $\Gamma(r)$ and $\Gamma(\mathbf{r}, \mathbf{r}_+)$ for the von Karman spectrum are valid for all ranges of source-receiver distance r , including $r \sim \kappa_0^{-1}$. In the limiting cases $\kappa_0 r \ll 1$ and $\kappa_0 r \gg 1$, these equations coincide with those calculated for the Kolmogorov and Gaussian spectra, respectively.

Acknowledgments

This material is partly based upon work done by V.E.Ostashev and G.Goedecke that was supported by the U.S. Army Research Office under contract number DAAH04-95-1-0593.

References

- [1] J.Hinze, *Turbulence*, McGraw-Hill (1975).
- [2] V.E.Ostashev, "Sound propagation and scattering in media with random inhomogeneities of sound speed, density and medium velocity (Review Article)," *Waves in Random Media* 4, 403-428 (1994).
- [3] V.E.Ostashev, G.Goedecke, F.Gerdes, R.Wandelt and J.Noble, "Line-of-sight sound propagation in the turbulent atmosphere with Gaussian correlation functions of temperature and velocity fluctuations," *Proc. 7th Intern. Symp. on Long Range Sound Propagation*, Lyon, France (1996).
- [4] V.I.Tatarskii, *The effects of the turbulent atmosphere on wave propagation*, Israel (1971).

Propagation of Acoustic Pulses in a Turbulent Refractive Atmosphere

Ph. Blanc-Benon and D. Juvé

Laboratoire de Mécanique des Fluides et d'Acoustique,
U.M.R. C.N.R.S. 5509 ,Ecole Centrale de Lyon,
B.P.163, 69131 Ecully Cedex, France

The propagation of short duration acoustic signals above the ground through a model atmosphere is studied by numerical simulations. In the numerical model a time independent turbulent medium is represented by a set of realizations of random fields composed of a series of Fourier modes. The propagation of an acoustic pulse with a Gaussian spectrum is calculated using Fourier synthesis. In a first step each frequency component of the pressure signal is propagated using a wide angle parabolic equation; and in a second step the acoustic pressure in the time-domain is obtained via an inverse Fourier transform.

Results are presented for the case of a sound speed profile decreasing with height and a turbulent medium with Gaussian temperature fluctuations. The spatial variability of the time signatures in the shadow zone is illustrated and energetic aspects are discussed for individual realizations of the turbulent field.

1 Introduction

An acoustic wave propagating through a turbulent atmosphere is significantly affected by the variation in the value of the refractive index along the propagation path. The influence of temperature and wind velocity fluctuations has been demonstrated in many experimental studies. In recent years several authors have taken into account the effect of turbulence on sound propagation through numerical simulations for realistic cases. As an example, for sound propagation over long distances when strong negative vertical sound-speed gradients refract sound upward, it has been confirmed that the increase of the mean sound-pressure level in the shadow zone is due to the scattering of sound by turbulence.

Because of the turbulent fluctuations, each frequency component of an acoustic source will be scattered in a different way. As a consequence an acoustic pulse propagating in a turbulent atmosphere will be distorted. In addition, when there exists a mean sound-speed gradient echoes will appear due to multi-path propagation. Exploration of the coupling effect between turbulence and mean sound-speed gradient on acoustic propagation is an important issue in the use of impulse responses for outdoor sound propagation investigation.

This paper is organized as follows. In section 2 the numerical model used to compute the propagation of acoustics pulses is formulated. The turbulent refracting index model is introduced in section 3. Numerical examples and discussion are given in section 4. Finally, the results are summarized and a conclusion is drawn.

2 Wave equation and time domain formulation

Two different approaches have been developed to model long range sound propagation of time signals. One can solve the wave equation directly in the *time domain*([1]) or solve

the Helmholtz equation in the frequency domain and use Fourier synthesis to go back to time domain ([2]). In this paper we have chosen the second approach which is more effective for long range propagation of narrow band pulses, and can be easily combined with a wide-angle parabolic equation formulation.

In an environment with azimuthal symmetry the pressure field can be represented as:

$$P(r, z, t) = \int_{-\infty}^{+\infty} H(f) p(r, z, f) e^{-2i\pi ft} df. \quad (1)$$

where $H(f)$ is the frequency spectrum of the source. In practice this integral(1) is evaluated by a fast Fourier transform at each spatial position (r, z) for which the pulse response is desired. The complex amplitude $p(r, z, f)$ satisfies the reduced wave equation:

$$\left(\frac{\partial^2}{\partial r^2} + \frac{1}{r} \frac{\partial}{\partial r} + \frac{\partial^2}{\partial z^2} + k_0^2 n^2 \right) p(r, z, f) = H(f) \delta(\vec{x} - \vec{x}_0) \quad (2)$$

where k_0 is the reference wave number, $\vec{x}_0 = (r_0, z_0)$ is the position of the source, δ is the Dirac function and n is the index of refraction. The farfield approximation of equation (2) is :

$$\left(\frac{\partial^2}{\partial r^2} + \frac{\partial^2}{\partial z^2} + k_0^2 n^2 \right) u(r, z, f) = 0 \quad (3)$$

where u is the variable $p\sqrt{r}$ ($r > 0$). For weak turbulence the backscattering by index fluctuations is very small and the acoustic field is dominated by forward propagating waves. The outgoing waves are solutions of the following one-way wave equation :

$$\frac{\partial}{\partial r} \Psi(r, z, f) = ik_0(Q - 1)\Psi(r, z, f) \quad (4)$$

where $\Psi(r, z, f)$ is the envelope ($\Psi(r, z, f) = u(r, z, f) \exp(-ik_0 r)$) and Q is the square root of the linear second order operator Q^2 defined as :

$$\begin{cases} Q^2 = n^2 + \frac{1}{k_0^2} \frac{\partial^2}{\partial z^2} = 1 + \mathcal{L} \\ \mathcal{L} = (n^2 - 1) + \frac{1}{k_0^2} \frac{\partial^2}{\partial z^2} \end{cases} \quad (5)$$

To advance the solution of Eq. 4 over a short range Δr , we assume that the operator $Q = \sqrt{1 + \mathcal{L}}$ is slowly varying with range. Then, locally, the solution takes the form:

$$\psi(r + \Delta r, z, f) = \exp [ik_0(Q - 1)\Delta r] \psi(r, z, f) \quad (6)$$

The exponential operator is approximated by a rational approximation. We used a second order Padé development which yields:

$$\exp [ik_0 \Delta r (\sqrt{1 + \mathcal{L}} - 1)] \sim \frac{1 + p_1 \mathcal{L} + p_2 \mathcal{L}^2}{1 + q_1 \mathcal{L} + q_2 \mathcal{L}^2} \quad (7)$$

where the coefficients p_1 , p_2 , q_1 and q_2 are expressed in term of the parameter $\sigma = ik_0 \Delta r$ as:

$$p_1 = \frac{3 + \sigma}{4}; \quad p_2 = \frac{\sigma^2 + 6\sigma + 3}{48};$$

$$q_1 = \frac{3 - \sigma}{4}; \quad q_2 = \frac{\sigma^2 - 6\sigma + 3}{48};$$

Numerically, this leads to an implicit integration scheme of the form:

$$[1 + q_1 \mathcal{L}_h + q_2 \mathcal{L}_h^2] \psi_h^{n+1} = [1 + p_1 \mathcal{L}_h + p_2 \mathcal{L}_h^2] \psi_h^n \quad (8)$$

Here \mathcal{L}_h and \mathcal{L}_h^2 represent the centered difference approximations to the partial differential operators \mathcal{L} and \mathcal{L}^2 with respect to the variable z . This corresponds to a linear system with pentadiagonal matrices. The resolution is performed with a standard LU decomposition method. We used a vertical step Δz of $\lambda/4$ and an horizontal marching step Δr of λ (λ is the wave length corresponding to the highest frequency of interest). The ground is considered as a rigid boundary. A non reflecting boundary condition is imposed at the top of the computational domain by adding an absorption layer of several wavelengths thickness, so that no significant energy is artificially introduced from the upper boundary of the mesh. The details of the method and its application for continuous wave propagation through a turbulent atmosphere can be found in Chevret ([3]) and Chevret *et al.* ([4]).

The time domain solution $P(r, z, t)$ is then computed by Fourier transform of $\frac{1}{\sqrt{r}} \psi(r, z, f)$. Because of the phase factor $e^{-i\omega \frac{r}{c_0}}$, the pressure field P is shifted around $t_0 = \frac{r}{c_0}$. For the numerical simulations presented in this paper, we chose an initial pulse centered around $f_0 = 500\text{Hz}$, with a Gaussian envelope :

$$P(0, 0, t) = \exp(-t^2/\tau_0^2) \cos(2\pi f_0 t). \quad (9)$$

The frequency response of the initial pulse is then:

$$H(f) = \frac{\tau_0 \sqrt{\pi}}{2} [\exp(-\alpha(f - f_0)^2) + \exp(-\alpha(f + f_0)^2)] \quad (10)$$

where $\alpha = \pi^2 \tau_0^2$ is equal to 2×10^{-5} (the bandwith Δf defined at -3dB is equal to 380Hz , see Fig. 2). The field $\psi(r, z, f)$ is computed for 64 frequencies between 0Hz and 1000Hz . Then the pressure $P(r, z, t)$ is evaluated with a fast Fourier transform over 256 points using a zero-padding technique to increase the time resolution.

3 Refraction index modeling

Here, we consider that the temperature fluctuations in the atmosphere are the only cause of the fluctuations of the sound speed c . To take into account the atmospheric turbulence in our numerical simulations we split the refraction index n in two components, i.e. a mean part $\langle n \rangle = c_0/c$ and a fluctuating part $\mu = -T'/2T_0$ (T_0 is the temperature reference). We simplify the problem by assuming that $\langle n \rangle$ varies only with the height above the ground z and that $T'(\vec{x})$ is a function only of z and the horizontal distance r .

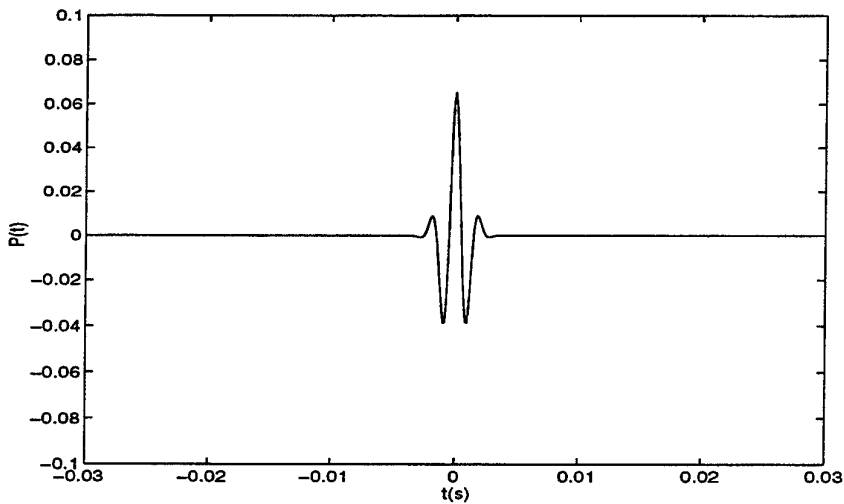


Figure 1: Time evolution of the initial pulse

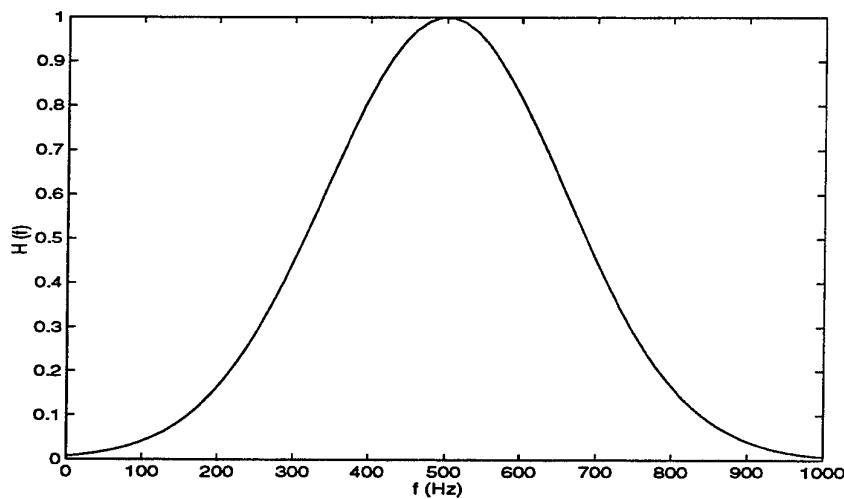


Figure 2: Frequency spectrum of the pulse

In this paper the turbulence is considered as isotropic and homogeneous and the spectral density of the turbulent eddies is modeled using a Gaussian distribution. Even though it is a simplified model for atmospheric turbulence near the ground, this approximation has been used successfully by Daigle *et al.* ([5]) to explain outdoors sound propagation experiments. It has also been introduced in numerical simulations to predict the effects of turbulence in an upward-refracting atmosphere by Gilbert *et al.* ([6]), Juvé *et al.* ([7]) and Havelock *et al.* ([8]). Assuming that the turbulence is frozen, the temperature fluctuations T' at a point \vec{x} can be represented by a sum of N random Fourier modes:

$$T'(\vec{x}) = \sum_{i=1}^N T(\vec{K}^j) \cos(\vec{K}^j \cdot \vec{x} + \varphi^j) \quad (11)$$

In the decomposition (11), for each Fourier mode, we have to choose four parameters: the modulus K^j and the orientation θ^j of the turbulent wave vector \vec{K}^j in Fourier space, the amplitude $T(\vec{K}^j)$ of the mode and the phase angle φ^j . To obtain a statistically homogeneous and isotropic field, θ^j and φ^j must be independent random variables with uniform distribution over $[0, 2\pi[$. The amplitude of each mode is picked from a prescribed energy spectrum $G(K)$. If the random field $T'(\vec{x})$ is characterized by a Gaussian correlation function, the associated energy spectrum is given by:

$$G(K) = \frac{\theta^2}{4} KL^2 \exp\left(-\frac{K^2 L^2}{4}\right) \quad (12)$$

where L is related to the integral scale of the turbulence l_{int} ($l_{\text{int}} = \sqrt{\pi}/2 L$). $G(K)$ is sampled uniformly by N values $K^j = ||\vec{K}^j||$ between a minimum value K_{\min} and a maximum value K_{\max} chosen so that the energetics of the field is well represented. The number of modes N is 100, the minimum value K_{\min} and the maximum value K_{\max} are respectively $0.1/L$ and $6/L$ with $L = 1.1$ m. The r.m.s. value of the index fluctuations μ_{rms} is equal to 1.414×10^{-3} .

Here we particularly focus on the propagation of acoustic waves in an upward refracting atmosphere. The sound speed profile $c(z)$ is defined as:

$$\begin{cases} c(z) = c_0 + a \ln(z/d) & z \geq z_0 \\ & \\ & = c_0 + a \ln(z_0/d) & z < z_0 \end{cases} \quad (13)$$

where $c_0 = 340$ ms $^{-1}$, $z_0 = 0.01$ m, $d = 6 \times 10^{-3}$ and $a = -2$ m/s (strong upward refraction).

4 Results for sound propagation over a rigid boundary

We now study the propagation of an acoustic pulse in an upward refracting atmosphere over a rigid boundary. In all the results discussed in this section the height of the source is $z_s = 5$ m. As illustrated on Fig. 3 by ray tracing, an acoustic shadow zone appears in the vicinity of the ground when the sound speed gradient is negative. In the following part

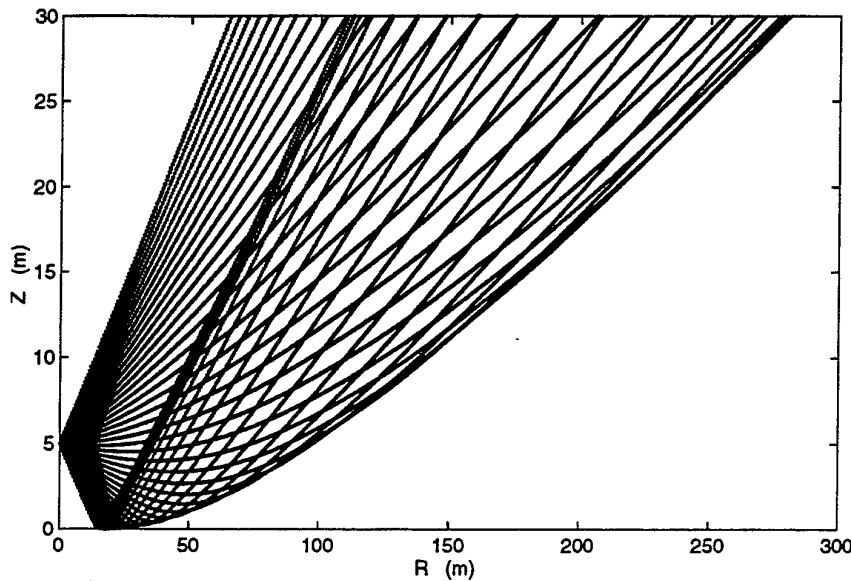


Figure 3: Ray trace for the upward-refracting sound speed profile

of this paper we will concentrate on energetic aspects; consequently only the amplitude of the pulse will be considered.

For a fixed height of the receiver $z_r = 5 \text{ m}$, we plot on Fig. 4 the amplitude level of the pulse $20 \log_{10}(\|P(r, z, t)\|)$ as a function of the distance r and of the reduced time $t - \frac{r}{c_0}$. On this figure, when the receiver is close to the source ($r < 50\text{m}$), we clearly identify the direct and the reflected paths which are well separated in time. For larger distances of propagation ($50\text{m} < r < 200\text{m}$), the direct and reflected paths merge and the amplitude of the signal decrease quickly as the receiver is moved inside the shadow zone. For $r > 200\text{m}$ the signal disappears almost completely. On Fig. 5 we have the same plot for one realization of the turbulent field. For short distances of propagation ($r < 100\text{m}$), the two plots look very similar. However, it appears that due to the turbulence scattering the pulse persists in the refractive shadow zone. Even in the deep shadow zone ($r > 200\text{m}$), it is still possible to identify a signal with arrival time in a well defined interval.

To clearly visualize this phenomena we plot the amplitude level as a function of time and altitude for two distances of propagation ($r = 120 \text{ m}$ and $r = 240 \text{ m}$). According to the ray-tracing of Fig. 3, the limit of the shadow zone in the z direction is $z = 7.25 \text{ m}$ for $r = 120 \text{ m}$ and $z = 24.5 \text{ m}$ for $r = 240 \text{ m}$. For $r = 120 \text{ m}$ (Fig. 7) the effects of turbulence are weak and the variations of the arrival time of the pulse are small with a maximum of 10ms near the ground ($z < 2\text{m}$). When the receiver is located in the deep shadow zone ($r = 120 \text{ m}$), the effects of turbulence are of great importance. If we compare Fig. 8 and Fig. 9, we see that the pulse can reach the ground ($0\text{m} < z < 10\text{m}$) with a significant amplitude and its arrival time is spread out in a band of width 20ms .

To illustrate the variability of the acoustic signal at the receiver location we plot the

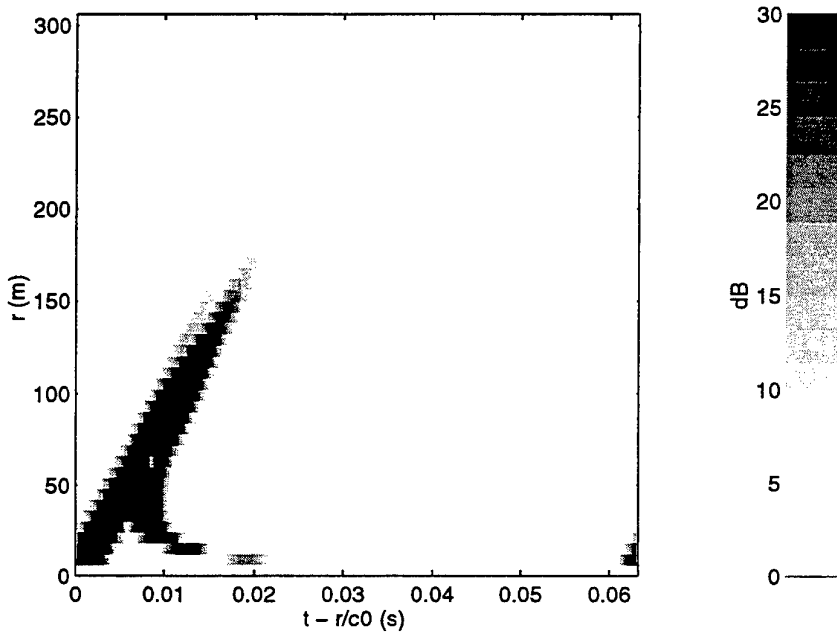


Figure 4: Evolution with the distance of propagation r of the amplitude level of the pulse for a non turbulent atmosphere ($z_s = z_r = 5 \text{ m}$)

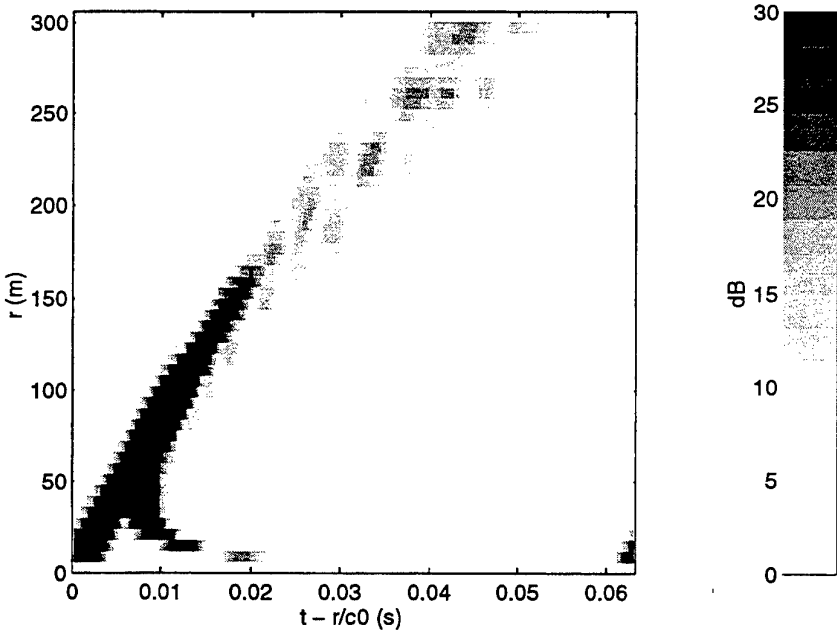


Figure 5: Evolution with the distance of propagation r of the amplitude level of the pulse for one turbulent realization ($z_s = z_r = 5 \text{ m}$)

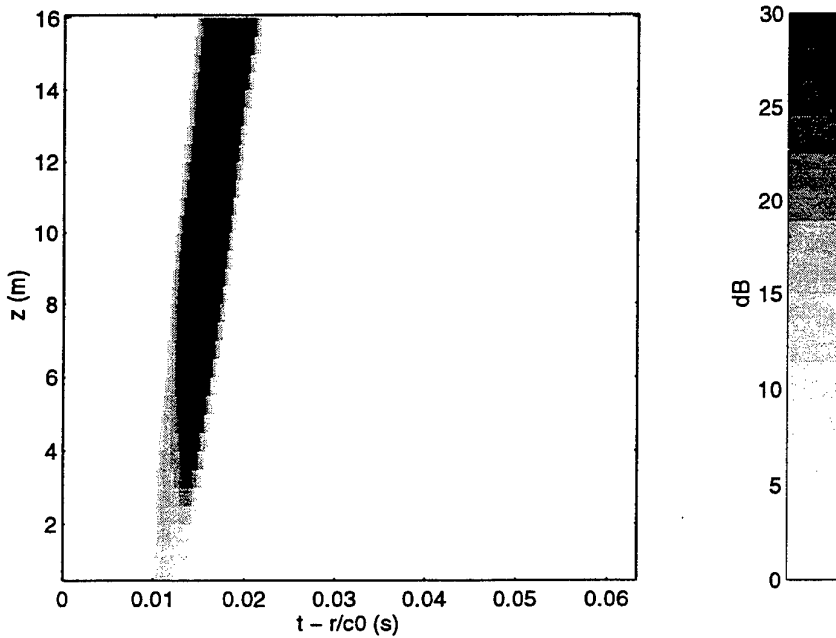


Figure 6: Evolution with the altitude z of the amplitude level of the pulse for a non turbulent atmosphere ($z_s = 5$ m and $r = 120$ m)

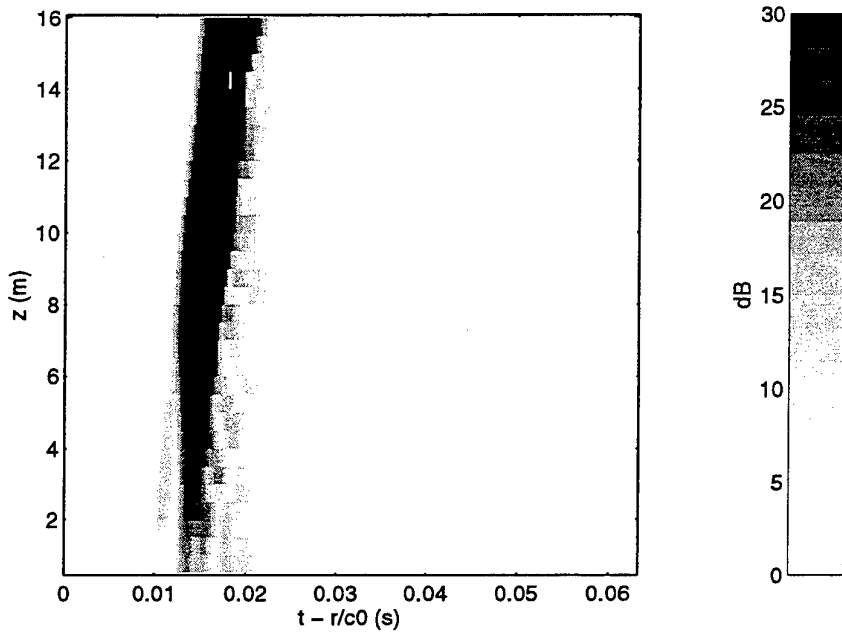


Figure 7: Evolution with the altitude z of the amplitude level of the pulse for one turbulent realization ($z_s = 5$ m and $r = 120$ m)

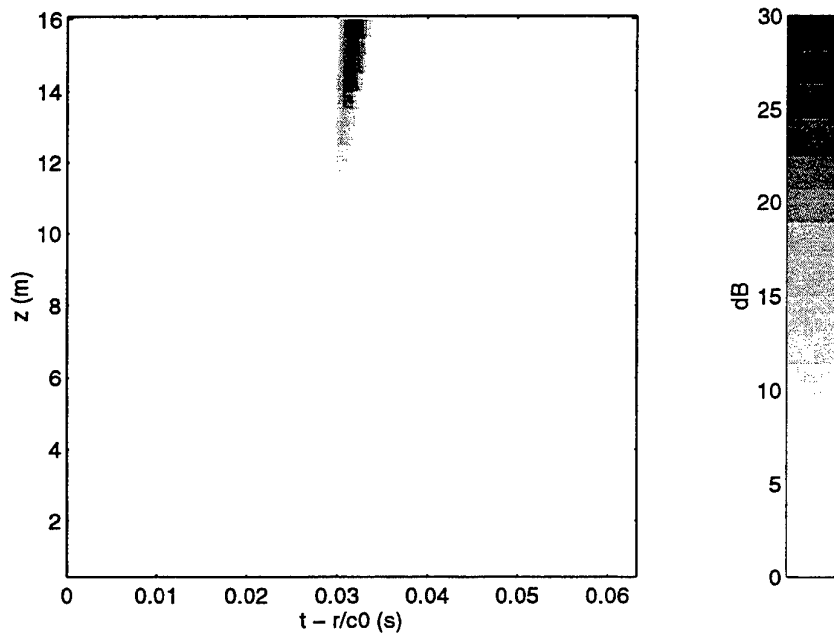


Figure 8: Evolution with the altitude z of the amplitude level of the pulse for a non turbulent atmosphere ($z_s = 5$ m and $r = 240$ m)

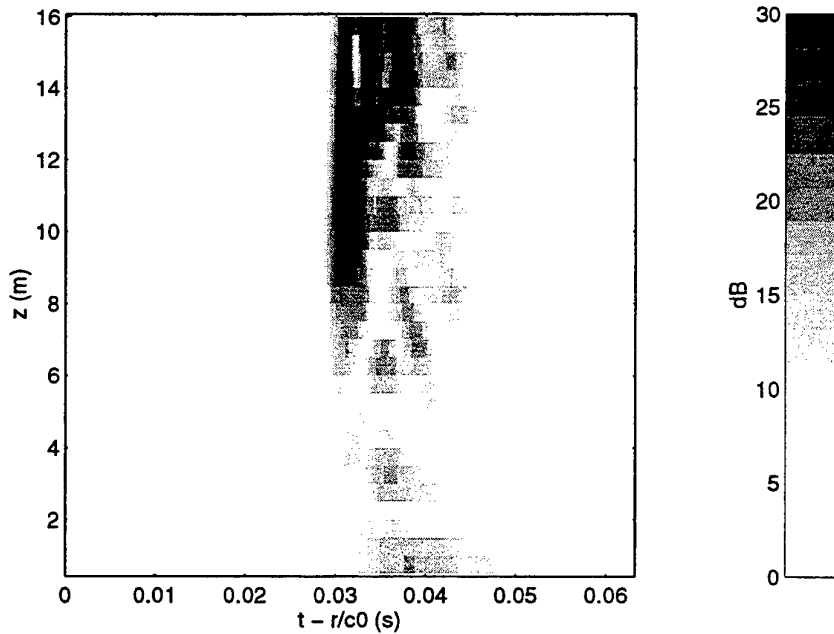


Figure 9: Evolution with the altitude z of the amplitude level of the pulse for one turbulent realization ($z_s = 5$ m and $r = 240$ m)

amplitude level $\|u \sqrt{r}\|$ as a function of the reduced time and of the realization number of the turbulent field N_{real} (see Fig.10-12). The height of the source and of the receiver are equal to 5 m, and the distances of propagation are respectively $r = 42$ m; 120 m; 240 m. As expected, for short distances of propagation (Fig. 10-11) the perturbations of the signal are weak. For $r = 42$ m (Fig. 10) there are no amplitude modulations of the signal and no fluctuations in the arrival time of the direct and of the reflected paths. At the beginning of the shadow zone (Fig. 11), we identify one signal arriving at a practically fixed time, and we note some fluctuations in the amplitude. When the receiver is located in the deep shadow zone (Fig. 12), the signature of the signal is very different from one realization to another one. The amplitude is reduced by a factor of 20 with respect to the level at $r = 42$ m, and strong fluctuations appear. The signal exhibits drop-outs (for example $N_{real} = 3$ on Fig. 12) and multiple arrival times with large fluctuations from one realization to another. These examples give an interesting way of visualization of the distortion introduced by turbulence in the shadow zone. They reveal the complexity of the arrival-time structure of the transmitted pulse, and the intermittency of the mean square pressure.

In addition, we compute the transmitted square pressure $P^2(t)$ of the pulse. For comparison we plot on the same figures: i) the results obtained without turbulence, ii) the results obtained for each realization of the turbulent field, iii) the mean square pressure averaged over 10 realizations. On these figures we have also indicated the limit of the shadow zone estimated from the ray-tracing figure (3). On Fig. 13 we plot the evolution of $P^2(t)$ with the distance of propagation r for a receiver located at 5 m from the ground. For short distances, $r < 100$ m (the limit of the shadow zone), the variations from one realization to another one are less than 3 dB, and the mean square pressure is practically equal to its "deterministic" value. When the distance of propagation increases, the influence of turbulence becomes important; we observe that the mean square pressure reaches a uniform level independent of r . We note also that the variations from one realization to another one can reach up to 20 dB.

On Fig. 14-16 we plot the transmitted mean square pressure $P^2(t)$ as a function of height, at different distances of propagation, respectively $r = 42$ m; 120 m; 240 m. We clearly see that as soon as the receiver is located inside the shadow zone the mean square pressure exhibits large fluctuations depending of the realization of the turbulent field. In the deep shadow zone ($r = 240$ m, Fig. 16) we note an "instantaneous" fluctuation of 20 dB close to the ground ($z < 6$ m).

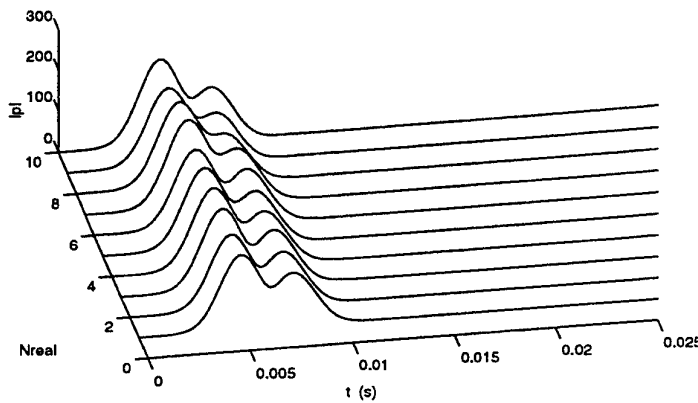


Figure 10: Amplitude level of the received pulses at $z_r = 5 \text{ m}$ and $r = 42 \text{ m}$, for different realizations N_{real} of the turbulent field.

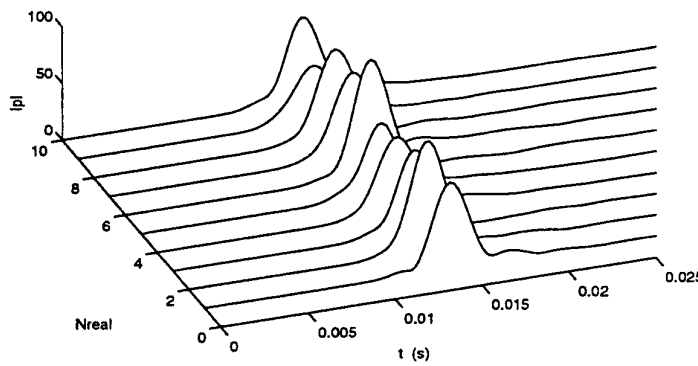


Figure 11: Amplitude level of the received pulses at $z_r = 5 \text{ m}$ and $r = 120 \text{ m}$, for different realizations N_{real} of the turbulent field.

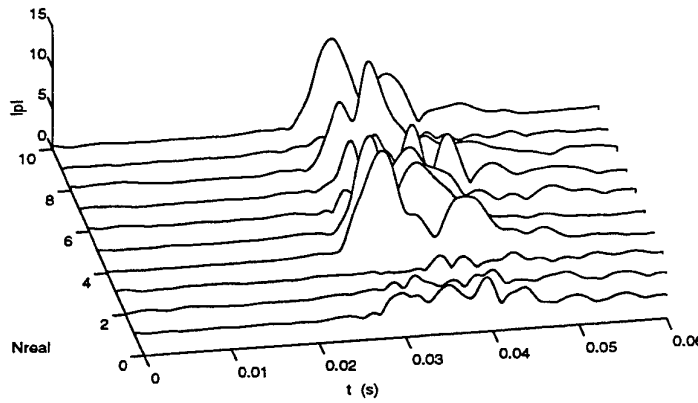


Figure 12: Amplitude level of the received pulses at $z_r = 5 \text{ m}$ and $r = 240 \text{ m}$, for different realizations N_{real} of the turbulent field.

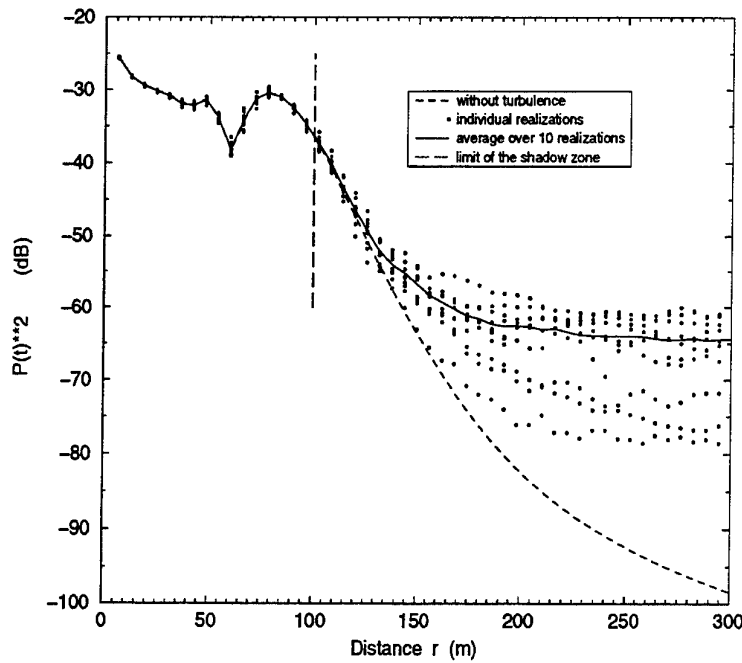


Figure 13: Evolution with the distance of propagation of the mean square pressure of the pulse ($z_s = z_r = 5 \text{ m}$)

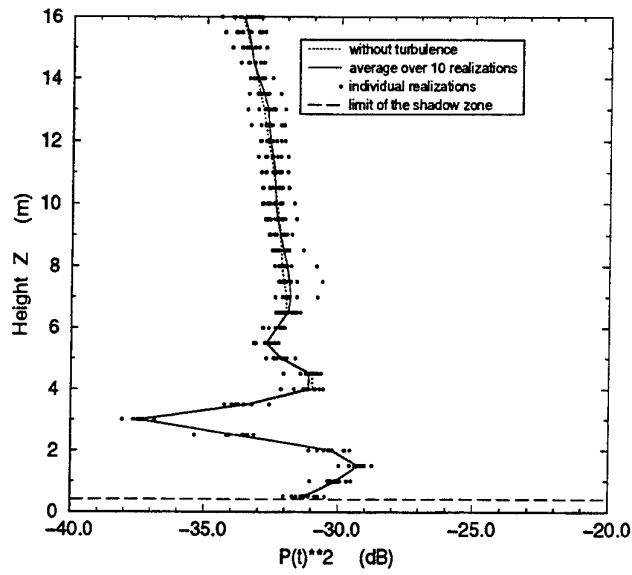


Figure 14: Evolution with the altitude z of the mean square pressure of the pulse for a distance $r = 42 \text{ m}$

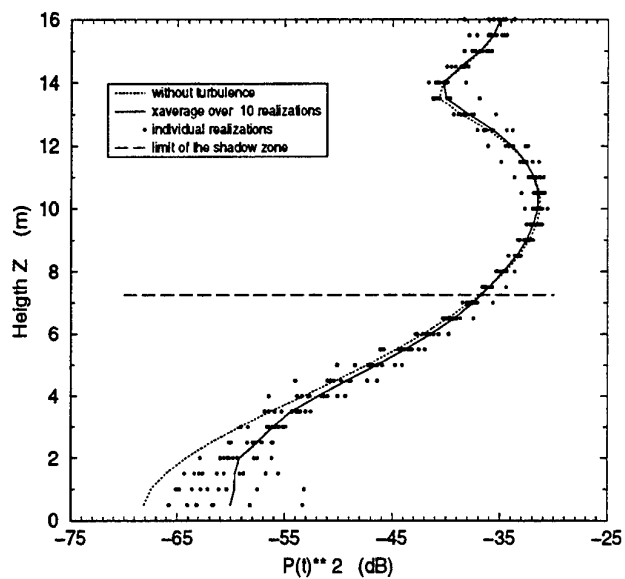


Figure 15: Evolution with the altitude z of the mean square pressure of the pulse for a distance $r = 120\text{ m}$

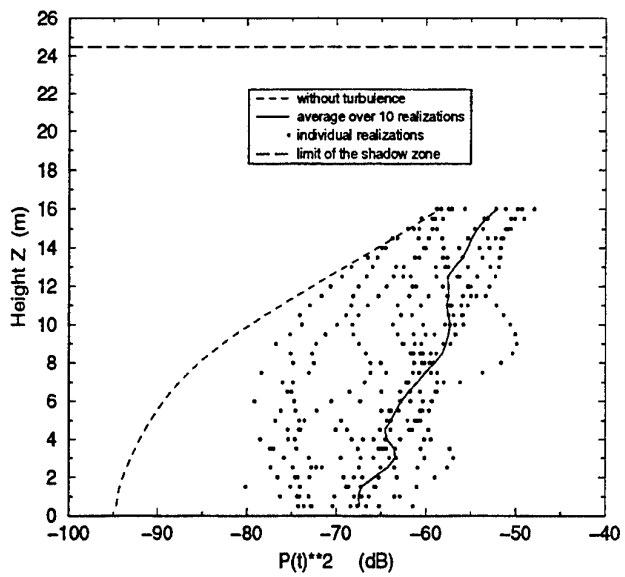


Figure 16: Evolution with the altitude z of the mean square pressure of the pulse for a distance $r = 240\text{ m}$

5 Conclusion

In this paper we have presented a numerical model to simulate the propagation of a pressure pulse in the atmosphere, near the ground and with the combined effects of turbulence and mean sound speed gradients. In our model a time-independent turbulent medium is generated by a set of realizations of random fields composed of a series of Fourier modes. The propagation of an acoustic pulse with a Gaussian spectrum is then performed via Fourier synthesis. In a first step each frequency component of the signal is propagated using a wide angle parabolic equation; and in a second step the acoustic pressure in the time-domain is computed using a fast Fourier transform.

Results have been given for sound propagation over long distances under strong upward-refraction conditions. The spatial variability of the time signatures in the shadow zone are illustrated and energetics aspects are discussed for individual realizations of the turbulent field. Because of the turbulent fluctuations, each frequency component of the pulse is scattered in a different way. As a consequence, when the distance between the source and the receiver increases, the arrival time structure of the pulse becomes more and more complex with additional echoes due to multi-path propagation. We also noticed that in the deep shadow zone, the mean square pressure becomes very intermittent with instantaneous fluctuations(up to 20dB in the studied cases).

Acknowledgment

This research was supported in part by CNRS under Project IDRIS n° 960742.

References

- [1] M. D. Collins *The time-domain solution of the wide-angle parabolic equation including the effects of sediment dispersion*. J. Acoust. Soc. Am., 84:2214–2125, 1988
- [2] L. Nghiem-Phu, and F. Tappert. *Modeling of reciprocity in th time domain using the parabolic method*. J. Acoust. Soc. Am., 78:164–171, 1985.
- [3] P. Chevret. *Simulation numérique des effets de la turbulence sur la propagation du son dans l'atmosphère*. PhD thesis, Ecole Centrale de Lyon, 1994. n° 94-18.
- [4] P. Chevret, Ph. Blanc-Benon, and D. Juvé *A numerical model for sound propagation through a turbulent atmosphere near the ground* . J. Acoust. Soc. Amer., 1996, (to appear).
- [5] G. A. Daigle, J. E. Piercy, and T. F. W. Embleton. *Line-of-sight propagation through atmospheric turbulence near the ground*. J. Acoust. Soc. Am., 74:1505–1513, 1983.
- [6] K. E. Gilbert, R. Raspet, and X. Di. *Calculation of turbulence effects in an upward-refracting atmosphere*. J. Acoust. Soc. Am., 87:2428–2437, 1990.
- [7] D. Juvé, Ph. Blanc-Benon, and P. Chevret. *Sound propagation through a turbulent atmosphere: influence of the turbulence model*. In *Proceedings of the Sixth Internationnal Symposium on Long Range Sound Propagation*, pages 270–282, Ottawa, June 1994. Canada.
- [8] D. I. Havelock, X. Di, G. A. Daigle, and M. R. Stinson. *Spatial coherence of a sound field in a refractive shadow: Comparison of simulation and experiment*. J. Acoust. Soc. Am., 98:2289–2302, 1995.

Distorted-wave Born approximation analysis of sound levels in a refractive shadow zone

K.E. GILBERT, X. DI, and R.R. KORTE

*Applied Research Laboratory and the Graduate Program in Acoustics,
Pennsylvania State University, State College PA, 16804, U.S.A.
FAX (1) 814-863-8783*

ABSTRACT

Almost forty years ago, Weiner and Keast observed that octave-band sound pressure levels in a refractive shadow zone depend weakly on frequency. Precise continuous-wave (cw) measurements made recently by Havelock et al. show a significantly stronger frequency dependence, a decrease of approximately 9 dB in going from 210 Hz to 940 Hz. We have found that both the weak frequency dependence seen by Weiner and Keast and the stronger frequency dependence seen by Havelock et al. can be predicted with parabolic equation calculations using a Kolmogorov spectrum for small-scale turbulence. The parabolic equation calculations, however, provide little understanding of the physical mechanisms that control the frequency dependence. In order to gain insight into the reasons for the observed frequency dependence, we use the "distorted-wave Born approximation" (DWBA) to analyze the experiments. We focus our attention on the precise cw measurements of Havelock et al. and analyze them in some detail. Using the DWBA, the problem of scattering from turbulence is formulated in terms of a "sampling function" which allows a more direct physical interpretation of scattering into a shadow zone than is possible with parabolic equation calculations. It is shown that in the experiment of Havelock et al., where the source and receivers were nearly on the ground, the frequency dependence is due mainly to interference between the direct path and the ground reflected path. For an experiment where the source and receivers are elevated, such as that of Weiner and Keast, the interference tends to "average out," and as a consequence, the shadow zone levels depend weakly on frequency.

INTRODUCTION

The purpose of the analysis presented here is to understand the physical mechanisms that control the frequency dependence of the sound pressure levels in a refractive shadow zone. The approach used, the so-called "distorted-wave Born approximation" (DWBA),¹ is the same as that in Ref. 2 except that the calculations are done in

wavenumber space (k -space) instead of coordinate space (R -space) as was done earlier. The wavenumber approach used in the present analysis has the advantage that the shadow zone levels can be directly related to the turbulence spectrum. In applying the approach, we have limited our investigation mainly to the measurements of Havelock et al.,^{3,4} since these data are apparently the only existing tonal measurements that cover a significant range of frequencies and have closely spaced receivers over the entire measurement distance. We begin with a brief discussion of the experiment geometry and the experimental results relevant to the theoretical analysis. For the details of the experiment, see Ref. 4.

The geometry of the experiment of Havelock et al. is shown in Fig. 1. The source was at .3 m, and the receivers were at .1 m and extended over a range of 700 m. The propagation was almost directly upwind. Nine tones at frequencies ranging from 40 Hz to 940 Hz were broadcast, and average levels were determined from 10-minute samples. At the two lowest frequencies, 40 Hz and 90 Hz, turbulence effects were negligible for the distances involved. Consequently, we consider here only the higher frequencies, 210 Hz to 940 Hz.

An initial key to understanding the measured frequency dependence of the shadow zone levels came from Juvé et al. who observed that it is important to accurately represent the inertial subrange in predictions of sound levels in shadow zones.⁵ That is, one should use a spectral representation consistent with measured power-law spectra which vary as (wavenumber)^{-5/3} in one dimension.⁶ The importance of the observation of Juvé et al. is demonstrated in Fig. 2 which shows predictions for the average relative sound pressure levels for the experiment of Havelock et al. The levels in Fig. 2 are ensemble averages for 200 realizations computed with a Kolmogorov spectrum (Fig. 2a) and with a gaussian spectrum (Fig. 2b). The Kolmogorov spectrum was inferred from measurements of horizontal windspeed made at the experiment site. As will be discussed, the spectrum used to represent small-scale turbulence can have a large effect on the predicted frequency dependence of shadow zone levels. For example, for the Kolmogorov spectrum, the predicted spread of levels in the shadow zone is approximately 9 dB between 210 Hz and 940 Hz and agrees well with the level spread observed by Havelock et al. In contrast, for the gaussian spectrum the predicted level spread is approximately 20 dB and consequently greatly overestimates the observed frequency dependence.

It is clear that using a Kolmogorov spectrum gives much better agreement with experiment. Nevertheless, an important question remains to be answered: "Why is the variation with level as large as 9 dB in the experiment of Havelock et al.?" As mentioned in the Abstract, the data of Weiner and Keast show very little frequency dependence for the shadow zone levels.⁷ Further, simple plane-wave Born approximation cal-

culations predict that for a Kolmogorov spectrum and a constant scattering volume, the shadow zone levels should vary weakly with frequency: Level \propto (frequency) $^{1/3}$ or 1 dB per octave.

In order to take a direct, systematic approach to the question of the dependence of shadow zone levels on frequency, we apply the DWBA. The DWBA is a generalization of the usual plane-wave Born approximation in that it accounts for a point source and for refracted (distorted) waves. Using the DWBA, the problem of scattering by turbulence is formulated in terms of a "sampling function" that shows what part of R -space and k -space are sampled by the acoustic field. The sampling function allows a straightforward analysis of the physical mechanisms that control the frequency dependence of shadow zone level.

The theory for the sampling function approach is given in Section I. Section II uses the sampling function theory to analyze the frequency dependence in the measurements of Havelock et al. A summary and our conclusions are given in Section III.

I. SAMPLING FUNCTION FORMULATION

In this section we outline the theory for the sampling function approach used to analyze the levels in a refractive shadow zone. In the analysis given here, the index of refraction fluctuations are treated as a homogenous, isotropic random scalar field. For the windy conditions that prevailed during the experiment of Havelock et al., the index of refraction fluctuations were dominated by fluctuations in the vector wind component in the direction of propagation. Hence, in reality, the refractive index fluctuations were not strictly isotropic. However, for ground-to-ground propagation into a shadow zone, the isotropic approximation is reasonably accurate⁸ and is certainly sufficient for the analysis given here.

To begin, we consider the inhomogeneous wave equation for the acoustic field due to a point source in a medium with a fluctuating index of refraction, n :

$$\nabla^2 G(\vec{R}, \vec{R}') + k_0^2 n^2 G(\vec{R}, \vec{R}') = -4\pi\delta(\vec{R} - \vec{R}'), \quad (1)$$

where k_0 is a reference wavenumber. The index of refraction is defined as the sum of a deterministic part n_d and a stochastic part μ : $n = n_d + \mu$. The deterministic part is taken to be a function only of z , while, at any instant of time, the stochastic part has arbitrary spatial variation. Hence the deterministic part of the wavenumber squared is

$$k_d^2 = k_0^2 n_d^2(z). \quad (2)$$

Similarly, at some instant of time, a “snapshot” of the fluctuating part is given by,

$$\delta k^2(\vec{R}) = k_0^2 \left(n_d(z) + \mu(\vec{R}) \right)^2 - k_0^2 n_d^2(z) \approx 2\mu(\vec{R})k_0^2. \quad (3)$$

Thus the wave equation we consider is

$$\nabla^2 G(\vec{R}, \vec{R}') + (k_0^2 n_d^2 + 2\mu k_0^2)G(\vec{R}, \vec{R}') = -4\pi\delta(\vec{R} - \vec{R}'). \quad (4)$$

To derive a sampling function formulation for acoustic propagation we need to write the wave equation in Eq.(4) as an integral equation. In terms of an integral equation, the acoustic field at a receiver point, \vec{R}_r , for a given point source at \vec{R}_s , is

$$G(\vec{R}_r, \vec{R}_s) = G_0(\vec{R}_r, \vec{R}_s) + \frac{1}{4\pi} \int G_0(\vec{R}_r, \vec{R}') \delta k^2(\vec{R}') G(\vec{R}', \vec{R}_s) d^3 \vec{R}', \quad (5)$$

where G_0 is deterministic and satisfies the same inhomogeneous wave equation as G , but with μ equal zero. Note that in Eq.(5), G_0 is the unperturbed (unscattered) field or the “insonifying field.” The scattered field is the second term on the right-hand side of Eq.(5) and is denoted here as δG_{rs} . Since δG_{rs} is the scattered field due to turbulence, it is a stochastic quantity and can be written as

$$\delta G_{rs} = k_0^2 \int W_{rs}(\vec{R}') \mu(\vec{R}') d^3 \vec{R}', \quad (6)$$

where W_{rs} is defined as

$$W_{rs}(\vec{R}') \equiv \frac{1}{2\pi} G_0(\vec{R}_r, \vec{R}') G(\vec{R}', \vec{R}_s). \quad (7)$$

The function $W_{rs}(\vec{R}')$ is called the “sampling” function because in R -space it defines what spatial volume is sampled by the acoustic wave.

As the formulation stands, it is exact and is entirely equivalent to the differential wave equation formulation in Eq.(4). The integral equation representation is important for our analysis because it allows systematic approximations to be made. For example, in the strongly insonified (non-shadow) region where the scattering takes place, δG is much less than G_0 . Hence, we can simplify the analysis considerably by treating the turbulence as a perturbation and approximating the total field ($G = G_0 + \delta G$) in the strongly insonified region as $G \cong G_0$. Then the sampling function in Eq.(7) becomes

$$W_{rs}(\vec{R}') \cong \frac{1}{2\pi} G_0(\vec{R}_r, \vec{R}') G_0(\vec{R}', \vec{R}_s). \quad (8)$$

Since we are interested here in what part of the turbulence spectrum is sampled rather than what part of space is sampled, we want to compute the integral in Eq.(6) in k -space instead of R -space. Hence we define the k -space forms of W_{rs} and μ :

$$\widetilde{W}_{rs}(\vec{k}) = \int e^{-i\vec{k}\cdot\vec{R}'} W_{rs}(\vec{R}') d^3\vec{R}'. \quad (9)$$

and

$$\tilde{\mu}(\vec{k}) = \int e^{-i\vec{k}\cdot\vec{R}'} \mu(\vec{R}') d^3\vec{R}'. \quad (10)$$

Then Eq.(6) becomes

$$\delta G_{rs} = k_0^2 \int \widetilde{W}_{rs}(\vec{k}') \tilde{\mu}^*(\vec{k}') d^3\vec{k}' / (2\pi)^3. \quad (11)$$

where $\tilde{\mu}^*(\vec{k}') = \tilde{\mu}(-\vec{k}')$.

Because of deterministic refraction upward and stochastic scattering downward, in the shadow region the deterministic field G_0 is much less than the stochastic field δG . Hence, the total field can be approximated as δG , so that the average level in the shadow region is

$$\langle |\delta G_{rs}|^2 \rangle = k_0^4 \int \int \widetilde{W}_{rs}(\vec{k}') \widetilde{W}_{rs}^*(\vec{k}'') \langle \mu^*(\vec{k}') \mu(\vec{k}'') \rangle d^3\vec{k}' d^3\vec{k}'' / (2\pi)^6. \quad (12)$$

After some straightforward manipulation Eq.(12) becomes

$$\langle |\delta G_{rs}|^2 \rangle = k_0^4 \int |W_{rs}(\vec{k}')|^2 \Phi(\vec{k}') d^3\vec{k}' / (2\pi)^3, \quad (13)$$

where the wavenumber spectrum $\Phi(\vec{k}')$ is the Fourier transform of the autocorrelation function $B(\vec{s})$:

$$\Phi(\vec{k}') = \int e^{i\vec{k}'\cdot\vec{s}} B(\vec{s}) d^3\vec{s}. \quad (14)$$

The turbulence is assumed to be homogeneous and isotropic so that the autocorrelation function $B(\vec{s})$ is a function only of $|\vec{s}|$, where $\vec{s} = \vec{R}' - \vec{R}$. The autocorrelation function itself is defined as

$$B(\vec{s}) = \langle \mu(\vec{R}) \mu(\vec{R} + \vec{s}) \rangle, \quad (15)$$

where $\langle \rangle$ denotes an ensemble average.

In the present application, the turbulence is taken to be two-dimensional, and the deterministic point-source solutions G_0 are computed with a parabolic equation algorithm.⁹ (Note that since G_0 is calculated without turbulence, it could be computed

with any algorithm that can handle a stratified medium such as, for example, the “fast-field program.”)

In terms of parabolic equation solutions, the two-dimensional sampling function is

$$W_{rs}^{2D}(x, z) = k_0^{3/2} \Gamma [\psi^{2D}(x, z) \psi^{2D}(|x - x_r|, z)], \quad (16)$$

where $\psi^{2D}(x, z)$ is the parabolic equation solution to a 2-D wave equation, and the constant Γ is

$$\Gamma = \frac{\exp(i k_0 x_r + \pi/4)}{\sqrt{2\pi x_r}}. \quad (17)$$

In the 2-D case, as in the 3-D case, we define the k -space sampling function as

$$\tilde{W}_{rs}^{2D}(\vec{k}) = \int W_{rs}^{2D}(x, z) e^{i(k_x x + k_z z)} dx dz. \quad (18)$$

Thus the average level in the shadow zone is

$$\langle |\delta G|^2 \rangle = k_0^3 \int |\tilde{W}_{rs}^{2D}(k_x, k_z)|^2 \Phi^{2D}(k_x, k_z) dk_x dk_z / (2\pi)^2, \quad (19)$$

where the 2-D turbulence spectrum is defined as

$$\Phi^{2D}(k_x, k_z) \equiv \int e^{i(k_x s_x + k_z s_z)} B(s_x, s_y = 0, s_z) ds_x ds_y \quad (20)$$

$$= \int \Phi(k_x, k_y, k_z) dk_y / (2\pi). \quad (21)$$

For isotropic turbulence, $\Phi^{2D}(k_x, k_z)$ can be written as a one-dimensional spectrum $\Phi^{1D}(k) = \Phi^{2D}(\sqrt{k_x^2 + k_z^2})$ where $k = \sqrt{k_x^2 + k_z^2}$, so that the two-dimensional integral in Eq.(19) can be reduced to one dimension:

$$\langle |\delta G|^2 \rangle = k_0^3 \int \Omega_{rs}^{1D}(k) \Phi^{1D}(k) k dk / (2\pi)^2, \quad (22)$$

where Ω_{rs}^{1D} is defined as $|\tilde{W}_{rs}^{2D}(k_x, k_z)|^2$ integrated over the polar angle θ in the (k_x, k_z) -plane:

$$\Omega_{rs}^{1D}(k) = \int |\tilde{W}_{rs}^{2D}(k, \theta)|^2 d\theta. \quad (23)$$

where $k = \sqrt{k_x^2 + k_z^2}$.

To give some idea of what the sampling functions W_{rs} and \tilde{W}_{rs} look like, in Fig. 3 we show gray-scale plots in (x, z) -space and (k_x, k_z) -space. The top panel in Fig. 3 shows $|W_{rs}^{2D}(x, z)|^2$ and the bottom panel shows $|\tilde{W}_{rs}^{2D}(k_x, k_z)|^2$, both for a frequency of 210 Hz. From the figure it is apparent that $|W_{rs}^{2D}(x, z)|^2$ extends over a large

volume of (x, z) -space. In contrast, $|\tilde{W}_{rs}^{2D}(k_x, k_z)|^2$ is relatively compact in (k_x, k_z) -space. Note especially that the spread in k_x values is significantly smaller than the spread in k_z values. For small-angle scattering, such a difference in the spreads of k_x and k_z is to be expected, because the vector Bragg wavenumber changes mainly in a direction perpendicular to the propagation direction (i.e., in the z -direction) and very little in the propagation direction itself (the x -direction).

For isotropic turbulence, as indicated in Eq.(22), the average level in a shadow zone can be written as an integral over a one-dimensional sampling function times the turbulence spectrum. In Fig. 4 we show the one-dimensional sampling function $\Omega_{rs}^{1D}(k)$ at 600 Hz and also the product of the turbulence spectrum $\Phi^{1D}(k)$ and $\Omega_{rs}^{1D}(k)$. It is clear from the figure that a relatively narrow band of wavenumbers contributes to the integral. (Note: Since the frequency in Fig. 4 is approximately three times greater than the frequency in Fig. 3, the wavenumber spread is also approximately three times greater.)

Figure 5 shows how the sampling region varies with frequency and what part of a Kolmogorov and Gaussian spectrum would be sampled at various frequencies. The arrows indicate the main part of k -space that contributes at each frequency. For reasons to be discussed in the next section, the arrows in Fig. 5 are drawn at heights (i.e., y -coordinates) proportional to the integral over $\Omega_{rs}^{1D}(k)$.

II. ANALYSIS OF FREQUENCY DEPENDENCE

In this section we consider an approximate analysis of the frequency dependence of the shadow zone levels in order to arrive at a better understanding of the physical processes involved. The analysis takes as its starting point the observation that, at a particular frequency and range, the band of wavenumbers contributing to the scattering is relatively narrow. Because the spread in wavenumbers is limited, the integral for the $\langle |\delta G|^2 \rangle$ in Eq.(22) can be evaluated at an average wavenumber and taken outside the integral:

$$\langle |\delta G|^2 \rangle = k_0^3 \Phi^{1D}(\bar{k}) \int \Omega_{rs}^{1D}(k) k dk / (2\pi)^2 \quad (24)$$

where we take \bar{k} to be the Bragg wavenumber for the mean scattering angle $\bar{\theta}$.

$$\bar{k} = \bar{k}_{Bragg} = 2k_0 \sin(\bar{\theta}/2) \quad (25)$$

The mean scattering angle can be estimated from ray tracing or gray-scale plots such as Fig. 1. For example, from Fig. 1 we can see that at a range of 700 m, the mean scattering angle (twice the propagation angle) is approximately 15° .

For a two-dimensional Kolmogorov spectrum, the associated one-dimensional spectrum $\Phi^{1D}(\bar{k})$ in Eq.(24) is proportional to (frequency) $^{-8/3}$, so that $k_0^3\Phi^{1D}(k)$ is proportional to (frequency) $^{1/3}$. The integral in Eq.(24) is the integral of $|\tilde{W}_{rs}|^2$ over (k_x, k_z) -space, which by Parseval's theorem, is the same as the integral of $|W_{rs}|^2$ over (x, z) -space. Hence, the integral in Eq.(24) can be interpreted as the effective scattering volume which we denote as V_{scat} . Thus, we have

$$V_{scat} = \int \Omega_{rs}^{1D}(k) dk / (2\pi)^2 \quad (26)$$

$$= \int |\tilde{W}_{rs}^{2D}(k_x, k_z)|^2 dk_x dk_z / (2\pi)^2 \quad (27)$$

$$= \int |W_{rs}^{2D}(x, y)|^2 dx dz \quad (28)$$

The dependence of $\langle |\delta G|^2 \rangle$ on frequency can hence be written in the form

$$\langle |\delta G|^2 \rangle \propto (\text{frequency})^{1/3} V_{scat} \quad (29)$$

Hence, for a Kolmogorov spectrum, we expect $\langle |\delta G|^2 \rangle$ to depend weakly on frequency as long as V_{scat} does not change with frequency. For the source-receiver geometry in the experiment of Havelock et al., however, V_{scat} decreases by more than a factor of ten (approximately 11 dB) as the frequency increases from 210 Hz to 940 Hz. In Fig. 5 the decrease in the scattering volume is indicated schematically by plotting the horizontal arrows at heights proportional to the integral in Eq.(28). The 11 dB decrease in scattering volume, together with a 2 dB increase (approximately) due to the factor $(\text{frequency})^{1/3}$, provides a quantitative explanation for the net 9 dB decrease in the shadow zone levels in the experiment of Havelock et al. in going from 210 Hz to 940 Hz.

The question to be answered at this point is: "What causes the scattering volume to decrease so dramatically with increasing frequency?" Figure 6, together with Fig. 1, can be used to arrive at an explanation. The dark "stripes" visible in Fig. 1 result from destructive interference between the source and its ground reflection. That is, the stripes are part of a dipole radiation pattern. For the frequency in Fig. 1 (940 Hz) the nulls in the dipole pattern are closely spaced, while at a lower frequency such as 210 Hz, the nulls are more widely spaced. The sampling function, which can be thought of as the "product" of a source dipole and a receiver dipole, is strongly affected by the frequency dependence of the dipole pattern. The frequency dependence is evident in Fig. 6 which shows the magnitude squared of the (x-z)-space sampling function $|W_{rs}^{2D}(x, y)|^2$ at 210 Hz (top) and 940 Hz (bottom). Since the constructive interference lobes are wide at 210 Hz, the scattering region is large. As the frequency increases from 210 Hz to 940 Hz, destructive interference leads to more closely spaced

nulls in the sampling volume so that the effective volume available for scattering is significantly reduced. At 940 Hz, the three small scattering regions visible in Fig. 6 result from multiplying together two dipole radiation fields having more closely spaced destructive interference nulls than at 210 Hz.

Surprisingly, in cases where the source and/or receiver are several wavelengths off the ground rather than almost on the ground, the destructive interference tends to "average out" so that the frequency dependence is lessened significantly. To demonstrate how the source and/or receiver height affect the frequency dependence of the shadow zone levels, we show in Fig. 7 predicted relative sound pressure levels at 210 Hz and 940 Hz for three cases. In case (a) the source is at .3 m, and the receivers are at .1 m. In case (b) the source has been raised to 4 m, while in case (c) both source and receiver are at 4 m. With both source and receiver 4 m off the ground, there is very little frequency dependence in the shadow zone sound levels. As was discussed in the Introduction, the Weiner-Keast measurements, which had elevated source and receivers, showed weak frequency dependence. The implication of the Weiner-Keast data and the calculations in Fig. 7 is that the experiment of Havelock et al., if repeated with elevated source and receivers, would show very weak frequency dependence for the sound levels in the refractive shadow.

III. SUMMARY AND CONCLUSIONS

Using a generalized perturbative method (DWBA), we have formulated the problem of scattering by turbulence in terms of a "sampling function". The approach allows a straightforward interpretation of the physical mechanisms that control the frequency dependence of average sound levels in a refractive shadow zone. The sampling function shows that a narrow band of wavenumbers contributes to the shadow-zone levels. Consequently, scattering into a refractive shadow zone can be simply viewed: the shadow-zone levels are proportional to $(k_0^4) \times (3\text{-D turbulence spectrum evaluated at the average Bragg wavenumber}) \times (\text{sampling volume})$. For 2-D turbulence, the factor k_0^4 becomes k_0^3 .

For situations where the scattering volume is constant, it was shown that a Kolmogorov spectrum leads to a weak frequency dependence for the shadow zone levels, $(\text{frequency})^{1/3}$. For elevated sources, as in the experiment of Weiner and Keast, the interference effects tend to average out so that the effective scattering volume is nearly constant. Consequently, for such experimental geometries, the sound levels in the shadow zone are weakly dependent on frequency.

For near-ground source and receivers, as in the experiment of Havelock et al., it was shown that multipath interference reduced the sampling volume dramatically

as the frequency went from 210 Hz to 940 Hz. The frequency dependent decrease of the scattering volume caused a corresponding decrease in the shadow zone levels with increasing frequency. It was conjectured that if the experiment of Havelock et al. were repeated with elevated source and receivers, the levels in the shadow region would depend weakly on frequency.

Finally, it is important to understand that the results of the analysis presented here apply only to the scattering of sound by turbulence in an upward-refracting atmosphere. For example, for downward-refracting propagation, the turbulence spectrum would be sampled at considerably smaller wavenumbers (larger turbulence scales), and hence would include wavenumbers outside the inertial subrange. Thus, even though the present analysis provides insight on the specific problem of turbulent scattering of sound into a shadow zone, it by no means fully addresses the more general problem of sound propagation in a turbulent atmosphere. In fact, the general problem can be theoretically investigated in a meaningful way only with a turbulence model that realistically represents the full spectrum of turbulent scales in the atmosphere. At present, no such model is available. Hopefully, in the near future, the atmospheric turbulence community will develop turbulence models that make it possible to include both inertial subrange structure and realistic large-scale atmospheric structure in acoustic propagation calculations.

ACKNOWLEDGMENTS

This work was supported by the Army Research Laboratory, the Defense Advanced Research Projects Agency, and the Applied Research Laboratory of Pennsylvania State University.

REFERENCES

1. L.S. Rodberg and R.M. Thaler, *Introduction to the Quantum Theory of Scattering* (Academic Press, New York, 1967).
2. K.E. Gilbert, X. Di, and L. Wang, "Distorted-wave Born approximation calculations for turbulence scattering in an upward-refracting atmosphere," Fourth International Symposium on Long-Range Sound Propagation, NASA Langley Research Center, Hampton, VA, May 16,17, 1990. NASA Conference Publication 3101, pp 211-225. Compiled by William L.Willshire, Jr.
3. D.I. Havelock, "Measurements of sound pressure levels within a refractive shadow," 29th meeting of NATO AC/243, Panel 3, RSG 11, Pennsylvania State University, State College, PA, September 26-30,1994.

4. X. Di, K.E. Gilbert, D.I. Havelock, M.R. Stinson, G.A. Daigle, "Wideband sound propagation in a refractive shadow zone," to be submitted to the J. Acoust. Soc. of Am.
5. D. Juvé, Ph. Blanc-Benon, and P. Chevret, "Sound propagation through a turbulent atmosphere: Influence of the turbulence model," Sixth International Symposium on Long-Range Sound Propagation, Ottawa, Canada, June 12-14, 1994.
6. R.B. Stull, *An Introduction to Boundary Layer Meteorology* (Kluwer Academic Publishers, Dordrecht, 1989).
7. F.M. Weiner and D.N. Keast, "Experimental study of the propagation of sound over ground," J. Acoust. Soc. of Am. **31**, 724-733 (1959).
8. X. Di and K.E. Gilbert, "On wind turbulence models for shadow-zone propagation: From measurement to simulation," to be submitted to the J. Acoust. Soc. of Am.
9. K.E. Gilbert and X. Di, "A fast Green's function method for outdoor sound propagation," J. Acoust. Soc. of Am. **94**, 2343-2352 (1993).

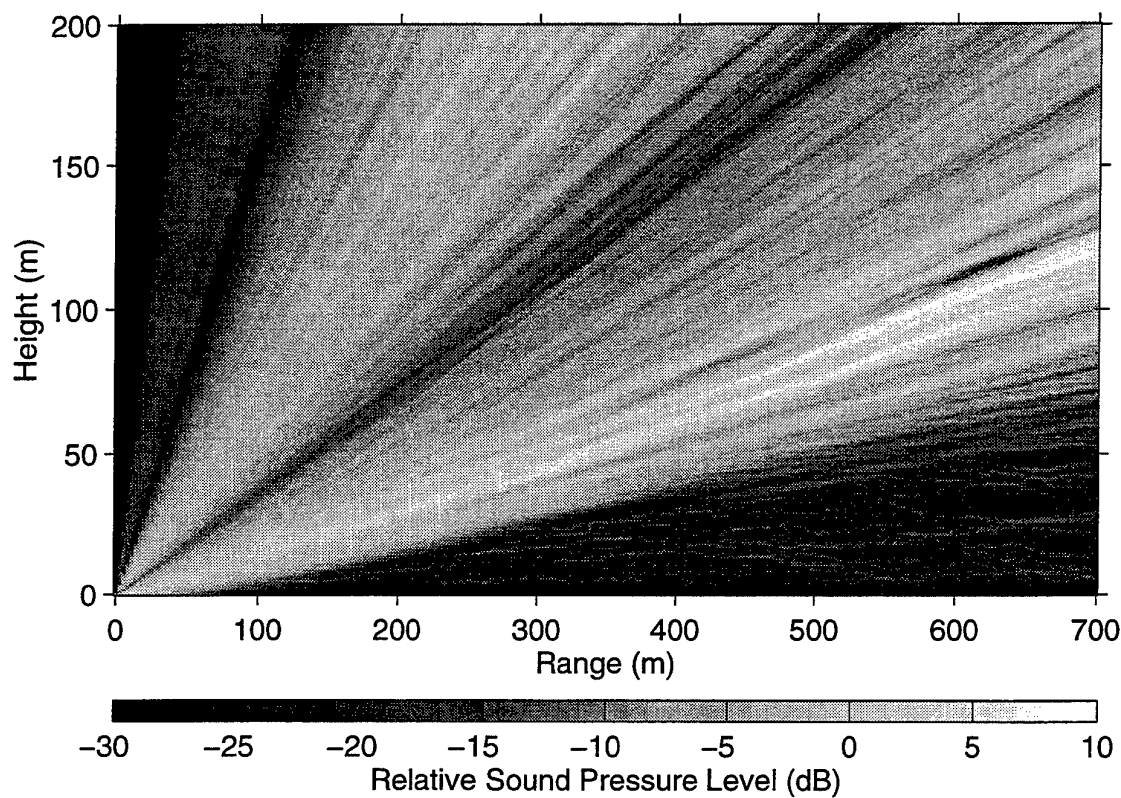


Fig. 1: Gray-scale plot of the relative sound pressure level for the experiment of Havelock et al. In the figure, the source height is 0.3 m and the frequency is 940 Hz. A Kolmogorov spectrum is used to represent the fluctuations in the index of refraction due to turbulence. The acoustic propagation is almost directly upwind.

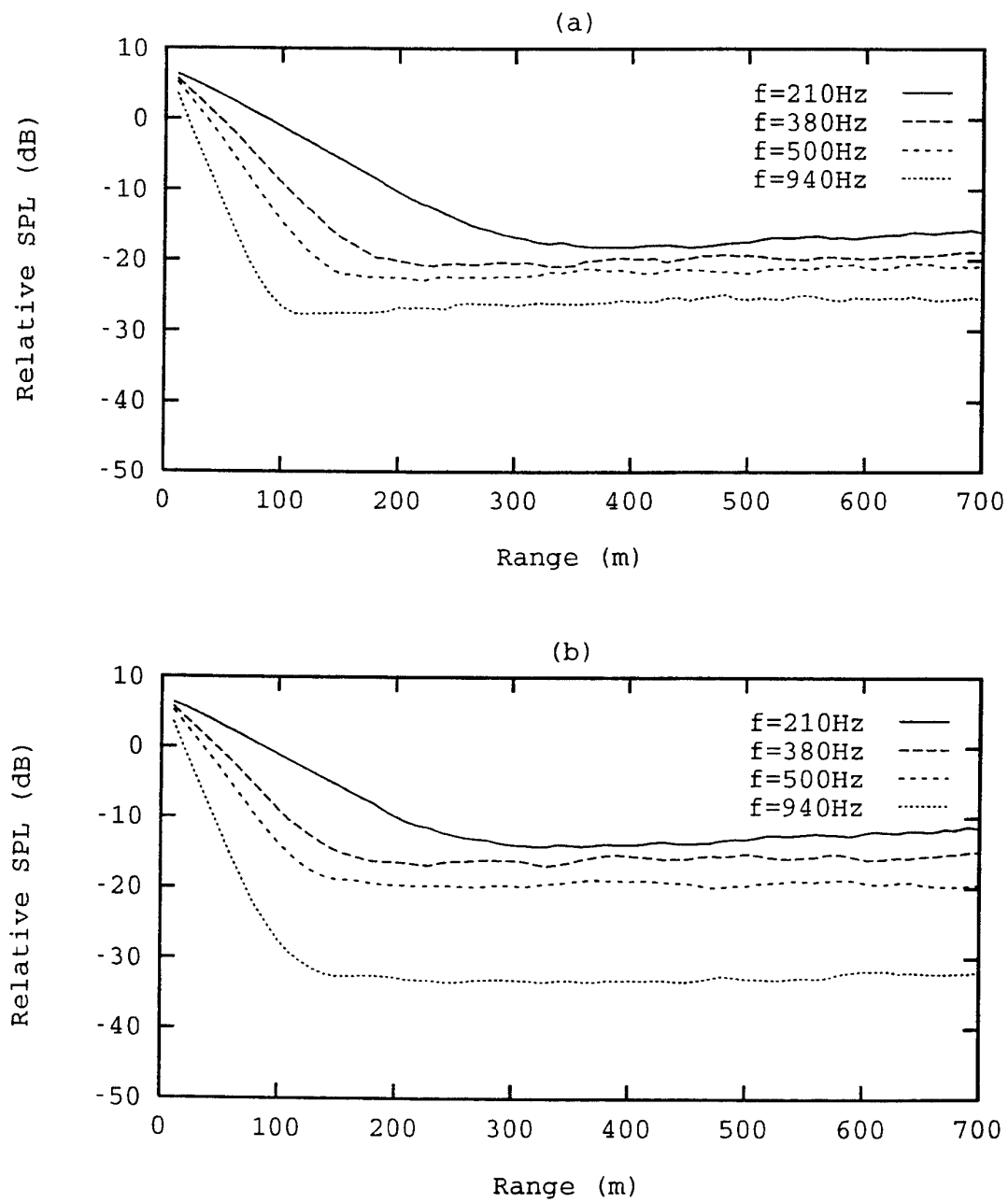


Fig. 2: Calculated frequency dependence of average relative sound pressure levels (SPL) in a refractive shadow: (a) for a Kolmogorov spectrum, and (b) for a Gaussian spectrum. Each curve is the ensemble average for 200 realizations of the turbulence model used. The predictions for the Kolmogorov spectrum are in good agreement with the data of Havelock et al., but the Gaussian spectrum significantly overestimates the dependence on frequency.

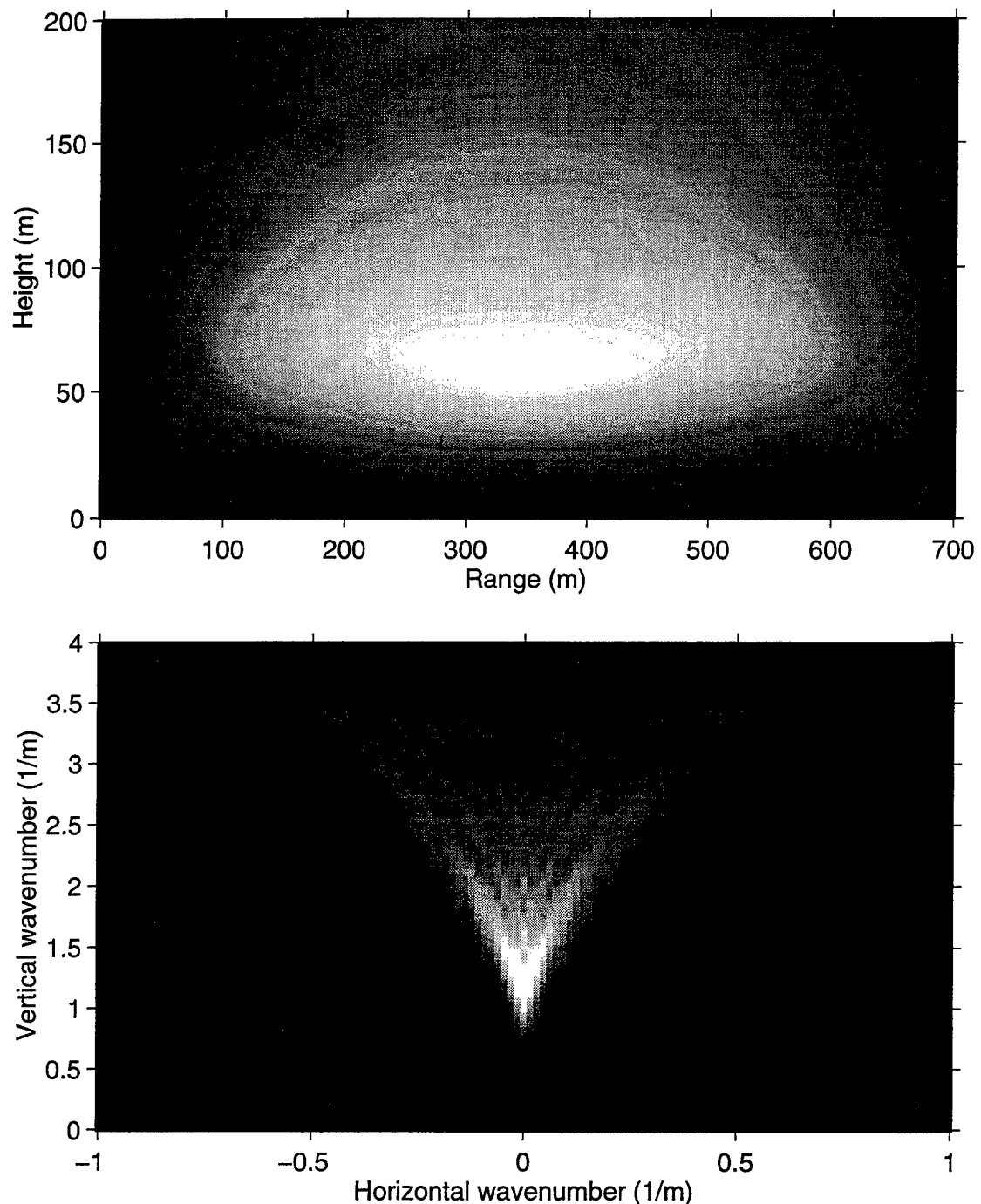


Fig. 3: Magnitude squared of the two-dimensional R -space sampling function $|W_{rs}(x, z)|^2$ (top). Magnitude squared of the two-dimensional k -space sampling function $|\tilde{W}_{rs}(k_x, k_z)|^2$ (bottom). In both figures, a shading change from white to solid black indicates a decrease of a factor of ten.

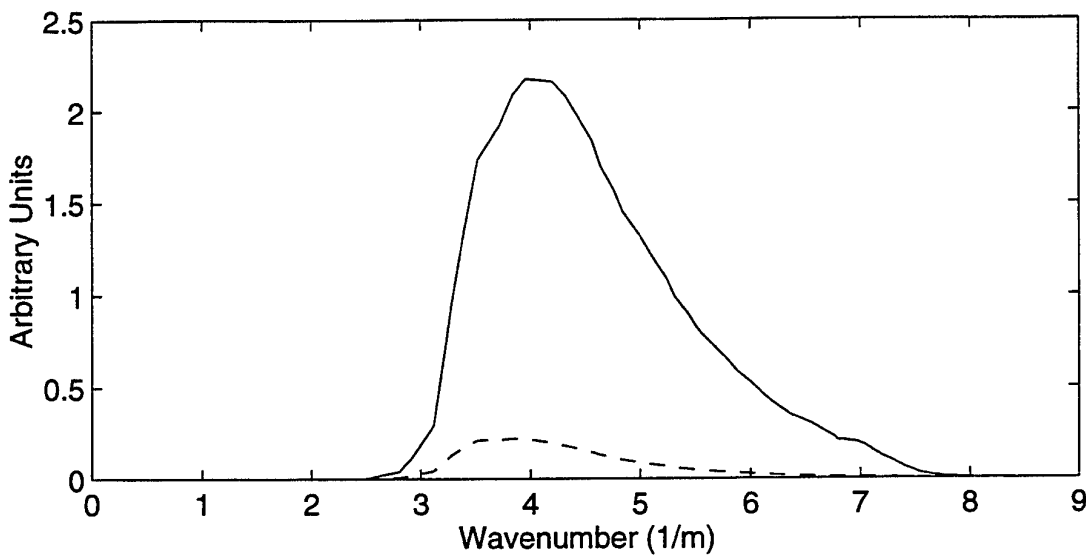


Fig. 4: The one-dimensional sampling function $\Omega_{rs}^{1D}(k)$ (solid line) and $\Phi^{1D}(k)\Omega_{rs}^{1D}(k)$ (dashed line), where $\Phi^{1D}(k)$ is the spectrum for index of refraction fluctuations due to turbulence. The sound level in a refractive shadow zone is proportional to the integral over $\Phi^{1D}(k)\Omega_{rs}^{1D}(k)$. Note that a relatively narrow band of wavenumbers contributes to the integral for the shadow zone sound level.

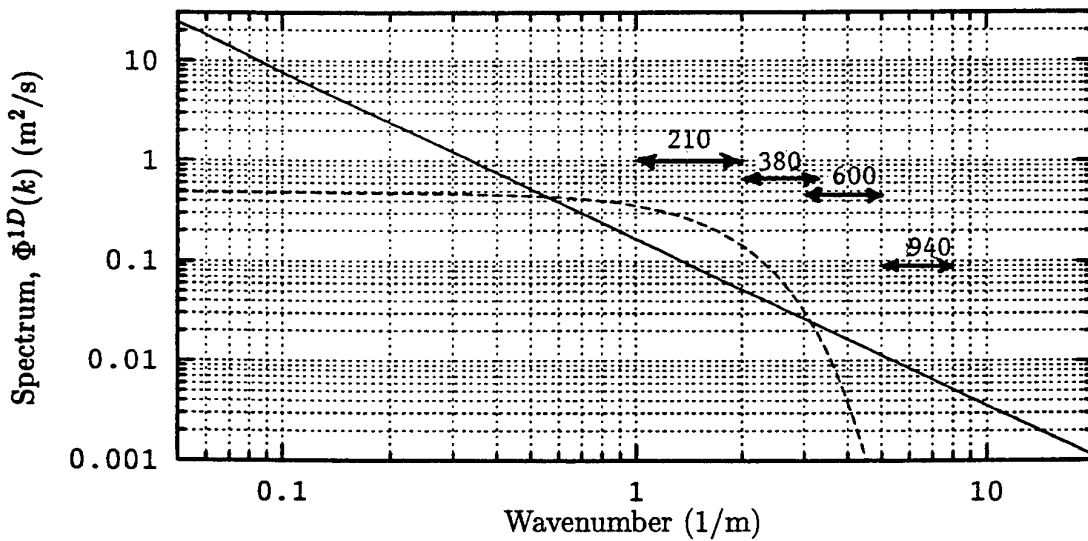


Fig. 5: Regions of k -space that contribute to the shadow zone level at various frequencies (shown by arrows). The solid and dashed curves are for Kolmogorov and Gaussian spectra, respectively. Because the region sampled at a given frequency is relatively narrow, the two spectra predict significantly different shadow zone levels, especially at higher frequencies.

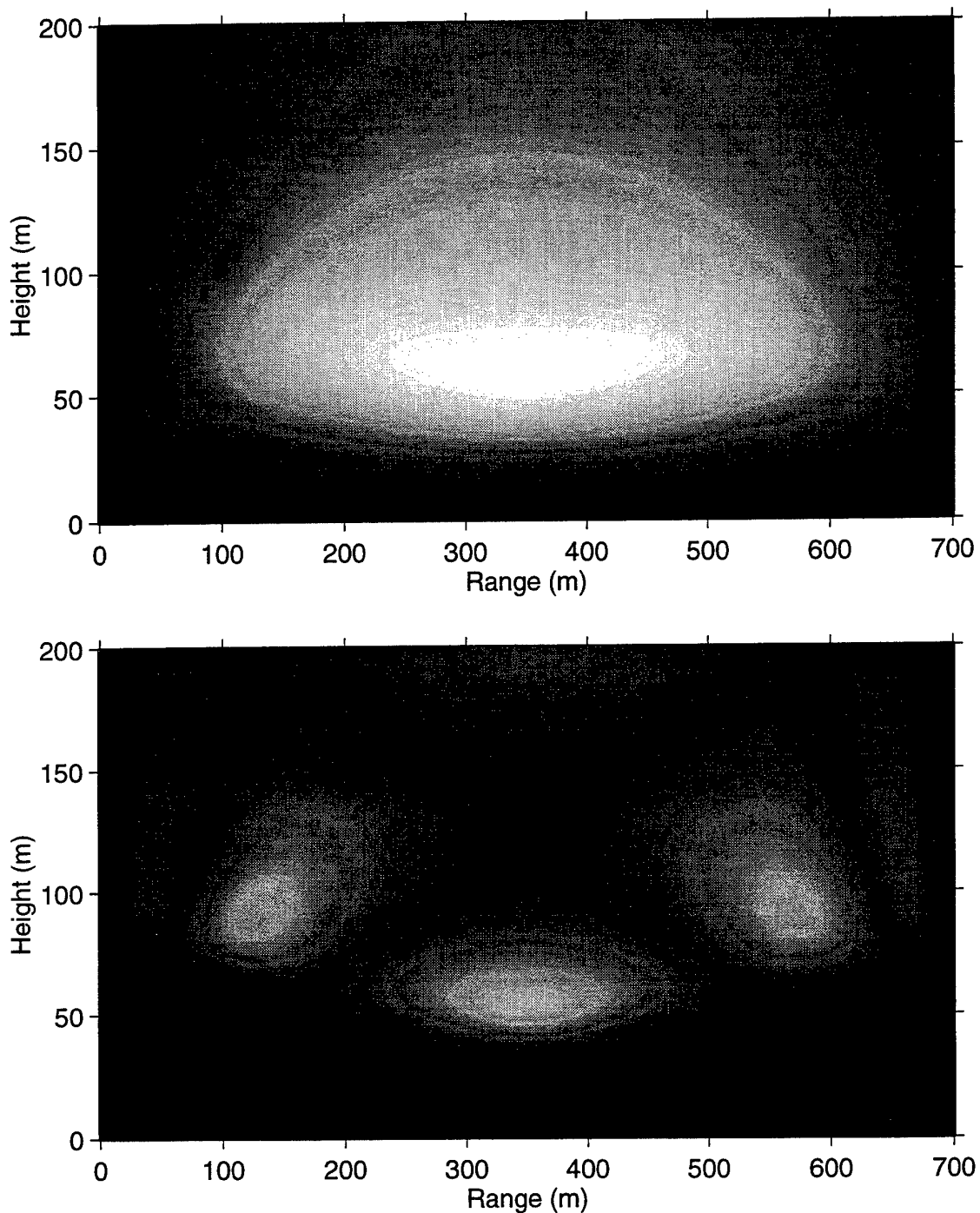


Fig. 6: Magnitude squared of the two-dimensional R -space sampling function $|W_{rs}(x, z)|^2$ at 210 Hz (top) and 940 Hz (bottom), respectively. Due to interference between the source and its ground reflection, the sampling volume depends strongly on frequency. At 210 Hz the interference is constructive, while at 940 Hz, regions of destructive interference are present, and consequently, the effective scattering volume is greatly reduced.

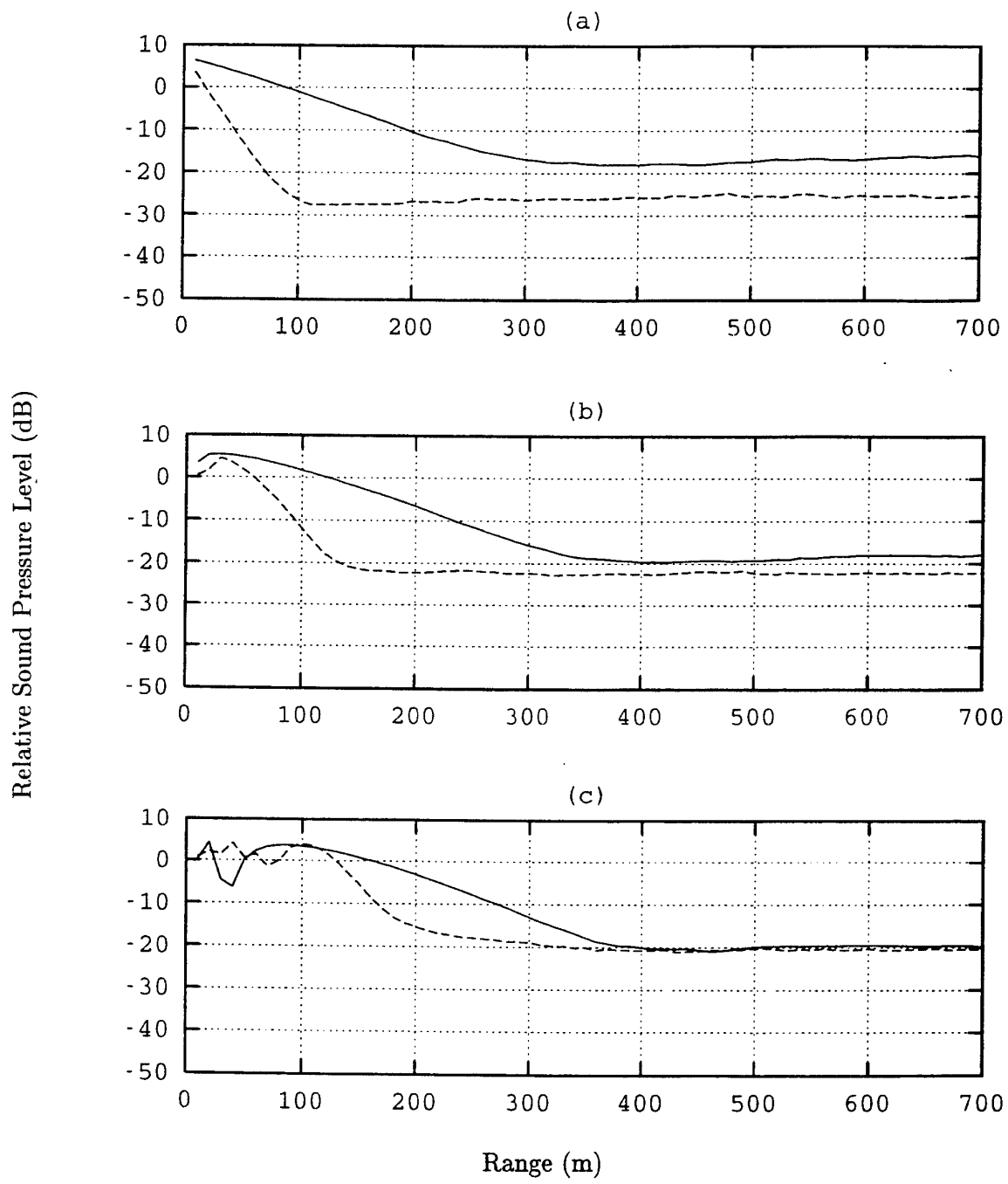


Fig. 7: The effect of source and receiver height on the frequency dependence in a refractive shadow zone. The solid and dashed lines are for frequencies of 210 Hz and 940 Hz, respectively. The cases shown are (a) source height of 0.3 m and receiver heights of 0.1 m, (b) source height of 4 m and receiver heights of 0.1 m, (c) source and receiver heights of 4 m. Each curve is the ensemble average for 200 realizations from a Kolmogorov turbulence model.

Correlation and Coherence Measurements of a Spherical Wave**Travelling in the Atmospheric Boundary Layer**

VOLKER MELLERT, BERNHARD SCHWARZ-RÖHR

*Dept. of Physics, University of Oldenburg**D-26111 Oldenburg**FAX (+49) 441 798 3698***Abstract**

Measurements of the first and second moments of the amplitude of a spherical wave propagating outdoors up to 200 m distance are carried out. Wind- and temperature data are monitored at the same time, the structure constant of wind and outer scale of turbulence are calculated from these. The measured acoustic amplitude fluctuations are evaluated with the parabolic equation method (PEM) assuming a von Karman spectrum of turbulence. The acoustic measurements yield comparable results to the meteorological data, the determination of the scale of turbulence is improved. The acoustic measurements show more consistent and reliable results, being more representative as a spatial average compared to local meteorological time history registrations. In order to evaluate second moment measurements careful monitoring of the number of averages and the grade of coherence is necessary to ensure sufficient precision for successful inversion.

1. Introduction

Based on the parabolic approximation it is possible to calculate the propagation through the turbulent atmosphere of the first and second moment of a plane and spherical wave for a variety of spectral representations of wind and temperatur [1]. One objective of the present study is to test the theoretical predictions for the boundary layer outdoors. The other objective is to provide a new remote measurement tool to determine acoustically turbulence parameters like structure constants C_f^2 , C_v^2 , and outer scale L_0 .

The fluctuating wind- and temperature field changes the amplitude and phase of the propagating acoustic wave. Measuring the time dependent complex amplitude with an arrangement of microphones allows to determine the first and second moment of the amplitude fluctuations, i.e. the time average of the complex amplitude at one location and the correlation between two locations. With the theoretical predictions given in [1] the interesting turbulence parameters are deduced from these measurements and compared with traditionally determined results from time series registrations of wind and temperature.

2. Theory

The statistical properties of wind and temperature are assumed to be homogeneous. Velocity and temperature fluctuate around an average value which is constant in time and space. Both assumptions do not hold for the real atmosphere but are approximately true for a time intervall of some minutes and in the stratified boundary layer over a distance of some hundred meters. Profiles are not investigated. The wave is assumed to propagate through a statistically homogeneous part. The fluctuations of wind and temperature are modeled by a von Kármán spectrum, modifying the infinite cascade of turbulence in the Kolmogorov spectrum by an outer and an inner scale of largest and smallest turbulent

structures. In this investigation, only the large scale L_0 , representing the largest structures of wind and temperature fluctuation within the time interval of measurement is of interest.

The sounding wave is reduced in amplitude due to geometrical spreading and to usual atmospheric absorption but not due to turbulence (provided the wave is not radiated as a narrow beam). The turbulent structures cause phase- and magnitude-fluctuations of the wave and some scattering. The energy of the wave is not reduced but spreaded over a larger volume. The amplitude is regarded as a complex quantity taking magnitude and phase informations into account. Spherical wave propagation is assumed in order to compare theoretical predictions [1] with experimental results, but the theory could deal with other wave geometries as well.

The theoretical description is based on the "parabolic equation method" (PEM) developed by *Klyatskin* and *Tatarskii* in the late sixties. Within the scope of this paper only the results of the theory will be given, a detailed description is found in [2]. Starting from a lossless wave equation isotropic, homogeneous and frozen turbulence is assumed. Two essential approximations enter into the theory. First, one assumes, that the wave propagation can be described in the parabolic approximation. The second approximation is to replace the correlation function of the medium by an effective one with vanishing correlation length in the direction of the propagation path ("Markov approximation"). Introducing Cartesian coordinates $(x, \mathbf{r}) = (x, y, z)$, where the x-axis is directed along the propagation path, the acoustical pressure $p(x, \mathbf{r}, t)$ is written as

$$p(x, \mathbf{r}, t) = A(x, \mathbf{r}) e^{ikx} e^{i\omega t}. \quad (1)$$

Here $A(x, \rho)$ denotes the complex amplitude, k the acoustical wavenumber ω/c_0 . For any set of points in the yz -plane $\mathbf{r}_1 \dots \mathbf{r}_n, \mathbf{r}'_1 \dots \mathbf{r}'_m$ the parabolic equation method leads to closed differential equations for arbitrary statistical moments of the form

$$\langle A(x, \mathbf{r}_1) A(x, \mathbf{r}_2) \dots A^*(x, \mathbf{r}'_1) A^*(x, \mathbf{r}'_2) \dots \rangle.$$

The differential equation for the first moment $\langle A(x, \mathbf{r}) \rangle$ has the formal solution

$$\langle A(x, \mathbf{r}) \rangle = A_0(x, \mathbf{r}) e^{-\gamma x} \quad \gamma = \gamma_T + \gamma_v \quad (2)$$

Here $A_0(x, \mathbf{r})$ is the sound field in absence of turbulence, γ_T and γ_v are the contributions of the turbulent temperature and velocity fluctuations to the extinction coefficient γ . Both contributions are determined by the spatial power spectrum of the turbulence. Assuming von Kármán spectra results in

$$\gamma_T = \mathcal{B} k^2 \frac{C_T^2}{T_0^2} \kappa_0^{-\frac{5}{3}}, \quad \gamma_v = 4 \mathcal{B} k^2 \frac{C_v^2}{c_0^2} \kappa_0^{-\frac{5}{3}}, \quad (3)$$

here $\mathcal{B} = \pi/(12 \Gamma(1/3)) \approx 0.098$, T_0 is the mean value of temperature corresponding to the sound speed c_0 . Note that the extinction of the first moment is independent of the

geometry of the wave. For a spherical source located at the origin the first moment is given explicitly by

$$\langle A(x, \mathbf{r}) \rangle = \frac{1}{4\pi x} e^{-\gamma x}. \quad (4)$$

In contrast the so called mutual coherence function

$$\Gamma(x, \mathbf{r}, \mathbf{r}') := \langle A(x, \mathbf{r}) A^*(x, \mathbf{r}') \rangle \quad (5)$$

depends on the wave geometry. Analytical solutions are known only for special wave types. For spherical waves and von Kármán spectra the mutual coherence function is given by [1]

$$\Gamma(x, \mathbf{r}, \mathbf{r}') = \frac{\exp(ik[\mathbf{r} + \mathbf{r}'][\mathbf{r} - \mathbf{r}]/2x)}{(4\pi x)^2} \Gamma_T(x, \mathbf{r} - \mathbf{r}') \Gamma_v(x, \mathbf{r} - \mathbf{r}'), \quad (6)$$

where $\Gamma_T(x, \mathbf{r} - \mathbf{r}')$ and $\Gamma_v(x, \mathbf{r} - \mathbf{r}')$ are contributions to $\Gamma(x, \mathbf{r}, \mathbf{r}')$ due to temperature and velocity fluctuations, given by

$$\Gamma_T(x, \mathbf{r} - \mathbf{r}') = \exp \left[-2\gamma_T x R_T(\kappa_0[\mathbf{r} - \mathbf{r}']) \right],$$

$$\Gamma_v(x, \mathbf{r} - \mathbf{r}') = \exp \left[-2\gamma_v x R_v(\kappa_0[\mathbf{r} - \mathbf{r}']) \right],$$

Here γ_T and γ_v are the extinction coefficients defined by Eq. (3), $R_T(\kappa_0[\mathbf{r} - \mathbf{r}'])$ and $R_v(\kappa_0[\mathbf{r} - \mathbf{r}'])$ are abbreviations for

$$R_T(\mu) = 1 - \frac{2^{\frac{1}{6}}}{\Gamma(\frac{5}{6})} \frac{1}{\mu} \int_0^\mu d\beta \beta^{\frac{5}{6}} K_{\frac{5}{6}}(\beta) \quad (7)$$

$$R_v(\mu) = 1 - \frac{2^{\frac{1}{6}}}{\Gamma(\frac{5}{6})} \frac{1}{\mu} \int_0^\mu d\beta \beta^{\frac{5}{6}} \left[K_{\frac{5}{6}}(\beta) - \frac{\beta}{2} K_{\frac{1}{6}}(\beta) \right] \quad (8)$$

where $K_{5/6}(\beta)$ and $K_{1/6}(\beta)$ denote modified Bessel-functions, $\Gamma(5/6)$ the Gamma-function.

Measurable quantities are obtained from the moment equations (4), (6) as follows. The acoustical pressure at a microphone located at (x, \mathbf{r}) is given by Eq. (1). Its Fourier transform is obviously

$$\tilde{p}(x, \mathbf{r}, \omega) = A(x, \mathbf{r}) e^{ikx}. \quad (9)$$

Averaging the $\tilde{p}(x, \mathbf{r}, \omega)$ linearly ("signal enhancement mode") allows to determine the first moment of the acoustical amplitudes:

$$\langle \tilde{p}(x, \mathbf{r}, \omega) \rangle = \langle A(x, \mathbf{r}) \rangle e^{ikx}.$$

A similar relationship can be found for the mutual coherence function. Of course two microphones—say at the locations (x, \mathbf{r}) and (x, \mathbf{r}') —are needed. From Eq. (1) the following relationship is readily obtained:

$$\langle \tilde{p}(x, \mathbf{r}, \omega) \tilde{p}^*(x, \mathbf{r}', \omega) \rangle = \langle A(x, \mathbf{r}) A^*(x, \mathbf{r}') \rangle = \Gamma(x, \mathbf{r}, \mathbf{r}'). \quad (10)$$

Therefore, the averaged cross spectrum of the two pressures turns out to be the mutual coherence function. Note that the averaged intensity $S(x, \mathbf{r}) := \Gamma(x, \mathbf{r}, \mathbf{r})$ corresponds to the power spectrum of $\tilde{p}(x, \mathbf{r}, \omega)$.

The parabolic equation method does not account for atmospheric absorption. Furthermore, it is desirable to eliminate source and receiver sensitivities from the measurements. But for homogeneous and isotropic turbulence the averaged intensity is not affected by medium fluctuations. This can be proven within the scope of the parabolic theory by taking the limit $\mu \rightarrow 0$ in Eqs. (7) and (8), leading to $R_T(0) = 0$ and $R_v(0) = 0$. Therefore, the transfer characteristics are normalized with the averaged intensity. The measured quantity for the first moment was chosen to be

$$\frac{|\langle A(x, \mathbf{r}) \rangle|}{\sqrt{\Gamma(x, \mathbf{r}, \mathbf{r})}} = e^{-\gamma_x}, \quad (11)$$

the right hand side of the equation follows immediately from Eq. (4). Using a FFT-signal-analyzer $\langle A(x, \mathbf{r}) \rangle$ can be determined from the time enhanced, the averaged intensity from the power spectra of the received signals. Normalizing the second moment leads to

$$\frac{\Gamma(x, \mathbf{r}, \mathbf{r}')}{\sqrt{\Gamma(x, \mathbf{r}, \mathbf{r})\Gamma(x, \mathbf{r}', \mathbf{r}')}} = \exp\left(ik\frac{[\mathbf{r} + \mathbf{r}'][\mathbf{r} - \mathbf{r}']}2\right) \exp\left(-2x[\gamma_v R_v(\kappa_0\rho) + \gamma_T R_T(\kappa_0\rho)]\right), \quad (12)$$

where the lateral distance $\mathbf{r} - \mathbf{r}'$ is abbreviated by ρ . The complex phase factor $\exp(ik[\mathbf{r} + \mathbf{r}'][\mathbf{r} - \mathbf{r}']/2)$ does not carry any information about the turbulence. Therefore, multiplying Eq. (12) with its complex conjugate leads to

$$\frac{|\Gamma(x, \mathbf{r}, \mathbf{r}')|^2}{\Gamma(x, \mathbf{r}, \mathbf{r})\Gamma(x, \mathbf{r}', \mathbf{r}')} = \exp\left(-4x[\gamma_v R_v(\kappa_0\rho) + \gamma_T R_T(\kappa_0\rho)]\right)$$

Using relationship (10) to express $\Gamma(x, \mathbf{r}, \mathbf{r}')$ by the averaged spectra of the acoustic pressure leads to

$$\frac{|\langle \tilde{p}(x, \mathbf{r}, \omega)\tilde{p}^*(x, \mathbf{r}', \omega) \rangle|^2}{\langle \tilde{p}(x, \mathbf{r})\tilde{p}^*(x, \mathbf{r}) \rangle \langle \tilde{p}(x, \mathbf{r}')\tilde{p}^*(x, \mathbf{r}') \rangle} = \exp\left(-4x[\gamma_v R_v(\kappa_0\rho) + \gamma_T R_T(\kappa_0\rho)]\right) \quad (13)$$

Within the context of signal processing the left hand side of the last equation is defined as the so called "coherence" α^2 . This coherence is directly evaluated by the FFT-analyzer. The normalized first moment (11) and the coherence (13) are used in the data exploitation. These quantities carry all information of the medium fluctuations that is hidden in the moments of the sound amplitude.

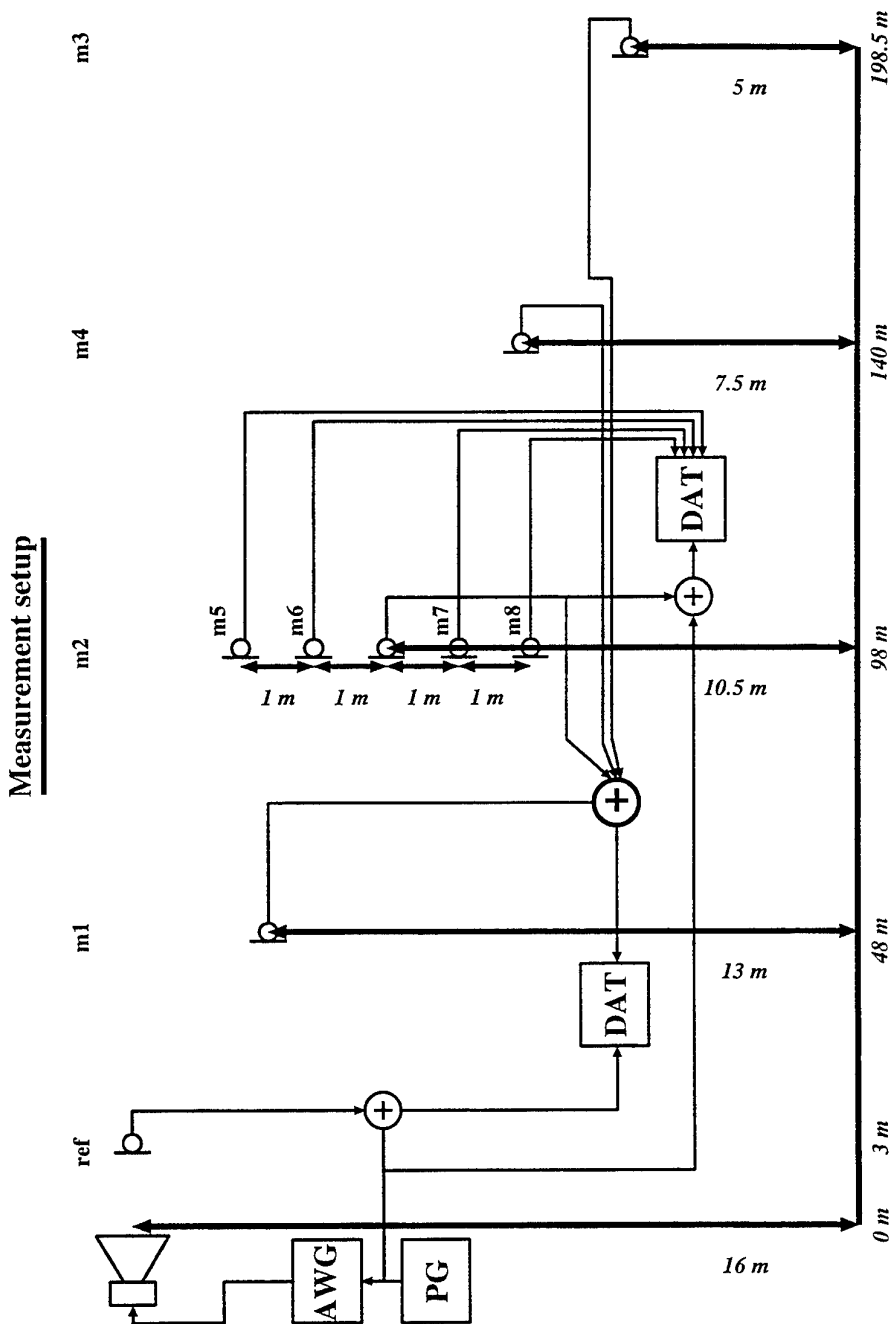


Fig. 1: Sketch of measurement setup. For details see text.

3. Measurement setup

Measurements were made over a flat lawn site surrounded by some medium height trees. Weather conditions were neutral with windspeed below 2.5 m/s, clouded sky and practically no temperature fluctuations. Fig. 1 gives a sketch of the measurement setup. A pulse generator (PG) triggers an arbitrary wave form generator (AWG) driving a wide angle horn loudspeaker (JBL) mounted on a mast at 16 m height. A reference micro-

phone is placed 3 m in front of the speaker. The other microphones pick up the signal at distances 48 m, 98 m, 140 m, and 198.5 m. The height of the microphones m1 to m4 is not kept constant but lowered gradually from 13 m to 5 m, aligned in the line of sight as depicted in Fig. 1. At a distance of 98 m a lateral arrangement of microphones m5 to m8 allows to pick up the spatial correlation of the wave at the given distance. All microphone signals are stored on digital tape recorders (DAT) together with synchronisation signals of the pulse generator. By using sinusoidal pulse-trains of appropriate length and due to the travel time it is possible to record all microphone signals in one DAT-channel without interference in information but with optimized synchronisation in time (signal flow depicted in Fig. 1).

The pulse-train was set up by five sinusoidal pulses with frequencies 650 Hz, 1.08 kHz, 1.8 kHz, 3 kHz, 5 kHz, and 100 ms duration. They were Hanning-switched with a frequency dependent rise- and fall-time from 40 ms to 20 ms. The repetition rate of the pulse-train was about 0.5 Hz. Hence, the statistics of an ensemble of 150 successive individual measurements at each frequency represents a time window of about 5 min.

The meteorological data were monitored in parallel with sensors mounted on the mast with the lateral microphone arrangement. Wind was registered with a three-component ultrasound anemometer and with a hotwire anemometer, which could be used as a fast temperature probe as well. A typical time series of the wind is shown in Fig. 2 over a period of 5 min. The power spectrum of the same sample is given in Fig. 3.

The temperature fluctuations were small during the reported measurement period. They do not considerably contribute to the acoustic amplitude fluctuations and are therefore omitted in this investigation.

4. Test for spherical wave propagation

The height of loudspeaker and microphones in connection with the biradial horn should ensure approximate spherical wave propagation under free field condition with reduced boundary reflections. The acoustic center of the source was calculated from the microphone signals for every distance and averaged. It then has been used to compute the spherical propagation for every frequency. Fig. 4 shows a double-log-plot of the $1/r$ behaviour for the test frequencies with adjusted distance and correction for atmospheric absorption. There is only a slight deviation for the lowest frequency of 650 Hz. Some interference with a ground reflected wave occurs due to unsufficient directivity of the horn speaker. At larger distances the deviation from $1/r$ is about 2 dB. The higher test frequencies show deviations from geometrical spreading below 1 db. Actually, the ground reflected wave could not be suppressed sufficiently. Calculations with a usual porous ground model reveal an interference pattern up to 8 dB. But the test frequencies were chosen not to fall into an interference minimum, which matched quite well except for 650 Hz due to the poor horn directivity characteristic.

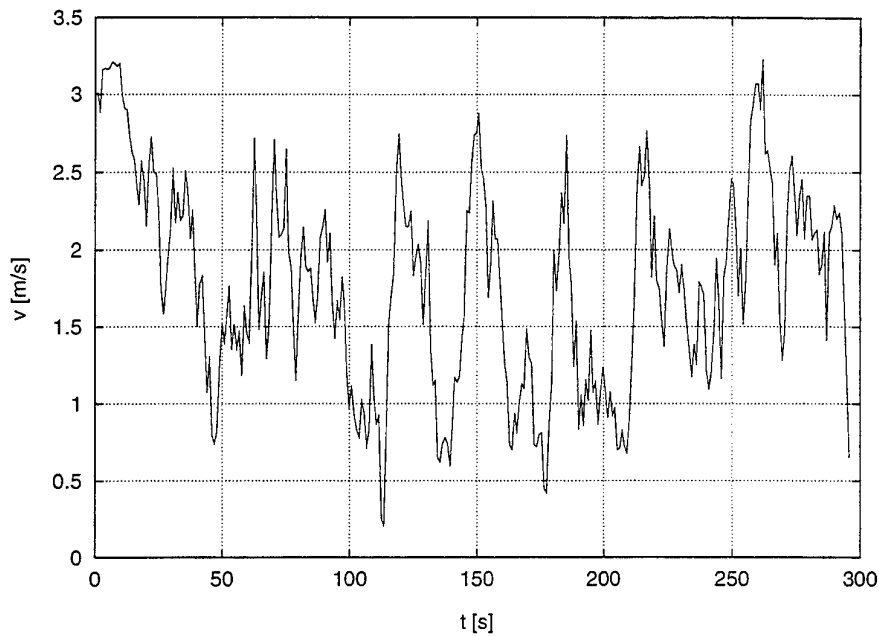


Fig. 2: Typical time series of the wind velocity during a measurement intervall of about 5 min, registrated with an ultrasound anemometer.

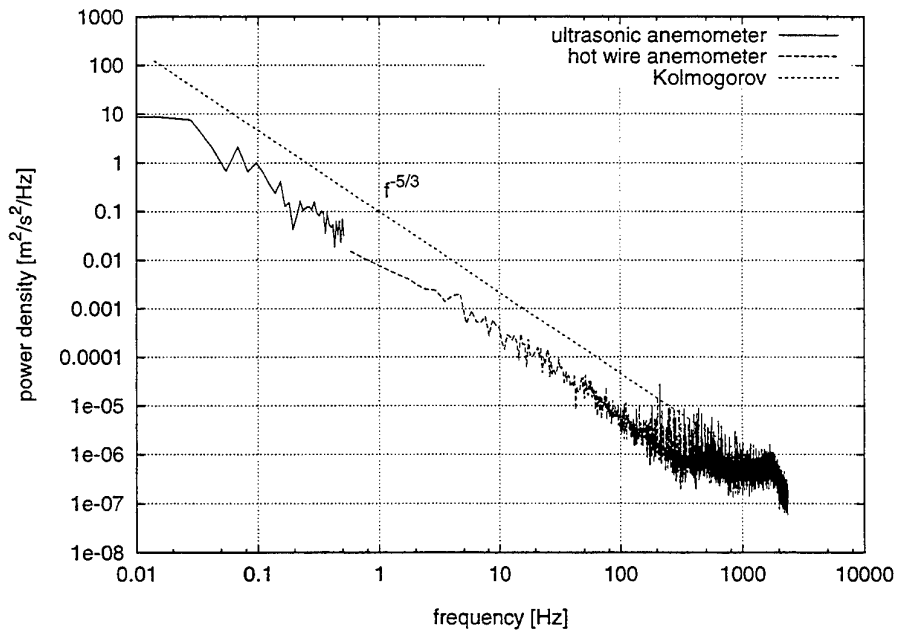


Fig. 3: Onedimensional power spectrum density (PSD) of the time series in Fig. 2, recorded with both, an ultrasound and hot wire anemometer (for rapid fluctuations). Both sensor outputs fit to each other and are well approximated in the inertial subrange by a Kolmogorov spectrum.

5. Extinction

The first moment (Eq. (4)) of the amplitude is proportional to $1/x$ due to spherical wave propagation. Additionally, the complex ensemble average is exponentially lowered due to extinction, i.e. out-of-phase summation of each measured sample. The expected result is depicted in Fig. 5: Instead of an amplitude dependence with $1/x$, the first moment should decrease with distance like the dashed line.

By measuring the power spectrum $S(x) = \langle \tilde{p}(x)\tilde{p}^*(x) \rangle = \langle A(x)A^*(x) \rangle$ at a given distance x and relating it to the spectrum at a reference distance x_{ref} one obtains $D_P = 10 \log S(x)/S(x_{ref})$. Measuring the first moment at both places, e.g. in the enhancement mode of a signal analyser, yields $D_1 = 20 \log \langle A(x) \rangle / \langle A(x_{ref}) \rangle$. Obviously $D_1 - D_p = -20 \log(e)\gamma(x - x_{ref})$.

This relation holds only for a sufficient high number of ensemble averages. Assuming that the samples of the first moment are completely uncorrelated, the average would result in a sum which is by $10 \log N$ smaller than with constant $A(x)$ (N = number of averages). For example, no extinction below 22 dB can be obtained with $N = 150$.

Given x and x_{ref} , γ may be determined from first moment measurements if the registered wave fronts "see" a representative sample of the atmosphere. Fig. 6 shows measurements of $D_1 - D_p$ for 650 Hz and 1.08 kHz. The estimated limit of evaluation according to the number of measurements ($N=150$) is depicted as "noise floor". C_v^2 was adjusted to $0.09 \text{ m}^2/\text{s}^2 \text{ m}^{-2/3}$ and κ_0 to 0.1 m^{-1} according to the best fit of the coherence measurements.

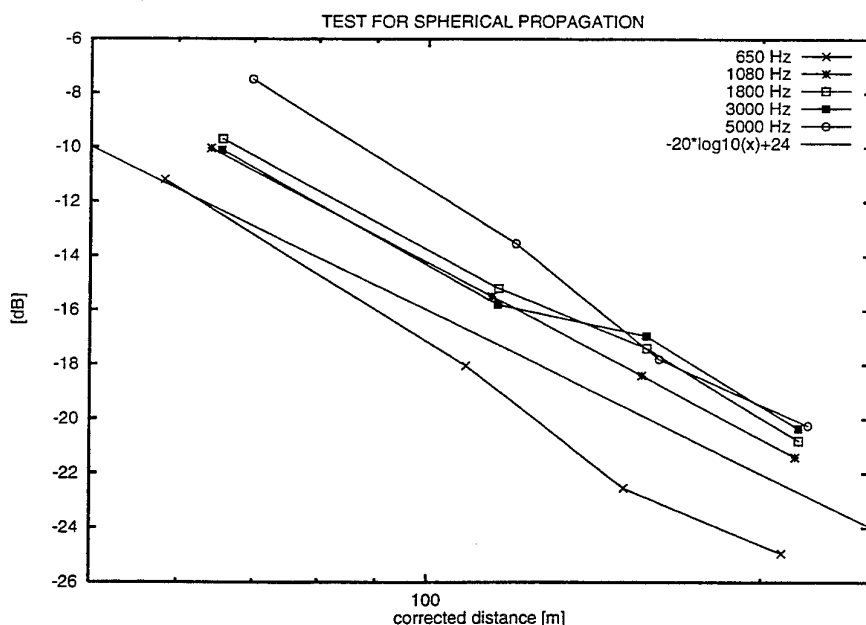


Fig. 4: Spherical wave propagation of the test frequencies: The sound pressure is plotted against a distance-scale, which was adjusted for the acoustic center of each frequency.

Obviously the measured extinction is larger than the predicted one, indicating that the amplitude fluctuations measured at 650 Hz and 1.08 kHz are too large. One reason could be the problem of ground reflection giving rise to increased amplitude fluctuations in unsteady interference minima. The problem of ground reflection should be reduced at higher frequencies, at least up to 150 m distance because of the improved directivity pattern. But the argument does not hold for larger distances because the declined arrangement of microphones in the present setup lowers the distance from ground.

The higher frequencies of 1.8 kHz and 3 kHz show indeed a better accordance to the theoretical expectation as can be seen from Fig. 7, at least up to 150 m distance. Higher frequencies cannot be evaluated because the extinction is below the limit of 22 dB. Surprisingly, the extinction is reduced at 200 m distance for all frequencies, indicating an improved coherence between the individual measurements in the ensemble. One possible explanation for this observation could be given by looking at the ground reflected wave which has a prominent contribution at the location of the farthest microphones. By geometrical reasoning the ground reflected portion of the wave suffers from much less amplitude fluctuations since the turbulence profile tends to zero near ground. Due to the larger angle of radiation the ground reflected wave "sees" a smaller layer of turbulence than the direct wave senses, even at reduced distance. Hence, the extinction at larger distance is even smaller than for the direct wave at less distance.

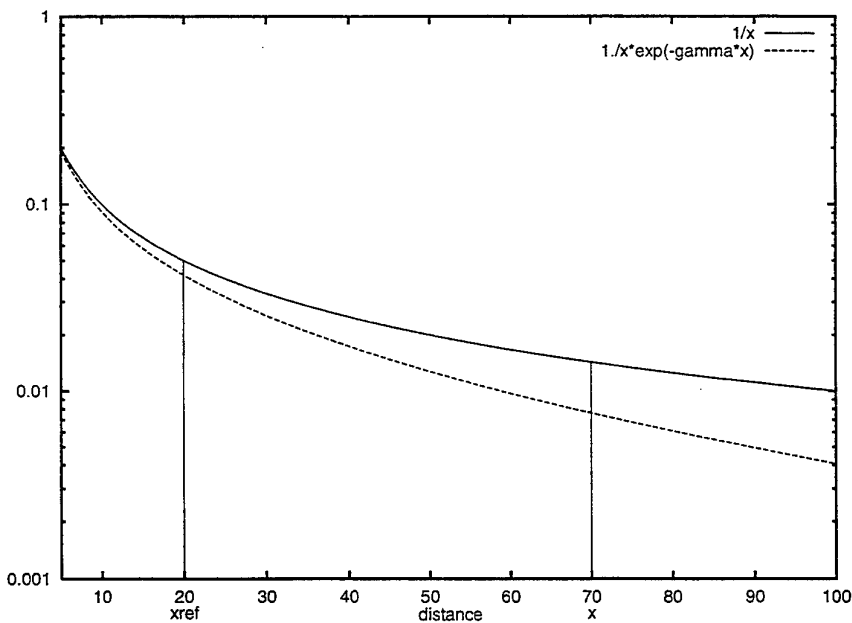


Fig. 5: Extinction of a spherical wave. The first moment is decreasing exponentially compared to the $1/x$ distance dependency.

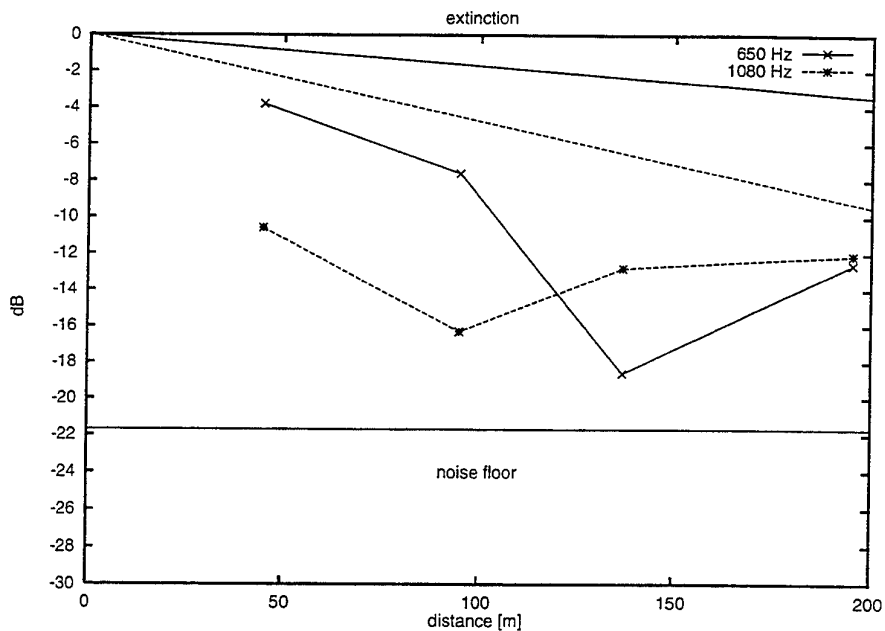


Fig. 6: Extinction measured for 650 Hz and 1.08 kHz. The limit of evaluation is depicted as "noise floor", according to the number of measurements. The estimated curves are adjusted to $C_v^2 = 0.09 \text{ m}^2/\text{s}^2 \text{ m}^{-2/3}$ and $\kappa_0 = .1 \text{ m}^{-1}$ from the coherence measurement.

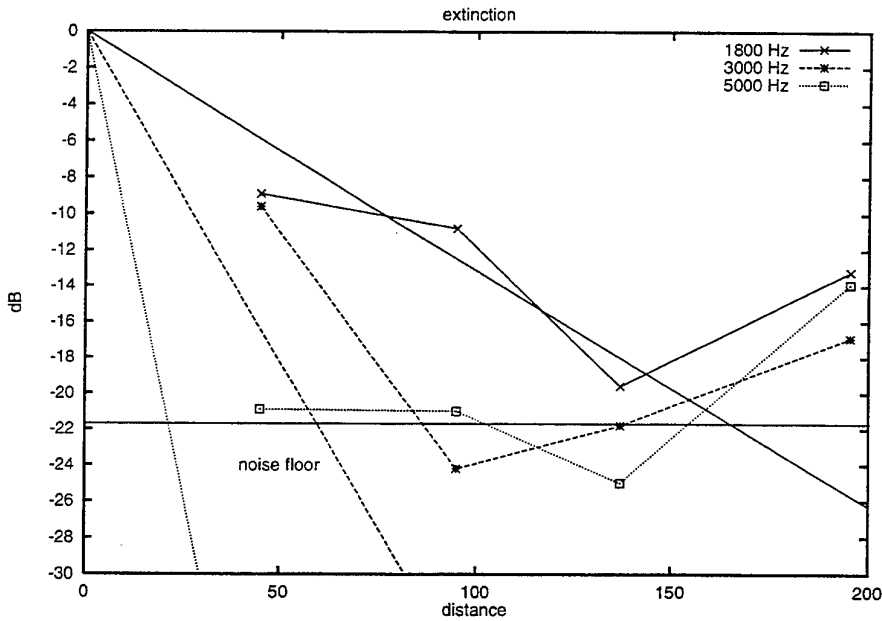


Fig. 7: Extinction measured for 1.8 kHz, 3 kHz and 5 kHz. The limit of evaluation is depicted as "noise floor", according to the number of measurements. The estimated curves are adjusted to the same parameter values given in Fig. 6. The estimated extinction for 5 kHz drops off such rapidly that it is out of range above 20 m.

6. Coherence

Coherence measurements were made with the lateral microphone arrangement at about 100 m distance in 10 m height (Fig. 1). Measurements were related to the microphone at middle location, the other lateral microphones were ± 1 m and ± 2 m apart. (Unfortunately there was a drop out of one microphone, located at -1 m.) The measured coherences are plotted in Fig. 8. The coherence function $\Gamma(x, \mathbf{r}, 0)$ was determined by the FFT-analyser according to Eq. (13). The number of measurements was again 150, the time the same as shown in Fig. 2.

Due to the nonlinear relations between coherence and acoustic frequency (Eq.(13)) it is not obvious that the estimated theoretical curves fit the measurements best. Therefore, the measured values are redrawn normalized to the frequency 1.08 kHz in Fig. 9. It is to emphasize that the estimated values of structure constant and turbulence scale are based only on the microphone signal at ± 1 m and ± 2 m. These are well fitted by the theoretical curve.

7. Determination of parameters

The next step is to calculate the parameters of the von Kármán spectrum from coherence measurements. During the experiments the neutral meteorological condition was characterized by neglible temperature fluctuations, therefore $C_T^2 = 0$ is assumed. Thus the structure constant of the velocity fluctuations C_v^2 and the upper bound of the inertial

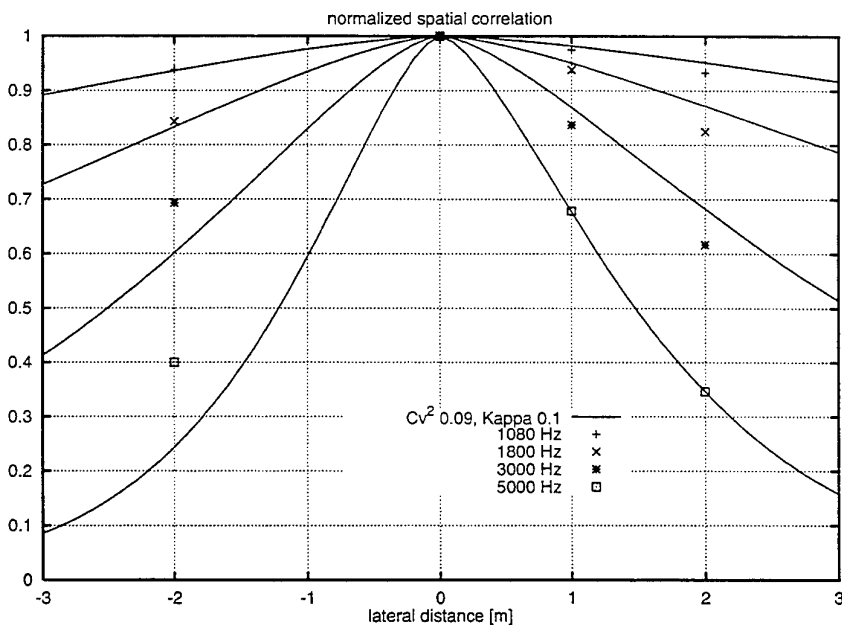


Fig. 8: Measured and estimated coherence at frequencies 1.08 kHz, 1.8 kHz, 3 kHz, and 5 kHz at 100 m distance. The solid lines are theoretical estimations according to Eq. (13) with parameters from a best fit (see Chap. 7).

subrange L_0 –or equivalently $\kappa_0 = 2\pi/L_0$ – remain to be determined. These two parameters are combined in the equation for the coherence (13). In the special case of two microphones at a distance x from the source with a lateral displacement ρ , this equation might be written as

$$\alpha^2(x, \rho) = \exp(-4x \mathcal{B} k^2 \frac{C_v^2}{c_0^2} \kappa_0^{-\frac{5}{3}} R_v(\kappa_0 \rho)). \quad (14)$$

Of course the determination of two parameters requires two measured values or at least three microphones. Denoting the two coherences measured at lateral distances ρ_1 and ρ_2 by α_1^2 and α_2^2 respectively, the following trick allows to separate the parameters. First determine κ_0 by computing the ratio

$$\frac{\ln \alpha_1^2}{\ln \alpha_2^2} = \frac{R_v(\kappa_0 \rho_1)}{R_v(\kappa_0 \rho_2)}.$$

According to the conditions of the experiment ($\rho_1 = 1 \text{ m}$, $\rho_2 = 2 \text{ m}$), the ratio $R_v(\mu)/R_v(2\mu)$ is plotted in Fig. (10). Furthermore, the ratios of $\ln \alpha_1^2 / \ln \alpha_2^2$ are shown in Fig. (10) for different frequencies. Because the function $R_v(\mu)/R_v(2\mu)$ increases monotonically with $\kappa_0 \rho$, each intersection point provides an estimate of $\kappa_0 \rho_1$. Obviously the measurement at 1800 Hz drops out of range. From the remaining data follows a value of κ_0 in the range of 0.09 m^{-1} to 0.105 m^{-1} . This corresponds to a length L_0 between 60 m and 70 m. With knowledge of κ_0 the structure constant can be calculated for each measured coherence by means of Eq. (14). The results of this computations are listed in Tab. 1.

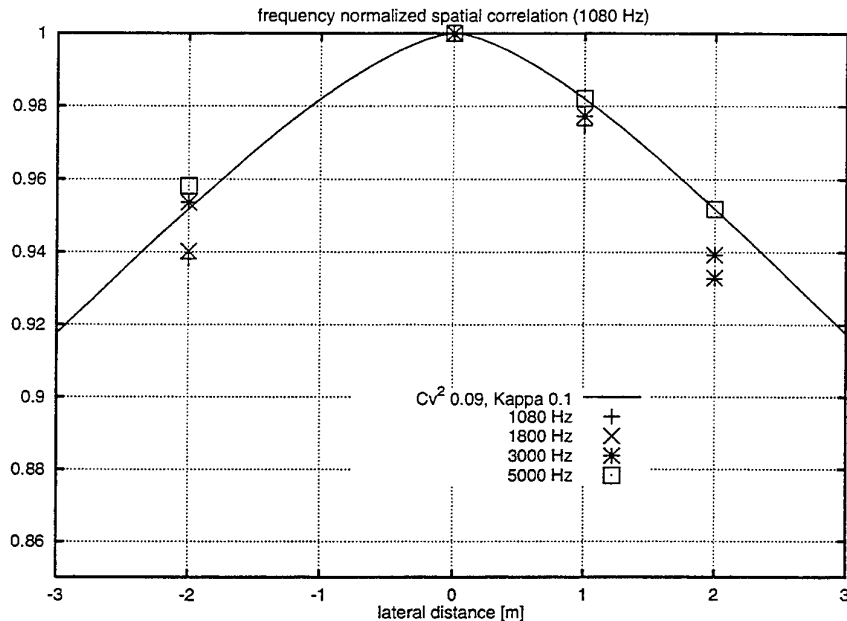


Fig. 9: Coherence measurements of Fig. 8 normalized to 1.08 kHz. The solid line gives the prediction of a best fit to the microphone signals at $+1 \text{ m}$ and $+2 \text{ m}$, according to the inversion procedure in Chap. 7.

The estimated parameters of turbulence from acoustical measurements are now compared with those derived from anemometer spectra. Noting that on the logarithmic scale the density of spectral points is apparently low at small frequencies, no significant bending of the spectral curve is visible at low frequencies. Therefore, only a lower bound of L_0 can be deduced from this curve. According to an averaged wind speed $\bar{v} = 1.78 \text{ m/s}$ an estimate of about 100 m for L_0 seems reasonable. This is at least not in contradiction to the acoustical measurement. A more meaningful agreement is found for the structure constant from anemometer spectra: $C_v^2 = 0.088 \text{ m}^2/\text{sec}^2 \text{ m}^{-2/3}$. Another test for consistency can be deduced from the variance of velocities. For a von Kármán spectrum this variance is given by [1]

$$\bar{v}^2 - \bar{v}^2 = \frac{1}{3} \frac{\sqrt{\pi}}{\Gamma(\frac{5}{6})} C_v^2 \kappa_0^{-\frac{2}{3}}.$$

Inserting $\kappa_0 = 0.1 \text{ m}^{-1}$ and variance determined from anemometer data ($\bar{v}^2 - \bar{v}^2 \approx 0.362 \text{ m}^2/\text{s}^2$) into this equation leads to $C_v^2 = 0.18 \text{ m}^2/\text{s}^2 \text{ m}^{-2/3}$ in not too bad agreement with the acoustical measurement.

Due to the finite number of averages, the coherence α^2 exhibits a statistical uncertainty $\delta\alpha^2$ that shows up in the calculated C_v^2 and κ_0 . For convenience the abbreviation

$$f(\alpha_1^2, \alpha_2^2) := \frac{\ln \alpha_1^2}{\ln \alpha_2^2}$$

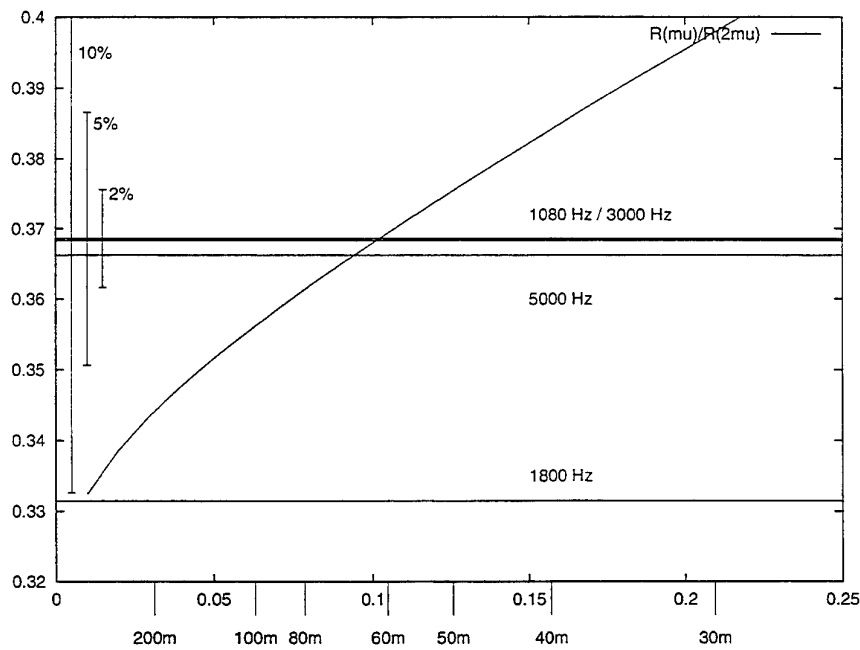


Fig. 10: The function $R(\mu)/R(2\mu)$ and the measured values of $f(\alpha_1^2, \alpha_2^2)$ used for the determination of spectrum parameters in Chap. 7.

is introduced. Up to first order the relative error of f is given by

$$\left(\frac{\delta f(\alpha_1^2, \alpha_2^2)}{f(\alpha_1^2, \alpha_2^2)} \right)^2 = \frac{1}{f^2} \left\{ \left(\frac{\partial f}{\partial \alpha_1^2} \delta \alpha_1^2 \right)^2 + \left(\frac{\partial f}{\partial \alpha_2^2} \delta \alpha_2^2 \right)^2 \right\} = \left(\frac{1}{\ln \alpha_1^2} \frac{\delta \alpha_1^2}{\alpha_1^2} \right)^2 + \left(\frac{1}{\ln \alpha_2^2} \frac{\delta \alpha_2^2}{\alpha_2^2} \right)^2.$$

Thus, f is increasingly sensitive to errors if any of the coherences tends to unity. In the limiting case of for example $\alpha_1^2 = 1$, any variation in α_1^2 causes an infinite change in f . This is a reasonable behavior, as can be seen from Eq. (14). A coherence of unity can arise from several causes: the microphones are close together ($\kappa_0 \rho \approx 0$), κ_0 is very large, or the structure constant vanishes. These three causes cannot be distinguished by this procedure of calculating the turbulence parameters. Rough estimates of the relative error in the f -function that are derived from the standard deviation of the coherences are listed in Tab. 1. Errorbars for 10%, 5%, and 2% error in f are shown in Fig. 10. Obviously the acoustical method of determining the parameters of turbulence calls for carefull geometrical arrangement and sufficient ensemble averaging.

8. Conclusions

Turbulent parameters of the atmosphere can be sounded with an acoustic wave by measuring statistical moments of the amplitude fluctuations. The first moment is very sensitive to disturbances of the wave field by interference. The measurement setup must ensure a free field propagation condition, but the wave geometry is not crucial. The first moment does not resolve the important turbulence parameters κ_0 and C_v^2 but only gives a product of both. The second moment can easiliy be determined by coherence measurements with a lateral arrangement of microphones. From two coherence measurements it is possible to compute κ_0 and C_v^2 . Though the necessity for a precise measurement must be considered depending on the grade of coherence. Neither high nor low coherence yield satisfying estimations for κ_0 and C_v^2 . The acoustic measurement yields parameters for a spatial average determined by wave propagation. This is advantageous compared to the local registration of wind- or temperature time series. Firstly, for the homogeneous atmosphere a representative result is achieved in a shorter time. Secondly, if spatial average in a locally inhomogeneous area is desired, the acoustic measurement substitutes numerous local registrations.

frequency [Hz]	α^2	$\rho=1\text{m}$		$\rho=2\text{m}$	
		C_v^2 [$\text{m}^2/\text{s}^2 \text{m}^{-\frac{2}{3}}$]	α^2	C_v^2 [$\text{m}^2/\text{s}^2 \text{m}^{-\frac{2}{3}}$]	est. $\delta f/f$
1080	.95	0.11	0.87	0.12	40 %
1800	.88	0.10	0.68	0.12	15 %
3000	.70	0.10	0.38	0.10	3 %
5000	.46	0.083	0.12	0.085	2 %

Tab. 1: Measured coherence α^2 and estimated structure constant with error $\delta f/f$ (see text).

The theoretical description used for inverting the acoustic measurements is the PEM. This approach proves to be very useful to obtain analytical expressions for different turbulence spectra. Further investigations must show if a precise determination of the spatial coherence function allows the discrimination of different turbulence spectra, especially for separating wind- from temperature-fluctuations.

Acknowledgements

Members of the working group acoustics in the department of physics supported the experiment by erecting masts and recording signals, in particular the meteorological data were measured and evaluated by R. Matuschek and A. Schomburg, the special waveform was generated by H. Harms.

Literature

- [1] V. E. Ostashev, G. Goedecke, B. Brähler, V. Mellert, H. Auvermann, "Coherence function of plane and spherical waves in the turbulent atmosphere with von Karman spectra of temperature and wind velocity fluctuations.", *Proc. 7th Intern. Symp. on Long Range Sound Propagation*, Lyon, France (1996)
- [2] V. I. Tatarskii, "The effects of the turbulent atmosphere on wave propagation", McGraw-Hill, New York, (1971)